ISSN 2434-9488

KURNS

Progress Report

2024

Institute for Integrated Radiation and Nuclear Science,
Kyoto University

KURNS Progress Report 2024

APRIL 2024 – MARCH 2025

Published by
Institute for Integrated Radiation and Nuclear Science,
Kyoto University,
Kumatori-cho, Sennan-gun, Osaka 590-0494, Japan

Preface for the KURNS Progress Report 2024

It is our pleasure to announce that the KURNS Progress Report 2024 has been published. This report contains all of the accomplishments of research and related activities at the Institute for Integrated Radiation and Nuclear Science, Kyoto University (KURNS) during the fiscal year 2024 (hereafter called as FY2024). A large number of research subjects have been enrolled in FY2024, which covers various fields of nuclear science and technology, materials science, radiation life science and radiation medical science. It means that our institute continues to play a distinctive role as a Joint Usage/Research Center, promoting an extensive range of studies from fundamental to applied research with research reactors and accelerators.

In FY 2024, KUR was operated for 679 hours and KUCA was for 0 hours. Note that here KUCA has zero operating hours due to efforts to move to low enriched uranium fuel and KUR will stop operating in May 2026. In addition to KUR and KUCA, we have conducted joint research at hot laboratories, various accelerator facilities, and so on. In total, we accepted 3024 man-day researchers and students for using research facilities and for attending scientific meetings.

We strive for safe and stable operations for nationwide use, making it our primary mission to provide scientists the opportunity to conduct research and education. We are happy to dedicate our support to enable users conduct significant interdisciplinary research at KURNS.

Kumatori, June 17, 2025
Ken Kurosaki Director,
KURNS

CONTENTS

1. Neutron Scattering

2. *Nuclear Physics and Nuclear Data*

3. *Reactor Physics and Reactor Engineering*

4. *Material Science and Radiation Effects*

5. Geochemistry and Environmental Science

6. Life Science and Medical Science

7. Neutron Capture Therapy

8. Neutron Radiography and Radiation Application

9. TRU and Nuclear Chemistry

10. Health Physics and Waste Management

11. Others

I. ANNUAL SUMMARY OF EXPERIMENTAL RESEARCH ACTIVITIES

I-1. PROJECT RESEARCHES

Project 1

PR1

Preclinical studies for applying BNCT to veterinary medicine

M. Suzuki

Institute for Integrated Radiation and Nuclear Science, Kyoto University

Radiation therapy has been incorporated as one means of treating cancer in companion animals. In university hospitals, state-of-the-art radiotherapy equipment which is used in human radiotherapy has been installed. BNCT for head and neck cancer has been performed as an approved treatment modality at medical institutes. To expand the application of BNCT to the veterinary field, the research project has been conducted with the inclusion of veterinary researchers.

In this research project, six research projects were included. Details of the four projects are referred to each progress report.

P1-1. The Basic Study Aimed at performing the BNCT for Canine Malignant Melanoma

Malignant melanoma is one of the most major cancers in dogs. Melanomas that occur in the canine oral cavity are highly invasive and difficult to surgically resect. In addition, they are known to be refractory tumors that are difficult to treat with conventional radiation therapy. Therefore, new treatment strategies are needed. In this study, the survival after the neutron irradiation using the canine malignant melanoma cell lines.

P1-2. Preparation of anti BSH/HER2 Chimeric Bispecific Antibody and Its Estimation of Binding Ability to BSH and HER2

The aim of this study is to create a chimeric bispecific antibody against BSH and HER2 by linking a humanized anti-HER2 antibody scFv to the Fc region of a previously prepared rabbit-canine chimeric anti-BSH antibody. These chimeric bispecific antibodies are expected to contribute to cancer treatment in dogs

P1-3. Development of carborane loading extracellular vesicles as a boron agent for boron neutron capture therapy.

In this study, extracellular vesicles (EVs) which have the important features such as excellent biocompatibility, low immunogenicity, and targeting properties to specific tissue, are investigated as potentially applicable as platforms for drug delivery systems in BNCT.

P1-4. Meg-BPA IL Delivery via Cerebrospinal Fluid Circulation for BNCT in a Rat Glioma Model

The aim of this study is to establish an optimal administration protocol for Meg-BPA IL via the CSF. Glioma model rats were treated using different CSF-based delivery methods— continuous infusion and bolus injection, varying in BPA concentration—and subsequently subjected to BNCT at the Kyoto University Research Reactor. This approach offers a minimally invasive, effective alternative for boron delivery in BNCT, paving the way for clinical use.

PR1-1

The Basic Study Aimed at perfoeming the BNCT for Canine Malignant Melanoma

S. Yoshihashi, A. Niimi, K. Tsuchimoto, R. Iwasaki[1], A. Uritani, Y. Sakurai[2], M. Suzuki[2]

Graduate School of Science, Kyoto University
[1] Obihiro University of Agriculture and Veterinary Medicine
[2]Institute for Integrated Radiation and Nuclea r Science, Kyoto University

INTRODUCTION: Malignant melanoma is one of the most major cancers in dogs. Melanomas that occur in the canine oral cavity are highly invasive and difficult to surgically resect. In addition, they are known to be refractory tumors that are difficult to treat with conventional radiation therapy. Therefore, new treatment strategies are needed.

BNCT is a therapeutic method that selectively destroys the tumor while leaving normal tissues al-most unharmed by utilizing the nuclear reaction with neutron and boron, which tends to accumulate in the cancer cells. In human malignant melanoma, LAT1, an amino acid transporter of boron com-pound, is shown to be overexpressed in many malignant tumor cells. In this study, the survival after the neutron irradiation using the canine malignant melanoma cell lines.

****

EXPERIMENTS: Two cell lines derived from canine malignant melanoma, primary skin melanoma (CMeC) and metastatic mandibular lymph nodes of oral melanoma cells (LMeC), were used for this study [1]. As boron agent, ^{10}B-p-boronophenylalanine (BPA) was used. Expression of LAT1 has also been found in canine melanoma [2]. CMeC and LMeC were neutron irradiated after incorporating BPA at boron concentrations of 50 ppm and 25 ppm, respectively. Cells after neutron irradiation were cultured for 7 days and cell viability was evaluated using the colony formation assay.

****

RESULTS: Fig. 1 shows the cell viability against neutron fluence of CMeC with and without BPA. This figure shows a clear difference between the cases with and without BPA at neutron fluence above 1 x 10^{12} n/cm^2, indicating that BNCT is effective against CMeC. Fig. 2 shows the cell viability to absorbed dose of CMeC with BNCT and gamma irradiation. This figure shows that BNCT resulted in lower cell viability than gamma irradiation at the same dose. Similar results were obtained for experiment results for LMeC. Furthermore, DNA damage was evaluated by fluorescent immunostaining, which showed more severe damage in BNCT cells than in gamma-irradiated cells.

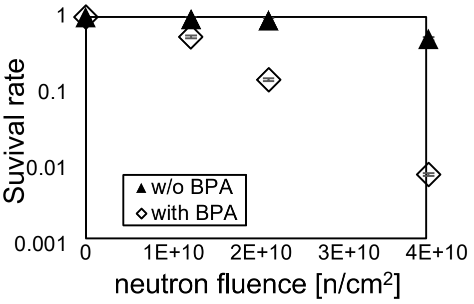

Fig. 1. Comparison of cell survival rate with and without boron for neutron irradiation.

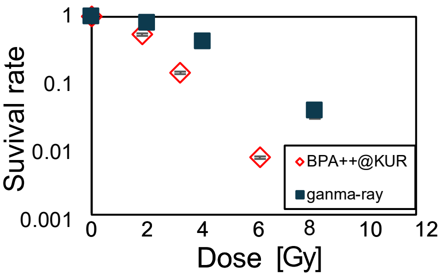

Fig. 2. Comparison of cell survival rate in the case of gamma and neutron irradiation

REFERENCES:

[1] K. Inoue *et al.,* J. Vet. Med. Sci., **66**(11) (2004) 1437-1440.
[2] S. Fukumoto *et al.,* Biochemical and Biophysical Research Communications, 439(1) (2013) 103.

PR1-2

Preparation of anti BSH/HER2 Chimeric Bispecific Antibody and Its Estimation of Binding Ability to BSH and HER2

N. Ueda, T. Kanai, N. Yasukawa, R. Kawasaki[1], Y. Sakurai[2], Y. Sanada[2], N. Kondo[2], M. Suzuki[2], and T. Nagasaki

Graduate School of Engineering, Osaka Metropolitan University
[1] Graduate School of Advanced Science and Engineering, Hiroshima University
[2]Institute for Integrated Radiation and Nuclear Science, Kyoto University

INTRODUCTION: Malignant tumors are the leading cause of death in dogs. Boron Neutron Capture Therapy (BNCT) has attracted attention as a solution to canine cancer. One of the BNCT drugs clinically used is mercaptoundecahydrododecaborate (BSH). Although BSH is a boron cluster with 12 ^{10}B atoms per molecule, resulting in a very high boron atom integration density, It has the disadvantage of no tumor cell selectivity. HER2 has a structure similar to the epidermal growth factor receptor and belongs to the EGFR family. It is a glycoprotein of approximately 185 kDa, and known as a cancer antigen that is highly expressed in various types of cancer, including breast cancer and gastric cancer. It has been revealed that HER2 is also overexpressed in canine cancer cells, and a single-chain humanized anti-HER2 antibody (scFv) with a HER2-binding domain has already been developed. In this study, we aimed to create a chimeric bispecific antibody against BSH and HER2 (Figure 1) by linking a humanized anti-HER2 antibody scFv to the Fc region of a previously prepared rabbit-canine chimeric anti-BSH antibody. By applying chimeric bispecific antibodies, we will try to contribute to cancer treatment in dogs.

EXPERIMENTS: PCR was performed using previously reported rabbit-dog chimeric anti-BSH heavy chain expression vector (pCAGEN chBSH HC) [1] as templates to produce 1st PCR products. Using the 1st PCR product as a template and linker sequence containing primer, 2nd PCR was performed to produce a linker sequence-containing 2nd PCR product. The 2nd PCR product was digested with restriction enzymes Nhe I and Not I and ligated to pCAGEN chBSH HC to afford linker-added chBSH heavy chain expression vector (pCAGEN chBSH HC linker). On the other hand, PCR was performed using gifted human anti-HER2 scFv-Fc expression vector (pCAGEN h4D5 scFv-Fc) as templates to produce 1'st PCR products. The 1'st PCR product was digested with restriction enzymes XhoI and Not I and ligated to pCAGEN chBSH HC linker, which had been previously digested with the same enzymes, to create a rabbit-dog chimeric anti-BSH/HER2 bispecific antibody heavy chain expression vector (pCAGEN chBSH h4D5scFv HC). Using ExpiCHO cells as a host, pCAGEN chBSH h4D5scFv HC and previously prepared light chain expression vectors (pCAGEN chBSH LC) [1] were cotransfected to produce rabbit-dog chimeric anti-BSH/HER2 bispecific antibody (cBhs: chBSH h4D5scFv). To confirm the simultaneous binding ability to BSH and HER2, sandwich ELISA between BSH-modified albumin (BEB) and mouse Fc-fused canine Her2 was performed using HRP-labeled secondary anti-mouse IgG antibody. (Fig. 2).

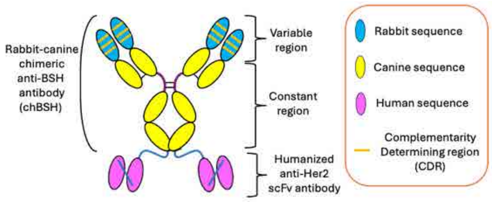

Fig. 1. Format of chimeric anti BSH/HER2 bispesific antibody (cBhs: chBSH h4D5scFv).

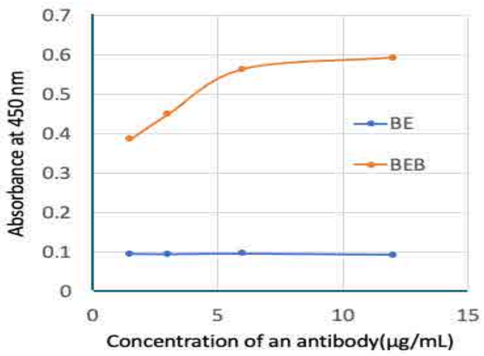

Fig. 2. Evaluation of simultaneous binding ability to BSH and HER2 with cBhs.

RESULTS: The amount of bispecific antibody produced per a liter of culture medium was 15.1 mg. The ELISA results are shown in Fig.2. As the concentration of antibody increased, the absorbance value at 450 nm also increased with immobilized BSH-modified BSA (BEB). Therefore, it was confirmed that cBhs simultaneously binds to BSH and HER2. Evaluation of cBhs as a BNCT boron delivery system is currently progressing by BNCT toward tumor-bearing mice using HER2-expressing cells.

REFERENCES:

[1] N. Ueda *et al.,* KURNS Prog. Rep., (2024) R5P2-2.

PR1-3

Development of carborane loading extracellular vesicles as a boron agent for boron neutron capture therapy

R. Kawasaki,[1] A. Oshige,[1] K. Yamana,[1] Y. Miura,[1] T. Saito,[1] Y. Sanada,[2] Y. Sakurai,[2] H. Tanaka,[2] M. Suzuki,[2] M. Sadakane,[1] Y. Hattori,[3] M. Kirihata,[3] R. Mizuta,[4] Y. Sasaki,[4] K. Akiyoshi,[5] S. Miyaki,[6] T. Nagasaki,[7] and A. Ikeda[1]

[1] *Applied Chemistry Program, Department of Advanced Science and Engineering, Graduate School of Advanced Science and Engineering, Hiroshima University*

[2] *Institute for Integrated Radiation and Nuclear Science, Kyoto University*
[3] *Research center for BNCT, Osaka Metropolitan University*
[4] *Department of Polymer Chemistry, Graduate School of Engineering, Kyoto University*
[5] *Graduate School of Medicine, Kyoto University*
[6] *Department of Orthopedic Surgery, Graduate School of Biomedical and Health Sciences, Hiroshima University*
[7] *Department of Applied Chemistry and Bioengineering, Graduate School of Engineering, Osaka Metropolitan University*

INTRODUCTION: With excellent biocompatibility, low immunogenicity, and targeting properties to specific tissue, extracellular vesicles (EVs) are potentially applicable as platforms for drug delivery systems. EVs can provide nanospace to encapsulate both hydrophilic and hydrophobic pharmaceuticals as well as lipid-based nanoparticles. Today, pre- and post-loading methods are the option in encapsulating drugs toward EVs, which is essential technique to utilize EVs as a delivery platform. Though post-loading technique are attractive due to their excellent efficiencies, the methods require external stimuli such as heating, sonication, and electric fields, which are potentially disrupt EVs structure and defunctionalize EVs. Moreover, in encapsulation of small drugs with high hydrophobicity, usage of organic solvent which can be mixed with water like dimethyl sulfoxide and ethanol are indispensable, which are also potentially harmful to EVs. For these perspectives, we have developed hydrophobic drug loading technique for EVs via exchanging reaction based on supramolecular chemistry strategy without using organic solvents. We employed this system for hydrophobic boron cluster molecule, carborane, and demonstrated the performance of BNCT.

RESULTS AND DISCUSSION: As the model EVs, we isolated EVs from milk via ultracentrifugation and the purified EVs exhibited representative properties found in EVs. Exchanging reaction of carborane from cyclodextrin complex to EVs were tracked by measuring H NMR spectra as the molecular dynamics of carborane changes drastically via exchanging reaction. As a result, the loading of carborane to EVs finished within 15 min and carboranes are highly condensed within lipid membrane, which is advantageous in increasing the efficiencies to achieve boron neutron capture reaction. We further addressed uniformity in loading drugs by single particle analysis using imaging flow cytometry and current method can introduce cargo molecules to EVs with high uniformity and without leaving any EVs empty.

We next investigated the performance of EVs trapping carborane as a boron agent for BNCT, and L-BPA/fructose complex and carborane loading liposomes are employed as control. As a result, EVs systems exhibited the highest BNCT activity against colon carcinoma cell line (Colon26) among these three systems. Moreover, our systems efficiently accumulated in tumor tissue mainly via EPR effect even in tumor bearing mice model which was established by transplantation of Colon26 cells to mice. For their excellent deliverability of boron agent to tumor tissues, thermal neutron irradiation to the mice treated with carborane loading EVs enabled to eliminate cancer cells in tumor tissue, compared to the other systems. For these results, our systems are potentially applicable as a boron agent for BNCT.

REFERENCES:

[1] R. Kawasaki *et al.,* ACS Applied Materials and Interfaces, **16** (2024) 47137-47149.

PR1-4

Meg-BPA IL Delivery via Cerebrospinal Fluid Circulation for BNCT in a Rat Glioma Model

S. Kusaka, M, Shirakawa[1], N.Voulgaris, K. Onishi[2], S. Saito[2], I. Murata, T. Takata[3], M. Suzuki[3]

Graduate School of Engineering, Osaka University
[1] *Neuron Therapy Research Center, Okayama University*
[2] *Graduate School of Medicine, Osaka University*
[3] *Institute for Integrated Radiation and Nuclear Science, Kyoto University*

INTRODUCTION: In our previous study, we demonstrated that boron neutron capture therapy (BNCT) using cerebrospinal fluid (CSF)-based delivery of boronophenylalanine (BPA) achieved comparable therapeutic efficacy to the conventional intravenous (IV) route, despite using less than one-thirtieth of the BPA dose [1]. To further enhance the efficiency of CSF drug delivery, we developed a novel ionic liquid (IL) formulation of BPA using meglumine (Meg-BPA IL), enabling stable delivery at concentrations ranging from 2 to 10 times the standard concentration (1400 ppm). [2]. In the present study, we aimed to establish an optimal administration protocol for Meg-BPA IL via the CSF. Glioma model rats were treated using different CSF-based delivery methods— continuous infusion and bolus injection, varying in BPA concentration—and subsequently subjected to BNCT at the Kyoto University Research Reactor. This approach offers a minimally invasive, effective alternative for boron delivery in BNCT, paving the way for clinical use.

****

EXPERIMENTS: The C6 rat glioma models were supplied for the present experiment 10 days after implantation. Eight rats were divided into three groups. Rats A–C received 4200 ppm continuous infusion, while rats D–F received 8400 ppm continuous infusion. Rats G and H were administered a bolus injection of Meg-BPA IL (4200 ppm) via CSF. All CSF administrations were performed via the cisterna magna. All rats were irradiated for 20 minutes at a 5 MW reactor using a heavy water neutron irradiation facility, with an average fluence of 3.8 × 10^{12} neutrons/cm^2. After the thermal neutron irradiation, all rats were kept under the same conditions for 14 days. MRI was used to evaluate the changes in tumor volume and overall therapeutic effects of BNCT.

****

RESULTS: Rats receiving 8400 ppm Meg-BPA IL via CSF (rats D–F) died within 30 minutes, suggesting potential toxicity related to osmotic stress or high concentration. In contrast, 4200 ppm infusion showed a trend of smaller tumor volume changes post-BNCT compared to bolus injection. (Figs. 1 and 2). Further studies are required to determine statistical significance.

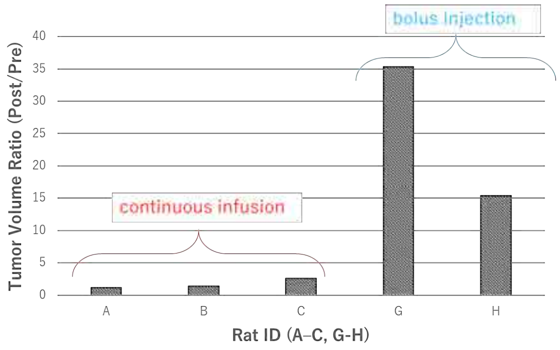

Fig. 1. Relative tumor volume in CSF infusion (A–C)

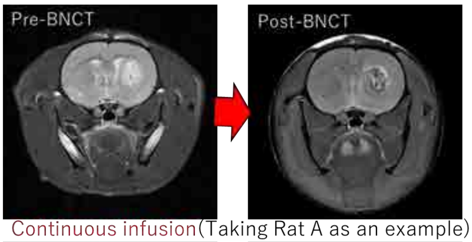

Continuous infusion(Taking Rat A as an example)

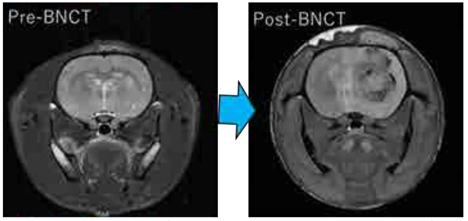

Bolus injection(Taking Rat G as an example)

Fig.2. T2-weighted MRIs pre- and post-BNCT. Top: continuous infusion; Bottom: bolus injection.

REFERENCES:
[1] S. Kusaka *et al.,* Cells, **13**(19) (2024) 1-14.
[2] M. Shirakawa *et al.,* Patent No. 7525095.

I-1. PROJECT RESEARCHES

Project 2

PR2

The effect of BNCT on normal tissues

M. Suzuki

Institute for Integrated Radiation and Nuclear Science, Kyoto University

Clinical trials of BNCT for head and neck cancer began at two medical institutes in 2020 as approved medical treatments. Several clinical trials of BNCT with accelerator BNCT are currently underway for new indications including malignant melanoma, angiosarcoma, malignant brain tumors, and breast cancer. In all clinical trials, the prescribed dose is the dose to normal tissues or organs. In conventional radiotherapy, on the other hand, the prescribed dose is the dose to the malignant tumors, and the dose to normal tissues is used as a dose limit. The reason for this is that real-time measurement of boron concentration in the tumors during irradiation is not realized. Therefore, the dose to critical normal organs in the irradiation field is used as the prescription dose, and the dose to normal tissues is estimated based on the boron concentration in the blood sampled from the patient just before irradiation.

The therapeutic efficacy of BNCT for malignant tumors depends on the accumulation of the boron drug in the tumor or tumor cells at the high boron concentration. Normal tissues, on the other hand, when considering the adverse effects of BNCT on them, those will differ depending on which of the multiple components (parenchymal cells, blood vessels, nonparenchymal cells, etc.) taken up the boron compound selectively. Borocaptate sodium (BSH), which has been used clinically, and boronophenylalanine (BPA), which is currently used in daily practice, have been studied with respect to their local distribution in normal tissues, but not enough research has been conducted. In addition, many new boron agents are currently being developed. To try the new boron drugs in first-in-human clinical studies, the prerequisites is the investigation of the BNCT effects on normal tissues. More BNCT researchers are expected to have interest in the research on BNCT for normal tissues and struggle with this research thema.

In this research project, two research projects were included in this year. One research was not performed. Details of one project are referred to the progress report.

P2-1. Evaluation of the Anticancer Effects and Side Effects of BNCT in a Mouse Model

In previous study, the anti-tumor effect of Boron Neutron Capture Therapy (BNCT) for a mouse model of pelvic recurrence of Colorectal cancer (CRC) was elucidated. In this study, the late ad-verse effect of BNCT on pelvic organs.

PR2-1

Evaluation of the Anticancer Effects and Side Effects of BNCT in a Mouse Model

S. Hagihara[1], J. Arima [1], K. Taniguchi[1,2], Y. Inomata[1], A. Miyamoto[1], M. Suzuki[3],
and Sang-Woong Lee [1]

[1] *Department of General and Gastroenterological Surgery, Osaka Medical and Pharmaceutical College, Osaka, Japan*
[2] *Translational Research Program, Osaka Medical and Pharmaceutical College, Osaka, Japan*
[3] *Department of Particle Radiation Oncology, Research Reactor Institute, Kyoto University, Kumatori, Osaka, Japan.*

INTRODUCTION: Previously, we reported the anti-tumor effect of Boron Neutron Capture Therapy (BNCT) for a mouse model of pelvic recurrence of Colorectal cancer (CRC). On the other hand, we could not fully evaluate side effects in terms of immune response or the later complications, because we examined the effectiveness of BNCT in the nude mouse model only a month after treatment. This study investi-gates early and late effect of pelvic BNCT.

****

EXPERIMENTS: We used Boronophenylalanine (BPA) as a boron compound. Also, we used seven-week-old female BALB/c mouse. Firstly, we established a mouse model of pelvic recurrence of CRC using Colon-26-Luc cells concentrated to 1.0×10^5/100μL in 0.1ml of PBS. We injected BPA intraperitoneally at 3h before irradiation. Animals were divided into three groups; the cold control (no treatment, no neutron irradiation), hot control (neutron irradiation only), and BNCT (intraperitoneal BPA administration and neutron irradiation) groups. Also, we conducted an irradiation experiment using BALB/c mice without tumor implantation to investigate the long-term effects on pelvic organs.

****

RESULTS: Our results are the first to show that BPA-mediated BNCT prolonged the survival of experimental in BALB/c mice with pelvic tumors. (**Fig.1**) There were the significant differences of body weight among three groups after BNCT (**Fig.2**) However, all mice did not have symptoms such as diarrhea and survived for 189 days. Based on the result, BNCT for the pelvis was considered to be safely feasible.

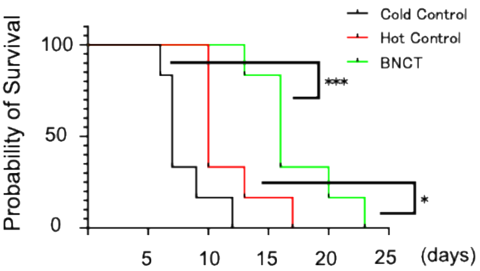

Fig.1 The survival was significantly prolonged in BNCT group.
N=6 in each group. Error bar: means±SD

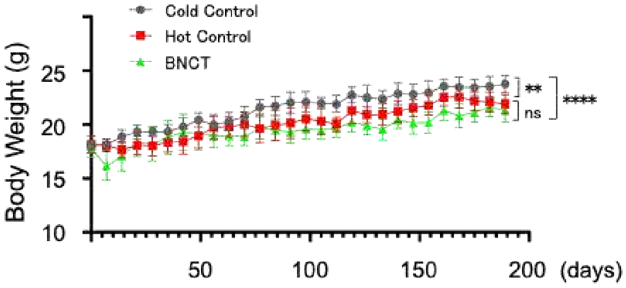

Fig.2 Body weight was reduced in BNCT group.
N=7 in cold group, N=6 in hot control and BNCT group, Error bar: means±SD

****

REFERENCES:

[1] Jun Arima *et al.*, Biomed. Pharmacother. **154** (2022) 113632, (doi) 10.1016/j.biopha.2022.113632.

I-1. PROJECT RESEARCHES

Project 3

PR3

Production of medical RI by reactor irradiation

T. Yamamura, H. Kimura[1], Y. Shimizu[2], K. Washiyama[3], K. Shirasaki[4]

KURNS, Kyoto University [1]Agency for Health, Safety and Environment, Kyoto University [2]Division of Clinical Radiology Service, Kyoto University Hospital [3]Advanced Clinical Research Center, Fukushima Medical University [4]Institute for Radiation Sciences, Osaka University

INTRODUCTION: Neutron irradiation of ^{176}Yb offers Japan the most practical route to a domestic supply of the β-emitter ^{177}Lu for cancer theranostics. Clinical tracers such as ^{177}Lu-DOTA-TATE and ^{177}Lu-PSMA-617 have already demonstrated therapeutic benefit [1, 2]. The 2024 (final) year therefore integrated on-line column separation, temperature-responsive liposomal formulation, and ultrafast radiolabeling of targeted probes into one GMP-oriented workflow.

EXPERIMENTS:

Step	Key conditions	**Purpose**
1. On-line column separation	Extraction-chromatography with real-time γ-monitoring; 1.5 M HNO_3 (300–400 min) elutes Yb, 4 M HNO_3 ($\geq$ 500 min) collects ^{177}Lu	Obtain n.c.a. ^{177}Lu rapidly with low operator dose
2. Thermosensitive liposome (TSL) formulation	Remote loading of [^{177}Lu]Lu-DTPA; labeling eff. > 70 %, purity > 95 %	Create heat-triggered DDS while preserving specific activity
3. Rapid probe radio-labeling	2-min chelation to DOTA derivatives at 50–90 °C; yield 75–86 %	Produce EphA2-targeted probes for pre-clinical testing

RESULTS AND DISCUSSIONS:

On-line Column Separation: A Ge-semiconductor γ-detector integrated into the extraction column enabled real-time monitoring of elution. Yb was completely removed with 1.5 M HNO_3 (300–400 min), while 4 M HNO_3 ($\geq$ 500 min) selectively yielded n.c.a. ^{177}Lu, cutting operator dose and QC time (Fig.1). Bis-2-ethylhexyl-phosphoric acid (HDEHP)-based resins and related extractants remain the work-horse for Lu/Yb separation [3, 4].

Thermosensitive Liposomal Formulation *& Pr*e-clinical Evaluation: Using the high-specific-activity ^{177}Lu fraction from Section 1, remote loading produced TSLs with labeling efficiency > 70 % and purity > 95 %. [^{177}Lu]Lu-DTPA leakage was < 5 % at 37 °C but > 70 % at 43 °C; mild heating in Colon-26 tumor mice improved the tumor-to-blood ratio, validating heat-triggered release. Radiolabeled liposomes have been widely explored for theranostics [5], and the present strategy builds on earlier urine-excretable TSL work [6].

Rapid Probe Radiolabeling *& Theranostic* Development: Purified ^{177}Lu supported **2-min** chelation to DOTA derivatives with 75 % (50 °C), 83 % (70 °C), 86 % (90 °C) yields (Fig.2), enabling assembly of EphA2-targeted probes now entering cytotoxicity and comparative studies versus commercial ^{177}Lu.

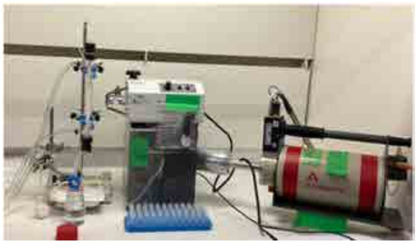

Fig.1. Extraction-chromatography set-up with on-line γ-ray detector for Yb/Lu separation.

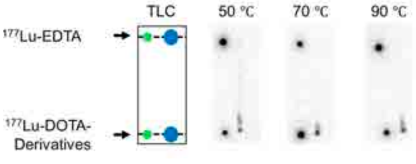

Fig.2 Radio-TLC analysis

REFERENCES:

[1] T. Das et *al*., Applied Rad. Isotopes, **65** (2007) 301.
[2] M. Benesova et *al*., J. Nucl. Med.,**56** (2015) 914.
[3] E. P. Hor-witz et *al*., Applied Rad. Isotopes **63** (2005) 23.
[4] F. F. Knapp Jr. et *al*., J. Radioanal. Nucl. Chem., **263** (2005) 503.
[5] H.-Y. Low et *al*., Molecules **28** (2023) 115-120.
[6] M. Munekane et *al*., Molecular Pharmaceutics **21** (2024) 5728-5735.

PR3-1

Development of tumor-targeted radiotheranostics probes and its clinical application

H. Kimura[1], T. Yamamura[2], K. Shirasaki[3]

[1]Research Center for Experimental Modeling of Human Disease, Kanazawa University
[2]Institute for Integrated Radiation and Nuclear Science, Kyoto University
[3]Institute for Radiation Science, Radioisotope Center, Osaka University

INTRODUCTION: Theranostics is a new medical technology that combines therapeutics and diagnostics. The key to the realization of theranostics is a drug known as theranostic probes. The characteristic of the radiotheranostics probes we are developing is that we consider a single molecule as an aggregate of target recognition units, linker units, and chelating units, and design molecular probes based on the concept of "unit-coupling molecular probes," in which independently developed units are freely combined. This drug design theory is not only effective for designing molecular probes with relatively large molecules such as antibodies and other proteins and bioactive peptides as the nucleus, but also can also be applied to organic small molecular compounds. In this study, we will utilize the theory of creation of unit-coupling molecular probes to develop drugs that can ultimately be applied clinically. First, a basic study of the production of ^{177}Lu in the KUR was conducted. Next, labeling with 1,4,7,10-tetraazacyclododecane-1,4,7,10-tetraacetic acid (DOTA) derivatives was investigated to evaluate whether ^{177}Lu produced at the KUR could be used as a radiopharmaceutical.

EXPERIMENTS: ^{177}Lu Production: To obtain ^{177}Lu, Lu_2O_3 and Yb_2O_3 were irradiated at 1 MW for 24 hours and 5 MW for 6 hours.
^{177}Lu-DOTA Labeling Study: An appropriate amount of 12M hydrochloric acid was added to the separated and purified ^{177}Lu, which was then heated at 100-140°C using a hot plate.$^{177}LuCl_3$ was reacted with DOTA derivatives in 0.1 M MES buffer. The reactions were carried out at different temperatures (50, 70, and 90°C) and reaction times of 2 min. The labeling ratios, defined as the ratios of the spot intensity of labeled material to the total spot intensity, was calculated using radio-TLC and autoradiography.

RESULTS: The HPGe energy calibration was performed using ^{133}Ba. The γ-ray spectrum from the HPGe measurement of ^{177}Lu used is shown in Figure A. The γ-ray spectrum confirms the presence of ^{177}Lu. Radio-TLC analysis in Figure B shows that the radiochemical yields were 75%, 83%, and 86% at 50°C, 70°C, and 90°C, respectively. These results suggest that ^{177}Lu produced at KUR can be used for labeling DOTA. In the future, we plan to evaluate the cell-killing effect of ^{177}Lu produced using cancer cells and compare it with commercially available ^{177}Lu.

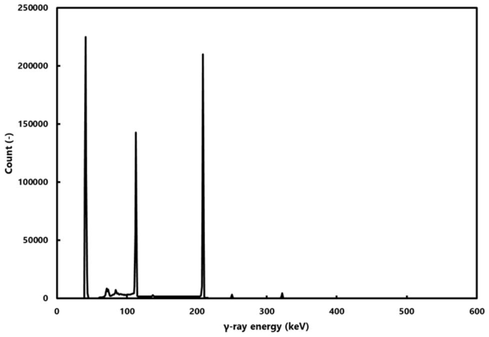

Figure A. HPGe spectrum for ^{177}Lu

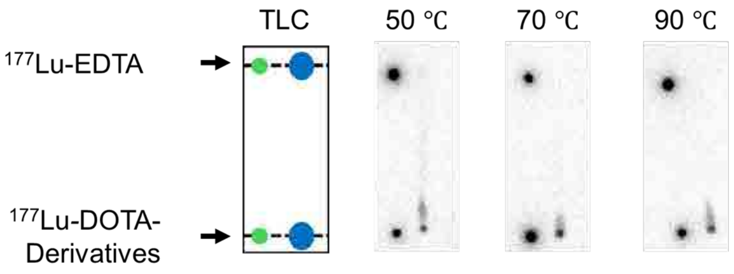

Figure B. Radio-TLC anaylsis

PR3-2

Development of thermosensitive liposomes encapsulating a ^{177}Lu-labeled urinary excretable compound for targeted radionuclide therapy

M. Munekane[1], M. Ozaki[1], K. Sano[2], T. Yamasaki[2], T. Mukai[2], K. Washiyama[3], K. Mishiro[1], T. Fuchigami[1], and K. Ogawa[1]

[1] *Graduate School of Medical Sciences, Kanazawa University*
[2] *Kobe Pharmaceutical University*
[3] *Advanced Clinical Research Center, Fukushima Medical University*

INTRODUCTION: Liposomes are useful drug delivery carriers for cancer treatment, and many radiolabeled liposomes have also been developed for radiotheranostics[1]. However, the high retention of radiolabeled liposomes in the blood results in a high background in diagnostic imaging and the occurrence of side effects such as bone marrow suppression in targeted radionuclide therapy. Then, we have developed thermosensitive liposomes (TSLs) encapsulating radiolabeled compounds that are excreted in urine[2]. The previously reported TSLs released the urinary excretable radiolabeled compounds, In-111-diethylenetriaminepentaacetic acid (^{111}In-DTPA), by heating blood in peripheral tissue of mice, resulting in rapid clearance of blood radioactivity and improved tumor-to-blood ratio. In this study, the TSL-based method was applied to targeted radionuclide therapy with Lu-177 (^{177}Lu) replacing ^{111}In.

EXPERIMENTS: TSLs (1,2-dipalmitoyl-sn-glycero-3-phosphocholine/1,2-distearoyl-sn-glycerol-3-phosphocholine/cholesterol/1,2-distearoyl-sn-glycero-3-phosphoethanolamine-N-[methoxy(polyethylene glycol)-2000] = 60:20:15:5 at molar ratio) were prepared by a thin-film hydration followed by an extrusion method. ^{177}Lu was produced at the Kyoto University Research Reactor, KURR. [^{177}Lu] Lu-DTPA loaded liposomes were prepared by a remote loading method with high labeling efficiency (>70%) and purity (>95%). The release of [^{177}Lu] Lu-DTPA from liposomes was evaluated at 37 and 43°C for 1 h by gel filtration chromatography. Biodistribution of radioactivity was evaluated in Colon-26 tumor-bearing mice at 0.5, 3, 6, and 24 h postinjection. In vivo release experiments were also performed using Colon-26 tumor-bearing mice. Biodistribution of radioactivity was analyzed with or without heating the tails of Colon 26 tumor-bearing mice for 1 h at 2 h postinjection.

RESULTS: [^{177}Lu] Lu-DTPA loaded liposomes released less than 5% and more than 70% of radioactivity at 37 and 43°C, respectively. In the biodistribution experiments using Colon-26 tumor-bearing mice, high blood retention of radioactivity and high accumulation in the spleen and liver were observed. The highest accumulation in the tumor was found at 3 h postinjection. These results were similar to the biodistribution of ^{111}In-labeled thermosensitive liposomes. In vivo release experiments showed the decreased radioactivity in blood for the heated group, resulting in the improved tumor-to-blood ratio. These results suggest that the TSL-based method can be applied to targeted radionuclide therapy with ^{177}Lu.

REFERENCES:

[1] HY. Low *et al.,* Molecules, **28(9)** (2023) 115-120.
[2] M. Munekane *et al.,* Mol. Pharm, **21(11)** (2024) 5728-5735.

R6P3-3

PR3-3

On-line monitoring of ^{177}Lu separation by extraction chromatography

K. Shirasaki and T. Yamamura[1]

Institute for Radiation Science, The University of Osaka
1 Institute for Integrated Radiation and Nuclear Science, Kyoto University

INTRODUCTION: ^{177}Lu (half-life: 6.64 d), produced indirectly by neutron irradiation of ^{176}Yb, is a b-emitter and one of the applicable nuclides for targeted radioisotope therapy (TRT). To date, ^{177}Lu-DOTA-TATE, ^{177}Lu labeled with DOTA-TATE for the treatment of somatosta-tin-overexpress-ing tumors [1], and ^{177}Lu-PSMA-617, ^{177}Lu labeled with PSMA-617 for the treat-ment of castration-resistant prostate cancer [2], have been investigated for TRT use.

In extraction chromatography, bis-2-ethylhexylphosphonric acid (HDEHP) [3] and 2-ethylhexylphosphonic acid (HEH[EHP]) [4] are well known as substrate adsorbed extractants for ^{177}Lu separation, and recently some extractants have explored. In these studies, typically the con-centrations of Yb and Lu in the eluate are determined by radiometric or elemental concentration measurements after collecting a certain volume of solution that has passed through the column. However, some technique that allows for faster analysis is desirable for the best condition survey.

In this study, we developed a real-time monitoring technique for ^{177}Lu and radioactive Yb using the on-line Ge semiconductor detector in the separation of ^{177}Lu from neutron irradiated Yb targets by extraction chromatography.

EXPERIMENTS: The experimental apparatus used in this study consists mainly of a pump, a column with a water jacket and a Ge semiconductor detector. The solution is pumped up and introduced into the column, which is filled with extraction resin (LN2, Eichrom, 50–100 µm). The column temperature is kept constant by a thermostatic water circulation system. The solution that has passed through the column is introduced into a lead shield with a γ-ray detector installed. Then, the solution is collected in a sample vial as it passes through a bundled flow path in the ring shape for γ-ray measurement.

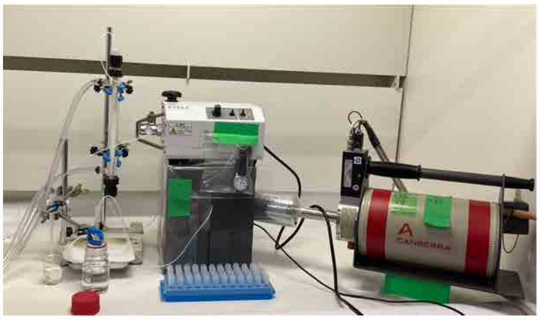

Fig. 1. Experimental apparatus used for the separation of ^{177}Lu and Yb by extraction

RESULTS: During the Lu/Yb separation experiment, the peak energies and their intensities in the γ-ray spectra change with time. Focusing on the γ-ray energy range above 100 keV, high intensities were detected at around 110, 131, 177, 198, 282, 308, and 396 keV for times between 300 and 400 min. These γ-ray peaks are attributed to ^{169}Yb (110, 131, 177, 198, and 308 keV) and ^{175}Yb (114, 282, and 396 keV), respectively. In the region around 510 min, high intensities were detected at 110 keV as well as 208 keV. Especially at the latter γ-ray energy, the intensity was confirmed only in this region. Since these can be attributed to ^{177}Lu (113 keV and 208 keV), it can be assumed that most of the Yb is leached out by passing 1.5 M HNO_3, and the remaining resin residue, composed mainly of Lu, is leached out by 4 M HNO_3 after 500 min.

REFERENCES:

[1] T. Das *et al.,* Applied Radiation and Isotopes, **65** (2007) 301.
[2] M. Benesova *et al.,* J Nucl Med, **56** (2015) 914.
[3] F. F. Knapp Jr. *et al.,* Journal of Radioanalytical and Nuclear Chemistry, **263** (2005)503.
[4] E. P. Horwitz *et al.,* Applied Radiation and Isotopes, **63** (2005) 23.

R6P3-4

I-1. PROJECT RESEARCHES

Project 4

PR4

Chemical and electronic properties of Actinide compounds and their applications

T. Yamamura, Y. Haga[1], M. Abe[2], M. Nakase[3], K. Shirasaki[4], S. Kambe[1], N. Ishikawa[5], T. Suzuki[6], M. Nogami[7], T. Kobayashi[1]

KURNS, Kyoto University, [1] Advanced Science Research Center, JAEA, [2] Graduate School of Advanced Science and Engineering, Hiroshima University, [3] Institute of Integrated Research, Institute of Science Tokyo, [4] Institute for Radiation Sciences, Osaka University, [5] Department of Chemistry, Graduate School of Science, Osaka University, [6] Ngaoka University of Technology, [7] Graduate school of Electronic Eng., Kindai University

INTRODUCTION: The 2024 fiscal year marks the second full cycle of the multi-institutional project aimed at elucidating the chemical and electronic properties of actinide 5f systems and translating them into practical applications in condensed-matter physics, coordination chemistry, separation science, and medical isotopes. The hot laboratories at the Institute for Integrated Radiation and Nuclear Science, Kyoto University, continue to provide the required infrastructure for handling gram-scale quantities of actinide materials. Building on the instrumentation and methodologies commissioned in 2023, the consortium expanded to nine research teams.

RESULTS AND DISCUSSIONS:

I. Metallic Intermetallic Physical Properties 1. Actinide Intermetallic Compounds (Haga, R6P4-1): Single-crystal X-ray diffraction revealed that replacing Ge with Si in $ThRh_6Ge_4$ destabilises the $LiRh_6P_4$-type structure. Weak super-lattice reflections emerge along the c* axis, indicating the onset of lattice softening that precedes a possible charge-density-wave state. 2. Hidden-Order Physics in URu_2Si_2 (Kambe, R6P4-5): Temperature-dependent ^{101}Ru NQR spectra under uniaxial stress $\sigma[100] = 0.23$ GPa showed that the electric-field-gradient symmetry at the Ru site remains four-fold down to 1.5 K, supporting an order parameter that preserves the C4 point group even in the hidden-order phase. 3. Physical Properties of Simulated Fuel Debris (Kobayashi, *R6P4-9):* Sample fabrication was delayed owing to beam-time scheduling at external hot cells. A contingency plan to synthesise three surrogate debris compositions $(U,Zr,Ca)O_{2-x}$ using spark-plasma sintering has been approved for early R7.

II. Theoretical Chemistry 4. Relativistic Multireference Electronic-Structure Theory (Abe, R6P4-2): The newly released X2C–RASPT2 program reproduces the vertical $1\Sigma_u^+ \rightarrow 1\Sigma g^+$ transition of UO_2^{2+} within 0.08 eV of spin–orbit CASPT2 and EOM-CCSD benchmarks. The code enables active spaces up to (24e,24o) with DMRG optimisation.

III. Coordination Chemistry 5. Data-Driven Discovery of Phthalocyanine Extractants (Nakase , P4-3): The AACE workflow clustered 512 synthetically accessible Pc derivatives by Hansen solubility parameters and π-electron descriptors. Twenty-four candidates were prioritised for synthesis, halving experimental overhead compared with the brute-force search in R5. 6. Spectroscopy of U–Porphyrin/Phthalocyanine Complexes (Ishikawa, R6P4-6): Variable-temperature MCD of $U(TPP)Cl_2$ exhibited a sign inversion of the Q-band at 92 K, suggesting thermal population of spin-orbit split $5f^2$ manifolds that couple to the porphyrin π system.

IV. Separation Chemistry 7. U(VI) Adsorption by Silica-Supported DMAA–TPMA Resin (Nogami, R6P4-8): A two-step grafting protocol afforded a hybrid resin whose distribution coefficient K_d(U) exceeds that for Ce^{3+} by an order of magnitude up to 6 M HNO_3. Batch adsorption isotherms followed a Langmuir model with $Q_{max} = 52$ mg-U g^{-1}.

V. Medical-Isotope Separation and Purification 8. Extraction Chemistry of ^{228}Ac with D2EHPA (Shirasaki, R6P4-4): Log–log plots of D_Ac versus $[(D2EHPA)_2]$ yielded a slope of 3.0 ± 0.1, consistent with a tri-dimeric extraction complex. At pH_ini 6.0 the distribution ratio exceeded 10^3, paving the way for one-cycle purification schemes. 9. Separation of ^{228}Ra for ^{225}Ac/^{229}Th Production (Suzuki, R6P4-7): Combining PVPP chromatography with $MgCO_3$ co-precipitation achieved 92 % retention of ^{228}Ra on MgO, while reducing Th carry-over below 0.05 %. The eluate meets radiochemical purity targets for generator fabrication.

PR4-1

Crystal Structure and Characterization of Actinide Intermetallic Compounds

Y. Haga

Advanced Science Research Center, Japan Atomic Energy Agency

INTRODUCTION: Actinide elements and their compounds are known to show unique physical properties. Actinides are often compared with lanthanides where both series of elements are characterized by f-shell electrons. As demonstrated by the complicated crystal structures of some of the actinide metals, unlike those of rare earth metals, the difference of electronic structure between these series might be involved in the crystal structure. Here, we report a comparison of isostructural lanthanide and actinide compounds, ARh_6X_4 (A = actinide or lanthanide, X = Si, Ge) crystallizing in the hexagonal structure, an analog of the heavy fermion ferromagnet $CeRh_6Ge_4$.[1]

EXPERIMENTS: The samples of ternary Th-Rh-Ge and Th-Rh-Si systems were synthesized by arc-melting with the starting composition 1:6:4. The crystal structures were measured by single-crystal X-ray diffraction on a single crystal extracted from the arc-melted ingot.

RESULTS: We confirmed that $ThRh_6Ge_4$ crystallizes in the hexagonal $LiCo_6P_4$-type structure. The cerium analog $CeRh_6Ge_4$ is reported to have the same structure. Because the formal valence electron count for both compounds are the same, electronic structure should also look alike. In fact we have already investigated electronic structure of $ThRh_6Ge_4$ [2] to discuss the correlated electronic behavior in $CeRh_6Ge_4$. However, when Ge is replaced by Si, this structure became unstable. Figure 1 shows the X-ray diffraction data mapped on (0 0 1) plane for $ThRh_6Ge_4$ and “$ThRh_6Si_4$”. In $ThRh_6Ge_4$, the reflections are indexed as hexagonal cell. In the “$ThRh_6Si_4$”, however, the diffraction data is completely different. Although strong reflections marked by large circles approximately maintain the similar hexagonal symmetry, there are weak super reflections. This result directly demonstrates that the structural instability occurs when Si is substituted, most likely caused by the Fermi surface instability. The detailed structural analyses are in progress.

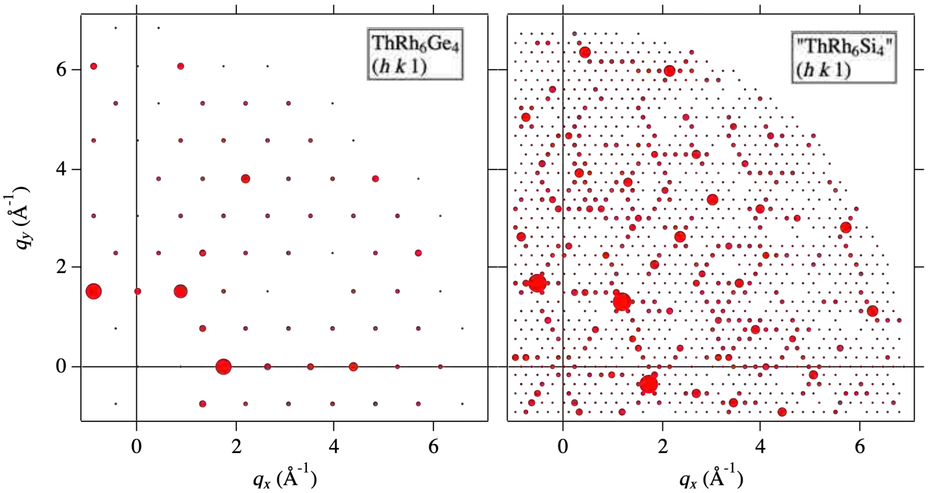

Fig. 1. X-ray diffraction data for $ThRh_6Ge_4$ and “ThRh Si ”.

REFERENCES:

[1] H. Kotegawa *et al.,* J. Phys. Soc. Jpn., **88** (2019) 093702.

[2] Y. Haga *et al.,* International Conference on Strongly Correlated Electron Systems 2023.

PR4-2

Development of relativistic multireference electron correlation methods for actinide compounds

M. Abe,[1] Y. Masuda,[1] S. Toda,[1] T. Yamamura[2]

[1] *Department of Chemistry, Hiroshima University*
[2] *Institute for Integrated Radiation and Nuclear Science, Kyoto University*

INTRODUCTION: Understanding the properties of actinide compounds is crucial for both engineering and academic research. Theoretical calculations, alongside experimental approaches, play a vital role in elucidating their characteristics and facilitating safe verification studies. However, accurately handling relativistic and electron correlation effects is essential for theoretical investigations of actinide compounds. As the atomic number Z increases, the relativistic effect becomes significant, challenging the accuracy of conventional scalar relativistic treatments or perturbative corrections of spin-orbit interactions. Rigorous relativistic effects demand the application of four-component Dirac or exact two-component (X2C) relativistic Hamiltonians. Moreover, because all s, p, d, and f orbitals serve as valence orbitals for actinide atoms, static electron correlation cannot be neglected, limiting the efficacy of conventional single reference methods like density functional theories. Multi-reference electron correlation theory becomes necessary but poses computational challenges due to its complexity. Our group has developed new quantum chemistry programs based on the X2C relativistic Hamiltonian to accurately calculate electronic states and properties of actinide compounds. Specifically, we have created a program for the CASPT2/RASPT2 method, employing multiconfigurational wave functions (CASCI/RASCI) as the 0th-order state of perturbation. CASPT2/RASPT2 is a well-established perturbation theory in the non-relativistic framework [1].

METHODS: The Hartree-Fock and molecular orbital integral transformation with the X2C relativistic Hamiltonian can be executed using the free software DIRAC [2,3]. Consequently, we have developed a CASPT2/RASPT2 program that utilizes molecular orbital information computed by the DIRAC software.

RESULTS: This year, we released our newly developed program as an open-source project on GitHub [4] and reported benchmark calculations of the vertical excitation energies of the UO_2^{2+} ion [5]. Because these excitations require a large active space, we applied the RASPT2 method. Figure 1 compares our results with those from previous studies. Our highest-accuracy protocol—RASPT2(3h,3e) incorporating Improved Virtual Orbitals (IVO)—yields excitation energies very close to EOM-CCSD and SO-CASPT2 benchmarks, whereas four-component TDDFT and IHFSCCSD show larger deviations. These observations indicate that, for the excited states studied here, the choice of electron-correlation treatment has a greater impact on accuracy than the relativistic Hamiltonian.

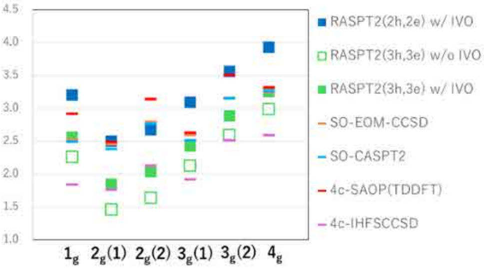

Fig. 1. Vertical excitation energies of UO_2^{2+} molecule

REFERENCES:

[1] K. Anderson *et al.,* J. Phys. Chem., **94** (1990) 5483–5488.
[2] H. J. Aa. Jensen *et al.*,DIRAC, a relativistic ab initio electronic structure program, Release DIRAC22 (2022).
[3] T. Saue *et al.,* J. Chem. Phys. **152** (2020) 204104.
[4] The software is downloadable from https://github.com/RQC-HU/dirac_caspt2
[5] Y. Masuda *et al.*, J. Chem. Theory Comput., **21** (2025) 1249–1258.

PR4-3

Synthesis of novel phthalocyanine derivatives and the effect of substituent on the recognition of light actinide and chemical property-4

M. Nakase[1], F. Ikhwan[1], T. Yamamura[2]

[1]*Institute of Innovative Research, Tokyo Institute of Technology*
[2]*Institute for Integrated Radiation and Nuclear Science, Kyoto University*

INTRODUCTION: Understanding actinide chemistry is crucial in the reprocessing of spent nuclear fuels, Fukushima waste treatment, and medical uses of actinium. My focus is on the Th fuel cycle, which avoids producing heavy actinides like Am and Cm, instead dealing with light actinides such as Th, Pa, and U. This cycle requires separating U from Th and other fission products in spent Th fuels. Recently, we investigated the use of phthalocyanine (Pc) derivatives as extractants for U/Th separation. This year, experiments were not conducted for several reasons; however, the chemoinformatic approach progressed.

INFORMATIC APPROACH: The scheme for exploring the extractant structure is as follows: First, structural data, physicochemical properties (calculated by regression using Hansen Solubility Parameter (HSP) values), and some calculated energy parameters are compiled. The structural fingerprint is created based on the Simplified Molecular Input Line Entry System (SMILES). Clustering methods are used to predict solubility, and the extraction performance is also predicted. All the steps of the approach are compiled in the computational program, Acceleration of Actinide Chemistry Experiment (AACE), which can deploy transfer learning (TL) and human-in-the-loop machine learning (HITL-ML) [1]. The code is written in Python, and modules are combined using Streamlit, which enables the creation of simple user interfaces and facilitates machine learning with reduced coding effort.

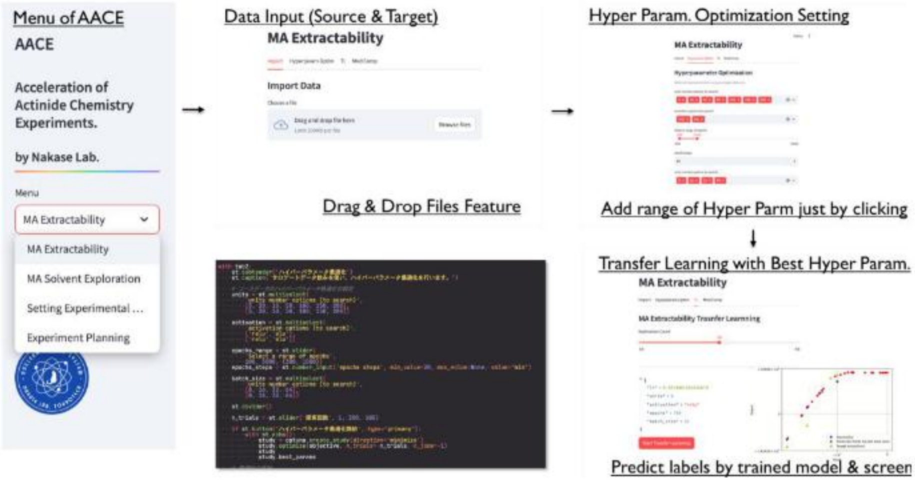

Fig. 1. AACE program developed in 2025 at Nakase-lab [1]

RESULTS: The functionalities and the operation check of the AACE program were completed, and an initial ML attempt was done by using the extracted data obtained for the other research project. To implement machine learning to find suitable Pc-derivatives for reprocessing Th-based fuels, we need more data.

CONCLUSION: The Pc-derivatives suitable for reprocessing in the Th-U fuel cycle were attempted by an informatics approach. The biggest hurdle was the synthesis part, which was difficult to accelerate in the current situation of my laboratory. Therefore, from the next fiscal year, we will focus our research more on informatics, utilizing data from previously published papers and databases, and, where possible, data collected at Kyoto University.

REFERENCES:

[1] M. Nakase *et al.*, EPJ Web of Conf., **317** (2025) 01007.

PR4-4

Evaluation of extraction behavior of ^{228}Ac by D2EHPA under pH range.

K. Shirasaki and T. Miyawaki[1]

Institute for Radiation Science, The University of Osaka
1 Institute for Materials Research, Tohoku University

INTRODUCTION: Actinium is the earliest element in the actinide series, which has 29 isotopes excluding metastable states, and is considered similar to lanthanum in chemical properties. In terms of oxidation state, actinium has only trivalent state like the elements after americium in the actinide series. Most isotopes of actinium are produced by nuclear reactions and have short half-lives of a few seconds to a few minutes. ^{225}Ac, one radioisotope of actinium, is used in targeted alpha therapy and has been reported to be highly effective to the cancer therapy, especially for prostate cancer [1]. ^{225}Ac is very therapeutic because it undergoes four alpha decays before becoming stable ^{209}Bi and does not pass through a noble gas. However, the resources of actinium isotopes, not only ^{225}Ac but also ^{227}Ac are quite rare and expensive. ^{228}Ac, one of the thorium series, reaches radiolytic equilibrium with the parent nuclide ^{228}Ra in about 30 hours. Therefore, once separated, the same amount of ^{228}Ac can be collected again [2]. ^{228}Ac emits photons over a wide energy range and its emission rate is very high among isotopes. With these properties, ^{228}Ac is expected to facilitate basic research on actinium, such as chelate chemistry, which is also required for labeling.

In this study, the extraction behavior of ^{228}Ac and La by D2EHPA in the pH range is evaluated using shaking time, extractant concentration dependence, and pH as indicators for study basic coordination chemistry of actinium.

EXPERIMENTS: Here, the buffer ADA is used as the aqueous phase, and n-dodecane (nDD), one of hydrocarbonate solvents with properties such as nonflammability, chemical stability and low viscosity, were used as the organic phase. Initially, ^{228}Ac was dissolved in the aqueous phase. Under the pH condition, ^{228}Ac in the aqueous phase was extracted into the organic phase by chelation between actinium and the D2EHPA compound. Here, the distribution ratio was used as an index to evaluate how much ^{228}Ac in the aqueous phase was extracted into the organic phase.

RESULTS: The distribution ratio of ^{228}Ac (D_{Ac}) increased with increasing extractant concentration (Fig. 1). The slope obtained from the fit in the range $-0.2<\Delta pH<0$ was 3.38 ± 0.2 at pH_{ini} 6.0. Based on the extraction data, we can compare the extractant distribution ratios of other compounds to determine the effect of side chains, and to devise and demonstrate extractants and buffers that are compatible with Ac. For more investigations, such as the extraction behavior of actinium and extraction data for heavy actinide elements, which have the same trivalent stable state as Ac and Am, are needed to clearly demonstrate the similarity between actinide and lanthanide series elements.

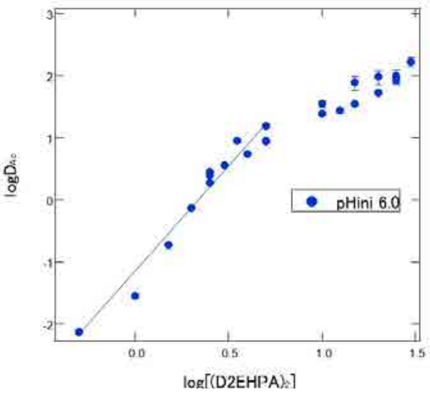

Fig. 1. Dependence of log $D_{Ac.}$ vs. $\log[(D2EHPA)_2]$

REFERENCES:

[1] C. Kratochwil *et al.,* J Nucl Med. **57(12)** (2016) 1941-1944.
[2] K.E. Aldrich *et al.,* In-organic Chemistry, **59(5)** (2020) 3200-3206.

PR4-5

Study of Heavy Fermion Superconductor URu_2Si_2 ^{101}Ru-NQR study II

S. Kambe, Y. Haga, H. Sakai, T. Ishitobi, Y. Tokunaga, H. Matsumura[1], S. Kitagawa[1], K. Ishida[1] and T. Yamamura[2]

Advanced Science Research Center, Japan Atomic Energy Agency
[1]Department of Physics, Kyoto University
[2]Institute for Integrated Radiation and Nuclear Science, Kyoto University

INTRODUCTION: Understanding of ”Hidden ordering” in URu_2Si_2 is fairly progressed recently [1], whereas the definitive answer is still missing. This issue is very exciting since the hidden ordering is supposed to be new spontaneous symmetry breaking. Considering the recent experimental results, a few possible space groups of hidden order symmetry have been selected previously [2,3]. If the hidden order symmetry is once determined, the corresponding multipolar order parameter is spontaneously determined.

* * *

EXPERIMENTS: In this study, the local symmetry of Ru site is determined in the hidden order state without uni-axial stress and with uni-axial stress along the [100] and [110] directions [4], by means of precise Ru-NQR measurements. These measurements again support the 4-fold symmetry at Ru site in the hidden order state without uni-axial stress. Furthermore, certain cases can be excluded from the previously proposed possible ones. In this year, the Ru-NQR measurements under uni-axial stress [100] direction are performed.

* * *

RESULTS: Fig. 1 shows the T-dependence of ^{101}Ru NQR frequency at zero field under uni-axial stress σ along [100] direction of 0.23GPa. As ^{101}Ru is I=5/2 nuclei, there are two NQR peaks are observed i.e. ν_{1Q} ($I = \pm 3/2 \Leftrightarrow I = \pm 1/2$) and ν_{2Q} ($I = 5/2 \Leftrightarrow I = \pm 3/2$). In the present case, the ν_{1Q} results are presented. Compared to the σ=0 case, T-dependence is small in the case under [100] stress. This may be natural since ν_{1Q} is related to the thermal expansion constant which is small in the c-plane due to σ[100].

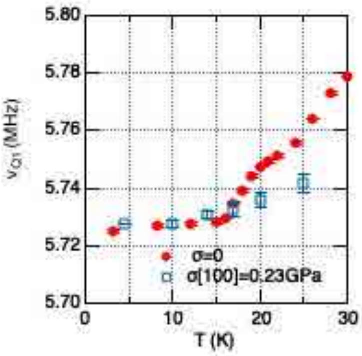

Fig. 1. T-dependence of ^{101}Ru NQR frequency at zero field under uni-axial stress σ[100]= 0.23GPa.

* * *

REFERENCES:

[1] J. Mydosh *et al.,* J. Phys.:Condens. Matter, **32** (2020) 143002.
[2] S. Kambe *et al.,* Phys. Rev. B, **97** (2018) 235142.
[3] S. Kambe *et al.,* JPS Conf. Proc., **30** (2020) 011035.
[4] See experimental methods: K. Karube *et al.,* J. Phys. Soc. Jpn., **83** (2014) 084706.

PR4-6

Exploration of new interactions between actinide 5f electron systems and photo-excited organic π-electron systems

N. Ishikawa, Ryosuke Amakatsu

Department of Chemistry, Graduate School of Science, Osaka University

INTRODUCTION: Metal complexes of actinide as well as those of lanthanide have high magnetic anisotropy due to the orbital angular momentum component in the total angular momentum of the f-electronic systems. In contrast to 4f electrons, 5f electrons are characterized by a large covalency involved in chemical bonding.

Another type of electronic angular momentum is known to be generated on a cyclic π -conjugated system of macrocyclic ligands, such as phthalocyanines (Pc) or porphyrins, by photo-excitation into degenerate π-π* excited states.

Previously, our group revealed the existence of a magnetic interaction between these two angular momenta (J-L interaction) in rare-earth Pc complexes by temperature- and magnetic-field-dependent magnetic circular dichroism (HT-VH-MCD) spectroscopy [1][2]. This interaction has been observed in sandwich-type bilayer complexes Pc_2Ln (Ln=Tb, Dy) and monolayer complexes PcLn(cyclen). Similar interaction was confirmed in the sandwich bilayer complex Pc_2Ln and the monolayer complex PcLn(cyclen).[3][4]

So far, we have conducted measurements of VT-VH-MCD in the visible energy region for the monolayer Pc complex of U(IV), $PcU(acac)_2$ (acac=acetylacetonate), as well as the bilayer complex Pc_2U to investigate magnetic interaction between the $(5f)^2$ system and the ligand π-conjugate system in a photo excited state.

This year, we conducted preliminary experiments for the synthesis of a new type of Pc-uranium complex having a different ligand, namely, $U(TPP)(acac)_2$ (TPP=tetraphenylporpyrinate).

EXPERIMENTS: The precursor $U(TPP)Cl_2$ was synthesized through the reaction of the metal-free $TPPH_2$ and UCl_4. The obtained $U(TPP)Cl_2$ and Na(acac) were placed in a flask in a glove box and THF was added. The mixture was then heated outside the glove box in a sealed condition using an oil bath. At the present stage, the target compound U(TPP)(acac)2 has not been identified. We have therefore conducted the VT-VH-MCD measurement of the precursor $U(TPP)Cl_2$ in a PMMA film.

RESULTS: Typical Soret band and Q band of metal porpyrins were observed in the visible region. Both bands exhibited temperature-dependent changes, but with completely opposite tendencies. The Soret band displayed a negative A-term pattern, with the MCD intensity increased as the temperature decreased. In contrast, the Q band exhibited a positive A-term pattern at 100 K, which gradually changed to a negative A-term pattern as the temperature decreased.

REFERENCES:

[1] K. Kizaki *et al.,* Chem. Commun., **53** (2017) 6168-6171.
[2] T. Fukuda *et al.,* Chemistry A European Journal, **23(64)** (2017) 16357-16363.
[3] K. Kizaki *et al.,* Inorg. Chem., **60(3)** (2021) 2037-2044.
[4] K. Kizaki *et al.,* Inorg. Chem. Front., **10** (2023) 915-925.

Fundamental Study on Extraction/Separation of Actinides and Their Decay Products for Medical Nuclide Production

T. Suzuki[1], F. Yin[1], S. Fukutani[2], M. Harigai[2], and T. Yamamura[2]

[1]Department of Nuclear System Safety Engineering, Nagaoka University of Technology
[2]Institute for Integrated Radiation and Nuclear Science, Kyoto University

INTRODUCTION: Many amounts of decay products are generated from uranium and/or thorium chemicals which are stored in long term. If these decay products are extracted and/or transmuted, we can obtain the several kinds of nuclides and can apply them to many fields such as medicine. While, concern of nuclear therapy using α-nuclides recently increases. Especially, ^{225}Ac is one of the most concerning α-nuclides. However, since ^{225}Ac don't exist in nature, it must be generated artificially. We have proposed ^{229}Th/^{225}Ac generator, ^{229}Th is generated by ^{228}Ra(n,γ) reaction. Our plain of obtaining ^{228}Ra is recovery of decay products from Th. We have plan to use the residue of rare earth ore and/or long storage ThO_2. For obtaining this type generator, development of the dissolution method of thorium compounds, extraction of ^{228}Ra from thorium and other decay products, manufacturing of stable target, irradiation of neutron, and separation of ^{229}Th, etc. are required. In this fiscal year, we investigated the separation of ^{228}Ra from ^{229}Th by polyvinylpolypyrrolidone (PVPP), the coprecipitation of ^{228}Ra separated by PVPP with $MgCO_3$, and the chemical conversion of $MgCO_3$ with Ra to MgO with Ra.

EXPERIMENTS: Th solutions dissolved by thermochemical conversion method using CBr4 were used. The separation experiment of Ra from Th was carried out using a column packed with 1.12 g of PVPP. This column height was approximately 5 cm. The solution with the isolated Ra was neutralized by $NaCO_3$. Then, 8mL of 1M $NaCO_3$ solution and 2mLof 1M $MgCl_2$ solution were added in the Ra solution. The obtained $MgCO_3$ precipitation was filtered. $MgCO_3$ was converted to MgO by heating at 400°C for 0.5h. The transfer rate of Ra from solution to precipitation and the retention rate of Ra from carbonate to oxide were evaluated. The radioactivity of ^{228}Ra was determined by γ-ray measurement of radio equilibrium ^{228}Ac, which is daughter of ^{228}Ra.

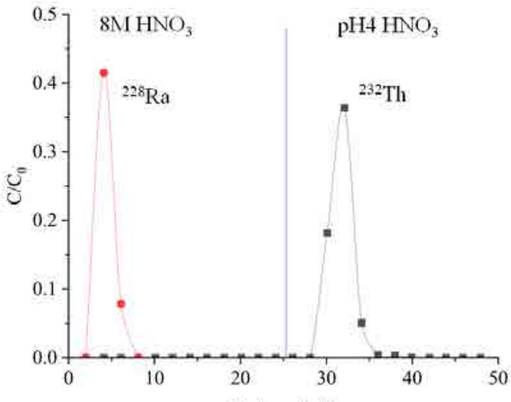

Fig. 1. Separation result of Ra from Th by PVPP.

RESULTS: Separation result of Ra from Th by PVPP was shown in Fig. 1. We can see the complete separation of Ra from Th. The transfer rate of Ra from solution to precipitation and the retention rate of Ra from $MgCO_3$ to MgO are shown in Table.1 From this table, we confirmed that almost all Ra is transfer from solution to precipitation by $MgCO_3$ precipitation method, and almost all Ra is remained in MgO after conversion from $MgCO_3$ to MgO.

Table 1. Transfer rate of Ra from solution to precipitation, and retention rate of Ra in MgO

Radioactivity of Ra in solution (Bq)	Radioactivity of Ra in $MgCO_3$ (Bq)	%transfer of Ra from solution to $MgCO_3$	Radioactivity f Ra in MgO (Bq)	%retention of Ra in MgO
5.56±0.77	5.28±0.57	95.0±16.7	4.87±0.58	92.2±14.8

PR4-8

Synthesis and Adsorptivity of Novel Bifunctional Monoamide- Diamide Resin for Selective Separation of Actinyl Ions

M. Nogami, K. Uchida, S. Matsumoto [1], C. Abe [2], M. Toyama [3], and T. Yamamura [3]

Faculty of Science and Engineering, Kindai University
[1]*Graduate School of Science and Engineering, Kindai University*
[2]*Institute for Materials Research, Tohoku University*
[3]*Institute for Integrated Radiation and Nuclear Science, Kyoto University*

INTRODUCTION: Development of highly selective compounds for hexavalent actinide species (actinyl ions, An(VI), AnO_2^{2+}) has been important. We have been focusing on monoamide compounds which coordinate with An(IV) and (VI) species in nitric acid media as promising candidates. However, as reported last year[1], forming six-coordinated structures where one AnO_2^{2+} ion is surrounded by two carbonyl oxygen atoms of two monoamide molecules might be difficult spatially in case of resins. In order to increase the possibility of these coordinations, we suggested the combined use of monoamide and diamaide compounds as bifunctional groups. Diamide compounds are famous for separating not only An(IV) and (VI) species but also An(III) and lanthanide(III) (Ln(III)) ones. In this study, a preliminary synthesis and adsorptivity of a novel bifunctional monoamide-diamide resin was investigated.

EXPERIMENTS: *N,N*-dimethylacrylamide (DMMA) and *N,N,N',N'*-tetrapentylmalonamide (TPMA) were used as monoamide and diamide, respectively. The synthetic scheme of the resin has two steps as shown in Fig. 1. DMAA, chloromethylstyrene (CMS), and divinylbenzene (DVB) were firstly copolymerized (8 % crosslinkage) at the mixed ratio of DMAA/CMS = 1 (w/w) with pore producing solvents and a porous silica support similarly to the earlier literatures[2,3]. Chlorine atoms of poly-CMS were then substituted by TPMA by following the earlier literature[4] and the final resin (Silica DMAA-TPMA) was obtained. Adsorptivity of the resin was examined by a batch method using U(VI) and Ce(III) up to 6 mol/dm^3 (= M) HNO_3 at room temperature.

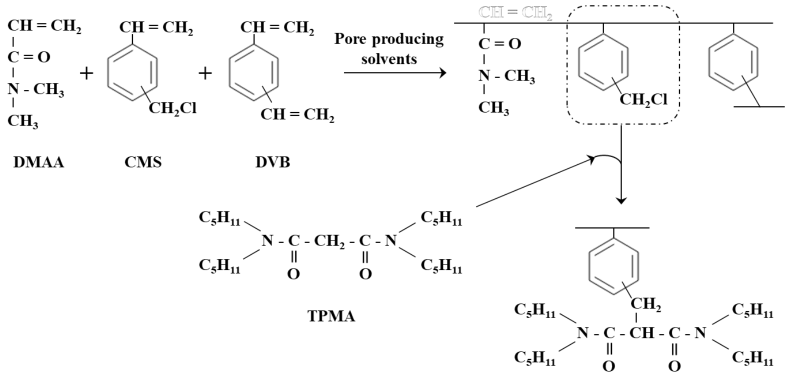

Fig. 1. Synthetic scheme of Silica DMAA-TPMA.

RESULTS: The resin showed adsorptivity basically with increasing concentration of HNO_3 for U(VI) and in HNO_3 higher than 3 M for Ce(III), Respectively. The K_d values for U(VI) were more than 10 times higher than those for Ce(III). In addition, those for U(VI) of Silica DMAA-TPMA was found to be higher than those of Silica DMAA resins[2] although the direct comparison for experimental conditions would be difficult. This suggests that, as expected, bifunctional monoamide-diamide resins may improve adsorptivity for An(VI) by suppressing the adsorption for Ln(III). It was also revealed that the resin has some points to be improved, *e.g.*, increase in adhesion ratio of the polymers to the silica support.

REFERENCES:

[1] M. Nogami *et al.*, KURNS Progress Report 2023 (2024) PR5-8.
[2] M. Nogami *et al.*, J. Radioanal. Nucl. Chem., **273** (2007) 37-41.
[3] M. Nogami *et al.*, Prog. Nucl. Energy, **50** (2008) 462-465.
[4] M. Nogami *et al.*, J. Solid State Chem., **171** (2003) 353-357.

I-1. PROJECT RESEARCHES

Project 5

PR5

Fundamental Resratch on Decommissioning of Reactor Facility

J. Hori

Institute for Integrated Radiation and Nuclear Science, Kyoto University

OBJECTIVES and RESEARCH SUBJECTS:

The main objective of this research project is to improve the method and the fundamental information on decommissioning of KUR and the Fukushima-Daiichi NPPs. This project consists of seven research subjects from four institutions, as follows.

R6P5-1: Neutron flux measurement for KUR facility activation modeling (2) (T. Sano *et al.*, Kindai Univ.)
R6P5-2: Measurement of the amount of activation of structures around KUR (K. Takamiya *et al.*, Kyoto Univ.)
R6P5-3: Fundamental Research about Radioactive Contamination Survey on Nuclear Reactor Facility - Elution tests with the irradiated KUR stack core - (S. Fukutani *et al.*, Kyoto Univ.)
R6P5-4: Neutron Capture Cross-Section Measurement at TC-Pn in KUR for Holmium among Nuclides in Decommissioning (S. Nakamura *et al.*, JAEA)
R6P5-5: Identification of Nuclear Material in Spent Fuel (3) (Y. Nauchi *et al.*, Central Research Institute of Electric Power Industry)
R6P5-6: External Neutron Source for Non-destructive Analysis of Fuel Debris (Y. Nauchi *et al.*, Central Research Institute of Electric Power Industry)
R6P5-7: Study on Non-destructive Analysis Method for Fuel Debris using Neutron Resonance Absorption (J. Hori *et al.*, Kyoto Univ.)

MAIN RESULTS and CONTENTS of this REPORT:

T. Sano *et al.* (R6P5-1) evaluated the neutron flux distribution in the KUR sub-pile room during 5-MW operation for the decommissioning of KUR by an activation experiment and numerical calculations.
K. Takamiya *et al.* (R6P5-2) measured the activity concentration of ^{60}Co for the stainless steel screws used in the B-2 experimental hole irradiation apparatus. A clear correlation was observed between the neutron dose and the radioactivity of ^{60}Co.
S. Fukutani *et al.* (R6P5-3) conducted elution tests with the irradiated KUR stack core. The results of elution with 0.1 N nitric acid solution were obtained.
S. Nakamura *et al.* (R6P5-4) performed the activation experiments by using the thermal column pneumatic tube (TC-Pn) of KUR. The thermal-neutron capture cross-section for production of ^{166m}Ho with the half-life of 1133 years was obtained.
Y. Nauchi *et al.* (R6P5-5) measured FPs of half-lives from 0.5 s to a few hours by way of OOPS (out of phase event spectroscopy) technique at the pulsed neutron source in the KURNS-LINAC. We decreased the lower threshold energy of measurement from 950 keV in the previous work.
Y. Nauchi *et al.* (R6P5-6) studied enhancement of the count rate of the γ ray and reduction of background using a fusion neutron source in an inertial electrostatic confinement device (IEC source) as an external source.
J. Hori *et al.* (R6P5-7) performed the verification experiment with a self-indication method as a non-destructive assay at the pulsed neutron source in the KURNS-LINAC. It was confirmed that the method using a high-enriched uranium sheet as an indicator makes it possible to determine the areal density of ^{235}U contained in a natural uranium sample.

PR5-1

Neutron flux measurement for KUR facility activation modeling (2

T. Sano, J. Hori[1], Y. Yashima[1], Y. Takahashi[1], K. Terada[1], Z. Zhang[1] and Y. Fujihara[1]

AtomicEnergy Research Institute, Kindai University
[1]Institute for Integrated Radiation and Nuclear Science, Kyoto University

INTRODUCTION: For the decommissioning of the KUR, it is important to evaluate the amount of radio activation materials such as the experimental equipment, the biological shield and so on. In general, the evaluation of the activation dose is mainly based on numerical calculations. In numerical calculations, the neutron spectrum and absolute neutron flux are important input information. However, the absolute values often differ by several 10% or more between the calculated and measured values. With that background, the research project has been conducting neutron flux measurements on the surface of biological shields and constructing a numerical calculational model [1]. In the FY2024, the neutron flux at the sub-pile room in the KUR was measured by the radio-activation foils and detail calculation of neutron flux distribution of the KUR facilities.

EXPERIMENT: Neutron flux measurement in the sub-pile room were using by Au-197 foils. An Au-197 foil sample was 10 mm in diameter and 0.05mm thickness (approximately 75 mg). The foils were placed at 4 locations around the primary cooling water outlet piping in the sub-pile room shown in Fig.1. Neutron irradiation was conducted from January 21 to 23 in 2024, and gamma rays (411 keV) emitted from Au-198 were measured using a Ge detector.

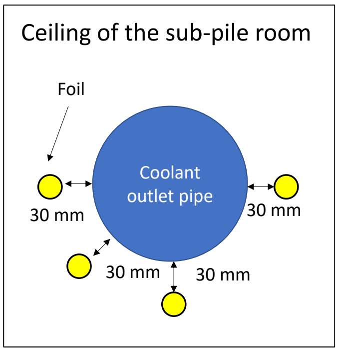

Fig.1 Location of Au foils setting

CALCULATION: Neutron flux calculations in the KUR facilities were performed in the following two steps:
1) A core calculation of KUR was performed using the Monte Carlo calculation code MVP3 [2] and JENDL-5 [3] to obtain the neutron spectrum in the KUR core.
2) Using the neutron spectrum as input, a neutron transport calculation was performed using PHITS2 version 3.31 [4] and JENDL-5 to obtain the neutron flux in the KUR sub-pile room.

RESULTS: The averaged counting rate was 0.015 cps by the Ge detector. Since the reactor power during the irradiation period was 46 hours for 1 MWt and 6 hours for 5 MWt, the neutron flux evaluation was performed by dividing the counting rate by 1:4 as an approximation. In addition, the neutron flux can be considered as approximate thermal flux. As the results, the thermal neutron flux was $1.11 \times 10^4\ (n/cm^2/sec)$ at the 1 MWt and at the $5.56 \times 10^4\ (n/cm^2/sec)$ at the 5 MWt. In the numerical calculations, the thermal neutron flux in the sub-pile room was $3.0 \times 10^4\ (n/cm^2/sec)$ at the 5 MWt. The experimental and calculated values agreed by an order of magnitude.

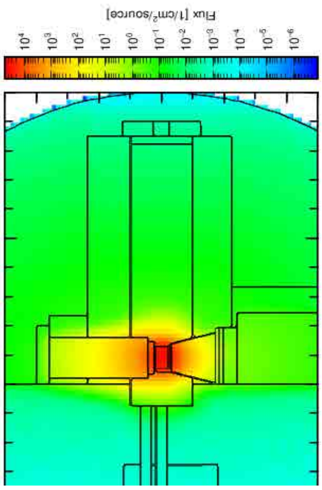

Fig.2 Calculated neutron flux distribution (relative value)

REFERENCES:

[1] T. Sano *et al.*, KURNS-Progress report 2022, (2023) pp.71.
[2] Y. Nagaya *et al.,* JAEA-Data/Code 2016-018, (2016).
[3] O. Iwamoto *et al.,* J. Nucl. Sci. Technol., **60** (2023) 1-60.
[4] T. Sato *et al.,* J. Nucl. Sci. Technol., **55** (2018) 684-690.

PR5-2

Measurement of the amount of activation of structures around KUR

K. Takamiya, H. Yoshino, J. Hori

Institute for Integrated Radiation and Nuclear Science, Kyoto University

INTRODUCTION: Unlike commercial nuclear reactors, safety measures for decommissioning research reactors require consideration of the activation of various experimental equipment such as experimental holes and irradiation holes. To provide basic data for safety assessments during the removal of these experimental structures, this study aimed to measure the amount of radioactive material present in some of these structures. To obtain a clear correlation between the actual measured values and the history of exposure to neutrons, the target structural materials were selected based on the condition that (1) there was no movement during the time they were installed, and (2) it was possible to estimate the irradiated neutron dose. The irradiation apparatus of the B-2 experimental hole met these criteria because its installation period is clear, and existing simulation-based calculated values and actual measured values obtained by activation analysis are available for the neutron dose within the experimental hole. Therefore, the irradiation apparatus of the B-2 hole was selected as the subject of this study.

EXPERIMENTS: The B-2 experimental hole irradiation apparatus was introduced as one of KUR's irradiation facilities in March 2012 and was removed in March 2021. This device was able to irradiate neutrons on large samples or liquid samples by transporting the truck with the samples from the adjacent laboratory into the experimental hole. A rail was installed within the inner sleeve of the experimental hole to transport the truck, and stainless steel screws were used to fix the rail. The position of these screws was precisely located using the apparatus drawings. Therefore, these screws were selected as the material for evaluating the amount of activation in this study. Six screws were collected at 30 cm intervals, starting from a range of 135 cm from the edge of the rail (i.e., at 135, 165, 195, 225, 255, and 285 cm from the edge). Gamma-ray spectra were subsequently measured using a Ge-semiconductor detector GC4020 (Canberra).

RESULTS AND DISCUSSION: As a result of a gamma-ray spectrum analysis, a photo-peak of ^{60}Co was observed, and ^{60}Co radioactivity was quantified by comparing it with the measurement results of a standard source of ^{60}Co. Figure 1 shows the correlation between the sample position and the radioactivity of ^{60}Co. The squares in the figure show the neutron doses previously estimated by the gold activation method. A clear correlation was observed between the neutron dose and the radioactivity of ^{60}Co. These results showed that by collecting a part of the structural material with a clear installation history among the experimental equipment and structures around the reactor, it was possible to infer the irradiation history of neutrons by measuring the radioactivity, and it was effective in assessing the effects of radiation exposure due to activation during decommissioning.

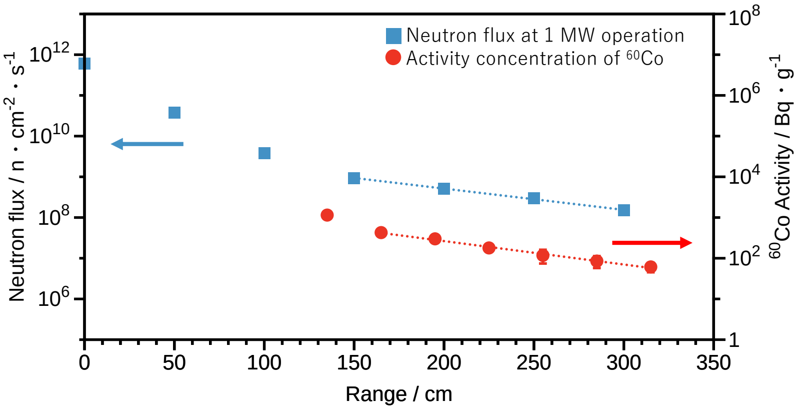

Figure 1 The correlation between the range from the edge of the rail and the activity concentration of ^{60}Co.

PR5-3

Fundamental Research about Radioactive Contamination Survey on Nuclear Reactor Facility - Elution tests with the irradiated KUR stack core -

S. Fukutani[1)], R. Tsuchiya[2)], M. Ikegami[1)], J. Hori[1)] and K. Takamiya[1)]

1) Institute for Integrated Radiation and Nuclear Science, Kyoto University
2) Graduate School of Engineering, Kyoto University

INTRODUCTION: It is important to survey radioactive contamination for decommission of nuclear reactor facilities. The KUR stack, which was built in 1963, made of RC (Reinforced Concrete) was demolished in 2013. We reported stable nuclide concentration in the KUR stack core [1] measuring by INAA [2]. In this study, we conducted elution tests with the irradiated KUR stack core.

EXPERIMENTS: The KUR stack core samples, which was irradiated by neutron at KUR (Pn-2, 5MW, 1hour) were placed in a 15 mL centrifuge tubes, and ultrapure water or 0.1 N nitric acid solution was added. The solid-liquid ratio was 1:10, and the centrifuge tubes were stirred for 6 hours using a magnetic stirrer. At this time, a wire was used to make a two-layer structure to prevent contact between the stirrer and each core. After the agitation was completed, filtration was performed using a 0.45 µm disposable membrane filter. The filtrate was collected in a U-8 container. The obtained measurement samples were measured for nuclides using a Ge semiconductor detector (ORTEC GEM30-70) and a multichannel analyzer (SEIKO EG&G MCA7600). The measurement time was 80,000 seconds or longer. The radioactivity of the eluted nuclides was calculated from the measurement results.

RESULTS: Radionuclides were hardly detected in the filtrate when the elution tests were performed with ultrapure water. Therefore, only the results of elution with 0.1 N nitric acid solution were shown in Table 1.

Table 1 Elution rate of each nuclide from core 1 and core 2

nuclide	Core 1 [%]	Core 2 [%]
Ce-141	16 ± 0.6	23 ± 0.9
Ce-144	3.9 ± 0.3	3.7 ± 0.5
Co-60	20 ± 0.1	39 ± 0.3
Cr-51	9.7 ± 0.3	32 ± 1.0
Eu-152	15 ± 1.1	24 ± 2.0
Fe-59	5.9 ± 0.2	15 ± 0.3
Mn-54	15 ± 0.4	25 ± 0.7
Sb-124	6.1 ± 0.5	16 ± 1.3
Sc-46	5.5 ± 0.0	17 ± 0.1
Zn-65	25 ± 0.2	45 ± 0.4

Elution rate (%) = (Radioactivity of eluted nuclide [Bq]) / (Radioactivity of nuclide in the core sample [Bq]) × 100

REFERENCES:

[1] S. Fukutani *et al.,* KURNS Prog. Report 2022, (2023) 72.
[2] S. Fukutani *et al.,* KURNS Prog. Report 2023, (2024) 45.

PR5-4

Neutron Capture Cross-Section Measurement at TC-Pn in KUR for Holmium among Nuclides in Decommissioning

S. Nakamura[1], S. Endo[1], R. Gerard[1], A. Kimura[1], Y. Shibahara[2]

[1]Nuclear Data Center, Japan Atomic Energy Agency
[2]Institute for Integrated Radiation and Nuclear Science, Kyoto University

INTRODUCTION: The present study is an attempt to measure accurate thermal-neutron capture cross-sections for nuclides of concern in decommissioning. From the viewpoint of clearance level [1] in decommissioning, we have performed the cross-section measurements by an activation method using the thermal column pneumatic tube (TC-Pn) of KUR [2-6]. The present work selected ^{165}Ho nuclide and measured its thermal-neutron capture cross-section for production of ^{166m}Ho with the half-life of 1133±8 years.

EXPERIMENTS: Two pieces of natural Ho foils were prepared with a purity of 99.9%, a diameter of 4mm, a thickness of 12.5 μm, and a weight of 15 mg. A gold-aluminum alloy wire, a cobalt foil and a Mo foil were used to monitor the neutron flux at the irradiation position. **Figure 1** draws a rough sketch of the target samples. The target was irradiated for 5 hours under 5-MW operation of KUR. After irradiation, the Ho samples and flux monitors were enclosed in a thin vinyl bag one by one. Gamma-rays emitted from each sample were measured with a high-purity Ge detector. A sample was placed at a distance of 110 mm from the front surface of the Ge detector. The γ-ray peak efficiencies of the Ge detector were measured in advance with a mixed γ-ray source and a gamma reference source of ^{152}Eu. Two Ho samples were measured together without overlapping each other. Gamma-rays emitted from ^{166g}Ho (26.8 hours) were measured with sufficient yields, therefore we also measured the cross section of the ^{165}Ho(n,γ)^{166g}Ho reaction. After ^{166g}Ho had decayed sufficiently, γ-rays from ^{166m}Ho were measured for 7 days. **Figure 2** shows a γ-ray spectrum of ^{166m}Ho. Four γ-rays originating from ^{166m}Ho were observed at 184, 280, 712, and 810-keV.

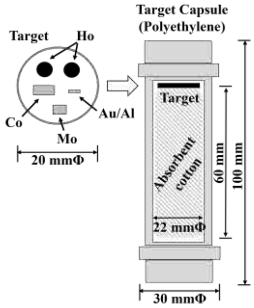

Fig.1 Target samples.

ANALYSIS AND RESULTS: The reaction rates of the Ho samples and flux monitors were calculated from their γ-ray yields. On the basis of Westcott's convention [7], the thermal-neutron flux was derived with the reaction rates of monitors. The cross sections for produced ^{166m,g}Ho were derived by dividing the reaction rates of Ho by the thermal-neutron flux. We tentatively obtained a value of 2.79±0.04 barn for the ^{165}Ho(n,γ)^{166m}Ho reaction, which was derived with an accuracy of 1.4% compared to the past reported value of 3.4±0.5 barn. As a by-product, we also obtained 61.2±0.6 barn for the ^{165}Ho(n,γ)^{166g}Ho reaction. Combining the cross sections for ^{166m}Ho and ^{166g}Ho presented 64.4±0.6 barn, which supports the past reported value of 64.4±2.8 barn by Time-Of-Flight method and the recently evaluated data of 64.69 barn and 64.4±1.2 barn within the limit of uncertainty.

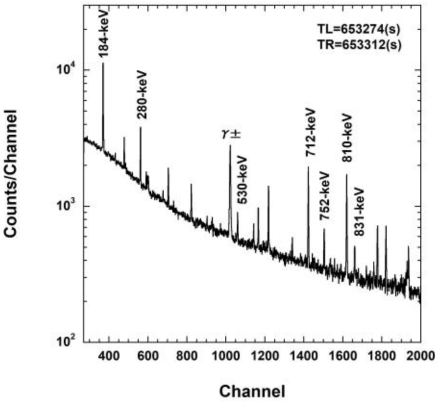

Fig.2 γ-ray spectrum of ^{166m}Ho .

REFERENCES:

[1] IAEA; 2004. (No. RS-G-1.7).
[2] S. Nakamura *et al.,* J.Nucl.Sci.Technol., **58**(10) (2021) 1061.
[3] S. Nakamura *et al.,* J.Nucl.Sci.Technol., **59**(11) (2022) 1388.
[4] S. Nakamura *et al.,* J.Nucl.Sci.Technol., **61**(11) (2024) 1415.
[5] S. Nakamura *et al.,* J.Nucl.Sci.Technol., **62**(3) (2025) 300.
[6] S. Nakamura *et al.,* J.Nucl.Sci.Technol., (2025) Published Online.
[7] C.H. Westcott *et al.,* P/202, Canada, **16** (1958) 70.

Identification of Nuclear Material in Spent Fuel (3)

Y. Nauchi, J. Hori[1], K. Terada[1], T. Sano[2] and S. Sato

Energy Transformation Research Laboratory, Central Research Institute of Electric Power Industry
[1]Institute for Integrated Radiation and Nuclear Science, Kyoto University
[2]Atomic Energy Research Institute, Kindai University

INTRODUCTION: γ ray emission data from short lived fission products (FPs) generated from ^{235}U had been measured to give reference data for delayed γ ray assay (DGA). We measured FPs of half-lives from 0.5 s to a few hours by way of OOPS (out of phase event spectroscopy) technique. The focused energy region was originally greater than 3 MeV for the purpose of DGA for spent nuclear fuel since γ ray spectroscopy for energy region less than 3MeV is impractical for such spent fuel. However, we had noticed γ ray intensity from FP is greater for lower energy region. In this work, we decreased the lower threshold energy of measurement from 950 keV in the previous work [1] to obtain full energy γ ray spectrum which is useful to validate decay heat data.

EXPERIMENTS: Measurement set up was almost same as that applied in the previous work [1]. The same Uranium (U) - Aluminum (Al) alloy sample was irradiated by neutrons periodically radiated from the tantalum target with frequency of 30 Hz. The γ rays emitted from the sample were measured with the HPGe detector. The time spectrum of γ ray detection after pulsed electron was injected on the target is shown in Fig. 1. The prompt rays from the fission and the capture reactions appear in the time region from 0 to 16 ms. We shielded the HPGe detector with collimators of lead disks and boron doped polyethylene ones. We focused on the event in the time region from 20 to 33.3 ms. The region is out of phase (OOP) of the pulsed neutron so that γ rays were measured from radioactive decay of FPs and 235U. The ray spectra were measured on irradiation conditions for 18 hours.

Table 1. γ ray count rate for pulse height region.

Pulse height range (keV)	Count rate (cps)	error
70~210	99.97	0.25
210~950	187.62	0.07
950~3000	58.54	0.03
3000~	4.16	0.01

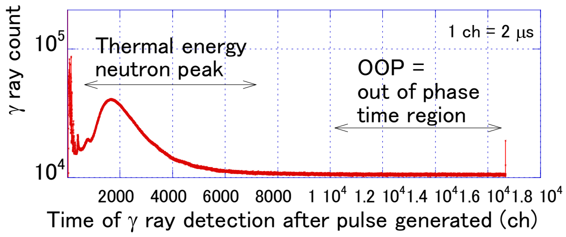

Fig. 1 Time spectrum of γ ray detection.

RESULTS: Measured spectra are shown in Fig. 2. By the sufficient collimation, we could reduce the ray detection threshold down to 70 keV. Below 210 keV, γ rays of energy 144, 163, 186, 205 keV, etc. from decay of ^{235}U are intense. The net count rate of the ray is shown in Table 1. The rate in the pulse height region extended in this work is 4.6 times larger than that in the previous work. Accord-ingly, these data are considered significant to validate total number of γ ray emission from FPs as well as the decay heat.

REFERENCES: [1] Y. Nauchi *et al.*, KURNS Progress Report 2023 (2024) 47.

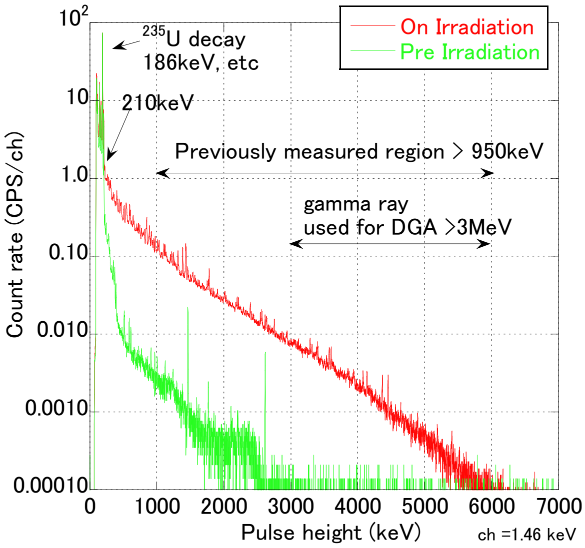

Fig. 2 γ ray spectrum in out of phase time region.

PR5-6

External Neutron Source for Non-Destructive Analysis of Fuel Debris (3)

Y. Nauchi, Y. Takahashi[1], J. Hori[1], K. Terada[1] and S. Sato

Energy Transformation Research Laboratory, Central Research Institute of Electric Power Industry
[1]Institute for Integrated Radiation and Nuclear Science, Kyoto University

INTRODUCTION: Neutron sources have been studied for neutron induced gamma ray spectroscopy (NIGS) for characterizing fuel debris retrieved from damaged cores [1]. A fusion neutron source from an inertial electrostatic confinement device (IEC source) is advanced since no significant γ ray emission is associated with the neutron emission. However, 4060 keV γ ray from the ^{238}U(n,γ) reaction had not yet been identified with a IEC source at KURNS [2]. In this work, enhancement of the count rate of the γ ray and reduction of backgrounds (BG) were studied.

EXPERIMENTS: NIGS with the IEC source was conducted in the measurement room of the KUCA building. Schematic view of geometry is shown in Fig. 1. The neutron source intensity was measured as 5×10^5 n /s. Metallic uranium (U) plates with the natural isotopic abundance were used. To enhance reaction rate of ^{238}U(n,γ), we made a unit cell which consists of a sheet of the U plate and two sheets of the polyethylene plates with 3.085 mm in thickness. The 5 units were loaded in a square shaped sheath made of aluminum. Polyethylene reflectors were placed on both sides of the units. The thickness of the reflectors was chosen to enhance the count rate of the 4060 keV γ rays. Sixteen sets of the U samples, polyethylene plates, and the sheath were employed, where the number of U plates was doubled compared to that employed in the previous work [1]. ^{238}U(n,γ) 4060 keV γ rays were measured with a HPGe detector. Dead time of it due to γ rays from ^{234m}Pa in the U plates is issue. To mitigate the dead time, 6 sheets of lead-bismuth plates were loaded at the end of the sheath. In the previous work, γ ray emission in the HPGe detector from neutron capture reactions of germanium isotopes was major BG [2]. To reduce BG, we placed lithium fluoride plates which absorb thermal neutrons without radiating γ rays. To avoid spectrum distortion due to high counting rate, shaping time of pulse signals by the linear amplifier was set to 2 μs.

RESULTS: Pulse height spectrum obtained by 3.5 hours of measurement is shown in Fig. 2. The pulse height was calibrated referring to 1001 keV γ ray from ^{234m}Pa and 2614.5 keV γ ray from ^{208}Tl assuming linearity of pulse height channel to energy. As the results, we identified 4060 keV γ ray peak above continuum fission prompt γ ray spectrum although counting statistics is not sufficient. However, the statistics can be enhanced just by extension of the measurement time up to a day. Accordingly, IEC neutron source is promising for NIGS for the fuel debris.

REFERENCES: [1] Y. Nauchi *et al.*, KURNS Progress Report 2022 (2023) 74.
[2] Y. Nauchi *et al.*, KURNS Progress Report 2023 (2024) 48.

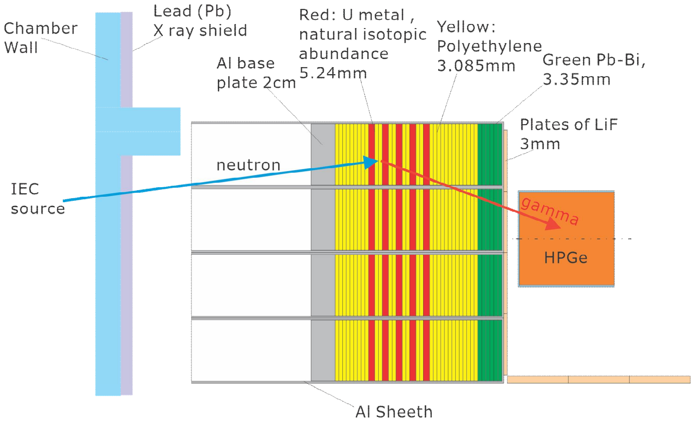

Fig. 1 Schematic view of measurement geometry.

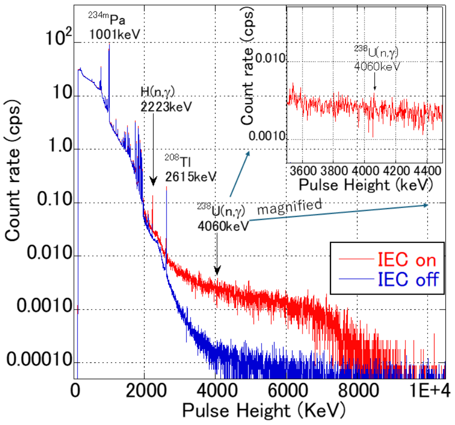

Fig. 2 γ ray spectrum from U irradiated by IEC n-source.

PR5-7

Study of Non-destructive Analysis Method for Fuel Debris using Neutron Resonance Absorption

J. Hori, K. Terada, T. Takahashi, H. Yashima and T.Sano[1]
Institute for Integrated Radiation and Nuclear Science, Kyoto University
[1]*Atomic Energy Research Institute, Kindai University*

INTRODUCTION: In the units 1 to 3 of Fukushima Daiichi Nuclear Power Plant (1F), the fuel, the metal cladding and the control rods were melted and large amount ware re-solidified in the bottom of the pressure vessel as fuel debris. In the decommission plan of 1F, the fuel debris will be collected and analyzed in the near future. Non-destructive nuclide assay is one of the important issues for nuclear material accountancy. We have studied the Neutron Resonance Densitometry (NRD) as a method of non-destructive nuclear assay. In the study, we proposed to apply a self-indication method to analysis of the fuel debris [1]. In the self indication method, an indicator consisting of the target nuclide is placed at the neutron beam downstream from a sample. The transmitted neutron though the sample can be measured indirectly by detecting the reaction products from the indicator with the neutron time-of-flight (TOF) method. We carried out the verification experiment.

EXPERIMENTS: The experiment was performed at the Institute for Integrated Radiation and Nuclear Science, Kyoto University (KURNS-LINAC). The linac was operated with a repetition rate of 200 Hz, a peak current of about 5 A, and an electron energy of about 30 MeV. We used a flight path in the direction of 135 degree with respect to the linac electron beam. A Cd sheet of 0.5 mm in thickness was inserted into the TOF beam line to suppress overlap of low energy neutrons due to the previous pulse. A high-enriched uranium (HU) sheet was used as an indicator. The HU indicator was made of U_3O_8-Al alloy and the areal densities of ^{235}U and ^{238}U were 1.3×10^{-4} and 9.5×10^{-6} /b, respectively. Prompt gamma-rays from the indicator which set at the position of 12m neutron flight path were measured by a 4π BGO spectrometer. Another measurement with a natural uranium in the upper beam side was also performed. The sample was 1 cm long, 2 cm wide and 5.8 g in weight.

RESULTS: Figure 1 shows the comparison of TOF spectra for prompt gamma-rays from the HU indicator with and without the natural uranium sample. The resonances due to fission reactions of ^{235}U and capture reactions of ^{235}U or ^{238}U were observed. It is noted that the effective reaction rate of the 20.9-eV resonance of ^{238}U becomes to be comparable to that of the 19.3-eV resonance of ^{235}U in the case of HU indicator. By inserting the natural uranium sample, the decrease in peak area depending on the areal density for each nuclide was observed. We succeeded in assaying the areal density of ^{235}U in the natural uranium sample by the self-indication method.

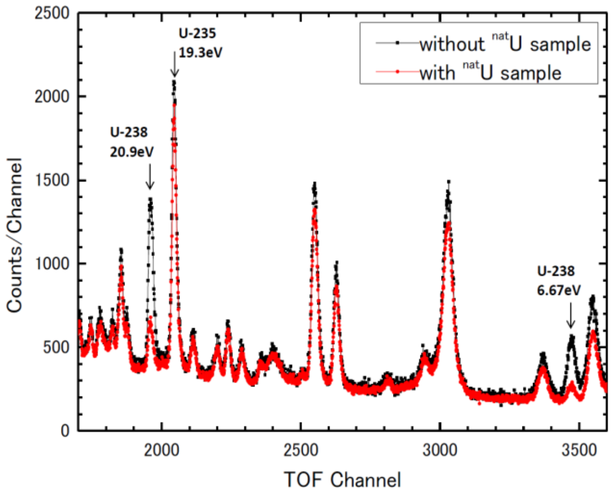

Fig. 1 Comparison of the TOF spectra for prompt gamma-rays from the HU indicator with and without natural uranium sample

REFERENCES:

[1] J. Hori *et al.,* EPJ Web of Conferences 146, 09042 (2017).

I-1.   PROJECT RESEARCHES

Project 6

PR6

Development on Neutron Imaging Application

Y. Saito

Institute for Integrated Radiation and Nuclear Science, Kyoto University

OBJECTIVES and ALLOTED RESEARCH SUBJECT: Neutron imaging provides valuable information which cannot be obtained from an optical or X-ray imaging. The purpose of this project is to develop the imaging method itself and the experimental environment for expanding the application area of the neutron imaging. The allotted research subjects are as follows:

ARS-1:	Measurements of Multiphase Dynamics by Neutron Radiography (Y. Saito et al.)
ARS-2:	Effect of Gravity on Void Fraction of Refrigerant Two-Phase Flows in Mini-channels (H. Asano et al.)
ARS-3:	Quality visualization of top flooding phenomena in vertical hole (H. Umekawa et al.)
ARS-4:	Evaluation of Meltwater Penetration During Defrosting Process (R. Matsumoto et al.)
ARS-5:	Spalling Phenomenon of High-Strength Concrete with Different Admixtures (M. Kanematsu et al.)
ARS-6:	Neutron Radiography on a 1/16-inch Tee-Shaped Mixer with an Inner Diameter of 1.3 mm Used in Supercritical Hydrothermal Reactor (S. Takami et al.)
ARS-7:	Visibility of Plant Roots in Different Artificial Soils via Neutron Imaging (U. Matsushima et al.)
ARS-8:	In-situ Observation of Lithium Migration in the Lithium-ion Conductor through Neutron Radiography under High-Temperature (S. Takai et al.)
ARS-9:	Measurement of coolant distribution in a flat laminate vapor chamber utilizing neutron radiography (Mizuta et al.)

MAIN RESULTS AND THE CONTENTS OF THIS REPORT:

ARS-1 performed visualization of boiling two-phase flow by high-speed imaging. This study aims to investigate the dynamics of boiling two-phase flow in a heated pipe using high-speed NRG and to clarify the temporal fluctuations.

ARS-2 applied to neutron imaging to void fraction measurements of two-phase flow in a small diameter tube. From measurement results, it was found that the image blur was caused by the beam divergence, resulting in a positive liquid thickness even in the range outside the tube.

ARS-3 investigated the quenching phenomena. Experimental results show the effect of test section geometry on the cooling behavior, including the counter current flow limitation (CCFL).

ARS-4 evaluates the meltwater penetration during defrosting process, which is one of the important phenomena to enhance the energy efficiency of the air conditioning system.

ARS-5 investigates the effect of admixtures in high strength concrete on the spalling phenomenon.

ARS-6 proposed a mixer for the instantaneous heating of the reactant solution and performed neutron radiography measurements. In this study, they tried to visualize the mixing behavior at a teeshaped mixer with an inner diameter of 1.3 mm.

ARS-7 compared the visibility of the root systems of plants cultivated in rice husks and perlite mixed media using neutron imaging.

ARS-8 applies the electric field to the model cell to observe the lithium migration in the solid electrolyte employing the NR.

ARS-9 investigated the change in coolant distribution in a flat vapor chamber with heat input by utilizing neutron radiography.

PR6-1

Measurements of multiphase flow dynamics using neutron radiography

Y. Saito, D. Ito and N. Odaira

Institute for Integrated Radiation and Nuclear Science, Kyoto University

INTRODUCTION: Neutron radiography (NRG) is useful for understanding multiphase flow phenomena. NRG proves effective in understanding thermal-hydraulic phenomena in metallic pipes due to its high transmissivity and has been applied in various applications. It can also measure the flow structure of boiling two-phase flow. Umekawa et al. measured the time-averaged void fraction distribution of boiling two-phase flow under the fluctuated flow rate condition by neutron radiography [1]. This study aims to investigate the dynamics of boiling two-phase flow in a heated pipe using high-speed NRG and to clarify the temporal fluctuations.

EXPERIMENTS: Neutron imaging experiments were conducted in the B-4 facility of KUR. A high-speed imaging system comprising an optical image intensifier and a high-speed camera was employed to acquire sequences of neutron transmission images of boiling flow at 1000 fps. A stainless steel tube with an inner diameter of 6 mm is used as a test section. The test section is heated by Joule heating using a DC power supply whose output can be controlled by the external signal from a function generator. The cross-sectional average void fraction was calculated from the instantaneous void fraction distribution estimated from the transmission images. The dynamics of the flow pattern in the tube were analyzed based on its spatio-temporal distribution.

RESULTS: The spatio-temporal void fraction distributions of boiling flow are shown in Fig.1. The horizontal axis denotes the time and vertical axis denotes the axial distance in the heated tube. The color map represents the cross-sectional averaged void fraction. At the constant heat flux, the generation of vapor bubbles near the center of the imaging area can be confirmed, as shown in Fig.1A. When the test section is heated by sinusoidal power, the distribution shows the fluctuated behavior, as shown in Fig.1B. The position of bubble generation moves in the axial direction as the heat flux changes. The high-speed NRG can measure changes in flow structure in opaque metal pipes and is an effective method for understanding the phenomena of boiling two-phase flow.

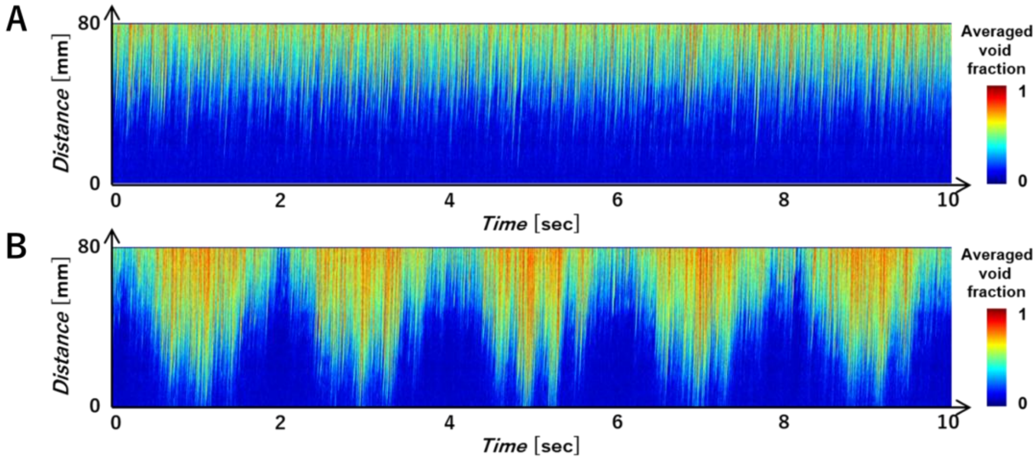

Fig.1. Spatio-temporal distribution of cross-sectional void fraction of constant heat flux of 830 kW/m^2 (A) and fluctuated heat flux with the frequency of 0.5 Hz, the amplitude of 390 kW/m^2 (B).

REFERENCES:

[1] H. Umekawa *et al.,* Physics Procedia, **43** (2013) 269-276.

PR6-2

Effect of Gravity on Void Fraction of Refrigerant Two-Phase Flows in Mini-channels

H. Asano, T. Maruyama, S. Saeki, K. Sugimoto, N. Yoshida, H. Murakawa, Y. Obayashi, K. Nakagawa, Y. Shirase[1], C. Schreiber[1], E. Dzramado[1], J. Inukai[1], N. Odaira[2], D. Ito[2] and Y. Saito[2]

Graduate School of Engineering, Kobe University
[1]Hydrogen and Fuel Cell Nanomaterials Center, University of Yamanashi
[2]Institute for Integrated Radiation and Nuclear Science, Kyoto University

INTRODUCTION: Low-GWP refrigerants are being considered to address the global warming issue, and hydrocarbon-based refrigerants, which are highly flammable natural refrigerants, are also considered as candidates. To apply hydrocarbons to heat pump system, a compact heat exchanger with mini-channels is essential to reduce the refrigerant charge and to improve the coefficient of performance. In this study, the effect of gravity on the void fraction in a mini-channel with an inner diameter of 1 mm, assuming a layered microchannel heat exchanger.

EXPERIMENTS: The test section was a SUS tube with the inner diameter of 1.0 mm and the thickness of 0.5 mm. R134a was used as the working fluid. Gas-liquid two-phase flow was supplied to the test section as a vertical upward flow from a steam generator installed vertically. Horizontal and vertically downward flows were supplied through a bend tube. An example of neutron radiograph is shown in Fig. 1. The tube was filled with liquid. The rectangular area in Fig. 1 shows the measurement area of void fraction. The distance from the entrance to the center of the measurement area is 167, 48, and 52 mm for vertically upward, horizontal and vertically downward flows, respectively. Pixel size was 12.7 μm/pixel with an exposure time of 30 s. The experiment was conducted with mass fluxes of 230, 300, and 400 kg/(m^{2}s) and varied vapor quality from 0.1 to 0.9. The saturation temperature was maintained at 20°C. The bond number, defined as the ratio of the inertia force to the surface tension, was approximately 1.35.

RESULTS: Liquid thickness along the neutron beam direction can be measured by comparison with the image with vapor single-phase at each pixel. Values corresponding to the liquid film thickness for the vertically downward flows are plotted against the distance from the center of the tube as shown in Fig. 2. The vertical axis shows the product of attenuation coefficient of liquid R134a and its thickness in arbitrary unit. The result for liquid single-phase flow represents the cross-sectional shape of the tube. It can be seen from the results that the liquid thickness was positive even in the range outside the tube. The reason is caused by blur due to due to non-parallelism of the neutron beams and the effect of neutron scattering in the object. To measure the cross-section occupied by liquid, it is necessary to integrate the liquid thickness over the area affected, including outside the tube. It was found that the difference in liquid distribution between vertically upward and downward was little.

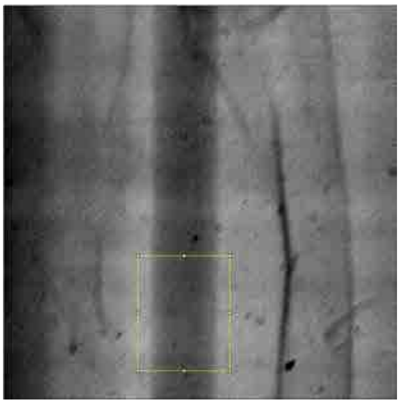

Fig. 1. Neutron radiograph take with reactor thermal out ut 5 MW.

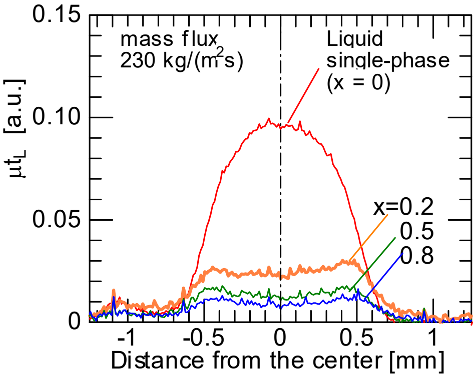

Fig. 2. Radial distribution of liqui thickness along neutron beam.

PR6-3

Qualitatively Visualization of Top Flooding Phenomena in Vertical Hole

H. Umekawa, T. Ami, A. Nanno, K. Inou, Y. Saito[1], D. Ito[1] and N.Odaira. [1]

Department of Mechanical Engineering, Kansai University
[1]Institute for Integrated Radiation and Nuclear Science, Kyoto University

INTRODUCTION: The continuous supply of cold water to a hot surface is a critical factor in the effective cooling of high temperature structures. These phenomena are commonly encountered across various industrial processes and accidents. Typical limitation of cooling process is caused by counter-current flow condition (CCFL) and film boiling. In this investigation, the flow behavior of the cooling water inside a vertical heated tube was qualitatively visualized.

EXPERIMENTS: In this investigation, the test section was initially heated by installing into the electric furnace. Once the temperature of the test section reached the predetermined level, the test section was removed from the furnace, and the cooling water is supplied as the top flooding configuration. During the visualization, the movement of the cooling water was continuously recorded by using highs speed camera. In this term, three kind of test sections was employed, i.e. two round tube (I.D.=3mm and I.D.=8mm, both with t=1mm) and one rectangular tube (I.D.2mm×10mm with t=2mm). The length of these test sections was 75mm, with a closed bottom end, and the top end connected to a water receiver.

Results:

Figure 1 shows the time-strip images of each test sections. These visualization image clearly visualized the influence of the tube geometry. In the case of the large diameter tube (I.D.=8mm), the cooling water reached the bottom end of the tube and periodical cooling behavior was observed. On the other hand, in the case of the small diameter tube (I.D.=3mm) the water could not reach the bottom and mostly stagnated near the entrance part owing to the CCFL condition. In the case of the rectangular tube, water movement expresses the more complex tendency, owing to the separating of the vapor flow and liquid flow at the entrance part. Overall, this visualization in this term, the fundamental procedure can be established, and these results can be utilized in the subsequent detail measurements.

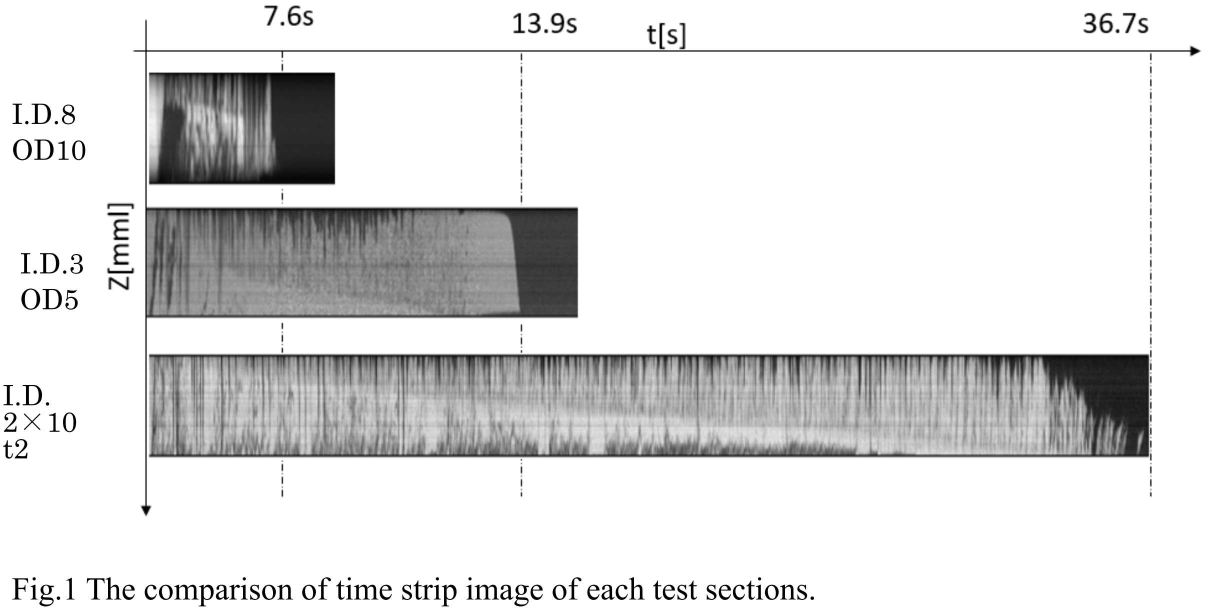

Fig.1 The comparison of time strip image of each test sections.

PR6-4

Evaluation of Meltwater Penetration During Defrosting Process

N. Fujikawa , Q. Chu , R. Matsumoto , S. Kimura , K. Munekiyo , Y. Saito[1] D. Ito[1] and N. Odai-ra[1]

Department of Mechanical Engineering, Kansai Universit
[1]Institute for Integrated Radiation and Nuclear Science, Kyoto University

INTRODUCTION: Frost formation on the heat exchangers of the air conditioning system causes the serious problem on the heat transfer performance. In order to recover the performance of the heat exchanger, a defrosting operation is performed periodically to remove the frost from the heat exchanger. Matsumoto et al. [1] reported the removal of meltwater by penetrating into the remaining frost layer. By using this phenomenon, effective defrosting can be achieved. However, the meltwater penetration mechanism and temperature distribution along the frost layer remain unclear. This study evaluates meltwater penetration behavior using neutron radiography.

EXPERIMENTS AND RESULTS: Frost was formed on the aluminum plate with a thickness of 0.5 mm by cooling it down to -25 °C. A temperature gradient was applied by raising the temperature at one edge of the plate to 1°C, thus, the defrosting was performed in one direction. The defrosting duration was 10 min. The water penetration image at 3 min after the start of defrosting is shown in Fig.1, where defrosting was occurred from left to right, the meltwater penetrates into the remaining frost layer for about 45 mm. The water contents were analyzed in a 50 mm × 5 mm region (marked by yellow lines) by dividing into 20 sections in Fig.2. Defrosting process was started at t = 100 sec. At t = 140 sec, rapid meltwater penetration occurred by reaching the x = 45 mm position at t = 180 sec. The local water content reached at about 9 mg in x = 45 mm at t = 380 sec. As the temperature of the flat plate increases while keeping the temperature gradient, the meltwater moves to the right side of the plate. Hardly any residual water was observed on the plate.

REFERENCES:

[1] R. Matsumoto *et al.,* Transactions of the Japan Society of Refrigerating and Air Conditioning Engineers, **37(3)** (2020) 249.

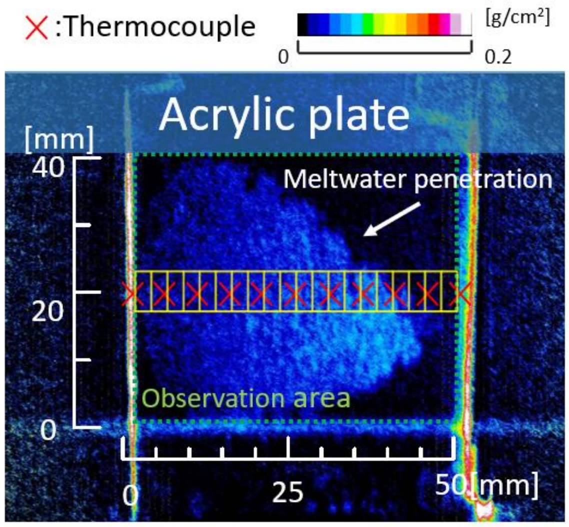

Fig. 1 Water penetration image.

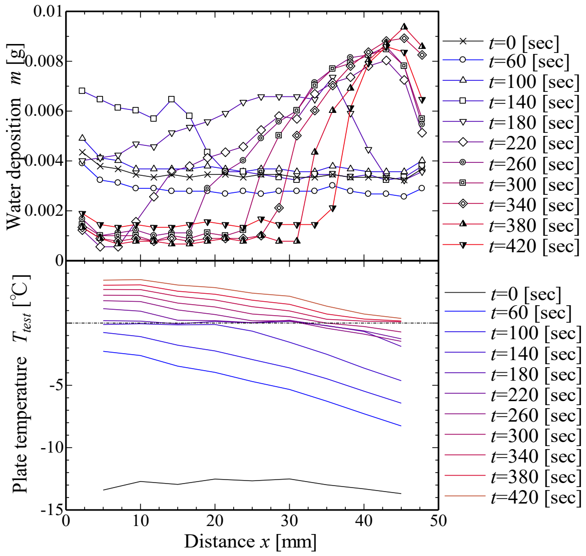

Fig. 2 Spatio-temporal distribution of meltwater penetration.

PR6-5

Spalling Phenomenon of High-Strength Concrete with Different Admixtures

K. Iwamura[1], M. Kanematsu[1], Y. Nishio[2], J. Kim[1], N. Odira[3], D. Ito[3] and Y. Saito[3]

[1]Department of Architecture, Tokyo University of Science
[2]Building Research Institute
[3]Institute for Integrated Radiation and Nuclear Science, Kyoto University

INTRODUCTION: Capturing detailed moisture movement in concrete under fire is essential to understanding the spalling mechanism [1]. In this study, using neutron radiography technology on high strength concrete with different admixtures, the effect of temperature and pressure changes and moisture movement inside the concrete during heating on the spalling phenomenon was examined.

EXPERIMENTS: 3 type concrete specimens (70×100×30 mm) with W / B of 18% are prepared. The first is general high-strength concrete(N), the second is N with replacing 40% blast furnace slag (BB) and the third is N with replacing rice husk ash (RHA). Temperatures and internal pressures were measured at the positions shown in Fig.1. In this experiment, specimens were heated from the bottom surface with quartz heater. Neutron radiography was performed at B-4 port of KUR.

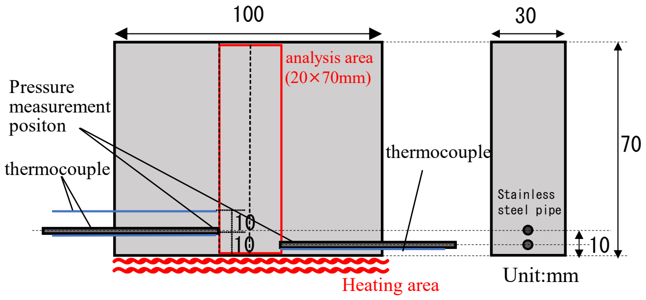

Fig. 1 Outline of concrete specimen

RESULTS: Fig. 2 and Fig. 3 show the result of a heating experiment with RHA. Fig. 2 shows the change in differential water intensity under heating, obtained by neutron radiography, and Fig. 3 shows the changes of temperature and pressure inside the concrete respectively. As shown in Fig. 2, areas with relatively high differential water intensity (dark blue areas) appeared at 5minutes. This trend was similar for the result with N and BB, which indicates forming moisture clog inside the concrete. As shown in Fig. 3, the maximum pressure was measured when the spalling occurred, and the measurement position was near the spalling depth. This suggests that the formation of water vapor pressure under heating affects the spalling occurrence. In the future, a more detailed investigation of the relationship between water vapor pressure and moisture clogs is expected

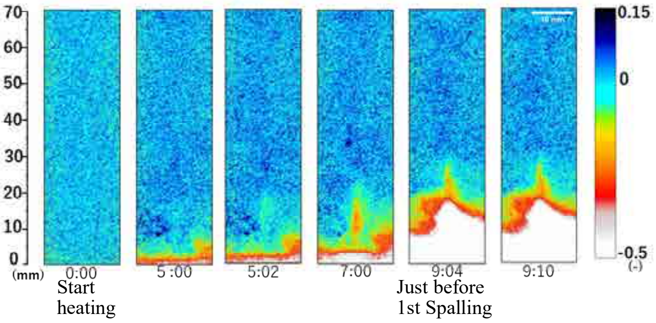

Fig. 2 Differential water intensity under heating (RHA)

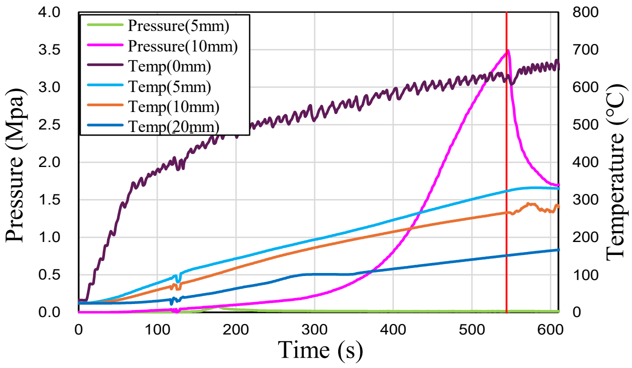

Fig. 3 Relationship between pressure and temperature in concrete under heating (RHA)

REFERENCES:

[1] JCI-TC-154A (2017). “Committee Reports:”

[2] T. Tanibe, (2014). “Ring restraining testing and spalling index of concrete at high temperature”

Neutron Radiography on a 1/16-inch Tee-Shaped Mixer with an Inner Diameter of 1.3 mm Used in Supercritical Hydrothermal Reactor

T. Kurono, S. Takami, Y. Azami[1], T. Saito[1], M. Kubo[1], K. Sugimoto[2], N. Odaira[3], D. Ito[3] and Y. Saito[3]

Graduate School of Engineering, Nagoya University
[1]Graduate School of Engineering, Tohoku University
[2]Graduate School of Engineering, Kobe University
[3]Institute for Integrated Radiation and Nuclear Science, Kyoto University

INTRODUCTION: Supercritical hydrothermal synthesis is a method to produce metal oxide nanoparticles in supercritical water. During supercritical hydrothermal synthesis using flow-type reactors, a stream of metal ion aqueous solution was instantaneously heated by mixing with a stream of supercritical water in a mixer. In the previous study, we visualized the mixing behavior of supercritical water and room temperature water in 1/8-inch and 1/4-inch tee-shaped mixers using neutron radiography. [1-3] We also found that a mixer with an inserted tube promoted faster mixing of reactant solutions with a stream of supercritical water.[4] In this study, we tried to visualize the mixing behavior at a tee-shaped mixer with an inner diameter of 1.3 mm.

EXPERIMENTS: In this study, we conducted neutron radiography measurements to visualize the mixing behavior in a flow-type reactor under operation. The measurements were performed at the B4 port of the Kyoto University Reactor (KUR). The KUR was operated at a 1 MW output with a neutron flux of ca. 1 or 5×10^7 n/cm^2 s at the beam exit of the B4 neutron guide tube. The experimental setup was similar to that used in previous studies.[1-4] The neutron beam that passed through the mixer was converted into fluorescent light using a 100 μm-thick ^{6}LiF/ZnS scintillator screen. A CMOS camera (ANDOR Zyla, 2048×2048 pixels) with a 180 mm telephoto lens (SIGMA APO MACRO DG HSM, f=3.5), a teleconverter (Nikon TC-201) and a close-up ring (Nikon PK-12) was used to capture the fluorescent light. The calculated spatial pixel resolution was around 13 μm. The distance between the neutron port and the converter was 2,310 mm

RESULTS: In this study, we tried to evaluate the mixing behavior of supercritical water and room temperature water in the 1/16-inch tee-shaped mixer with an inner diameter of 1.3 mm, which is expected to realize faster mixing. Due to the unexpected limitation of beam time availability, we were only able to visualize the mixer with room temperature water as shown in Fig. 1. As we can confirm, the room temperature water was precisely visualized using this setup. Therefore, we think the mixing behavior of supercritical water and room temperature water in 1/16 inch tee-mixer can be visualized using the similar setup.

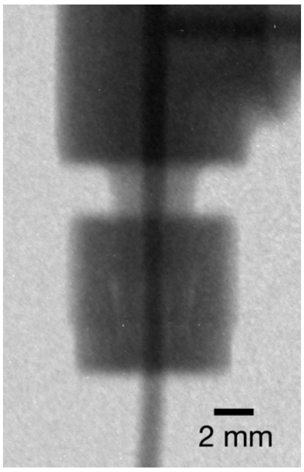

Fig. 1. Neutron radiography image of room temperature

REFERENCES:

[1] K. Sugioka *et al.,* AIChE J., **60** (2014) 1168-1175.
[2] S. Takami *et al.,* Phys. Proc., **69** (2015) 564-569.
[3] R. Sasaki *et al.,* J. Phys.: Conf. Ser., **2605** (2023) 012029.
[4] K. Sato *et al.,* Chem. React. Eng., **8** (2023) 1449-1456.

PR6-7

Visibility of Plant Roots in Different Artificial Soils via Neutron Imaging

U. Matsushima, O. Naoya[1], D. Ito[1], Y. Saitoh[1]

Faculty of Agriculture, Iwate University
[1]Institute for Integrated Radiation and Nuclear Science, Kyoto University, Japan

INTRODUCTION: This study compared the visibility of the root systems of plants cultivated in rice husks and perlite mixed media using neutron imaging.

EXPERIMENTS: *Brassica rapa* var. “perviridis” (Komatsuna) was the study material grown in rice husk (rice husks:soil = 3:1) and perlite mixed (perlite:soil = 9:1) media, in aluminum pots 14 × 14 × 14 mm. A thickness of 14 mm allowed neutrons to penetrate even wet media. The root system was observed using a neutron CT imaging device at the B4 beam hole, KUR, Kyoto University.

RESULTS: The rice husk medium, which contained organic matter, had low neutron permeability (Fig. 1-a), whereas perlite, which was mainly glassy with large grains and many voids, demonstrated high permeability (Fig. 1-b). In the peripheral region of the rice husk medium, roots developed well, root ball formation was apparent, and the root structure was confirmed. However, in the central part, the neutron permeability of the roots and the medium were similar, making it difficult to distinguish between them. As the neutron permeability in the perlite-mixed medium increased, the root visibility also improved. However, root development was inferior to that in the rice husk, and root identification in the central part of the medium was challenging. To observe plant root systems using neutron imaging, it is necessary to consider the neutron permeability and root development in the culture medium.

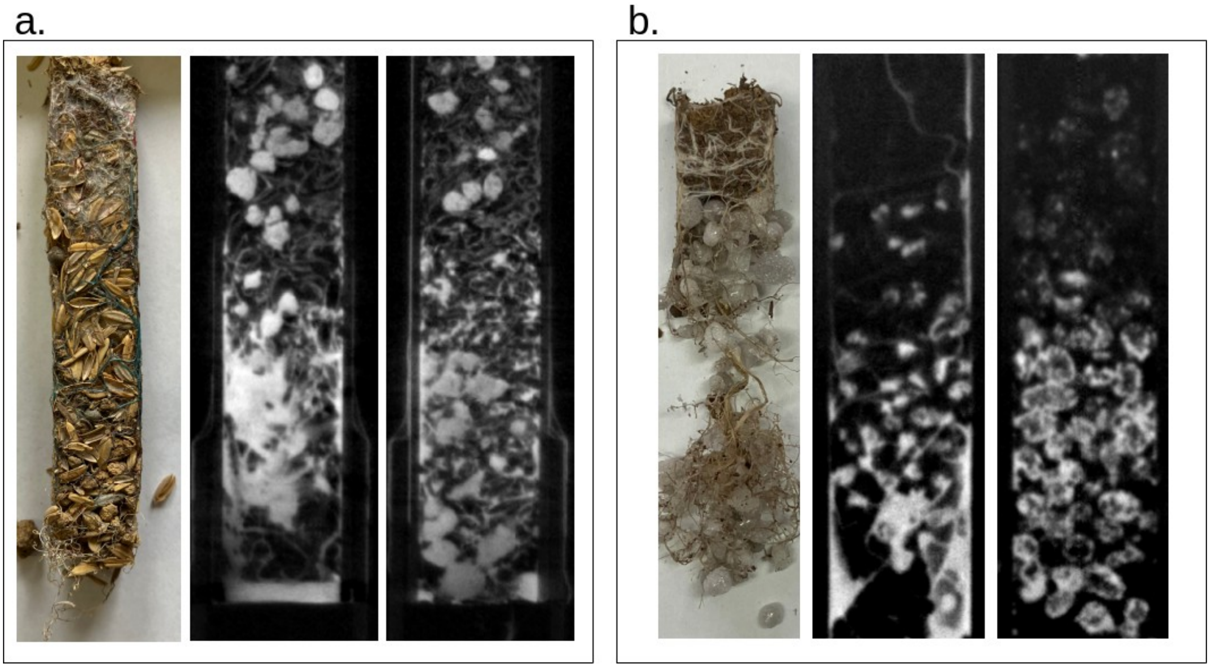

Fig. 1. Root systems of *Brassica rapa* var. “perviridis” (Komatsuna) grown in two culture medium and their neutron CT images.
From the left, root growth in the culture medium, and CT images of the peripheral and central areas of the culture medium. a. rice husks, b. perlite.

PR6-8

In-situ Observation of Lithium Migration in the Lithium-ion Conductor through Neutron Radiography under High-Temperature

S. Takai[1], H. Takagi[1], H. Ezaka[1], T. Yabutsuka[1], N. Odaira[2], D. Ito[2], and Y. Saito[2]

[1]*Graduate School of Energy Science, Kyoto University*
[2]*Institute for Integrated Radiation and Nuclear Science, Kyoto University*

INTRODUCTION: Lithium-ion migration in the solid electrolyte is the essential property for the operation of All-solid-state batteries. While the Li^+ ions migrate from the anode to the cathode through the electrolyte during battery operation, such behavior is hardly visualized due to the light element of lithium ions and the lack of appropriate radio isotopes. We have carried out the lithium diffusion coefficient measurement using the neutron radiography (NR) technique. We have measured the diffusion coefficient from the isotope profiles of the annealed samples by using the large difference in the neutron attenuation factors between ^6Li and ^7Li.

In the present study, we applied the electric field to the model cell to observe the lithium migration in the solid electrolyte employing the NR.

EXPERIMENTS: ^{7}Li-LAGP ($Li_{1.5}Al_{0.5}Ge_{1.5}(PO_4)_3$ using ^7Li) solid electrolyte and ^{6}Li-LMO ($LiMn_2O_4$ using ^6Li) electrode material were prepared by the conventional solid-state reaction method. A test cell consisting of Cu / ^{6}Li-LMO / PEO / ^{7}Li-LAGP / PEO / ^{6}Li-LMP / Al was constructed and electrolyzed at 300°C. Higher temperature operation than the previous (140°C) for the higher mobility of lithium ions. The mounted amount of cathode and anode materials are 3 and 6 mg, respectively. Before, after, and during the electrolysis, NR data were collected by CCD camera at the B4 guide tube in IIRNS, Kyoto University.

RESULTS: Fig. 1 shows the NR images of (a) before and (b) after the electrolysis. The ^{6}Li-containing part (electrode) in the test cell shows a darker image. The intermediate area between the electrodes corresponds to the LAGP electrolyte. Fig. 2 (a) shows the neutron-transmitted intensities of the image before and after the electrolysis. The divided data of (before) / (after) is represented in Fig. 2 (b). The electrolyte in the vicinity of the anode exhibits a little higher values, which indicate the introduction of ^{6}Li at the anode.

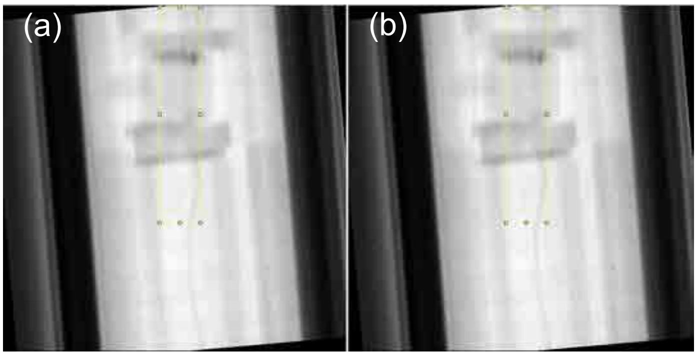

Fig. 1 NR images of test cell consisting of ^{7}Li-LAGP. (a) before and (b) after the electrolysis.

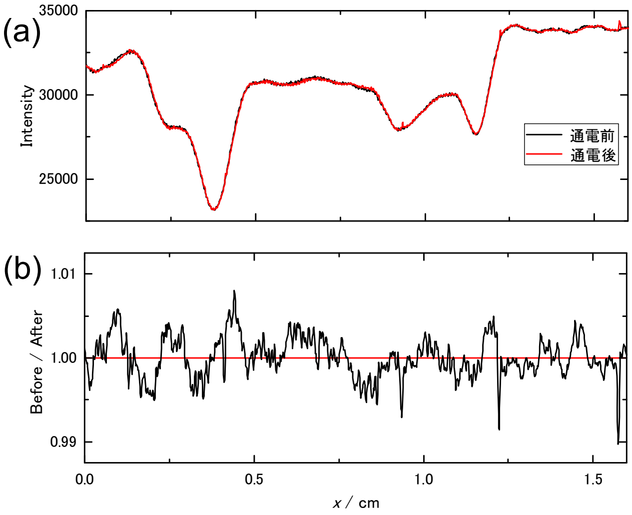

Fig. 2 (a) Neutron intensity profiles for the test cell before and after the electrolysis. (b) Division intensities of the cell.

PR6-9

Measurement of coolant distribution inside a flat laminate vapor chamber Utilizing neutron radiography

K. Mizuta, S. Shibata, Y. Saito[1], D. Ito[1]

Faculty of Engineering, Kagoshima University
[1]Institute for Integrated Radiation and Nuclear Science, Kyoto University

INTRODUCTION: Cooling electronic devices is becoming increasingly difficult due to rapid increase in performance and decrease in size of such devices, so more efficient cooling techniques are required to achieve sufficient reliability. We have been developing a flat laminate vapor cham-ber called FGHP(Fine Grid Heat Pipe) to contribute to tackle thermal problems in this field. In the previous studies, we found that FGHP has the highest thermal performance among various vapor chambers [1], and also found that thermal conductivity of FGHP in planar direction reached as high as 10,000 W m^{-1} K^{-1} at about 360 K [2]. Now we are developing larger size of FGHP than in the previous studies aiming at contributing wider range of applications. In this study, we tried to inves-tigate how the thermal performance of a newly developed FGHP changes with heat input and the change in coolant distribution with heat input by utilizing neutron radiography.

EXPERIMENTS: E-2 port of KUR was utilized for our experiments. Thermal neutron flux at the sample position was about $3x10^5$ cm^2s at 5MW operation. A test sample of FGHP utilized in this experiment was 100 mm square and 8 mm thick. The test sample was set vertically. A CCD camera (BU-53LN, BITRAN Co. Ltd., 4008×2672 pixels) and 6LiFZnS (50 µm thickness) were used. The effective spatial resolution was about 50 µm/pixel due to the scintillator screen characteristics. Neutron imaging of the sample was performed at the 1 MW operation mode and the exposure time was 300 s. Neutron images of the sample were utilized to calculate liquid thickness in the FGHP.

RESULTS: Fig 1 shows the variation of thermal resistance of the test sample with heat input and heater temperature, respectively. Circle key shows the data obtained through increasing heat input, and triangle key shows that obtained through decreasing heat input respectively. This figure shows that thermal resistance decreased with increasing heat input, which was the similar tendency found in our previous results [1]. Fig. 2 shows the variation of liquid thickness with heat input calculated at some points. From this figure, it was found that liquid thickness was almost constant regardless of heat input as found in our previous study [3], which means that the inner structure of a test sam-ple utilized in this study was still adequate enough for effective coolant circulation.

REFERENCES: [1] Mizuta, K., *et al.*, *Applied thermal management*, **104** (2016) 461-471. [2] Mizuta, K., *et al.*, *Ap-plied thermal management*, **146** (2019) 843-853.[3] Mizuta, K., *el al.*, *Physics Procedia*, **69** (2015) 556-563

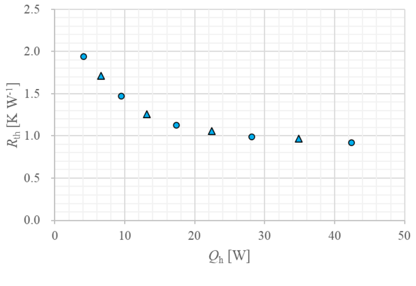

Fig. 1 Variation of thermal resistance with heat input.

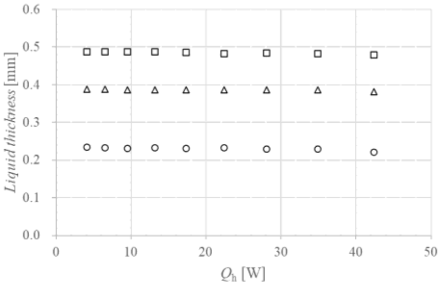

Fig. 2 Variation of liquid thickness of coolant with heater input.
(○:top, □:bottom, △:horizontal average)

I-1. PROJECT RESEARCHES

Project 7

PR7

Estimation for 3D Distribution of Biological and Chemical Doses for BNCT

Y. Sakurai

Institute for Integrated Radiation and Nuclear Science, Kyoto University

BACKGROUNDS AND PURPOSES: For the further advancement of BNCT, it is important to improve the estimation for biological effect due to neutrons. At Heavy Water Neutron Irradiation Facility of Kyoto University Reactor (KUR-HWNIF), the fundamental studies for BNCT in the fields of medicine, biology, chemistry and pharmacology, etc., have been performed. Through these studies, the difficulty in the estimation for neutron biological effects is being acutely realized. In the BNCT irradiation field, it is difficult to monochromatically generate neutrons with a specific energy, and neutrons with the various energy ranges such as thermal, epi-thermal and fast neutrons, and also gamma rays are mixed. Furthermore, the neutron energies and the types and energies of secondary charged particles due to the nuclear reactions in living body are different. The biological effect estimation for BNCT are being studied by multiple groups in the world, but the consistent estimations have not been possible due to the difficulty of estimation for the biological effects, particularly regarding neutrons. The final goal of this project research is to develop a consistent estimation method of the biological effects for BNCT. In 2024, the developments of the estimation method for the 3D dose distribution, focused on the biological and chemical effects were continued. For the biological dose estimation, the estimation methods using three-dimensional co-culture, which can model the structure of living tissues and organs, were mainly studied. For the chemical dose estimation, the estimation methods using chemical dosimeters such as gel dosimeters were studied.

RESEARCH SUBJECTS: The collaboration and allotted research subjects (ARS) were organized as follows;

ARS-1 (R6P7-1: “Establishment of beam-quality estimation method in BNCT irradiation field using dual phantom technique (VIII)”, Y. Sakurai, *et al.*.
ARS-2 (R6P7-2: “Biological effects of BNCT on glioma cells in 3D culture”, N. Kondo and Y. Sakurai.
ARS-3 (R6P7-3: “The response after BNCT on 3D oral cancer model using patient-derived cancer-associated fibroblasts”, K. Igawa, *et al.*.
ARS-4 (R6P7-4: “Verification of BNCT effect on hematological cancer cells and dosimetry for expansion of BNCT cases”, S. Yoshihashi, *et al.*.
ARS-7 (R6P7-7: “Development and evaluation of 3D gel dosimeter for the measurement of dose distribution in BNCT”, S. Hayashi, *et al.*.
ARS-8 (R6P7-8: “Establishment of three-dimensional dose distribution estimation method for BNCT using radiochromic gel dosimeter (II)”, Y. Sakurai, *et al.*.
ARS-10 (R6P7-10: “Measurement of neutron depth distribution for quality assurance in boron neutron capture therapy”, M. Takada, *et al.*.
ARS-11 (R6P7-11: “Measurement of wavelength-dependent luminescence for beam quality assurance of BNCT”, K. Tanaka, *et al.*.
ARS-12 (R6P7-12: “Feasibility of water/fat decomposition technique using multi-energy X-ray computed tomography for BNCT dose calculation”, T. Takata, *et al.*.

ARS-5 (R6P7-5), ARS-6 (R6P7-6), ARS-9 (R6P7-9), ARS-13 (R6P7-13) could not be performed due to the scheduling and preparation issues. So, the reports of these subjects are not appeared.

PR7-1

Establishment of Beam-quality Estimation Method in BNCT Irradiation Field using Dual Phantom Technique (VIII

Y. Sakurai, N. Kondo, T. Takata, H. Tanaka and M. Suzuki

Institute for Integrated Radiation and Nuclear Science, Kyoto University

INTRODUCTION: Before the start of treatment with BNCT, the relative biological effectiveness (RBE) for the fast neutrons incident to the irradiation field must be estimated. Measurements of RBE are typically performed by biological experiments with a phantom. Although the dose deposition due to secondary gamma rays is dominant, the relative contributions of thermal and fast neutrons are virtually equivalent in a water and/or acrylic phantom. Uniform contributions to the dose deposited from thermal and fast neutrons are based in part on relatively inaccurate dose information for fast neutrons. The aim of this study is to establish the accurate beam-quality estimation method mainly for fast neutrons by using two phantoms made of different materials [1]. In 2024, verification experiments for the dual phantom technique were continued using Heavy Water Neutron Irradiation Facility installed in Kyoto University Reactor (KUR-HWNIF) as in the previous year [2].

MATERIALS AND METHODS: One of the dual solid phantoms was made of polyethylene with natural lithium fluoride for 30 weight percent (LiF-polyethylene phantom), and the other phantom was made of polyethylene with 95%-enriched lithium-6 fluoride for 30 weight percent (^{6}LiF-polyethylene phantom). Glioblastoma cells were divided in two groups. One was treated group using p-boronophenylalanine (BPA, containing B-10) for B-10 concentration of 25 ppm, and the other was non-treated group. In addition to the conventional cell suspension, the cell in collagen gel was also prepared. These cell samples were placed at the depths of 0 cm, 2 cm, 5 cm and 8 cm in the phantoms. Figure 1 shows the arrangement of the cell samples within the phantom plate. The depth dose distributions for the thermal neutron, fast neutron and gamma-ray components were determined based on the simulation calculation results normalized referring to the measured values. The epi-thermal neutron irradiation mode was used for the phantom experiments.

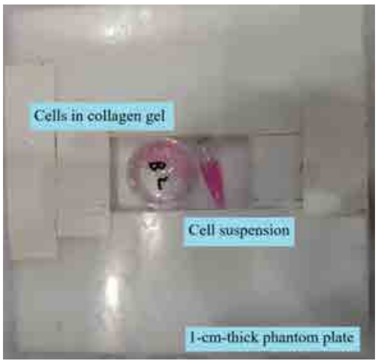

Fig. 1. Arrangement of the cell samples within the phantom plate.

RESULTS: It was confirmed that the survival fraction became smaller as the thermal neutron flux became larger in the LiF-polyethylene phantom. The survival fraction for the non-treated cell was higher than that in BPA-treated cell. In the ^{6}LiF-polyethylene phantom, the survival fraction showed no difference between non-treated and BPA-treated cells. These confirm the results from the previous years, with the same trends observed for the cells in suspension and gel. Incidentally, the differences were observed in the slopes of the dose-survival curves between these cell sample types.

ACKNOWLEDGMENT: This work was supported by JSPS KAKENHI Grant Number JP 24K03082.

REFERENCES:

[1] Y. Sakurai *et al.,* Med. Phys., **42** (2015) 6651-6657.
[2] Y. Sakurai and T. Kobayashi, Nucl. Instr. Meth. A, **453** (2000) 569-596.

PR7-2

Biological effects of BNCT on glioma cells in 3D culture

Natsuko Kondo[1] and Yoshinori Sakurai[1]

[1] *Particle Radiation Oncology Research Center, Institute for Integrated Radiation and Nuclear Science, Kyoto University (KURNS)*

INTRODUCTION: Boron Neutron Capture Therapy (BNCT) have been applied to recurrent malignant glioma and even after standard therapy (surgery, chemo-radiation therapy) because of the selective damage to the tumor. Especially, glioblastoma (GBM) is the most miserable cancer, whose patient survival is 14.6 months and remarkably resistant to chemo-radiation and immuno-therapy. With BNCT, we achieved better local control and survival benefit in malignant glioma using thermal neutrons produced by the reactor in Kyoto University. However, the recurrence locally or dis-tantly is inevitable after BNCT. To clarify the underlying mechanism in recurrence of glioma after BNCT is an urgent issue. On the other hand, 3D culture is more advanced and useful method than 2D culture to recapitulate the in vivo situation. Therefore, we firstly investigated the biological ef-fects of BNCT on glioma cells in 3D culture and compared with 2D culture.

EXPERIMENTS:

Cells:

We used mouse glioma GL261 cells. They were cultured in DMEM with 10% heat-inactivated fetal bovine serum in 5 % CO_2 incubator. For the adherent 2D culture, cells were disseminated on the tissue-treated 6-well plates. For 3D culture, cells were suspended in the mixture of Cell matrix type 1A collagen (3mg/ml, pH 3), 5 x DME concentrated culture medium and the reconstitution buffer on ice, according to the manufacturer's protocol (Nitta Gelatin, Osaka Japan). Next, the suspended cells in the 500 µL of collagen solution were disseminated into each well of a 24-well plate and placed in the 5 % CO_2 incubator at 37 °C for 30 minutes for gel formation. Then, 500 µL of DMEM was poured over the gel. The DMEM was changed every three or four days.

p-Boronophenylalanine (BPA) treatments:

~~For 2D culture, BPA was added to the cult~~ure medium at 0 to 20 ppm final concentration, two hours before irradiation. For 3D culture, medium was changed to BPA containing DMEM (0 to 20 ppm), the day before irradiation. The medium was removed just before irradiation.

Neutron irradiation

We irradiated thermal neutrons for 5 minutes to the glioma cells in 2D culture, and 50 minutes to the glioma cells in 3D culture using the heavy water neutron irradiation facility in KUR. The cells was placed in 5 % CO_2 incubator with fresh DMEM after irradiation.

Sampling

One week after irradiation, we counted the survived cells. To suspend the cells, for 2D culture, we treated the cells with trypsin. For 3D culture, we treated collagenase to dissolve the collagen gel.

RESULTS:

The higher the BPA concentration, the lower the surviving rate. Compared with 2D culture, the glioma cells in 3D culture were resistant.

PR7-3

The Response After BNCT on 3D Oral Cancer Model Using Patient-Derived Cancer-Associated Fibroblasts

K.Igawa, I.Yamamoto[1], N.Kondo[2], M.Suzuki[2] and Y.Sakurai[2]

Neutron Therapy Research Center, Okayama University

[1]Department of Oral and Maxillofacial Surgery, Okayama University Graduate School of Medicine, Dentistry and Pharmaceutical Sciences

[2]Institute for Integrated Radiation and Nuclear Science, Kyoto University, Particle Radiation Oncology Research Center

INTRODUCTION: Cancer-associated fibroblasts (CAFs) are one of the most important components of tumor microenvironment (TME). Many studies have revealed that CAFs promote cancer progression, invasion, metastasis, and treatment resistance. In this study, we developed a three-dimensional oral cancer model with patient-derived CAFs and oral cancer cells, and to simulate the TME. We aimed to investigate radiation-induced effects on CAFs using X-ray irradiation and BNCT.

EXPERIMENTS: A 3D oral cancer model was fabricated using our previously reported protocol. The 3D oral cancer models were consisted of two layers; a stromal layer composed of either patient-derived normal oral fibroblasts (NOFs) or patient-derived cancer-associated fibroblasts (CAFs) (provided by Niigata University) and a cancer layer using the oral cancer cell line HSC-4 (JCRB0624). ***X-ray irradiation:*** 3D models were irradiated at single doses of 0, 5, 10 and 20 Gy using an X-ray desktop-operated machine at Okayama University. ***Neutron irradiation:*** Neutron beams were applied at the Heavy Water Neutron Irradiation Facility of KUR at 1MW operation for 0, 20 and 40 minutes. 10% BPA-supplemented medium was added 24 hours before irradiation. ***Histological analysis:*** The samples were collected 5 days after irradiation and stained with Masson's trichrome for histological evaluation.

RESULTS: Figure 1 shows the Masson's trichrome stained histopathological specimen including 0, 5, 10, and 20 Gy of X-ray irradiation (i) and 0-, 20-, 40-minute neutron irradiation (ii). After BNCT was conducted, a decline in the depth of cancer cell invasion in 3D cancer-CAFs model was observed (Figure 2 (i)), which didn't significantly change after X-ray irradiation (Figure 2 (ii)) [1].

Figure 1

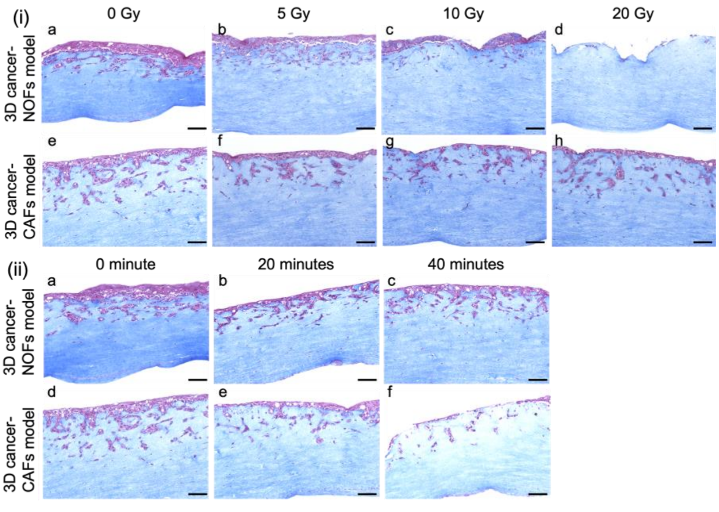

Figure 2

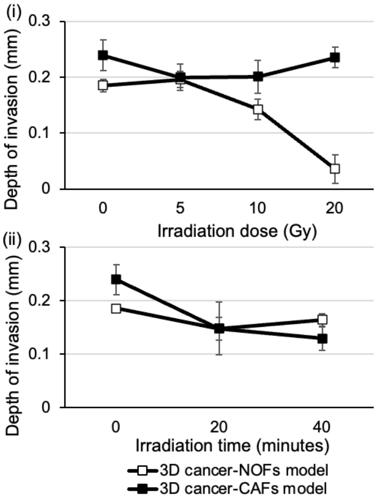

REFERENCES:

[1] I. Yamamoto *et al*., Int. J. Transl. Med., **5** (2025) 12.

PR7-4

Verfication of BNCT Effect on Hematological Cancer Cells and Dosimetry for Expansion of BNCT Cases

S. Yoshihashi, O. Suzuki, T. Kasai, Y. Sakurai[1], A. Uritani, K. Tsuchimoto, A. Niimi, K. Tsuchida, T. Nishitani

Graduate School of Engineering, Nagoya University
[1]Institute for Integrated Radiation and Nuclear Science, Kyoto University

INTRODUCTION: The number of newly diagnosed patients with major hematologic cancers (malignant lymphoma, multiple myeloma, and leukemia) in Japan was 58,547 in 2019 [1], and 5,853 hematopoietic stem cell transplants were performed in FY2022 as the last treatment option for these refractory hematologic cancer patients [2]. While autologous transplantation is a desirable medical technique for patients because it does not require long-term administration of immunosuppressive drugs and prevents immune reactions (GVHD) caused by HLA incompatibility, the grafts contain tumor cells, which must be removed and treated with chemotherapy and radiotherapy, which are pre-treatment procedures. We are now conducting basic research to remove tumor cells in grafts by Ex Vivo BNCT. In this study, the response of PVA-GTA-I gel dosimeter to thermal neutrons, fast neutrons, and gamma-ray was evaluated to use the gel dosimeters for dose assessment in cell bags.

****

EXPERIMENTS: PVA-GTA-I gel is prepared by adding PVA as the main component, KI as the reactant, Fructose as the reducing agent, GTA as the gelator, and GDL as the gelation promoter by adding GTA. In this study, 100 mM of B-$(OH)_3$ was added to PVA-GTA-I gel to make it sensitive to thermal neutron beams. The prepared gels were sealed in an optical cell with a 1 cm optical path length.

Two irradiation systems were prepared: System A, in which an optical cell was placed in the beam direction, and System B, in which a Teflon plate containing LiF, which absorbs thermal neutrons, was placed in front of System A to remove the thermal neutron component.

In both systems A and B, irradiation was performed using the KUR heavy water irradiation facility, and the irradiation time was 60 minutes. The 486 nm absorbance of each of the neutron-irradiated gels was measured using a UV-visible spectrophotometer.

****

RESULTS: The distribution of absorbance in the depth direction in system A and B shows that the PVA-GTA-I gel with B-$(OH)_3$ is sensitive to thermal neutron radiation. The total dose was assumed to be the sum of thermal neutrons, fast neutrons, and gamma ray radiation, and the response of PVA-GTA-I gel to each dose was determined. The response to thermal neutron was calculated from the difference in sensitivity between System A and System B. The response to gamma ray was calculated using the results of calibration experiment using a ^{60}Co source. These results indicate the potential use of gel dosimeters for dose assessment within cell backing.

****

REFERENCES:

[1] National Cancer Center (Japan), Current Cancer Statistics, https://ganjoho.jp/reg_stat/statistics/stat/summary.html (2024.02.19).
[2] Japan Hematopoietic Cell Transplantation Center (JDCHCT): Hematopoietic Cell Transplantation in Japan Annual Report of Nationwide Survey 2022, http://www.jdchct.or.jp/data/report/2022/ (2024.02.19).

PR7-5

Development and evaluation of 3D gel dosimeter for the measurement of dose distribution in BNCT

S. Hayashi, Y. Sakurai[1], M. Suzuki[1], T. Takata[1], and R. Narita[2]

Faculty of Health Sciences, Hiroshima International University
[1] *Institute for Integrated Radiation and Nuclear Science, Kyoto University*
[2] *Graduate school of Engineering, Kyoto University*

INTRODUCTION: Three-dimensional (3D) gel dosimeters have been developed for the 3D dose measurement of the complex conformal dose distributions in radiation therapy [1]. These devices are composed of radio-sensitive substances and an aqueous gel matrix to preserve spatial information about the absorbed dose. The 3D absorbed dose distribution is deduced from the distribution of the reaction products measured by 3D imaging modalities such as MRI and Optical CT. In previous studies, we have developed a PVA-GTA-I radiochromic gel dosimeter that utilizes red color development due to the complex formation of polyvinyl alcohol (PVA) and iodide [2]. In this work, to compare the neutron sensitization effect with that of ^{10}B, gadolinium contrast agent for MRI was added to the gel dosimeter in different concentrations and the response to a neutron beam from a nuclear reactor was evaluated.

EXPERIMENTS: The PVA-GTA-I gel dosimeter is composed of partially saponified PVA, potassium iodide (KI), glutaraldehyde, fructose, glucono-δ-lactone, and water. As a thermal neutron sensitizer, a Gd contrast agent (Gadovist®) was added into the gel dosimeters. The resulting solution was subdivided by pouring into PMMA cuvettes (4.5 mL, 1 cm path length). The neutron irradiations were performed using the HWNIF of KURR (1 MW) in the air at room temperature. The three different modes (mixed, thermal, and epi-thermal modes) of neutron beams made by heavy water spectrum shifter and cadmium thermal-neutron filters were applied to the samples. After irradiation, the response was evaluated on the change in absorbance at the absorption peak wavelength (486 nm) using a UV-Vis spectrophotometer.

RESULTS: Figure 1 shows the samples irradiated in each mode and the change in absorbance with respect to the Gd concentration. In all cases, the addition of a small amount of Gd caused a rapid increase in color development. For example, in the mix mode, even with 10 mM Gd, the response was approximately 6 times higher than that of the unadded sample. On the other hand, the increase in absorbance was almost saturated at 50 mM or more. ^{157}Gd has an absorption cross section for thermal neutrons that is about 60 times larger than that of ^{10}B. These results indicate that ^{157}Gd contained in the contrast agent can be stably added to the radiochromic gel dosimeter, enabling it to detect thermal neutrons with higher sensitivity.

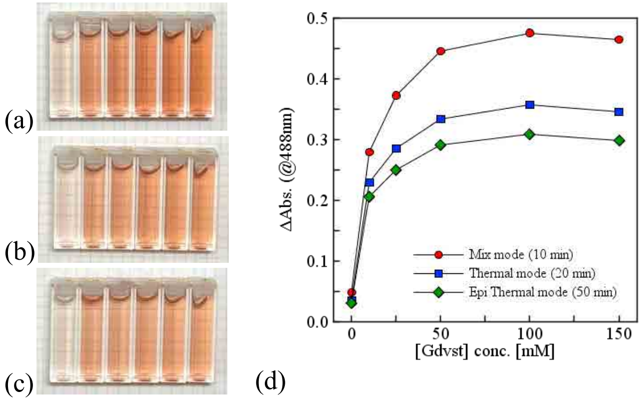

Figure 1 (a), (b), and (c) are PVA-GTA-I gel samples containing different concentrations of Gd (from left to right: 0, 10, 25, 50, 100, and 150 mM) irradiated in mixed, thermal, and epi-thermal modes, respectively. (d) shows their absorbance changes.

REFERENCES:

[1] Y. De Deene, Gels, **8** (2022) 599.
[2] S. Hayashi *et al.,* J. Phys.; Conf. Ser., **2167** (2022) 012014.

PR7-6

Establishment of Three-dimensional Dose Distribution Estimation Method for BNCT using Radiochromic Gel Dosimeter (II

Y. Sakurai, R. Narita[1], J. Prateepkaew[1] and T. Takata

Institute for Integrated Radiation and Nuclear Science, Kyoto University
[1]Graduate School of Engineering, Kyoto University

INTRODUCTION: Development in accelerator-based irradiation systems for BNCT is underway. BNCT using newly developed accelerator systems is being implemented at multiple facilities around the world. However, there are still issues that need to be improved for further advancement of BNCT. The advancement of dose estimation is one of these, and the estimation of biological dose is particularly important. As part of the advancement of biological dose estimation for BNCT, we focus on chemical effects, which are the precursor to biological effects. We are studying on the estimation method using chemical dosimeters, especially gel dosimeters. Gel dosimeters are made of materials similar to living tissue and can be formed into any shape. Using a phantom made from gel dosimeter that models human body, three-dimensional dose distribution estimation becomes possible. Among the various types of gel dosimeters, we are especially focusing on “radiochromic gel dosimeters” that can be read out using optical CT, etc.. The purpose of this study is to establish three-dimensional dose distribution estimation method for BNCT using multiple types of radiochromic gel dosimeters. In 2024, the characterization for micellar gel dosimeters was continued.

MATERIALS AND METHODS: Leucocrystal violet (LCV) was selected as dye of micelle gel dosimeters, because it is extremely clear before irradiation, based on our previous study [1]. The micelle gel dosimeters were prepared based on 1 mM of LCV in the 96% water and 4% gelatin according to the method of Babic et al. [2]. For dose rate independency and temporal coloration reduction, the type and concentration of surfactant and sensitizer were changed. In addition, boric acid or urea was added for the estimation of boron or nitrogen dose components, referring to Gambarini et al. [3]. Furthermore, a dosimeter in which heavy water was replaced with light water was also prepared to estimate hydrogen dose component [4]. The amount of additives was based on our previous study. The characterization experiments were mainly performed using Heavy Water Neutron Irradiation Facility of Kyoto University Reactor (KUR-HWNIF) [5]. In the experiments, three irradiation modes, such as the standard mixed neutron irradiation mode, the standard epi-thermal neutron irradiation mode and the standard thermal neutron irradiation mode, were used. The absorbance of the gel dosimeters after the irradiation was measured at the peak wavelength of 600 nm using a spectrophotometer (V730-Spectrophotometer, Japan Spectroscope Co., Ltd.).

RESULTS: From the experiment results, it was confirmed that the dose response of each gel dosimeter depended on the linear energy transfers (LETs) of the particles produced in each dosimeter. Using these results, the factors for dose-component discrimination method were determined and verified for different energy spectra, and the validity was confirmed.

REFERENCES:

[1] R. Narita and Y. Sakurai, J. Phys: Conf. Ser., **2630** (2023) 012016.
[2] S. Babic *et al.,* Phys. Med. Biol., **54** (2009) 6791-6808.
[3] G. Gambarini *et al.,* Nucl. Instrum. Meth. A, **353** (1994) 406-410.
[4] G. Gambarini *et al.,* IEEE Trans. Nucl. Sci., **48** (2001) 780-784.
[5] Y. Sakurai and T. Kobayashi, Nucl. Instr. Meth. A, **453** (2000) 569-596.

R6P7-8

PR7-7

Measurement of Neutron Depth Distribution for Quality Assurance in Boron Neutron Capture Therapy

M. Takada, K. Kamimura[1], K. Harada[1], H. Endo[2], Y. Shuto[2], S. Nishina[2], Y. Sakurai[3], H. Tanaka[3], T. Takata[3], S. Nakamura[2]

National Defense Academy of Japan
[1] *National Defense Academy of Japan*
[2] *National Cancer Center Hospital*
[3] *Institute for Integrated Radiation and Nuclear Science, Kyoto University*

INTRODUCTION: Thermal neutron depth distributions in acrylic and water phantoms have been generally measured using a gold neutron activation analysis for conducting quality assurance (QA) program in boron neutron capture therapy. For evaluation of thermal neutron distribution, radioactivity of gold wires are measured by using a high purity germanium detector, and gold wires are covered with and without a cadmium case to measure thermal neutron contribution in each measurement point. Hence, huge amount of medical staff manpower and time are required to perform the QA program. Thus, a simpler and less costly technique of measuring the depth distributions in the phantom is required to improve frequency and time of the QA procedure.

In this study, a technique of easy-to-use aluminum indirect neutron computed radiography was applied to measure the in-phantom 2D thermal neutron depth distribution to improve the BNCT QA procedure.

EXPERIMENTS: The neutron depth distributions were measured to verify this technique at heavy water irradiation facility. The aluminum sheet was inserted into an acrylic phantom with 300×300×300 mm. Neutron beam was irradiated to the aluminum sheet in the acrylic phantom for 10 minutes (5MW), then the radioactivated aluminum sheet was exposed to an imaging plate (IP). The neutron-induced radioactivity distribution in the aluminum was transferred to the IP. The radioactivity distribution on the IP was scanned by the IP reader. By just one neutron irradiation, the neutron depth distributions of 0-300 mm in depth and further offset neutron depth distributions were obtained. In addition, the neutron depth distribution was measured by the gold neutron activation method to verify this research result.

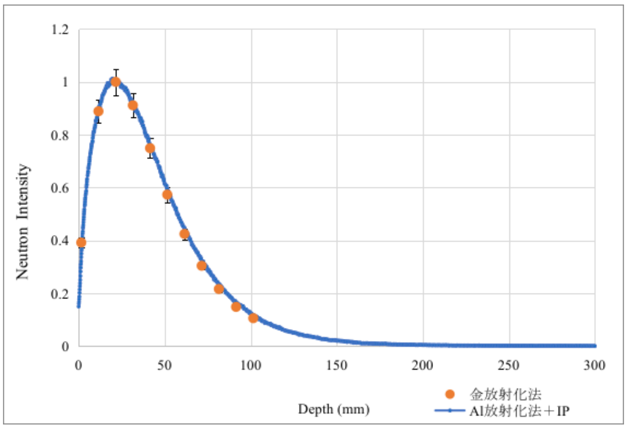

Fig. 1. Comparison of depth neutron distribution using aluminum- and gold-activation methods.

RESULTS: Figure 1 shows the measured neutron depth distribution at neutron beam center, as a solid line. The distribution is compared with the gold saturation radioactivity, shown as closed circles. The distributions were normalized at the peak around the 20-mm depth. The experimental depth distribution shows the neutron peak of 19.7 mm with FWHM of 54.5 mm. Both experimental results were in good agreement. The ratio of the aluminum to the gold neutron activation results showed 1.0–1.06 in the 0-80 mm depths. Based on the agreement within 0-6% difference, the aluminum neutron activation method was validated to measure the neutron depth distribution of BNCT neutron beam in the acrylic phantom. Although relative neutron distributions were obtained using this method, an absolute neutron distribution could be obtained with the help of the gold activation method.

Measurement of wavelength-dependent luminescence for beam quality assurance of BNCT

Kenichi Tanaka, Yoshinori Sakurai[1], Takushi Takata[1], Hiroki Tanaka[1]

Laboratory of Physics, Kyoto Pharmaceutical University
[1]Institute for Integrated Radiation and Nuclear Science, Kyoto University

INTRODUCTION: In boron neutron capture therapy, measurement of beam fluence spatial distribution is required for quality assurance in the irradiation field. Previously, the imaging plate was tested for usage in this purpose[1]. The luminescence material for imaging plate, BaFBr:Eu, has multiple peaks in its excitation spectrum[2]. The dependence of the quantity of the luminescence on the wavelength of the excitation light, or possibly luminescence, will specify the beam quality. Thus, this study investigated the use of the luminescence for measurement of both quantity and quality of the radiation. A candidate of the luminescent material, BaFBr:Eu, has been proposed[3]. In this report, additional candidate was been surveyed to improve the measurement of beam quality.

EXPERIMENTS: As candidates, BeO, Al_2O_3:Cr, and Al_2O_3:CrMnCo were tested. The samples were irradiated with gamma rays from ^{60}Co, and neutrons and gamma rays at the standard mixed neutron irradiation mode of Kyoto University Reactor Heavy Water Neutron Irradiation Facility[4] at 1 MW of the power. In the latter, the samples were driven with Irradiation Rail Device. The dependence of the fluorescence quantity on the wavelength was measured with the fluorescence spectrofluorometer (Hitachi corporation, F-2700).

RESULTS: An example of the excitation spectrum is shown in Fig. 1 for Al_2O_3:Cr, and Al_2O_3:CrMnCo. The ratio of the luminescence quantity by excitation at 458 nm to that at 550 nm is about 10-20% lower for KUR than that for Co, where the uncertainty of the measured ratio is several %. Though the figure is not shown, the luminescence spectra for Al_2O_3:Cr and Al_2O_3:CrMnCo suggest the dependence of the quantity of the luminescence on the wavelength of the excitation light for Al_2O_3:Cr, and Al_2O_3:CrMnCo possibly indicates the quality of the irradiated beam. In this case, the spectrum does not show apparent difference between KUR and Co in this case. Also, the results for BeO did not show the spectrum with the peaks at proper wavelength. This may be because the samples are in glass tube, and the placement of the samples in the analyzer was not proper. Thus, the attempt to measure the beam quantity by using the luminescence dependence on wavelength is undergoing for usage of BAS-TR and fabricated BaFBr:Eu mainly, and Al_2O_3:Cr and Al_2O_3:CrMnCo as additional options to improve the identification.

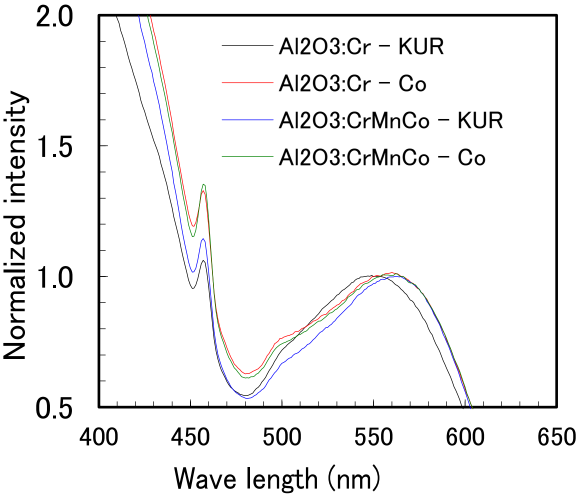

Fig. 1. Excitation spectrum

REFERENCES:
[1] K. Tanaka *et al.*, Appl. Rad. Isot., **115** (2016)212-220.
[2] K. Abe, Rad., **25** (1999)31-49. (in Japanese).
[3] K. Tanaka *et al.,* KURNS. Prog. Rep., 2023 (2024) 71.
[4] Y. Sakurai *et al.,* NIM, **A453** (2000)569-59.

Feasibility of Water / Fat Decomposition Technique Using Multi-Energy X-ray Computed Tomography for BNCT Dose Calculation

T. Takata, Y. Tamari[1], Y. Sakurai, H. Tanaka and M. Suzuki

Institute for Integrated Radiation and Nuclear Science, Kyoto University
[1] School of Medical Sciences, Fujita Health University

INTRODUCTION: The Monte Carlo method is frequently used in dose calculations for Boron Neutron Capture Therapy (BNCT), where radiation transport calculations are conducted by specifying material information for each tissue in the body, such as density and elemental composition. Traditionally, reference values from literature, like those in ICRU Report 44 and 46, are assigned as fixed values [1, 2]. However, this approach fails to capture detailed material information, such as variations among patients or the precise distribution of water/fat content in tissues and organs. In this study, we aim to develop a method for quantitatively evaluating material density and water/fat content using data obtained from multi-energy X-ray Computed Tomography (CT), and to incorporate this material information into dose calculations. We examined the feasibility of water/fat decomposition by fundamentally estimating differences in attenuation coefficients by X-ray energy.

MATERIALS AND METHODS: The X-ray CT system (ECLOS-4, Hitachi, Ltd.) installed at KURNS is the subject of this study. The X-ray tube voltage can be selected from 100, 120 and 130 kV in the system. The linear attenuation coefficients of water, soft tissue, muscle, and adipose tissue were derived and compared at each of these tube voltages. The density and elemental composition of each material were obtained from the reference values in ICRU Report 44 [1]. The attenuation coefficients for the estimated X-ray energy spectrum of each tube voltage were derived from the mass attenuation coefficient dataset from NIST [3].

RESULTS: The estimated linear attenuation coefficients for each material are presented in Table 1. Due to the increased photoelectric effects induced by low-energy photons, the attenuation coefficients for all substances were higher at lower tube voltages. This difference is greater in adipose tissue compared to other tissues. When comparing the coefficients for water or soft tissue at 130 kV and 100 kV, the difference was 5.5%, whereas for adipose tissue, it was 4.2%. This system confirmed that a difference in CT values of approximately 1% is necessary between 100 and 130 kV tube voltages to differentiate between water and fat composition in tissues. Based on these findings, further studies on CT imaging conditions will be conducted.

Table 1 X-ray linear attenuation coefficients of the CT system.

Tube voltage	**Linear attenuation coefficient [cm^{-1}]**			
[kV]	Adipose Tissue	Muscle Skeletal	Tissue Soft	Water Liquid
100	1.97×10^{-1}	2.32×10^{-1}	2.34×10^{-1}	2.22×10^{-1}
120	1.91×10^{-1}	2.23×10^{-1}	2.26×10^{-1}	2.14×10^{-1}
130	1.89×10^{-1}	2.20×10^{-1}	2.22×10^{-1}	2.10×10^{-1}

REFERENCES:

[1] International Commission on Radiation Units and Measurements (ICRU) Report 44 (ICRU, Bethesda, MD, 1989).
[2] International Commission on Radiation Units and Measurements (ICRU) Report 46 (ICRU, Bethesda, MD, 1992).
[3] J. H. Hubbell and S. M. Seltzer, X-Ray Mass Attenuation Coefficients, NIST Standard Reference Database 126.

R6P7-12

I-1. PROJECT RESEARCHES

Project 8

PR8

Advancement of radiation detectors aimed at application in accelerator BNCT

H. Tanaka

Institute for Integrated Radiation and Nuclear Science, Kyoto University

BACKGROUNDS AND PURPOSE: With the initiation of insurance-covered treatments using accelerator-based BNCT systems at medical institutions, the number of BNCT cases is expected to increase significantly. As part of the quality assurance (QA) and quality control (QC) processes for clinical treatments, it is necessary to measure the thermal neutron flux and gamma-ray dose prior to irradiation. Currently, conventional methods developed for reactor-based BNCT, such as the gold foil activation technique and thermoluminescent dosimeters (TLDs), are still in use. However, these methods are complex, and the continued availability of TLDs is uncertain. Consequently, there is a strong demand from medical institutions for simplified, yet highly accurate, measurement techniques.

Furthermore, there is an increasing need for the development of advanced radiation detectors applicable to BNCT, including those capable of measuring epithermal and fast neutron fluxes, prompt gamma emissions, and neutron energy spectra. In response to these demands, this project aims to enhance radiation detector technologies for practical application in accelerator-based BNCT systems.

RESEARCH SUBJECTS:

R6P8-1: Study on the Measurement of Neutron Fluence and Gamma-ray Distributions Using a Combination of Thermoluminescent Plate and Converter (K. Shinsho *et al.*)

R6P8-2: Comparison of optical observation of boron dose by using of boron-added liquid scintilla-tors: a property of Insta-Fluor Plus (A. Nohtomi *et al.*)

R6P8-3: Development and demonstration of a Bonner sphere spectrometer and investigation on neutron dose measurement with a modified neutron servey meter (A. Masuda *et al.*)

R6P8-4: Radiation quality evaluation method for neutron irradiation field (N. Hu *et al.*)

R6P8-5: Evaluation of response characteristics of semiconductor detectors in neutron irradiation field (N. Hu *et al.*)

R6P8-6: Development of Scintillator for Thermal Neutron Detector in BNCT (N. Matsubayashi *et al.*)

R6P8-7: Study of Optically Stimulated Luminescent Dosimeter in BNCT Irradiation Field (N. Matsubayashi *et al.)*

R6P8-8: Establishment of Characterization Estimation Method in BNCT Irradiation Field using Bonner Sphere and Ionization Chamber (VIII) (Y. Sakurai *et al.*)

R6P8-9: Development of Real-time Boron-concentration Estimation Method using Gamma-ray Telescope System for BNCT (III) (Y. Sakurai *et. al,*)

R6P8-11: 4H-SiC Neutron Image Sensor for Boron Neutron Capture Therapy（V. T. Ha *et. al,*)

R6P8-12: Improvement of the SOF detector system for energy-dependent discrimination and long-term stability (M. Ishikawa *et al.)*

R6P8-13: Etch Pit Analysis of Solid-State Nuclear Track Detectors Using a 3D Confocal Laser Microscope for Fast Neutron Dosimetry in BNCT (T. Takata *et al.*)

R6P8-14: Development of a Real Time Dose Rate Monitor for BNCT Using Novel Scintillation Materials (S. Kurosawa *et al.*)

R6P8-15: Measurement of Current-to-Flux Ratio in Neutron Fields for BNCT (I. Murata *et al.*)

R6P8-16: Performance Evaluation of a Real-Time Thermal Neutron Detector for BNCT (H. Tanaka *et al.*)

R6P8-17: Characterization of a Thermal Neutron Detector for Measuring the Shielding Performance of Thermal Neutron Shielding Materials (H. Tanaka *et al.*)

Research subjects R5P9-1,4-7, 11,13,15, and 17 are research and development on methods to measure thermal and fast neutrons and γ-rays. R5P9-2 and 9 propose methods to obtain boron distributions in realtime. R5P9-3,8, and 12 propose new methods for measuring neutron spectra. R5P9-14, and 16 have succeeded in obtaining real-time measurements of gamma rays, thermal and epithermal neutrons in the irradiation field of BNCT. All of them are expected to be applied to accelerator BNCT.

R6P8

PR8-1

Study on the Measurement of Neutron Fluence and Gamma-ray Distributions Using a Combination of Thermoluminescent Plate and Converter

K. Shinsho, M.Kawane, L.Takahashi, H. Tanaka[1], T. Takata[1], S. Matsumoto, G. Wakabayashi[2], G. Okada[3], Y. Koba[4]

Graduate School of Human Health Science, Tokyo Metropolitan University

[1] Research Reactor Institute, Kyoto University
[2] Graduate school of Science and Engineering Research, Kindai University
[3]Co-creative Research Center of Industrial Science and Technology, Kanazawa Institute of Technology
[4]Center for Radiation Protection Knowledge, QST-NIRS

INTRODUCTION: Boron Neutron Capture Therapy (BNCT) is one of the radiation therapies that uses neutrons and ^10B drugs, which accumulate in tumors. BNCT is expected to be a next-generation cancer therapy that can improve patients' quality of life (QOL), as it enables selective irradiation of cancer cells at the molecular level. However, dosimetry techniques in mixed neutron–gamma fields have not yet been established. Therefore, in this study, we focused on the measurement of neutrons and gamma rays using a two-dimensional thermoluminescence dosimeter (2D-TLD).We have previously reported that the thermoluminescence (TL) of a Cr-doped Al_2O_3 ceramic plate sandwiched between Cd plates can selectively measure the thermal neutron fluence in a BNCT irradiation field without being affected by mixed γ-rays [1,2], and that the TL characteristics of a high thermal conductivity type BeO ceramic plate (Na-undoped) can selectively measure the γ-ray fluence without being affected by neutrons [2,3].

In this study, we investigated a new method for selective fast neutron measurement using a novel thermoluminescent plate combined with a converter based on the elastic scattering reaction between fast neutrons and hydrogen atoms.

EXPERIMENTS: A 3 mm thick polyethylene converter was placed in front of a BeO ceramic plate (11 mm square) and affixed using heat-shrink film. Irradiation was conducted using both the epi-thermal mode and the mixed mode. Three BeO ceramic plates with the converter and three without it were each irradiated for one hour. In the mixed mode, a 3 mm thick LiF plate was used to eliminate thermal neutrons, which would otherwise act as noise.

RESULTS: A comparison of the TL responses of BeO ceramic plates with and without the converter is shown in Table 1. In the epi-thermal mode, except for sample No.10, the plates with the converter exhibited approximately 13% higher TL responses, indicating an increase attributable to fast neutrons. Only sample No.10 showed a lower TL response, which is likely due to insufficient contact between the converter and the ceramic plate.

Table 1. TL responses of BeO ceramic plates with and without converter

Epi-thermal mode				
converter	No.	TL intensity	Ave.	S.D.
Without	BeO07	6699597	6637626	58620
	BeO08	6630220		
	BeO09	6583061		
With	BeO10	6265652	7196678	811354
	BeO11	7571694		
	BeO12	7752687		
converter	No.	TL intensity	Ave.	S.D.
Without	BeO13	9328973	9775622	425445
	BeO14	9821797		
	BeO15	10176097		
With	BeO16	9441903	9345213	86850
	BeO17	9273821		
	BeO18	9319916		

In contrast, in the mixed mode, no significant difference in TL response was observed between plates with and without the converter. This may be due to the relatively smaller contribution of fast neutrons to the TL response, as a large proportion of γ-rays is present in the mixed mode, and possibly due to insufficient shielding of thermal neutrons. Further evaluation will be conducted by comparing these results with Monte Carlo simulation data to assess the utility of the method.

REFERENCES:

[1] R. Oh, K. Shinsho *et al.,* Sens. and Mater., **33(6)** (2021) 2129-213.
[2] K. Shinsho *et al.,* Jpn. J. Appl. Phys., **62** (2023) 010502.
[3] M.Tanaka *et al.,* J. Mater. Sci.: Mate. Elec., **33** (2022) 20271–20279.

PR8-2

Comparison of optical observation of boron dose by using of boron-added liquid scintillators: a property of Insta-Fluor Plus

A. Nohtomi, H. Maeda, A. Moriguchi, H. Moriguchi, G. Wakabayashi[1], Y. Sakurai[2], H. Tanaka[2] and T. Takata[2]

Graduate School of Medicine, Kyushu University
[1]Atomic Energy Research Institute, Kindai University
[2]Institute for Integrated Radiation and Nuclear Science, Kyoto University

INTRODUCTION: For boron-neutron capture therapy (BNCT), the information of boron dose plays a significant role. In our previous paper [1], a boron-added liquid scintillator has been proved to be very useful for the direct evaluation of boron dose by observing the luminescence with a CCD camera during the neutron irradiation. In that paper, as an attempt, we dissolved trimethyl borate in a commercially-available liquid scintillator, Insta-Gel Plus. Hence, at the last machine time, we tested other two types of liquid scintillators and the results inferred a possibility of high light-output yield when using Insta-Fluor Plus from the view point of its chemical composition. In the present work, in addition to other three types of commercially-available liquid scintillators, Insta-Fluor Plus was examined as boron-added liquid scintillator for comparison.

EXPERIMENTS: We dissolved trimethyl borate in four types of commercially-available liquid scintillator (Insta-Fluor Plus, Insta-Gel Plus, Ultima Gold XR and Ultima Gold F: Perkin Elmer) approximately 1 wt% in natural boron concentration. The main component of Insta-Gel Plus is pseudocumene with a certain amount of addition of alkylphenol polyglycol ether as emulsifier. On the other hand, Insta-Fluor Plus is made of mainly sole pseudocumene. The main component of Ultima Gold XR is diisopropyl naphthalene isomers with a certain amount of addition of alkylphenol polyglycol ether as emulsifier. On the other hand, Ultima Gold F is made of mainly sole diisopropyl naphthalene isomers. The boron-added liquid scintillator was filled in a quartz bottle phantom and was irradiated by thermal neutrons (~10^5 n/cm^2/s) during 150, 300 and 450 seconds at E-3 irradiation port [2]. Luminescence of each boron-added liquid scintillator was observed by a cooled CMOS camera (Bitran, CS-67M) during the irradiation in a black box.

RESULTS: The luminescence were clearly observed for all types of boron-added liquid scintillators for 450 seconds irradiation. The luminance was proportional to the irradiation time as indicated in Fig. 1 for all types of boron-added liquid scintillators. However, the luminance was different for each type of liquid scintillator. Contrary to our inference, the luminescence of Ultima Gold F was the brightest among the four and approximately 1.6 times higher than that of Insta-Gel Plus. And, unexpectedly, the luminescence of Insta-Fluor Plus was approximately equivalent to that of Ultima Gold XR and was approximately 80 % of that of Insta-Gel Plus.

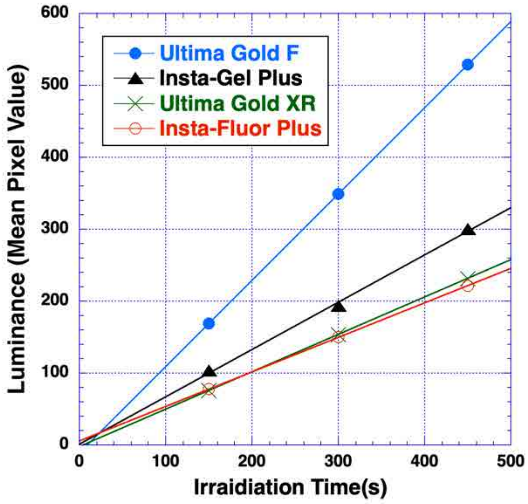

Fig. 1. Luminance value for different types of boron-added liquid scintillators as a function of neutron irradiation time.

REFERENCES:

[1] A. Nohtomi *et al.,* Radiol. Phys. Technol., **15** (2022) 37-44.
[2] T. Kobayashi and, K. Kanda. Nucl. Instrum. Meth., **204** (1983) 525–531.

PR8-3

Development and demonstration of a Bonner sphere spectrometer and investigation on neutron dose measurement with a modified netron servey meter

A. Masuda, T. Matsumoto, S. Manabe, K. Watanabe[1], A. Ishikawa[2], H. Tanaka[3], Y. Sakurai[3],
H. Harano, T. Takata[3], N. Matsubayashi[3], A. Uritani[4] and H. Kumada[5]

National Metrology Institute of Japan, National Institute of Advanced Industrial Science and Technology
[1]Graduate School of Engineering, Kyushu University
[2]Nuclear Science Research Institute, Japan Atomic Energy Agency
[3]Institute for Integrated Radiation and Nuclear Science, Kyoto University
[4]Graduate School of Engineering, Nagoya University
[5]Proton Medical Research Center, University of Tsukuba

INTRODUCTION: Neutron spectral fluence measurement techniques are required in boron neutron capture therapy (BNCT). A BSS for intense neutron beams is developed and tested in this study. A small lithium-glass scintillator is adopted to the Bonner sphere detectors to accommodate the neutron intensity of 10^9 cm^{-2} s^{-1}. Demonstration measurements of the assembled BSS were performed at the Kyoto University Research Reactor (KUR). A simple technique for measuring neutron dose in BNCT facilities is also needed. In this study, we fabricated a commercially available gas-based neutron survey meter customized for high-intensity neutrons and demonstrated it at the KUR.

EXPERIMENTS: The Bonner sphere detectors with the small lithium-glass scintillator coupled with an optical fiber [2] and a photomultiplier (PMT, Hamamatsu R9880U-21) were set and irradiated by the standard mixed neutrons in rotation at the measurement position of the heavy water irradiation facility of the KUR [3]. Output signals from PMT were processed using a preamplifier (ORTEC 113) and a signal processing and acquisition system (Amptek PX5). Previous studies had suggested the effectiveness of measurements using spheres with thinner moderators, so in this study, spheres with diameters of 1.5", 2", and 2.5" were added. In the demonstration of the survey meter, the direct signal from the detector was amplified by a linear amplifier, and the pulse height distribution was acquired by an ADC (Amptek MCA8000D).

RESULTS: The measurement results using a Bonner sphere detector are shown in Figure 1. The count rate was confirmed to be dependent on the sphere diameter, and a reasonable decrease in the count rate was observed with a small diameter detector that is sensitive to the low energy region. The results for the neutron survey meter are shown in Figure 2. A pulse height spectrum was obtained that appears to be a superposition of the 14N(n,p)14C reaction caused by low-energy neutrons and the H(n,n)p reaction caused by fast neutrons.

This study is supported by Grant-in-Aid for Scientific Research, Japan Society for the Promotion of Science (JSPS KAKENHI Grant Number JP22K12667).

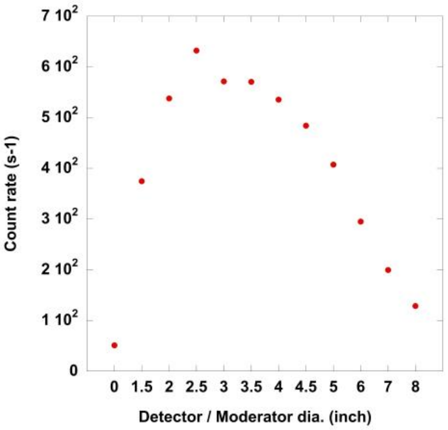

Fig. 1. Results of Bonner sphere measurements.

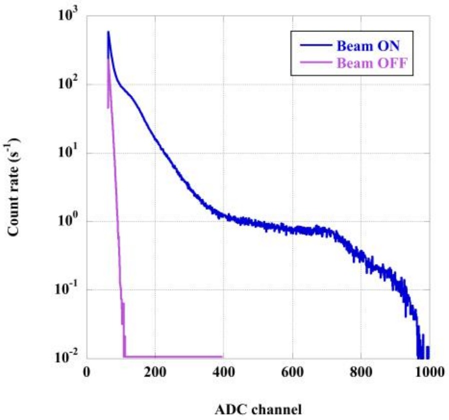

Fig. 2. Results of neutron survey meter measurements.

PR8-4

Radiation quality evaluation method for neutron irradiation field

N. Hu, R. Yamazaki[1], N. Matsubayashi[2], T. Takata[2], Y. Sakurai[2], and H. Tanaka[2]

Kansai BNCTMedical Center, Osaka Medical and Pharmaceutical University
[1] Graduate School of Engineering, Department of Nuclear Engineering, Kyoto University
[2] Institute for Integrated Radiation and Nuclear Science, Kyoto University

INTRODUCTION: In a typical BNCT irradiation field, a mixture of radiation types is present, and measurements are by no means simple. A proportional gas counter is commonly used to measure the radiation beam quality of a mixed irradiation field, such as a neutron/gamma radiation field. To measure the biological effect of a neutron beam, a tissue equivalent proportional counter (TEPC) was used, and the gas density was reduced to mimic a micrometer sized cell volume.

****

EXPERIMENTS: Experiment was performed using the epithermal irradiation mode of KUR at 1 MW. The TEPC was placed free-in-air in the center of the irradiation field with 1 hour measurement time. The raw data was converted to lineal energy spectrum (y distribution) and compared with simulation results calculated using Monte Carlo simulation (Particle and Heavy Ion Transport code System: PHITS).

****

RESULTS: Figure 1 shows the experimental set up and the results. The proton edge at approximately 100 keV/μm was clearly visible and closely matched the PHITS Monte Carlo simulation results. Deviation in the high lineal energy region (> 200 keV/μm) was observed. Possible reason could be due to the overestimation of the PHITS calculation in the high lineal energy region, which has been reported previously [1].

Repeating the experiment with a higher reactor power (5MW) or longer exposure time may improve the statistical uncertainty.

****

REFERENCES:

[1] T. Sato *et al.,* Phys. Med. Biol., **68** (2023).

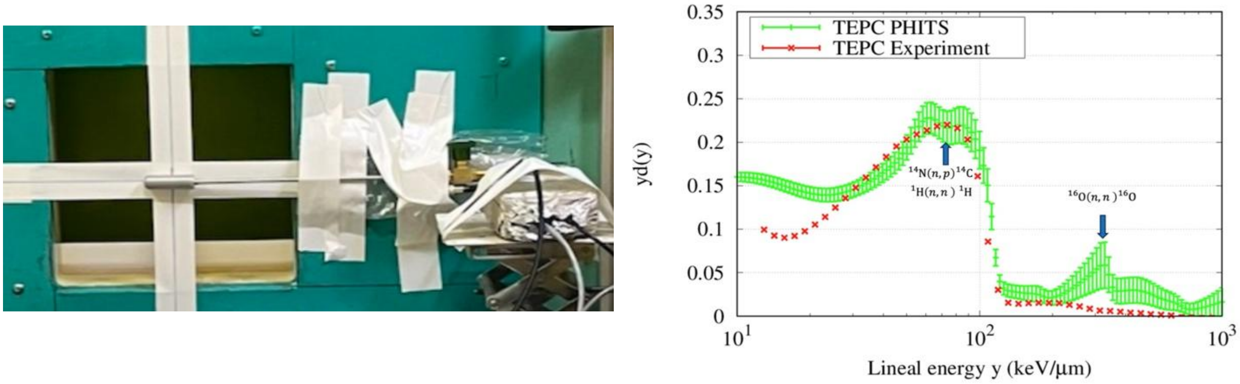

Fig. 1. Left) Experimental set up. Right) Experimentally measured lineal energy distribution (ydy) of KUR epithermal mode.

PR8-5

Evaluation of response characteristics of semiconductor detectors in neutron irradiation field

N. Hu, R. Yamazaki[1], N. Matsubayashi[2], T. Takata[2], Y. Sakurai[2], and H. Tanaka[2]

Kansai BNCT Medical Center, Osaka Medical and Pharmaceutical University
[1]Graduate School of Engineering, Department of Nuclear Engineering, Kyoto University
[2] Institute for Integrated Radiation and Nuclear Science, Kyoto University

INTRODUCTION: The Centre for Medical Radiation Physics, University of Wollongong, Australia, has developed a silicon microdosimeter to measure directly the microdosimetric spectrum. The detector has an array of micro-sized sensitive volumes, which can measure the energy deposition at the cellular-level. The use of this detector in a mixed neutron/gamma ray radiation field is of high interest, particularly for evaluating the dose deposited to a volume mimicking a single cell. A commonly used detector to measure the microdosimetric distribution is a gas filled proportional counter [1]. Initial experiments were performed using this detector as a base for comparison with the silicon microdosimeter.

****

EXPERIMENTS: The microdosimetric spectrum of the heavy water irradiation facility (epithermal irradiation mode) of the Kyoto University Research Reactor was measured using a proportional gas counter. Both a tissue equivalent walled (tissue equivalent proportional counter: TEPC) and graphite walled counter (carbon walled proportional counter: CWPC). Measurements were performed free-in-air at the center of the irradiation field. One-hour measurements were performed with the reactor power at 1 MW.

****

RESULTS: Figure 1 represents the frequency distribution curve of the KUR epithermal mode measured with both types of proportional counters. Proton events (20 – 100 keV/µm) were observed with the TEPC (nitrogen and hydrogen component of the wall) but not with the CWPC (no hydrogen component). By subtracting these two results, gamma ray events can be separated from neutron events. These results will be compared with the silicon microdosimeter results.

****

REFERENCES:

[1] H. Rossi, Radiation Research Supplement, **2** (1960) 290-299.

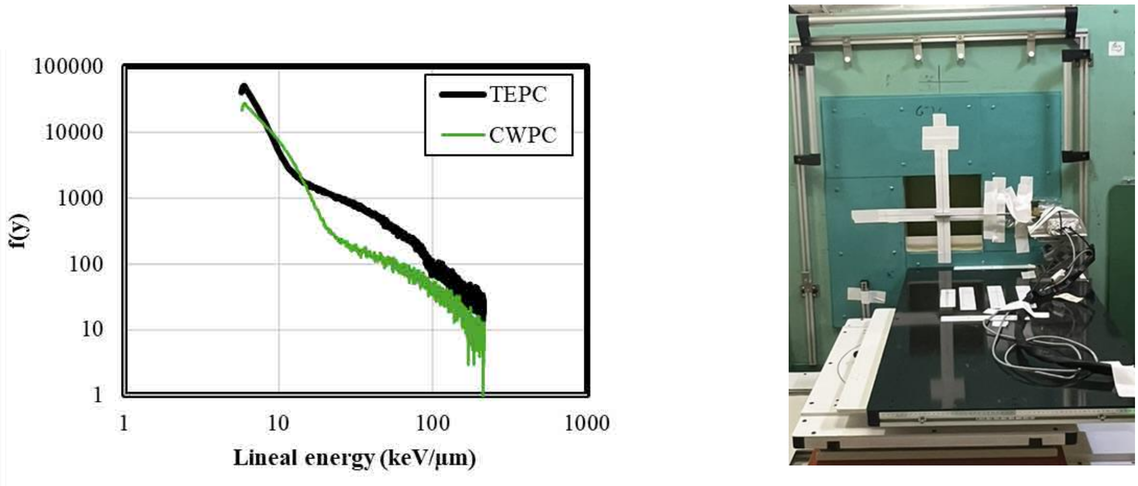

Fig. 1. Left) The frequency distribution curve of the KUR epithermal mode measured with the TEPC (black line) and CWPC (green line). Right) Image of the experimental set up.

PR8-6

Development of Scintillator for Thermal Neutron Detector in BNCT

N. Matsubayashi, H. Tanaka, S. Kurosawa[1], A. Yamaji[1], Y. Sakurai, T. Takata

Institute for Integrated Radiation and Nuclear Science, Kyoto University
[1]Institution for Materials Research, Tohoku University

INTRODUCTION: In recent years, accelerator-based BNCTs have been developed worldwide, and clinical cases are increased. The activation method has been used for measurement of thermal neutron flux but cannot measure in real-time. The development of thermal neutron detectors as neutron monitors is needed. The neutron monitor using Eu:LiCaAlF$_6$ (LiCAF) scintillator with quartz fiber was developed [1]. It is necessary for the use of the scintillator as neutron monitor to determine the relationship between the count rates obtained by the detector and thermal neutron flux. Considering the increase in the clinical cases, we must calibrate the detector in primary national standard field. However, the neutron intensity of the standard field is much lower than that of the BNCT irradiation field. In this study, we developed a new scintillator with fast response and high detection efficiency.

****

EXPERIMENTS: As the thermal neutron detector for BNCT, a scintillator with 0.3~0.6 mm is mounted on the tip of the fiber to reduce gamma-ray sensitivity. In this study, we selected LiBr/CeBr$_3$ and Ce:LiBr/LaBr$_3$ eutectics, which have fast response and high light yield [2][3]. Since the selected scintillators were hygroscopic, they were packaged using quartz glass and cement to prevent exposure to the outside air. The irradiation tests of each detector were performed at Kyoto University Research Reactor-Heavy Water Neutron Irradiation Facility (KUR-HWNIF) [4]. A Cd shutter was installed to change the thermal neutron flux with each aperture. The irradiation tests were carried out by changing the aperture to 0, 100, 200, 300, 400, 500, and 600 mm. The scintillation lights though the fiber were measured by a photomultiplier tube (PMT). The signal from the PMT was processed by a multi-channel analyzer (MCA). The pulse height distributions were measured by the MCA and the neutron count rates were evaluated by summarizing high channel area to remove the gamma-ray events.

****

RESULTS: In the irradiation tests at KUR-HWNIF, neutron peaks were not formed in the pulse height distribution. However, neutron events were identified in higher channel area than gamma-ray events, and the count rate varied with Cd shutter aperture. As shown in Fig. 1, the neutron count rates obtained by the detectors and thermal neutron flux showed good linearity. It is confirmed that the detectors developed in this study can be used as neutron monitor for BNCT. In the future, we will carry out the irradiation tests repeatedly to evaluate the long-term stability of the detector.

****

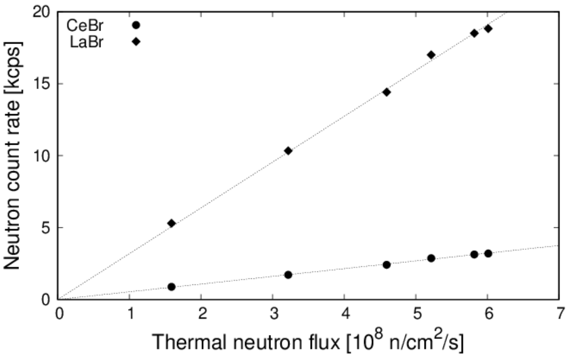

Fig. 1. Relationship of the thermal neutron flux

REFERENCES:

[1] H. Tanaka *et al.,* Rev. Sci. Instrum., **88 (5)** (2017) 056101.
[2] R. Yajima *et al.,* Jpn. J. Appl. Phys., **61** (2022) SC1028.
[3] Y. Takizawa *et al.,* Nucl. Instrum. Methods. Phys. Res A., **1028** (2022) 166384.
[4] Y. Sakurai *et al.,* Nucl. Inst. Methods. Phys. Res., **453(3)** (2000) 569-596.

PR8-7

Study of Optically Stimulated Luminescent Dosimeter in BNCT Irradiaiton Field

N. Matsubayashi, H. Tanaka T. Takata, Y. Sakurai

Institute for Integrated Radiation and Nuclear Science, Kyoto University

INTRODUCTION: The BNCT irradiation field consists of neutrons with a wide energy range and undesired gamma-rays, which are mainly caused by nuclear reactions with surrounding structures. For quality control/quality assurance (QA/QC), the undesired gamma-ray dose in a phantom must be measured [1]. To evaluate gamma-ray dose in the BNCT irradiation field, a thermoluminescent dosimeter (TLD) composed of beryllium oxide power enclosed in a quartz glass capsule, which is less sensitive to thermal neutrons, has been used. However, as the TLD was out of production, a new gamma-ray dosimeter is required for QA/QC of BNCT [2]. In this study, we selected optically stimulated luminescent dosimeter (OSLD), which is made of Al_2O_3:C. The OSLD has been used in other radiation therapies, has almost no fading effect and can be measured repeatedly. To use the OSLD in the BNCT irradiation field, the sensitivity to thermal neutron needs to be evaluated [3]. In this study, before the irradiation tests of the OSLD, the characteristics of the irradiation field were evaluated.

****

EXPERIMENTS: The irradiation tests of the BNCT irradiation field were performed at Heavy Water Neutron Irradiation Facility (HWNIF) at Kyoto University Research Reactor (KUR) [4]. A cadmium shutter, which shields only thermal neutrons, was installed to control the thermal neutron flux with each openness. To investigate the thermal neutron flux per the cadmium shutter openness, the irradiation tests were carried out by changing the openness to 0, 100, 200, 300, and 600 mm. A gold foil was placed in the center of the irradiation field, and the radioactivity of the gold foil was measured by high-purity germanium detector. Thermal neutron flux was measured using the reaction rate of the gold foil, the detection efficiency of the germanium detector, the gamma-ray emission rate of the gold, the irradiation time, and the measurement time.

****

RESULTS: Fig.1 shows thermal neutron flux by changing the cadmium shutter openness. The thermal neutron flux of KUR-HWNIF was found to be from 1.4×10^{7} to 1.2×10^{9} cm^{-2} s^{-1} depending on the openness. It was found that the range of thermal neutron flux was over an order of magnitude at KUR-HWNIF. Since the cadmium had a large cross section in the thermal neutron energy region, the high energy neutron was not changed depending on the cadmium shutter openness. The OSLD was manly sensitive to thermal neutron, and the KUR-HWNIF is a suitable irradiation field for evaluating the thermal neutron sensitivity of the dosimeter.

****
****

REFERENCES:

[1] K. Yamamoto *et al.,* Res. Dev. NCT, **46** (2002) 499-503.
[2] N. Matsubayashi *et al.,* Radi. Meas., **161** (2023) 106900.
[3] Y. Sakurai *et al.,* Nucl. Inst. Methods. Phys. Res., **453(3)** (2000) 569-596.

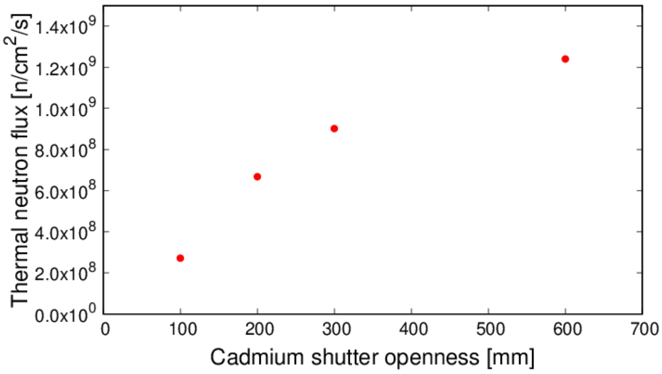

Fig. 1. Relationship of the thermal neutron flux and the cadmium shutter openness.

PR8-8

Establishment of Characterization Estimation Method in BNCT Irradiation Field using Bonner Sphere and Ionization Chamber (VIII

Y. Sakurai, J. Prateepkaew[1], R. Narita[1], T. Takata and H. Tanaka

Institute for Integrated Radiation and Nuclear Science, Kyoto University
[1]Graduate School of Engineering, Kyoto University

INTRODUCTION: Development in accelerator-based irradiation systems for BNCT is underway. BNCT using newly developed accelerator systems is being implemented at multiple facilities around the world. Considering this situation, it is important that the estimations for dose quantity and quality are performed consistently among several irradiation fields, and that the equivalency of BNCT is guaranteed, within and across BNCT systems. Then, we are establishing QA/QC system for BNCT. As part of the QA/QC system, we are developing estimation method for neutron energy spectrum using Bonner-sphere technique [1]. In our spectrometer, liquid such as pure water and/or boric acid solution is used as the moderator. A multi-layer case with multiple moderator layers is prepared. The moderator and its thickness are changeable without entering the irradiation room, by the remote supply and drainage of liquid moderator in the several layers. For the detector, activation foils are remotely changed, or online measurement is performed using SOF detector, etc. As a new type of spectrometer, we are developing the Cylindrical Hemisphere Accurate Remote Multilayer Spectrometer (CHARMS) [2,3]. In 2024, a prototype of CHARMS was manufactured and a validation experiment was performed to verify its effectiveness.

MATERIALS AND METHODS: A LiCaAlF6 scintillation neutron detector is positioned at the center of CHARMS, and it is surrounded by three layers of liquid moderators. With a remote operation of liquid moderator supply and drainage system from outside the irradiation room, we can realize a fully remote-operating neutron spectrometer. The performance of CHARMS in measuring the neutron energy spectrum was evaluated at Heavy Water Neutron Irradiation Facility of Kyoto University Reactor (KUR-HWNIF) [4].

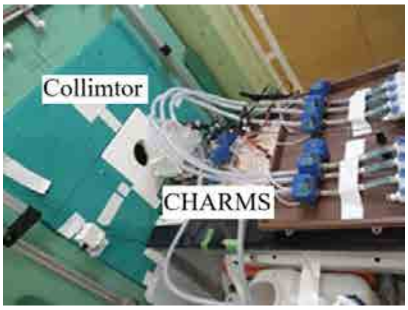

Fig. 1. Experimental setup for CHARMS measurements at KUR-HWNIF.

RESULTS: The neutron energy spectrum of the BNCT irradiation at KUR-HWNIF was measured using CHARMS without the need to enter the irradiation room. The evaluated neutron energy spectrum closely matched the results of simulation calculations. The entire measurement process took approximately one hour by using CHAMRS. It was confirmed that CHARMS can provide a reliable neutron energy spectrum with a short measurement time compared to conventional methods. It is considered that CHARMS is a promising neutron spectrometer for use in BNCT irradiation field in the future.

REFERENCES:

[1] S. Shiraishi *et al.,* Appl. Radiat. Isot., **163** (2020) 109213.
[2] J. Prateepkaew *et al.,* Nucl. Instr. Meth. A, **1059 (**2024) 168948.
[3] J. Prateepkaew *et al.,* Appl. Radiat. Isot., **219** (2025) 111717.
[4] Y. Sakurai and T. Kobayashi, Nucl. Instr. Meth. A, **453** (2000) 569-596.

PR8-9

Development of Real-time Boron-concentration Estimation Method using Gamma-ray Telescope System for BNCT (III

Y. Sakurai, J. Prateepkaew[1], R. Narita[1], T. Takata, H. Tanaka and M. Suzuki

Institute for Integrated Radiation and Nuclear Science, Kyoto University
[1]Graduate School of Engineering, Kyoto University

INTRODUCTION: It is important to decide the boron concentrations for tumor and normal parts in the dose estimation for BNCT. To improve the dose estimation in BNCT, a method for estimating the spatial distribution of boron concentration online in real time is expected. The information about the boron concentration distribution can be obtained using the prompt gamma-ray analysis (PGA) for the prompt gamma rays from boron-10 (B-10). The improved gamma-ray telescope system is settled at Heavy Water Neutron Irradiation Facility of Kyoto University Reactor (KUR-HWNIF) [1-3]. This system consists of an HPGe semiconductor detector and a collimation system including two lead collimators. The gamma rays through these collimators can be detected, and the telescope view-filed can be changed by moving the two collimators independently. The experimental verification for the ability to distinguish between tumor and normal parts was continued in 2024 as well.

MATERIALS AND METHODS: The phantom experiment was performed using the epi-thermal neutron irradiation mode at KUR-HWNIF. The phantom size was 20 cm × 20 cm × 20 cm. Within the phantom, a 5-cm diameter acrylic hollow sphere was placed as the tumor. Both the phantom and tumor sphere were filled with different concentrations of boric acid water. For example, the tumor spheres with the B-10 concentration of 70, 100 and 200 ppm were put into a phantom with B-10 concentration of 20 ppm. The irradiation field was set to 12 cm in diameter. The tumor sphere was fixed at the center of the telescope view-field. The 1st and 2nd telescope collimators were set at the bottom of the telescope. The simulation calculation was performed using Particle and Heavy Ion Transport code System (PHITS) version 3.25 [4]. To simplify the simulation process, the irradiation room and the telescope system were separately used as the simulation geometry.

RESULTS: The count rates for 478-keV prompt gamma rays with the different irradiation conditions were obtained from the experimental results. In the case of the 70-ppm tumor sphere, the experimental count rate was 29.6 cps (s^{-1}). Therefore, because the time required to reach 1000 counts was just over 30 seconds, the time course of B-10 concentration can be estimated almost in real-time. From the results of the experimental verification, the effectiveness and usefulness of the improved gamma-ray telescope system were confirmed. The more precise estimation will be performed for the B-10 concentration, size and position of the tumor sphere, and for the position of two telescope collimators. Moreover, the effective range for the discrimination between tumor and normal parts will be clarified.

REFERENCES:

[1] Y. Sakurai *et al.,* Appl. Radiat. Isot., **61** (2004) 829-833.
[2] Y. Sakurai *et al.,* Appl. Radiat. Isot., **165** (2020) 109256.
[3] Y. Sakurai and T. Kobayashi, Nucl. Instr. Meth. A, **453** (2000) 569-596.
[4] T. Sato *et al.,* J. Nucl. Sci. Technol., **61** (2024) 127-135.

PR8-10

4H-SiC Neutron Image Sensor for Boron Neutron Capture Therapy

V. T. Ha[1], T. Meguro[1], H. Tanaka[2], and S.-I. Kuroki[1]

[1]*Research Institute for Semiconductor Engineering, Hiroshima University*
[2] *Institute for Integrated Radiation and Nuclear Science,*
Kyoto University Graduate School of Science, Kyoto University

INTRODUCTION: Boron neutron capture therapy (BNCT) has been attracting attention as an advanced treatment method on cancer because this therapy has a great advantage on a minimally invasive and selective treatment. In the BNCT, for making this therapy more accurate one, it is better to measure the neutron beam's position and profile in real time. On the other hand, silicon carbide (SiC) semiconductors integrated circuits have been developed as radiation hardened electronics [1], and the SiC CMOS image sensors also have been demonstrated [2]. We are suggesting a neutron CMOS image sensor by combining the SiC CMOS image sensor and neutron conversion layer for the neutron real time imaging [2]. In this year, we continue to design and fabricate the neutron CMOS image sensors and simulate the device operations by using circuits simulator.

EXPERIMENTS: The structure of our neutron sensor is based on a three- and four-transistor type CMOS image sensor pixel. The neutron sensor is based on an image sensor pixel using SiC, which has been developed in our laboratory, focusing on stable operation under neutron irradiation for a long time. The neutron sensors are equipped with boron-10 layer as a neutron conversion layer. In this layer, the injected neutrons have a reaction with boron-10, and then, alpha and lithium particles are emitted. The alpha particles penetrate the device, and generate electron-hole pairs, electrons are collected at gate electrode of SF(source-follower) transistor, and then the induced charge is detected as the output voltage from the sensor.

RESULTS: Figure 1 shows the device layout of neutron image sensors. Now this chip is under fabrication. On the other hand, circuit-level simulation was also carried out. In this simulation with the realistic device parameters, real time output signals were observed.

REFERENCES:
[1] Masayuki Tsutsumi *et al.,* IEEE Electron Device Lett., **44(1)** (2023)100 - 103.
[2] Tatsuya Meguro *et al.,* Appl. Phys. Ex-press, **17** (2024) 081005-1 - 081005-5.
[3] M. Taniguchi *et al.,* "Neutron Image Sensor for Boron Neutron Capture Therapy", The International Symposium on Biomedical Engineering 2022 (2022) 66.

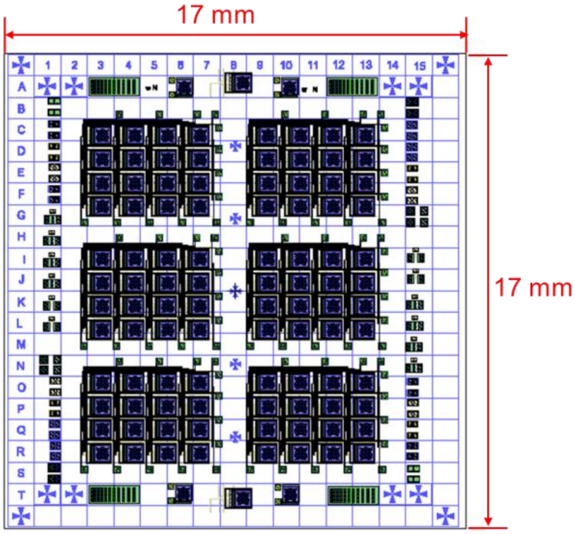

Fig. 1. Chip layout of the neutron CMOS

PR8-11

Improvement of the SOF detector system for energy-dependent discrimination and long-term stability

M. Ishikawa[1,2], Y. Ikeda[2], K. Takamiya[3] and Y. Sakurai[3]

[1]*Faculty of Health Sciences, Hokkaido University*
[2]*Graduate School of Biomedical Science and Engineering, Hokkaido University*
[3]*Institute for Integrated Radiation and Nuclear Science, Kyoto University*

INTRODUCTION: We have been conducting research on SOF detectors as thermal neutron flux monitors in BNCT for many years.[1,2] However, degradation of the SOF detector due to long-term irradiation has been reported.[3] As anti-degradation methods, we have replaced plastic optical fibers, which cause degradation, with quartz fibers, and developed degradation monitors using blue laser source. In addition, since epithermal neutron irradiation has become mainstream in recent years, it is desirable to be able to measure the epithermal neutron flux. In this study, we tried to estimate the neutron energy spectrum at KUR HWNIF (Heavy Water Neutron Irradiation Facility) using 2-dimensional thermal neutron flux distribution.

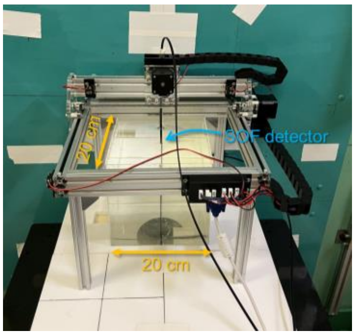

Fig. 1. Measurement geometry for neutron energy spectrum estimation using MLEM unfolding method.

EXPERIMENTS: For energy spectrum estimation, the MLEM (Maximum Likelihood Expectation Maximization)-based energy spectrum estimation was tested using Monte Carlo simulation (PHITS ver 3.32) data assuming 2D thermal neutron flux distribution using SOF detectors prior to actual experiment. As shown in Fig. 2 (a), the estimated energy spectrum showed a good agreement with energy spectrum used for neutron source.

In measuring 2D thermal neutron flux distribution, the assigned machine time of 3 hours is insufficient for accomplish data acquisition. So, we expected efficient data acquisition by using high-sensitivity SOF probe. Figure 1 shows the 2D scanning measurement experiment at KUR-HWNIF, where the SOF detector probe was located at a pitch of 1 cm in the lateral direction and 5 mm in the depth direction inside a 20 x 20 x 20 cm^3 PMMA phantom, and measurements were performed at each point for 10 sec. However, as shown in Fig. 2(b), the estimated neutron energy spectrum using the measured data shows a rather large deviation in the fast energy region. This is because photon signals were saturated due to high thermal neutron flux with 5MV operation, so measurement data was not adequate for analysis.

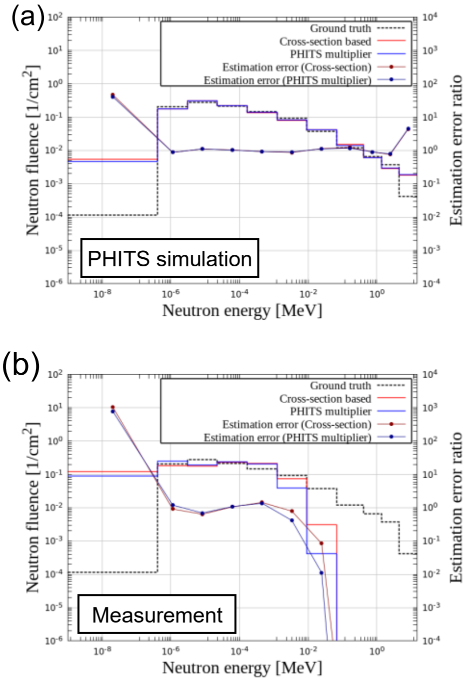

Fig. 2. Estimated neutron energy spectrum bv SOF detector.

REFERENCES:

[1] M. Ishikawa *et al.,* Appl. Radiat. Isot., **61** (2004) 775-779.
[2] M. Ishikawa *et al.,* Nucl. Instr. Meth. A, **551** (2005) 448-457.
[3] M. Komeda *et al.,* Appl. Radiat. Isot., **67** (2009) 254-257.

PR8-12

Etch Pit Analysis of Solid-State Nuclear Track Detectors Using a 3D Confocal Laser Microscope for Fast Neutron Dosimetry in BNCT

T. Takata, N. Matsubayashi, Y. Sakurai and H. Tanaka

Institute for Integrated Radiation and Nuclear Science, Kyoto University

INTRODUCTION: In dosimetry of boron neutron capture therapy (BNCT), separate measurements of doses from thermal neutrons, fast neutrons, and gamma rays are required. In such a mixed neutron and gamma-ray field, a paired ionization chamber method is a standard for fast neutron dosimetry. In principle, the method requires compensation of gamma-ray dose, causing an uncertainty of the derived fast neutron dose. Also, perturbation of the radiation field caused by the gas cavity must be taken into account.

In this study, utilization of solid-state nuclear track detector (SSNTD), which is not sensitive to gamma-rays and has less field perturbation than ionization chambers, has been investigated as an alternative method. It is known that a pit shape formed on the SSNTD by chemical etching depends on LET of incident particles [1]. In the application to BNCT, small and shallow pits formed by low-energy recoil protons need to be analyzed. We report the applicability of a 3D-measuring confocal laser microscope for the pit-shape measurements.

MATERIALS AND METHODS: Commercially available SSNTDs (Baryotrack, Nagase Landauer, Ltd.) were irradiated with two types of charged particles induced by low energy neutron beam from the E-3 guide tube at KUR [2]. One is an alpha particle from $^{10}B(n,\alpha)^{7}Li$ reaction occurred in the boric acid solution. Another is a proton from $^{14}N(n,p)^{14}C$ reaction occurred in the atmospheric air [3]. The irradiated detectors were etched with 6M NaOH solution for 2 hours at 70°C. The surface profiles of the etched detectors were measured by using a 3D confocal laser microscope (LEXT4000, Evident Corporation) with 100× objective lens. The measurement was performed with the support of the Kyoto University Nanotechnology Hub under “Advanced Research Infrastructure for Materials and Nanotechnology Project” sponsored by the Ministry of Education, Culture, Sports, Science and Technology (MEXT), Japan.

RESULTS: The formation of pits was observed on the SSNTDs with a variety of its size. An example of the measured surface profile is shown in Fig. 1. The elliptical shape of the pit aperture and the conical shape along the direction of the particle track can be clearly observed, confirming that the 3D shape measurement has more advanced feature than the usual 2D pit measurement with an optical microscope. We will develop a tool to quickly analyze the shapes of many pits and investigate the measurement of the energy and angular distribution of incident radiation.

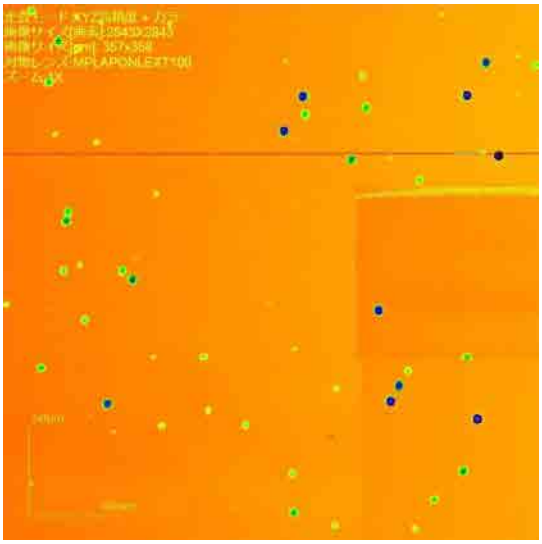

Fig. 1 Surface profiles with conical-shaped etch pits formed on SSNTD.

REFERENCES:

[1] M. Caresana *et al.,* Nucl. Instrum. Methods Phys. Res. Sect. A, **638** (2012) 8-15.
[2] T. Kobayashi and K. Kanda, Nucl. Instrum. Methods, **204** (1983) 525-531.
[3] T. Takata *et al.,* KURNS Progress Report 2023, R5P9-10 (2023) 86.

Development of a Real-Time Dose Rate Monitor for BNCT Using Novel Scintillation Materials

S. Kurosawa[1,2,3], Y. Urano[2,4], C. Fujiwara[2,4], A. Yamaji[1,2], T. Takata[5], H. Tanaka[5]

[1] *New Industry Creation Hatchery Center, Tohoku University*
[2] *Institute for Materials Research Tohoku University*
[3] *Institute of Laser Engineering, Osaka University*
[4] *Department of Materials Science, Graduate School of Engineering, Tohoku University*
[5] *Institute for Integrated Radiation and Nuclear Science, Kyoto University*

INTRODUCTION: Boron neutron capture therapy (BNCT) is radiation therapy based on the nuclear reaction of boron (^{10}B) and thermal neutrons. To estimate the treatment effect in real-time, the use of prompt gamma rays (478 keV) emitted by the ^{10}B(n,α)^{7}Li reaction has been proposed using a collimator [1]. Although the proposed detector uses a collimator, the collimator led to a decrease in detection efficiency due to the collimator space and an increase in gamma-ray background by scattering. From the above results, we have developed a new detector consisting of a scintillator, optical fiber and photomultiplier tube without such a collimator.

The scintillators are required to have high output, good non-proportionality (NPR), and low hygroscopicity. In this study, we focused on Tl-doped $Cs_3Cu_2I_5$ (Tl:CCI) scintillator [2] because of a high light output of more than 98,200 photons/MeV and low hygroscopicity.

EXPERIMENTS: Tl:CCI crystals were grown by the vertical Bridgman-Stockburger method, and the crystal phase was verified by powder X-ray diffraction. To evaluate the light output and NPR, the pulse height spectra excited by several line gamma rays from ^{137}Cs source and other sources were measured with a photomultiplier tube (R7600U-200, Hamamatsu K.K.), shaping amplifier (572A, ORTEC) and multichannel analyzer (Pocket MCA8000D, AMPTEK).

Using Tl:CCI and optical fiber, we measured 478-keV gamma rays originating from samples containing ^{10}B at The Heavy-Water Thermal Neutron Facility at Kyoto University Research Reactor. The scintillation photons were measured with a photomultiplier tube and pico-ammeter. Here, the target samples had different concentrations of ^{10}B, and the samples were irradiated with neutrons with a flux of around 10^9 cps.

RESULTS: The scintillation photons were converted to current with a pico-ammeter, and Figure 1 shows current values as a function of ^{10}B concentration. These results indicated our system has concentration sensitivity. Here, the typical ^{10}B concentration in the actual application is the order of 10 ppm (10-50 ppm). Since the detection lower limit of our system was found to be 100 ppm, the sensitivity of this system should be improved by an order of magnitude. Thus, now we have developed scintillation materials, their size and the detection sensitivity of the photo sensor, and this detection lower limit is found to be a few ppm. As a next step, we also measured and found the position sensitivity.

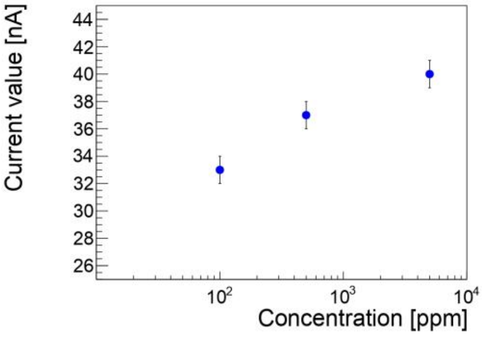

Fig. 1. Current value from scintillation signal as a function of concentration of ^{10}B in the target sample.

REFERENCES:

[1] K. Okazaki *et al.,* NUCL INSTRUM METH A, **1055** (2023) 168546.
[2] L. Stand *et al.,* Instrum. Methods Phys. Res. A, **991** (2021)164963.
[3] T. Jun *et al.,* Adv. Mater., **30** (2018) 1804547.

PR8-14

Measurement of Current-to-Flux Ratio in Neutron Fields for BNCT

I. Murata, K. Sagara, H. Asano, R. Kawahata, H. Nagasawa, S. Tamaki, S. Kusaka, T. Takata[1], H. Tanaka[1], Y. Sakurai[1]

Graduate School of Engineering, Osaka University
[1]Institute for Integrated Radiation and Nuclear Science, Kyoto University

INTRODUCTION: BNCT is a promising cancer therapy which kills only tumor cells selectively. The neutron field for BNCT includes not only thermal and epi-thermal neutrons but also fast neutrons that are harmful to the human body. Therefore, we have to measure the absolute integral flux intensity of fast neutrons (10 keV ~ 1 MeV) to evaluate their exposure dose. Now we are developing a monitor to precisely measure it and repeatedly improving the monitor [1]. In the previous research, the experimental value is overestimated by about 196 % compared to the calculated value. We discussed one possible reason for this error was the unknown current-to-flux (C/F) ratio of the neutron source in KUR, Kyoto University Reactor. Therefore, the objective of this work is to measure the C/F ratio of the neutron source for BNCT in KUR.

EXPERIMENTS: We have developed a device to measure the C/F ratio. The device consists of an acrylic container with two tubes passing through it. The two tubes are set so that one is perpendicular to the surface of the neutron source and the angle between the two tubes is 30 deg. As shown in Fig. 1. The acrylic container is filled with B_4C powder and water to shield neutrons. As an activation foil, two Au foils covered with a Cd sheet are placed at an equal distance from the neutron source. Because the angular distribution of the neutron beam is determined by the C/F ratio, the C/F ratio can be estimated from the ratio of the radioactivity of the Au foils. Using the device in Fig. 1, we conducted an experiment to measure the C/F ratio at KUR. Irradiation was carried out for 8 min in 5 MW operation.

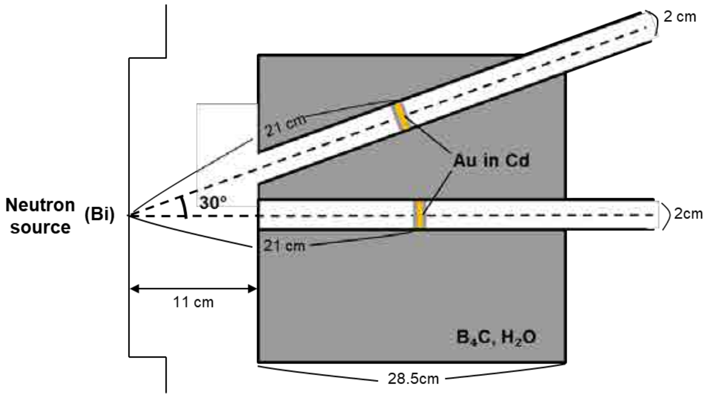

Fig.1 Device for measurement of C/F ratio.

RESULTS: The results of the experiment are shown in Table 1. The C/F ratio was deduced to be 0.543±0.042 from the ratio of the ^{198}Au activities. However, the calculated value of the C/F ratio obtained by the simulation was 0.501±0.002, which was slightly different from the experimental results. Since the device is not completely shielded from neutrons, the discrepancy could be due to neutrons entering the device from the side surface of the tube. Therefore, in the future, we will remove the contribution of neutrons coming from the side surface of the tube and measure a more accurate C/F ratio.

Table.1 C/F Ratio.

	0°	**30°**
Au Radioactivity [Bq]	544±6	526±6
Nomalized Au Radioactivity [Bq]	544±6	514±5
C/F Ratio	0.543±0.042	

REFERENCES:

[1] K. Aoki, "Development of absolute epi-thermal and fast neutron flux intensity detector for BNCT", Thesis, University of Osaka, 2021.

PR8-15

Performance Evaluation of a Real-Time Thermal Neutron Detector for BNCT

H. Tanaka[1] and A. Ishikawa[2]

[1] *Institute for Integrated Radiation and Nuclear Science, Kyoto University*
[2] *Japan Atomic Energy Agency*

INTRODUCTION: In quality assurance and quality control (QAQC) for boron neutron capture therapy, it is necessary to measure the thermal neutron flux in a water phantom. Until now, the thermal neutron flux has been measured using the gold activation method. Since the start of accelerator BNCT in medical institutions, the number of measurements required for QAQC has increased. Therefore, a method that can measure more quickly than the gold activation method is desired.

We have developed a thermal neutron real-time neutron detector using a combination of LiCAF scintillators and optical fibers [1], and are considering the use of scintillators with fast scintillation light decay. In this study, we report the results of adapting a lithium glass scintillator with a fast decay time to a heavy water neutron irradiation facility.

EXPERIMENTS: A lithium glass scintillator was installed at the tip of an optical fiber, and the scintillation light was guided through the optical fiber to a photomultiplier tube. The signal was amplified in the photomultiplier tube, and the pulse height distribution was acquired using a multichannel analyzer.

The scintillator was placed at a depth of 2 cm in a water phantom, and an epithermal neutron beam with a collimator diameter of 12 cm was irradiated.

RESULTS: Figure 1 shows the results of the pulse height distribution. The peak around 100 channels is formed by the total energy absorption of the Li(n,α)T reaction. Since gamma rays are events with energies of approximately 50 channels or less, events with energies of 70 channels or more were considered to be neutron-induced events. Figure 2 shows the time trend of the thermal neutron flux. A constant thermal neutron flux distribution was confirmed.

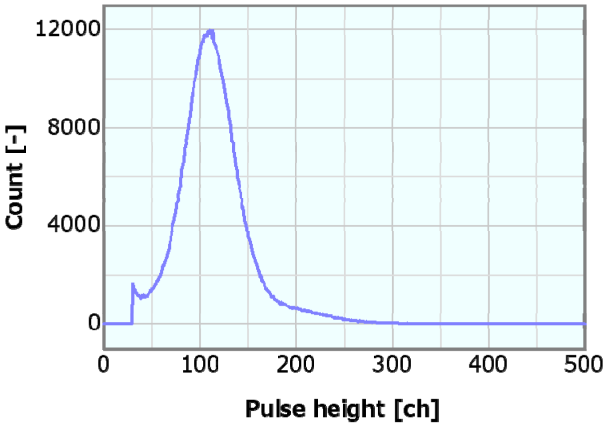

Fig. 1. Pulse height distribution of lithium glass scintillator.

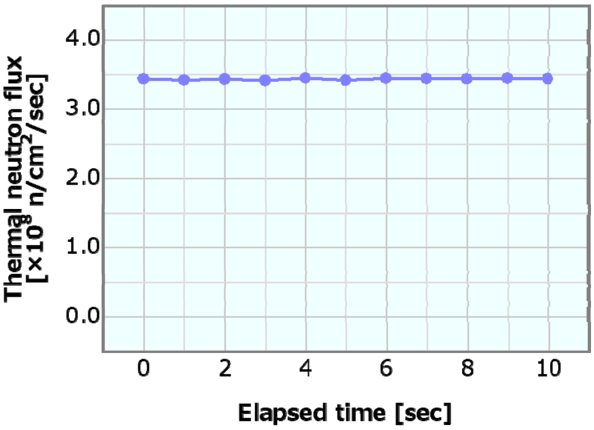

Fig. 2. Time trend of thermal neutron flux.

REFERENCES:

[1] H. Tanaka *et al.,* Review of Scientific Instruments, **88 (5)** (2017) 056101.

R6P8-16

PR8-16

Characterization of a Thermal Neutron Detector for Measuring the Shielding Performance of Thermal Neutron Shielding Materials

H. Tanaka, N. Matsubayashi, T. Takata, S. Sakurai

Institute for Integrated Radiation and Nuclear Science, Kyoto University

INTRODUCTION: Since the start of insurance-covered treatment with accelerator-based BNCT (Boron Neutron Capture Therapy) systems, a significant increase in the number of clinical cases is anticipated. In BNCT irradiation fields, there is a possibility that semiconductor-based electronic devices—such as neutron monitors, patient monitoring cameras, and implanted pacemakers—will be exposed to irradiation. If a semiconductor device contains nuclides with large thermal neutron cross sections, the irradiation of thermal neutrons may induce the generation of charged particles within the semiconductor material. These charged particles create electron-hole pairs along their tracks, and the resulting charge can lead to noise currents within the semiconductor device. Such noise currents may cause malfunctions of the semiconductor devices. To prevent radiation damage induced by thermal neutrons, we are developing materials capable of efficiently shielding thermal neutrons.

To evaluate the performance of these thermal neutron shielding materials, a thermal neutron beam is required. By placing a thermal neutron detector behind the shielding material and measuring the resulting count rate, the attenuation performance of the shielding material can be assessed. In the current fiscal year, we have characterized the thermal neutron detector intended for this evaluation.

EXPERIMENTS: The thermal neutron beam extracted from the E3 guide tube facility was used in this study. The thermal neutron detector needed to fulfill two requirements: it had to measure thermal neutrons transmitted through the shielding material, and it had to have a sensitive volume smaller than the size of the thermal neutron beam in order to minimize the effects of scattered neutrons.

In this study, we employed a thermal neutron detector consisting of a 0.3 mm square LiCAF scintillator coupled to an optical fiber with a core diameter of 0.6 mm. The optical fiber was connected to a photomultiplier tube, and the resulting signals were processed using a multichannel analyzer.

RESULTS: The obtained pulse height distribution is shown in the figure 1. To minimize the contribution from gamma rays, the integration was performed over the higher pulse heights from the peak center. The thermal neutron flux measured using the gold foil activation method was 2×10^6 (n/cm^2/s), and the corresponding count rate was 17 cps, resulting in a thermal neutron sensitivity of 9×10^{-6} (cps/(n/cm^2/s)). Measurement of the shielding performance of a typical shielding material yielded a transmission rate of 0.01, indicating that evaluation with a statistical error of 2% can be achieved within 1.5 hours.

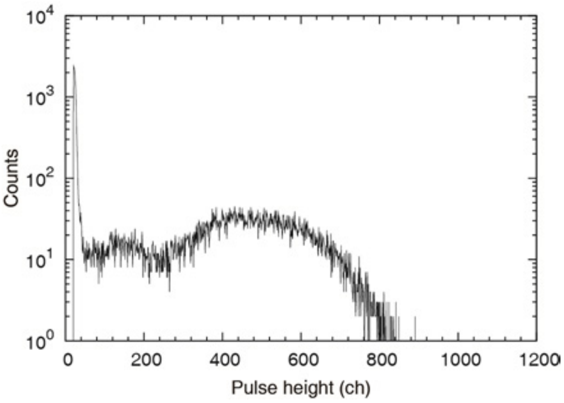

Fig. 1. Pulse height distribution of small LICAF scintillator.

I-1. PROJECT RESEARCHES

Project 9

PR9

Project Research on Advances of Mössbauer Spectroscopy in Isotope-Specific Studies

M. Seto
Institute for Integrated Radiation and Nuclear Science, Kyoto University

OBJECTIVES OF RESEARCH PROJECT

One of the most irreplaceable features of the Mössbauer spectroscopy is to extract several information such as electronic states and magnetic properties for a specific isotope. The main objectives of this project research on advanced isotope-specific investigation on the frontier of materials science by the methods of Mössbauer spectroscopy. Developments of Mössbauer spectroscopy provides more useful and valuable methods in modern materials science.

In this project research, each group performed their research by specific isotopes:

^{61}Ni in R6P9-1; ^{197}Au in R6P9-2, R6P9-3; ^{57}Fe in R6P9-4 to R6P9-12; and other isotopes in R6P9-13, R5P1-14.

MAIN SUBJECTS AND RESULTS OF THIS REPORT

Main subjects and results are as follows:

(R6P9-1, T. Kitazawa) ^{61}Ni Mössbauer spectroscopy of the $PbMn_2Ni_6Te_3O_{18}$-type oxides

Y. Doi et al. investigated magnetic behavior of low-dimensional Ni chain system in Mg-doped $PbMn_2(Ni_{0.95}Mg_{0.05})_6Te_3O_{18}$. The ^{61}Ni Mössbauer spectra of the compound showed unexpectedly little broadening due to internal magnetic field. The result may imply the magnetic interactions are weakened by the incorporation of diamagnetic Mg^{2+} ions.

(R6P9-2, H. Ohashi) Differences in ^{197}Au Mössbauer Spectra between Adsorbed Gold Samples Prepared with Different Acidity

H. Ohashi et al. investigated mechanism of partial reduction of Au(III) catalysts in different preparation conditions. The ^{197}Au Mössbauer spectra were measured in Au(III) catalysts adsorbed on MnO_2 prepared from acidic solution and alkaline solution. It was found the amount of gold(0) varied greatly depending on preparation conditions.

(R6P9-3, Y. Kobayashi) Recoilless Fraction on ^{197}Au Mössbauer Spectroscopy of Au Particles Supported on TiO_2 and SiO_2

Y. Kobayashi et al. evaluated Debye temperatures of Au particles on TiO_2 and SiO_2. It was found that of Au/TiO_2 is lower than that of metallic Au, while Au/SiO_2 is similar to metallic. It is considered to be due to fine particle size.

(R6P9-4, M. Tabuchi) Utilization of Fe ion in Fe and Ni substituted Li_2MnO_3 positive electrode material for lithium-ion battery

M. Tabuchi et al. evaluated the change of Fe oxidation value before and after charging of the electrode materials.

(R6P9-5, S. Ishiwata) Search for novel spin-charge ordered phases in anomalously high-valence iron oxides

Z. Ma et al. investigated the behavior of magnetic transition of $Ba_{1-x}La_xFeO_3$ ($x = 0.1, 0.2, 0.25$ and 0.33) and evaluated spin-charge ordered phase in charge disproportionation of Fe^{4+} to $Fe^{3+} + Fe^{5+}$.

(R6P9-6, K. Shinoda) An Intensity Tensor of Quadrupole Doublet due to Fe Ions Occupying M-sites of Hornblende

K. Shinoda et al. evaluated intensity tensor of hornblende single crystal successfully.

(R6P9-7, S. Takai) Temperature Dependence of Mössbauer Spectra of Fe_2O_3-Al_2O_3 Solid Solution in the Al-rich Region

S. Takai et al. evaluated composition dependence of QS value, which is due to deviation from spherical symmetry.

(R6P9-8, T. Ohto) Mossbauer Measurement of Spin-Crossover Complex

T. Ohto confirmed the spin crossover behavior in reduced graphene oxide template at high temperature of 410 K.

(R6P9-10. Y. Kamihara) Research on Magnetism and Electronic Phase in a H-doped Iron-based Superconductor

Y. Kamihara et al. studied temperature dependence of H-doped $SmFeAsO_{1-x}F_x$ to evaluate Debye temperature.

(R6P9-11, K. Yonezu) Experimental Preliminary Approach on the Precipitation Mechanism of Banded Iron Formation (BIF): Precipitation Behavior of Iron-bearing Siliceous Deposit Formed at Higher Temperature

K. Yonezu et al. prepared the scale samples from geothermal power plant and evaluated iron-baring compounds.

(R6P9-13, R. Masuda) ^{166}Er Mössbauer spectroscopy of ErB_{66}

R. Masuda et al. evaluated the hyperfine field of Er in magnetic ordering of ErB_{66} at 20K.

(R6P9-14, S. Kitao) Search of ^{166}Er Mössbauer Single-Line Materials

S. Kitao et al. evaluated ^{166}Er Mössbauer spectra of ErF_3 at about 20K, which is a candidate for single-line Er material. It is unfortunately found that a broadened component was observed in ^{166}Er Mössbauer spectrum.

The experiments have not been performed in this term in R6P9-9 and R6P9-12.

PR9-1

^{61}Ni Mössbauer spectroscopy of the $PbMn_2Ni_6Te_3O_{18}$-type oxides

Y. Doi[1, 2], H. Fukuda[1], K. Kitase[1], T. Kitazawa[1, 2], S. Kitao[3], Y. Kobayashi[3], T. Kubota[4], and M. Seto[3].

[1]*Department of Chemistry, Faculty of Science, Toho University, Japan*
[2]*Research Centre for Materials with Integrated Properties, Toho University*
[3]*Institute for Integrated Radiation and Nuclear Science, Kyoto University*
[4]*Agency for Health, Safety and Environment, Kyoto University*

INTRODUCTION: The compounds featuring low-dimensional arrangements of magnetic ions are known to exhibit distinctive magnetic behaviors at low temperatures. Among them, one-dimensional chain systems have attracted a great deal of interest since the proposal of Haldane's conjecture, which has led to the discovery of various quantum phenomena, such as the spin-gap behavior observed in Ni^{2+} (S = 1) chains. Recently, we investigated the compound $PbMn_2Ni_6Te_3O_{18}$, which contains zigzag Ni^{2+} chains, and found that it exhibits low-dimensional magnetic behavior and an antiferromagnetic transition at 86.0 K arising from the collinear ordering of both Ni^{2+} and Mn^{2+} magnetic moments[1]. Furthermore, this compound has very recently been identified as a potential candidate for a novel ferrotoroidic material[2]. The fundamental magnetic properties of this compound are primarily gov-erned by the Ni^{2+} chain structure. To gain further insights into the local environment and magnetic characteristics of Ni^{2+} ion, we conducted the ^{61}Ni Mössbauer spectroscopy measurements.

EXPERIMENTS: Polycrystalline samples of $PbMn_2Ni_6Te_3O_{18}$ and its Cd- and Mg-doped derivatives were synthesized via a conventional solid-state reaction method. The starting materials used were PbO, CdO, MnO, NiO, MgO, and TeO_2. Stoichiometric mixtures of these oxides were thoroughly ground, pressed into pellets, and calcined in a muffle furnace at 973–1073 K for 12–36 hours. Phase purity and structural characterization were confirmed by powder X-ray diffraction combined with Rietveld refinement, revealing that all samples crystallize in the hexagonal structure with space group $P6_3/m$, identical to that of undoped $PbMn_2Ni_6Te_3O_{18}$. For ^{61}Ni Mössbauer spectroscopy meas-urements, approximately 0.5 g of powdered sample was loaded into a 10 mm diameter sample holder.

RESULTS: Figure 1 presents the ^{61}Ni Mössbauer spectrum of Mg-doped $PbMn_2(Ni_{0.95}Mg_{0.05})_6Te_3O_{18}$ at 20 K. The spectrum appears to exhibit a single peak; however, it shows slight broadening compared to that of the standard $Ni_{86}V_{14}$ alloy, suggesting the possible presence of magnetic hyperfine splitting. The Néel temperature of the compound is approximately 80 K, indicating that the Ni^{2+} ions are situated in an internal magnetic field generated by long-range antiferromagnetic ordering. Curve fitting yields an internal field of approximately 4.6 T, which is unexpectedly small given the relatively high transition temperature. This result may imply that the magnetic interactions are weakened by the incorporation of diamagnetic Mg^{2+} ions, which likely disrupt the exchange pathways.

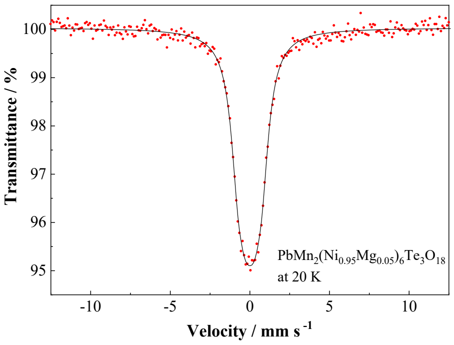

Fig. 1. The ^{61}Ni Mössbauer spectrum of Mg-doped $PbMn_2Ni_6Te_3O_{18}$.

REFERENCES:

[1] Y. Doi *et al.,* J. Inorg. Chem., **54** (2015) 10725−10731.
[2] R. Nakamura *et al.,* J. Phys. Soc. Jpn., **93** (2024) 063703.

PR9-2

Differences in ^{197}Au Mössbauer Spectra between Adsorbed Gold Samples Prepared with Different Acidity

H. Ohashi, M. Taguchi, S. Ikeda, T. Okuyama, N. Takahashi, Y. Kobayashi[1], S. Kitao[1]

Faculty of Symbiotic Systems Science, Fukushima University
[1]Institute for Integrated Radiation and Nuclear Science, Kyoto University

INTRODUCTION: Gold catalysts have been very famous as heterogeneous catalysts. When preparing gold catalysts from Au(III) compounds, it was known that the preparation conditions differ depending on the support metal oxides. Preparation of Au/MnO_2 from $HAuCl_4$ compounds was known to be difficult. This was because Au(III) ions were partially reduced to Au(0) on the surface of MnO_2.

We have investigated the mechanism of this automatic reduction to Au(0)[1]. As a conclusion, the Au(III) component with relatively high IS and QS values was important. However, the reason why Au(III) ions were effectively reduced to Au(0) was unknown. In this study, we focused on the slow ligand substitution of Au(III) ions and aimed to observe the change in ^{197}Au Mössbauer spectrum when Au(III) aqueous solution was prepared from the alkaline side and the acidic side.

EXPERIMENTS: Manganese dioxide was added to the $HAuCl_4$ aqueous solution to adjust the pH 6 from acid media or alkaline media, and the mixture was stirred. The solution of ionic strength was adjusted to 0.10 M with NaCl. The suspension solution was filtered using 0.45 μm membrane filter, and the filtrate was dried at 30oC for 12 hours. The amount of gold was approximately 5wt%.

^{197}Au Mössbauer spectra were measured at Kyoto University Research Institute of Nuclear Science. The ^{197}Pt isotope (T1/2 = 18.3 h), γ-ray source feeding the 77.3 keV Mössbauer transition of ^{197}Au, was prepared by neutron irradiation of isotopically enriched ^{196}Pt metal at the Kyoto University Reactor. The measurement temperature was 20 K, and the measurement was performed by the transmission method.

RESULTS: Figure 1 shows ^{197}Au Mössbauer spectra at 20 K for the sample of Au(III) adsorbed on MnO_2. It was found that the amount of gold(0) varied greatly depending on whether the aqueous solution was acidic or alkaline (Table 1).

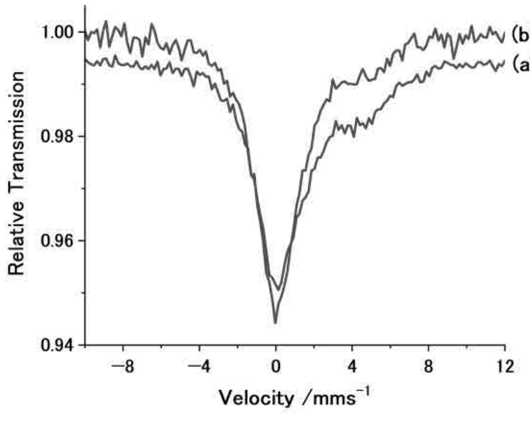

Fig. 1. ^{197}Au Mössbauer spectra at 20 K for the sample of Au(III) adsorbed on MnO_2. (a) prepared from acid solution, (b) from alkaline.

REFERENCE:

[1] H. OHASHI, K. YONEZU, D. KAWAMOTO, and T. YOKOYAMA, Anal. Sci., **37** (2021) 1321-1330.

Table 1 Mössbauer parameters for Au(III) adsorbed on MnO_2 samples. (a) Au loaded 5wt%, stirred with pH 6 adjusted from acid solution, (b) Au loaded 5wt%, stirred with pH 6 adjusted from alkaline solution.

		Component A	**Component B**		**Component A**	**Component B**
	Γ /mms^{-1}	**IS /mms^{-1}**	**IS /mms^{-1}**	**QS /mms^{-1}**	**Area (%)**	**Area (%)**
Sample (a)	**2.49**	**0.01**	**3.24**	**2.90**	**68.3**	**31.7**
Sample (b)	**2.40**	**0.01**	**3.17**	**3.27**	**82.3**	**17.7**

PR9-3

Recoilless Fraction on ^{197}Au Mössbauer Spectroscopy of Au Particles Supported on TiO_2 and SiO_2

Yasuhiro KOBAYASHI[1], Hironori OHASHI[2] and Makoto SETO[1]

[1]Institute for Integrated Radiation and Nuclear Science, Kyoto University
[2]Faculty of Symbiotic Systems Science, Fukushima University

INTRODUCTION: The recoilless fraction is a parameter that reflects lattice vibrations and provides important knowledge in physics, chemistry, etc. In ^{197}Au Mössbauer spectroscopy, the energy of γ-rays is higher than ^{57}Fe, so differences and changes in the recoilless fraction appear significantly. We have succeeded in estimating the Debye temperature not from the absolute amount of spectral absorption area but from its temperature dependence curve and estimated that of $Au(OH)_3$ and Au_2S [1]. We applied this technique to Mössbauer measurements of Au-supported catalysts. The characteristics of Au-supported catalysts change depending on the supporters. To investigate the influences of the supporters on the Au particles, we measured the ^{197}Au Mössbauer spectrum and the recoilless fraction.

EXPERIMENTS: Prepared samples were Au particles on a TiO_2 supporter (Au/TiO_2) and Au particles on a SiO_2 supporter (Au/SiO_2). The Au contents were 2~10wt% in Au/TiO_2 and 2wt% in Au/SiO_2. The TiO_2 or SiO_2 powder was put in the $HAuCl_4$ aqueous solution, and $Au(OH)_3$ was precipitated on the powder surface by adjusting the pH while stirring. The obtained powder was dried and calcined at 300°C for 4 hours to prepare the sample [2].

Using KUR, the ^{197}Pt γ-ray sources for ^{197}Au Mössbauer measurements were prepared by neutron irradiation to 98%-enriched ^{196}Pt metal foil. The γ-ray source and samples were cooled to the same temperatures using a helium refrigerator.

RESULTS: In the ^{197}Au Mössbauer spectra of the Au/TiO_2 and Au/SiO_2 samples, all components showed a single peak like metallic Au. It was found that Au was chemically in the metallic Au state in all samples. No interface or surface components were observed, even in the Au 2wt% Au/TiO_2 sample, which is considered the smallest Au particles.

The Debye temperatures of the Au/TiO_2 samples and Au/SiO_2 sample obtained from the temperature change of the spectral absorption area. It was close to that of bulk metallic Au in the Au 10wt% Au/TiO_2 sample. However, it was lower than metallic Au in the Au 2wt% sample. This is thought to be due to a decrease in the recoilless fraction due to fine particle size. On the other hand, the Au 2wt% Au/SiO_2 sample had a Debye temperature close to that of metallic Au, suggesting that the particles were not as small as those in Au/TiO_2. In X-ray diffraction, the peaks of metallic Au were not observed in the 2wt% Au/TiO_2 sample due to the fine particle size, whereas it was observed in the Au/SiO_2 sample. The results of the recoilless fractions are consistent with the X-ray diffraction. The lattice vibrations affect the adsorption and movement of adsorbed molecules on the Au particle surface. Therefore, it is thought to affect catalytic activity.

REFERENCES:

[1] Yasuhiro kobayashi *et al.,* Interactions, **245** (2024) 42.
[2] Luong Xuan Dien *et al.,* Applied Catalysis B: Environmental, **241** (2019) 539-547.

R6P9-3

PR9-4

Utilization of Fe ion in Fe and Ni substituted Li_2MnO_3 positive electrode material for lithium-ion battery

M. Tabuchi and Y. Kobayashi[1],
National Institute of Advanced Industrial Science and Technology (AIST)
[1]Institute for Integrated Radiation and Nuclear Science, Kyoto University

INTRODUCTION: Large scale lithium-ion battery (LIB) is needed for EV and ESS applications. To stabilize a cost of the LIB, low-cost positive electrode material is necessary. Especially, utilization of Fe ion redox is attractive. Fe and Ni substituted Li_2MnO_3 is a suitable positive electrode material for above object [1, 2]. In this report, $Li_{1+x}(Fe_{0.2}Ni_{0.1}Mn_{0.7})_{1-x}O_2$ ($0<x<1/3$) was selected to check the change in valence state of Fe ion using ^{57}Fe Mössbauer spectroscopy during the electrochemical activation process.

EXPERIMENTS: The sample was prepared by coprecipitation-calcination method [2]. After calcination in air, the sample was calcined by reductive atmosphere (4%H_2-96%N_2 gas) at 425 °C for 3h. The electrochemical activation process was constructed as follows; The charged capacity increased from 80 mAh/g (1st) by 40 mAh/g step until 200 mAh/g (4th) after discharged to 2.0 V for Li/sample cell. At 5th cycle, the cell charged to 4.8 V and then discharged to 2.0 V to finish activation process. The active material was sealed in Al-laminate sheet for ^{57}Fe Mössbauer measurement. The isomer shift (IS) value was calculated using α-Fe as standard material.

RESULTS: The as-prepared (asp.) and first charged (1c) sample's XRD pattern can be fitted by a single-phase of monoclinic Li_2MnO_3 structure, whereas fifth charged (5c) and then discharged (5d) samples had monoclinic $NaNiO_2$ one. Both structures belong to layered rock-salt one.

^{57}Fe Mössbauer spectra (Fig. 1) for the as-prepared sample fitted by two symmetric doublets. The main A component (90%, IS=+0.34 mm/s) was assigned as high-spin trivalent Fe [3], whereas minor B one (10%, IS=-0.22 mm/s) was attributed as tetravalent state (4+δ state, $0<\delta<0.5$) [3]. After first charging (1c), minor B (20%) and C (7%) components appeared. Both components had highly negative IS values (-0.32 and -0.46 mm/s for B and C ones, respectively). The B and C components were assigned as 4.5+ and 5+ states [4]. The fact indicates that attractive $Fe^{3+/5+}$ redox coexisted with normal $Fe^{3+/4+}$ one on initial charging. At the end of charging (5c) state, the IS values of the B (21%) and C (8%) components were raised to +0.15 and +0.16 mm/s, respectively. These components are assigned as 3.5+ state [3], indicating that oxidized Fe ion was reduced incompletely at the end of charging. At the end of discharging (5d) state, all of Fe component was trivalent state. The result showed that the $Fe^{3.5+}$ ion utilized on fifth discharging. In summary, at $Li_{1+x}(Fe_{0.2}Ni_{0.1}Mn_{0.7})_{1-x}O_2$ composition, constituent Fe ion act as redox center on both charging and discharging. The obtained result contributes to accelerate the development of low-cost positive electrode material.

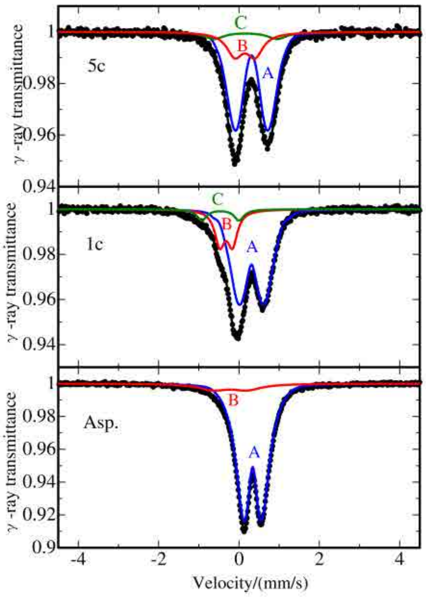

Fig. 1 ^{57}Fe Mössbauer spectra for before and after charged samples.

REFERENCES:[1] M. Tabuchi et al., Electrochim. Acta, **303** (2019) 9-20. [2] M. Tabuchi et al., Mat. Res. Bull., **149** (2022) 11743. [3] G. Prado et al., J. Electrochem. Soc., **147** (2000) 2880-2887. [4] F. Menil, J. Phys. Chem. Solids, **46** (1985) 763-789.

PR9-5

Search for novel spin-charge ordered phases in anomalously high-valence iron oxides

Z. Ma[1], M. Onose[1,2], H. Takahashi[1], S. Kitao[3], M. Seto[3], S. Ishiwata[1]

[1] *Graduate school of engineering science, Osaka University*
[2]*Department of Engineering, University of Tokyo*
[3]*Institute for Integrated Radiation and Nuclear Science, Kyoto University*

INTRODUCTION: Charge disproportionation of Fe^{4+}, described by $2Fe^{4+} \rightarrow Fe^{3+} + Fe^{5+}$, was widely observed in perovskite-type iron oxides with anomalous high valence state, and is closely linked to the emergence of novel magnetic phases. For instance, charge disproportionation of iron was observed in $Sr_{2/3}La_{1/3}FeO_3$, originated from the spin-charge ordering (SCO) phase, where the three-fold charge ordering was coupled with the six-fold spin ordering. [1] In our previous work, we revealed a plausible SCO phase in $Ba_{1-x}La_xFeO_3$ when $x = 0.2$. In order to further understand the magnetic ordering, the valence of iron was studied with the Mössbauer spectra for $Ba_{1-x}La_xFeO_3$ with $x = 0.1$, 0.2, 0.25 and 0.33, measured below the phase transition temperature.

EXPERIMENTS: Polycrystalline samples of $Ba_{1-x}La_xFeO_3$ were synthesized by annealing $Ba_{1-x}La_xFeO_{3-\delta}$ with oxidizing agent ($NaClO_3$) at 500 °C and 8 GPa for 1h in a cubic-anvil-type high-pressure apparatus. The ^{57}Fe Mössbauer spectra were measured with a ^{57}Co source in Rh. The velocity was calibrated with α-Fe.

RESULTS: Figure 1(a) shows the Mössbauer spectra for $Ba_{1-x}La_xFeO_3$ with $x = 0.1$, 0.2, 0.25 and 0.33, measured below the phase transition temperature. The spectrum for $x = 0$ was reproduced from previous report.[2] The spectra for $x = 0.1$, 0.2, 0.25 and 0.33 can be well fitted by the superposition of two sexts corresponding to two Fe ions with different valence states, indicating charge disproportionation. As shown in Figures 1(b-c), the sextet with an isomer shift (IS) of approximately 0.5 mm/s and a hyperfine field (HF) around 45 T is attributed to Fe^{3+}. The other sextet, with an IS of around 0.1 mm/s and an HF of approximately 25 T, is attributed to Fe^{5+}. For $x = 0.25$ and 0.33, the charge disproportionation is consistent with the emergence of SCO I phase.[3] For $x = 0.2$, the ratio for Fe^{3+} and Fe^{5+} are 53% and 47%, respectively, which is close to the expected ration of 3:2, suggesting a novel SCO II phase. The broadening of the sexts for the Fe^{3+} and Fe^{5+} is observed for lower La content x. The broadening of the peaks in $x = 0.25$ is attributed to the coexistence of HM and SCO I phases, as it is at the boundary of the phase diagram. For $x = 0.2$, the significant broader peaks indicate spin fluctuations.

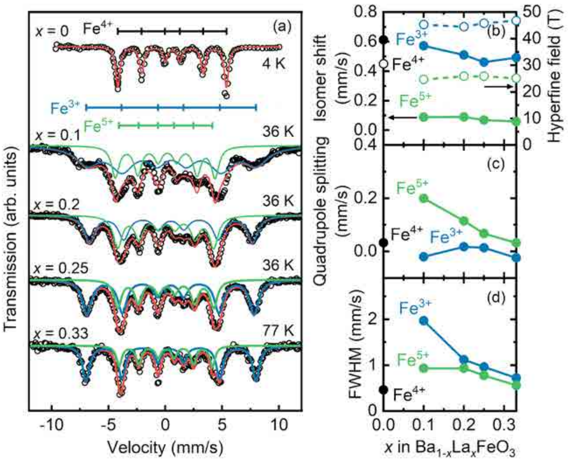

Fig. 1. (a) The Mössbauer spectra for $Ba_{1-x}La_xFeO_3$ ($x = 0.2$, 0.2, 0.25 and 0.33) under phase transition temperature. (b) Isomer shift, and hyperfine field, (c) quadrupole splitting, (d) Full width at half maximum (FWHM) obtained by the fitting of the Mössbauer spectra.

REFERENCES:

[1] J. Q. Li *et al.,* Phys. Rev. Lett., **79** (1997) 297 .
[2] N. Hayashi *et al.,* Angew. Chem., **123** (2011) 12755.
[3] M. Onose *et al.,* Phys. Rev. Mater., **4** (2022) 094401.

PR9-6

An Intensity Tensor of Quadrupole Doublet due to Fe Ions Occupying *M*-sites of Hornblende

K. Shinoda and Y. Kobayashi[1]

Department of Geosciences, Graduate School of Science, Osaka Metropolitan University
[1]Institute for Integrated Radiation and Nuclear Science , Kyoto University

INTRODUCTION: Hornblende is a typical amphibole mineral that widely occurs in igneous and metamorphic rocks. General chemical composition of hornblende is $NaCa_2(Mg, Fe^{2+}, Al)_5$ $(Si, Al)_8$ O_{22} $(OH)_2$. Hornblende is a major multi-site solid solution mineral that includes M1, M2, M3 and M4 sites. Mg and Fe^{2+} ions occupy the smaller M1, M2, and M3 sites and Na and Ca ions occupy the larger M4 site. Pyroxene is also multi-site solid solution minerals the include M1 and M2 sites. The intensity tensor for Fe ions at M-sites is important property for analyzing Mössbauer spectra of single crystal of multi-site solid solution minerals. Although chemical dependences of intensity tensors in Ca-rich pyroxene [1] and Ca-poor orthopyroxene [2] are revealed, intensity tensor due to Fe ions in M-sites of amphibole is not revealed. The intensity tensor is a symmetric tensor of which components are I_{XX}, I_{YY}, I_{ZZ}, I_{XY}, I_{YZ} and I_{XZ}. I_{YZ} and I_{XZ} of monoclinic crystal can be fix as 0 by its symmetry. The peak intensity (I) defined as $I_h/(I_h+I_l)$, where I_l and I_h are the lower and higher peak's intensity, respectively [3].

EXPERIMENTS: A single crystal of hornblende from Ikenohukuro, Sakai, Suwa, Nagano prefecture, Japan was used for this study. Three crystallographically oriented thin sections perpendicular to ***a***, ***b*** and ***c*** were prepared by measuring X-ray diffraction methods. Nine Mössbauer spectra of oriented thin sections and one powder spectrum were measured. Cartesian coordinate (X Y Z) is set as X//***c****, Y//***a***, Z//***b****. Mössbauer measurements were carried out in transmission mode on a constant acceleration spectrometer with an Si-PIN semiconductor detector (XR-100CR, AMPTEK Inc.) and multichannel analyzer of 1024 channels. A 3.7GBq $^{57}Co/Rh$ of 4mmϕ in diameter was used as γ-ray source. An ^{57}Fe-enriched iron foil was used as velocity calibrant. The two symmetric spectra were folded, and velocity range was ± 4mm/s. Mosswinn program was used for peak separation.

RESULTS: Peak separation of powder sample was performed by three quadrupole doublets of equal intensity peak (I =0.5) assuming Fe ions at three M-sites. As the result, three kinds of successful peak separation were obtained. Peak separations of single crystal were done in the three ways by fixing IS_n, QS_n and LW_n (n=1, 2, 3) of powder sample, and unfixing peak intensity (I). For three different peak separations, three intensity tensors $(I^{'()}_{("),\%\&}(p, q = X, Y, Z))$ were obtained by fixing I_{YZ} and I_{XZ} as 0. To examine the validity of three intensity tensors, intensity tensors $(I^{*'''\ 0}_{("),\%\&})$ by unfixing I_{YZ} and I_{XZ} as 0 were also calculated. Comparing $I^{'()}_{("),\%\&}$ and $I^{*'''\ 0}_{("),\%\&}$, the best matched intensity tensor was selected as the intensity tensor of this hornblende. Fig.1 shows Mössbauer spectrum of hornblende single crystal under γ-ray //a-axis and the best peak separation among three different parameters (IS_n, QS_n and LW_n).

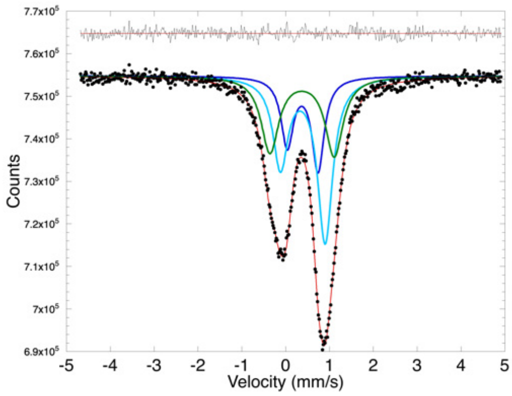

Fig. 1. Mössbauer spectra of hornblende single crystal under γ-ray //a-axis and a peak separation with three QS doublets.

REFERENCES:

[1] D. Fukuyama *et al.,* J. Mineral. Petrol. Sci., **117** (2022) 011.
[2] K. Shinoda *et al.,* J. Mineral. Petrol. Sci., **118** (2023) 020.
[3] R. Zimmermann, Nucl. Instr. and Meth., **128** (1975) 537-543.

Temperature Dependence of Mössbauer Spectra of Fe_2O_3-Al_2O_3 Solid Solution in the Al-rich Region

S. Takai[1], D. Luo[1], T. Yabutsuka[1], S. Kitao[2], M. Seto[2]

[1]*Graduate School of Energy Science, Kyoto University*
[2]*Institute for Integrated Radiation and Nuclear Science, Kyoto University*

INTRODUCTION: While α-Fe_2O_3 and α-Al_2O_3 exhibit the corundum-type structure, the solid solution range is much restricted around the endmembers of the composition. We have reported the successful preparation of Fe_2O_3-Al_2O_3 solid solutions across the entire compositional range using mechanical alloying techniques starting from γ-Fe_2O_3 and γ-Al_2O_3. The compositional dependence of the solid solution exhibits Vegard's law, and the radial distribution function obtained by EXAFS shows the gradual decrease at Fe-Fe distance, whereas it remains almost constant at Fe-O. We measured the Mössbauer spectra of $(Fe_2O_3)_{1-x}(Al_2O_3)_x$ solid solutions at room temperature in the previous study. The spectra change from sextet to doublet with increasing aluminum concentration, which should be ascribed to the spin interaction decrease due to the substitution of non-magnetic aluminum ions for iron. While the doublet profile is observed for the solid solution of x = 0.5 at room temperature, it changes to a sextet with decreasing temperature. The spin fluctuation is thought to be restricted by reducing the temperature, and long-range spin interaction becomes evident. In the present study, we deduced the magnetic parameters from fitting the spectra with the doublet and sextet profiles.

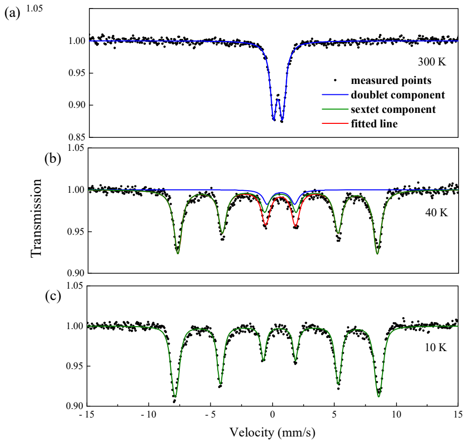

Fig. 1 Measured and fitted Mössbauer spectra for $(Fe_2O_3)_{0.5}(Al_2O_3)_{0.5}$. (a) 10 K, (b) 40 K, and (c) 300 K.

EXPERIMENTS: Mössbauer spectroscopy was performed on $(Fe_2O_3)_{0.5}(Al_2O_3)_{0.5}$ through the conventional transmission mode using a ^{57}Co in Rh γ-ray source (1.85 GBq). Liquid helium and liquid nitrogen were employed as coolants below and above 77 K, respectively. The Doppler velocity scale was calibrated using an iron foil reference, and the spectral profiles were analyzed in Velocity Buffer File (VBF) mode. The profile fitting was carried out by RECOIL program to yield some magnetic parameters.

RESULTS: Fig. 1 shows measured and fitted profiles of the Mössbauer spectra for on $(Fe_2O_3)_{0.5}(Al_2O_3)_{0.5}$. Single doublet peaks are employed for the spectra of 300K, while sextet peaks are for 10 K. These combinations are used at intermediate temperatures. Fig. 2 represents the quadrupole splitting obtained from the sextet and doublet components. The negative values of QS for sextet components indicate a weak-ferromagnetic state rather than antiferromagnetic for the measured temperature range. As for the doublet component, the QS values increase with decreasing temperature, which should be ascribed to the deviation from spherical symmetry due to the suppression of spin fluctuation.

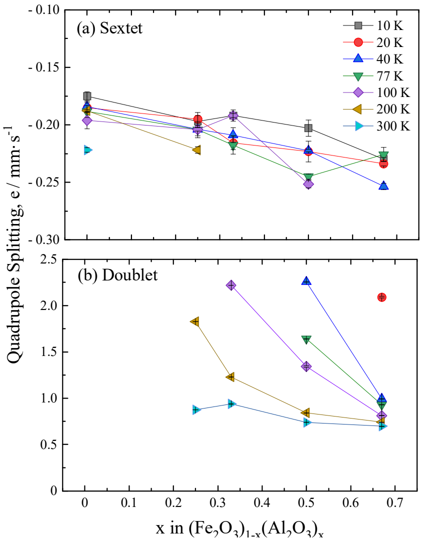

Fig. 2 Compositional dependence of the quadrupole splitting of $(Fe_2O_3)_{1-x}(Al_2O_3)_x$ under variable temperatures obtained from (a) sextet and (b) doublet component.

PR9-8

Mössbauer Measurement of Spin-Crossover Complex

T. Ohto

Graduate School of Engineering, Nagoya University

INTRODUCTION: Despite a clear demonstration of bistability in spin-crossover (SCO) materials, the absence of long-range magnetic order and poor electrical conductivity limit their prospect in spintronic and nanoelectronic applications. Intending to create hybrid devices made of spin-crossover (SCO)-2D architecture, here, we report an easily processable Fe-based SCO nanostructures grown on 2D reduced graphene oxide (rGO). The heterostructure shows enhanced cooperativity due to formation of interfacial charge transfer induced inter-molecular interaction. The spin transition temperature is controlled by tuning the coverage area of SCO nanostructured networks over the 2D surfaces, thus manipulating hysteresis (aka memory) of the heterostructure. The enhanced magnetic coupling of the heterostructure leads to the spontaneous magnetization states with a large coercive field of ~ 3000 Oe. Additionally, the low conductivity of the pristine SCO nanostructures is addressed by encapsulating them on suitable 2D rGO template, enabling detection of magnetic bistable spin states during high-spin/low-spin conductance change. This adds spin functionality in conductance switching for realizing hybrid 2D spintronic devices. Ab-inito calculations, on the experimentally proposed nanostructures, corroborate the enhanced magnetic interaction in the proposed architecture facilitated by interfacial charge transfer and provide insights on the microscopic mechanism.

****

EXPERIMENTS: Conventional ^{57}Fe Mössbauer spectroscopy was performed using ^{57}Co source in Rh matrix with nominal activity of 1.85 GBq. The velocity scale was calibrated with α-Fe. For the low temperature measurements, a mixture of the compound with silicone grease was used as the Mössbauer absorber. We pelletized mixture of the compound with BN and polyethylene powder for the room temperature ~ high temperature measurements.

****

RESULTS:

The ^{57}Fe Mössbauer spectroscopy was performed for the low concentration and high concentration samples starting from room temperature (297K) to different temperatures until 410K high temperature to reveal the electronic states of Fe centres in the nanocomposites and to confirm the Fe II SCO behaviour in a rigorous and accurate way. The low spin and high spin states of Fe(II) can be clearly distinguished through their different hyperfine parameters in a quadrupolar interaction.

****

REFERENCES:

[1] B. Shatabda *et al.,* submitted.

PR9-9

Research on Magnetism and Electronic Phase in a H-doped Iron-based Superconductor III

Y. Kamihara, A. Matsuura, Y. Kobayashi[1], S. Kitao[1], and M. Seto[1]

Department of Applied Physics and Physico-Informatics, Faculty of Science and Technology, Keio University
[1]Institute for Integrated Radiation and Nuclear Science, Kyoto University

INTRODUCTION: The research in 2024 is to clarify the bulk element specific magnetic properties of polycrystalline superconducting $SmFeAsO_{1-x}H_x$ (H-doped Sm1111) prepared by high temperature and high pressure synthesis and $SmFeAsO_{1-x}F_x$ (F-doped Sm1111) prepared by conventional method.[1-5] ^{57}Fe Mössbauer spectra are demonstrated for the H-doped Sm1111 at several low temperatures. Present spectra are very similar to that of superconducting F-doped Sm1111. [5, 6]

EXPERIMENTS: The phase purity, lattice constants, and crystal structure of the sintered powders were examined by powder x-ray diffraction (XRD) Rigaku Rint2500 using Cu K alpha radiation from a rotating anode. The magnetic moment (M) of polycrystalline H-doped Sm1111 was measured using a SQUID magnetometer (Quantum Design MPMS) at several temperatures (T) and magnetic fields (H). ^{57}Fe Mössbauer spectroscopy was observed at T = 4.2, 10, 20, 50, 77, 300 K for the H-doped Sm1111. The ^{57}Fe Mössbauer spectroscopy was performed using 14.4 keV γ-rays from a ^{57}Co source.

RESULTS: Figure 1 exhibits ^{57}Fe Mössbauer spectra at T = 4.2, 10, 20, 50, 77, 300 K for H-doped Sm1111. The Mössbauer spectra of H-doped Sm1111 were analyzed using the code Mosswinn [7], and the apparent isomer shift was determined. In this study, the spectrum was refined by considering the electronic state around the Fe nucleus as a mixture of singlet and doublet. Subsequently, the obtained isomer shift (δ) values, which were obtained at each T, were used along with the theoretical formula to refine the δ-T plot data. In 2025, we will derive and refine the Debye temperature for the H-doped Sm1111. Magnetic phases of the H-doped Sm1111 are paramagnetic at T = 4.2-300 K.

REFERENCES:

[1] For a review, Y. Sakai, Ph. D thesis (Keio University, 2015).
[2] K. Miyazawa *et al.,* Appl. Phys. Lett., **96** (2010) 07254.
[3] P. M. Shirage *et al.,* Phys. Rev. Lett., **105** (1010) 037004.
[4] Y. Muraba *et al.,* Inorg. Chem., **54** (2015) 11567-11573.
[5] Y. Kamihara *et al.,* New J. Phys., 12, 033005 (2010).
[6] Y. Kamihara *et al.,* American Physical Society March Meeting, Dallas, USA (2011).
[7] Z. Klencsar, Mosswinn Program (Budapest, 2001). [http://www.mosswinn.com/].

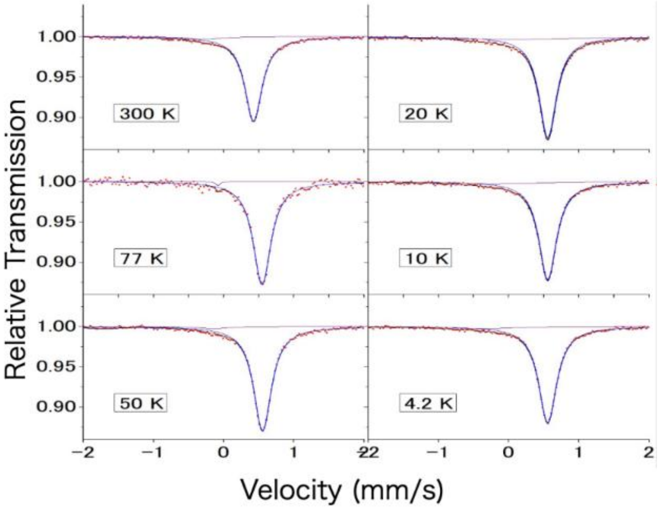

Fig. 1. ^{57}Fe Mössbauer spectra at T = 4.2, 10, 20, 50, 77, 300 K for H-doped Sm1111.

PR9-10

Experimental Preliminary Approach on the Precipitation Mechanism of Banded Iron Formation (BIF: Precipitation Behavior of Iron-bearing Siliceous Deposit Formed at Higher Temperature

K. Yonezu[1], E. Wanyonyi[1], S. Juhri[1], Y. Kobayashi[2] and T. Yokoyama[3]

[1]Department of Earth Resources Engineering, Faculty of Engineering, Kyushu University
[2] Institute for Integrated Radiation and Nuclear Science, Kyoto University
[3]Department of Chemistry, Faculty of Sciences, Kyushu University

INTRODUCTION: Banded Iron Formation (BIF) is chemically precipitated sedimentary rock at Precambrian age. Current iron resource widely used in our industries largely depends on BIF. Commonly the hydrothermal water, anoxic water was mixed with oxic seawater (e.g., Otake and Otomo, 2021). However, the formation mechanism of BIF was not yet clarified. In order to ap-proach the formation mechanism, we have done ambient temperature batch experiments, elevated temperature batch experiments and the experiments using natural system (geothermal fluid mixed with seawater and silica scale characterization formed at around 100 degree C). Therefore, this study aims to understand the formation mechanism of iron-bearing siliceous deposits at higher temperature in Olkaria geothermal power plant in Kenya.

EXPERIMENTS: Several scale samples were collected from multiple locations of the Olkaria geothermal power plant, including separators, atmospheric silencers, brine lines, scrubbers, vent stations, and cooling towers. The samples were analyzed by XRD, XRF, petrograph and NMR (^{29}Si and ^{27}Al).

RESULTS: As shown in Fig. 1, ^{27}Al NMR results suggested that most of Al is present as 4-coordinated structure with minor 6 coordinated structure. Combined with the data from SEM-EDX, aluminum was seen to be uniformly distributed in the silica phase, especially in the samples from the separators, suggesting that the 4-coordinate aluminum ion (AlO_4 unit) was present at the silicon site (SiO_4 unit) in the silica phase by isomorphous substitution. The chemical composition of those samples are mainly composed of SiO_2, followed by Al_2O_3 and Fe_2O_3 (up to 2.3wt%). Mineralogically, those samples are amorphous phase. Additionally, ^{29}Si NMR spectra indicated that the structure considered for Si was Q^4. The detailed peak deconvolution was conducted and revealed that there are several mineral phases in one sample as suggested by XRD pattern with the presence of opal. The role of Al in the precipitation of siliceous deposit was well discussed, however iron-bearing siliceous deposit in neutral to alkaline pH conditions with high temperature has not yet discussed. For further discussion on the formation mechanism of iron-bearing siliceous deposit would be an important key to understand the formation mechanism of BIF.

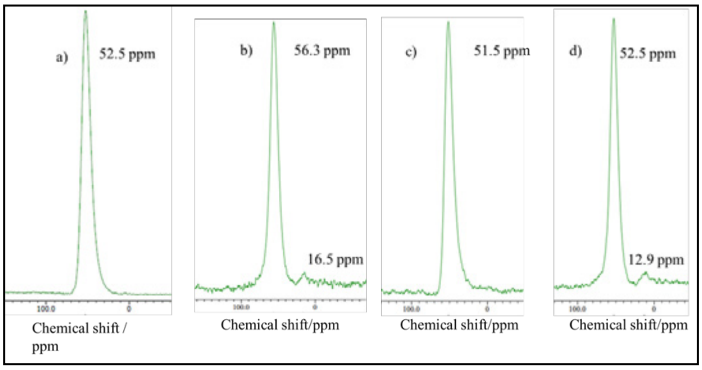

Fig. 1. ^{27}Al MAS NMR spectrum for the representative samples

REFERENCES:

[1] T. Otake *et al.,* Shi-gen-Chishitsu, **71** (2021) 57-73.
[2] E. Wanyonyi *et al.,* Geo-thermics **117** (2024) 102871.

PR9-11

^{166}Er Mössbauer spectroscopy of ErB_{66}

R. Masuda, F. Iga[1], S. Kitao[2], Y. Kobayashi[2], K. Murakami, T. Kato, H. Shimizu, and M. Seto[2]

Graduate School of Science and Technology, Hirosaki University
[1]*Graduate School of Science and Technology, Ibaraki University*
[2]*Institute for Integrated Radiation and Nuclear Science, Kyoto University*

INTRODUCTION: Boron-rich rare earth borides recently attract researchers as magnetically-diluted insulators. In fact, we can control the ratio of the constituent magnetic atom, i. e. rare earth atoms; REB_4, REB_6, REB_{12}, and REB_{66} (RE=rare earth) are typically stable. Erbium atom is a rare earth element with L=6 and S=3/2 (J = 15/2) and ErB_{66} is a semiconductor boride with diluted magnetic atoms. Its crystal structure is cubic $Fm\bar{3}c$, same as other rare earth REB_{66}. The clear magnetic ordering is seen below 0.5 K as the maximum in the ac susceptibility measurement and above the temperature, a spin glass state is discussed [1]. Recently, ^{166}Er Mössbauer spectroscopy using ^{166}Ho ($T_{1/2}$=26.8h) source is available in KURNS [2,3]. Therefore, we performed ^{166}Er Mössbauer spectroscopy to observe the electronic state of ErB_{66} in microscopic viewpoint.

EXPERIMENTS: The Mössbauer spectroscopy was performed at Tracer Laboratory at KURNS using cryostat by a refrigerator by cooling both source and sample. The source was (^{166}Ho,Y)H_2 powder synthesized by the neutron irradiation to the dihydride with natural Ho, that is, Ho consisted of only ^{165}Ho. The irradiation condition was 2.5 hours under 1MW KUR operation. The sample was non-enriched ErB_{66} powder, that is, including 33.5 % of ^{166}Er, shaped to the pellet of 10 mmφ. The γ-rays from the source penetrated the sample and were detected by a $CeBr_3$ scintillator. The detail of the Mössbauer measurement system is shown in ref. [3].

RESULTS: The Mössbauer spectrum of ErB_{66} at 20 K is shown in Fig. 1. The magnetic hyperfine splitting is clearly shown even at 20 K, by far higher than the temperature of maximum of the ac susceptibility. This result is clear evidence for the existence of a kind of magnetic ordering, which is discussed as spin-glass state. Furthermore, the spectrum was not a typical shape of the simple one element with magnetic splitting. It can be analyzed by a model with the distribution of magnetic hyperfine fields. The normal distribution of magnetic hyperfine fields with the mean of 628 T and the standard deviation of 38.4 T explains the spectra, as shown in Fig. 1. The existence of such distribution agrees with the spin-glass state and implies that the glass state includes the distribution of atomic magnetic moments. If we use the conversion factor 87.1 T/μ_B derived from the ^{166}Er Mössbauer spectroscopy of antiferromagnetic Er_3Ge_4 [4], these parameters correspond to the mean of 7.21μ_B and the standard deviation of 0.441μ_B.

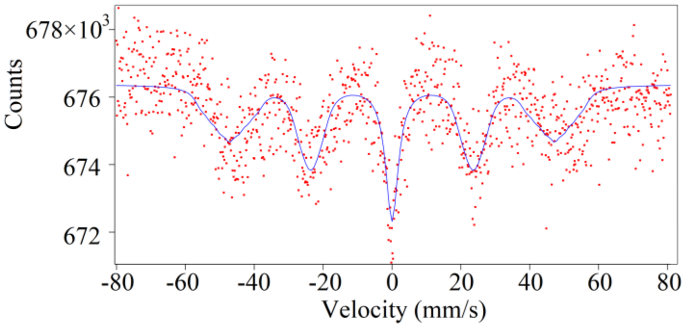

Fig. 1 The Mössbauer spectrum of ErB_{66} at 20 K. The red dots are experimental data and the line is a fitting with a distribution of the magnetic hyperfine interaction.

REFERENCES:

[1] H. Kim *et al.,* J. Supercond. Nov. Magn., **25** (2012) 2371-2375.
[2] S. Nakamura, *et al.*, Hyperfine Interact., **241** (2019) 75 .
[3] S. Kitao *et al.*, Hyperfine Interact., **244** (2023) 10.
[4] D. H. Ryan *et al.,* Hyperfine Interact., **153** (2004) 43-55.

PR9-12

Search of ^{166}Er Mössbauer Single-Line Materials

S. Kitao[1], Y. Kobayashi[1], H. Yamashita[2], R. Masuda[3], and M. Seto[1]
[1]*Institute for Integrated Radiation and Nuclear Science, Kyoto University*
[2]*Graduate School of Science, Kyoto University*
[3]*Graduate School of Science and Technology, Hirosaki University*

INTRODUCTION:

The Mössbauer spectroscopy is one of the most powerful methods to investigate electronic states and magnetic properties by extracting the information of a specific isotope. Mössbauer spectroscopy in general is performed for quite limited isotopes, such as ^{57}Fe and ^{119}Sn. On the contrary, the neutron irradiation facility at Kyoto University Reactor (KUR) at KURNS can be used to produce various radioactive isotopes for the Mössbauer sources. Moreover, some isotopes can be complementarily produced by high-energy γ-ray irradiation converted from electron beam from the electron linear accelerator (KURNS-LINAC). We have been developing practical methods for Mössbauer spectroscopy for various isotopes. Mössbauer spectroscopy are available at present in following isotopes(source in parentheses): ^{61}Ni(^{61}Co), ^{125}Te(^{125m}Te), ^{129}I(^{129}Te,^{129m}Te), ^{161}Dy(^{161}Tb), ^{166}Er(^{166}Ho), ^{169}Tm(^{169}Er), ^{170}Yb(^{170}Tm), ^{197}Au(^{197}Pt), etc.

Among these isotopes, ^{166}Er Mössbauer spectroscopy is one of the most useful methods for studies of electronic or magnetic state for Er compounds. For some former studies, $HoAl_2$ was used as a Mössbauer source [1]. However, the measurement temperature had not to be cooled below around 40 K, since $HoAl_2$ has magnetic transition at 25 K. To overcome this disadvantage, another source material, $Ho_{0.4}Y_{0.6}H_2$ had been successfully synthesized with similar method in the references [2,3] and confirmed a single-line ^{166}Er Mössbauer spectra as low as 18K [4]. As for ^{166}Er Mössbauer spectroscopy, not only the source material, but also single-line Er compound is important. The single-line Er compound can also be used as a reference material for synchrotoron-radiation-based Mössbauer spectroscopy. Although ErH_2 can be used as a single-line Er compound, it has disadvantages of low recoilless fraction and degradation at ambient atmosphere. Er-Al alloys can also be used as a single-line Er compound, which is stable at ambient atmosphere. However, the recoilless fraction is still low. Therefore, it is important to search for another useful single-line Er compound.

In this report, a study of an Er compound, ErF_3 is described. ErF_3 is expected as a compound with high recoilless fraction. However, the Mössbauer spectra of ErF_3 has not been well known at low temperature.

EXPERIMENTS AND RESULTS:

The source material $Ho_{0.4}Y_{0.6}H_2$ has been synthesized by hydridation of $Ho_{0.4}Y_{0.6}$ alloy. The neutron irradiation was performed at pneumatic tube of KUR for 150 minutes at 1MW operation or 30 minutes at 5MW operation. The ^{166}Ho source with a half-life of 26.8 h was obtained and used for the ^{166}Er Mössbauer measurement for 2 or 3 days. The source material can be irradiated repeatedly, when it is kept in a vacuum desiccator after use to avoid degradation. The ErF_3 was purchased from Mitsuwa Chemicals Co., Ltd. The measurement temperature was controlled by keeping both the source and the absorber in a He-gas filled space using a closed cycle He-refrigerator.

The obtained spectra of ErF_3 at about 20K are shown in Fig. 1. The spectrum showed that magnetic splitting was not clearly observed. However, the spectra contained a broadened component. It may result from relaxation phenomenon of magnetic ordering. Therefore, ErF_3 is unfortunately found to be unsuitable for a single-line material. However, it is worth researching on property of ErF_3 to search for another candidate for single-line compounds in related compounds.

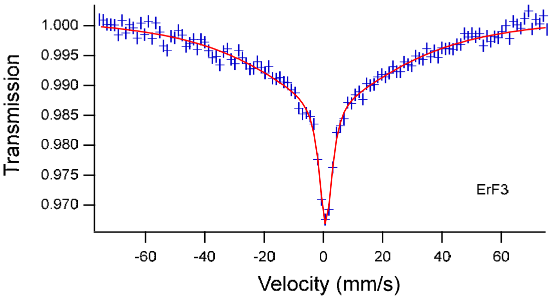

Fig. 1. ^{166}Er-Mössbauer spectrum of ErF_3 using $^{166}Ho_{0.4}Y_{0.6}H_2$ source at about 20 K.

REFERENCES:

[1] S. Nakamura, H. Yokota, S. Kitao, Y. Kobayashi, M. Saito, R. Masuda, and M. Seto, Hyperfine Interact., **240** (2019) 75.

[2] J. Stöhr and J. D. Cashion, Phys. Rev. B, **12** (1975) 4805.

[3] D. B. Prowse, A. Vas, and J. D. Cashion, J. Phys. D:Appl. Phys., **6** (1973) 646.

[4] S. Kitao, Y. Kobayashi, M. Kurokuzu, T. Kubota, and M. Seto, Hyperfine Interact., **244** (2023) 10.

I-1. PROJECT RESEARCHES

Project 10

PR10

Operando system for observing the dynamic structure of polymers under ionisation

H. Nakamura, T. Kubota[1], M. Ikegami, Y. Shirakawa[2,3], H. Kitamura[3]

Institute for Integrated Radiation and Nuclear Science, Kyoto University
[1]Agency for Health, Safety and Environment, Kyoto University
[2]Research Organization for Nano & Life innovation Adjunct Researcher, Waseda University
[3]Faculty Department of Innovation Strategy Senior Research Administrator, National Institutes for Quantum Science and Technology

PROGRAM OVERVIEW:

Readily available aromatic ring polymers undoped with fluorescent molecules have attracted attention for use in radiation measurements. However, the mechanism underlying the fluorescence, as the key element, has not been elucidated. When the polymers are exposed to charged particles with low intensity, optical signals that are difficult to understand from the fluorescence mechanism of traditional polymers doped with fluorescent molecules are observed. It is speculated that the signals arise from a transient change in the intrinsic properties of the polymers upon exposure to charged particles. However, this phenomenon disappears when the irradiation is stopped. Thus, there are limitations of the indirect approach for inferring the intramolecular electronic states “under ionisation” from those of the “after irradiation” polymer. To solve this problem, a direct approach is required to determine the intramolecular electronic states in the ionised state. Here, we aim to develop a system that can measure the changes in the bond strengths among the constituent elements, the arrangements of the constituent elements, and the electron distributions in polymers in real time while controlling the on/off state of the irradiation.

IMPLEMENTATION:

After extensive testing, we have hypothesised that the charged particles, resonating with the dynamic structure of the base adjacent to the aromatic ring, temporarily delocalise the intramolecular electron distributions, inducing new molecular modes and changing the intrinsic properties. According to the hypothesis, the dynamic structures of the bases adjacent to the aromatic ring should change in response to the presence of charged particles. To directly investigate the electronic states in molecules under ionisation, we are preparing to sequentially mount various radioactive sources on instruments, such as a Raman spectrometer, an infrared spectrometer, a fluorescence spectrometer, and an ultraviolet/visible spectrophotometer. The data from these instruments need to be systematically understood. The amount of space available for each instrument is different, so the mounting unit is being developed, which includes adjusting the size and shape of the radioactive source. The realisation of this new measurement environment will clarify the changes that occur in the bond strengths among the constituent elements and the intramolecular electron distributions in polymers under ionisation, and how they relate to the changes in the optical properties. In addition, clarification of the dynamic structures of polymers under ionisation could lead to the improvement of the properties of traditional polymers doped with fluorescent molecules.

ACKNOWLEDGEMENTS:

This work was supported by JSPS Grant-in-Aid for Challenging Research Exploratory Grant Number 24K21749.

PR10-1

Elucidation of dynamic structures of polymers under ionisation

H. Nakamura, T. Kubota[1], M. Ikegami, Y. Shirakawa[2,3], H. Kitamura[3]

Institute for Integrated Radiation and Nuclear Science, Kyoto University

[1]Agency for Health, Safety and Environment, Kyoto University
[2]Research Organization for Nano & Life innovation Adjunct Researcher, Waseda University
[3]Faculty Department of Innovation Strategy Senior Research Administrator, National Institutes for Quantum Science and Technology

INTRODUCTION:

Optical signals difficult to explain and are attributed to internal light have been captured in synthetic molecules irradiated with charged particles. These signals likely arise from a switching phenomenon in which exposure to weak charged particles temporarily induces changes in the intrinsic optical properties of the molecule. The phenomenon disappears when irradiation is stopped, so details have been difficult to obtain. Electronic states within the molecule appear to be switched between steady and ionised states when the irradiation is turned on or off. Changes in bond strengths between the constituent elements, the arrangement of the constituent elements, and the electron distributions are observed in real time. Here, we aim to establish the mechanism underlying this unknown phenomenon.

IMPLEMENTATION:

Polymers of undoped fluorescent molecules can temporally exhibit unknown optical signals that cannot be explained by internally generated fluorescence. This occurs only when they are exposed to environmental levels of charged particles. Through extensive verification, we developed an hypothesis that ‘ionising radiation that resonates with the dynamic structure of the base adjacent to the aromatic ring temporarily delocalises the intramolecular electron distribution, inducing a new molecular mode and modifying the inherent optical properties.’ Based on our hypothesis, the dynamic structure of the base adjacent to the aromatic ring changes depending on whether ionising radiation is present. Therefore, we used Raman, infrared (IR, and fluorescence spectrometers to directly observe intramolecular electron states sequentially exposed to strontium-90 or americium-241 radiative sources. The Raman, IR, and Rayleigh spectra for familiar polymers such as polyethylene terephthalate were obtained when the irradiation was on and off. Positions and shapes of each peak were compared, and differences led to the presence of dynamic structure transformations. In addition, singular points where the optics switches when changing the irradiation dose will be identified. In the near future, we reveal the process of changes in bond strengths between constituent elements, as well as those in the intramolecular electron distribution, and elucidate the mechanisms.

ACKNOWLEDGEMENTS:

This work was supported by JSPS Grant-in-Aid for Challenging Research Exploratory Grant Number 24K21749.

PR10-2

Development of an operando ionisation measurement system

T. Kubota, H. Nakamura[1], M. Ikegami[1], Y. Shirakawa[2,3], H. Kitamura[3]

Agency for Health, Safety and Environment, Kyoto University

[1]Institute for Integrated Radiation and Nuclear Science, Kyoto University
[2]Research Organization for Nano & Life innovation Adjunct Researcher, Waseda University
[3]Faculty Department of Innovation Strategy Senior Research Administrator, National Institutes for Quantum Sci-ence and Technology

INTRODUCTION:

In radiation measurements, the research focus on polymer-based scintillation materials has begun to shift from fluorescent-molecule-doped to undoped fluorescent polymers. Hence, emission is conventionally interpreted in terms of a ladder model based on electronic transitions within the molecular structure. However, pulsed fluorescence emission, different from that predicted when measuring environmental-level charged particles, has been repeatedly observed. This only occurs in the presence of charged particles. The key to elucidating this observation is via operando measurements to observe changes in intermolecular bond strengths and intramolecular electron distributions when turning the irradiation on and off.

IMPLEMENTATION:

There is a strong desire to elucidate the mechanism of radiation-induced luminescence in undoped fluorescent polymers. However, there are limitations to indirectly inferring the molecular electronic states 'during irradiation' from the polymer luminescence 'after irradiation.' We identify the singular point at which the optical properties of the polymer change under charged particle irradiation (approximately ten of Bq) as it is turned on and off. To realise operando measurements to investigate the properties of polymers under ionisation, support stands for mounting samples and radiation sources were developed for several spectrometers. This allowed us to directly monitor molecular states exposed to the charged particles. After documenting inherent characteristics of fluorescence and ultraviolet-visible absorption spectrometers equipped with a radiative source, excitation, fluorescence and absorption spectra were obtained for versatile aromatic ring polymers, such as polyethylene terephthalate, polyethylene naphthalate, polystyrene, polyvinyl toluene, polycarbonate and polyether sulphone under conditions with or without charged particles. The comparisons identify singular points where orbital energies change and optical properties switch. These results elucidate the process by which bond strengths between constituent elements and the electron distributions within molecules change under ionisation.

ACKNOWLEDGEMENTS:

This work was supported by JSPS Grant-in-Aid for Challenging Research Exploratory Grant Num-ber 24K21749.

A radioactive source unit for an operando ionisation measurement system

M. Ikegami, H. Nakamura, T. Kubota[1], Y. Shirakawa[2,3], H. Kitamura[3]

Institute for Integrated Radiation and Nuclear Science, Kyoto University

[1]Agency for Health, Safety and Environment, Kyoto University
[2]Research Organization for Nano & Life innovation Adjunct Researcher, Waseda University
[3]Faculty Department of Innovation Strategy Senior Research Administrator, National Institutes for Quantum Sci-ence and Technology

INTRODUCTION:

Recently, polymers with aromatic rings have been used as radiation detection elements for safety management in radiation facilities and nuclear reactors. The triggering event for their use is the ionising effect of radiation. Knowledge of macroscopic reactions that occur after polymer ionisation has been well developed over a century. However, there is still little known about microscale responses during ionisation. Thus, this project established an operando measurement system that can investigate microscale changes in polymers in real time during irradiation. One of the core technologies was to adjust the shape of the radiation source installed inside the equipment.

IMPLEMENTATION:

To investigate intramolecular electronic states in polymers under environmental-level charged particle irradiation, it was necessary to mount both a polymer sample and a radiative source in instruments such as an X-ray diffractometer, as well as Raman, infrared, fluorescence and ultravio-let-visible absorption spectrometers. However, the amount of available space on each piece of equipment varied, and the measurement conditions had to be standardised to understand the data obtained from each piece of equipment. Commercially available radiation sources have fixed shapes and dimensions, which limit incorporation into the equipment. These difficulties were overcome by adjusting the size and shape of the radioactive sources. We established a simple method for devel-oping a radiation source that offers a high degree of freedom. A three-dimensional printer will eventually solve these problems, where samples will be made by mixing a radioactive standard so-lution into the printer solution resin, with full knowledge of the resulting printer contamination. In the meantime, as a cold test, we prepared a potassium chloride solution to create a prototype radio-active source that emitted beta particles. The surface profiles of the prototype radioactive sources were evaluated with a tabletop scanning electron microscope. Then source samples with different doses by controlling the amount used of standard radioactive solution (strontium-90) will then be fabricated.

ACKNOWLEDGEMENTS:

This work was supported by JSPS Grant-in-Aid for Challenging Research Exploratory Grant Number 24K21749.

I-1. PROJECT RESEARCHES

Project 11

PR11

Advanced Applications of Materials Irradiation and Characterization Techniques Using High Energy Particles

A. Kinomura
Institute for Integrated Radiation and Nuclear Science, Kyoto University

OBJECTIVE:

We have developed and maintained various irradiation facilities (KUR SSS and KURNS-LINAC targets) and characterization facilities (positron annihilation spectroscopy and thermal desorption spectroscopy systems) in Institute for Integrated Radiation and Nuclear Science. This project aims to further advance the development and the improvements of facilities for stimulating joint-use research projects in this area.

RESEARCH SUBJECTS:

R6P11-1 Study to improve transport and measurement performance of a slow positron beamline

The relationship among positron pulse shapes of the KUR slow positron beamline was investigated for quick and easy adjustment of system parameters.

R6P11-2 Micro-vickers hardenss in neutron-irradiated Fe-Cr alloys

The progress of phase separation in Fe-Cr binary alloys was detected using PAS for the correlation between the hardness and phase separation irradiated with neutrons at 473K and 573 K.

R6P11-3 Effect of rhenium doping on vacancy formation in electron-irradiated tungsten studied with positron annihilation spectroscopy

Simple Frenkel pairs were introduced into W-Re dilute alloys through electron irradiation, and the resulting vacancy-type defects were analyzed using positron annihilation spectroscopy.

R6P11-4 Gamma-ray excited photo-emission from nano, micro, and bulk diamonds

Gamma-ray induced luminescence of three types of diamonds, bulk, micrometer-sized, and nano-sized particles was investigated.

R6P11-5 Multiple hydrogen trapping by vacancies in B2-type Fe-Al alloys

Slow positron beam measurements for electron irradiated and hydrogen introduced $Fe_{50}Al_{50}$ alloys were performed as well as computer simulations of positron annihilation in Fe-Al alloys with hydrogen trapping vacancies.

R6P11-6 Change of free volume in highly hydrogenated DLC films due to desorption

Positron annihilation spectroscopy measurements were performed to investigate structural changes in the free volume of H DLC films by soft X ray irradiation and temperature increase.

R6P11-7 Structural analysis of diamond-like carbon coatings using positron annihilation spectroscopy

The microstructural defect behavior of DLC coatings deposited under varying bias voltages was investigated by employing positron annihilation spectroscopy.

R6P11-8 Valuation of the effect of the CHF3 plasma treatment on Si surfaces using the positron annihilation method

CHF_3 plasma treated Si surfaces were investigated using the different plasma conditions to clarify the formation, deposition and sputtering processes of the C related materials.

R6P11-9 Effects of pulse irradiation by charged particles on damage structures in metals

The effects of pulse irradiation on the damage defect evolution were investigated using numerical simulation and electron irradiations.

R6P11-10 Development of slow positron beamline using electron linear accelerator

Preliminary experiments of a slow positron beamline using KURNS-LINAC were performed to confirm the performance of the storage section and beam transport to the sample chamber.

Study to improve transport and measurement performance of a slow positron beamline

A. Kinomura, N. Oshima[1], and A. Yabuuchi

Institute for Integrated Radiation and Nuclear Science, Kyoto University
[1]National Institute of Advanced Industrial Science and Technology (AIST)

INTRODUCTION: Positron annihilation spectroscopy is an important analytical method to detect vacancy-type defects and vacant spaces of materials. Energy-variable mono-energetic positron beams (slow positron beams) are essential to perform depth-dependent positron annihilation spectroscopy of surface layers such as ion-implanted layers or thin films. As moderation efficiencies to obtain slow positron beams are typically $<10^{-4}$, intense positron sources are required for practical use. A positron source using pair-creation by gamma-rays from a nuclear reactor have been developed by using Kyoto University research Reactor (KUR) to obtain a slow positron beam for materials analysis. In the KUR slow positron beamline, a lifetime measurement system based on a pulsing system using a radiofrequency-driven buncher was developed for the KUR slow positron beamline. In the KUR slow positron beamline, typically it takes about one hour to adjust parameters of the pulsing system. It is desired to reduce the time required for the adjustment for efficient use of the beamline. In this report, the relationship among pulse shapes was investigated for quick and easy adjustment of the pulsing system.

EXPERIMENTS: The pulsing system was adjusted using a standard sample (Kapton) at 2 keV. The lifetime of the Kapton samples was confirmed to be close to the lifetimes found in published papers. The pulsing system consists of three pulse/radiofrequency (RF) circuits (i.e., chopper, prebuncher and buncher) [1]. Each RF circuit was turned on and off to observe the contribution of individual circuits.

RESULTS: Figure 1 shows the pulse shapes measured as lifetime spectra. In Fig. 1(a), broken and solid lines correspond to the spectrum obtained with all the circuits and spectrum obtained without the buncher (with the chopper and prebuncher), respectively. Fire 1(b) shows three spec-tra obtained only with the buncher, where a phase shifter was changed to ±5 % with respect to the best value (0%). Fig. 1 indicates that the pulses, corresponding to the indi-vidual RF circuits, should be at different positions. If this relationship can be recorded or formulated, the adjustment time for the pulse system can be significantly reduced.

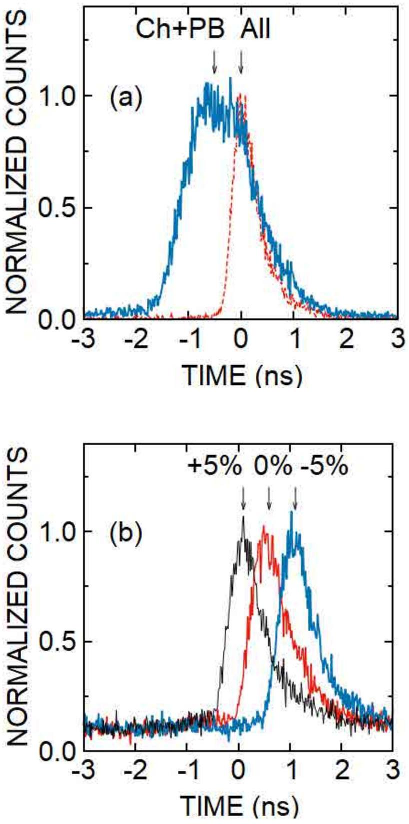

Fig. 1. Lifetime spectra to observe pulse shapes.

REFERENCES:

[1] M. Nakajima *et al.,* Rev. Sci. Instrum., **91**(2020) 125109.

PR11-2

Micro-Vickers Hardenss in Neutron-irradiated Fe-Cr Alloys

K. Sato, Y. Noshita, R. Kasada[1], Q. Xu[2], A. Yabuuchi[2], A. Kinomura[2]

Graduate School of Science and Engineering, Kagoshima University
[1]Institure for Materials Research, Tohoku University
[2]Institute for Integrated Radiation and Nuclear Science, Kyoto University

INTRODUCTION: Ferritic stainless and heat resistant steels used as nuclear reactor peripheral materials have high Cr content [1]. In these materials, ductility and toughness remarkably decrease, and hardness and tensile strength increase by aging from 593 to 813 K. This phenomenon is caused by the formation of Fe-rich and Cr-rich phase, and is called 475˚C embrittlement [2]. These changes in mechanical properties are an important issue in terms of evaluation of aged deterioration when it was used as a reactor structural material. Positron annihilation spectroscopy (PAS) is very powerful tool to obtain the information of vacancy-type defects (even single vacancies) and precipitates. In Fe-Cr alloys used in this study, positron affinity of Fe is lower than that of Cr [3]. Therefore, we can detect the formation of Fe-rich phase in phase separation of Fe-Cr alloys using PAS. The purpose of this study is to detect the progress of phase separation using PAS, and to obtain the correlation between the hardness and phase separation in Fe-Cr binary alloys irradiated with neutrons at 473K and 573 K.

EXPERIMENTS: Fe-x wt.%Cr (x = 0, 9, 15, 30, 45, 50, 70, 85, 91, and 100) binary alloys were used in this study. The weight of high purity Fe (99.99%) and Cr (99.99%) were measured, and samples were melted by the arc melting. For neutron irradiation, samples with diameters of 3 mm and thickness of 0.25 mm were cut using the wire electric discharge machine. Fe-xCr (x = 30, 45, 50, 70, 85, 91, and 100) were annealed at 1273K for 1h, and Fe-xCr (x = 0, 9, 15) were annealed at 1073K for 1h in a vacuum ($< 4 \times 10^{-4}$ Pa), and then water-quenching was performed for the suppression of phase separation. The neutron irradiation was carried out at the Material Controlled Irradiation Facility (SSS) of Kyoto University Reactor (KUR) [4]. The irradiation doses were 0.44×10^{-3} , 0.5×10^{-3} and 2.1×10^{-3} dpa. The irradiation temperature was 473K (0.5×10^{-3} dpa) and 573K (0.44×10^{-3} and 2.1×10^{-3} dpa). Vickers hardness tests were conducted using HMV-T2 (SHIMADZU corp.) at room temperature with the test load of 0.9807 mN ($Hv_{0.1}$) and the load holding time of 15 s.

RESULTS: The hardness increased after neutron irradiation in all samples. This is due to the progress of phase separation and the formation of irradiation-induced defects. In Fe-xCr (x = 0, 9 and 15), hardness is highest in the 473 K irradiation. Since the vacancy clusters were detected in the PAL measurements in the 473 K irradiation, the greatest cause of the highest hardness was the formation of irradiation-induced defects. In Fe-xCr (x = 30, 45, 50, 85 and 91), the hardness of samples irradiated at 473 K for 47 h is almost the same as that of samples irradiated at 573 K for 42 h. The contribution of irradiation-induced defects on the increase in the hardness is difference in each samples. Because the formation of vacancy clusters is detected by the PAL measurements in the 473 K irradiation.

REFERENCE:

[1] R.L. Klueh *et al.,* J. Nucl. Mater., **191** (1992) 116.
[2] R.O. Williams, Trans. AIME, **212** (1958) 497.
[3] M.J. Puska *et al.,* J. Phy. Condes. Matter., **1** (1989) 6086.
[4] T. Yoshiie *et al.,* Nucl. Instr. Meth. Phys. Res. A, **498** (2003) 522.

PR11-3

Effect of rhenium doping on vacancy formation in electron-irradiated tungsten studied with positron annihilation spectroscopy

T. Toyama, Z. Zhang, K. Inoue, Y. Nagai, A. Yabuuchi[1], A. Kinomura[1]

Institute for Materials Research, Tohoku University
[1]Institute for Integrated Radiation and Nuclear Science, Kyoto University

INTRODUCTION: In tungsten (W), which is considered a promising material for fusion reactors, the retention and accumulation of hydrogen isotopes due to neutron irradiation pose a significant problem. Recently, it has been reported that the addition of rhenium (Re) significantly reduces hydrogen isotope accumulation [1], which is believed to be due to the suppression of irradiation defect formation, the primary trapping sites for hydrogen. In fact, it has been found that the formation of vacancy-type defects is significantly suppressed in W-5Re compared to pure W [2].
The aim of this study is to further investigate the effect of Re addition on vacancy formation. To this end, simple Frenkel pairs were introduced into W-Re dilute alloys through electron irradiation, and the resulting vacancy-type defects were analyzed using positron annihilation spectroscopy.

EXPERIMENTS: The specimens used were pure W and W-xRe alloys (x = 0.1, 0.3, 1.0, and 5.0 at.%). After annealing at 1800°C for 1 hour (1600°C for 1 hour for x = 5.0), electron irradiation was performed at the Kyoto University Institute for Integrated Radiation and Nuclear Science (KURNS) Linac facility (8 MeV, <100°C, approximately 3.5×10^{23} e^-/m^2). After irradiation, vacancy-type defects were investigated via positron annihilation measurements (lifetime measurements and coincidence Doppler broadening measurements).

RESULTS: Figure 1(a) shows the dependence of the average positron lifetime (τ_{ave}) on Re composition. Before irradiation, τ_{ave} ranged from 110 to 117 ps. Since these values are close to the positron lifetime in bulk W, it is assumed that almost no vacancy-type defects existed before irradiation. After irradiation, τ_{ave} increased in all samples, indicating positron trapping at vacancy-type defects introduced by irradiation. In all samples, long-lifetime components were barely observed in the positron lifetime spectra, suggesting little positron trapping by vacancy clusters. Figure 1(b) shows the increase in τ_{ave} ($\Delta\tau_{ave}$) due to irradiation. Compared to pure W, $\Delta\tau_{ave}$ increased with Re composition up to about 1%, indicating an increase in positron trapping at vacancy-type defects. On the other hand, at 5% Re composition, $\Delta\tau_{ave}$ was smaller than that of pure W, consistent with previous findings on W-5Re [2]. Theoretical calculations have proposed that Re strongly binds with W interstitial atoms, lowering their mobility and increasing the frequency of interstitial-vacancy recombination, thereby suppressing the formation (retention) of vacancy-type defects [3]. However, based on the present results, it is suggested that other mechanisms may also need to be considered. For example, since Re has a positive (attractive) binding energy of 0.22 eV with vacancies in W [3], it is possible that Re stabilizes vacancies.

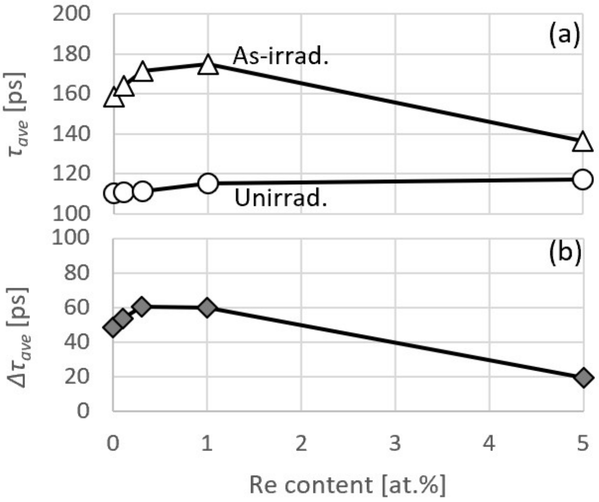

Fig. 1. Re content dependency of (a) average positron lifetime, (b) increase of average positron lifetime.

PR11-4

Gamma-ray excited photo-emission from nano, micro, and bulk diamonds

T. Nakamura[1], T. Nishimura[1], K. Kuriyama[1], Atsushi Kinomura[2]

[1]Research Center of Ion Beam Technology, Hosei University, Koganei, Tokyo 184-8584, Japan
[2]Institute for Integrated Radiation and Nuclear Science, Kyoto University, Kumatori, Osaka 590-0494, Japan

INTRODUCTION: Diamonds are known to emit defects- and impurity-related green, yellow, and red fluorescence when exposed to ultraviolet light [1] as well as blue to green visible lights [2]. Recently, the authors have observed gamma-ray irradiation-induced luminescence in the bulk wide gap semiconductors, such as GaN [3], although it has a smaller band gap than that of diamond. As an application of gamma-ray irradiation, we have already reported the gamma-ray-enhanced quenching phenomenon of photoconductance in GaAs [4]. Recently, research on gamma-ray detectors using single-crystal bulk diamond has been progressing [5]. Therefore, studying gamma-ray induced emission from diamond powders with a wide diameter range from nano- to micro-meters and bulk diamond substrate will lead to fundamental research as a material for future gamma-ray detectors. In this work, we investigate gamma-ray induced luminescence of three types of diamonds, bulk, micrometer-sized, and nano-sized particles.

EXPERIMENTS: Samples used for the present study are bulk single crystal substrates, transparent diamond particles with a size of 90 to 165 μm (micron-sized), and white to gray nano-diamond particles with a size of about 10 nm. Bulk and micro-sized diamond samples were purchased from Sumitomo Electric Industries Ltd. Nano-diamond samples were purchased from Tokyo Chemical Industry Co., Ltd. The diamond crystals were irradiated at room temperature with gamma-rays of 1.17 and 1.33 MeV from a cobalt-60 source of Institute for Integrated Radiation and Nuclear Science, Kyoto University. The gamma-ray irradiation induced photo luminescence measurements were performed by using a charge coupled device (CCD) equipped spectrometer (QE Pro, Ocean Insight Co. Ltd.).

RESULTS: Figure 1(a) shows gamma-ray-induced luminescence spectra of nano, micro, and bulk diamonds measured at room temperature with an absorbed dose of 1.0 kGy/h. The gamma-ray induced luminescence for the bulk-diamond sample is more intense than those for nano- and micro-diamond ones. It should be noted that the luminescence intensity of the bulk-diamond is one-third as weak as that of GaN wafer [6]. The gamma-ray induced luminescence from micro and bulk diamonds was observed from 375 nm to 850 nm with a peak at around 525 nm, whereas the luminescence from nano- diamond was observed from 375 nm to 800 nm si 200 with a peak at 450 nm.

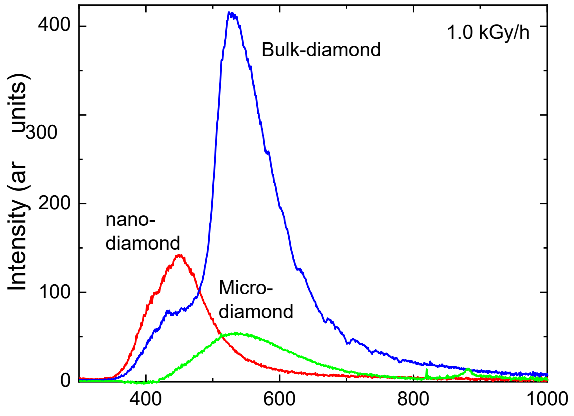

Fig. 1. Gamma-ray-induced luminescence spectra of nano, micro, and bulk diamonds measured at room temperature with an absorbed dose of 1.0 kGy/h.

REFERENCES:

[1] S. Eaton-Magaña *et al.,* Geology, **36** (2008) 83.
[2] K. Beha *et al.,* Phys. Rev. Lett., **109** (2012) 097404.
[3] T. Nakamura *et al.,* Appl. Phys. Lett., **118** (2021) 032106.
[4] K. Kuriyama *et al.,* Appl. Phys. Lett., **53** (1988) 1074.
[5] K. Ueno *et al.,* Jpn. J. Appl. Phys., **58** (2019) 106509.

PR11-5

Multiple hydrogen trapping by vacancies in B2-type Fe-Al alloys

F.Hori, J.Tian, K.Miyazumi, K.Ohsawa[1], Q.Xu[2], A.Kinomura[2], N.Abe[2]

Department of Quantum and Radiation Engineering, Osaka Metropolitan University
[1]Res. Inst. of Appl. Mech., Kyushu University
[2]Institute for Integrated Radiation and Nuclear Science, Kyoto University

INTRODUCTION: B2 ordered Fe-Al alloy is used as high strength at high temperature material because of its good properties such as specific strength to weight ratio, oxidation resistance. However, it is known that Fe-Al alloy with B2 ordered structure is easy to form vacancy and anti-site atom defects. On the other hand, the vacancy type defects in this alloy first principles calculation result indicate that not only one hydrogen atom but also several hydrogen atoms can be trapped in a single vacancy in B2 ordered Fe-Al alloy. However, the interaction between vacancies and hydrogen atoms in this type of Fe-Al alloy is not cleared yet. So far, we have investigated the nature of defect structures in B2 type Fe-Al alloy [1]. In this study, we have performed slow positron beam measurements for electron irradiated and hydrogen introduced $Fe_{50}Al_{50}$ alloys, and also performed computer simula-tions of positron annihilation in Fe-Al alloys with hydrogen trapping vacancies, and discussed the experimental results from these results.

EXPERIMENTS: B2 ordered $Fe_{50}Al_{50}$ alloy was prepared by arc melting method. Sliced samples with the thickness of 0.5 mm were irradiated with an 8 MeV electron beam at room temperature to a dose of 4×10^{18} /cm^2 at KURRI, Kyoto University. Hydrogenated samples by electro-chemical method after electron irradiation were examined by positron lifetime measurement by using slow positron beam with the energy of 4 keV at KURRI facility. Positron lifetime calculation of super imposed atom method have performed for B2 ordered 80x80x80 cell including an atomic vacancy and a hydrogen atom.

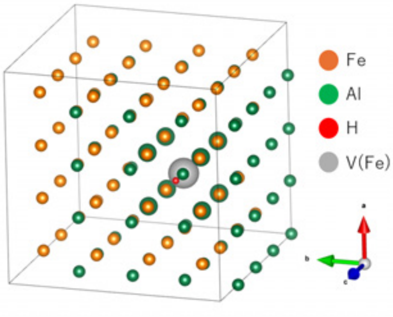

Fig. 1. Calculated atomic position of hydrogen trapped by Fe vacancy in Fe-Al alloy.

RESULTS: Fig. 1 shows the atom site of B2 ordered Fe-Al alloy with iron vacancy (V_{Fe}) and hydrogen calculated by the first principles calculation. Hydrogen atom trapped in a vacancy not the center of vacancy but near the octahedral site. Fig. 2 show the positron annihilation lifetime of electron irradiated (vacancy introduced) Fe-Al at around 400 nm depth as a function of hydrogen charging time. Positron lifetime decreases with increasing hydrogen charging time showing that hydrogen trapping by vacancies. The calculated positron lifetime considering the arrangement of one hydrogen atom in an iron vacancy is shown by the arrow in Figure 2. The positron lifetime after 80 hours of hydrogen charging is almost the same as the calculated value. Furthermore, after 160 hours of charging, the positron lifetime comes down to about 160 ps, which is the same as the value calculated when two hydrogen atoms are arranged at the o-sites facing each other in the vacancy.

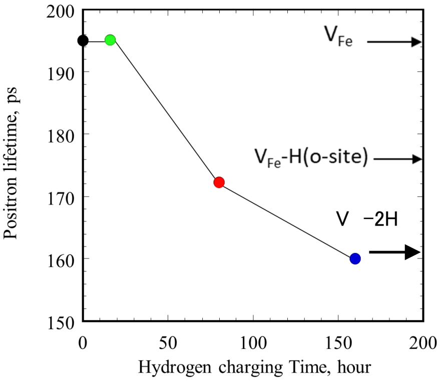

Fig. 2. Positron annihilation lifetime in hydrogen charged Fe-Al measured with 4 keV positrons and calculated values of H-V complexes.

References
[1] F. Hori *et al.,* KURNS Progress Report 2023 (2024) CO4-2 p.108.

PR11-6

Change of Free Volume in Highly Hydrogenated DLC Films due to Desorption

K. Kanda, F. Hori[1], A. Yabuuchi[2] and A. Kinomura[2]

Laboratory of Advanced Science and Technology for Industry, University of Hyogo
[1] *Department of Materials Science, Osaka Metropolitan University*
[2] *Institute for Integrated Radiation and Nuclear Science, Kyoto University*

INTRODUCTION: Highly hydrogenated diamond-like carbon films (H-DLC films) have been found to release hydrogen and other elements upon soft X-ray irradiation or temperature increase, resulting in a decrease in volume, an increase in density, and an increase in the $sp^2/(sp^2+sp^3)$ ratio of carbon atoms [1]. In this study, positron annihilation spectroscopy (PAS) measurements were performed to investigate the differences in the structural changes in the free volume of H-DLC films between the desorption processes induced by soft X-ray irradiation and temperature increase.

EXPERIMENTS: H-DLC films, whose hydrogen content was 50%, were deposited on Si wafers using Plasma Enhanced CVD method with film thickness of 400 nm. The H-DLC films were heated from room temperature to 1100°C using an electric furnace and were irradiated with white light up to 1000 eV at BL06 of NewSUBARU. PAS measurements were performed using a slow positron beam system installed at the B-1 hole of KUR. Positrons generated in the reactor were thermalized, and accelerated up to 30 keV just before the irradiation chamber, and irradiated onto the sample. The γ rays generated by annihilation were observed using a Ge detector.

RESULTS: The dependences of S parameter, which indicates the momentum shift of the γ-rays produced by positron annihilation, and the positron annihilation lifetime (PAL), on soft X-ray irradiation dose and rising temperature are shown in Figs. 1 and 2, respectively. In both desorption processes, the PAL increased, which indicated that the free volume in the H-DLC film increased. The S parameter increased with temperature for desorption by temperature rise, but decreased with increasing soft X-ray dose for soft X-ray irradiation. This is thought to be due to the increase in annihilation with the inner shell electrons of carbon due to desorption of hydrogen without inner shell electrons around the free volume in the H-DLC film. In conclusion, the difference in the desorption processes, in which both carbon and hydrogen are desorbed at rising temperatures, whereas only hydrogen is desorbed by soft X-ray irradiation, is considered to make a difference in dependence of the PAL and S parameter.

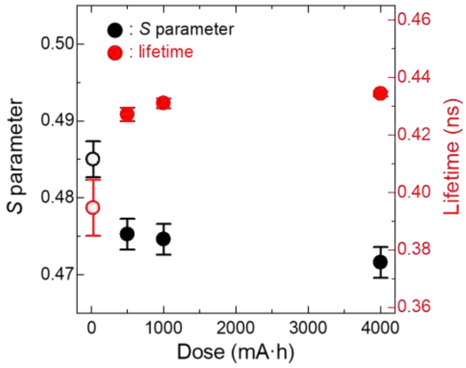

Fig. 1. Dependence of S-parameter and Positron annihilation lifetime on soft X-ray dose.

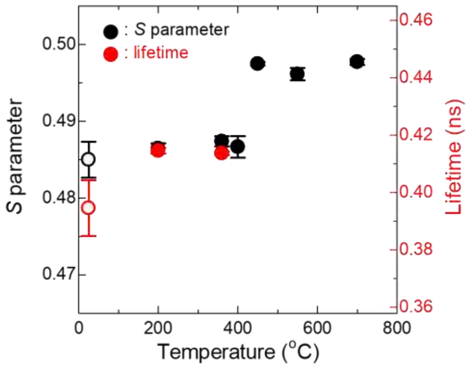

Fig. 2. Dependence of S-parameter and Positron annihilation lifetime on rising temperature.

REFERENCES:

[1] R. Imai *et al.,* Diam. Rel. Mat., **44** (2018) 8.

PR11-7

Structural Analysis of Diamond-Like Carbon Coatings Using Positron Annihilation Spectroscopy

Junho Choi

Department of Mechanical Engineering, Tokyo City University

INTRODUCTION: Enhancing the efficiency of mechanical systems has led to a growing interest in coatings that reduce friction. Among these, diamond-like carbon (DLC) coatings have gained considerable attention due to their outstanding tribological and mechanical properties [1]. The microstructure of DLCs can be tailored to suit various industrial applications, with potential structures ranging from graphite-like carbon (GLC) to polymer-like carbon (PLC), depending on fabrication techniques and deposition conditions [2]. These structural variations are primarily influenced by factors such as hydrogen content and the ratio of carbonaceous bonds (sp^2 and sp^3). In addition, research suggests that defects also contribute to the overall properties of these coatings [3]. To analyze defect behavior in materials, positron annihilation spectroscopy (PAS) serves as an effective investigative tool. This study aims to explore the microstructural defect behavior of DLC coatings deposited under varying bias voltages by employing PAS.

EXPERIMENTS: The hydrogenated coatings were synthesized using the plasma-based ion implantation (PBII) technique. Deposition was carried out on standard Si (100) wafers. To control the microstructural characteristics, varying negative bias voltages between -1 and -10 kV were directly applied to the target as a deposition parameter. The deposition time was adjusted to achieve a coating thickness of approximately 1 μm. The defect behavior within the coating's microstructure was analyzed based on the S-parameter and positron lifetime, both measured at a positron energy of 5 keV.

RESULTS: Figure 1 shows the S-parameter profiles (a) and the corresponding normalized S-parameter and positron lifetime values (b) for F-DLC films deposited at different bias voltages using PBII. In Figure 1(a), the S-parameter increases with positron energy, reflecting typical positron diffusion behavior. A higher negative bias leads to an increase in the S-parameter, suggesting larger open-volume defects. Figure 1(b) summarizes the bias dependence of S/S_{Si} and positron lifetime, both of which rise from –5 to –10 kV. This trend indicates that void size increased with implantation energy, while π-electron density remained largely unchanged.

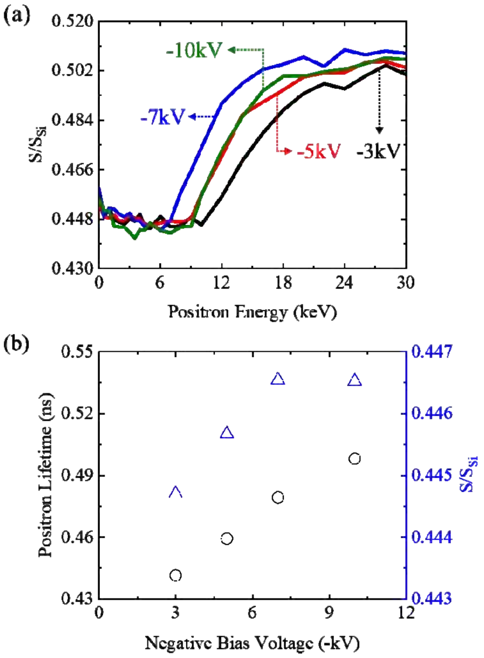

Fig. 1 (a) S- arameter depth profiles o F-DLC films. (b) bias voltage dependence of normalized S- arameter and positron lifetime at different bias voltages.

REFERENCES:

[1] J. Robertson, Surf. Coat. Technol., **50** (1992) 185-203.
[2] J. Choi *et al.,* Diam. and Relat. Mater., **20** (2011) 845-848.
[3] T. Ishikawa *et al.,* Diam. and Relat. Mater., 89 (2018) 94-100.

PR11-8

Valuation of the Effect of the CHF3-Plasma Treatment on Si Surfaces using the Positron Annihilation Method

J. Yanagisawa, S. Ito, Q. Xu[1], A. Yabuuchi[1], K. Takamiya[1], and A. Kinomura[1]

School of Engineering, The University of Shiga Prefecture
[1]Institute for Integrated Radiation and Nuclear Science, Kyoto University

INTRODUCTION: In our previous study [1], we have found that the S-parameter of the CHF_3-plasma-treated Si surface was smaller than that of untreated Si, especially in the surface region, indicating the formation and the deposition of C-related materials during the process. In the present study, to clarify the formation, deposition and sputtering processes of the C-related materials, the CHF_3-plasma-treated Si surfaces were investigated using the different plasma conditions.

EXPERIMENTS: The CHF_3-plasma with the gas pressure of 10 Pa and the RF power of 40 W was irradiated for 30 or 120 min. on Si substrates with the size of 18 mm x 18 mm cleaved from a Si (100) wafer in the experiment. The Si substrates were mounted on the sample stage of the plasma chamber, which was connected to the blocking condenser and negatively charged during the plasma treatment, or on the cover of the chamber, which was directly connected to ground. The S-parameters were obtained from the Doppler broadening for the energy of the γ-ray by the positron-electron annihilation and the elemental analyses were obtained from the energy dispersive X-ray analysis (EDX) and the X-ray photoelectron spectroscopy (XPS).

RESULTS: As shown in Fig. 1, the S-parameters of all CHF_3-plasma-treated samples were smaller than that of Si. The S-parameters of the samples mounted on the cover were smaller than those of Si and the samples on the stage, and affected on deeper region by increasing process time, indicating the growing of deposited new materials on the surfaces. From the EDX analysis, the element composition of the material was C:Si = 64.3:35.7, indicating the deposited material was C-related one which was formed from involatile materials by the gaseous decomposition of the CHF_3 gas during the plasma process. Figure 2 shows the more precise component of the deposited materials obtained by the XPS measurement. F was also detected. For the samples mounted on the stage, however, the smaller S-parameters relative to Si were observed only near the surface region, indicating the sputtering of the deposited materials by energetic ions from the plasma. The effect of the CHF_3-plasma treatment directly on Si surfaces, which show the almost the same tendency with that of the BF^{2+}-implanted Si, is still an issue in the future.

REFERENCE:

[1] J. Yanagisawa *et. al.,* KURNS Progress Report 2023 (Kyoto University) 121 (CO4-15).

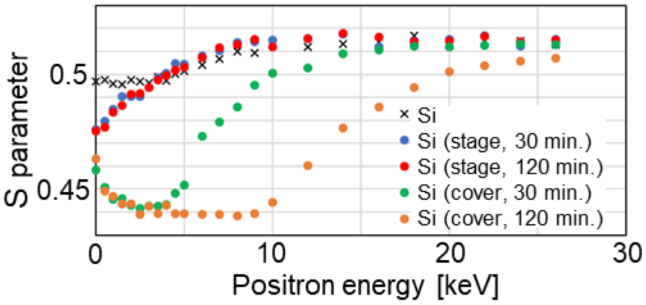

Fig. 1. S-parameters of Si and CHF_3-plasma- treated Si positioned on the sample stage or the cover of the plasma chamber, exposed for 30 or 120 min.

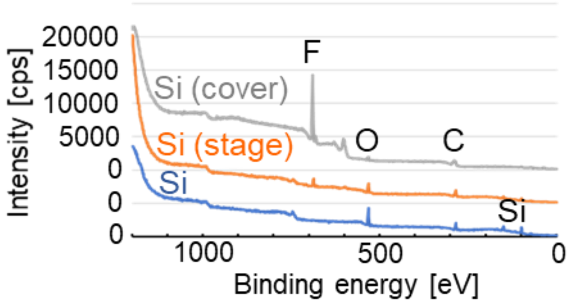

Fig. 2. XPS spectra for Si and CHF_3-plasma-treated Si positioned on the sample stage or the cover of the plasma chamber.

PR11-9

Effects of Pulse Irradiation by Charged Particles on Damage Structures in Metals

T. Yoshiie, F. Hori, T. Nishimura[1], A. Kinomura[2]

Department of Quantum Beam Science, Osaka Metropolitan University
[1]Research Center of Ion Beam Technology, Hosei University
[2]Institute for Integrated Radiation and Nuclear Science, Kyoto University

INTRODUCTION: Irradiation experiments are crucial for the development of nuclear materials. High-energy charged particles like ions and electrons, which are created in accelerators, are commonly employed in these experiments. The time structures of ion and electron beams from accelerators that use radio frequency or beam scanners are characterized by periodic/discontinuous intensities. The purpose of this study is to clarify the effects of pulse irradiation on the damage defect evolution.

EXPERIMENTS: Self-ion irradiation of Fe with the accelerating energy of 2 MeV was performed by tandem accelerator in Research Center of Ion Beam Technology, Hosei University. The irradiation temperature and total dose were 573 K and 1 dpa, respectively. The other irradiation conditions are in Table 1, where τ and T are the pulse dulation and fluquency, respectively. The effect of irradiation damage was investigated with positron annihilation spectroscopy in the slow positron beamline at the Kyoto University Research Reactor.

Table 1. The irradiation conditions of Fe by tandem accelerator with 2 MV at 573 .K.

Specimen	Fe	Fe	Fe
Beam train	Pulse τ/T: 10^{-4}s/10^{-3}s, 1kHz	Pulse τ/T: 1^{-1}s/1s, 1Hz	Continuous
Average damage rate	6.1x10^{-6} dpa/s	8.1x10^{-6} dpa/s	6.5x10^{-6} pa/s

RESULTS: By changing the accelerating voltage, the penetration length of positron changes. S parameter depends on the total amount of spaces in Fe, such as vacancies and their clusters formed by irradiation. Near the surface, the effect of the surface is significant, and we chose the area from 300 to 800 nm for S parameter as shown in Figure 1. The clear difference between unirradiated specimens and irradiated specimens, and the effect of beam structures is detected.
Reaction kinetic analysis was performed based on the rate theory. It describes the reaction rates among point defects and their defect clusters. Figure 2 shows the accumulation of point defects after 0.1 dpa irradiation at 300°C with three irradiation conditions, 1kHz (τ/T=, 10^{-4}s/10^{-3}s), 1Hz (0.1s/1s), and continuous beams (Cont.). The accumulation of interstitials (I in Fig. 2) in clusters are almost the same. However, clear differences in vacancy accumulation (V in Fig. 2) can be seen. The order of vacancy accumulation is the same as that of slow positron measurements.

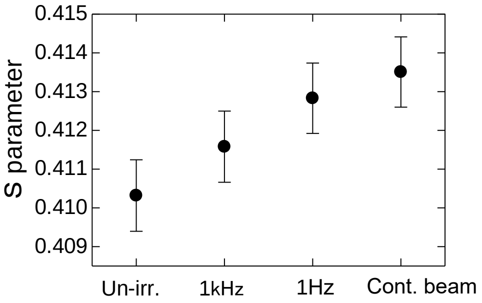

Fig.1 Time structures of pulse beams

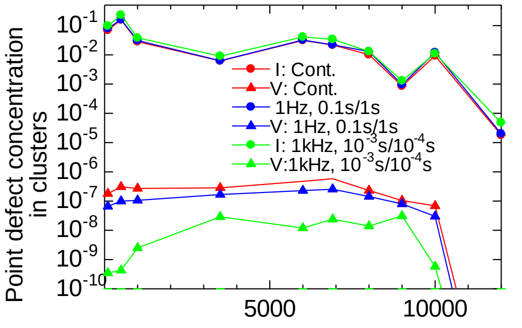

Fig.2 Distance from the surface(atoic distance)

PR11-10

Development of slow positron beamline using electron linear accelerator

A. Kinomura, Q. Xu, T. Takahashi, and N. Abe

Institute for Integrated Radiation and Nuclear Science, Kyoto University (KURNS)

INTRODUCTION: Slow positron beams (energy-variable monoenergetic positron beams) have been widely used to investigate vacancy-type defects in thin films or near-surface layers in ion irradiated materials. Intense slow positron beams can be generated through pair-creation reactions by large-scale experimental facilities such as nuclear reactors and accelerators. In terms of accelerator-based positron sources, so far, radiofrequency-driven electron linear accelerators (LINAC) have been mainly used. In principle, LINAC-generated positron beams are not continuous (i.e., pulsed beams), while reactor-based positron beams are continuous. The pulsed beams can be potentially applied for unique applications such as pump-probe type measurements [1]. This study aims at such unique applications using KURNS-LINAC.

EXPERIMENTS: A 30 MeV electron beam with a pulse width of 5 μs was generated using the KURNS-LINAC. A water-cooled tungsten converter and a Pt-mesh moderator were used at the source part. Generated positrons are extracted with a bias voltage of 10 V and magnetically guided to the beamline. A linear storage section was installed to control time structures of the slow positron beam. The original pulse with a width of 5 μs can be stretched or delayed by controlling the waveforms applied the entrance and exit electrodes in the linear storage. The beamline was extended to the sample chamber with a pulsing system for positron lifetime measurements in the measurement room next to the target room. The pulse system consists of transmission-type chopper electrodes and radiofrequency (RF) driven prebuncher and buncher electrodes.

RESULTS: Preliminary experiments showed that the slow positron beam was successfully transported to the sample chamber. Annihilation gamma-rays were detected by a scintillation detected behind the sample chamber. Fig. 1 shows the annihilation gamma-ray signals recoded by an oscilloscope at the end of the linear storage section. When the delay of the storage were changed from 50 μs to 250 μs, gamma-rays signals (negative pulses) were shifted accordingly. It indicates that the linear storage successfully worked. The pulse stretching performance can be indicated in Fig. 1 as well. The original pulse width of 5 us was stretched to ~100 μs. The pulse system for positron lifetime measurements was examined by feeding appropriate pulse/RF signals. The pulse formation and bunching were confirmed for individual electrodes.

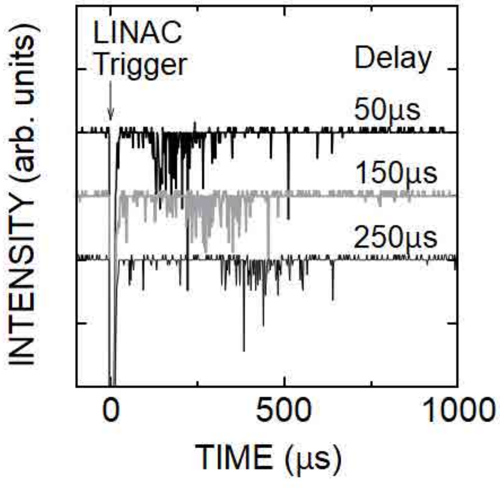

Fig. 1 Positron signals recorded for different delay times of the linear storage.

REFERENCES:

[1] A. Kinomura *et al.,* Rev. Sci. Instrum., 85 (2014) 123110.

I-2. COLLABORATION RESEARCHES

1. *Neutron Scattering*
2. *Nuclear Physics and Nuclear Data*
3. *Reactor Physics and Reactor Engineering*
4. *Material Science and Radiation Effects*
5. *Geochemistry and Environmental Science*
6. *Life Science and Medical Science*
7. *Neutron Capture Therapy*
8. *Neutron Radiography and Radiation Application*
9. *TRU and Nuclear Chemistry*
10. *Health Physics and Waste Management*
11. *Others*

CO1-1

Development of absorption grating devices with CN-3 beamline at KURNS

M. Hino[1], M. Li[2], T. Hosobata[3], M. Takeda[3], Y. Yamagata[3] and Y. Seki[4]

[1]*Institute for Integrated Radiation and Nuclear Science, Kyoto University*
[2]*Department of Nuclear Engniering, Kyoto University*
[3]*RIKEN Center for Advanced Photonics, RIKEN*
[4]*Institute of Multidisciplinary Research for Advanced Materials, Tohoku University*

INTRODUCTION: Neutron imaging techniques are very powerful as a versatile nondestructive analyzing tools in many research fields. Neutron Talbot-Lau interferometry (nTLI) has attracted considerable attention since it was proposed in 2006[1]. The nTLI consists of three gratings, a source grating G0, a beam splitter grating G1 and an analyzer grating G2. G0 and G2 are absorption gratings and G1 is a phase grating. The absorption gratings are very important key devices, and Gadolinium (Gd) is used in the fabrication of absorption gratings due to its high absorption cross section. This study presents a novel fabrication method for absorption gratings using a Gd-based multilayer optimized for ultra-high precision cutting.

EXPERIMENTS: The Gd-based multilayer consists of Gd and Ti (titanium), and the G0 and G2 gratings were created by micro-cutting the Gd/Ti multilayer on a substrate. The gratings were subjected to an evaluation at an actual nTLI installed to CN-3 port of the Kyoto University Reactor (KUR) [2], with the visibility of moiré fringes being assessed. In the case of nTLI at CN-3, the required effective thickness of Gd is larger than 20 μm. The coating of Gd film in this development was performed by an ion beam sputtering instrument (KUR-IBS) at KURNS [3].The number of Gd/Ti bilayers for G0 fabrication was 2000 and the deposition time of each Gd and Ti layers were 5 minutes and 30 seconds, respectively, which was same as that of the above cutting test. The total thickness of the films was estimated to be 46μm. After sputtering, the Gd/Ti multilayer was shaped using the ultra-high precision cutting machine NPIC-M200 (Nagase Integrex Co.,Ltd.) at RIKEN and a V-shape binder-less nanodiamond cutting tool, the apex angle of which is 62 degrees within a range of 50 mm square. The total number of grooves was 400 with a pitch of 125 μm in 50 mm square.

RESULTS: Fig.1 shows the groove depth of different parts of the micro cut G0 grating measured by confocal laser microscope VK-X1000 (KEYENCE Co.,Ltd.) at RIKEN. It shows that the Gd/Ti multilayer of the newly fabricated G0 was totally penetrated to surface of Al substrate. The small peaks in bottoms of grooves were caused by Al residues from cutting. The G0 grating has also been used with another joint-use research in the nTLI at the CN-3 port.

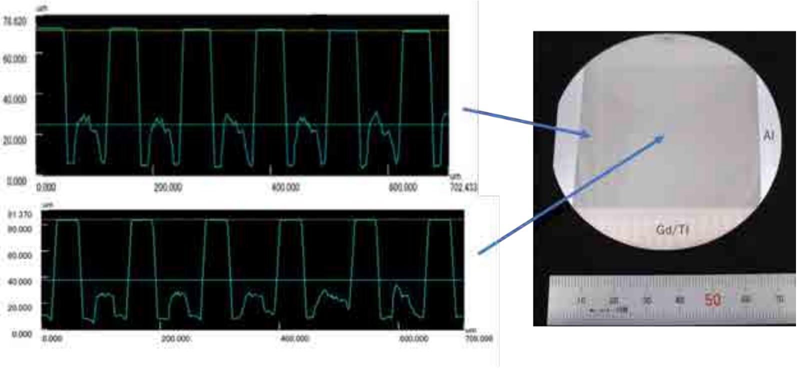

Fig.1 Groove depth of different parts of the micro-cut G0 grating.

REFERENCES:

[1] N. Kardjilov *et al.,* Materials Today, **21** (2018) 652 .
[2] Y. Seki *et al.,* Rev Sci Instrum, **94** (2023) 103701.
[3] M. Hino *et al.,* Nucl. Instr. and Meth., **797** (2015) 265.

R6055

CO1-2

Trial of mass production of *m*=6 neutron focusing supermirrors II

M. Hino[1], T. Hosobata[2], M. Takeda[2], Y. Yamagata[2] T. Oda[3] and H. Endo[4]

[1]*Institute for Integrated Radiation and Nuclear Science, Kyoto University*
[2]*RIKEN Center for Advanced Photonics, RIKEN*
[3]*Institute for Solid State Physics, the University of Tokyo*
[4]*Institute of Materials Structure Science, KEK*

INTRODUCTION: A new research reactor construction project is underway at the "Monju" site in Tsuruga City, Fukui Prefecture. One of main purposes of the research reactor is to make more extensive use of neutron beams, to produce results including those for industrial use, and to contribute to various fields, especially the local community. The actual use of the focusing mirror is one of the very important things to be at par with the top-level institute for neutron science and technology. We have established a fabrication method for aspherical focusing supermirrors with metal substrate [1]. The metal substrate is robust and ductile, which can produce a steeply curved surface with high shape accuracy. It is also applicable to use under high radiation irradiation and high temperature field, even at a place close to the neutron target and moderator. We have realized smooth surface for high-m supermirror coating. Here, m is the maximum critical angle of the mirror in units of the critical angle of natural nickel. In this study, we report on the status of mass production for high-m neutron focusing supermirrors.

EXPERIMENTS: We fabricated ellipsoidal metallic substrates with electroless nickel-phosphorus plating, based on the technology using ultrahigh precision cutting with correction processing, followed by mechanical precision polishing. The first precise manufacturing was conducted at a CNC machine for development of neutron optical devices at workshop of the KURNS. The ultra-precise manufacturing, polishing and cleaning of the metallic sub-strate were conducted at RIKEN. The supermirror coating was conducted with ion beam sputtering machine at the KURNS (KUR-IBS)[2]. Fig.1 shows photograph of ellipsoidal supermirror deposited on one LOT (three pieces) and two Si substrates. The semi-major and semi-minor axes of the ellipsoidal supermirror were 1250 mm and 65.4 mm, respectively. Eventually, we have fabricated m=6 NiC/Ti(C) supermirrors in which maximum effective number of layers was 12180, where the half of the layers were very thin carbon interlayers. The performance of supermirrors deposited on the Si substrates were evaluated by neutron reflectivity at CN-3 port of KURNS and C3-1-2(MINE) port of JRR-3.

Fig.1 Photograph of three parts of ellipsoidal neutron supermirrors coated by the ion beam sputtering instru-ment (KUR-IBS) at KURNS.

RESULTS: Although the measured reflectivity was not expected due to some problems such as grid problems, we succeeded in producing m=6 supermirrors from LOT-34 to LOT-38. Including the m=6 supermirrors, in which the number of layers was 9750 , fabricated last year, we now completed 18 LOTs (54 pieces) required for the full-circumference ellipsoidal supermirror with a length of 0.9m.

REFERENCES:

[1] T. Hosobata *et al.,* , Optics Express **25**(2017) 20012, Optics Express **27**(2019)26807.
[2] M. Hino *et al.,* Nucl. Instr. and Meth., **797** (2015) 265.

R6056

CO1-3

Measurement and improvement with neutron interferometer

M. Kitaguchi, T. Fujiie[1], T. Nambu[1], and M. Hino[2]

KMI, Nagoya University
[1]*Graduate School of Science, Nagoya University*
[2]*Institute for Integrated Radiation and Nuclear Science, Kyoto University*

INTRODUCTION: Neutron interferometry is a powerful technique for studying fundamental physics. Numerous interesting experiments [1] have been performed since the first successful test of a single-crystal neutron interferometer [2]. However, the single-crystal interferometer is inherently not able to deal with a neutron that has a wavelength longer than twice its lattice constant. In order to investigate problems of fundamental physics, including tests of quantum measurement theories and searches for non-Newtonian effects of gravitation, the interferometry of cold neutrons is extremely important, since the sensitivity of interferometer for small interaction increases with the neutron wavelength. A large scale of interferometer also has the advantage to increase the sensitivity to small interactions. One of the solutions is an interferometer using neutron multilayer mirrors [3,4]. We can easily control parameters such as Bragg angle, reflectivity, and Bragg peak width by selecting the deposited material and tuning the bilayer thickness and the number of layers. We have demonstrated a multilayer interferometer for pulsed cold neutrons at the beamline 05 NOP in J-PARC MLF [5]. In the case of pulsed neutrons, the phase of interference fringes depends on neutron wavelength which is resolved by time-of-flight.

EXPERIMENTS AND RESULTS: We tried to measure the neutron scattering lengths of ^{3}He and ^{4}He gas with the interferometer. The gas cell which can be installed into the narrow gap of the interferometer was developed. Although the accuracy was not yet good, a clear phase shift was observed. We consider that the gas cell is the cause of the contrast reduction and are currently working on improving it.

In order to enlarge the number of neutrons, neutron supermirrors which can reflect wide bandwidth of wavelength were developed for interferometer by using Ion Beam Sputtering facility in KURNS. The number of layers of the multilayer mirrors was reduced compared to the conventional supermirrors to suppress deformation of the mirror, that causes contrast loss of the interferogram. Figure 1 shows the reflectivity of the half mirrors with wide bandwidth. We will apply the mirrors to the interferometer.

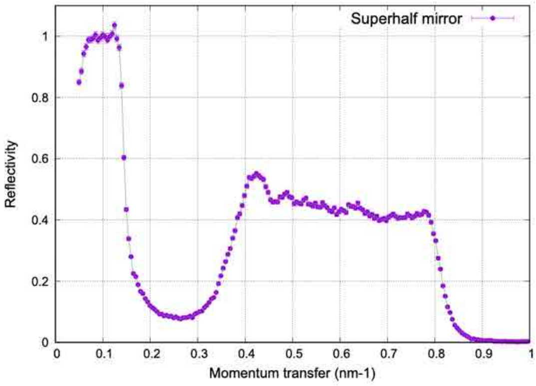

Fig. 1. Reflectivity of the half mirror with wide band of neutron wavelength measured at MINE2 in JRR3.

REFERENCES:

[1] H. Rauch and S. Werner, Neutron Interferometry Oxford University Press, Oxford, 2000.
[2] H. Rauch, W. Treimer, and U. Bonse, Phys. Lett. A, **47** (1974) 369.
[3] M. Kitaguchi *et.al.,* Phys. Rev. A, **67** (2003) 033609.
[4] Y. Seki *et. al.,* J. Phys. Soc. Jpn., **79** (2010) 124201.
[5] T. Fujiie *et. al.,* Phys. Rev. Lett., **132** (2024) 23402.

CO1-4

Iron films on an aluminum substrate for polarization analysis of ultra-cold neutrons

T. Higuchi, R. Fujitani[1], M. Hino, S. Kawasaki[2,4], M. Kitaguchi[3]

Institute for Integrated Radiation and Nuclear Science, Kyoto University

[1]*Department of Nuclear Engineering, Kyoto University, Kyoto University*
[2]*Institute of Particle and Nuclear Studies, KEK*
[3]*Kobayashi-Maskawa Institute for the Origin of Particles and the Universe, Nagoya University*
[4]*School of High Energy Accelerator Science, The Graduate University for Advanced Studies (Sokendai), Tsukuba305-0801, Japan*

INTRODUCTION: A finite electric dipole moment (EDM) of the neutron implies violation of time-reversal symmetry, and has been searched since the 1950s. Searches for a non-zero neutron EDM in high sensitivity constitute stringent tests of theories beyond the Standard Model of particle physics and shed light in the mystery of baryon asymmetry of the universe. In the state-of-the-art neutron EDM experiment, spin-precession frequencies of ultracold neutrons (UCNs), neutrons with kinetic energies on the order of 300 neV or less, are compared under different electromagnetic configurations. One of the key components required for neutron EDM experiments is spin analyzer of UCNs, whose efficiency directly impacts the precision of the spin-precession frequency measurement, thus the sensitivity of the neutron EDM search. Because of extremely low energies of UCNs, magnetized Fe thin films with small coercivities can be used as effective UCN spin analyzers, functioning as filters that selectively transmit the high-field seeking state of UCNs. In this project at the Institute for Integrated Radiation and Nuclear Science, Kyoto University, we have developed sputtered thin Fe films produced with KUR-IBS [1,2,3]. In FY2024 we succeeded in developing Fe films on 0.1-mm thick Al foils as substrate, which have minimum neutron absorption and suited for application to UCNs.

****

EXPERIMENTS: Polarized neutron reflectometry measurement was performed using a monochromatic cold neutron beam at 0.88 nm wavelength from the JRR-3/MINE2 beamline. A dedicated θ-2θ stage with an electromagnet was constructed for measurement with variable magnetic fields.

****

RESULTS: The results of the reflectometry at an applied filed of 288 Oe are presented in Fig. 1 for Fe films on Al foils and Fe films on glass. It can be observed that the reflectivity on the plateau for spin slipper off are comparable between the Fe films on Al and glass substrates. The systematic measurements sweeping the magnetic field on the sample were taken for each sample.

****

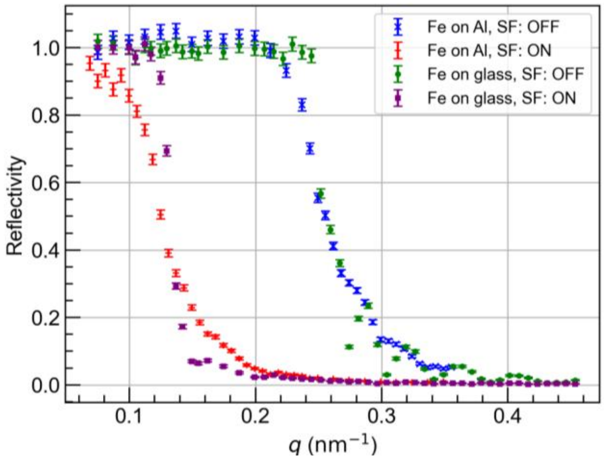

Fig. 1. Polarized neutron reflectometry with a monochromatic 0.88-nm neutrons from the MINE2 beamline. The beam was polarized with a magnetic Fe/SiGe multilayer mirror. The applied magnetic field was 288 Oe for all the measurements shown.

REFERENCES:

[1] M. Hino *et al.*, Nucl. Instr. and Meth. A, **797** (2015) 265.
[2] H. Akatsuka *et al.,* JPS Conf. Proc., **37** (2022) 020801.
[3] T. Higuchi *et al,* J. Phys. Soc. Jpn., **93** (2024) 091009.

R6139

CO2-1

Measurement system requirements for photofission signal detection with coincidence neutron counting method

Kim Wei Chin[1], Hiroshi Sagara[1], Jun-ichi Hori[2] and Yoshiyuki Takahashi[2]

[1]*Laboratory for Zero-Carbon Energy, Tokyo Institute of Technology*
[2] *Institute for Integrated Radiation and Nuclear Science, Kyoto University*

INTRODUCTION: This work focuses on numerical simulation on design of coincidence neutron counting system to detect photofission signal coming from uranium target consisting of ^{235}U and ^{238}U with in the experimental condition of LINAC Kyoto University. The information of photofission by two different energy beams can lead to the different enrichment of these two isotopes or multi-nuclide of nuclear material using the Photofission Reaction Ratio (PFRR) methodology. Photofission signal detection via neutron detection encounters difficulties of background by not only the bremsstrahlung converter target, the surrounding structural material and collimator which could contribute photo-neutrons as background. Another challenge is the separation of neutrons signal by photonuclear reactions from photofission reactions. This work proposes coincidence counting method for the neutron signal separation, and qualitative assessment on background reduction of neutrons. The coincidence counting method is a technique for separating.

****

METHODOLOGY: With MCNP code, bremsstrahlung photon source by Tantalum target with LINAC and the photo-nuclear reactions of uranium and structure materials were simulated including the neutron detector response by He-3 tubes for coincidence counting method with neutron multiplicity. The photonuclear data library used in this work is the ENDF/B-VII.0.

****

RESULTS: The impact analysis was performed on the measurement possibility with accidental injections of single neutrons coming from mainly background neutron collision in nuclear material, and background neutron reduction requirement and possible neutron absorber designing were finally deduced. The existence of the neutron absorber such as pure ^{10}B and High Density Poly Ethylene (HDPE) with 10% of fully enriched ^{10}B with certain length of thicknesses have successfully reduced the accidental injection noise down to the measurement goal defined as 1% of the total doubles of photofission neutrons, also improved the distinguishability of photofission neutrons from the background neutrons by about four orders magnitude difference (Fig. 1).

****

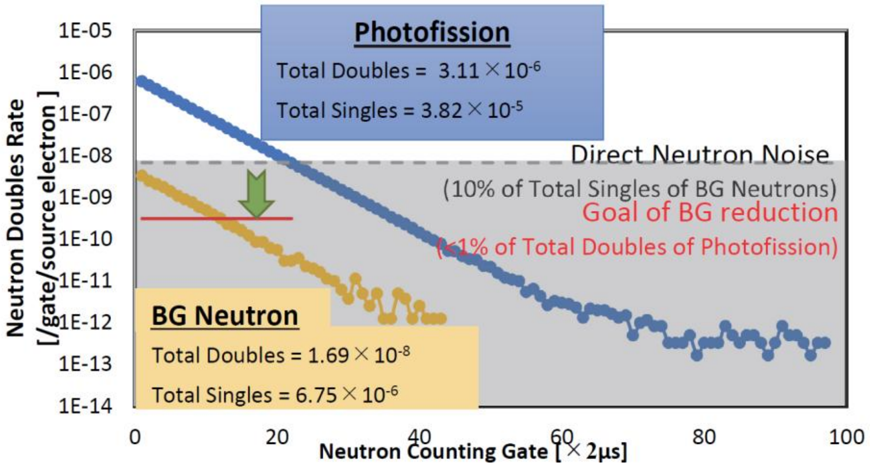

Fig. 1 Accidental neutron injection noise reduction goal.[1]

REFERENCES:

[1] Kim Wei Chin. *et al.,* Progress in Nuclear Science and Technology, **7** (2025) 91-96.

CO2-2

Measurement of Th-232 Capture Cross Section for Thorium Reactor System

T. Sano, Y. Takahashi[1], K. Terada[1], H. Yashima[1], J. Hori[1] and H. Unesaki[1]

AtomicEnergy Research Institute, Kindai University
[1]Institute for Integrated Radiation and Nuclear Sci-ence, Kyoto University

INTRODUCTION: In thorium fuel loaded nuclear reactor systems, it is important to have reliable evaluated nuclear data on the neutron capture reaction of the parent material Th-232 and the fission reaction of U-233. The authors have previously carried out differential experiments using the electron linear accelerator at the Institute for Integrated Radiation and Nuclear Science, Kyoto University (KURNS-LINAC) to measure the fission cross section of U-233 and the neutron capture cross section of Th-232. In the FY2024, shielding of gamma-ray and X-ray from photonuclear reaction in a Ta target was improvement and Th-232 capture cross sections were measured.

EXPERIMENTS: The experiment was performed on the 12 m neutron flight path shown in Figure 1. The samples were Th-232 and B-10 for neutron flux measurement. Th-232 and its daughter nuclides emitted γ rays as background. To reduce the background γ rays, a 10-mm-thick piece of lead was placed between the Th-232 sample and the BGO detector. In the measurement of B-10 for neutron measurement, a single γ ray of 478 keV emitted by the (n,α) reaction between the B-10 sample and neutrons was measured, and the TOF information was observed with the Ta target incident of accelerated electrons as the start signal and the prompt gamma ray emitted by the reaction be-tween the sample and neutrons as the stop signal.

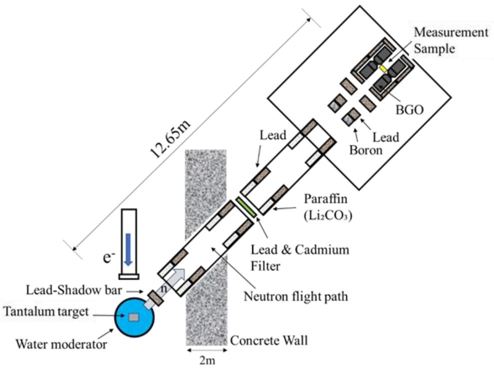

Fig.1 Experimental geometry

RESULTS: Table 1 shows the observed Th-232 resonances in this work. In this measurement, 17 resonances in the 10-350 eV energy region were observed. Compared with the evaluated values after correcting for the neutron self-shielding effect using the cross section of JENDL-5[3], the C/E values were ± 20 % except for the fourth resonance (69.2 eV). On the other hand, the C/E of the 4th resonance was clearly excessive compared to that of JENDL-5. Therefore, more detailed measurement of the 4th resonance is needed.

Table 1. Observed resonances

No.	Peak energy (eV)	No.	Peak energy (eV)	No.	Peak energy (eV)		Peak energy (eV)
1	21.80	6	120.89	11	221.33	16	329.16
2	23.47	7	129.21	12	251.69	17	342.07
3	59.53	8	170.42	13	263.28		
4	69.24	9	192.76	14	285.97		
5	113.06	10	199.45	15	305.69		

ACKNOWLEDGMENT: A part of this study was supported by CHUBU Electric Power Co., Inc.

REFERENCES:

[1] J. Lee *et al.,* Energy Procedia, **131** (2017) 306-311.
[2] O. Iwamoto *et al.,* J. Nucl. Sci. Technol., **60(1)** (2023) 1-60.

CO2-3

Analysis of Tetraneutron Search Experiment by the (^{4}n, n) Reaction in KUR

S. Oikawa, H. Fujioka and K. Takamiya[1]

Department of Physics, Institute of Science Tokyo
[1] Institute for Integrated Radiation and Nuclear Science, Kyoto University

INTRODUCTION: Tetraneutron is a nucleus that is composed of four neutrons. It is not clear whether it exists from theoretical calculations, but recent experimental studies have suggested its existence. For example, M. Duer et al. reported the discovery of a tetraneutron in a resonant state [1], and T. Faestermann et al. claimed the observation of a bound tetraneutron [2]. We have conducted a tetraneutron search experiment by the (^{4}n,n) reaction in KUR, assuming that bound tetraneutrons are emitted by fission of uranium in a nuclear reactor. As the first step, an experiment with $^{88}SrCO_3$ was conducted in FY2022, and an upper limit of the emission rate of tetraneutron was determined [3]. In this experiment, we performed a similar irradiation experiment with mononuclidic elements.

EXPERIMENTS: We used the (^{4}n,n) reaction on ^{93}Nb or ^{127}I to detect long-lived tetraneutrons from the fuel. High purity niobium metal and NH_4I samples were placed near the reactor core through hydraulic (Hyd) and pneumatic (Pn-2) transport tubes. They were irradiated for 4 hours and 1 hour, respectively, at a thermal power of the reactor of 5 MW. Then, we measured the gamma rays emitted from the samples with a germanium detector. If tetraneutrons reacted with ^{93}Nb or ^{127}I, γ-rays from ^{96}Nb or ^{130}I are expected to be observed.

RESULTS: As shown in Figs. 1 and 2, photopeaks originating from various nuclides were identified. In Fig. 1, we identified photopeaks not only from niobium, but also from tantalum, which was contained in the sample. In Fig. 2, we identified γ-rays from the silica tube in which NH_4I was sealed as well.

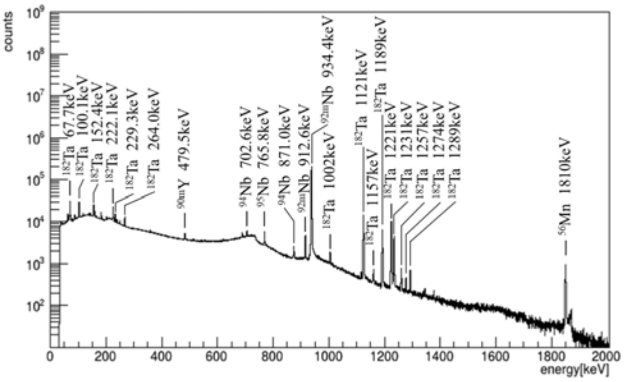

Fig. 1. Spectrum measured for 30 minutes from niobium metal about 70 hours after irradiation.

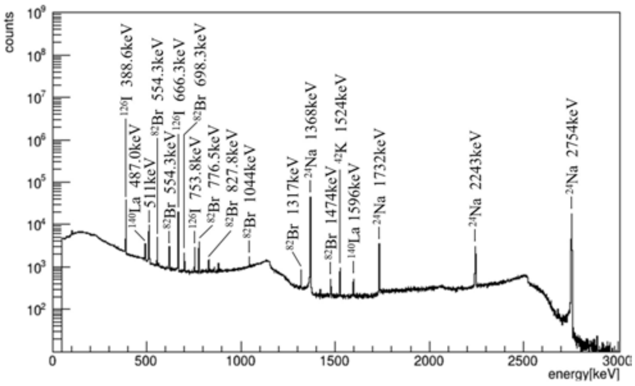

Fig. 2. Spectrum measured for 30 minutes from NH_4I about 69 hours after irradiation.

REFERENCES:

[1] M. Duer *et al.,* Nature, **606** (2022) 678-682.
[2] T. Faestermann *et al.,* Phys. Lett. B., **824** (2022) 136799.
[3] H. Fujioka *et al.,* Phys. Rev. C, **108** (2023) 054004.

CO2-4

Effects of lead addition on tritium recovery for advanced Li_2TiO_3-Li_4SiO_4 mixed breeder material

Y. Oya[1], A. Sanfukuji[1], Q. Zhou[2]

[1]Graduate School of Integrated Science and Technology, Shizuoka University
[2]School of Materials Science and Engineering, Wuhan University of Technology

INTRODUCTION: Tritium will be produced by (n, α) reaction with lithium (Li) in the fusion reactor because the amount of tritium in nature is limited. Tritium breeder requires good chemical stability and ease of tritium recovery. Lithium silicate (Li_4SiO_4) and lithium titanate (Li_2TiO_3) have different characteristics. For example, lithium silicate has a high lithium density, while lithium titanate is good chemical stability and has a good crushing load. Advanced tritium breeder materials should have both of higher tritium production rate and recovery efficiency. LTO-LSO mixed ceramic materials are expected to have both advantages. Lead (Pb) is a neutron multiplier that contributes to the improvement of the tritium breeding ratio and has a lower affinity with tritium. The addition of Pb into Li ceramics is expected to have a potential advantage for efficient tritium recovery.

EXPERIMENTS: LTO-LSO-x wt.%Pb, a powder sample of lithium titanate and lithium silicate mixture with 2, 5, 25wt.%Pb addition, was prepared at Wuhan University of Technology. Those samples were irradiated by neutron at Kyoto University Research Reactor (KUR) with the neutron fluence of 8.0×10^{15} n cm^{-2} and 8.0×10^{16} n cm^{-2}. After the neutron irradiation, tritium release behavior was evaluated by Tritium-thermal desorption spectroscopy (T-TDS) system by heating the samples separately from R.T. to 1113 K with the heating rates of 10, 20, and 30 K min^{-1}. Liquid scintillation counter (LSC) was used to measure the total T amount trapped by the water bubbler at Shizuoka University. For each sample, the surface chemical states were characterized by X-ray Photoelectron Spectroscopy (XPS), and the bandgap was evaluated using Reflection Electron Energy Loss Spectroscopy (REELS).

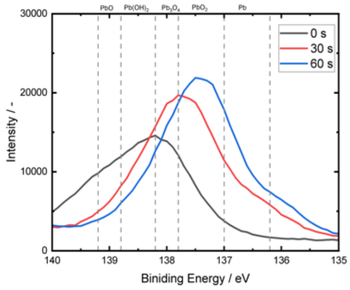

Fig. 1 XPS spectra of Pb-4f in LTO-LSO-20 wt.% Pb.

RESULTS: Fig. 1 shows the XPS spectra of Pb-4f for LTO-LSO-20 wt.%Pb. It was found that the oxidation state of Pb increased with depth from the surface. This suggests that Pb forms oxides with LTO and LSO. The bandgap of LTO-LSO was found to be 2.78 eV, whereas that of LTO-LSO-20 wt.%Pb increased to 4.53 eV, as determined from REELS measurements. This increase can be attributed to the larger energy difference between the conduction band of Pb and the valence band of highly electronegative oxygen. These results suggest that the Pb-added sample is more resistant to external influences such as radiation and exhibits better thermal stability. Fig. 2 shows the T-TDS spectra for LTO-LSO and LTO-LSO-5 wt.%Pb with different LTO/LSO compositional ratios. The addition of Pb caused the shift of major tritium desorption toward lower temperature side. The T release behavior also varied depending on the relative proportions of the two oxides. Therefore, it is considered necessary to investigate not only the Pb content but also their mixing ratio.

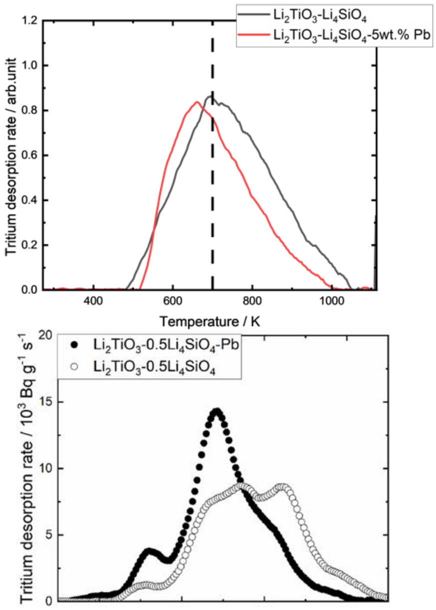

Fig. 2 TDS spectra of samples with different LTO/LSO ratios (top: LTO-LSO, bottom : LTO-0.5LSO).

CO2-5

Development of neutron resonance analysis technique in neutron time-of-flight for fissile material identification and quantification

J. Lee[1], F. Rossi[1], Y. Yoshimi[1], T. Shiba[1], K. Terada[2], and J. Hori[2]

[1]*Integrated Support Center for Nuclear Nonproliferation and Nuclear Security, Japan Atomic Energy Agency*
[2]*Institute for Integrated Radiation and Nuclear Science, Kyoto University*

INTRODUCTION: The Japan Atomic Energy Agency (JAEA) has been developing a neutron resonance analysis (NRA) technique as an active neutron non-destructive assay for the identification and quantification of fissile materials. NRA combines neutron resonance transmission analysis (NRTA), neutron resonance capture analysis (NRCA), and neutron resonance fission neutron analysis (NRFNA) [1]. In the JAEA NRA system, we employed EJ-276D plastic scintillators, which allow for pulse shape discrimination (PSD) of gamma rays and fast neutrons for NRCA and NRFNA. Additionally, we used the GS20 lithium glass scintillator for NRTA [2]. An NRA experiment was conducted at the neutron time-of-flight (TOF) beamline of the KURNS-LINAC using enriched uranium (EU) samples. This paper reports the measurement results and discusses the NRA system's ability to identify and quantify fissile materials.

EXPERIMENTS: **Fig. 1** shows the experimental setup. The KURNS-LINAC was operated with a pulse width of 2 μs, a repetition rate of 50 Hz, an average current of 47.5 μA, and a beam energy of 31.5 MeV. The pulsed neutrons were collimated using lead and borated polyethylene and directed toward the sample. In this experiment, three EU samples with different thicknesses (1, 2, and 3 mm) were used, each containing approximately 93.14 wt% of ^{235}U. The EU samples were placed at the center of the two EJ-276D detectors, which detected fast fission neutrons and gamma rays emitted by the EU sample. A 6-mm-thick GS20 detector was used to measure the neutrons transmitted through the EU samples.

RESULTS: **Fig. 2** shows the obtained TOF spectra for the 3-mm-thick EU sample. The resonance dips and peaks corresponding to the ^{235}U(n, tot) and the ^{235}U(n, γ) reactions (in blue and black respectively) were observed in the TOF range of 170–450 μs. Additionally, the resonance peaks from the ^{235}U(n, f) reactions (in red) were observed in the TOF range of 100–2000 μs. These results indicate that the JAEA NRA system is sufficiently capable of identifying fissile materials. Currently, analysis is ongoing to quantify the fissile material using data obtained from the EU samples of different thicknesses.

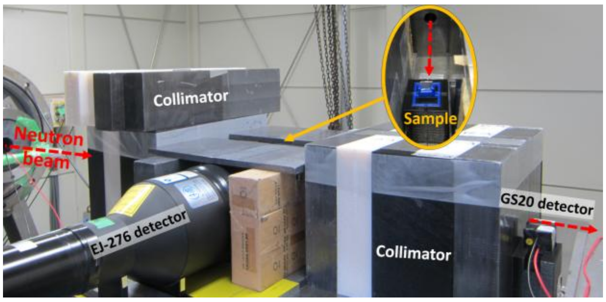

Fig. 1. Experimental setup.

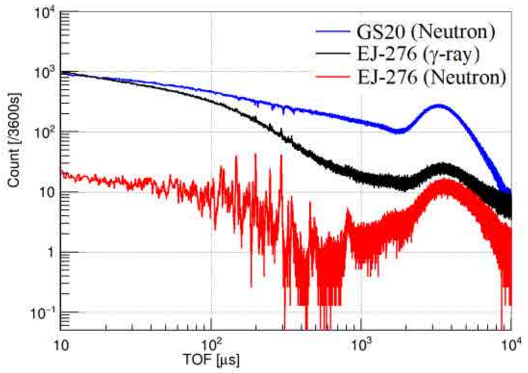

Fig. 2 Obtained TOF spectra of 3-mm-thick EU.

ACKNOWLEDGEMENTS: This research was implemented under a subsidy for "promotion of strengthening nuclear security and the like" of the Ministry of Education, Culture, Sports, Science, and Technology, Japan.

REFERENCES:

[1] K. Hironaka *et al.,* NIM-A, **1054** (2023) 168467.
[2] J. Lee *et al.,* Annals of Nuclear Energy, **211** (2025) 111017.

CO2-6

Measurements of neutron capture cross sections of P-31

K. Terada, J. Hori, Y. Takahashi, H. Yashima and T. Sano[1]

Institute for Integrated Radiation and Nuclear Science, Kyoto University
[1]Atomic Energy Research Institute, Kindai University

INTRODUCTION: The thermal neutron capture cross section data of ^{31}P are scarce, as it has only been measured by Salama et al [1]. This is because it was not regarded as an important nuclide in the applications of nuclear power and stellar nucleosynthesis. The evaluations of JENDL-5 [2] and ENDF-B/VIII.0 [3] are 16% and 18% larger than that of Salama et al. Therefore, we measured neutron capture cross sections of ^{31}P at the thermal energy with the Kyoto University Institute for Integrated Radiation and Nuclear Science-Linear Accelerator (KURNS-LINAC).

EXPERIMENTS: The KURNS-LINAC is an L-band electron linear accelerator having a maxi-mum acceleration voltage of 46 MeV and a beam power of 10 kW. Accelerated electron beams with a repetition rate of 50 Hz, an energy of 31 MeV, and an average beam current of 60 μA are bom-barded to a water-cooled Ta target, generating bremsstrahlung X-rays. Neutrons produced via (γ, n) reactions are moderated by light water sealed in the tank with a diameter of 20 cm and a height of 30 cm. 6.935 g of red phosphorus powder was sealed in an aluminum container with a diameter of 30.0 mm and a thickness of 16.5 mm. Furthermore, we measured a dummy case to subtract sam-ple-dependent background. The measurement was performed using a time-of-flight (TOF) method. The distance between the sample and the neutron source was 12.7 m. Neutron capture gamma-rays from the ^{31}P sample were measured with twelve BGO detectors. Signals from the detectors were recorded event-by-event as two-dimensional data of TOF and pulse height data. Incident neutron energy distribution was determined by measuring 478 keV gamma-rays via ^{10}B(n, γα) reactions. Figure 1 shows the obtained TOF spectra of the ^{31}P sample and the dummy case. The net TOF spec-trum of ^{31}P was determined by subtracting the sample-dependent and sample-independent back-ground. Finally, the neutron capture cross sections of ^{31}P was derived.

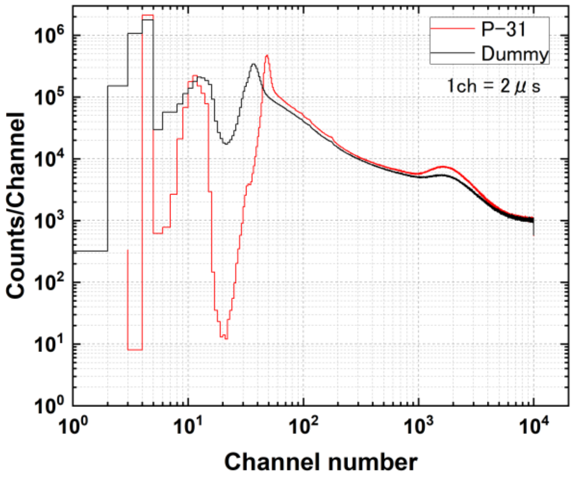

Figure 1. Measured TOF spectra were shown. The red line is the ^{31}P TOF spectrum. The black line is the Dummy TOF spectrum. 1 ch is 2μs.

REFERENCES:

[1] M. Salama *et al.,* Nuclear Science, **23(5)** (1986) 327.
[2] O. Iwamoto *et al., J.* Nucl. Sci. Technol., **60(1)** (2023) 1-60.
[3] D. A. Brown *et al.,* Nuclear Data Sheets, **148** (2018) 1-142.

R6160

CO2-7

Neutron cross-section measurement of molybdenum

Y. Takahashi, J. Hori, K. Terada

Institute for Integrated Radiation and Nuclear Science, Kyoto University

INTRODUCTION:

The Kyoto University Critical Assembly (KUCA) is preparing to adopt a new reactor fuel composed of uranium-molybdenum (UMo). This will be the first reactor in the world to utilize this type of fuel, which is expected to be widely used in research reactors in the future. While the reliability of nuclear data has been sufficiently validated for conventional uranium-aluminum alloy fuel, core analysis using UMo fuel, particularly for molybdenum, remains insufficient. Therefore, improving the nuclear data related to molybdenum is essential.

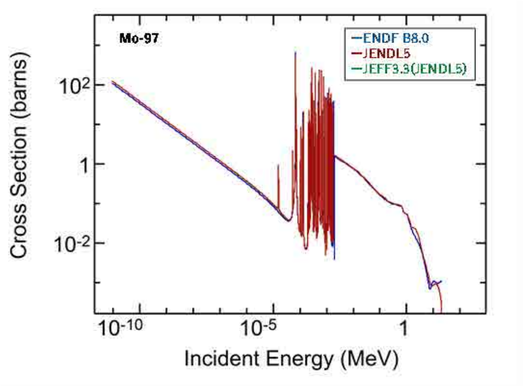

Fig. 1. Cross-section of Mo-97

Figure 1 shows a comparison of Mo-97 data in JENDL-5 and ENDF/B-VIII.0, revealing some discrepancies. This study aims to contribute to the improvement of molybdenum nuclear data by measuring neutron cross-sections of selected molybdenum isotopes using the KURNS-Linac, thereby enhancing the accuracy of KUCA core analyses.

EXPERIMENTS:

For the preliminary test, a natural molybdenum plate was used as the sample. The plate was 3.0 mm thick, with dimensions of 15 × 15 mm. In the time-of-flight (TOF) setup, the sample was placed 12 meters from the target at a 135-degree angle. The target was surrounded by a carbon moderator. A total of 12 BGO scintillators were arranged around the sample to measure the total energy of absorbed gamma rays. No shielding materials were used. The accelerator operated in short-pulse mode with the following parameters: average beam current of 17 μA, frequency of 200 Hz, pulse width of 33 ns, and beam diameter of 50 mm. The measurement time was 1 hour for both the sample and the blank.

RESULTS:

Figure 2 presents the TOF measurement results for both the sample and the blank (no sample). The data are normalized to measurement time. One channel corresponds to 100 ns. For example, a difference was observed in the TOF region between 10 and 50 μs, which was attributed to hydrogen capture gamma rays. Several peaks were clearly detected, and further analysis will be necessary.

In future experiments, cross-section measurements will be conducted using thinner samples, with the sample thicknesses determined through preliminary calculations

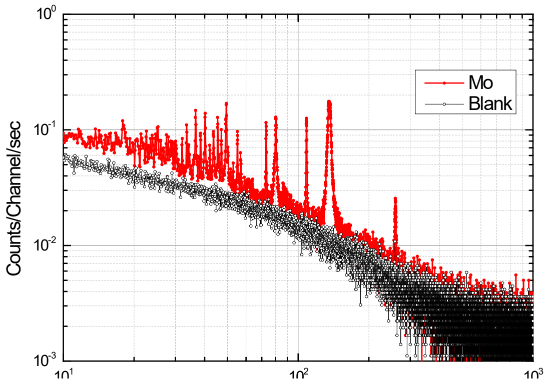

Fig. 2 Result of TOF

CO3-1

Tritium release behavior from neutron irradiated FLiNaBe mixed with Ti

K. Katayama, Y. Setoguchi[1], T. Ichikawa[1], H. Isogawa[1], Y. Mori[1], K. Akashi[2], Y. Iinuma[3]

Faculty of Engineering Science, Kyushu University
[1]Interdisciplinary Graduate School of Engineering Sciences, Kyushu University
[2]Faculty of Engineering, Kyushu University
[3]Institute for Integrated Radiation and Nuclear Science, Kyoto University

INTRODUCTION: FLiNaBe is a promising liquid blanket material of a deuterium – tritium fusion reactor due to chemical stability, low MHD effect and low melting point. Since hydrogen solubility in FLiNaBe is quite low, one concern is permeation loss of bred tritium in transport process to the tritium recovery system. In order to increase effective solubility for tritium, the addition of Ti powder has been proposed [1]. The understanding of tritium release behavior from FLiNaBe is an important issue in the design of fuel recovery systems and radiation safety measures. However, the tritium release behavior from FLiNaBe mixed with Ti is not sufficiently understood. In this work, solid-state samples of FLiNaBe were irradiated by neutrons in Kyoto University Research Reactor. Ti powder was mixed in the irradiated FLiNaBe and tritium release behavior from the FLiNaBe with Ti by heating to 600 °C was observed in Kyushu University.

****

EXPERIMENTS: FLiNaBe prepared by the present authors are packed in quartz tubes with vacuum. The quartz tubes were packed in polyethylene capsules and irradiated by neutrons with 5.5×10^{12} $\mathrm{cm^{-2}\cdot s^{-1}}$ in flux and 5 minutes in irradiation period. After neutron irradiation, the samples were transported to Kyushu University for tritium release experiments. The schematic diagram of the experimental apparatus is shown in Fig.1. The irradiated sample was put in a Mo crucible, and it was installed in the quartz reaction tube. The sample was heated by an electric furnace to 600 °C in Ar gas flow. The water soluble tritium such as tritiated water vapor (HTO) and tritium fluoride (TF) and gaseous tritium (HT) were separately collected in water bubblers. Ti power was mixed in the irradiated FLiNaBe with 5 wt% and the similar experiment was conducted.

****

RESULTS: Most of tritium was released in water-soluble chemical form. Fig.2 shows the cumulative amount of water-soluble tritium released from neutron irradiated FLiNaBe and FLiNaBe mixed with Ti powder. As this figure shows, the amount of tritium released from the FLiNaBe with Ti was smaller than that from the FLiNaBe. This result clearly indicates that the amount of tritium released in the gas phase from FLiNaBe can be largely suppressed by mixing Ti. At temperatures below 500 °C, tritium was effectively absorbed and retained in Ti powder.

****

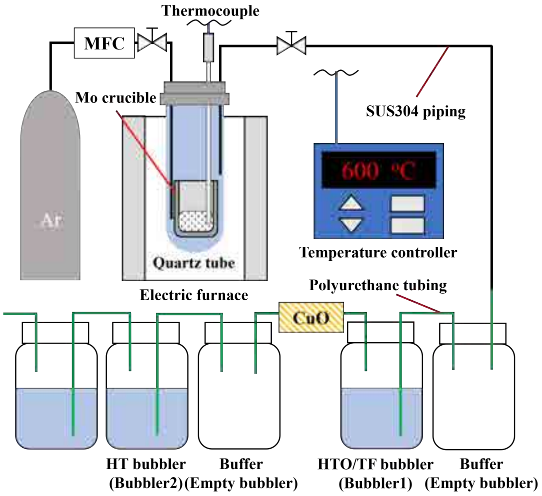

Fig. 1. Experimental apparatus.

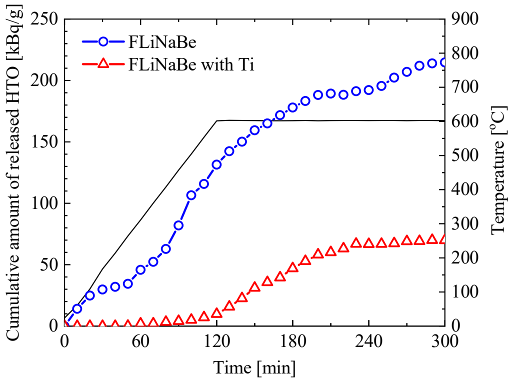

Fig. 2. Cumulative amount of water-soluble tritium released from FLiNaBe and FLiNaBe with Ti powder.

REFERENCES: [1] A. Sagara *et al.,* Fusion Eng. Des., **89** (2014) 2114–2120.

CO4-1

Characterization of ion-irradiated yttria stabilized zirconia (YSZ) single crystal substrates using a slow positron beam

T. Ozaki, H. Sakane[1] and A. Yabuuchi[2]

School of Engineering, Kwansei Gakuin University
[1] *SHI-ATEX Co., Ltd.*
[2] *Institute for Integrated Radiation and Nuclear Science, Kyoto University*

INTRODUCTION: The rare-earth (RE)-based cuprate superconductor $REBa_2Cu_3O_y$ (REBCO) exhibits high in-field performance, and is expected to be useful for magnetic coils. Critical current properties in applied magnetic fields are enhanced by introducing structural defects using ion-irradiation techniques. Positrons are sensitive to vacancy-type defects, and they are useful for characterizing irradiation-induced defects. However, it is difficult to characterize irradiation-induced defects in GdBCO coated conductors (CCs), which were industrially produced with a roll-to-roll process because GdBCO CCs initially contain vacancy clusters, whose size is larger than that of the newly-formed defects induced by the irradiation [1]. In this study, we probed ion-irradiated yttria stabilized zirconia (YSZ), which is an oxidized material and almost the same density as GdBCO, single crystal substrates using a slow positron beam, so that we will evaluate the irradiation defect in these substrates using the positron annihilation measurement.

EXPERIMENTS: The YSZ single crystal substrates were irradiated with 600 keV He^+ or 10 MeV Au^{4+} ions. The unirradiated and irradiated samples were probed by the KUR slow positron beam and the Doppler broadening of annihilation radiation (DBAR) spectra were acquired with incident positron energies $E_+ = 9$ keV.

RESULTS: Figure 1 shows the positron lifetime spectra for the unirradiated and the irradiated YSZ single crystal substrates. We observed longer lifetimes of positron in the irradiated samples than that in the unirradiated sample. In addition, a longer lifetime component was clearly observed for the sample irradiated with 10 MeV Au-ions compared with that irradiated with 600 keV He-ions, suggesting that the size of lattice defects produced by 10 MeV Au-ions is larger than that produced by 600 keV He-ions.

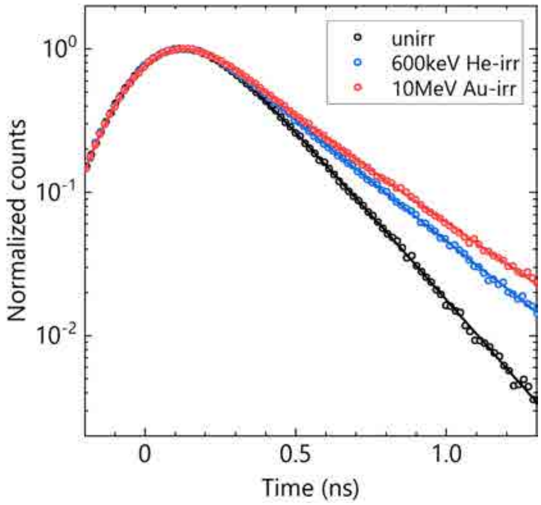

Fig. 1. Positron lifetime spectra for the unirradiated and the irradiated YSZ single crystal substrates.

REFERENCES:

[1] A. Yabuuchi *et al.,* Appl. Phys. Ex-press, **13** (2020) 123004.

CO4-2

Reducing Parasitic Scattering in Small-Angle X-Ray Scattering using Single Crystal Pinhole

Y. Oba, R. Inoue[1], K. Morishima[1] and M. Sugiyama[1]

Department of Mechanical Engineering, Toyohashi University of Technology
[1]Institute for Integrated Radiation and Nuclear Science, Kyoto University

INTRODUCTION: Small-angle X-ray scattering (SAXS) is a powerful tool for nanostructural characterization and used in a wide variety of research fields, such as polymer science, biology, and metallurgy [1,2]. To enhance the performance of SAXS, scatterless slit techniques have attracted attention [3-5]. They can drastically reduce parasitic scattering in X-ray collimation systems and allow efficient X-ray collimation. In this study, one of these techniques using single-crystal pinholes were applied to the SAXS instrument with Mo Kα radiation (Mo-SAXS) at the Institute for Integrated Radiation and Nuclear Science, Kyoto University.

EXPERIMENTS: SAXS experiments were carried out using Mo-SAXS (NANO-Viewer, Rigaku) with a conventional three-pinhole collimation system. Scattering patterns were measured using a photon-counting-type two-dimensional detector (PILATUS 100k, Dectris). The X-ray path from the X-ray entrance pinhole to the window just before the detector was evacuated to reduce the background scattering from air. The scattering patterns were reduced using our original program written in Igor Pro (WaveMetrics).

The single-crystal pinholes were made of tantalum discs with the thickness of 0.5 mm. A round hole with the diameter of 0.3-1.0 mm was opened at the center of each disc. In the current experiments, the two-pinhole collimation system was built using the normal X-ray entrance pinhole and the single-crystal pinhole just before the sample.

RESULTS: Fig. 1shows the comparison of the SAXS profiles between the conventional three-pinhole and new two-pinhole systems with the same primary beam size on the detector. The two-pinhole system provided almost 1/10 background intensity at $q < 0.15$ nm^{-1}, where q is the magnitude of the scattering vector. As the result, the data quality in this low q region was significantly improved and the practical low q limit reached 0.05 nm^{-1}. The background intensity in the high q region was also decreased. In addition, the incident X-ray intensity at the sample position increased 2.4 times.

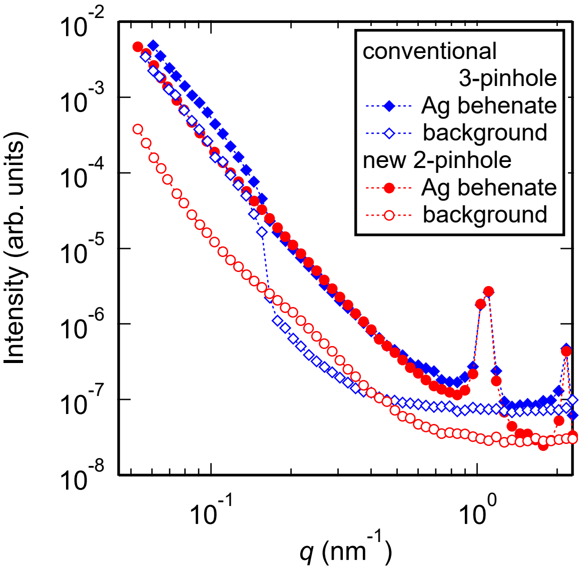

Fig. 1. SAXS profiles of background and Ag behenate obtained using conventional three-pinhole and new two-pinhole systems.

REFERENCES:

[1] Cy M. Jeffries *et al.,* Nat. Rev. Methods Primers, **1** (2021) 70.
[2] S. Da Vela, D. I. Svergun, Curr. Res. Struct. Biol., **2** (2020) 164.
[3] Y. Li *et al.,* J. Appl. Cryst., **41** (2008) 1134-1139.
[4] A. Schwamberger *et al.,* Nucl. Instrum. Met. Phys. Res. B, **343** (2015) 116-122.
[5] J. Lyngsø J. S. Pedersen, J. Appl. Cryst., **54** (2021) 295-305.

CO4-3

Neutron shielding performance of wood-based products

K. Murata[1], Y. Mimoto[1], M. Tsuchiya[2], K. Kariya[2], Y. Yamashiki[3], K. Takamiya[4]

[1]*Graduate School of Agriculture, Kyoto University*
[2]*Sumitomo Forestry Co., Ltd.*
[3]*Graduate School of Advanced Integrated Studies in Human Survivability, Kyoto University*
[4]*Institute for Integrated Radiation and Nuclear Science, Kyoto University*

INTRODUCTION: Neutron shielding is achieved using hydrogen-rich materials, such as water, polyethylene, and concrete, while elements with a large neutron absorption cross-section, such as boron, cadmium, and lithium, are used as absorbers. Because wood is primarily composed of carbon, oxygen, and hydrogen, and like polyethylene, is a hydrogen-rich compound, wood-based materials are also expected to exhibit good neutron shielding performance. In addition, fire-retardant wood products containing boron, which are commercially available, should have excellent neutron shielding performance. In this study, the neutron shielding performance of wood products was evaluated at a heavy water neutron irradiation facility (HWNIF) in the KUR.

EXPERIMENTS: The table 1 shows the materials prepared for neutron shielding test, which have a cross section of 80 mm × 80 mm and a thickness of 60 mm. Au foils and a cadmium-covered Au foils were placed in front of and behind the specimen, and the specimen was irradiated with mixed-mode neutron radiation in the HWNIF for 10 min. Gamma rays from the activated Au foils were measured using a Ge semiconductor detector, and shielding rates were obtained.

Table 1 Materials for estimating neutron shielding performance.

Symbol	Material	Symbol	Material
ASG	Air-dried sugi wood	FSG	Fire retardant sugi wood (boron)
DSG	Densified sugi wood	FPW	Fire retardant karamatsu plywood (boron)
WSG	Water impregnation sugi wood	PE	Polyethylene
KPW	Karamatsu plywood		

RESULTS: Fig. 1 shows a comparison of the neutron shielding rates of each product. Because PE and WSG have high shielding rates for epithermal neutrons, products rich in hydrogen atoms can effectively shield epithermal neutrons. However, because FSG and FPW have a high thermal-neutron shielding rate, it can be noted that elements with a large neutron absorption cross-section are effective in shielding thermal neutrons.

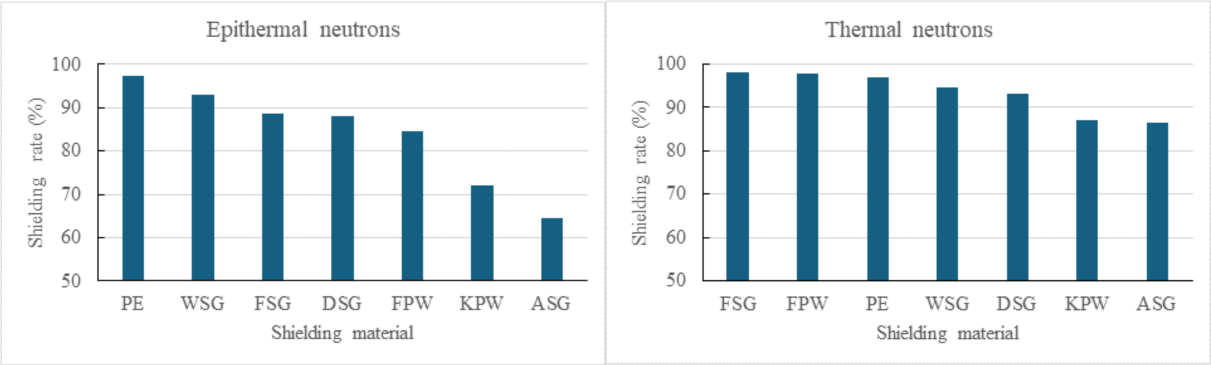

Fig. 1. Neutron shielding rates of wood products shown in Table 1.

CO4-4

Study on HPLC Elution Behavior of Heavy Lanthanide Metallofullerene Using Chlorobenzene Eluent

K. Akiyama, D. Nakamura, T. Kuroda, K. Takamiya[1], and S. Kubuki

Department of Chemistry, Tokyo Metropolitan University
[1]Institute for Integrated Radiation and Nuclear Science, Kyoto University

INTRODUCTION: Lanthanide (Ln) metallofullerene (EMF): Ln@C_{82} is a clathrate compound encapsulating metal atom in fullerene C_{82} and known that two or three electrons are transferred to C_{82} cage from the encapsulated Ln atom [1]. In the previous work, we succeeded to obtain the high-performance liquid chromatography (HPLC) elution behavior on a pyrenyl stationary phase for Ln@C_{82} of La, Ce, Pr, Nd, Gd, Tb, Dy, Ho, and Er with a toluene as an eluent by the thermal neutron activation method [2]. In this study, we used chlorobenzene (CB), which has a similar structure to toluene, as an eluent in order to obtain further knowledge about the HPLC elution behavior of Ln@C_{82}.

EXPERIMENTS: Ln@C_{82}s of Tb, Dy, and Ho were prepared by previously reported [2]. These purified samples were injected into a Buckyprep column using CB as an eluent. The eluate from the column was fractionated every 2 minutes at room Temperature (RT) and every 30 seconds at 50 °C. These fractionated eluates were evaporated to dryness and re-dissolved to carbon disulfide and then dropped onto paper filters with 12 mm diameters and dried for 2 or 3 days in the evacuated desiccator. After sufficient drying, these samples were sealed into polyethylene bags and were activated by a thermal neutron in the KUR of the Institute for Integrated Radiation and Nuclear Science, Kyoto university. After the irradiation, the γ rays emitted from the samples were measured by a Ge detector.

RESULTS: Figure 1 shows HPLC chromatograms of Ln@C_{82} (Ln: Tb, Dy, Ho) using CB as a developing solvent at room temperature (left) and 50 oC (right). The retention times for each Ln@C_{82} were found to be 44.76 and 44.92 minutes for Dy, and Ho at room temperature and 40.73 minutes, 40.57 minutes, and 40.56 minutes for Tb, Dy, and Ho at 50 °C. Although the retention time for Tb at room temperature is missing because accurate data was not available, adsorption desorption enthalpy for Dy and Ho were roughly estimated and found to be 3.5 and 3.6 kJ/mol for Dy and Ho respectively.

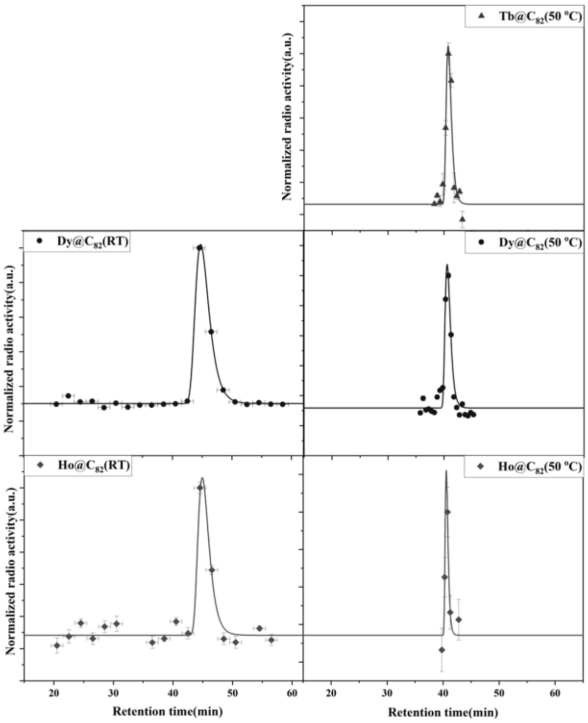

Fig. 1. HPLC chromatogram of Ln@C82 (Ln = Tb, Dy, and Ho) using CB as a developing solvent (left: room temperature, right: 50°C)

REFERENCES:

[1] H. Shinohara, Rep. Prog. Phys., **63** (2000) 843-892.
[2] K. Akiyama *et al.,* KURNS Prog. Rep. 2022 CO4-1.

CO4-5

Study on ^{99m}Tc separation/concentration technology from ^{99}Mo by (n, γ) method (3)

H. Suematsu, Y. Yang, T. Kitagawa, T. M. D. Do, T. Suzuki, Y. Fujita[1], Y. Fujihara[2], H. Yoshinaga[2] and J. Hori[2]

Graduate School of Engineering, Nagaoka University of Technology
[1]Fuels and Materials Department, Japan Atomic Energy Agency
[2]Institute for Integrated Radiation and Nuclear Science, Kyoto University

INTRODUCTION: ^{99}Mo production methods by neutron irradiation of MoO_3 targets were studied and an effective extraction method using ^{99}Mo hot atoms was developed[1]. In the former research, β-MoO_3 whiskers were used as the neutron irradiation targets[1]. However, it was not certain whether the high extraction rate was caused by the short diffusion path of ^{99}Mo in the whisker or the wide spacing of MoO_5 pyramids in the β-MoO_3 crystal. Furthermore, α-MoO_3 was also present in the target. In this work, high purity β-MoO_3 particles were synthesized by a thermal evaporation method using a metal filter to separate large α-MoO_3 crystals from fine β-MoO_3 particles for the neutron irradiation and ^{99}Mo extraction experiments.

EXPERIMENTS: α-MoO_3 powder was placed in a tube furnace heated at 900 °C in flowing O_2 gas at 60 kPa with a flow rate of 8L/min. In the downstream side of the furnace, a # 500 metal filter was placed to catch large α-MoO_3 crystals. Then fine β-MoO_3 particles were collected on a membrane filter. The β-MoO_3 particles were irradiated by neutrons in KUR at $3\text{x}10^{13}$ n/cm^{2}s for 20 min. The irradiated particles (solid sample) was dispersed in water at room temperature up to 24 hour. The irradiated particles were separated by a centrifuge and a membrane filter to prepare solution sample. The activities of solid and solution samples were measured by a Ge detector were used to estimate the extraction rate of ^{99}Mo from the solid to solution samples.

RESULTS: Scanning electron microscopy (SEM) image of the β-MoO_3 particles is shown in Fig. 1. From the image, the geometric mean diameter was measured to be 130 nm. The time dependence of extraction rate is shown in Fig. 2. 75% of the formed ^{99}Mo in β-MoO_3 particles by the neutron irradiation was successfully extracted even at room temperature. From these experiments, it was concluded that β-MoO_3 particles can work as a target to produce and extract ^{99}Mo in water.

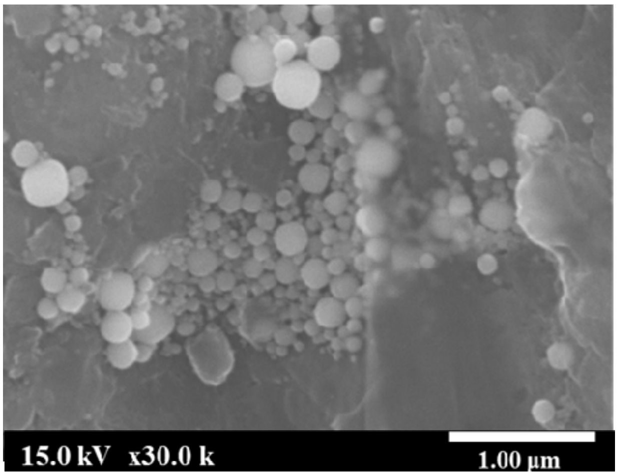

Fig. 1. SEM image of β-MoO_3 particles

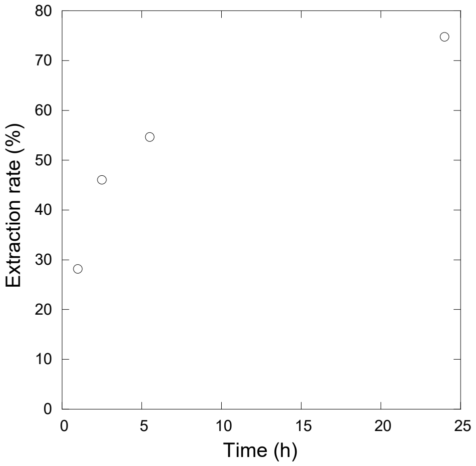

Fig. 2. Extraction rate of ^{99}Mo to water

REFERENCES:
[1] M. C. Ngo *et al.,* Inorganic Chem., **62** (2023) 131040.

CO4-6

Complex Structure of Ions Coordinated with Hydrophilic Polymer 25. Examination for "Diffusion-induced Orientation" Observed in PA6 Considering Dynamic Structure of Polyiodides.

A. Kawaguchi , A. Kita, Y. Morimoto

IIRNS, Kyoto University (KURNS)

INTRODUCTION: We have been investigating dynamical and interacted structures between iodine and polymers. Here, "iodine" is mentioned containing "polyiodide ions" (I_n^{m-}, m, n: integer, n > 1: "Poly-Iod." mentioned below), which are defined as charged molecules constructed with more than one iodine atom. And, Poly-Iod.(s), mono iodide ion (I^-) and iodine (I_2) can actively interact with each other as molecular (re)structuring between (or among) them originated by "halogen (iodine) bonding". Such structured iodine arrays can be often observed in coordination within organic crystals.[1] And interaction and structuring are more emphasized through coordination with macromolecular matrices as both hydrophilic and hydrophobic polymers.

Interaction and (re)structuring among Poly-Iod., I^-, and I_2 are characterized by "charge conjugation" and "iodine bonding", which is loose and anisotropic; it means that iodine arrays behave as "pseudo polymer" under charge shearing. And, polyamide 6 (PA6) is one of hydrophilic polymers showing active interaction with Poly-Iod. Additionally, PA6 is crystalline polymer and is induced phase transition through coordination with Poly-Iod.[2]

EXPERIMENTS: As starting PA6, non-oriented film ("Rayfan^{TM}", 100μm in thickness) provided by TORAY was prepared. And, while "non-oriented PA6" was annealed without stretching, "doubly oriented PA6" was annealed after stretched keeping filmy form. They were doped in 0.1N I_2-KI(aq) at 5deg. (iodine doping).

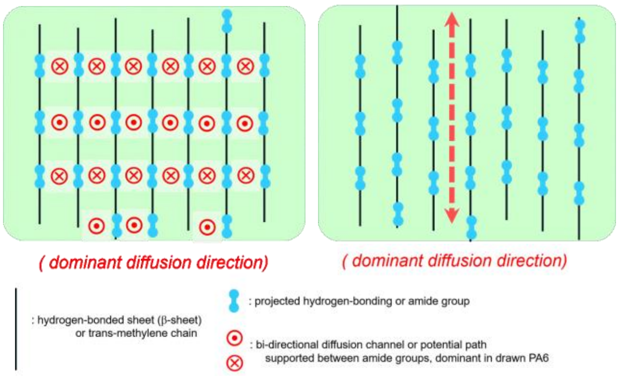

RESULTS AND DISCUSSION: After "iodine doping", (1) "non-oriented PA6" without chain orientation by stretching showed formation of chain axis normal to filmy surface of the sample. On the other hand, (2) "doubly oriented PA6" with chain orientation (c-axis of PA6 α-crystal) by stretching showed both "parallel orientation (to film surface)" of bc-plane of the crystal and "normal orientation (to film surface)" of the bc-plane while chain orientation (c-axis) was maintained before and after doping.[3] These results indicate that dynamic modification of chain orientation and crystalline axes (or maintenance for some of them) advance on iodine doping for PA6, but that not only diffusion of Poly-Iod. into matrices but their coordination with host polymer are implemented in structure anisotropy.

Then, "modified orientation" reported previously should also be explained by such dynamism; hypothesized "dynamic amphiphilicity" which guarantees self-organization can explain both diffusion and coordination of Poly-Iod.'s normal and parallel to chain axis. While driving force originated "iodine bonding" enables normal orientation of chains (Fig; right) to non-oriented sample surface, it performs normal and bi-directional diffusion normal to chains in doubly oriented sample. (Fig; left) Such scheme may suggest that diffusion of Poly-Iod.'s and charge conjugation along them are constructed both parallel and normal to chain axis as self-organized (modified) structure.[4]

REFERENCES:

[1] T.J. Marks & D.W. Kalina, "Extended Linear Chain Compounds" vol.1 ch.6., ed. J.S. Miller (Plenum Press, 1982).
[2] H. Arimoto, J. Polym. Sci. A, **3** (1964), 2283-2295.
[3] A. Kawaguchi, Polymer, **35** (1994) 3797-3798.
[4] A. Kawaguchi, Polym. Prep. Jpn., **71** (2022) 1J-20.

R6063

CO4-7

Research and Develop of M/HEA as Structure Materials For Nuclear Reactor

N. Hashimoto, K. Saito[1], H. Oka

Department of Materials Science and Engineering, Hokkaido University, Sapporo 060-8628
[1]Graduate Student, Graduate School of Engineering, Hokkaido University, Sapporo 060-8628

INTRODUCTION: To investigate the effect of compositional complexity on the microstructural evolution, the face-centered cubic (fcc) Medium Entropy Aloys were electropolished, and thin-foil samples were prepared for in-situ electron irradiation experiments at Hokkaido University. Electron-irradiated bulk samples were also prepared at the Institute for Integrated Radiation and Nuclear Science, Kyoto University, for the positron annihilation spectroscopy (PAS) at the International Research Center for Nuclear Materials of the Institute of Materials Research (IMR), Tohoku University. (MEAs), CrFeNiMn-type HEAs and a CrFeNi ternary alloy, were subjected to e^- irradiation.

EXPERIMENTS: $Cr_{0.8}FeMn_xNi$ (x = 0.4, 1.0, 1.5) alloys and CrFeNi were prepared by arc-melting and subjected to homogenization heat treatment (1160℃, 24h), cold-rolling (90%), and recrystallization heat treatment (1000℃, 4h) to prepare the test materials. Electrolytic polishing was used to prepare thin films for electron microscope observation, and the formation and growth process of dislocation loops were observed by electron beam irradiation experiments using a high-voltage electron microscope. The growth rate of the obtained dislocation loops and the supersaturation number density were organized as a function of temperature to measure the vacancy and interstitial migration energy. Additionally, after e^- beam irradiation of the bulk samples, positron annihilation measurements were performed to calculate the migration energy of atomic vacancies.

RESULTS: The migration energy of vacancies can be determined by measuring the lifetime of positrons introduced into an alloy (positron lifetime method). The vacancy concentration in an alloy is calculated by measuring the time it takes for a positron to be captured by an electron and annihilated, taking advantage of the property that the electron density is relatively low around the vacancies. In this study, the change in the residual vacancy ratio in an annealed sample was experimentally investigated, and the vacancy migration energy was selected so that the calculated value (by means of the equation as bilow) of the residual vacancy ratio was most consistent.
First, the positron lifetimes of the unirradiated and irradiated alloys were 106.7±0.5 (ps) and 146.1±0.2 (ps), respectively, confirming that atomic vacancies were introduced into the alloy by electron beam irradiation. Fig. 1 shows the annealing temperature dependence on positron lifetime in CrFeNi and $Cr_{0.8}FeMnNi$. In this experiment, the migration energies of vacancies in CrFeNi and $Cr_{0.8}FeMnNi$ were similar, suggesting that there was no significant change in the microstructural change due to irradiation damage. This result differs from the findings obtained from a separate in-situ electron beam irradiation experiment, and it was confirmed once again that it is not easy to calculate the vacancy migration energy by experiment. Furthermore, previous research has shown that the mobility of point defects is strongly affected by the impurity concentration in the alloy, reaffirming the need for further precise experiments in the future.

ACKOWLEDGEMENT: This study was supported by the Institute of Integrated Radiation and Nuclear Science, Kyoto University, for the electron irradiation experiment and the Institute for Materials Research, Tohoku University for the positron lifetime measurement experiment.

REFERENCES: [1] Z. Zhang *et al.* Progress in Materials Science 123, (2022), 100807.
[2] Dusadi., Computational Materials Science 237, (2024), 112912.

R6073

CO4-8

Neutron shielding and activation characteristics of novel iron oxide ceramics

H. Terato, and Y. Sakurai[1]

Advanced Science Research Center, Okayama University
[1]Institute for Integrated Radiation and Nuclear Science, Kyoto University

INTRODUCTION: Shielding is an essential procedure in the handling of ionizing radiation and radioisotopes. Shielding materials must be appropriately selected based on the type and energy of the radiation. Lead blocks are commonly used to shield gamma rays and X-rays; however, due to the toxicity of lead, there is a global trend toward avoiding its use. We have developed a novel iron oxide-based ceramic and evaluated its gamma-ray shielding capability, demonstrating its potential as a gamma-ray shielding material [1]. Furthermore, shielding materials used in reactor and accelerator facilities must also be evaluated for their effectiveness against neutrons and their activation characteristics. In this study, we evaluate the neutron shielding performance and activation behavior of the developed material using reactor neutrons. Additionally, we assess the generation of secondary gamma rays (prompt gamma rays) induced by neutron irradiation.

EXPERIMENTS: The neutron shielding effectiveness was evaluated using the carrying system of Heavy Water Neutron Irradiation Facility (HWNIF). The shielding performance of iron oxide ceramics with varying thicknesses was assessed using activation foils, such as gold foils. In this experiment, samples measuring 10 cm × 10 cm with a thickness of 1 cm were prepared and used in stacked configuration. The experiment was conducted at 1 MW for approximately 3 hours. To evaluate the activation characteristics, additional experiments were performed using the rail system of HWNIF. Iron oxide ceramic samples measuring 2 cm × 2 cm with a thickness of 1 cm were irradiated for approximately 5 or 50 minutes, and their activation was analyzed using an HPGe semiconductor detector. The experiment was also conducted at 1 MW for about 3 hours. To investigate the characteristics of prompt gamma-ray generation, experiments were conducted using the prompt gamma-ray analysis (PGA) system installed in Neutron Guide Tube (E-3). Iron oxide ceramic samples measuring 2 cm × 2 cm with a thickness of 1 cm were used, and the experiment was carried out at 1 MW for approximately 5 hours. In all experiments, control tests were also performed using iron and lead samples of the same dimensions as the iron oxide ceramics for comparison.

RESULTS: The thermal neutron shielding performance of the iron oxide ceramics was found to be intermediate between that of lead and iron, while the shielding performance against epithermal neutrons was closer to that of lead than to iron. In other words, the material demonstrated better neutron shielding than lead but was inferior to iron. As the gamma-ray shielding ability of ceramics and iron is generally proportional to their densities, similar results were observed in this aspect. Therefore, within the required shielding performance range, the ceramics are expected to offer a weight-reduction advantage. The characteristics of secondary gamma-ray generation in the ceramics were found to be nearly equivalent to those of iron. For thermal neutrons, the observed values were more than an order of magnitude higher than those of lead, mainly due to the (n,γ) reactions of iron. Regarding activation, the induced radioactivity ratio was approximately iron : ceramics : lead = 20 : 1 : 0.00003. This is primarily attributed to the generation of Mn-56 from iron. These results indicate that while the ceramics possess a certain level of neutron shielding capability, additional measures are required to address issues related to secondary gamma-ray generation and activation.

REFERENCES:

[1] M. Isobe *et al.,* Radiat. Safety Management, **22** (2023) 1-6.

R6081

CO4-9

Radiation Properties of Wide-bandgap Semiconductor Sensors for High-Energy Physics Experiments

T. Kishishita, H. Yashima[1], Y. Sakurai[1], R. Kosugi[2], T. Nakano[3,4], R. Kudo[4], T. Sakurai[4], Y. Hashimoto[4]

High Energy Accelerator Research Organization, KEK
[1] *Institute for Integrated Radiation and Nuclear Science, Kyoto University*
[2] *National Institute of Advanced Industrial Science and Technology*
[3] *Department of Electronics and Materials Science, Shizuoka University*
[4] *Research Institute of Electronics, Shizuoka University*

INTRODUCTION: Wide-bandgap semiconductor sensors have been considered as a potential alternative to Si for the manufacture of dosimeters, spectrometers, and charge particle detectors in high energy physics experiments, by virtue of its operation capability in strong radiation and/or high-temperature environments. To take advantage of such properties for future radiation detectors with a comparable size of silicon, we investigated two different semiconductor materials, SiC and BGaN this year. This study focuses on the influence of the SiC's bulk defects on the radiation sensor characteristics under the reverse-bias condition and neutron-detectability with BGaN sensors, by irradiating neutrons at Institute for Integrated Radiation and Nuclear Science, Kyoto University.

EXPERIMENTS: The reverse blocking characteristics and leakage current characteristic are primary concerns of the radiation effects on SiC. On the other hand, BGaN, a mixed semiconductor of GaN and BN, is expected to be a novel neutron detection material because it contains boron (B), a neutron-capturing element, as a semiconductor constituent. Therefore, we conducted different measurements with each sensor. As for the SiC sensor, we irradiated fast neutrons to SiC pn-diodes under the bias condition of 1 kV [1]. Fig. 1 shows the photograph of the measurement setup. We installed two SiC sensors at the front of the rail-instrument. After the 1MW operation, we carried out measurements of the leakage current and compared with those of the pre-irradiation samples. As for the BGaN, the sensor signals have been taken during the irradiation by external DAQ system and signal amplitudes and rise times were evaluated in off-line. The irradiation tests were both conducted at KUR.

RESULTS: The typical I-V characteristics of SiC sensors before and after irradiation showed similar characteristics, and we did not observe any degradation in leakage currents after the irradiation of 1E+12 n_{eq}/cm^2 fluence. The reverse blocking property was also retained up to 1 kV, which is required for full depletion of the SiC devices. We also conducted the Slant-irradation test for 4 hours for higher fluence, however, the device was heavily radio-activated, and thus, we could not measure the I-V characteristics. According to those results, we are currently developing a prototype muon beam monitor for the COMET experiment. The preliminary result was published in Ref. [1]. We will cotinue the measurement in 2025. As for the BGaN sensors, neutron-detectability was confirmed with sufficient event rates.

REFERENCES:

[1] T. Kishishita *et al.,* “Prototype of SiC beam monitor for the COMET experiment at J-PARC”, JINST 20 (2025) C02016.
[2] K. K. Lee *et al.,* Nucl. Instrum. Methods Phys. Res. B, **210** (2003) 489-494,

Fig. 1. Photograph of the measurement setup.

CO4-10

Influence of Hydrogen Isotopes on Growth of Vacancy Clusters in Tungsten-Based Materials

Y. Hatano, E. Taguchi, A. Matsumoto, K. Fukuda[1], T. Takahashi[2], N. Abe[2] and A. Kinomura[2]

Graduate School of Engineering, Tohoku University
[1]Guraduate School of Science and Engineering, University of Toyama
[2]Institute for Integrated Radiation and Nuclear Science, Kyoto University

INTRODUCTION: As a plasma-facing material of a fusion reactor, tungsten (W) will be exposed to fuel particles, deuterium (D) and tritium (T), and products of fusion reactions, helium and 14 MeV neutrons. Vacancies and vacancy clusters formed by neutron irradiation act as strong traps against hydrogen isotopes and increase T inventory in W [1]. Understanding of vacancy formation and clustering is necessary for accurate evaluation of T inventory in a vacuum vessel of a fusion reactor. Displacements by neutrons occur under exposure to hydrogen isotope plasma, and hence hydrogen isotopes may affect the growth and decomposition of vacancy clusters.

The objective of this study is to investigate the influence of hydrogen isotopes on behaviors of vacancy and vacancy clusters to construct a kinetic model of clustering and annihilation. To reach this goal, W samples with monovacancies and vacancy clusters are prepared by electron beam irradiation. Then, the irradiated samples are heated with and without hydrogen isotopes, and the difference in size distributions of vacancy clusters is examined using positron annihilation spectroscopy.

****

EXPERIMENTS: Disk samples of W were irradiated with 8 MeV electrons using KURNS-LINAC to 10^{-3} displacement per atom (dpa). A part of irradiated samples was exposed to D atoms at 200 ℃ to introduce D atoms and then heated under D_2 gas atmosphere at 0.1 MPa and 400 ℃ for 20–40 h. The other part of samples without D atoms were also heated at 400 ℃ for 20–40 h in vacuum. Positron lifetime was measured by using ^{22}Na source at Institute for Materials Research, Tohoku University [1].

****

RESULTS: The positron lifetime was 143 ps before the irradiation. As summarized in Fig. 1, the electron beam irradiation resulted in the generation of long-life components around 363 ps which is attributable to the formation of vacancy cluster [2].

The exposure to D atoms reduced the long-life component to 329 ps. This is because each trapped D atom brought 1 electron into a vacancy cluster. Subsequent annealing at 400 ℃ in vacuum led to shorter in long-life component. This observation can be ascribed to reduction in vacancy cluster size due to decomposition. The sample annealed under the presence of D atoms systematically showed larger values of long-life component than that annealed in vacuum. These observations suggest that D atoms hindered the decomposition of vacancy clusters.

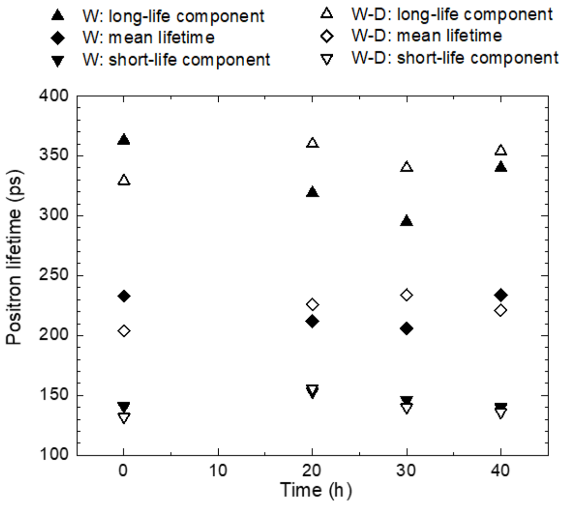

Fig. 1. Positron lifetime of electron irradiated W after annealing at 400 °C with and without deuterium (D).

****

REFERENCES:

[1] T. Toyama *et al.,* J. Nucl. Mater., **499** (2018) 464.
[2] T. Troev *et al.,* Nucl, Instr. Meth. B, **267** (2009) 535.

R6085

CO4-11

Structural Response of Guar-gum Hydrogels to Temperature via Small Angle X-ray Scattering

T. Tominaga, R. Inoue[1], and M. Sugiyama[1]

Neutron Science and Technology Center, Comprehensive Research Organization for Science and Society (CROSS)
[1]Institute for Integrated Radiation and Nuclear Science, Kyoto University

INTRODUCTION: Soft matter is characterized by its ability to undergo large deformation. A hydrogel is a soft material capable of extensive deformation [1]. Furthermore, additives can either enhance or inhibit its mechanical properties of the hydrogels. Guar-gum (GG) hydrogels can achieve significantly greater deformation when proper amounts of borax (cross-linker, Bx), glycerin (Gly), and vinyl acetate resin particles (Bd) are added, compared to GG gels containing only borax.
Previous small-angle X-ray scattering (SAXS) analysis of the hydrogels prepared from GG with the incorporation of Bx, Gly, and particles revealed that Gly mainly contributed to the structural homogenization, whereas Bx and Bd induced the structural inhomogeneity [2]. Structural changes during the elongation process of slime could not be evaluated due to extremely rapid relaxation. In this study, the influence of individual additives on temperature-dependent behavior was assessed through measurement of thermal responses in the internal structure of the hydrogel specimens utilizing SAXS.

EXPERIMENTS: GG hydrogels were synthesized with the following weight ratios: GG (2–3 wt.%), Gly (7 mL), Bx (0.4 g), Bd (2–3 g), and water (88 g). The samples were sandwiched between polyetherimide film (0.5 mm, Sperio, Mitsubishi, Japan). Cu-SAXS (RIGAKU Nanopix) in high-resolution mode was conducted at the Institute for Integrated Radiation and Nuclear Science, Kyoto University. The sample temperature was varied from 15–55°C using a Peltier temperature control system. The empty cell correction was applied to account for transmission, and the scattering profile, I(Q), was obtained via circular averaging.

RESULTS: SAXS profiles of GG hydrogels are shown in Figure 1. The top panel represents GG + Bx + Bd, while the bottom shows GG + Gly + Bx + Bd. Without Gly, high Q scattering intensity increased with temperature, whereas with Gly, the slope at $Q < 0.1$ Å^{-1} decreased, showing the suppression of temperature dependency of hydrogel.
Bx forms cross-links, introducing structural irregularities, while Gly reduces heterogeneity by enhancing fluidity near GG chains. The internal structures at $Q < 0.02$ Å^{-1} depend on resin on the other hand, it remains stable regardless of temperature change. Because Gly and Bx affect the opposing structural features, their ratio, distribution relative to GG, and respective functions could tend to contribute significantly to the slime's mechanical properties.
We plan to analyze the data with and without other additives and combine them in an original paper.

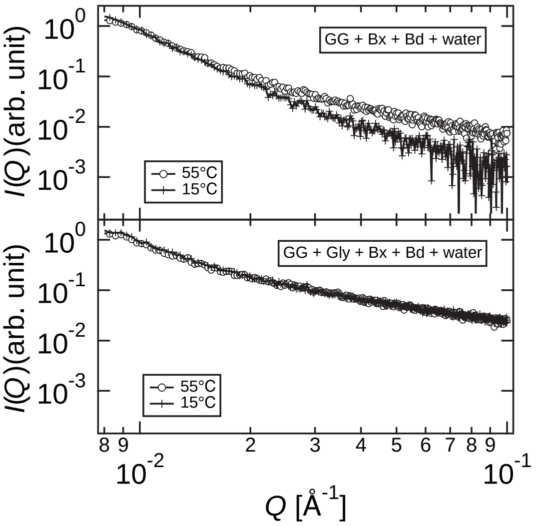

Fig. 1. Temperature dependence of SAXS profiles of GG + Bx + Bd + water hydrogel (top) and, GG + Gly + Bx + Bd + water hydrogel (bottom).

REFERENCES:

[1] T. Kanaya *et al.,* Polymer Journal, **44** (2012) 83–94.
[2] T. Tominaga *et al.,* KURNS Progress Report 2022, CO4-14 (2022) 105.

R6086

CO4-12

Thermal Behavior of Vacancies and Absorbed Hydrogen Atoms in Palladium Metal

W. Sato, M. Furumoto[1], Y. Shimizu[1], H. Shimizu[2], Y. Ohkubo[3] and A. Taniguchi[3]

Institute of Science and Engineering, Kanazawa University
[1]Graduate School of Natural Science and Technology, Kanazawa University
[2]Nishina Center for Accelerator-Based Science, RIKEN
[3]Institute for Integrated Radiation and Nuclear Science, Kyoto University

INTRODUCTION: Palladium (Pd) can occlude a large amount of hydrogen in the lattice interstitial sites; thus the metal is expected to be applied in industry as hydrogen storage material. However, the occlusion of hydrogen is likely to induce the formation of lattice defects, which causes the deterioration of its storage performance. Such a problem could be an obstacle to its practi-cal uses. In order to realize high performance of hydrogen occlusion in Pd, therefore, it is im-portant to understand the characteristics of the hydrogen-induced lattice defects as well as the ther-mal behavior of hydrogen impurities themselves in Pd [1]. In the present work, we have obtained atomic level information on those defects using two different nuclear spectroscopic techniques: positron annihilation lifetime spectroscopy (PALS) and perturbed angular correlation (PAC) spectroscopy.

EXPERIMENTS: A commercially available Pd plate of a purity of 99.95% was irradiated with thermal neutrons in the research reactor of Kyoto University (KUR) to produce the ^{111}Cd(←^{111}Ag←^{111}m, ^{111}Pd) probe, and TDPAC measurements were performed by the detection of the 97-245 keV cascade γ rays with the intermediate level of I = 5/2 having a half life of 85.0 ns. Apart from the PAC experiment, PALS measurements with a positron source of ^{22}Na were performed for a pristine and hydrogen-absorbed/desorbed Pd at room temperature. The PALS spectra were analyzed with a fitting program PALSfit [2]. For the absorption of hydrogen atoms into Pd lattice, we adopted an electrochemical method [3].

RESULTS: PALS measurements disclosed the effect of hydrogen occlusion on the local structure in the Pd lattice, suggesting the formation of dislocation and open-volume defects. It was also found that heat-treatments at 383 K thoroughly evacuate the absorbed hydrogen from the lattice of Pd. PAC spectroscopy with the ^{111}Cd probe revealed temperature-dependent dynamic behavior of hydrogen atoms as shown by the exponential relaxation of the PAC spectra in Fig. 1, and the spectral analyses have shown that the activation energy of their thermal motion is 47(3) meV.

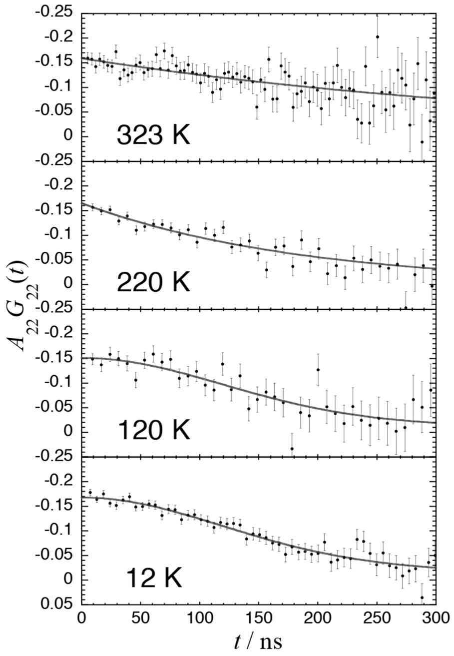

Fig. 1. Temperature-dependent TDPAC spectra of the ^{111}Cd(←^{111}Ag←$^{111m,\ 111}$Pd) probe in a hydrogen-absorbed Pd plate.

REFERENCES:

[1] M. Mihara *et al.,* JPS Conf. Proc., **21** (2018) 011031.
[2] J. V. Olsen *et al.,* Phys. Status Solidi C, **4** (2007) 4004-4006.
[3] W. Sato *et al.,* J. Appl. Phys., **135** (2024) 245103.

R6089

CO4-13

Investigation of Temperature-Dependent Cd Dopant Sites in $Cd_{0.2}Sr_{0.8}TiO_3$ Studied by TDPAC Spectroscopy

S. Komatsuda, W. Sato[1], A. Taniguchi[2], M. Tanigaki[2], and Y. Ohkubo[2]

Institute of Human and Social Sciences, Kanazawa University
[1]*Institute of Science and Engineering, Kanazawa University*
[2]*Institute for Integrated Radiation and Nuclear Science, Kyoto University*

INTRODUCTION: $SrTiO_3$ is one of the most promising candidates for photocatalytic materials. It is known that trivalent cation doping at the Ti^{4+} site is one of the effective methods to improve photocatalytic activity. According to our previous research, it was suggested that the doped In contributed to the improvement of the photocatalytic activity by substituting Ti[1]. Furthermore, it was found from our other experiments that Cd^{2+} occupies the same Ti^{4+} site as In^{3+} in $Cd_xSr_{1-x}TiO_3$ perovskite structure at high Cd concentrations ($0.06 \leqq x \leqq 0.20$). For a practical use of $Cd_xSr_{1-x}TiO_3$, it is necessary to obtain microscopic information on impurity sites at various temperatures. Therefore, for the microscopic study of the local fields at Cd sites, the TDPAC measurements were performed for $^{111}Cd(\leftarrow{}^{111m}Cd)$ in $Cd_{0.2}Sr_{0.80}TiO_3$ at room temperature and at 500 K.

EXPERIMENTS: Stoichiometric amount of $SrCO_3$, $CdCO_3$, and TiO_2 powders was mixed in a mortar. The powders were pressed into disks. For TDPAC measurements, about 3 mg of CdO enriched with ^{110}Cd was irradiated with thermal neutrons at Kyoto University Research Reactor, and radioactive ^{111m}Cd was generated by the $^{110}Cd(n, \gamma)^{111m}Cd$ reaction. The neutron-irradiated CdO powder was dissolved in 6M HCl and added in droplets onto the pre-sintered $Cd_{0.2}Sr_{0.80}TiO_3$ disk. The disk was sintered in air at 1373 K for 90 min. TDPAC measurements were carried out for the 151-245 keV cascade γ rays of $^{111}Cd(\leftarrow{}^{111m}Cd)$ probe with the intermediate state of $I = 5/2$ having a half-life of 85.0 ns.

RESULTS: Figure 1 shows the TDPAC spectra of the $^{111}Cd(\leftarrow{}^{111m}Cd)$ probe embedded in $Cd_{0.2}Sr_{0.80}TiO_3$ at room temperature and at 500 K. From the fitting parameters of TDPAC spectra in Fig. 1, spectral patterns can be reproduced by a fit with unique quadrupole frequencies. It is suggested from our previous study that Cd dopants replace Ti^{4+} in the lattice sites where defect exists in the vicinity of the Cd probes[1]. The value of the electric quadrupole frequency decreased slightly at 500 K, suggesting that the lattice expanded at 500 K. No other significant differences were observed in the spectra of the two, which suggests that the local structure around Cd remains stable at high temperatures. For more information on temperature dependence, TDPAC measurements of $Cd_xSr_{1-x}TiO_3$ perovskite at 500~100 K are now in progress.

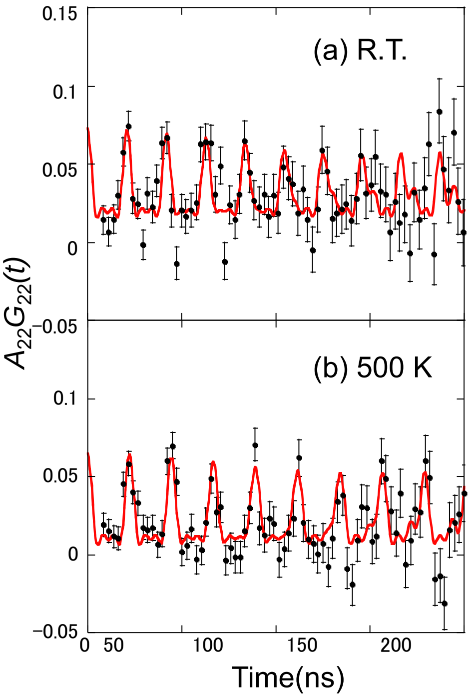

Fig. 1. TDPAC spectra of $^{111}Cd(\leftarrow{}^{111m}Cd)$ in $Cd_{0.2}Sr_{0.80}TiO_3$ (a) at room temperatures and (b) at 500 K.

REFERENCES:

[1] S. Komatsuda *et al.*, Interactions, **245** (2024) 37.

R6101

CO4-14

Investigation of the Dynamics of Rigid Helical Polymers via Small-Angle X-Ray Scattering, Dynamic Light Scattering, and Molecular Dynamics Simulations

Y. Nagata[1], M. Sugiyama[2], R. Inoue[2], N. Sato[2], and K. Morishima[2]

[1] *Institute for Chemical Reaction Design and Discovery, Hokkaido University*
[2]*Institute for Integrated Radiation and Nuclear Science, Kyoto University*

INTRODUCTION: Poly(quinoxaline-2,3-diyl)s (PQXs) represent a novel macromolecular scaffold that exhibits solvent-induced switching of helical chirality. For instance, a 100-mer PQX bearing (R)-2-octyloxymethyl side chains (**2oct**) adopts distinct helical conformations: a right-handed (P-helical) structure in tetrahydrofuran (THF) and a left-handed (M-helical) structure in a 4:1 (v/v) mixture of 1,1,2-trichloroethane (1,1,2-TCE) and THF. [1]

To elucidate the mechanism underlying the solvent-dependent helix inversion of **2oct**, both experimental and theoretical investigations have been conducted. Small-angle neutron scattering (SANS) studies revealed differences in the spatial arrangement of the side chains relative to the main chain in THF-d_8 and 1,1,2-TCE-d_3/THF-d_8. [2] Furthermore, quasielastic neutron scattering (QENS) directly probed the side-chain dynamics of **2oct** in these solvents. By combining QENS results with molecular dynamics (MD) simulations, a coupling between main-chain and side-chain dynamics was uncovered, suggesting that differences in side-chain mobility may drive the switching of helical chirality. [3]

Remarkably, solvent-dependent helix inversion has also been observed in PQXs dissolved in simple saturated hydrocarbon solvents. A PQX bearing (S)-3-octyloxymethyl side chains demonstrates a pronounced solvent effect, undergoing helix inversion from an M-helical structure in n-octane to a P-helical structure in cyclooctane. The efficiency of this solvent effect, induced purely by switching between alkane solvents, is particularly noteworthy. [4]

Despite these compelling observations, the precise molecular mechanism underlying helix inversion in the 3-octyloxymethyl-substituted PQX induced by alkane solvents remains poorly understood. In the present study, we are trying a comprehensive investigation of the solvent-dependent helix inversion of a 100-mer PQX bearing (S)-3-octyloxymethyl side chains (**3oct**) in n-octane and cyclooctane. By performing SAXS, DLS, SANS and QENS experiments in conjunction with improved MD simulations.

EXPERIMENTS & RESULTS: Prior to the experimental investigations, molecular models of **3oct** were constructed using computational chemistry. Initially, the structures of the repeating monomeric units, comprising two conformational isomers (δ-monomer and λ-monomer), were optimized using the Forcite optimizer in BIOVIA Materials Studio 2024 with the COMPASS III force field at the ultra-fine level. Based on these optimized monomers, right-handed and left-handed 100-mer helical structures (P-δ-**3oct**, M-δ-**3oct**, P-λ-**3oct**, and M-λ-**3oct**) were constructed and further optimized. Currently, molecular dynamics (MD) simulations are being performed on each of these models under varying temperature conditions, and the results will be compared with those obtained from quantum beam scattering experiments.

REFERENCES:

(1) Nagata Y. *et al.,* J. Am. Chem. Soc., **135** (2013) 10104-10113.
(2) Nagata Y. *et al.,* J. Am. Chem. Soc., **140** (2018) 2722-2726.
(3) Inoue R. *et al.,* J. Chem. Phys., **161** (2024) 054905.
(4) Nagata Y. *et al.,* J. Am. Chem. Soc., **136** (2014)15901-15904.

CO4-15

Magnetic Measurements of Irons in Soda-lime Glass by Mössbauer Spectroscopy (3

K. Okada, and Y. Kobayashi[1]

SPring-8/JASRI
[1]Graduate School of Engineering, Kyoto University

INTRODUCTION: Glass is used in many applications in our every-day lives and has exciting new applications related to the energy. Soda-lime glass is made of mainly silica (SiO_2) and additive many other materials, such as magnesium, sodium, calcium, aluminum, iron, sulfur, and so on. Our reference glass composition, in percent by weight (wt%), was 72.25 SiO_2, 1.75 Al_2O_3, 4.00 MgO, 8.00 CaO, 14.00 Na_2O as basic components, and 0.015-5 iron in terms of Fe_2O_3 as coloring components. Iron contaminants of less than 0.0005-0.01 wt% from raw materials, and iron injection up to 1.5-5 wt%. We added compatible $CaCO_3$ and Na_2CO_3 as CaO and Na_2O, respectively. The iron oxides in a glass composition are thought to be present in forms of Fe^{3+} and Fe^{2+}. The control parameters for irons are two: (1) the total iron mass weight percent in terms of Fe_2O_3, and (2) the ratio of $Fe^{2+}$to total iron ions ($Fe^{2+}/\Sigma_n Fe$). The Fe^{3+} component adds a light yellow tint to the glass and absorption in the ultraviolet and visible band, while the Fe^{2+} component adds a blue tint to the glass and absorption in the near-infrared band (1 μm). The transmission from ultraviolet to infrared in glass cannot be explained by simple Fe^{2+} and Fe^{3+} structures. Then, to reveal the exact local structures of irons (Fe^{2+} and Fe^{3+}) is necessary. Many scientists proposed many new theories and local structures [1-2], but they did not resolve it completely.

We have prepared reference glass samples with using the Mössbauer isotope ^{57}Fe (natural abundance is about 2.119 %) for measurements. The chemical composition of iron oxide in the ^{57}Fe enrichment glass was from 0.015 to 5 wt%, and the $Fe^{2+}/\Sigma_n Fe$ was from 0 to 0.6. We have investigated these samples by nuclear resonant inelastic scattering and XAFS methods at synchrotron radiation to reveal the local atomic structure around and neighboring iron atoms in sub-nanometer region [3].

EXPERIMENTS: We observed two samples with 0.2 $Fe^{2+}/\Sigma_n Fe$ and 0.6 $Fe^{2+}/\Sigma_n Fe$ of 0.5 wt% alpha-Fe_2O_3. The measurements were performed using conventional Mössbauer spectrometer at 297, 370, and 450 K. The specimens for Mössbauer measurements were tuned to 10 mm-phi pellet.

RESULTS: There were no difference between the three temperatures data with 0.2 $Fe^{2+}/\Sigma_n Fe$ and 0.6 $Fe^{2+}/\Sigma_n Fe$ of 0.5 wt% alpha-Fe_2O_3 as shown in Fig. 1.

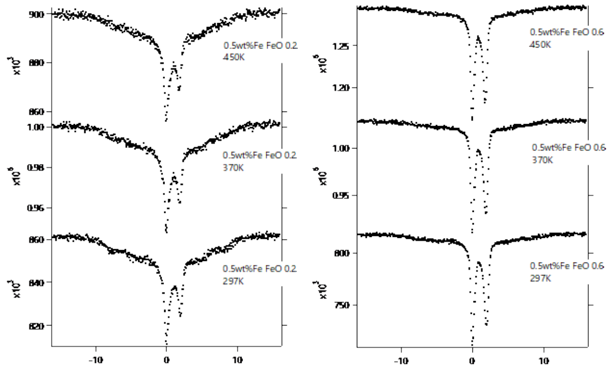

Fig. 1. Mössbauer spectra of the glass with 0.2 $Fe^{2+}/\Sigma_n Fe$ and 0.6 $Fe^{2+}/\Sigma_n Fe$ of 0.5 wt% alpha-Fe_2O_3. The measurements were performed at 297 K, 370 K, and 450 K.

REFERENCES:

[1] C. Ruessel *et al.,* Phys. Chem. Glasses, **47** (2006) 563.
[2] F. Farges *et al.,* Physica Scripta, **T115** (2005) 957.
[3] K. Okada *et al.,* X-ray Spectrometry, **47** (2018) 359-371.

R6105

CO4-16

Study on Resonant Frequency Change of Piezoelectric PZT with Radiation Irradiation

S. Takechi, S. Katayama, M. Okumoto[1], K. Nagasawa[1], S. Yamauchi[1], M. Kobayashi[2], T. Miyachi[2]

Graduate School of Engineering, Osaka Metropolitan University
[1]Department of Engineering, Osaka City University
[2]Planetary Exploration Research Center, Chiba Institute of Technology

INTRODUCTION: As a novel application of piezoelectric elements, we are exploring their use for radiation measurement. A key performance index of a piezoelectric element is the electromechanical coupling coefficient (*k*), which can be estimated from its resonance and anti-resonance frequencies. We found that the *k* value of a lead zirconate titanate (PZT) element, a type of piezoelectric material, changes when exposed to a 400 MeV/n Xe ion beam [1-3]. We are currently conducting electron beam irradiation experiments at the KURNS-LINAC to investigate how the *k* value of PZT elements changes under exposure to different types of radiation [4]. It is known that the *k* value of a PZT element decreases when the temperature exceeds a certain threshold. In FY2023, we investigated the changes in the *k* value of PZT element over several days under electron beam irradiation conditions, where the temperature was controlled to make the effects of temperature negligible. As a result, we found that the *k* value decreased monotonically with the cumulative dose of the 20 MeV electron beam and remained constant even after irradiation ceased [5].

EXPERIMENTS: The purpose of the experiment in FY2024 was to confirm the reproducibility of the experimental results obtained in FY2023 and to investigate the radioactivity of PZT due to irradiation. Experiments were conducted twice, in July and December 2024, each lasting three days, in which a PZT piezoelectric element was irradiated with an electron beam similar to that used in FY2023. The element is disk-shaped with a radius of 9 mm and a thickness of 1 mm, which was the same shape as in FY2023. The surface temperature of the PZT piezoelectric element during electron beam irradiation was monitored using a thermocouple. The electron beam irradiation time for each cycle was approximately 15 minutes. After the irradiation was stopped, the surface temperature of the PZT element was confirmed to be approximately at room temperature, and then the frequency-impedance characteristics of the element were measured. These measurements were performed 4 to 8 times per day. In the December experiment, after the frequency-impedance characteristics of the element had been measured, the radioactivity of the PZT piezoelectric element was measured for 10 minutes using an anti-Compton Ge detector.

RESULTS: After irradiating a PZT piezoelectric element with an electron beam for three days, we confirmed that the *k* value decreased monotonically with the increasing cumulative irradiation dose and that this decrease was sustained even after irradiation ceased. Gamma-ray measurements of the PZT piezoelectric element after electron beam irradiation, conducted using an anti-Compton Ge detector, revealed that the radioactive nuclides Pb-203 and Zr-89, which are isotopes of Pb and Zr—key constituent elements of PZT—were generated.

REFERENCES:

[1] M. Kobayashi *et al.*, Jpn. J. Appl. Phys., **52** (2013) 126604.
[2] M. Kobayashi *et al.*, Jpn. J. Appl. Phys., **53** (2014) 066602.
[3] S. Takechi *et al.*, Jpn. J. Appl. Phys., **60** (2021) 038003.
[4] S. Takechi *et al.*, Jpn. J. Appl. Phys., **61** (2022) 128001.
[5] S. Takechi *et al.*, Jpn. J. Appl. Phys., **63** (2024) 078002.

R6110

CO4-17

Positron Lifetime of β-FeSi$_2$ Film Probed by a Short-Pulsed Slow Positron Beam

A. Yabuuchi

Institute for Integrated Radiation and Nuclear Science, Kyoto University

INTRODUCTION: β-FeSi$_2$ is expected to be an environmentally friendly infrared light-emitting material. However, further enhancement of luminescence intensity is desired for practical applications. The Doppler broadening of annihilation radiation measurements using the KUR slow positron beam suggested that Al doping, which has been reported to enhance luminescence intensity, promotes the formation of Fe vacancies. In this study, positron annihilation lifetime measurements using the KUR slow positron beam were performed to investigate the size of atomic vacancies in β-FeSi$_2$ thin film.

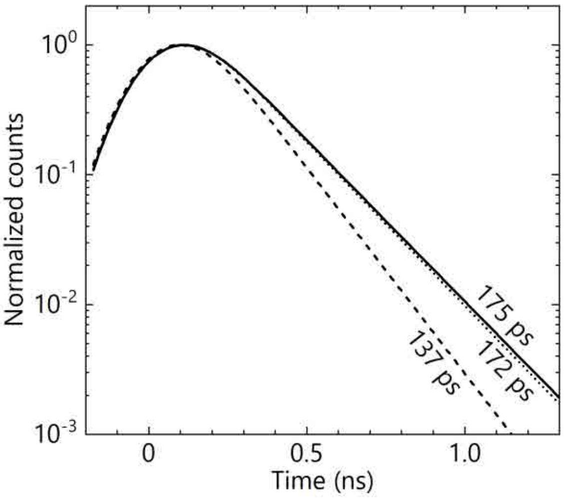

Fig. 1. Simulated positron annihilation lifetime spectra showing positron lifetimes of 137 ps.

EXPERIMENTS: A polycrystalline β-FeSi$_2$ film was fabricated on a Si substrate using the ion beam synthesis method. The positron annihilation lifetime of the film was measured using the KUR short-pulsed slow positron beam. The incident positron energy was determined to be 2 keV to probe the film region. In addition, yttria-stabilized zirconia (YSZ) single crystal, whose positron lifetime is well known [1], was also measured as a reference. The positron lifetime spectra obtained from the measurements were compared with simulated spectra based on the calculated positron lifetimes for β-FeSi$_2$ that have been reported [2].

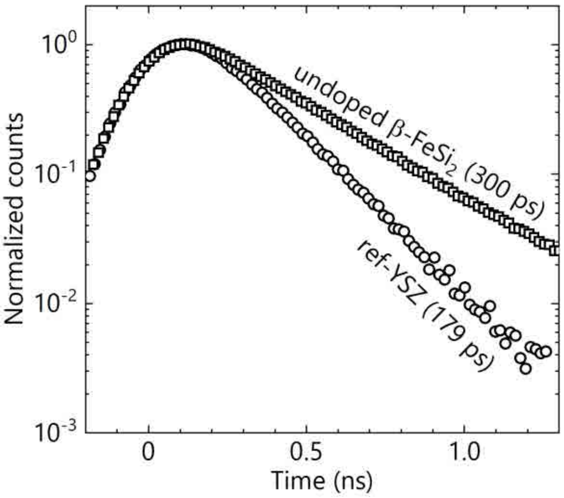

Fig2. Measured positron annihilation lifetime spectra of reference YSZ and the β-FeSi film.

RESULTS: The calculated positron lifetimes for defect-free β-FeSi$_2$ crystal, Fe monovacancy, and Si monovacancy have been reported as 137 ps, 172 ps, and 175 ps, respectively [2]. Figure 1 shows simulated positron annihilation lifetime spectra corresponding to these positron lifetimes. Figure 2 shows the positron annihilation lifetime spectra obtained from measurements of the reference YSZ and undoped β-FeSi$_2$. The measured positron lifetime for YSZ (179 ps) agrees with the reported value [1]. On the other hand, a positron lifetime component of 300 ps is observed from the positron lifetime measurements of the β-FeSi$_2$ film. This suggests the following possibilities: (i) vacancy clusters larger than monovacancies exist, or (ii) positrons are trapped at grain boundaries rather than within grains. Additionally, the possibility of influence from positron annihilation in the surface oxide layer cannot be excluded, as hydrofluoric acid treatment for oxide layer removal was not performed before measurement in this study.

REFERENCES: [1] O. Melikhova *et al.,* J. Phys.: Conf. Ser. **674** (2016) 012016.

[2] M. Mizuno, and H. Araki (2015) Chemical Bonding, Point Defects and Positron Lifetimes in FeSi$_2$ from First-Principles Calculations. In: T. Ishii, H. Wakita, K. Ogasawara, YS. Kim (eds) The DV-Xα Molecular-Orbital Calculation Method. Springer, Cham.

R6112

CO4-18

TDPAC Measurement of ^{111}Cd(←^{111}In) in Ultrafine Bubble Water

K. Takeshita, M. Tanigaki[1], A. Taniguchi[1], Y. Ueda[2], Y. Tokuda[3], and Y. Ohkubo[1]

Graduate School of Science, Kyoto University
[1] Institute for Integrated Radiation and Nuclear Science, Kyoto University
[2]Research Institute for Sustainable Humanosphere, Kyoto University
[3]Faculty of Education, Shiga University

INTRODUCTION: Ultrafine bubbles, the gaseous cavities with diameters less than 1 μm, have recently attracted much attention because of their multi-functionalities [1]. Fundamental studies on such multi-functionalities of ultrafine bubbles are not well extended because they are smaller than the wavelength of radiant rays. Following the previous study [2], we continue investigating the interface of ultrafine bubbles by the time differential perturbed angular correlation (TDPAC) of ^{111}Cd(¬ ^{111}In) to investigate the essential origins of its multi-functionality. This time, the pH dependence of $A_{22}G_{22}(t)$ was investigated over a much broader pH range than in the previous study.

EXPERIMENTS: Typical four-counter TDPAC measurements were performed for the 171-245 keV cascade in ^{111}Cd(←^{111}In) in oxygen water and water with oxygen-ultrafine bubbles. The average diameter and the density of the ultrafine bubbles were 200 nm, respectively. The aqueous solution of $^{111}InCl_3$ at pH 2 from Nihon Medi-Physics was added to each sample and adjusted to pH 4, 7, 8.5, 10, and 13 by dilution with the respective solvent [2]. The angular correlation term $A_{22}G_{22}(t)$ is given by:

$$A_{!!}\ G_{!!}\ (t)=\frac{2(N(180°,t)-N(90°,t)0}{N(180°,t)+2N(90°,t)}$$

where N(90°, t) and N(180°, t) are the counting numbers at 90 and 180 degrees, respectively. The time-dependent term $G_{22}(t)$ for each sample was obtained by normalizing $A_{22}G_{22}(t)$ by the asymmetry parameter A_{22} of 171-245 keV cascade in ^{111}Cd.

RESULTS: Typically observed $A_{22}G_{22}(t)$ spectra for ^{111}Cd(←^{111}In) in oxygen ultrafine-bubble water and those in oxygen-saturated water are shown in Fig. 1. No significant difference was not found in the spectra of oxygen ultrafine-bubbles and oxygen-saturated water, and the spectra for pH 4, 7, 8.5 are consistent with those reported by Demille [3]. In the cases of pH 10 and 13, $A_{22}G_{22}(t)$ in both oxygen-saturated water and oxygen ultrafine bubble water show a characteristic pattern around 40 ns, suggesting the existence of a non-axial symmetric electric field gradient at In site, which could lead to new insights into the structure of In complex ions.

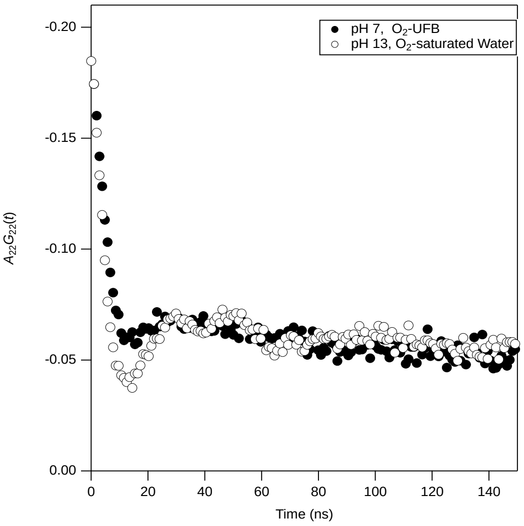

Fig. 1 Typical $A_{22}G_{22}(t)$ spectra of ^{111}Cd(←^{111}In) in oxygen ultrafine bubble water at pH 7 and in oxygen-saturated water at pH 13.

REFERENCES:

[1] E. G. Denis, “The fine bubble breakthrough,” ISO News, 2014. Available: https://www.iso.org/news/2014/05/Ref1844.html.
[2] M. Tanigaki *et al.,* KURNS Progress Report 2023 (2024) 130.
[3] G. R. Demille *et al.,* Chemical Physics Letters, **44** (1976)164–168.

CO4-19

Fundamental study of damage on tungsten by heat and particle loading

K. Tokunaga, S. Akamaru[1], M. Matsuyama[1], Y. Hatano[2], M. Hasegawa, K. Nakamura and Q. Xu[3]

Research Institute for Applied Mechanics, KyushuUniversity
[1]Hydrogen Isotope Research Center, University ofToyama
[2]School y ofEngineering, Tohoku University
[3]Institute for Integrated Radiation and Nuclear Science, Kyoto University

INTRODUCTION: It is of a great importance to clarify phenomena of implantation, retention, diffusion and permeation of tritium (T) on surface of the armor materials of the first wall/ blanket and the divertor on the fusion devices from a viewpoint of precise control of fuel particles, reduc-tion of tritium inventory and safe waste management of materials contaminated with tritium. In the present works, T exposure experiments have been carried out on tungsten (W) samples which were irradiated by high energy electrons and hydrogen beams to investigate effects of high energy elec-trons irradiation and high heat loading on microstructure and tritium retention of W. In this fiscal year, pure W were irradiated by repeated high energy negative hydrogen beams to investigate the effect of high heat loading of ELMs in fusion devises on T retention.

EXPERIMENTS: Stress relieved pure W (SR-W) has been exposed by multiple irradiations of a negative hydrogen ion beam with a energy of 3 MeV to investigate the influence of the repeated short pulse heat loading. After that, T exposure experiments on the exposed SR-W, non-irradiated SR-Ws and recrystallized W (RC-W) have been carried out using a T exposure device in University of Toyama. Pressure of the T gas was 1.3 kPa and T exposure was kept for 4 h at 100 ºC. T concen-tration in the gas was about 5 %. After the exposure to T gas, T amount retained in surface layers of the samples was evaluated by imaging plate (IP) measurements and γ-ray-induced X-ray spectrom-etry (BIXS).

RESULTS: As shown in Fig. 1, microstructures of pure Ws are elongated to the roiling direction. After recrystallization, grain coarsening is generated and its sizes are almost the same. Microstruc-ture near the surface of H$^-$ irradiated pure W changes to fine grains(B) and large grains (C) from rolling structure（A）as shown in Fig. 2. IP measurement after the T exposure indicates that T retention dependent on the microstructures as shown in Fig. 3. Distribution of T on cross section of the H$^-$ irradiated pure W is now investigating.

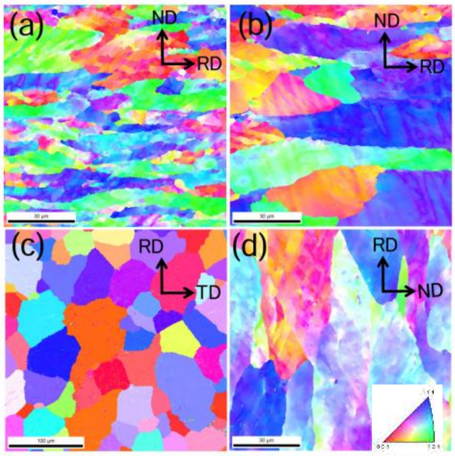

Fig. 1. IPF map (ND) (a)SR-W(PFW-672 TD), (b)SR-W(PFW-737 TD), (c)RC-W(ND), (d)SR-W(PFW-657-1 TD, H$^-$-irradiated)

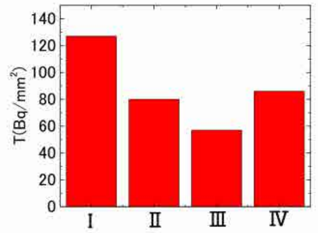

Fig. 3. Result of IP measure-ment Ⅰ, Ⅱ, Ⅲ and Ⅳ are (a), (b), (c) and (d) in Fig. 1

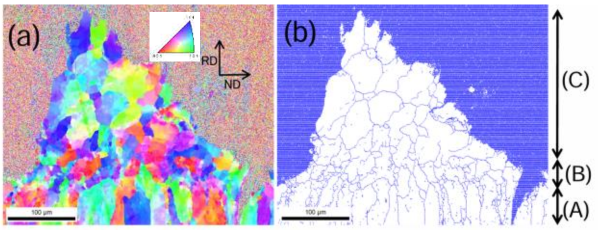

Fig. 2. Cross section near surface of H$^-$ irradi-ated SR-W, (a) IPF map (ND), (b) RA(15º-180º)

CO4-20

Positron annihilation coincidence Doppler broadening of chromium oxynitride epitaxial films on magnesium oxide substrates

M. Kitaura, T. Sumi, A. Kinomura[1], M. Ishizaki, S. Watanabe[2], T. Suzuki[3]

Faculty of Science, Yamagata University
[1]*Institute for Integrated Radiation and Nuclear Science, Kyoto University*
[2]*Inovative Technology Laboratories, AGC Inc.*
[3]*Faculty of Engineering, Nagaoka University of Technology*

INTRODUCTION: Chromium oxide epitaxial films grown on magnesium oxide substrates have the rock salt structure of a cubic system,as same as the chromium nitride [1]. The hardness of this material is superior to that of the chromium nitride which is used as a hard coating film [2] . The chemical composition is Cr_2O_3, the same as the corundum structure of a trigonal system, and is different from that of chromium nitride (CrN). The chromium oxide epitaxial film is thus regraded as a defective rock salt structure with chromium-poor composition. Stacking faults of rock salt and corundum structures were found in chromium oxide epitaxial films. They occurred in chromium oxynitride epitaxial films with oxygen contents greater than 33%. The introduction of oxygens and chromium vacancies seems to be correlated with the formation of stacking faults in chromium oxynitride epitaxial films. So far, we have measured positron annihilation lifetimes of undoped and 3% oxygen doped CrN epitaxial films and chromium oxynitride epitaxial film with the oxygen content of 33% ($CrN_{0.67}O_{0.33}$) [3]. In the former two, positrons annihilated at the sites of chromium monovacancy. In the latter, the positron annihilation lifetime was drastically changed compared to the former two, but it remained unclear where positron annihilation occurs predominantly. In the present study, we have investigated positron annihilation Doppler broadening of CrN and $CrN_{0.67}O_{0.33}$ epitaxial films.

EXPERIMENTS: The sample of undoped and 3%O doped CrN and $CrN_{0.67}O_{0.33}$ epitaxial films were grown on MgO substrates by a pulse laser deposition method ion. The thickness was nearly 400 nm. It was confirmed that they have a cubic structure of the rock-salt type [3]. CDB experiments were performed at the slow positron beam line in KUR. The incident energy of the slow positron beam was set to 6 keV. The γ-ray photons emitted due to positron-electron pair annihilation were accumulated over 3 million counts.

RESULTS: Figure 1 shows CDB spectra of CrN and $CrN_{0.67}O_{0.33}$ epitaxial films on Mg substrates, which were obtained at 300 K. The integrated areas of the CDB spectrum were normalized to unity. The CDB spectra are almost the same between CrN and $CrN_{0.67}O_{0.33}$. Detailed analyses are currently underway.

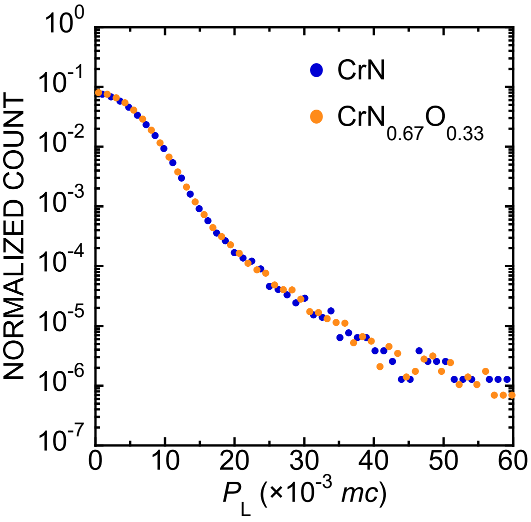

Fig. 1 CDB spectra of CrN and $CrN_{0.67}O_{0.33}$ epitaxial films.

REFERENCES:

[1] K. Suzuki *et al.,* APL Mater. **3** (2015) 096105.
[2] K. Suzuki *et al.*, Thin Solid Films **625** (2017) 111.
[3] M. Kitaura *et al.,* to be published from J. Phys.: Conf. Ser.

R6131

CO4-21

Research on radiation damage of new material (Ti high entropy alloy and industry steel (316L under and after irradiation

E. Wakai, A. Yabuuchi[1], T Yoshiie[2], K. Sato[3], T. Wakui, Y. Kobayashi[1], T. Takahashi[1], T. Ishida[4]

J-PARC Center, Japan Atomic Energy Agency
[1]Institute for Integrated Radiation and Nuclear Science, Kyoto University
[2]Department of Physics, Osaka Metropolitan University
[3]Research Field of Engineering, Kagoshima University
[4]J-PARC Center, High-Energy Accelerator Research Organization (KEK)

INTRODUCTION: Materials and instruments used in a radiation environment must have irradiation resistant properties. Therefore, it is important to promote research and development not only of existing applied and industrially developed materials, but alsoof innovative materials such as high entropy alloys [1,2] with even better properties. One of the objectives of this study is to understand the basic process of irradiation damage of high-entropy alloys as innovative materials. The electron-beam irradiation method, which can produce the simplest lattice defect, the Frenkel pair (energy must be adjusted), is an important experimental technique. Our efforts in this study have another objective. This is to detect the appearance of elastic waves produced by the stresses to which the material is subjected by the pulsed beam, and to measure and evaluate them using the four-terminal electrical resistance method as a nondestructive testing technique.

EXPERIMENTS: The electron irradiation experiments were performed using the electron linear accelerator at Kyoto University. In order to investigate the threshold energy of the atomic displacement process in Ti-64 (Ti-6Al-4V) alloy and Ti-based high-entropy alloys (Ti-V-Cr-Zn-Ta) caused by collisions with energetic incident particles, the temperature of the samples was kept at temperature about 4.0 K in a vacuum and the acceleration voltage of the electron beam was varied from 0.3 MV to 2.0 MV, and the electrical resistance of the sample was measured at each acceleration voltage by the four-terminal electrical resistance method [3]. Elastic waves excited in the 316L by pulsed electron beam waves (10, 20, 30, 50, and 100 Hz) around room temperature were also measured by the same 4-terminal electrical resistivity method in air at an energy of 8.0 MeV.

RESULTS: The electrical resistance of Ti-based HEA was found to change for the first time from at about 1.8 MeV, which is considered to be much higher than the generally assumed threshold energy of Ti alloys. This is an important result indicating the high threshold energy of this material and is an important factor in evaluating irradiation resistance performance. In the evaluation of the threshold energy of Ti-64 alloy, it was found to be higher than that of pure Ti. It was also evaluated to have a stepwise threshold energy. On the other hand, the results of the measurement by the 4-terminal electrical resistance method for elastic waves (stress waves) in solids induced by pulsed electron beams in the temperature region above room temperature were as follows. In 316L steel, the changes in electrical resistance tended to increase with increasing frequency (10-100 Hz). The results of this research and a detailed investigation of these material properties will be submitted to journals [4,5].

REFERENCES:
[1] E. Wakai *et al.,* Mater. Char., **211**(2024)113881.
[2] E. Wakai *et al.,* Sci. Talks, **8** (2023)100278.
[3] Y. Iwamoto *et al.,* J. Nucl. Mater., **458** (2015) 369-375.
[4] E. Wakai *et al.,* Advanced Mater. or Nature Com. or Materials Today to be submitted in 2025.
[5] E. Wakai or T. Wakai, *et al.,* Journal to be submitted in 2025.

R6132

Electrical Signals from Electron Device Measurement System under Irraditaion of Bremsstrahlung X-rays Produced by LINAC

Y. Gotoh, A. Kinomura[1], and T. Takahashi[1]

Graduate School of Engineering, Kyoto University
[1]Institute for Integrated Radiation and Nuclear Science, Kyoto University

INTRODUCTION: Electric and electronic circuits tolerant to radiation are important not only for decommissioning of Fukushima Daiichi Power Plant but also for the other nuclear power plants and radiation facilities [1]. To check the radiation tolerance, use of radioisotope (RI) is one of the good ways because radiation can be performed specific energy. Furthermore, RI does not cause electrical noise. However, it is rather difficult to observe individual event caused by the high energy particle, due to continuous radiation. To understand the events happening on electronic devices, its response after quick cease of the irradiation may give us some information. However, measurements of the electrical signals in radiation fields may have difficulties in acquiring such response from the device, due to the presence of unexpected noises. The purpose of the present study is to observe the response of the device together with electric noises produced in the measurement system under irradiation of Bremsstrahlung x-rays.

EXPERIMENTS: The samples were a silicon diode and an InGaP solar cell [2], which were installed in a small capsule made of stainless steel. Several samples were irradiated by pulsed X-rays generated by Bremsstrahlung of platinum target irradiated by 6 MeV electron beams. The output signal was taken out from the capsule via tri-axial cable. Current and voltage signals were acquired by a pico-ammeter and a digital oscilloscope. The pulse width was 4 μs and one pulse contained charges of 0.853 μC. Irradiations were performed at pulse repetition rates of 1 Hz and 60 Hz.

RESULTS: The ammeter detected little noise when the accelerator was not operated. Figure 1 shows a typical example of the voltage signal observed with the InGaP solar cell under x-ray irradiation. Rapid increase followed by a long tail, of which decay time was about several tens millisecond, was observed. The reason for the long decay time is currently unclear. The ammeter also recorded pulsed signal, and the observed pulse had also a longer time than the beam pulse. Further investigation will be necessary whether this method is applicable to extract some information on the effect of radiation to the electronic device, but the present InGaP solar cell may be used as a monitor of the beam pulse for low pulse repetition rate experiments.

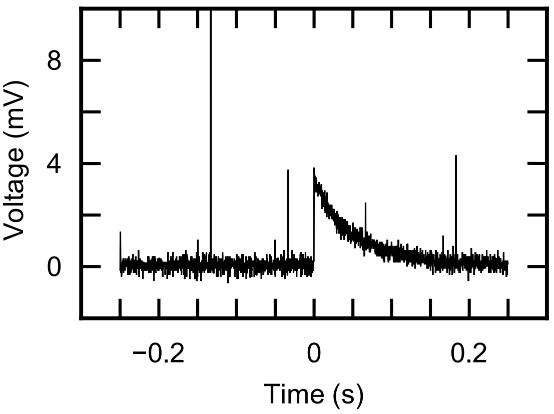

Fig. 1. Waveform of the X-ray induced signal obtained with an InGaP solar cell.

ACKNOWLEDGMENTS: The InGaP solar cells were provided by Dr. Mitsuru Imaizumi, Japan Aerospace Exploration Agency.

REFERENCES:

[1] Y. Gotoh *et al.,* IEEE Trans. on ED, **67** (2020) 1660-1665.
[2] Y. Okuno *et al.,* J. Nucl. Sci. Technol. **56** (2019) 851-858.

CO4-23

Vacancy Migration Energy in $CoCrFe_{0.25}MnNi$ High-Entropy Alloy

H. Araki, M. Mizuno, A. Yabuuchi[1] and A. Kinomura[1]

Graduate School of Engineering, Osaka University
[1]Institute for Integrated Radiation and Nuclear Science, Kyoto University

INTRODUCTION: Tsai et al. [1] originally proposed the concept of sluggish diffusion in the high-entropy alloy(HEA). However, the reason for the sluggishness of diffusion is not quite clear. $CoCrFe_{0.25}MnNi$ is known to form a quinary single-phased face-centered cubic structured solid solution. In the $CoCrFe_{0.25}MnNi$ HEA at high temperatures, atomic diffusion is expected to proceed via a vacancy mechanism because they are substitutional solid solutions. Therefore, vacancy formation and migration energies in the $CoCrFe_{0.25}MnNi$ HEA are important indexes for understanding the sluggish diffusion. In this work we have evaluated the vacancy migration energy in $CoCrFe_{0.25}MnNi$ HEA by observing the vacancy migration and annihilation behavior during an annealing process after electron irradiation, with the use of the positron lifetime spectroscopy.

EXPERIMENTS: An ingot of $CoCrFe_{0.25}MnNi$ HEA was carried out with solid solution heat treatment at 1373K for 24 h under argon atmosphere, and cut into 10 mm × 10 mm × 0.5 mm plates. The specimens were subjected to strain relief annealing at 1373K for 10 h and then rapidly cooled to prevent secondary phase precipitation and to stabilize single-phase FCC structure. Then, the specimens in water flow were exposed to 8 MeV electron beam irradiation for 3 h in KURNS-LINAC. The irradiation damage was evaluated at $(1.3 - 1.8) \times 10^{-4}$ dpa. The irradiated samples were isochronally annealed in a temperature range from 373 to 673 K. The temperature step during the isochronal annealing was 25 K and the duration of exposure to each temperature was 1 h. The positron lifetime measurements were made at 297–299 K.

RESULTS: Before the electron irradiation the positron lifetime spectrum for the solution-treated alloys was represented by only one component of 108 ps, which indicates that positrons annihilate in the bulk. After electron irradiation, the mean positron lifetime was increased to 132 ps. The analysis of positron lifetime spectra for the as-irradiated sample shows that many positrons are trapped and annihilate in the monovacancies introduced by electron irradiation, because the lifetime component, τ_2 , of trapped positrons was about 180 ps. The mean positron lifetime after isochronal annealing of the electron irradiated samples is shown in Fig.1. The mean positron lifetime is found to decrease sharply around 373K. This can be attributed to the decrease in vacancy concentrations triggered by the free vacancy-migration. It demonstrates the vacancy migration enthalpy in the $CoCrFe_{0.25}MnNi$ high entropy alloy is very similar to that in the CrFeNi alloy. These results indicate that the “'sluggish diffusion” hypothesis is not supported in $CoCrFe_{0.25}MnNi$ high entropy alloys at least in view of vacancy migration behavior.

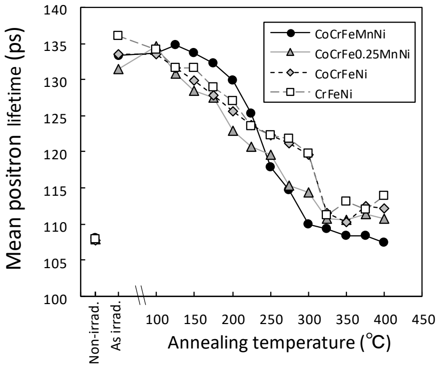

Fig. 1 Mean positron lifetime in the electron-irradiated $CoCrFe_{0.25}MnNi$ alloys after isochronal annealing.

REFERENCES:

[1] K. Y. Tsai, M. H. Tsai and J. W. Yeh, Acta Mater., **61** (2013) 4887.

R6141

CO4-24

Neutron Irradiation Tests for ITER Diagnostic Systems in JADA

T. Ushiki, K. Nojiri. T. Yokozuka, T, Kikuchi, S. Tainaka, E. Yatsuka, S. Kitazawa and Y. Nunoya

Department of ITER Project, Naka Institute for Fusion Science and Technology, National Institutes for Quantum Science and Technology

INTRODUCTION: ITER is the world's largest fusion experiment reactor and is under construction in southern France [1]. Components of diagnostic systems installed in the ITER tokamak are exposed to high neutron radiation. Therefore, it is important to investigate the effect of neutron irradiation on these components. In this study, neutron irradiation tests on components of ITER diagnostic systems in JADA (ITER project Japan Domestic Agency) have been conducted. This report presents the result of the neutron irradiation test on the optical fibers and electric devises for Infrared Thermography system (IRTh) [2] and pressure gauges for shutter on Divertor Impurity Monitor system (DIM), Edge Thomson Shattering system (ETS) and IRTh [3].

1. Irradiation test for IRTh

IRTh plans to use a steering mirror driven by an ultrasonic motor for optical axis adjustment in the ITER. A fiber optical rotary encoder and a precise limit switch are planned to be used for measuring the mirror angle and reference position. In this study, neutron irradiation tests on the fiber optical rotary encoder, optical fiber and limit switch were conducted.

EXPERIMENTS: The fiber optical rotary encoder, optical fiber and limit switch were irradiated at neutron fluence up to 1.0 x 10^{16} n/cm^2, equivalent to neutron fluences during 20 years of ITER operation. An evaluation of the transmittance at 800 nm, the use wavelength of the optical fiber, before and after irradiation, as well as functional tests of the fiber optical rotary encoder and the precise limit switch, were conducted.

RESULTS: It was confirmed that no significant degradation in transmittance was observed in the optical fiber before and after irradiation. Additionally, the precise limit switch was confirmed to function properly even after irradiation. The functional test of the fiber optical rotary encoder after irradiation is scheduled to be conducted around June 2025.

2. Irradiation tests of pressure gauges for shutter on DIM, ETS and IRTh

Pressure gauges are planned to be used on DIM, ETS and IRTh in the port cell area of ITER. Neutron irradiation tests on pressure gauges (K-P8AP) were performed to estimate neutron shielding that would last for 20 years ITER operation.

EXPERIMENTS: The irradiation position was outside of the graphite reflector in Slant Expose Tube (SLANT), and the thermal neutron flux at 5 MW operation was 4.8 x 10^{12} n/cm^2/s. The gauges irradiated up to 2.0 x 10^{12} n/cm^2 in the previous year were irradiated up to 3.0 x 10^{13} n/cm^2. The performance of the pressure gauge was compared before and after irradiations.

RESULTS: No change in the performance of the gauges was observed before and after the irradiation up to 3.0 x 10^{13} n/cm^2. The tested pressure gauges K-P8AP proved to be available at neutron fluence up to 1.0 x 10^{13} n/cm^2, equivalent to neutron fluences during 20 years of ITER operation.

REFERENCES:

[1] https://www.iter.org
[2] T. Ushiki *et al.,* J. Nucl. Mater., **595** (2024) 155047.
[3] K. Itami *et al.,* J. Plasma and Fusion Res., **92** (2016) 433.

R6143

CO4-25

Slow Positron Beam Analysis of Layered Structure Membrane

Z. Chen, Y. Kobayashi[1] A. Yabuuchi[2] and A. Kinomura[2]

Department of Material Science and Engineering, Wuhan Institute of Technology, People's Republic of China
[1]Department of Environmental Sciences, Tokyo Gakugei University
[2]Institute for Integrated Radiation and Nuclear Science, Kyoto University

INTRODUCTION: Membrane separation is an effective method for water treatment due to its low cost and low energy consumption [1]. Polyamide (PA) thin film composite membranes are widely studied owing to the tunable nature of their selective top layer and porous substrate. Since the thick selective layer may lead to the decrease of water flux, commercial composite membrane usually contains a thin selective layer. However, the defects in the thin selective layer would lead to serious decline of rejection, which is the main concern for membrane preparation. In order to solve the problem, introducing 2D material may be a potential method. Since the 2D material, such as $Ti_3C_2T_x$ (MXene), exhibits uniform nanochannels which is comparable to the ion size, PA/MXene/Polysulfone (PA/MX/PSF) layered structure may possess excellent performance. In this case, the PA/MX/PSF layered composite membranes have been prepared and investigated via positron annihilation techniques coupled with a positron beam.

EXPERIMENTS: The MXene aqueous solutions with different concentrations (0.03mg/L, 0.06mg/L, 0.12 mg/L and 0.18 mg/L) were filtrated by polysulfone membrane at 0.1 MPa, respectively. The piperazine (PIP) aqueous solution was poured on the surface of obtained MXene/polysulfone membrane for vacuum filtration. Then the trimesoyl chloride (TMC) was poured onto the obtained membrane surface for 1 min. The excess TMC solution was expelled after the PIP and TMC had reacted sufficiently to form the PA layer. Positron measurements were performed with the positron beam system at the Institute for Integrated Radiation and Nuclear Science, Kyoto University.

RESULTS: As shown in Fig. 1, the S-E curves of the four membranes suggested the difference of the layer structures. The S-E shape is similar to the positron results of PA/PSF membranes in the previous study [2]. In this study, all the four membranes are PA/MXene/PSF layered structure with different thickness of the MXene layer. Moreover, it can be found that thicker MXene layer would lead to the lower S parameter in the incident energies lower than 10 keV. The long-lived ortho-positronium (o-Ps) lifetime results at the incident energy of 1.65 keV and membrane rejections were shown in Table 1. It can be found that shorter o-Ps lifetime is corresponding to higher rejection. During the interface polymerization process, the existence of the MXene layer may hinder the loss of polymer monomer through porous substrate. In this case, thicker MXene layer may result in denser polyamide layer.

Table 1 The o-Ps lifetime and rejection of membrane

	o-Ps lifetime [ns]	Rejection of $MgSO_4$
PA/MX-3/PSF	2.17	70.1%
PA/MX-6/PSF	2.20	68.8%
PA/MX-12/PSF	2.16	81.1%
PA/MX-118/PSF	2.10	90.7%

REFERENCES:
[1] Y. Cui *et al.,* Water Research, **200** (2021) 117207.
[2] Z. Chen *et al.,* J. Phys. Chem. C, **115** (2011)18055-19060.

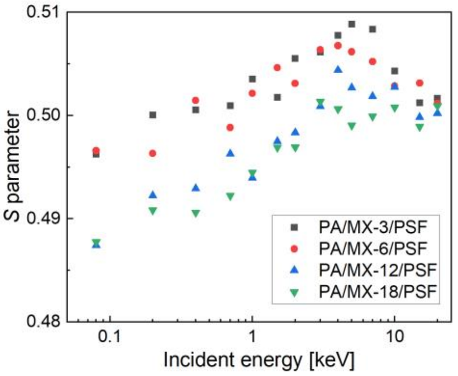

Fig. 1 The S-E plots for the samples.

CO4-26

Changes in oxidation states of electrode material including Fe during discharging process

T. Wada and Y. Arachi
Department of Chemistry, Materials Engineering, Kansai University

INTRODUCTION: Oxide-based all-solid-state batteries (ASSBs) are expected to be the next-generation storage battery with both high energy density and chemical stability. Much research has been conducted on lithium metal as the anode. However, as the current density increases, there is a fatal problem that the precipitation of lithium metal in the sintered solid electrolyte leads to a short circuit between the electrodes. We believe that the anode of this battery requires an insertion electrode in which the charge/discharge reaction proceeds through the insertion and desorption reaction of Li ions into the crystal structure.

Electrochemical charge/discharge measurements confirmed that the charge/discharge reaction occurred at an average discharge voltage of 2.1 V in the first cycle, but the discharge capacity at the cutoff voltage of 1.8 V was only about 60% of the theoretical capacity (153 $mAhg^{-1}$), based on a one-electron reaction with Fe^{3+}. Furthermore, a significant capacity fading was observed toward the second cycle, and the reversible capacity gradually decreased with following cycles. Previous our research has shown that this material shows an ionic distribution of $[Li_{0.5}Fe^{3+}_{0.5}]^{8a}[Li_{0.25}Fe^{3+}_{0.25}Ti_{0.5}]^{16d}{}_2O_4$. Therefore, when Li is inserted into spinel-type $LiFeTiO_4$, it is possibly to change to rock salt-type Li_2FeTiO_4. In order to clarify the Fe oxidation state of the sample as well as the movement of Fe between sites (change in coordination environment) during charge/discharge reaction. For this purpose, we believe that Mössbauer spectroscopy is the most effective method.

EXPERIMENTS: The sample was prepared by conventional solid state reaction. As starting materials, Li_2CO_3, $FeC_2O_4 \cdot 2H_2O$ and TiO_2(anatase) were used and mixed by ball-milling for 30 min at 400 rpm and followed with sintering at 1273 K for 12 h in air. The obtained samples were charactered by powder X-ray diffraction and electrochemical testing. The electrode was treated by carbon-coating with acetylene black. As anode and electrolyte the lithium metal and 1 M $LiPF_6$ in EC-DMC (3:7) were used respectively.

RESULTS: A single cubic phase of the sample including Fe was confirmed by XRD pattern. Then the Rietveld refinement was carried out and yielded a relatively good fitting, based on the inverse spinel type structure. As shown in Fig. 1(1) and (4), both spectra showed magnetic splitting under trivalent Fe state. On the other hands, Fig. 1 (2) and (3) indicated an existence of divalent Fe, in addition to a small amount of trivalent one. These results can be explained by the electrochemical reduction reasonably. A further quantitative analysis are under progress to clarify the discharge and charging mechanism, focusing on local environment of Fe.

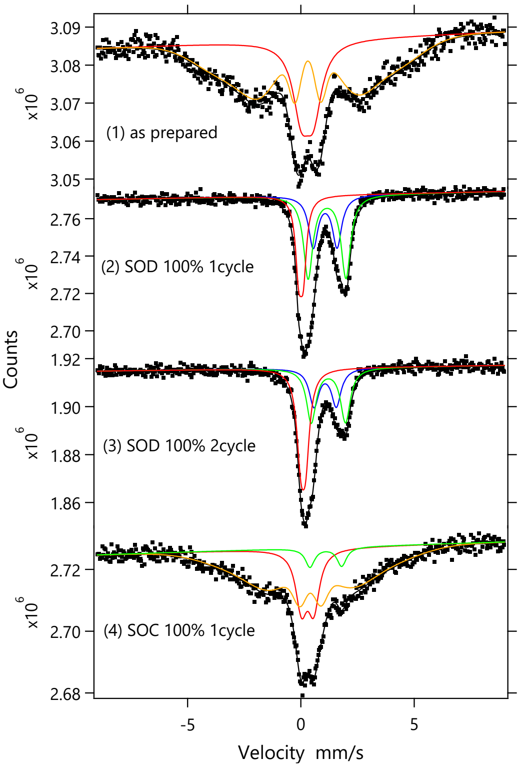

Fig. 1. ^{57}Fe Mössbauer spectra of various electrochemical oxidation states at 300 K. (1): as-prepared, (2): fully discharged at the first cycle, (3): fully discharged at the next 2nd cycle and (4) 1st cycled.

REFERENCES:

[1] Y. Arachi *et al.,* J. Jpn. Soc. Powder Powder Metallurg, **48(3)** (2001) 274-276.

[2] Y. Sakai, K. Ariyoshi and T. Ohzuku, Hyperfine Interactions, **139/140** (2002) 67-76.

CO4-27

Mössbauer spectrometric study of SrTiO$_3$ doped with dilute ^{57}Fe and Sn.

K. Nomura[1)], M. Takahashi[1)], Y. Kobayashi[2)], T. Naka[3)], Y. Yoshimura[4)], Y. Koike[4)], S. Kubuki[5)], J. Okabayashi[6)], and C. Barrero[7)]

[1] *Tokyo Medical University*
[2] *Institute for Integrated Radiation and Nuclear Science, Kyoto University*
[3] *National Institute of Material Science,*
[4]*Faculty of Science and Engineering, Meiji University,*
[5]*Radio-Isotope Center, Tokyo Metropolitan University,*
[6] *School of Science, The University of Tokyo,*
[7] *Faculty of Exact and Natural Sciences, University of Antioquia*

INTRODUCTION: Dilute magnetic semiconductors are required to have a Curie temperature above room temperature [1], and to achieve this, wide bandgap semiconductors doped with magnetic ions have been investigated [2]. In this study, we synthesized a strontium titanate (SrTiO$_3$: STO) doped with 1 at% ^{57}Fe^{3+} and several at% Sn^{4+} using a complexation/pyrolysis method. The local chemical states of iron were studied by Mössbauer spectrometry. At room temperature (RT), the two doublets due to the paramagnets and a broad relaxation peak were observed. The purpose is to clarify the origin of the broad peak by the low-temperature spectra.

EXPERIMENTS: The samples were prepared by the decomposition of the ethylene glycol complexes at 500 C for 2 hours and post-heating for 4 hours until 850 ºC. The formation of STO doped with 1 at% ^{57}Fe^{3+} and with and without several at% Sn^{4+} were mainly confirmed by XRD. VSM and SQUID measurements were carried out for 1 at% ^{57}Fe and 0–4 at% Sn samples.

RESULTS: We observed a very weak ferromagnetic behavior for 1 at% ^{57}Fe and 0–4 at% Sn co-doped samples. Mössbauer spectra of 1 at% ^{57}Fe doped and 1 at% ^{57}Fe + 4 at% Sn co-doped STO at RT, 200, and 75 K are shown in Fig. 1. The Mössbauer spectra of doped-STO at 75 K consist of four Fe^{3+} sites; two paramagnetic components and two magnetic relaxation components with different internal fields (about 50 and 20 T). Introducing Fe^{3+} and Sn^{4+} to Ti^{4+} sites can cause oxygen defects and lattice distortion. The ferromagnetic behavior can be attributed to the formation of clusters incorporating the oxygen vacancies, two Fe^{3+} atoms, and the strain-inducing Sn^{4+}. In some clusters, Fe^{3+} atoms achieved a long-range order [3].

REFERENCES:

[1] J.M.D. Coey *et al.,* Nature Materials, **172** (2005) 4.
[2] K. Nomura *et al.,* Hyperfine Interactions, **241** (2020) 6.
[3] A.M. Mudarra Navarro *et al.,* Interactions, **245** (2024) 21.

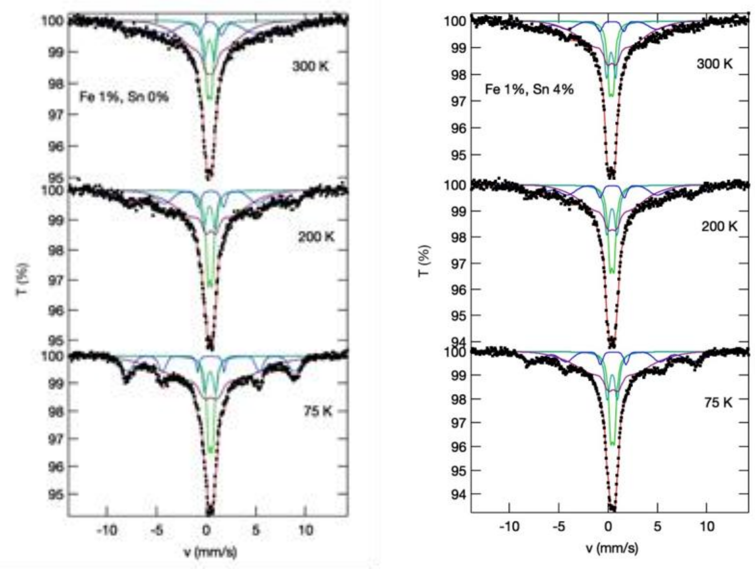

Fig. 1. Mössbauer spectra of 1% Fe doped STO (left) and 1%Fe +4%Sn doped STO (right) at 75, 200, and 300 K.

CO5-1

Artificial Alpha Recoil Track Formation on Synthetic Zircon: Preliminary Observation

N. Hasebe, Z. Shi[1], M. Hamada[2], Y. Iinuma[3], and K. Takamiya[3]

Institute of Nature and Environmental Technology, Kanazawa University
[1]Graduate School of Natural Science and Technology, Kanazawa University
[2]College of Science and Engineering, Kanazawa University
[3] Institute for Integrated Radiation and Nuclear Science, Kyoto University

INTRODUCTION: ^{238}U, ^{235}U, and ^{232}Th decay through emission of alpha particles to stable lead. Alpha Recoil Track (ART) is the damage formed when daughter nuclides move back in responce to alpha decay (Fleisher, 2003). Given the known decay constants of uranium and thorium, the age since the start of ART accumulation can be calculated by measuring the number of ARTs and the uranium and thorium concentrations. Zircon is rich in uranium and thorium, and is often analysed in geochronological studies. Unlike the layered silicates such as muscovite or biotite, ART in zircon has never been observed before, despite its potential to date samples whose ages are in order of thousand years old or older.

The purpose of this research is to establish a method to identify the ARTs in zircon by using the synthetic zircon and the artificial formation of ARTs using ^{241}Am source.

EXPERIMENTS: Synthetic zircon was formed by the flux method from the reagents of ZrO_2, MoO_3, Li_2MoO_4, and Li_2SiO_3 (Shinno, 1987). Synthetic zircons with well-developed plane parallel to the crystallographic c-axis were then handpicked and mounted in Teflon sheet. After polishing with diamond paste and colloidal silica, the zircon crystals were irradiated with ^{241}Am source for 10 hours at the Institute for Integrated Radiation and Nuclear Science, Kyoto University. Based on the experiments with muscovite, the expected areal ART density is around 0.02 ART/μm^2 (Nakashima et al., 2024)). The irradiated zircon, together with zircon without irradiation, were etched stepwisely with KOH:NaOH=1:1 eutectic etchant at 230°C, which is the same condition with fission track (FT) reveal in zircon, and surface topography was observed by the atomic force microscopy.

RESULTS: We run synthesis experiments with two cooling rates after heating at 1270°C for two hours: 10°C/hr and 5°C/hr. The slow cooling experiment resulted in larger crystals and more number of skeletal crystals. AFM observation shows no significant differences between irradiated and non-irradiated samples up to 6 hours etching. This may imply that the etching condition necessary to make ART visible is different from that for FT observation, or that the registration factor for zircon is different from that of muscovite and we need more irradiation to leave a suficient number of ART on the mineral surface.

REFERENCES:

[1] Fleischer, R.L. Geoch. Cosmoch. Acta, **67** (2003) 4769-4774.
[2] Sinno, I., Mineral. Jour., **13** (1987) 239-253.
[3] Nakashima, T., *et al.,* Rad. Meas., **173** (2024) 107087.

R6004

CO5-2

Concentration Distribution of the Elements in Aerosol Coarse Particle during Kosa Event

Norio Ito and Hisao Yoshinaga[1]

Radiation Research Center, Osaka Metropolitan University
[1] Institute for Integrated Radiation and Nuclear Science, Kyoto University

The particles which are suspended in the atmosphere, called atmospheric aerosols , have particle size ranging from several tens of nanometers to 100 µm, and the composition differs within each particle size range. Here, we will discuss the elemental composition of soil particles, which are mainly coarse particles (particle size > 2 µm). The soil particles increases its concentration mainly at the time when yellow sand (Kosa particle) arrives. Kosa particles originate in the desert regions of mainland China and arrive in Japan between March and May. From April 16th to 23rd, 2024, Kosa particles also flew into the Kansai region, and we were able to collect Kosa particles. Even when Kosa particles are not arriving, the area is affected by soil particles originating from China and soil particles around the observation point[1].

Here, we will discuss how the concentrations of Al and Ca (main element of soil particle) change and the changes in particle size distribution when Kosa particles arrive. The atmospheric aerosol particles observed on Kosa arriving(April 16th to 23rd, 2024) were collected at Osaka Metropolitan University (Sakai City, Osaka Prefecture) in one-week period using an Andersen sampler, collecting with the particle size ranges divided into nine ranges (<0.43, 0.43-0.65, 0.65-1.1, 1.1-2.1, 2.1-3.3, 3.3-4.7, 4.7-7.0, 7.0-11, >11 µm) and collected onto polyethylene sheets. The average of coarse particle (PM-C) concentration from April 16 to April 23 was 60 µg/m^3, about five times the average concentration for other non-Kosa periods (14 µg/m^3). The elemental composition of the collected atmospheric aerosol was analyzed by neutron activation analysis in neutron irradiation with Kyoto University Research Reactor. The average concentrations of Al and Ca during the Kosa event (April 16-23) were 3700ng/m^3 and 1700ng/m^3, respectively, which were 4.7 times (Al) and 3.2 times (Ca) higher than the average concentrations during other periods, which were 790ng/m^3 (Al) and 530ng/m^3 (Ca).The increase in Ca concentration during the arrival of Kosa particles was not as large as that of PM-C and Al, and it is estimated that the Ca concentration in Kosa particles is lower than that in soil particles near the observation point.

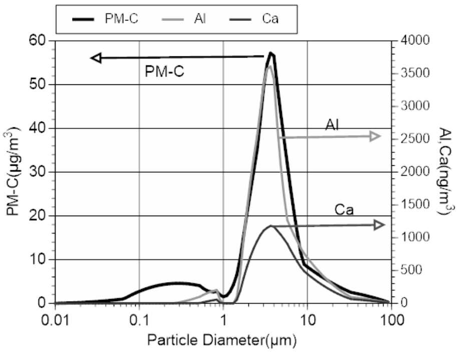

Fig.1 Concentration distribution on particle size for PM-C, Al,Ca

Figure 1 shows the particle size distribution of PM-C, Al, and Ca concentrations during the arrival of Kosa particles. The average particle size and standard deviation obtained from this distribution are shown in Table 1. When Kosa particles arrive, the average particle size and its standard deviation decrease, and it can be assumed that particles with a narrower particle size range are arriving.

Table 1 Mean diameter and standard deviation obtained from concentration distribution on particle size

	Mean diameter(µm)		Standard deviation of diameter(µm)	
Items	4/16-23	Other periods	4/16-23	Other periods
PM-C	6.5	8.9	5.1	7.4
Al	5.8	8.7	4.4	6.3
Ca	7.0	8.9	5.6	7.5

REFERENCES:

[1] I. Mori *et al.,* Atmospheric Environment, **36** (2002) 4569-4575.

CO5-3

Basic Research on Trace Elemental Analysis of Airborne Particulate Matters Derivated from Concrete in an Environment by INAA & IBA

I. Sato[1,2,3], S. Okano[3], K. Sato[1], N. Hagura[1,2,3], T. Uchiyama[2]

[1] *Nuclear Safety Engineering, Science and Engineering, Tokyo City University*
[2] *Atomic Energy Research Laboratory, Science and Engineering, Tokyo City University*
[3] *Cooperative Major in Nuclear Energy, Integrative Science and Engineering, Tokyo City University*

INTRODUCTION: To clarify the behavior of cesium compound aerosols in sodium-cooled fast reactor (SFR) during severe accident (SA), the aerosol behavior is divided into elementary processes, and simulation experiments will be performed for each process [1] (see Fig.1). In this work, the deposition of CsOH (one of the chemical forms of Cs during SA) to concrete material (one of the SFR structural materials, containing Ca) is focused on. That is, coexistence of these elements containing in the reaction products is investigated with INAA.

EXPERIMENTS: The concrete specimen (15mm×15mm×30mm) with 1g of CsOH at its top was placed in the center of a quartz tube (ϕ 30 ㎜). The specimen was heated in an cylindrical electric furnace (Asahi Rika Seisakusho, ARFH-30KC) for 30 minutes at a temperature of 800 ℃ under atmosphere of relative humidities: 0% and 80% in Ar. After heating, the top surface (reaction products) of specimens were grinded with abrasive paper (#60) to obtain fine powder for INAA (30 s irradiation at PN6 of KUR). These powder specimens (amount for 1mm thickness) were placed in polyvinyl bags, and were sealed.

RESULTS&DISCUSSION: During irradiation, neutron absorption reactions will be happened to make gamma emitter species as shown as Cs-133+n→Cs-134 and Ca-48+n→Ca-49. Radioactive species of Cs-134 and Ca-49 have half-lives of 2.06 y and 8.7 min, respectively. It is interest in the coexistence behavior of Cs and Ca, therefore gamma rays emitted from Cs-134 and Ca-49 were measured by Ge semiconductor detector. Generally, when Ca is present in rock materials such as sand or aggregate of concrete materials, it is incorporated into the silt structure that they possess. However, when Cs enters this location, it is believed that Ca gives up its space and is replaced by Cs [2]. Fig.2 shows a spectrum measured for a concrete specimen at full range 4 MeV instead of normal full range of 2 MeV. The depth profile for Ca-49 for a specimen heated at 800 ℃ for both humidity are identical, in which those intensities were high near the surface and those were low at at deep positions. This trend is same as in the Cs penetration profiles in concrete materials. If site-exchange reaction happens between free Cs, and Ca located at the silt structure, the depth profiles would show opposite trend each other. This behavior will be continuously researched by obtaining more precise measurements with INAA and/or other analysis methods.

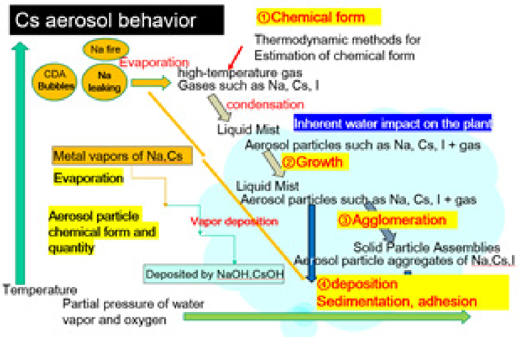

Fig. 1 Aerosol behavior map.

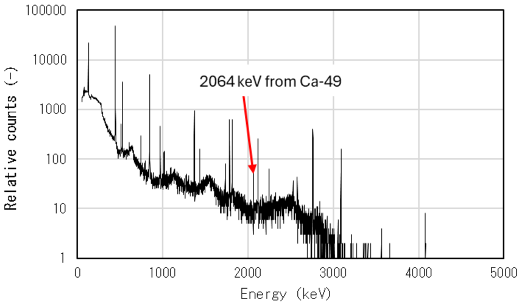

Fig. 2 A spectrum from an irradiated concrete

REFERENCES:

[1] O. Kawabata *et al.,* Proceedings of ICONE19, 43796, May 16-18, Makuhari, Japan, 2011.
[2] K. Ito *et al.,* Surface technology, **68** (2017) 430 (in Japanese).

CO5-4

Absorption of alkali metal ions by white radish sprouts (VI

M. Yanaga, T. Nakamura[1], S. Nishiwaki[2], H. Yoshinaga[3], R. Okumura[3] and Y. Iinuma[3]

Center for Radioscience Education and Research, Faculty of Science, Shizuoka University
[1]Department of Science, Graduate School of Integrated Science and Technology, Shizuoka University
[2]Department of Chemistry, Faculty of Science, Shizuoka University
[3]Institute for Integrated Radiation and Nuclear Science, Kyoto University

INTRODUCTION: Radioactive ^{137}Cs, which was released in the Fukushima Daiichi Nuclear Power Plant accident, still remains and is the cause of reputational damage. It is considered necessary to extract ^{137}Cs from soil in some way. However, ^{137}Cs has the property that it is strongly adsorbed when it enters soil and cannot be easily extracted. Previous research in our laboratory has shown that when stable isotope cesium is added to contaminated soil, ^{137}Cs is released from the soil by exchange with ^{137}Cs adsorbed in the soil[1, 2]. Therefore, in this study, we focused on ion exchange with alkali metal ions as a decontamination method. We created simulated contaminated soil with ^{137}Cs and performed decontamination using a decontamination solution containing stable isotope alkali metal ions (K^+, Rb^+, Cs^+) with similar properties, to examine which alkali metal ions are effective for decontamination. We also compared conditions for extracting more ^{137}Cs, such as the addition of nitric acid and dispersants, and temperature changes. In addition, from the perspective of practical application, radish sprouts were grown in the presence of alkali metal ions and the effects of decontamination on plant growth were considered in terms of changes in trace element concentrations.

EXPERIMENTS: After radish sprouts were germinated on absorbent cotton moistened with pure water, 10 mL each of $CsNO_3$ or $RbNO_3$ solutions of various concentrations and culture medium were added to the absorbent cotton, and the radish sprouts were hydroponically grown and harvested. The trace elements contained in the harvested samples were quantified and compared by neutron activation analysis. Radish sprouts were also grown in soil using androsol and vermiculite to which alkali metal ions had been added, and they were harvested. Neutron activation analysis was then performed to examine the effect of the addition of alkali metal ions on the absorption of various trace elements.

RESULTS: In this experiment, radish sprouts were grown hydroponically or in soil in the presence of alkali metal ions, and the effects of decontamination on plant growth were examined. The indicator was the change in trace elements contained in the radish sprouts. When alkali metal ions were added, a decrease in the K content in the radish sprouts was confirmed. This is thought to be because competition with alkali metal ions inhibited the absorption of K into the radish sprouts. On the other hand, the Mn content in the radish sprouts increased with the addition of alkali metal ions. Since Mn is an essential element for plants, if its absorption is promoted, it can be said to have a positive effect on plants. In addition, the increase in Mn content was reduced by washing with pure water, which is thought to allow the increase to be controlled, and it is speculated that the risk of Mn excess can be managed. As changes and trends were observed in the contents of several elements, it is thought that the addition of alkali metal ions (decontamination solution) has an effect on plants.

REFERENCES:

[1] M. Yanaga *et al.,* NMCC ANNUAL REPORT, **22** (2015) 185-190.
[2] M. Yanaga *et al.,* NMCC ANNUAL REPORT, **23** (2016) 172-179.

R6051

CO5-5

Development of ^{40}Ar-^{39}Ar Dating Equipment in IIRNS, Kyoto University

N. Iwata, Y.N. Miura[1], M. Inagaki[2]

Faculty of Science, Yamagata University
[1]Earthquake Research Institute, University of Tokyo
[2]Institute for Integrated Radiation and Nuclear Science, Kyoto University

INTRODUCTION: Radiometric dating is a valuable tool for unveiling terrestrial and planetary material formation and evolution. The K-Ar and ^{40}Ar-^{39}Ar methods are invaluable in determining the timing of volcanic eruption, cooling process estimation for plutonic rock and resolving the timing of heating events on planetesimals and asteroids (e.g. Fernandes, 2024 [1]). The ^{40}Ar-^{39}Ar dating method and the method with laser heating technique are suitable for tiny samples (e.g. Kelley, 1995 [2] and Hyodo, 2008 [3]). To obtain ^{40}Ar-^{39}Ar dates of the rock and mineral separate samples from terrestrial and extraterrestrial material using the facility in IIRNS, we have continued developing a ^{40}Ar-^{39}Ar dating system, which includes laser-heating gas extraction and gas purification lines. The system was initially designed by Dr. R. Okazaki (Kyushu University) and has been developed for several years. Previous progress reports have described details and the schematic diagram of the system (Nos. 31126, R2079, R3121, R4068, R5122).

EXPERIMENTS: In FY2024, we continued assembling the gas extraction and purification system. We added an activated charcoal trap to the gas purification lines for the purpose of transferring sample gas from the sample holder to the gas analyser. We also checked the current condition of the Nd-YAG laser.

RESULTS: The activated charcoal traps, which include 0.12 g of activated charcoal grains, were installed in the gas extraction and purification system. When this trap is chilled with liquid nitrogen externally, sample gases are adsorbed on the surface of activated charcoal, and the gases are released when the trap is heated up by hot water. Combining this with valve manipulation can transfer the sample gas within the vacuum line. A Nd-YAG laser (LEE Laser model 812TQ), which was installed in 2019 at IIRNS, had a continuous wave power output of 57 W at the time of installation. However, no laser power output was observed in the latest operation test in March 2025. We must consider replacing the laser equipment to achieve argon isotope measurements in the IIRNS.

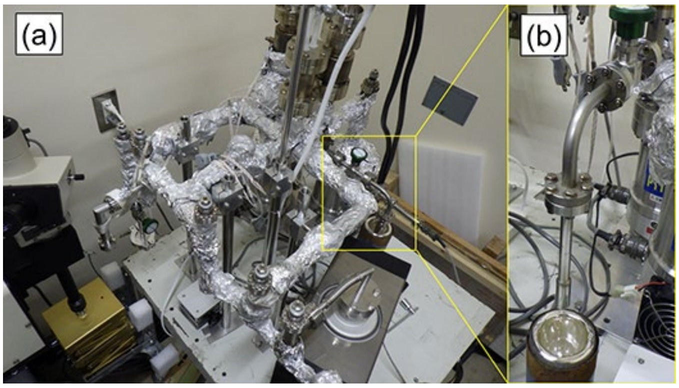

Fig. 1. (a) A photo of an upper view of the gas extraction and purification system. (b) A close-up photo of an activated charcoal trap.

REFERENCES:

[1] Fernandes, V.S., Burgess, R. and Sumino, H. (2024), in Methods and applications of Geochronology, edited by Shellnutt, Denyszyn and Suga, (Elsevier, 2024) 297-343.
[2] S. P. Kelley, in Microprobe techniques in the earth sciences, edited by Potts, Bowles, Reed, Cave (Chapman & Hall, London, 1995) 327-358.
[3] H. Hyodo., Gondwana Res., **14** (2008) 609-616.

R6057

CO5-6

Measurement of tritium concentration in modern commercial heavy water reagents used for estimating the migration of radioactive nuclides

T. Ohta, Y. Mahara[1], S. Fukutani[2], Y. Shibahara[2] and T. Kubota [3]

Department of Nuclear Technology, Nagaoka University of Technology
[1] *Kyoto University*
[2] *Institute for Integrated Radiation and Nuclear Science, Kyoto University*
[3] *Agency for Health, Safety and environment, Kyoto University*

INTRODUCTION:

Vast forest was markedly contaminated by radioactive plums containing radiocesium in the wide range of the eastern part of Japan in 2011 [1–7]. As forests have an important role in preventing landslides and maintaining the ecological and hydrological system, the destructive forest should be avoided and an appropriately managed tree-felling should be conducted. In our previous field study [1], most of the radiocesium in the tree rings was directly absorbed by the atmospheric direct uptake via the bark and leaves rather than by roots.-We directly measured root distribution of Cryptomeria japonica [3], indicating that mature it is not effective to absorb radiocesium by the root uptake due to the distribution of the fine root [3, 5]. The radiocesium is higher in Konara than in Cryptomeria japonica [1]. The velocity of migration of the nuclide in the unsaturated layer is key to evaluating the absorption of nuclides from the roots. The infiltration rate of soil water in the unsaturated zone is an important factor in evaluating the migration of the nuclides, and heavy water is used to estimate the infiltration rate. However, heavy water contains tritium. We clarified the tritium concentration of commercially available heavy water reagents and examined the environmental impact in field tests.

EXPERIMENTS:

We selected eleven commercially available heavy water reagents and one ^{18}O-water ($H_2{}^{18}O$) deuterium reagent for six markers and one $H_2{}^{18}O$ reagent for one marker available in 2016. These samples will contain high concentration of tritium, a range which fell within direct counting detection limits of modern LSC and does not require any ^{3}H pre-enrichment. The reagents were distilled 20-fold with ultrapure water. The radioactivity of tritium in the reagents was measured directly by a liquid scintillation counter (LSC) after the addition of a cocktail of liquid scintillation [8].

RESULTS:

Commercially available the reagents contain tritium ranging from 61 Bq/L to 2.5 x10^3 Bq/L. The concentration in the reagent was higher than that detected in the unsaturated layer in Fukushima [9]. However, the tritium concentration in the reagents was below WHO regulation. After the reagent is used as a field tracer in the environment, since the tritium in the reagents in the surface layer is further diluted by water in the unsaturated zone and then recover to background level quickly.

REFERENCES:

[1] Y. Mahara *et al.,* Sci. Rep., **4** (2014) 7121. [2] T. Ohta *et al.,* J. Radioanal. Nucl. Chem., **310** (2016) 109-115. [3] Y. Mahara *et al.,* Sci. Rep., **11** (2021) 8404.

[4] T. Ohta *et al.,* Radiological Issues for Fukushima’s Revitalized Future, Ed Takahashi (Springer) (2016) 13-24. [5] T. Ohta *et al.,* KURNS Progress Report 2021 (2022) 151.

[6] T. Ohta *et al.,* Ana. Sci., **29** (2014) 941-947. [7] T. Ohta *et al.,* J. Environ. Radioact., **111** (2012) 38-41. [8] T. Ohta *et al.,* Ana. Sci., **40** (2024) 1927-1930. [9] Ohta *et al.,* Sci. Rep., **14** (2024) 19672.

R6058

CO5-7

Determination of Abundance of Rare Metal Elements in Seafloor Hydrothermal Ore Deposits by INAA Techniques-11: Determination of Barium in Sulfide-sulfate Ore

J. Ishibashi, R. Kinugasa[1], S. Toyoda[1], H. Yoshinaga[2], Y. Iinuma[2] and K. Takamiya[2]

Ocean-bottom Exploration Center, Kobe University
[1]Department of Applied Physics, Okayama University of Science
[2]Institute for Integrated Radiation and Nuclear Science, Kyoto University

INTRODUCTION: We have studied application of INAA technique to quick search for elemental abundance in mineralized samples collected from seafloor hydrothermal deposits. Barite ($BaSO_4$ as chemical formula) is one of important gangue minerals in such deposits, and Ba content of sulfide-sulfate ores widely varies from a few hundred ppm to more than 50 wt%. On the other hand, it is not easy to determine Ba content in ore samples using conventional ICP-MS analysis. In this study, we report determination of Ba content of sulfide-sulfate ore using INAA technique.

****

EXPERIMENTS: For determination by the peaks at 165.85 keV of Ba-139 (t½=1.38 hours) and at 661.66 keV of Ba-137m (t½=2.552 minutes), powdered samples of 10-20 mg were irradiated at Pn-3 (thermal neutron flux = 4.68×10^{12} n/cm^2/sec) for 30 seconds and the gamma ray activity was measured for 3 minutes after adequate cooling time (2-5 minutes). For determination by the peak at 496.26 keV of Ba-131 (t½=11.8 days), powdered samples of 10-20 mg were irradiated at Pn-2 (thermal neutron flux = 5.50×10^{12} n/cm^2/sec) for 20 minutes and the gamma ray activity was measured for 15 minutes after adequate cooling time (~30 hours). Barium content of samples was calculated based on relative comparison of peak areas with a pure barite crystal grain collected from the Kosaka mine.

****

RESULTS: Because of low background compared with those of Ba-139 and Ba-131, Ba-137m was revealed as useful for determination of Ba in sulfide-sulfate ore in spite of its rather short half-time. Figure 1 shows comparison of results of quantitative determination using these three nuclides. Barium content determined by Ba-139 sometimes showed lower values than that determined by Ba-137m (Fig. 1a), which would reflect high background of the peak in the low energy range. Barium content determined by Ba-131 sometimes showed about 10-20 % higher values than that determined by Ba-137m (Fig. 1b), which would reflect high background caused by As-76 included in coexist sulfide minerals.

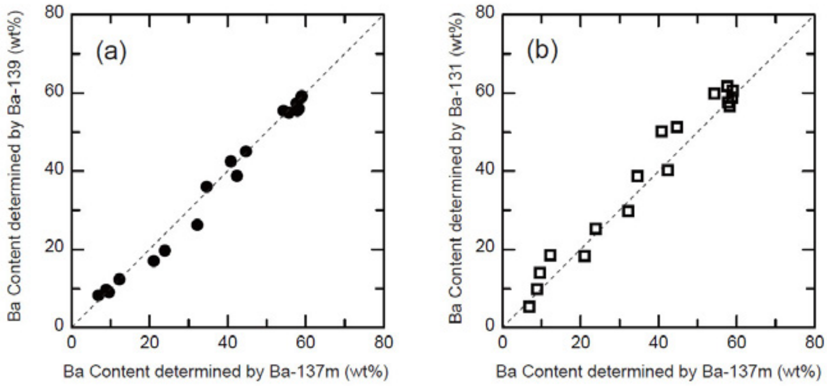

Fig. 1. Comparison of Ba content determined by Ba-131, Ba-137m and Ba-139. (Note that Ba content of pure barite crystal is 58.8 wt%).

CO5-8

Experimental evaluation of shock-induced reactions of carbonate minerals: Implications for understanding environmental change by planetary impacts

Y. Umeda[1, 2], T. Sekine[3], Y. Seto[4], N. Tomioka[5], and T. Okuchi[1,2]

[1]*Institute for Integrated Radiation and Nuclear Science, Kyoto University*
[2]*Graduate School of Engineering, Kyoto University*
[3]*Center for High Pressure Science and Technology Advanced Research*
[4]*Graduate School of Science, Osaka Metropolitan University*
[5]*Kochi Institute for Core Sample Research, X-star, Japan Agency for Marine–Earth Science and Technology*

INTRODUCTION:

Planetary impacts by asteroids and comets can dramatically alter the state of the planetary surface due to their high energy density. Carbonate minerals are the main reservoirs of carbon species (e.g., CO_2 and C) on the Earth's surface, and have significant effects on the carbon cycle and atmospheric circulation in the Earth. To model planetary impacts and evaluate impact-induced environmental changes, we need to understand the shock behavior of carbonate minerals under extreme conditions induced by the impact process. In this study, we aimed to evaluate the shock-induced behavior of calcite ($CaCO_3$), a potential source of CO and/or CO_2. To this end, we experimentally investigated the time evolution of calcite during shock compression and decompression processes using an ultrafast time-resolved X-ray diffraction (XRD) coupled with a laser-driven shock compression system.

EXPERIMENTS:

We conducted the high-power laser shock compression experiments coupled with femtosecond XRD to analyze the structural changes of calcite under high-temperature and high-pressure conditions. Laser-shock XRD experiments were performed in Experimental Hatch 5 at Beamline 3 of the SPring-8 Angstrom Compact Free-Electron Laser (SACLA) facility. The natural calcite crystals used (~1 cm pieces; density, 2.71 g/cm^3) were polished to a thickness of 50 ± 1 μm (~4 mm square plates) and were similar to those used by Umeda et al. (2022) for Hugoniot measurements [1]. We investigated the structural evolution of calcite under shock compression up to 234 ± 19 GPa and during decompression from this peak pressure to ambient pressure conditions. The target was composed of 50-μm thick polypropylene $(C_3H_6)_n$ and a 50-μm thick single crystal of calcite ($CaCO_3$). An optical drive laser pulse with a rectangular shape (5-ns width) and a wavelength of 532 nm was focused onto the polypropylene, which served as an ablator to generate a near-planer shock wave propagating through the calcite crystal. The X-ray free-electron laser (XFEL) probe pulse with a photon energy of 10.0 keV was focused on the target to a spot size of 40 × 13 μm. The XFEL beam was pointed at the calcite (25 μm center of depth). The X-ray diffraction (XRD) detector had a 2θ range of ~20° to ~70°. To estimate the shock velocity and the shock pressure of calcite, velocity interferometer system for any reflector (VISAR) measurements were used to determine the breakout time when the shock wave reached the rear surface of the calcite sample.

RESULTS:

In this study, we analyzed the structural evolution of calcite during shock compression and decompression as a function of time. The XRD results obtained for the nanosecond shocked calcite provided the direct evidence for the transformation of calcite to the amorphous state during the compression stage at shock pressures above 86 ± 7 GPa and during the decompression stage at shock pressure of 33 ± 3 GPa. Additionally, the results obtained for shock-decompressed calcite indicated that its decomposition reaction ($CaCO_3 = CaO + CO_2$) does not occur within the nanosecond shock process [2, 3]. These observations suggests that the shock duration as well as shock pressure and temperature are critical factors that determine shock-induced structural changes [3]. In future, we will conduct shock recovery experiments to investigate the shock-induced deformation structure in post-shock processes.

REFERENCES:

[1] Y. Umeda *et al.,* Review of Laser Engineering, **49** (2021).
[2] Y. Umeda *et al.,* Icarus, **377** (2022).
[3] Y. Umeda *et al.,* Physics and Chemistry of Minerals, in Press.

R6075

CO5-9

NAA and Ar-Ar dating for small-sized meteorite samples

R. Okazaki[1], N. Shirai, and M. Inagaki[2]

[1]*Department of Earth and Planetary Sciences, Kyushu University*
[2]*Department of Chemistry, Kanagawa University*
[3]*Research Reactor Institute, Kyoto University*

INTRODUCTION: Meteorites experienced complicated processed prior to the recovery on the Earth, including thermal metamorphism, aqueous alteration, impacts alteration, and irradiation of energetic particles in space. Timing and physicochemical conditions of these events could be recorded in minor element abundances and Ar-Ar ages of meteorites. We have developed and applied the combination analytical method that enables us to carry out gamma-ray measurements and Ar-Ar dating for the same individual samples of sub-milligram mass (e.g., Projects #R3007, R3038, R3127, and R5006). Through the previous projects, we have measured ordinary chondrites and eucrites (Vesta-derived meteorites). In this project of R6083, we applied this analytical method to Martian meteorites.

EXPERIMENTS: Samples were plagioclase and maskelynite (shock-melt glass) separates prepared from the A12325 Martian meteorite. Grains of orthoclase [1], wollastonite, and sanidine were used as the standard samples. The meteorite samples and our standard samples were placed in a conical dimple (φ1, depth ~ 0.5 mm) of a sapphire disk (φ5.5, 1.5 mm thick), and covered with a sapphire disk (φ5.5, 0.3 mm thick). Each of the sapphire container was wrapped with pure aluminum foil. These Al-wrapped containers were stacked and sealed in the capsules for the Hydro irradiation. The sample irradiation was conducted in October 2024 under our nominal condition (1MW × 47 hours + 5MW × 6 hours). The irradiated samples were recovered and transported to Kyushu Univ. in November after the decays of short-lived nuclides.

RESULTS: Our original plan was to conduct two irradiation experiments for NAA and Ar-Ar dating. However, due to the failure of the mass spectrometer for noble gas isotopes, the analysis scheduled for November could not be performed. In addition, the irradiation planned in early 2025 had to be cancelled. The irradiated samples have been preserved, and we plan to conduct noble gas isotope analysis as soon as possible after the repair of the mass spectrometer is completed.

REFERENCES:

[1] S. Weiss, Mineralien Magasin Lapis., **16** (1991) 13–14.

R6083

CO5-10

Volcanic and Tectonic History of Philippine Sea Plate (South of Japan Revealed by ^{40}Ar/^{39}Ar Dating Technique

O. Ishizuka, Y. Yoshino[1], H. Yoshinaga[1],Y. Iinuma[1],R. Okumura[1], T. Fujii[2]

Geological Survey of Japan, AIST
Graduate School of Science, Kyoto University
1 Institute for Integrated Radiation and Nuclear Science, Kyoto University
2 Graduate School of Engineering, Osaka University

INTRODUCTION: The origin and history of spreading of the West Philippine Basin and its tectonic relation to the adjacent Izu-Bonin-Mariana arc in the Philippine Sea Plate remains poorly-understood. Especially, understanding of the temporal and tectonic relationship between the birth of the Izu-Bonin arc and the West Philippine Basin is critical for reconstruction of Philippine Sea plate tectonics, which closely links to subduction initiation of the Pacific Plate along its margin.

The YK22-11S cruise aimed to investigate the origin and age of magmatism and structure of intersection between the spreading center of the West Philippine Basin (CBF Rift) and the Kyushu-Palau Ridge, i.e., remnant Izu-Bonin-Mariana arc. Two Shinkai6500 submersible dives were conducted in the CBF Rift spreading center. One dive (6K1646) observed an ESE-WNW trending ridge, which might be one of the youngest volcanic features in the rift. This dive recovered sam-ples of basaltic lava flows, quite often showing morphological characteristics of pillow lava. An-other dive (6K1647) in the rift examined a section of the CBF Rise, further west from the inter-section point than the previous dive. This dive again recovered a number of basalt samples of pil-low lava origin and also hyaloclastite. This year we determined ^{40}Ar/^{39}Ar ages for 20 basaltic rock samples which were recovered during the two dives mentioned above.

EXPERIMENTS: Ages of the igneous rocks were determined using the ^{40}Ar/^{39}Ar dating facility at the Geological Survey of Japan/AIST. 10-15 mg of phenocryst-free groundmass, crushed and sieved to 180 – 250 μm in size, was analyzed using a stepwise heating procedure. The samples were treated in 6N HCl for 30 minutes at 95°C with stirring to remove any alteration products (clays and carbonates) present in interstitial spaces. After this treatment, samples were examined under a microscope. Sample irradiation was done either at the Kyoto University Reactor (KUR). The neutron irradiation was performed for 10 h at the hydro-irradiation port under 1 MW operation, where thermal and fast neutron fluxes are 1.6×10^{13} and 7.8×10^{12} n/ cm^2 s, respectively, or for 2 h under 5 MW operation, where thermal and fast neutron fluxes are 8.15×10^{13} and 3.93×10^{13} n/cm^2 s respectively. Argon isotopes were measured in a peak-jumping mode on an IsotopX NGX noble gas mass spectrometer fitted with a Hamamatsu Photonics R4146 secondary electron multiplier.

RESULTS: 10 samples from the dive 6K1646 show age range between 28.3 and 30.9 Ma. These samples show geochemical variation with age, which shows enrichment in incompatible elements and radiogenic isotopes with time from relatively depleted MORB like composition. These data can be interpreted to show magmatic process at the last stage of spreading or rifting along the spreading center. As the extension along the spreading center was wanning, degree of mantle melting decreased, which causes increase in content of the incompatible elements and also preferential melting of mantle domain enriched in radiogenic isotopes. On the other hand, 10 samples from the dive 6K1647 show age range between 31.5 and 33.1 Ma, clearly older than those from 6K1646. Source of these basalts are estimated to have more enriched mantle, with similarity to EM-2 mantle component. These temporal geochemical variations discovered along the CBF Rift spreading center can be used to decipher processes when the seafloor spreading center approaches and clashes with volcanic arc.

R6093

CO5-11

Amorphization of $NaAlSi_3O_8$ feldspar by shock compression

N. Tomioka[1], T. Okuchi[2], Y. Umeda[2]

[1]*Kochi Institute for Core Sample Research, Japan Agency for Marine-Earth Science and Technology*
[2]*Institute for Integrated Radiation and Nuclear Science, Kyoto University*

INTRODUCTION: Strongly-shocked stony meteorites record hypervelocity collision events on their parent asteroids. Such meteorites often contain $NaAlSi_3O_8$-rich feldspar (albite) as a major mineral constituent. Based on X-ray diffraction and infrared spectroscopy of samples from laboratory shock experiments, it has been shown that albite begins to metastably transform into dense glass at ~34 GPa and completes at ~45 GPa [1-2]. This process is one of the indicators of the shock pressure, but the microstructural changes of albite during amorphization and the structure of the dense glass have not been sufficiently investigated. For a detailed understanding of the pressure-induced amorphization, we demonstrate shock recovery experiments of albite and X-ray diffraction (XRD) and transmission electron microscopy (TEM) of the recovered samples.

EXPERIMENTS: Single crystals of albite were processed into thin sections with smaller than 10 mm in size and with 1.0 mm in thickness. Each section was placed into a stainless steel (SUS304) container, and shock loaded using a single-stage propellant gun at 12 GPa (Shot1) and 29 GPa (Shot2). In one of the shots, the space between the inner wall of the container along the compression axis and the sample was filled with Al powder, to obtain a higher cooling rate than the shots without Al power, shocked at 29 GPa (Shot3). The central portions of the recovered thin section samples were first observed by TEM operated at 200 kV accelerating voltage, and then analyzed by XRD (Rigaku Ultima IV) at 1.6 kW X-ray power.

RESULTS: Under TEM, the Shot1 sample does not show any deformation and transformational features. Meanwhile, the Shot2 sample is mostly amorphized. Relict plagioclase crystal appears as thin lamellae less than 1 μm thick. Electron diffraction patterns show that the lamellae are oriented on the (010) plane of albite. The Shot3 sample shows the same microstructure as Shot2. These results suggest that the onset pressure of amorphization of albite is lower than 34 GPa which value was previously estimated by bulk sample analysis, regardless of the cooling rate after shock heating.

Shot1 and 2 were also analyzed by XRD. Both of the samples show broad First Sharp Diffraction Peak（FSDP）at ~0.2 ($Å^{-1}$). The FSDP of Shot #2 is 0.006 ($Å^{-1}$) greater than that of Shot1, indicating a denser glass structure. The results suggest that the FSDP shift is a potential indicator of shock pressure.

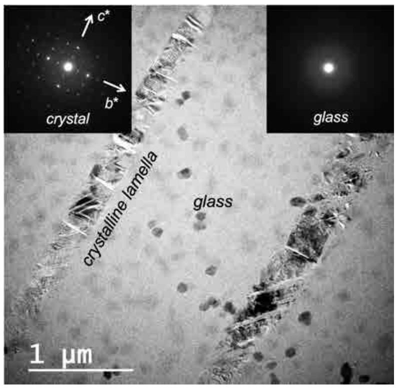

Fig. 1. TEM image of albite shocked at 229 GPa.

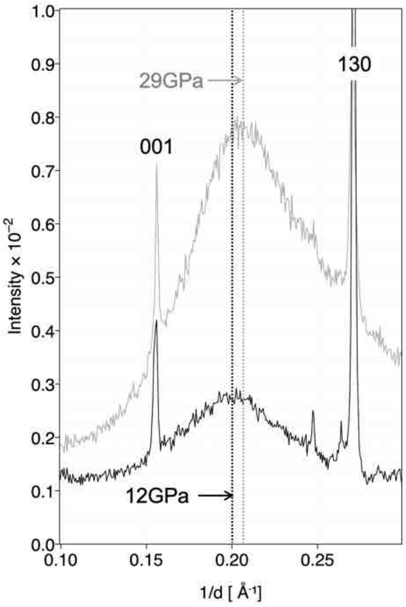

Fig. 2. XRD patterns of albite shocked at 12 and 29 GPa. Sharp diffraction peaks are due to weakly shocked part of albite at the edges of the sample.

REFERENCES:

[1] R. Ostertag *et al.*, J. Geophys. Res., **88** (1983) 364–376.
[2] D. Stöffler *et al.,* Meteorit. Planet. Sci., **53** (2018) 115–120.

CO5-12

Evaluation of Cs and Sr dynamics in forest ecosystems

Y. Shimada, Y. Motoie, M. Yoneda, S. Fukutani[1], M. Ikegami[1]

Graduate School of Engineering, Kyoto University
[1]Institute for Integrated Radiation and Nuclear Science, Kyoto University

INTRODUCTION: Forests contaminated by radionuclides released in the Fukushima Daiichi nuclear accident have yet to be decontaminated except for an area about 20 meters from the forest edge and there are areas of high air dose rates scattered throughout the forest. Because forests make up about 70% of Fukushima Prefecture, decontamination of forests more than 20 meters from the forest edge is necessary to reduce the air dose rate in the forests and restore life and industry surrounding the forests. But it is impossible to decontaminate the entire forest. In this study, in order to consider the feasible scope and methods of decontamination according to local conditions, we aim to develop a model that can quantitatively evaluate behavior of radioactive Cs and Sr in forest ecosystem. This year, we measured Cs in forest slope soil, analyzed the movement of Cs in the slope soil through experiments. The results of the measurement and experiment were reflected in the parameter values of our previous developed model for the transport of radioactive Cs in the forest slope and air dose rate estimation model.

EXPERIMENTS: We measured the distribution of Cs concentration in forest slope soil collected from Mt. Mari in Kawauchi Village, Fukushima Prefecture on Nov. 1, 2024. The results show that the concentration does not simply increase the further down the slope, is the highest in the 0-5 cm layer and the second highest in the 5-10 cm layer.

A Soil column was constructed using the above soils. The equipment is shown in Fig.1. The simulated rainfall was applied to it and measure the runoff rate of Cs on the soil slope.

Using the measurement data obtained in the experiment, Cs runoff rate in the surface slop soil was calculated to be 6.93×10^{-9} s^{-1}.

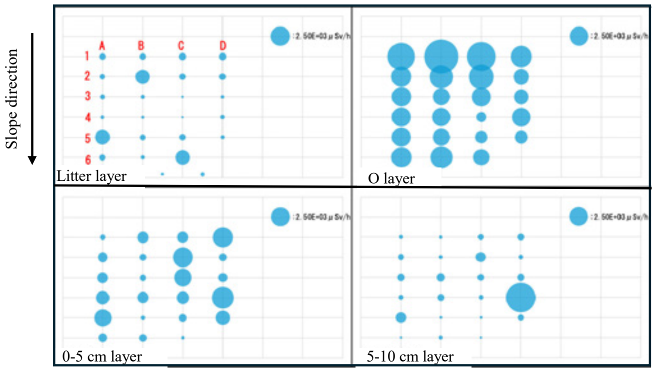

Fig. 1. Measurement results of Cs concentration in soil

RESULTS: The results of the measurement and experiment were reflected in the parameter values of our previous developed model for the transport of radioactive Cs in the forest slope and air dose rate estimation model. As a result, we could roughly reproduce the measured Cs concentration in the slope soils by model calculation. Using the calculated Cs concentration in soil, future air dose rate in the monitored area were also simulated using our previous air dose rate estimation model.

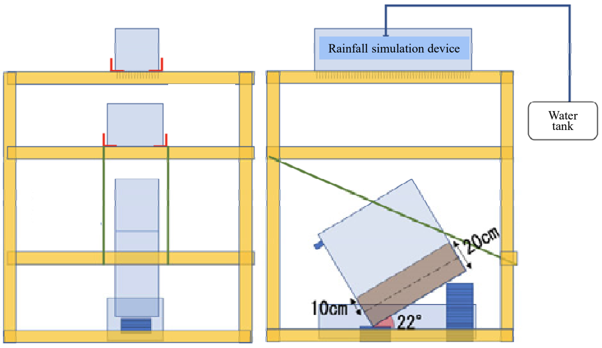

Fig. 2. Experimental equipment

REFERENCES:

[1] Y. Motoie *et al.,* The 13th Environmental Radiation Decontamination Research Conference S1-3, Iwaki City, Fukushima Pref., Japan (2024).

CO5-13

Fission Track Analysis of Fissile Material in Fallout Sample Collected on Daigo Fukuryu Maru

K. Takamiya, M. Ikegami and Y. Igarashi

Institute for Integrated Radiation and Nuclear Science, Kyoto University

INTRODUCTION: In the event of nuclear weapon explosions or nuclear disasters, particles originating from nuclear fuels are formed under conditions of high temperature and high pressure. During the Fukushima Daiichi Nuclear Power Plant accident, particles containing high concentrations of radioactive Cs have been discovered in environmental samples [1, 2]. Analysis of these particles provides important information for estimating the conditions inside the reactors. We have developed a method for detecting particles containing high concentrations of fissile substances such as ^{235}U and ^{239}Pu in environmental samples. This detection method combines fission track analysis using a research reactor with heavy liquid separation [3]. In the previous work, we analyzed soil samples presumed to contain fallout materials from the Hiroshima atomic bomb using this method. It was found that fission track analysis with appropriate neutron irradiation conditions could clearly distinguish particles originating from the A−bomb from natural uranium in the environment [4]. However, these particles could not be identified and analyzed using a SEM because their size was smaller than the spatial resolution of the SEM used in that study. This study aims to detect fallout particles containing fissile material, focusing on the detection of larger particles, by analyzing radioactive fallout samples from the Bravo nuclear weapon test.

EXPERIMENTS: The fallout sample, mixed with rust, was collected from a drum can placed on the Daigo Fukuryu Maru. After the sample was spread on the medicine wrapping paper, distribution of the radioactive isotopes was observed by autoradiography. Most of the sample was then collected in a sample container. Small particles remaining on the surface of the paper were subsequently collected on a paraffin film by pressing the film against it. The fission track detector was wrapped in the paraffin film so that the collected particles were in contact with the detector, and then irradiated with approximately 3×10^{12} n/cm^2 of thermal neutrons using the pneumatic irradiation facility (TC-Pn) at Kyoto University Research Reactor. After irradiation, the track detector was etched, and the resulting tracks were observed using an optical microscope.

RESULTS: The image of the radioactive material distribution obtained by autoradiography indicated that the radioactive fallout in the sample was not homogeneous, as there was no correlation between particle size and radioactivity. Observations of the detector surface revealed multiple clusters of tracks. Similar analysis of soil samples collected in Hiroshima also detected clusters of tracks. These clusters are thought to have been produced by fine particles containing high concentrations of enriched uranium derived from the atomic bomb. In this study, the number of tracks in each cluster ranged from tens to hundreds. Furthermore, the ratio of the number of tracks to the irradiated neutron fluence was similar to those observed for Hiroshima soil samples. This indicates that the radioactive fallout collected on the Daigo Fukuryu Maru contains fissile material at a level comparable to that in the enriched uranium particles derived from the atomic bomb. Based on the observed track distribution, the particle size is estimated to be smaller than several μm. Future analysis of the samples using SEM/EDX will be conducted to examine their appearance and elemental composition.

REFERENCES:

[1] K. Adachi *et al.,* Scientific Reports, **3** (2013) 2554.
[2] Y. Satou *et al.,* Geochemical Journal, **52** (2018) 137.
[3] K. Takamiya *et al.,* KURNS Progress Report 2022 (2023) 134.
[4] K. Takamiya *et al.,* KURNS Progress Report 2023 (2024) 163.

R6129

CO5-14

Three halogens (Cl, Br, and I) in mantle-derived samples

N. Shirai, M. Ebihara[1] and H. Yoshinaga[2]

Faculty of Science, Kanagawa University
[1]Department of Chemistry, Tokyo Metropolitan University
[2]Institute for Integrated Radiation and Nuclear Science, Kyoto University

INTRODUCTION: Among the four halogens, F, Cl, Br, and I are present in the environment as stable elements. Halogens are highly mobile, volatile, and incompatible elements in a range of geochemical processes. Due to their chemical characteristics, these elements have been widely used to trace the water cycle in subduction zones, understand the mechanism of magma degassing, and evaluate the recycling of solid earth materials in the crust and mantle. Despite the importance of halogens in geochemical processes, the determination of halogens in geological samples is scarce. The reason for this is the difficulty in determining these elements due to their volatility and low concentrations in geological samples. In the previous studies [1,2], USGS and GSJ geochemical reference materials were analyzed by both instrumental neutron activation analysis (INAA) and radiochemical neutron activation analysis (RNAA) to evaluate the accuracy of RNAA data. In this study, we analyzed mantle-derived samples to evaluate the applicability of our RNAA procedure to geological samples.

EXPERIMENTS: Two MORB samples were analyzed in this study. Together with these two MORB samples, USGS geochemical reference samples (BCR-2 and DTS-2b) also analyzed as control samples. The analytical procedure of RNAA is described in Ebihara et al. [1]. Samples were weighed into plastic vials and an appropriate amount of each halogen standard solution dropped on a filter paper was sealed in polyethylene as halogen reference samples. Both of these were irradiated for 20 min at the Kyoto University Research Reactor Institute. Know amounts of three halogens and Mn carriers were added into a Ni crucible with the irradiated reference materials and then were fused in NaOH. The fuse cake was digested in water, and a hydroxide precipitate was removed from the supernatant, which contained the halogens. After acidification of the supernatant, iodine was precipitated as PdI_2, and Cl and Br were precipitated as a mixture of AgCl and AgBr precipitates. These precipitates were subjected to the measurement of ^{128}I, ^{38}Cl, and ^{82}Br. The chemical yields of the three halogens during radiochemical separation were determined using the reactivation method. To correct the effects of neutron flux gradient and neutron attenuation, samples were sandwiched by a reference standard, which was prepared by dropping a known amount of I standard solution on a filter paper.

RESULTS: For the geochemical reference materials (BCR-2 and DTS-2b), our RNAA data of the three halogens (Cl, Br, and I) were consistent with those reported in the previous study [1], confirming that our RNAA values in this study are reliable. The two analyzed MORB samples have similar trace element abundances such as REE to each other, while significant differences in the three halogens can be seen. One of the MORB samples has approximately ten times higher abundances of Cl and Br compared with the other. A similar trend cannot be seen in I. In a plot of Br/Cl vs. I/Cl, our two MORB samples are plotted on the trend observed from the previous study [3]. The sample with higher Cl and Br abundances shows a lower I/Cl ratio compared with the other MORB samples. This lower I/Cl ratio indicated that this sample was contributed by seawater.

REFERENCES:

[1] M. Ebihara *et al.,* Geostand. Geoanal. Res., **47** (2023) 931-944.
[2] N. Shirai *et al.,* Minerals, **14** (2024) 1213.
[3] Kendrick *et al.,* Geochim. Cosmochim. Acta, **123** (2013) 150-165.

R6133

CO5-15

Noble gases and halogens in serpentinite-related metasomatic rocks in the Cretaceous Sanbagawa metamorphic belt, SW Japan

H. Sumino, K. Aida[1], S.R. Wallis[1], H. Kawamura, H. Yoshino[2], Y. Iinuma[2], H. Yoshinaga[2] and R. Okumura[2]

Research Center for Advanced Science and Technology, University of Tokyo
[1]Department of Earth and Planetary Science, University of Tokyo
[2]Institute for Integrated Radiation and Nuclear Science, Kyoto University

INTRODUCTION: Since some of the halogens (fluorine, chlorine, bromine, and iodine) are converted to corresponding noble gas isotopes by neutron irradiation and detection limits for noble gas isotopes by mass spectrometry are low (down to ten thousand atoms), they can be analyzed with high sensitivity by using neutron irradiation and noble gas mass spectrometry [1]. Deep earthquakes are generally recognized where subducting oceanic plates are in contact with the shallow mantle. High fluid pressure is commonly invoked as an essential factor in the generation of slow earthquakes, and the associated fluids are thought to be derived from the breakdown of hydrous minerals such as chlorite and serpentine in the subducting slab and the base of the mantle wedge. When considering how such fluids may cause earthquakes, it is crucial to consider both the quantities and fluid paths. Serpentinite developed along the base of the mantle wedge may act as an effective channel for the fluids along the subduction boundary. Numerous serpentinite bodies are exposed throughout the Sanbagawa belt. We analyzed noble gases and halogens in the two separate kilometer-scale serpentinite bodies, the Shiraga Yama (SY) and Kamabuse Yama (KY) bodies, which ascended from depths of ~35 km and ~25 km, respectively [2], to help identify the source of fluids related to hydration and material transport.

EXPERIMENTS: The samples of 5-50 mg each and standards for neutron fluence were wrapped with aluminum foil and put in aluminum capsules of ϕ10 mm x 30 mm. The capsules were irradiated with neutrons in KUR. After the irradiation, the samples were sent to the University of Tokyo. The samples were loaded into an ultra-high-vacuum, noble gas extraction, purification, and separation line. Noble gases were extracted from the samples by heating up to 1800°C, purified with hot Ti-Zr getters, separated into each noble gas with temperature-controlled cold traps, and then their isotope compositions were determined with a noble gas mass spectrometer [1]. The thermal and fast neutron flux was estimated from the production of ^{39}Ar and ^{38}Ar from ^{39}K and ^{37}Cl in the Hb3gr hornblende standard, in which K and Cl contents have been determined.

RESULTS: The results for KY are more complex, with distinct fluids responsible for serpentinization (1) and metasomatism (2). The metasomatism can be further divided into a chlorite-forming stage (2-1) and a later talc-forming stage (2-2). The sources for the fluids involved in each of these stages were likely derived from (1) altered oceanic crust, (2-1) altered oceanic crust + sedimentary porosity, and (2-2) sedimentary porosity + serpentinized slab. Combining the results from SY and KY suggests that channeling of subduction fluids in the Sanbagawa subduction zone was important at depths of around 35 km, which is consistent with the observation of subduction fluids in the Higashi-akaishi peridotite body exhumed from a depths of 100 km [3]. On the other hand, although the fluid channel was less effective at shallower levels, it was possible to rise close to the surface, as preserved in the subduction mélange in the Shimanto accretionary complex [4]. The change in the source region of the fluids with time, as shown in KY, suggests fluid flow may become more channelized as a shear zone develops along the subduction interface.

REFERENCES:

[1] M. Kobayashi *et al.,* Chem. Geol., **582** (2021) 120420.
[2] H. Kawahara *et al.,* Lithos, **254-255** (2016) 53-66.
[3] H. Sumino *et al.,* Earth Planet. Sci. Lett., **294** (2010) 163-172.
[4] N. Nishiyama *et al.,* Earth Planet. Sci. Lett., **538** (2020) 116199.

R6149

CO5-16

Validation of acid compounds by simulating a model screen (made of red copper leaf)

T. Mukai[1,2], N. Toe[1], Y. Shibahara[1], M. Ikegami[1], H. Yashima[1], S. Fukutani[1], K. Takamiya[1],
T. Adachi[1,3], and Y. Igarashi[1]

[1]*Institute for Integrated Radiation and Nuclear Science, Kyoto University,*
[2]*Osaka Metropolitan University*
[3]*ATOX Co., Ltd*

INTRODUCTION: Analyses by using SEM and XRD of the “Black Rain” traces on a gold folding screen (red copper leaf: copper alloy foil containing zinc), discovered in Hiroshima in 2022, showed that copper sulfate hydrate was presumed to be mixed. However, copper nitrate compounds were undetectable. Therefore, we conducted a simulation experiment of a model screen using sulfuric acid and nitric acid, being contained in the “Black Rain,” to verify the results.

EXPERIMENTS: After dropping 20 μℓ of pH 1 solution containing sulfuric acid, nitric acid, and mixed acids of both in Chinese ink on a model screen piece "RSY-001" (red copper leaf), each dissolved part was observed with an optical microscope and analyzed with a fully automated X-ray diffractometer (Rigaku SmartLab Cu Kα source, tube voltage 40 kV, tube current 200 mA, micro-incident optics, scan speed 0.5°/min) in 10 days and 4 months exposed indoors.

RESULTS: The black traces were observed under an optical microscope (reflected light/transmitted light images; Fig. 1), and dissolution of the red copper leaf was observed in both light images. Analysis by XRD of the samples after 10 days of the experiment revealed copper sulfate hydrate peaks in the case of sulfuric acid, and copper nitrate compound-derived peaks in the case of nitric acid (Fig. 2). The XRD analysis of the samples exposed for 4 months showed that the peaks decreased in all cases, and in the case of the mixed acid, the copper sulfate hydrate peak remained, but the one from the copper nitrate became minute. The copper nitrate compound could not be detected owing to its deliquescence [1].

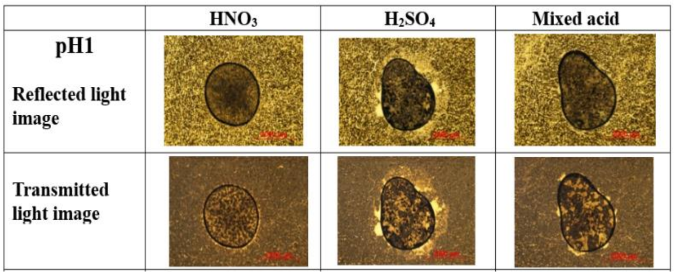

Fig. 1. Reflected and transmitted light images of a model screen after dropping acid solutions.

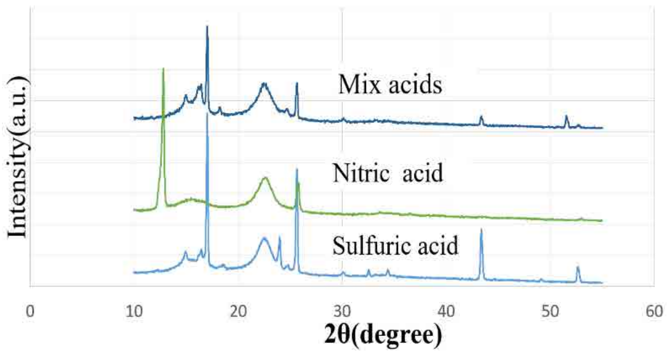

Fig. 2. XRD spectra of products of model screens.

REFERENCES:[1] H. Suzuki., Encyclopedia of Nitrogen Oxides, Maruzen, Tokyo (2008).

ACKNOWLEDGMENTS: We are grateful to the staff of the Hiroshima Peace Memorial Museum, especially the curatorial staff and the donor for permission to cut the gold folding screen. We thank Rekiseisha Co., Ltd. for a model screen. Lastly, Prof. Takuo Okuchi, KURNS is acknowledged for his guidance in the XRD analysis.

CO6-1

Development of Boron Cluster-Loaded Nanoparticles for BNCT

A.B. Fithroni, S. Zhou, T.F.N. Hakim, T. Tada, M. Suzuki[2], Y. Sakurai[2], N. Yamada[3], K. Watanabe, T. Ohtsuki, and E. Matsuura[1,4]

Department of Interdisciplinary Science and Engineering in Health Systems, Okayama University
[1]Collaborative Research Center for OMIC, Graduate School of Medicine, Dentistry, and Pharmaceutical Sciences, Okayama University
[2]Institute for Integrated Radiation and Nuclear Science, Kyoto University
[3]Nihon Fukushi Fuiin Holding, Co., Ltd.
[4]Neutron Therapy Research Center (NTRC), Okayama University

INTRODUCTION: Boron neutron capture therapy (BNCT) is a less-invasive nuclear therapeutic approach that highly selective to induce cancer apoptosis, without any cytotoxic effects in neighboring cells [1]. BPA and BSH as current clinically approved boron compounds have several limitations related to selectivity and effectivity [2]. To address the issues, a novel self-forming nanoparticle, which is consisted of biodegradable polymers, namely, “Lactosome” with a hydrophobic boron cluster have been developed [3]. In the previous study, the BNCT effects were successfully obtained after exposing neutron irradiation to the AsPC-1 cells (human pancreatic cancer cells) in vitro and in vivo [4]. In this study, we compared in vitro BNCT effect on a boron cluster loaded with different type of Lactosome “type 1” and “type 2” particles.

EXPERIMENTS: For in vitro study, AsPC-1 cells were subjected to irradiation at reactor power 1 MW for 10 min or 40 min after 2 hr incubation with boron cluster-loaded Lactosome particles. After the neutron irradiation, the cells were cultured in 12-well plates and incubated under 5% CO_2 at 37 °C for 14 days. Then, colony formation assay was performed after staining.

RESULTS: In vitro irradiation showed that Lactosome loaded with boron cluster significantly inhibited the AsPC-1 cells growth. Interestingly, Lactosome “type 1” particles loaded with boron cluster showed significant inhibition as compared to Lactosome “type 2” ones loaded with boron cluster after irradiation for 10 min. Moreover, both types of Lactosome particles loaded with boron cluster respectively showed remarkable inhibition of cancer cells at 40 min. Overall, in vitro irradiation study showed that both type of Lactosome loaded with boron cluster respectively are promising candidates for BNCT.

Table 1 In vitro inhibitory effect of AsPC-1 cells treated with Lactosome particles loaded with boron clus-ter.

Group	Colony formation rate		
	0 min	10 min	40 min
Control (DPBS)	1	0.82 ± 0.14	0.42 ± 0.08
Lactosome "type 1"	1	0.90± 0.09	0.33± 0.04
Lactosome "type 2"	1	1.00± 0.12	0.42± 0.04
Lactosome "type 1" loaded with boron cluster	1	0.03± 0.05	0.03± 0.02
Lactosome "type 2" loaded with boron cluster	1	0.25± 0.09	0.01± 0.00

REFERENCES:

[1] M. Suzuki. Int. J. Clin. Oncol., **25** (2020) 43-50.
[2] J.H. Goodman*et al.,* Neurosurgery, **47** (2000) 608-621.
[3] A.B. Fithroni *et al.,* Cells, **11** (2022) 3307.
[4] A.B. Fithroni *et al.,* Cells, **14** (2025) 60.

R6005

CO6-2

Mechanism of amyloid fibril formatin by serum amyloid protein A

T. Okunishi[1], K. Morishima[2], R. Inoue[2], M. Sugiyama[2] and M. Hoshino[1]

[1]*Graduate School of Pharmaceutical Sciences, Kyoto University*
[2]*Institute for Integrated Radiatio n and Nuclear Science, Kyoto University*

INTRODUCTION: Systemic amyloidosis is the protein-misfolding disease characterized by the deposition of amyloid fibril-forming proteins in multiple organs. Fibril formation by serum amyloid A (SAA), 104 amino acid residue protein, could cause systemic AA amyloidosis. SAA is a kind of apolipoprotein, which contribute to the formation of high-density lipoprotein (HDL), and plays a vital role in the transport of lipids and cholesterol in the blood. The HDL is mainly composed of apolipoprotein AI (apoA-I), and the concentration of SAA is usually low (≤ 10 μg/mL). However, in the acute phase, its serum level increases approximately 1000-fold under the action of inflammatory cytokines. The remarkable elevation of its serum level is considered to a risk factor of amyloid deposition.

EXPERIMENTS: The fusion protein of histidine-tagged ubiquitin and serum amyloid A (H6UbSAA), and yeast ubiquitin hydrolase-1 (YUH-1) were expressed by Escherichia coli strain BL21(DE3)-Gold. The protein expression was induced by isopropyl b-D-thiogalactopyranoside (IPTG). The protein was purified with histidine affinity chromatography, followed by the proteolytic digestion at the C-terminus of ubiquitin by YUH-1. The digested purified by reverse-phase HPLC with a linear gradient of acetonitrile, and SAA moiety was collected. Circular dichroism (CD) spectra were measured using Jasco J-820 spectropolarimeter with 1-mm light path length at protein concentration of 20 μM. Amyloid fibrillation was monitored as the increase in fluorescence of thioflavin T (ThT). After the incubation of protein at 20 μM and 37°C for the indicated time, an aliquot (66.7 μL) was added to 1.93 mL of 5 μM ThT. Fluorescence at 490 nm was measured at an excitation wavelength of 446 nm on a Shimadzu RF-5300 spectrofluorometer.

RESULTS: We analyzed the secondary structure of SAA at 4°C and 37°C by far-UV CD spectroscopy (Figure 1A). The spectrum at 4°C showed typical double minima at 222 and 208 nm, suggesting that the protein assumed mostly α-helical conformations. On the other hand, the spectrum recorded at 37°C was significantly different from that at 4°C and the signal intensity decreased significantly. Next, we examined the amyloid fibril formation by SAA1 at 4°C and 37°C (Fig1B). We found that the protein spontaneously formed ThT-active aggregates at 37°C. On the other hand, such a spontaneous fibril formation was not observed at 4°C. The results suggested that the fibril formation was closely related to the structure of the protein, and the loss of α-helical secondary structure seems to be the prerequisite for amyloid fibrillation by SAA1.

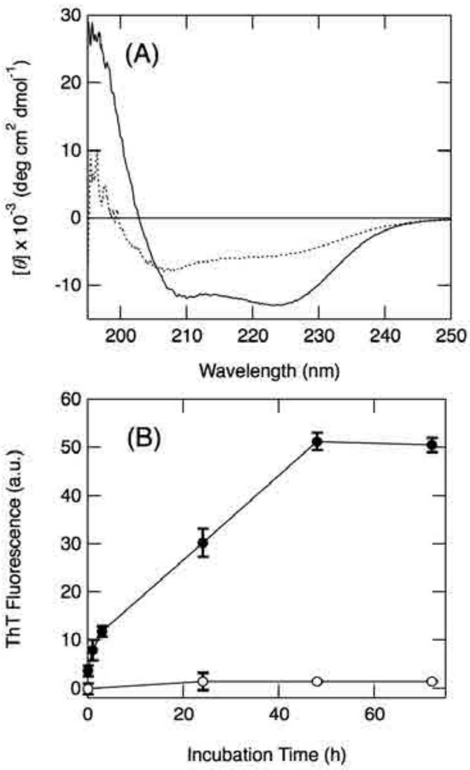

Fig. 1 (A) Far-UV CD spectra of SAA1 at 4°C (solid) and at 37°C (dotted) (B) Change in the ThT-fluorescence after the incubation at 4°C (open cicle) and at 37°C (closed circle)

R6008

CO6-3

Multi Element Neutron Activation analysis in the Gum Samples of the Diet of Small Primates

M. Fukushima, Y. Iinuma[1], H. Imai[2], Y. Tsuji

Faculty of Science and Engineering, Ishinomaki Senshu University
[1]Institute for Integrated Radiation and Nuclear Science, Kyoto University
[2]Center for the Evolutionary Origins of Human Behavior, Kyoto University

INTRODUCTION: Calcium is one of the essential ion to make bone and reproductive physiology of animals. Callithrix primates tend to consume plant extrudes which is known as high calcium. In this study four different natural gum samples and Arabic gum sample (purchased) were analyzed by neutron activation analysis (NAA) for eight element levels in them. Calcium levels were compared with the results obtained by colorimetric method.

EXPERIMENTS: Four different gum samples were extracted from Siniguena (Spondias purpurea), Barauna (Schinopsis brasiliensis), Algaroba (Prosopsis juliflora), and Ansico (Anadenanthrera macrocarpa). Gum samples except Arabic gum sample were extracted, freeze dried, and pulverized for further experiment. One portion of dried power was supplied for short irradiation in KUR. Eight elements of Ca, Cl, Cu, K, Mg, Mn, Na, and V were analyzed by the condition of TcPn irradiation (1.5 min. irradiation, 3.0 min. cooling, 10 min gamma counting by Ge detector with Compton suppression system). Colorimetric method for analyzing calcium was done by using QuantiChrom Assay kit (BioAssay Systems), absorbance at 612 nm of gum sample aquatic solutions were measured, and Ca levels were calculated from the standard curve.

RESULTS: Elemental levels obtained for the gum samples are shown in Table 1. Also, levels of Ca in the gum samples are shown in Fig. 1. There are variations of the Ca concentration between the gums. Interestingly, some of the gum (A, D) showed higher concentration when measured by NAA compared to the results of colorimetric method.

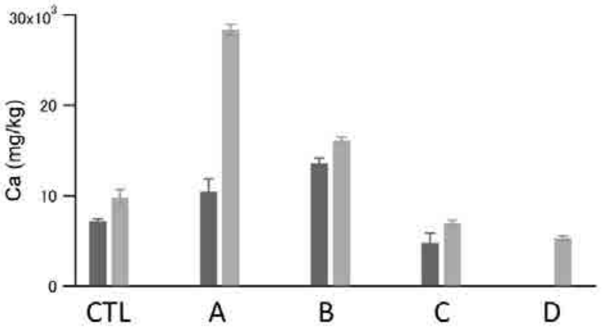

Fig. 1. Ca levels in the gum samples measured by the methods of chrorimetric (black) and neutron activation analysis (gray). CTL sample is Arabic gum, and natural gums from (A) Siniguena (*Spondias purpurea*) (B) Barauna (*Schinopsis brasiliensis*) (C) Algaroba (*Prosopsis juliflora)* (D) Ansico (*Anade-nanthera macrocarpa*) are shown.

Table 1. Elemental levels in gum samples (unit: mg/kg, dry weight).

	Mg	Cu	Na	V	K	Cl	Mn	Ca
Arabic gum	2390				9310			9760
Siniguela	1850		226	0.19	1140	128		28400
Barauna	1760		91		2490		39.7	16100
Algaroba	1020	22	474		9230	1090	38.0	7010
Ansico	627		153		7650		20.7	4320

These results suggest the presence of insoluble fraction of Ca in some gum which would appear after the fermentation of gum in the cecum.

REFERENCES:

[1] M. L. Power S D Tardif, D G Layne, J Schulkin, Am. J. Primatol., **47** (1999) 255-261.

[2] H. Imai, N. Suzuki, Y. Ishimaru, T. Sakurai, L. Yin, W. Pan, K. Abe, T. Misaka, H. Hirai, Biology letters, **8** (2012) 652-656.

[3] Y. Maruyama, R. Yasuda, M. Kuroda, Y. Eto, PLoS ONE, **7** (2012) e3448.

CO6-4

Quantitative Determination of a Neutron-sensitizing reagent, *p*-Borono-L-phenylalanine (BPA), Absorbed in Rice Seeds by Prompt Gamma-Ray Analysis

Y. Hattori, T. Kinouchi[1], S. Segami[2], and M. Kirihata

Research Center of Boron Neutron Capture Therapy, Osaka Metropolitan University, Japan
[1] Institute for Integrated Radiation and Nuclear Science, Kyoto University, Japan
[2] Research Institute of Environment, Agriculture and Fisheries, Osaka Prefecture, Japan

INTRODUCTION: In boron neutron capture therapy (BNCT), the efficient absorption of boron-10 (^{10}B) compounds, as neutron sensitizers, by tumor cells determines their clinical effect. BPA, *p*-borono-L-phenylalanine, is a primary ^{10}B compound in BNCT because it effectively delivers to tumor cells and induces DNA double-strand breaks (DSBs) in the cells by the BNC reaction. In recent studies, we have attempted to apply these properties of the combination of BPA and BNC reaction to crop breeding. In the case of BNCT, the induction of a large number of DSBs produces an anti-tumor effect, but if a small number of DSBs is generated, it leads to genetic mutation, which implies selective breeding. Therefore, we first attempted to absorb BPA in rice seeds and measure the amount of absorbed BPA by prompt gamma-ray analysis.

EXPERIMENTS: Preparation of BPA-absorbed rice seeds> Unhulled rice seeds were immersed in BPA solution (300 ppm) for 24 hours. After drying, the rice seeds were solubilized sequentially by dry and wet ashing treatments. Dry ashing was performed in an electric oven at 550°C for 5 hours. For wet ashing, the ashed samples were placed in a mixture of 68% (w/w) nitric acid and 30% (w/w) hydrogen peroxide water at 7:3 and decomposed using MARS 6, a microwave digestion system, at 210°C for 30 minutes.
Prompt gamma-ray analysis for ^{10}B determination in BPA-absorbed rice seeds > Solubilized rice seeds were irradiated by thermal neutrons during 600 sec at E-3 irradiation port of KUR under 5 MW operation to demonstrate the measurement of 478 keV prompt gamma rays.

RESULTS: After preparing a calibration curve of the ^{10}B concentration by boron standard solution, the concentration of ^{10}B in the blank group, consisting of only ultrapure water, the control group, in which only ultrapure water was absorbed by unhulled rice seeds, and the experimental group, in which BPA was absorbed, was measured by E-3 irradiation port. As shown in Table 1, all measured values were negative in the control group, and in some cases, the values were also negative in the BPA-treated group. This phenomenon was observed repeatedly, even when the BPA concentration was increased to 1,000 ppm. On the other hand, because alpha-ray autoradiography using CR-39, a solid-state nuclear tracking detector, visualizes that BPA absorbed by rice seeds accumulates in their embryo and outer coat, there is no doubt that the rice seeds absorb BPA (cf. R6142). Therefore, some obstacles might exist in measuring the ^{10}B concentration in the rice seeds by prompt gamma-ray analysis.

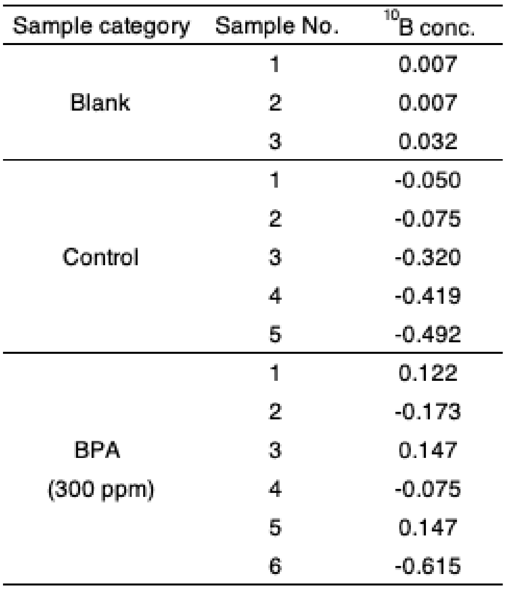

Sample category	Sample No.	^{10}B conc.
Blank	1	0.007
	2	0.007
	3	0.032
Control	1	-0.050
	2	-0.075
	3	-0.320
	4	-0.419
	5	-0.492
BPA (300 ppm)	1	0.122
	2	-0.173
	3	0.147
	4	-0.075
	5	0.147
	6	-0.615

Table 1. ^{10}B concentration in rice seeds: Each sample's estimated ^{10}B conc is in ppm. Sample No. indicates several independent trial samples.

CO6-5

Structural analysis of surfactant-induced α-synuclein protofibrils by small-angle X-ray scattering combined with analytical ultracentrifugation

S. Kitano, K. Morishima[1], R. Inoue[1], M. Sugiyama[1], E. Chatani

Graduate School of Science, Kobe University
[1]Institute for Integrated Radiation and Nuclear Science, Kyoto University

INTRODUCTION: Amyloid fibrils are protein aggregates involved in amyloidoses and neurodegenerative diseases. In the early stages of their formation, oligomers and protofibrils have been identified, particularly in neurodegenerative diseases. These aggregates are suggested to be the main culprits of cellular toxicity rather than mature amyloid fibrils; however, their physicochemical properties have still been awaiting clarification. Referring to a previous report [1], we have focused on the formation of α-synuclein protofibrils in the presence of sodium dodecyl sulphate (SDS) and investigated their structural properties by using small-angle X-ray scattering (SAXS) and analytical ultracentrifugation (AUC).

EXPERIMENTS: A recombinant α-synuclein protein was prepared and dissolved at a final concentration of 2.0 mg/mL in 25 mM Tris-HCl buffer (pH7.4) containing 100 mM NaCl, 1 mM ethylenediamine-N,N,N',N'-tetraacetic acid, and 0.5 mM SDS. The sample was incubated at 37 °C for 24 hours in quiescence to proceed the formation of protofibrils. The samples were then subjected to SAXS and AUC measurements to investigate the size distribution and averaged shape of the aggregates formed. SAXS profiles were measured at 25 °C and 30-minute exposure time by a NANOPIX equipped with a HyPix-6000 (Rigaku Corporation). A Cu K-α line (MicroMAX-007HFMR) was used as a beam source, which was further focused and collimated with a confocal multilayer mirror (OptiSAXS). AUC data were obtained at 25 °C and 40000 rpm with a ProteomeLab XL-I analytical ultracentrifuge (Beckman Coulter) and analyzed using SEDFIT based on a sedimentation velocity protocol.

RESULTS: The SAXS profile of the protofibril sample exhibited a characteristic scattering pattern with intensity intermediate between those of monomers and of amyloid fibrils (Fig. 1A, orange). The slope of the I(q) at low q region was close to −1, showing the rod-like shape of protofibrils. Although the fraction of protofibrils was only 1%, which was revealed from the AUC analysis, it was confirmed that the unreacted α-synuclein monomers had negligible effects and there was little change in the profile after subtracting their contribution (Fig. 1A, red). Using cross-sectional Guinier plot (Fig. 1B), the diameter of protofibril was calculated to be approximately 15 nm. It has been suggested that SAXS is a powerful technique to identify and characterize protofibrils, which is available even when protofibril population is small.

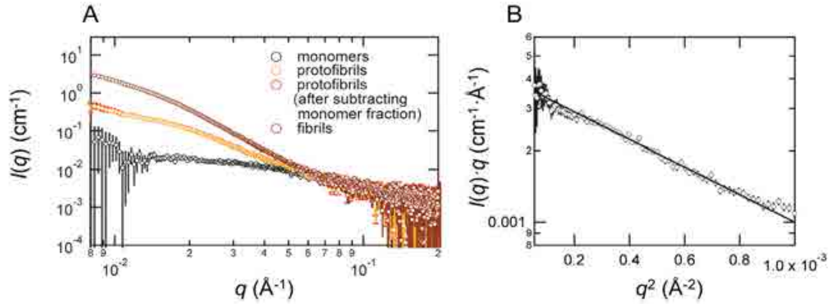

Fig. 1. SAXS profile (A) and its cross-sectional Guinier plot (B) of the α-synuclein protofibrils formed in the presence of 0.5 mM SDS. In panel A, the profiles of α-synuclein monomers and amyloid fibrils are also shown.

REFERENCE:

[1] L. Giehm *et al.*, J. Mol. Biol. **401** (2010) 115-133.

CO6-6

Neutron activation of gold complex

A. Toyoshima, K. Kajiyama[1], M. Murakami, A. Mitsukai[2], and J. Kataoka[3]

Institute for Radiation Sciences, Osaka University
[1]*School of Science, Osaka University*
[2]*Graduate School of Science, Osaka University*
[3]*Graduate School of Advanced Science and Engineering, Waseda University*

INTRODUCTION: Radiopharmaceuticals play a vital role in both the diagnosis and treatment of cancer. They are conventionally synthesized via chemical labeling, in which a medically applicable radioisotope, produced using a nuclear reactor or an accelerator, is attached to a precursor molecule. In this study, we propose a novel methodology for the direct synthesis of radiopharmaceuticals through neutron activation in a reactor. When a stable isotope within a precursor molecule is irradiated with thermal neutrons, prompt gamma rays are emitted following a neutron absorption reaction. This causes nuclear recoil of the activated atom, which may alter molecular structure and affect the chemical integrity of the molecule. Previously, we have investigated this approach using gold nanoparticles (AuNPs). Under specific irradiation conditions, dried AuNP samples were successfully re-dissolved after activation and used in subsequent animal experiments. In the present study, we extend this approach to examine the structural stability of a gold complex, Auranofin, following neutron activation.

EXPERIMENTS: A weighted amount of Auranofin was dissolved in acetone. An aliquot corresponding to 0.1 mg of Auranofin was transferred into a quartz tube and was dried by solvent evaporation. After evaluating the interior, the tube was sealed. Neutron irradiation was conducted for one hour at the Kyoto University Research Reactor. The irradiated sample was then recovered by dissolving it in 1 mL of acetone, followed by drying and re-dissolution in 0.5 mL of acetonitrile. High performance liquid chromatography (HPLC) was used to analyze the Auranofin sample. The HPLC system was equipped with a series of UV and NaI detectors to identify non-activated compounds and to detect gamma-ray, respectively.

RESULTS: The radioactivity of ^{198}Au produced by neutron irradiation was determined using a Ge detector to be 2.4±0.1 MBq on average. The activated Auranofin was quantitatively recovered in acetone. HPLC analysis showed that main peak of ^{198}Au has the same retention time as that detected with the UV detector. This indicates that the ^{198}Au peak attributes to activated Auranofin. Minor ^{198}Au peaks were also observed, probably suggesting that decomposed by-products are formed by nuclear recoils.

CO6-7

Study on the Amyloid Fibril Disaggregation Mechanism of Hsp104 from *Chaetomium thermophilum*

M. Yohda[1], K. Noi[1,2], K. Shibata[1], Y. Goto[1], M. Matsui[1], M. Hayata[1], K. Shinohara[1], K. Morishima[3], R. Inoue[3], M. Sugiyama[3]

[1]*Department of Biotechnology and Life Science, Tokyo University of Agriculture and Technology*
[2]*Engineering Biology Research Center, Kobe University*
[3]*Institute for Integrated Radiation and Nuclear Science, Kyoto University*

INTRODUCTION: Neurodegenerative diseases, such as Parkinson's disease, are thought to result from the deposition of abnormally aggregated proteins in various tissues. Molecular chaperones are considered potential biological inhibitors that counteract the formation of such aggregates. Among these chaperones, Hsp104 has demonstrated the ability to disaggregate protein aggregates and reduce their cytotoxicity. Hsp104, along with its bacterial homolog ClpB, forms hexameric ring structures that mediate protein disaggregation [1]. It is believed that the disaggregated polypeptide threads through the central channel of the ring. However, the detailed mechanism underlying the disaggregation process remains unclear. We have been investigating the protein disaggregation mechanism of Hsp104 from Chaetomium thermophilum (CtHsp104) [2]. In this study, we examined its reactivity toward various pathogenic amyloid fibrils derived from human α-synuclein, Huntingtin (Htt)/PolyQ, and insulin.

EXPERIMENTS: Wild-type and N-terminal deletion mutant forms of CtHsp104 were expressed in E. coli and purified using anion exchange chromatography, hydrophobic interaction chromatography, and gel filtration chromatography. Human α-synuclein and Huntingtin (Htt)/PolyQ were also expressed in E. coli and purified by affinity chromatography. Human insulin was purchased commercially. Amyloid fibril formation was confirmed by atomic force microscopy (AFM) and by monitoring changes in Thioflavin T fluorescence. Real-time disaggregation was directly visualized using high-speed AFM.

RESULTS: When wild-type (WT) CtHsp104 and its N-terminal deletion mutant (ΔN) were each added to amyloid fibrils and incubated at room temperature for 2 hours, a reduction in fibril content was observed for both α-synuclein and Htt/PolyQ fibrils compared to the control. However, no reduction was observed in insulin fibrils. Next, the disaggregation activity of Hsp104 was evaluated using Thioflavin T fluorescence. After allowing sufficient time for fibril formation, samples of α-synuclein, Htt/PolyQ, and insulin fibrils were incubated with CtHsp104 WT and ΔN, and fluorescence intensity was monitored over a 2-hour period. A time-dependent decrease in fluorescence was observed for α-synuclein and Htt/PolyQ fibrils compared to the control. In contrast, no significant change in fluorescence was observed for insulin fibrils. Finally, real-time disaggregation was directly visualized using high-speed atomic force microscopy (AFM). This analysis revealed that CtHsp104 WT was capable of fragmenting and disaggregating α-synuclein and Htt/PolyQ fibrils. These results suggest that CtHsp104 can disaggregate α-synuclein and Htt/PolyQ fibrils, but may not be effective against insulin fibrils, indicating that Hsp104 exhibits substrate-specific activity depending on the chemical stability of each amyloid fibril. Furthermore, the data indicate that CtHsp104 can disaggregate α-synuclein and Htt/PolyQ fibrils independently, without the need for additional cofactors. In addition, the findings suggest that, in fungal Hsp104—as opposed to the yeast-derived Hsp104 previously studied by other groups—the N-terminal domain may not be essential for amyloid fibril disaggregation.

REFERENCES:

[1] J.R. Glover *et al.,* Cell, **94** (1998) 73-82.
[2] Y. Inoue *et al.,* Structure, **29** (2021) 721-730.

CO6-8

Visualization of intrinsically disordered structure of F_1-ATPase ε subunit through integration of AUC-SAXS measurement and MD simulation

T. Oroguchi[1], K. Morishima[2], R. Inoue [2], M. Sugiyama[2], Y. Yamada[3]

[1] Department of Physics, Faculty of Science and Technology, Keio University
[2] Institute for Integrated Radiation and Nuclear Science, Kyoto University
[3] Department of Life Science, College of Science, Rikkyo University

INTRODUCTION: The ε subunit of F_oF_1-ATPase synthase plays as an intrinsic regulator of ATPase activity of F_1-ATPase depending on ATP concentration. The C domain of this subunit is an intrinsically disordered region, and the specific binding to ATP induces the structural formation of this domain and switches the inhibitory state off [1,2]. Furthermore, it has been recently reported that the disordered structure of the ε subunit is also involved in regulating the rotational coupling between F_o and F_1-ATPase [3]. Therefore, to elucidate the regulatory mechanism by the ε subunit, it is necessary to visualize its disordered structure. However, such visualization is difficult for the existing structural analyses methods such as X-ray crystal structure analyses, cryo-electron microscopy, etc. In this study, we challenge to visualize the disordered structure of the ε subunit through the technique integrating SAXS experiments and MD simulation [4]. Due to its tendency to aggregate, the ε subunit was measured using AUC-SAXS [5], which allows to confirm oligomeric states during measurement.

****

EXPERIMENTS: We condensed the purified isolated ε subunit to a concentration of 4 mg/ml, where SAXS intensity could adequately obtained, and conducted AUC-SAXS measurements. The measurements were conducted for both the ATP-unbound and the ATP-bound states. The ionic strength of the measurement buffer was adjusted to 150 mM to minimize aggregation.

****

RESULTS: Through the measurements from the last year, we were able to observe the structural change of the ε subunit due to ATP binding. The SAXS data revealed that the adopted condensation protocol and measurement conditions allowed us to obtain the non-aggregated ε subunit. The measurements in the last year revealed that the ε subunit exists in a monomer-dimer equilibrium for both ATP-unbound and ATP-bound states. Therefore, we surveyed the solution condition, in which we can obtain the data for monomer state. Then, we succeeded to obtain the data for the monomer state for ATP-unbound state, which is under analysis by MD simulation. For ATP-bound state, we elucidated the monomer-dimer equilibrium (Fig. 1(A)), and succeeded to account for the AUC-SAXS data by MD simulation (Fig. 1(B)).

****

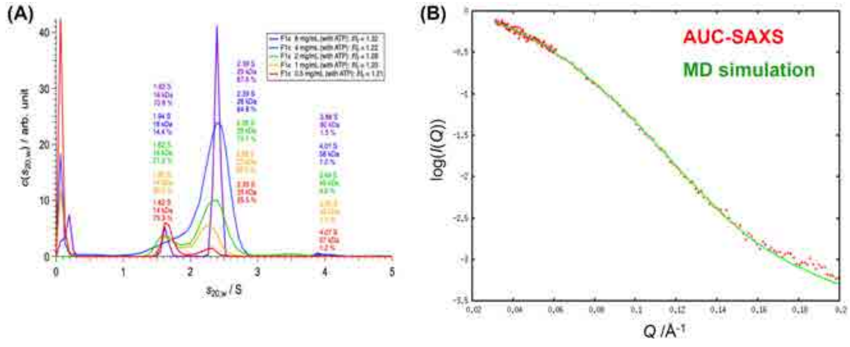

Fig. 1 (A) AUC data for the ATP-bound state of the ε subunit. (B) Comparison of SAXS and MD data.

REFERENCES:

[1] Y. Kato-Yamada & M. Yoshida, J. Biol. Chem., **278** (2003) 36013-36016 .
[2] S. Kato, M. Yoshida & Y. Kato-Yamada, J. Biol. Chem., **282** (2007) 37618-37623.
[3] F. Kadoya, S. Kato, K. Watanabe & Y. Kato-Yamada, Biochem. J., **437** (2011) 135-140.
[4] T. Oroguchi *et al.,* Biophys. J., **96** (2009) 2808-2822.
[5] K. Morishima *et al.,* Comm. Biol., **3** (2020) 294.

R6031

CO6-9

Evaluation of oxidized lens βB2-crystallins involved in age-related cataract

T. Takata, J. Sun and K. Lampi[1]

Institute for Integrated Radiation and Nuclear Science, Kyoto University
[1] Oregon Health & Science University

INTRODUCTION: The transparency of the lens is maintained by the stable long-lived protein interactions, comprising three kinds of crystallin families. Those proteins are very stable, but are decreased their stability with age. A kind of intrinsic damages of lens crystallins, such as heat damage, or extrinsic damages such as UV damage are increased with life time. Several researches suggested the amount of heat/UV damage on lens crystallins could be well described by the amount of modifications of amino acid residues [1]. Oxidation is one of the primary damages for crystallins after heat/UV exposure. In this year, we would like to examine investigating distribution of oxidation of tryptophan residues (Trp: W) in lens βB2-crystallins of different sizes after gamma-ray irradiation. Due to the technical troubles, we could not perform quantitative analysis of modifications depending on the each size of oligomer. However, all of five Trps had oxidation even in lower irradiated samples. Therefore, we focused on the result of oxidations and analyzed the contributions of oxidations for lens βB2-crystallins structure/stabilities.

EXPERIMENTS: Due to the structural similarity between oxidative derivatizes of Trp and phenylalanine (Phe: F), five Trp residues in βB2-crystallin were replaced by Phe respectively to simulate the oxidation effect of Trp in βB2-crystallin by site-directed mutagenesis (W59F, W82F, W85F, W151F and W196F). Each sample were prepared to 4.0 mg/mL in 50 mM Tris buffer (pH 7.8), 150 mM NaCl, and were injected into the Superdex™ 200 Increase 10/300 column equipped on an AKTA GO purifier system (Cytiva) at the Institute for Integrated Radiation and Nuclear Science, Kyoto University.

RESULTS: All mutants, except for W151F, showed a huge peak for dimer and a small peak for tetramer; W151F only showed a peak for dimer. Comparison of the peak area of the tetramer and dimer for each showed that W59F formed more tetramers than the other samples (Fig. 1). Shoulder peaks in the W59F chromatogram were indicative of multiple oligomeric states. Those results are consistent with previous studies that W59 are critical to βB2-crystallin structure and stability. Our results implies that the oxidation of W59 unstabilizes βB2-crystallin, leading to lens dysfunction and cataract formation. This also may impact on subunit-subunit interaction among lens crystallins, result in inhibiting formation of normal-lens protein complexes [2].

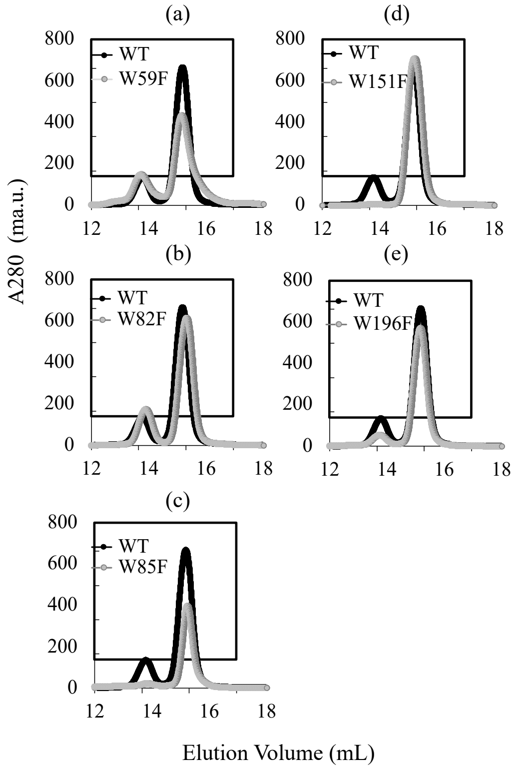

Fig. 1. Size exclusion chromatograms of βB2 mimics. WT are in black solid lines, mimics are in grey lines respectively. (a)(b)(c)(e) W59F, W82F, W85F, W196 all showed both those dimer and tetramer. (d) Only W151F only showed the dimeric peak.

REFERENCES:

[1] B. Searle *et al.,* J Proteome Res., **4** (2005) 546-554.
[2] A. Rolland *et al.,* Structure., **31** (2023) 1052–1064.

R6036

CO6-10

Spectroscopic Analysis of Tumor Model Dried Tissue in Sub-THz Region

Norio Miyoshi[1], Hidetoshi Sato[2], Bibin B. Andriana[2], and Toshiharu Takahashi[3]

[1] *Department of Cellular Immunology, Graduate School of Medical Sciences, Nagasaki University.*
[2] *Department of Life Sciences, Graduate School of Life Environment, Kwansei-Gakuin University.*
[3] *Institute for Integrated Radiation and Nuclear Science, Kyoto University*

INTRODUCTION: Spectroscopic analysis in sub-THz region in tumor pathology field is of interest in viewpoint of water interactions and important for the hydro bonding in viewpoint of MRI.

EXPERIMENTS: The experiment was performed with KURNS-LINAC. The energy of the electron beam was 39 MeV and the peak beam current measured by CT was 1.9 A. The repetition rate of the macro pulse was 60 pulses/s. Coherent transition radiation (CTR) from a titanium window was guided to the Fourier transform interferometer in the experimental room through the coherent radiation beam line [1]. A liquid-helium cooled silicon bolometer was used as the detector of CTR. The sample was prepared as tahe tumor model by cancer drug in Kwansei-Gakuin university. The sample tissue was sandwiched with two sheets of PVC plate 0.5mm thick as shown in Fig. 1.

RESULTS: As shown in Fig. 2, the spectra of tumor tissue (circle) and normal one (square) were measured. The result is shown on Fig. 3. The spectra have structure by the interference inside the PVC plate superimposed on it. Figure 4 shows the transmittivity calculated from the observed spectra. The absorption appeared in the tumor area compared with the normal one.

REFERENCES:

[1] T. Takahashi *et al.,* Rev. Sci. Instrum., **69** (1998) 3770.

Fig. 1 Experimental setup of the sample.

Fig. 2 Measurement points of tumor tissue (circle) and normal one (square).

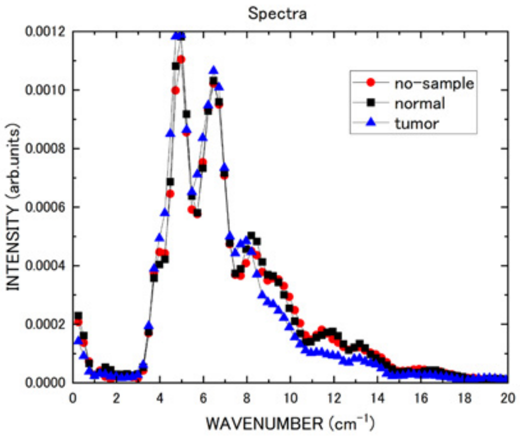

Fig. 1 The observed spectra.

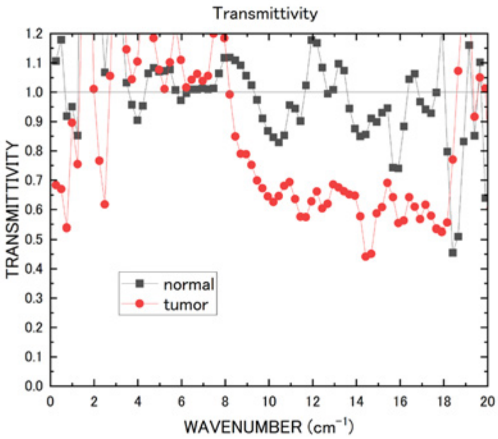

Fig. 2 The transmittivity spectra.

CO6-11

Elucidating the Molecular Basis for the Increased Risk of Nuclear Cataract Development with Global Warming

N. Yamamoto[1] and T. Takata[2]

[1] *Fujita Health University*
[2] *Institute for Integrated Radiation and Nuclear Science, Kyoto University*

INTRODUCTION: The transparency of the lens is important for focusing target onto retina. Lens cells contain rich stable long-lived structural proteins, which is called as crystallin. Recently, the worldwide epidemiological survey confirmed that the risk of nuclear cataract (NUC) is significantly higher in residents living in areas where the annual number of days with temperatures of 30°C or higher is higher. Furthermore, in an in silico simulation study, the applicant group showed that the incidence of NUC differs within a range of internal temperature differences (35.0-37.5°C) [1]. Based on these results, this study aims to clarify the relationship between the formation of NUC and temperature. There were also significant changes in cell proliferation and expression of crystallins during the process, indicating that temperature-dependent changes occur during protein biosynthesis inside the cell. After reviewing these results, we came to the hypothesis that there is a temperature dependence in the crystallin folding pathways inside the cell, and decided to conduct the following study to demonstrate temperature dependent different folding pathway in vitro.

EXPERIMENTS: Last year, recombinantly expressed human βB2-crystallin was unfolded, then refolded by dilution in the presence of each concentration of urea. The ratio of fluorescence intensities between folded (320 nm) and unfolded (360 nm) states were used for the folding index under at two different temperature environment (35.0°C vs 37.5°C). There were no differences of folding pathway between 35.0°C and 37.5°C. We, therefore, decided to create two mimics that are expected to have low thermal stability and have been reported to cause congenital cataracts [2]. Followed by previous reports, each of two tryptophan residues (Trp: W) were altered to cysteines (Cys: C) and recombinantly expressed in E.coli. at various conditions.

RESULTS: The recombinant human βB2-crystallin W59C and W151C were not well expressed in conventional vector (pET-28a vector) and BL21(DE3)pLysS cells. Therefore, we constructed his-tag and sumo tag (pET-sumo-vector) for both proteins to be expressed under mild condition and purify by Ni-column. As a result, a sufficient amount of target proteins were expressed and purified during the initial Ni-column purification (Fig. 1). However, after enzymatic treatment to cleave the his-tag and sumo, the majority was found to be lost during the second stage of purification. We think that the purification process should be further reviewed (e.g., lower temperature expression, shorter enzymatic digestion time, or use of a reducing reagents) for making those heat unstable βB2-crystallin mimics.

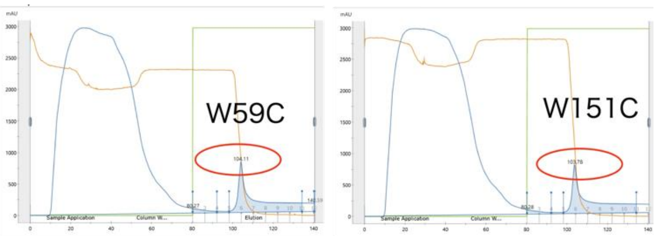

Fig. 1. Results from the first nickel column purification of βB2-crystallin mimics. Both enough amount of W59C and W151C bound to columns under current conditions.

REFERENCES:

[1] N. Yamamoto *et al.,* Cells., **12** (2020) 2670.
[2] W. Zhao *et al.,* J Biol Macromol., **103** (2017) 764–770.

R6048

CO6-12

Structural analysis of ferritin in a polyplacophoran

M. Nemoto[1], M. Shimizu[2]

[1]*Graduate School of Environmental, Life, Natural Science and Technology (Faculty of Agriculture), Okayama University*

[2]*Institute for Integrated Radiation and Nuclear Science, Kyoto University*

INTRODUCTION: Polyplacophora, a kind of mollusk, has a feeding organ called radula, in which magnetite precipitates in the cusp. Understanding the mechanism of magnetite formation by polyplacophora could lead to an environmentally friendly method for synthesizing magnetite. Since magnetite is usually produced industrially at high temperatures and with harmful substances, biosynthesis-based magnetite production will have a significant impact on the field of materials science. We have discovered a novel iron-storage protein from radula of *Acanthopleura japonica* , a species of *Polyplacophora* . To elucidate function and availability of this protein, we performed analytical ultracentrifuge and small-angle X-ray scattering on this iron-storage protein.

****

EXPERIMENTS: Analytical ultracentrifugation was performed at 40,000 rpm using a ProteomeLab XL-I analytical-ultracentrifuge (Beckman Coulter). Distribution of sedimentation coefficient was calculated by SEDFIT [1]. Small-angle X-ray scattering was performed using NANOPIX (Rigaku). One-dimension scattering profile was obtained by SAngler software [2].

****

RESULTS: Small-angle X-ray scattering data showed a characteristic profile of ferritin. Thus, this protein was suggested to have the structure of a typical ferritin protein. Ultracentrifugal analysis of this protein showed single peak in the sedimentation coefficient, and its corresponding molecular weight was around 580 kDa. Its value was almost similar to that of the protein 24-mer. These results suggest that this protein forms a typical ferritin 24-mer in aqueous solution.

****

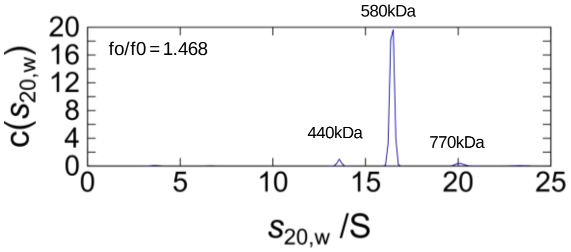

Figure 1. Sedimentation coefficient distribution of the protein

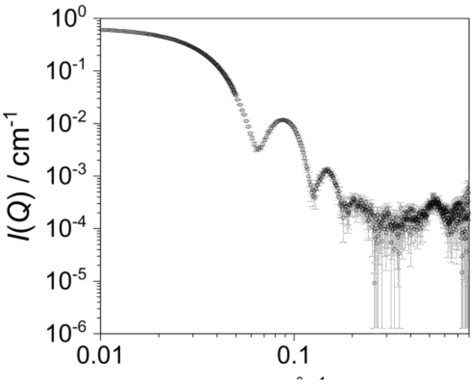

Figure 2. Small-angle X-ray scattering profile of the iron storage protein

REFERENCES:

[1] P. Schuck, Biophys. J., **78** (2000) 1606-1619.
[2] Shimizu, N. *et al.,* AIP Conf. Proc., **1741** (2016) 050017.

CO6-13

Asp racemization/isomerization in shedding products of cell adhesion molecule 1 is potentially involved in the neurodegeneration induced by elevated pressure

A. Yoneshige[1], A. Ito[1] and T. Takata[2]

[1]Department of Pathology, Kindai University
[2]Institute for Integrated Radiation and Nuclear Science, Kyoto University

INTRODUCTION: The elevation of internal pressure is often involved in neurodegeneration; intraocular and intraventricular pressure elevations over 20–30 cm H_2O cause glaucoma and hydrocephalus, respectively. Previously, to investigate the mechanisms by which elevation of intraluminal pressure causes cell or tissue de-generation, we devised a novel two-chamber culture system that enabled us to subject cultured cells to low levels of water pressure (2-50 cm H_2O pressure load) [1,2]. We found that mouse primary neurons degenerated when the water pressure was above 30 cm H_2O, and that ectodomain shedding of synaptic cell adhesion molecule 1 (CADM1) increased in a water pressure-dependent manner [1]. We also discovered that the increase of intracellular product of CADM1 shedding (C-terminal fragment, CADM1-CTF) resulted in decreased neurite density with punctate localization of CADM1 suggesting its aggregation in neurites [1]. CADM1-CTF is rich in Asp residues neighbored by Ala residues, and the conversion of these amino acids to poly-Gly diminished its aggregation state. Since the racemization and isomerization of Asp residues contributes to aggregation of various proteins and it likely occurred when the neighboring residues are small [3,4], these in-sights led us to hypothesize an involvement of Asp racemization/isomerization in the neurodegeneration induced by internal pressure elevation.

EXPERIMENTS: (1) Synthetic peptide of internal sequence of CADM1-CTF (GADDAADADTAIINAEGGQNNSEEK) was incubated at 50℃ for 0-15 days and applied to LC-MS to identify Asp isomer-containing peptides. (2) Mouse neuroblastoma cell line Neuro-2a cells with exogenously expressed CADM1-CTF were cultured un-der 50 cm H_2O and were prepared for LC-MS analysis. (3) To mimic oxidative stress induced by internal pressure elevation, Neuro-2a cells expressing CADM1-CTF were treated with hydrogen peroxide and the cells were subjected to the isolation of CADM1-CTF by immuno-precipitation (IP). The amounts and purity of CADM1-CTF-IP were quantified using immunoblotting and silver staining.

RESULTS: (1) In LC-MS analysis of CADM1-CTF synthetic pep-tide, multiple peaks were detected after 1 day at pH 6.0 or pH 7.0 indicating that Asp racemization/isomerization could occurred under neutral pH. (2) CADM1-CTF proteins in Neuro-2a cells were solubilized with water, Triton X-100 containing buffer, or SDS containing buffer after 3 days culture under 50 cm H_2O, and CADM1 immunoblot was carried out. CADM1-CTF protein yields (CADM1-CTF / total proteins) were in the order Triton X-100 > SDS > water, however, the peptide peak was not identified using with LC-MS. (3) Previously, we found that CADM1 shedding was increased by oxidative stress as a cause of pulmonary emphysema in cigarette smoke exposure [5]. We furthermore showed that Lipocalin-2, an iron binding protein was upregulated in the retinae under 50 cm H_2O pressure [6]. Since iron dysregulation induces oxidative stress, we decided to explore the linkage between oxidative stress and Asp racemization/isomerization of CADM1-CTF. We obtained partial purified CADM1-CTF from large-scale Neuro-2a cell culture, coupled with IP purification. However, the identification of Asp isomer by LC-MS remains challenging, probably because of sample purity.

REFERENCES: [1] A. Yoneshige *et al.,* Mol. Neurobiol., **54** (2017) 6378-6390. [2] M. Hagiyama *et al.,* Front. Physiol., **8** (2017) 997. [3] N. Fujii *et al.,* J. Biochem., **116** (1994) 663-669. [4] T. Takata *et al.,* Protein Sci., **29** (2020) 955-965. [5] A. Ri *et al.,* Front. Cell Dev. Biol., **6** (2018) 52. [6] A. Yoneshige *et al.,* Front. Cell Dev. Biol., **9** (2021) 664327.

R6054

CO6-14

Small-angle X-ray scattering analysis of MDP1-DNA mixture

M. Shimizu

Institute for Integrated Radiation and Nuclear Science, Kyoto University

INTRODUCTION: MDP1 is a protein of Mycobacterium sp. that is involved in intracellular Fe ion dynamics [1]. At the same time, the protein binds to nucleic acids and functions to bundle them [2]. To further elucidate the structure and function of MDP1, we analyzed the structure of mixed state of peptide whose sequence is characteristic of MDP1 and DNA by small-angle X-ray scattering measurements.

EXPERIMENTS: Peptide and DNA were purchased from Eurofins Genomics. Both peptide and DNA were dissolved in D_2O. Small-angle X-ray scattering was performed using NANOPIX (Rigaku). One-dimension scattering profile was obtained by SAngler software [3].

RESULTS: Radius of gyration (R_g) was calculated for the mixture system. The R_g was 18.7 Å. On the other hand, the R_g for DNA alone was 16.9 Å. Thus, DNA and peptides were shown to form a complex. We note that the detailed size distribution of the complex cannot be determined from the scattering profile alone. Considering that the molecular weight of the peptide alone is around 2,000 Da, there can be a mixture of free peptide and a much larger complex. This peptide is strongly positively charged and has been reported in the past to interact strongly with DNA [4]. This experiment showed consistency with the present experiment. On the other hand, no other characteristic scattering profiles appeared by mixing. In other words, the mixing of peptide and DNA did not dictate the formation of a new regular structure.

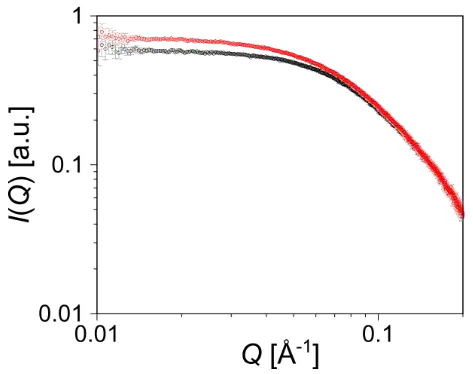

Figure 1. Small-angle X-ray scattering profile of the mixture of DNA and MDP1 peptide (red) and DNA (black).

REFERENCES:

[1] S. D. Pandey *et al.,* J. Bacteriol., **196** (2014) 1853-1865.
[2] A. Nishiyama *et al.,* Nucleic Acid Res., **52** (2024) 816-830.
[3] N. Shimizu *et al.,* AIP Conf. Proc., **1741** (2016) 050017.
[4] M. Furugen *et al.,* Microbial Pathogenesis, **30** (2001) 129-138.

CO6-15

Effect of salt concentration on solution structure of intrinsically disordered protein

R. Inoue, T. Oda[1], and M. Sugiyama

Institute for Integrated Radiation and Nuclear Science, Kyoto University
[1]J-PARC Center, JAEA

INTRODUCTION: Compared to the solution structure of folded globular protein (FDP), the solution structure of intrinsically disordered protein (IDP) exhibits a different susceptibility against external environment dependence due to the high content of hydrophilic and polar residues. For example, radius gyration (R_g) increases with increasing temperature for FDP, on the other hand it decreases with increasing temperature for IDP [1]. It is considered that enhancement of hydropho-bic interaction at high temperature could be concerned for such anomalous temperature-dependent structural change observed for IDP, however direct experimental proof for such an expectation have not obtained yet. In this work, we investigated the solution of IDP at two different salt concentra-tions and discussed whether or not enhancement of hydrophobic interaction at high temperature is the main contributor for the anomalous temperature-dependent structural change of IDP

EXPERIMENTS: As an example of IDP, we used intrinsically disordered region of Hef (Hef-IDR) [2]. To examine the solution of structure of Hef-IDR, we performed small-angle X-ray scattering (SAXS) measurements. SAXS measurements were conducted using a Photon Factory BL-6A instrument (Tsukuba, Japan). The X-ray wavelength and the sample-to-camera distance were set to 1.5 Å and 2038.9 mm, respectively. The Hef-IDR solution at the concentration of 12 mg/mL was prepared in a buffer containing 10 mM Tris (2-carboxyethyl) phosphine hydrochloride and TCEP (10 mM HEPES pH 7.5, 100 mM NaCl, 0.1 mM EDTA, 10 mM TCEP).

RESULTS: Fig. 1 shows the temperature dependence of R_g at two different salt concentrations. It is evident that R_g value is not affected by change of salt concentration, denying the possibility that decrease of R_g with increasing temperature is not caused by the enhancement of hydrophobic interaction at high temperature. From the complementary uses of various techniques, it was revealed that loss of polyproline type II helix at high temperature was mainly responsible for the decrease of R_g at high temperature observed for Hef-IDR [3]. At present, we are planning to perform SAXS measurement of Hef-IDR at different external environment such as high pressure.

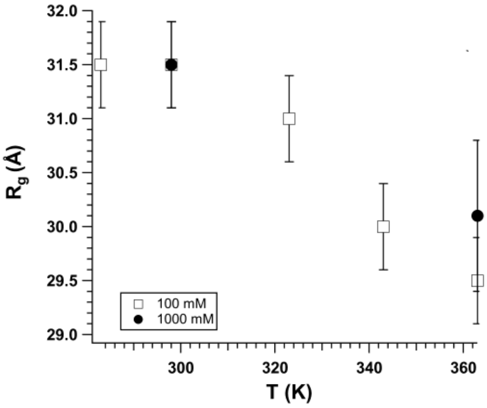

Fig. 1. Temperature dependence of R_g of Hef-IDR at 100 mM and 1000 mM.

REFERENCES:

[1] V. N. Uversky, J.R. Gillespie, and A.L. Fink. Pro-teins, **41** (2000) 415–427.
[2] S. Ishino *et al.,* J. Biol. Chem., **289** (2014) 21627-21639.
[3] R. Inoue *et al.,* Biophys. J., **124** (2025) 540-548.

R6064

CO6-16

Complex formation of cyanobacterial circadian clock proteins in solution

K. Morishima, R. Sakamoto, M. Shimizu, R. Inoue, and M. Sugiyama

Institute for Integrated Radiation and Nuclear Science, Kyoto University

INTRODUCTION:

Cyanobacterial circadian clock is composed of three clock proteins, KaiA, KaiB and KaiC, and its circadian rhythm is observed as a 24-hour cycle of the degree of phosphorylation of KaiC. The phosphorylation of KaiC is promoted by the formation of the KaiA-KaiC complex, and conversely, it is dephosphorylated by the formation of the KaiB-KaiC complex. In other words, to understand the oscillation mechanism of the circadian rhythm, it is essential to elucidate the competitive complex formation behaviour of KaiA and KaiB towards KaiC. In the previous research, we have clarified the phosphorylation state dependence of the KaiA-KaiC complex. Then, in this study, we focus on the KaiB-KaiC complexes formation utilizing phosphorylation-mimicking KaiC mutants

EXPERIMENTS:

Analytical ultracentrifugation (AUC) measurements was performed for titration samples of KaiB+KaiC. To mimicking the phosphorylation states of KaiC, we used the following mutants: S/T–mimicking S431A/T432A mutant (KaiC$_{AA}$), S/pT–mimicking S431A/T432E mutant (KaiC$_{AE}$), pS/pT–mimicking S431D/T432E mutant (KaiC$_{DE}$), and pS/T–mimicking S431D/T432A mutant (KaiC$_{DA}$). KaiB+KaiC titration sample series was prepared by mixing KaiB and KaiC solutions with the composition of [KaiB] : [KaiC] = x : 6 (x = 0 – 12), where [KaiB] and [KaiC] mean the molar concentration for their monomer. The partial concentration of KaiC was fixed at 2.0 mg/mL. The solution was subjected to measurements after incubation at 30 °C for 24 hours. AUC measurements were performed using ProteomeLab XL-I (Beckman Coulte). Sedimentation velocity analysis was performed using Rayleigh interference optics at 30 °C. The rotor speed was set at 60,000 rpm. The weight-concentration distributions as a function of sedimentation coefficient c($s_{20,w}$) and average frictional ratio f/f_0 were obtained through computational fitting to the time evolution sedimentation data with the multi-component Lamm formula using SEDFIT software version 15.01c [1]

RESULTS:

Fig1(a) show the titration-AUC result for the mix solution of KaiB+ KaiC$_{DE}$. With the KaiB mixing ratio increased, the peak shifted continuously to the higher $s_{20,w}$ side, and converged at $s_{20,w}$ = 12.3 S which corresponds to B_6C_6. Fig1(b) show the KaiC-phosphorylation dependence of the B_6C_6 formation. It is very noteworthy that, other than KaiC$_{DE}$, the phosphorylation mimics do not form B_6C_6. This means that the ability to form BC complexes is dramatically different between the highly phosphorylated state (DE) and other states. This phosphorylation-state-dependent affinity is one of the principles that generates the circadian oscillation of this system.

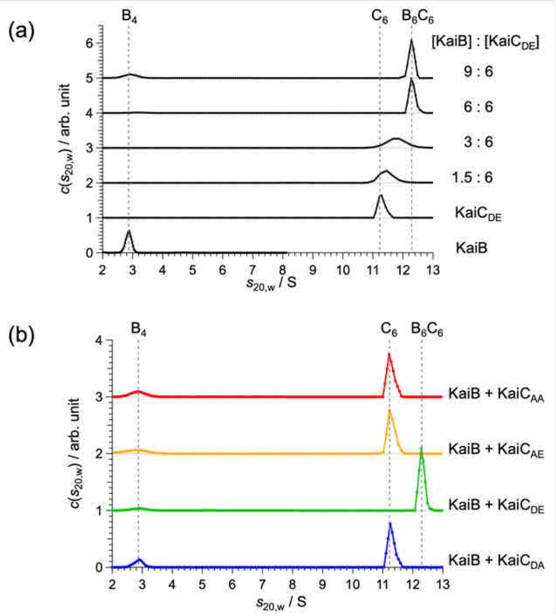

Fig. 1. (a) Titration-AUC result for the mix solution of KaiB+ KaiC$_{DE}$ with various mixing ratios. (b) AUC results for the mix solution of KaiB+ KaiC$_{DE}$ at the mixing ratio of [KaiB] : [KaiC] = 7.5 : 6 for various KaiC mutants.

REFERENCES:

[1] P. Schuck, Biophys, J., **78** (2000) 1606-1619.

CO6-17

Character of DNA damage induced by nuclear plant neutron beams

H. Terato, T. Hanafusa[1], M. Isobe, Y. Sakurai[2], H. Tanaka[2], and T. Saito[2]

Advanced Science Research Center, Okayama University
[1]Neutron Therapy Research Center, Okayama University
[2]Institute for Integrated Radiation and Nuclear Science, Kyoto University

INTRODUCTION: Radiation-induced biological effects are expressed through damage to DNA. Therefore, analyzing radiation-induced DNA damage is essential for elucidating the molecular mechanisms underlying these biological effects. High-LET radiation, such as heavy ion beams and neutron radiation, induces types of DNA damage that differ from those caused by low-LET radiation like gamma-rays [1, 2]. Two specific forms of DNA damage associated with high-LET radiation are cross-linked DNA damage (CLD) and clustered DNA damage (CDD). These types of damage show strong inhibitory effects on DNA synthesis and their low repair efficiency [3–5]. In this study, we aimed to analyze DNA damage caused by reactor neutrons, the two types of damage, CLD and CDD, also play a significant role in the expression of neutron-specific biological effects. Furthermore, we also analyzed the forms of DNA damage associated with Boron Neutron Capture Therapy (BNCT), a medical application of neutron radiation.

EXPERIMENTS: pUC19 DNA was dissolved in TE buffer (10 mM Tris-HCl, pH 7.5, 1 mM ethylenediaminetetraacetic acid) containing 1 M dimethyl sulfoxide and dispensed into microtubes. Samples with and without BSH (^{10}B-sodium mercaptododecaborate), one of BNCT agent, were prepared, and neutron irradiation was carried out at the KUR. The BSH concentration was set to 10% (w/v). Radiation doses were up to 5 Gy as a total physical dose. After irradiation, DNA was dialyzed against TE buffer to remove BSH, separated using 0.8% agarose gel electrophoresis, and the generated DNA damage was analyzed [1, 2].

RESULTS: The DNA damage in pUC19 was assessed using neutral agarose gel electrophoresis, which allows the separation of the circular plasmid DNA into three forms: type I (undamaged circular DNA), type II (single-strand break, SSB), and type III (double-strand break, DSB), thus enabling the observation of SSBs and DSBs in the DNA [1]. The results of agarose gel electrophoresis of irradiated DNA showed that DNA damage increased in a dose-dependent manner. The damage-enhancing effect of BSH was particularly prominent at low-dose regions, with a maximum increase in damage of up to fivefold. Most of the DNA damage detected by agarose gel electrophoresis was DSBs rather than SSBs. This suggests that high-LET radiation including neutrons and alpha particles with BNCT, efficiently induces DSBs. DSB is one of CDD induced by ionizing radiation directly and indirectly. In future studies, we plan to investigate another BNCT drug, BPA (^{10}B-4-Borono-L-phenylalanine), to further clarify the effects of BNCT.

REFERENCES:

[1] H. Terato *et al.*, J. Radiat. Res., **49** (2008) 133-146.
[2] Y. Tokuyama *et al.,* J. Radiat. Res., **56** (2015) 446-455.
[3] Y. Kinashi *et al.,* Radiat. Oncol., **6** (2011) 106.
[4] H. Terato *et al.,* KURNS Progress report 2022, (2023) 158.
[5] T. Nakano *et al.,* J. Biol. Chem., **284** (2009) 27065-27076.

CO6-18

Small-angle X-ray scattering analysis of di-nucleosomes

S. Sato[1], K. Morishima[2], R. Inoue[2], A. Okuda[2], M. Dacher[1], N. Horikoshi[1], M. Sugiyama[2], H. Kurumizaka[1]

[1]Institute for Quantitative Biosciences, The University of Tokyo
[2]Institute for Integrated Radiation and Nuclear Science, Kyoto University

INTRODUCTION: In eukaryotes, including human pathogenic parasites, genomic DNA forms chromatin structure and is packed within the nucleus. Chromatin plays an essential role in regulating biological events such as gene transcription, DNA repair, and replication by dynamically changing its conformation. The conformation of chromatin, in terms of compaction and relaxing forms, is regulated by histone modifications and binding proteins. Chromatin is an array of nucleosomes, each composed of 145-147 base-pairs of DNA wrapped around a histone octamer containing two molecules each of histone proteins H2A, H2B, H3, and H4. The relative positioning and flexibility between nucleosomes are important for chromatin conformation. Therefore, we tried to establish a method for analyzing the structures of adjacent nucleosomes in solution. We used di-nucleosomes in which two nucleosomes are connected by a linker DNA, and applied small-angle X-ray scattering (SAXS). This approach is important for understanding the mechanisms of chromatin dynamics regulated by epigenetic factors in eukaryotic cells.

EXPERIMENTS: Di-nucleosomes were prepared by in vitro reconstitution [1]. Recombinant histones were mixed with a DNA fragment under high salt conditions, followed by a gradual decrease in salt concentration to promote nucleosome formation. Di-nucleosomes were then purified using a method based on polyacrylamide gel electrophoresis [1]. The di-nucleosomes thus obtained were analyzed by SAXS. SAXS intensity of the buffer solution was measured for background subtraction, using the same procedure as for the di-nucleosome samples. These SAXS data were collected using a laboratory-based instrument equipped with a high-brilliance point-focused generator of a Cu Kα source. To assess aggregation and dissociation of the sample, sedimentation velocity was measured by analytical ultracentrifugation (AUC) [2].

RESULTS: We confirmed the formation of di-nucleosomes on the DNA fragment containing two strong nucleosome positioning sequences with 15-base pairs of linker DNA by polyacrylamide gel electrophoresis. We carefully removed precipitates by centrifugation and the di-nucleosome solution was prepared at a sufficient concentration for SAXS analysis. The AUC results showed a major peak corresponding to the di-nucleosome, and a small amount of dissociated and aggregated components were detected. Scattering profile (one-dimensional intensity data I(q) as a function of (q)) of the di-nucleosome was calculated as aggregated components were removed. Radius of gyrations (R_g) were estimated from the fitting curves of the I(q) data using Guinier plot, as previously described [3]. This analysis will be further pursued to establish a method for observing chromatin compaction in solution.

REFERENCES:

[1] T. Kujirai *et al.,* Methods Mol. Biol., **1832** (2018) 3-20.
[2] K. Morishima *et al.,* J. Appl. Crystallogr., **56** (2023) 56, 624-632.
[3] Y. Arimura *et al.,* Sci. Rep., (2013) 3510.

R6084

CO6-19

Design, Synthesis, and Evaluation of Macrocyclic Polyamine-Based Multiboron Carriers for BNCT

S. Aoki[1,2], H. Ueda[3], W. Yoshida[1], M. Suzuki[3], Tanaka, T.[1,4] S Masunaga[3], N. Kondo[3], and Y. Sakurai[3]

[1]*Faculty of Pharmaceutical Sciences, Tokyo University of Science*
[2]*Research Institute for Science and Technology, Tokyo University of Science*
[3]*Research Reactor Institute, Kyoto University*
[4]*Faculty of Pharmaceutical Sciences, Okayama University*

INTRODUCTION: Neutron capture therapy using boron-10 (^{10}B) (BNCT) is one of powerful therapies for local tumor control in the treatment of brain tumor, melanoma, and related diseases. We previously designed and synthesized phenylboronic acid-pendant 9-, 12-, and 15-membered macrocyclic amines such as **^{10}B-1a~3a** and the corresponding Zn^{2+} complexes **^{10}B-1b~3b** (Fig. 1) [1,2], based on high intracellular uptake of cyclen (1,4,7,10-tetraazacyclododecane) derivatives in cancer cells. It was reported that the metal-free **^{10}B-1a~3a** are introduced into cancer cells (A549 and HeLa S3 cells) more efficiently than their Zn^{2+} complexes **^{10}B-1b~3b** with considerably high cancer/normal cells selectivity. Besides, it was found that 12- and 15-membered derivatives **^{10}B-2a~3a** exhibit a higher BNCT effect than **^{10}B-1a**, possibly because **^{10}B-2a~3a** form the corresponding Zn^{2+} complexes **^{10}B-2b & 3b**, which strongly interact with DNA in living cells [3], resulting in the efficient breakdown of DNA upon the neutron irradiation.

Next, we synthesized dimeric macrocyclic polyamines having one phenylboronic acid unit such as **4~9** and their corresponding Zn^{2+} complexes (Fig. 1), because it was well established that polymeric Zn^{2+} complexes would form more stable complexes with DNA double strand than monomeric Zn^{2+} complexes [4]. However, the intracellular uptake of **4~9** and their Zn^{2+} complexes were lower than monomeric compounds **1~3**, possibly due to their lower hydrophobicity than that of **1~3.**

EXPERIMENTS AND RESULTS:

The aforementioned results have prompted us to synthesize monomeric polyamines equipped with two boronic ester units for higher intracellular uptake and BNCT effect. In 2024, **10a~15a** and their corresponding Zn^{2+} complexes **10b~15b** (Fig. 1) were synthesized. The evaluation of intracellular uptake and BNCT effect of **10a~15a** and **10b~15b** has suggested that **14a** has highest intracellular uptake and BNCT effect among these compounds [5].

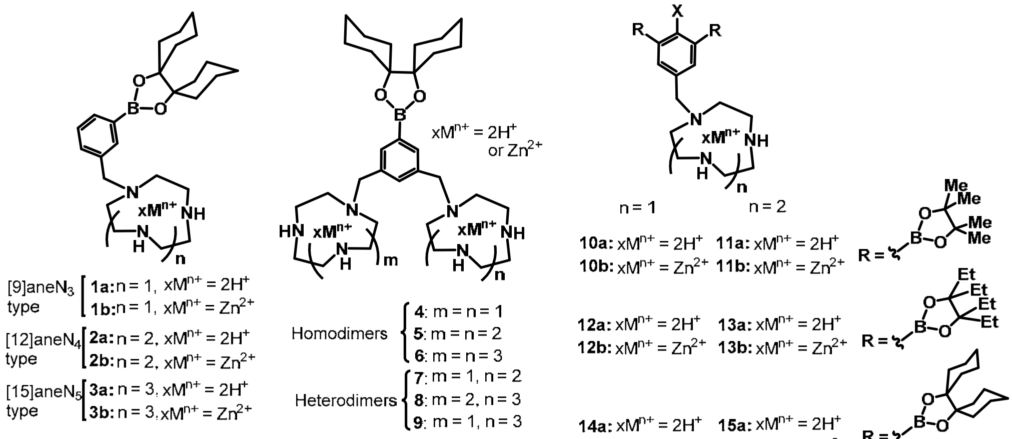

Figure 1. Chemical Structures of Borono Compounds **1~15**

REFERENCES:

[1] H. Ueda *et al.,* J. Med. Chem., **64** (2021) 8523-8544.
[2] S. Aoki *et al.,* In "*Characteristics and Applications of Boron*" 2022, pp 83-105, Charchawal Wongchoosuk, Ed., IntechOpen, Croatia.
[3] S. Aoki *et al.,* Chem. Rev., **104** (2004) 769-788.
[4] H. Ueda *et al.,* Eur. J. Inorg. Chem., **2022** (2022) e202100949 (24 pages).
[5] W. Yoshida *et al.,* Manuscript in preparation.

R6087

CO6-20

Quantitative change on microglia and astrocytes in the brain after immuno- and/or radiation therapy for cancer

Natsuko Kondo[1], Yoichi Shimizu[2], Nao Kobayashi[2] and Yoshinori Sakurai[1]

[1] *Particle Radiation Oncology Research Center, Institute for Integrated Radiation and Nuclear Science, Kyoto University (KURNS)*
[2]*Dept. of Diagnostic Imaging and Nuclear Medicine, Graduate School of Medicine, Kyoto University.*

INTRODUCTION: Radiotherapy such as X-rays and γ-rays is used as a standard treatment as a safe and effective cancer treatment. There are many unknown points, such as the interaction between infiltrated immune cells and residual tumors in the microenvironment, the effects of immune cells on organs and tumors outside the irradiated area. In addition, immune checkpoint inhibitors have come into use, and interactions mediated by immune cells have been emphasized. In this study, we investigated how immune cells infiltrate and interact with irradiated tissues and organs throughout the body (outside the field of irradiation), including the brain, after irradiation. We will also investigate the changes that occur when immune checkpoint inhibitors are used in combination with radiation therapy.

EXPERIMENTS:

Cells:

We used Lewis Lung Cell Carcinoma cell line (LLC). They were cultured in RPMI 1640 medium with 10% heat-inactivated fetal bovine serum in 5 % CO_2 incubator.

Innoculation of tumor and drug treatment to animals

We used C57BL/6 mice. $5E^5$ LLC cells were inoculated subcutaneously in a thigh of the mice. We created four groups (non-treatment, immunotherapy alone, radiation therapy alone, and immunotherapy and radiation therapy combined) and each group contained 9 animals. After the inoculation, we administrated anti-mouse PD-1 antibody on the day 6 and 12 (250 μg/body).

Irradiation:

We used the Cobalt 60 gamma-ray irradiation device in KURNS. On the day 13, we irradiated the tumor on the thigh of mice at the dose of 20 Gy shielding the body and head with lead.

Measurement of tumor size and sampling of tumors and brains

After the irradiation, we measured the major and minor axes of the tumors until mice were sacrificed. We sacrificed three mice in each group on 2, 7, 14 days after irradiation. The brain and tumor were removed and fixed in 10 % buffered formalin for pathological samples.

Immunohistochemistry:

We prepared paraffin sections, and stained microglia or macrophages using a monoclonal Iba-1 antibody for 1st antibody. DAB staining was used for second antibody. We analyzed the numbers of Iba-1 or GFAP positive cells in the hippocampus and cortex of the brain or in the tumor.

Mouse behavioral analysis

We performed the behavioral analysis with the mice after drug-treatment and/or irradiation.

RESULTS:

Tumor size: Only in the combination group, tumor size was significantly reduced compared with the control at 14 days after irradiation.

Pathology: The number of microglia in hippocampus tended to increase in immunotherapy alone group at 2 and 7 days after irradiation. In the tumor, the macrophages increased 7 days after irradiation.

Mouse behavioral analysis

Currently we are conducting mouse behavior analysis.

R6095

CO6-21

^{11}C Medical-isotope Production via ^{12}C(γ,n)^{11}C Reaction with Single-walled Carbon Nanotubes

N. Takahashi[1,2], M. Kurosawa[1], M. Tamura[1], M. Fujiwara[1,2], T. Kubota[3], N. Abe[4], and T. Takahashi[4]

[1]Research Center for Nuclear Physics, Osaka University
[2]Kyoto Medical Technology
[3]Agency for Health, Safety and Environment, Kyoto University
[4]Institute for Integrated Radiation and Nuclear Science, Kyoto University

INTRODUCTION: L-[^{11}C]-Methionine is used as a positron emission tomography (PET) reagent for medical diagnosis of brain tumors [1]. The medical ^{11}C radioisotopes are mostly produced in a cyclotron via the ^{14}N(p,α)^{11}C reaction by bombarding enriched nitrogen gas with a proton beam [2]. Instead of producing ^{11}C with the cyclotron, we developed a novel method of producing ^{11}C using the bremsstrahlung γ-rays with a single-walled carbon nanotubes (SWCNT) to get a reasona-ble number of the ^{11}C activity.

EXPERIMENTS: Figure 1 shows the experimental scheme for the ^{11}C production via the ^{12}C(γ,n)^{11}C reaction. Bremsstrahlung γ-rays were produced by impinging a 40 MeV electron beam on platinum converter at the electron LINAC facility. The γ-rays were irradiated to SWCNT sealed in aluminum vessel with non-woven masks as gas inlet/outlet filter. The produced ^{11}C inside the vessel were oxidized to ^{11}CO or ^{11}CO$_2$ in O$_2$ gas, which was continuously flown during the irradiation. The ^{11}C gas (^{11}CO and ^{11}CO$_2$) were trapped in two 13X molecular sieve columns and 511-keV γ-rays from positron-electron annihilation were detected with CdZnTe detectors. The SWCNT with a diameter of 2-3 nm were used as target.

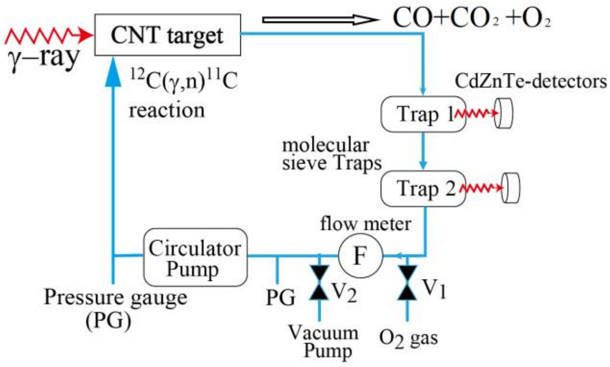

Fig. 1 Experimental scheme to produce ^{11}C and measure the extraction rate of ^{11}C gas.

RESULTS: Table 1 shows the normalized activity of ^{11}C gas for SWCNT which have different bulk density. The normalized activity slightly increases as bulk density increased. All the values shown in Table 1 are higher than 8.71 kBq/μA/g/min for SWCNT with a diameter of 1-1.4 nm used in the previous experiments.

Based on the experimental production rate of ^{11}C gas, we estimate that we can obtain the ^{11}C activity of 58 GBq when we use a SWCNT target under the conditions with 1) a length of 50 cm, 2) weight of 1.13 kg for 0.155 g/cm^3, 3) a 40 MeV electron beam intensity of 100 μA for 40 minutes bombardment.

Table 1 Normalized activity of ^{11}C gas for each bulk density

Bulk density of SWCNT (mg/cm^3)	Normalized activity of ^{11}C gas (kBq/μA/g/min)
3.27	13.30±0.07
6.53	13.94±0.07
9.80	14.41±0.06
13.06	14.92±0.05

REFERENCES:

[1] Kobayashi K. *et al.,* Eur. J. Nucl. Med. Mol. Imaging, **42** (2015) 1071-1080.
[2] David R. Christman *et al.,* Int. J. appl. radiat. isot., **26** (1975) 435-442.

R6100

CO6-22

Analysis of flexible structure of multi-domain protein Hef

T. Oda, R. Inoue[1], K. Morishima[1], A. Okuda[1], M. Sugiyama[1]

J-PARC Center, Japan Atomic Energy Agency.
[1]Institute for Integrated Radiation and Nuclear Science, Kyoto University.

INTRODUCTION: Hef is a protein that is required for DNA repair in hyperthermophilic archaea [1,2]. Hef consists of an N-terminal helicase domain, a C-terminal nuclease domain and intrinsically disordered region (IDR) connecting them [1,2]. Due to flexibility of the IDR, structural analysis of Hef using crystallography or cryo-electron microscopy is difficult. In this study, we attempted to analyze the flexible structure of Hef using small angle X-ray/neutron scattering (SAXS/SANS). Since the entire molecule contributes to scattering in SAXS, it is difficult to determine the ensemble structure of a multi-domain protein based solely on the SAXS profile. Therefore, to obtain another experimental constraint, we prepared a full-length Hef with 75% deuteration in only the helicase or the nuclease domain (segmentally deuterated samples, Fig.1(a)). If SANS measurement of the segmentally deuterated samples is performed in 100% D_2O solvent, the 75% deuterated domain is matched out, and only scattering of the non-deuterated region can be observed. Therefore, it is expected that the ensemble structure can be determined correctly by combining it with the SAXS profile.

EXPERIMENTS: Deuteration of Hef or D_2O solvent may affect the structure of Hef. In this study, prior to the SANS experiment, we performed SAXS analysis of the segmentally deuterated samples to confirm the presence or absence of structural modulation due to deuteration or D_2O solvent. The segmentally deuterated samples were prepared by ligation the 75% deuterated domain and the non-deuterated region using a protein ligation enzyme. After protein preparation, the solvent of samples was exchanged to D_2O buffer. The SAXS measurements were performed with BL10C installed PF. To avoid aggregation, SAXS measurements were carried out using dilute samples (0.6 mg/ml).

RESULTS: The SAXS profiles of the segmentally deuterated samples in D_2O and the fully hydrogenated sample in H_2O are shown in Fig1(b). The R_g values of segmentally deuterated samples (44 ±1Å and 47±2Å,) were equivalent to that of the fully hydrogenated sample (45±1Å). There was no difference between the SAXS profiles of the segmentally deuterated samples and the fully hydrogenated sample. These results show that there is no structural difference between the segmentally deuterated samples in D_2O and the fully hydrogenated sample in H_2O.

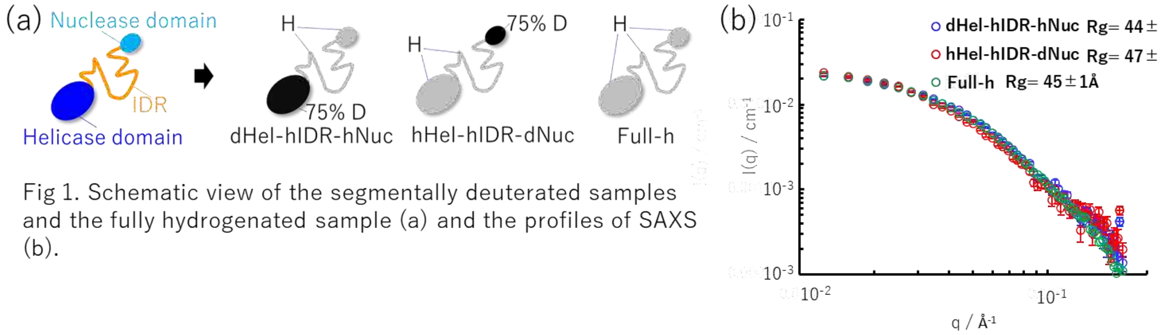

Fig 1. Schematic view of the segmentally deuterated samples and the fully hydrogenated sample (a) and the profiles of SAXS (b).

REFERENCES:

[1] Fujikane *et al.,* Genes Genet. Syst., **85** (2010) 243.
[2] Ishino *et al.,* J. Biol. Chem., **289** (2014) 21627.

CO6-23

Biophysical analysis of higher-order multimers of p53 DNA binding domain

E. Hibino[1], R. Hijikata[1], K. Morishima[2], R. Inoue[2], M. Sugiyama[2] and H. Hiroaki[1,3,4]

[1]*Graduate School of Pharmaceutical Sciences, Nagoya University*
[2]*Institute for Integrated Radiation and Nuclear Science, Kyoto University*
[3]*BeCellBar LLC.*
[4]*COMIT*

INTRODUCTION: The p53 protein functions as a crucial transcription factor for suppressing oncogenesis. Under cellular stress, p53 is activated and its expression levels rise, leading to the transcription of target genes that induce cell cycle arrest and apoptosis[1]. However, p53 can be inactivated through two distinct pathways: aggregation promoted by p53 DNA-binding domain (p53-DBD) and MDM2-mediated degradation[2]. Both mechanisms significantly contribute to tumorigenesis. Restoring functional p53, either by using p53 aggregation inhibitors or MDM2 inhibitors, has become a central approach in the development of anticancer therapies. Recently, we examined the p53 aggregation inhibitory activity of 16 flavonoids. We found that baicalein, which has been reported to exhibit some anticancer activity[3,4], suppresses aggregation of p53-DBD in vitro. In this study, we aimed to elucidate the mechanism of the anticancer effect of baicalein via p53 and analyzed the effect of baicalein on p53.

EXPERIMENTS: p53-DBD was produced using an E. coli overexpression system[5]. The purified p53-DBD solution was mixed with baicalein and incubated at 37°C for 1 h. The samples were then analyzed by Blue Native PAGE, nanoparticle tracking analysis (NTA), and dynamic light scattering (DLS), and observed by transmission electron microscopy (TEM).

RESULTS: After incubation of p53-DBD solution at 37°C for 1 h, amorphous aggregates and amyloid aggregates were formed, but it was found that the addition of baicalein suppressed these aggregate formations. Accordingly, we hypothesized that monomeric p53-DBD molecules remained, and confirmed the size of the molecules contained in the solution by Blue Native PAGE. As a result, it was suggested that p53-DBD forms relatively large particles by baicalein. Therefore, the formed particles were examined by NTA, TEM, and DLS, and it was found that higher-order multimers were formed in a concentration-dependent manner of baicalein (Fig. 1). We propose that the formation of p53-DBD higher-order multimers by baicalein leads to the inactivation of p53-DBD and maintains its function.

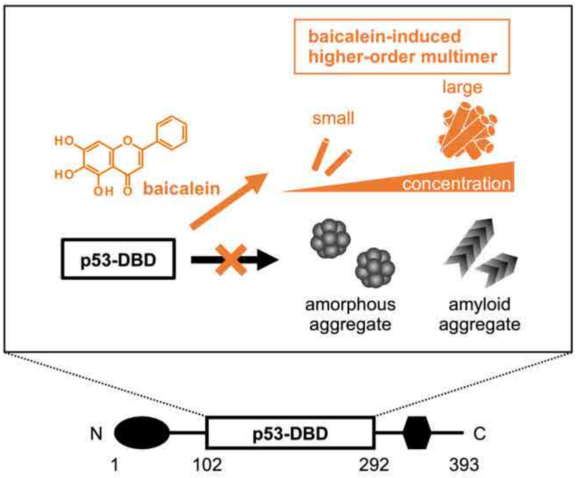

Fig. 1 Baicalein inhibits both amorphous and amyloid aggregation of p53-DBD and induces another higher-order multimer of p53-DBD in a concentration-dependent manner.

REFERENCES:

[1] B. Vogelstein *et al.,* Nature, **408** (2000) 307–310.
[2] E. Hibino *et al.,* Biophys. Rev, **14** (2022) 267–275.
[3] W. Yan *et al.,* Drug Des. Devel. Ther., **12** (2018) 3961–3972.
[4] Y. Gao *et al.,* Medicinal Chemistry Research, **25** (2016) 1515–1523.
[5] E. Hibino *et al.,* Front. Mol. Biosci., **9** (2022) 869851.

CO6-24

Distribution analysis of the chemical modification of the amino acid residues in mice lens structural proteins during age-related cataract

S. Matsushita[1], Y. Suzuki[1] and T. Takata[2]

[1] *Dept of Materials and Applied Chemistry, Nihon University*
[2] *Institute for Integrated Radiation and Nuclear Science, Kyoto University*

INTRODUCTION: Age-related cataracts are the leading causes of blindness in world. Several risk factors, contributing to the development of cataracts, have been reported. Above all, abnormal lens protein aggregation and insolubilization has been believed as the main process. Alteration of lens protein structure, caused by covalently post-translational modifications, are thought to be critical for maintaining lens protein homeostasis [1]. We have shown that covalent modifications of amino acid residues as a scale for a lens aging. To do this, mass spectrometry is an efficient tool to quantitative analysis, however the distributions of modifications were very obscured. Therefore, we are to address revealing the distribution of modifications (isomerization/racemization of Asp) in the lens section using by Imaging Mass Spectrometry (IMS) [2]. This technique requires the preparation of high-quality sections, but we could not have prepared the samples available for IMS so far. Since it has been very difficult to attach water-rich lens tissues to analytical glass plate, we tried to analyze lens model peptide with matrix solution on the sample plate to identify peptide by molar mass.

EXPERIMENTS: We synthesized, purified lens model peptides and mixed with CHCA ((4-hydroxyphenyl) acrylic Acid)), which is matrix for MALDI TOF-MS, in the presence of 50% acetonitrile. Each of modification site (L-α-Asp, L-β-Asp, D-α-Asp, D-β-Asp) were confirmed using by LC-MS/MS systems in Institute for Integrated Radiation and Nuclear Science, Kyoto University (data not shown). Then, we directly those samples with CHCA and loaded onto the imaging plate under three different concentration of peptide (Fig. 1). This is because of that to obtain subtracted MS images before digestion. The data was obtained by positive ion mode at m/z 100-2500 using by JMS-S3000 (JEOL). The peak at m/z 1311.70-1312.05 was observed (Fig. 2).

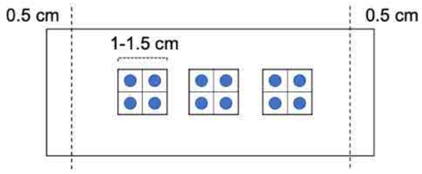

Fig. 1. The schematic drawings for added samples/CHCA mixtures into glass plate under three different concentrations.

RESULTS: The result suggested that the peptide concentration above 2.5 mg/mL show the images of peptides. The each of peptide had the same m/z, but D-α-Asp and D-β-Asp containing intense images. The mixed state with matrix and ionized state may have some differences between L-Asp or D-Asp. The shape is not simple image but heterogeneity. Drying from droplets mixing samples and matrix can form debris on the plate. To escape from this issue, the uniformed spraying system for samples/matrix should be constructed. Last year, we prepared that system and protease for D-Asp containing peptide/protein. To the end, we success to obtain the optimized samples concentrations, right m/z and specific enzyme for this study. After check the activity of this enzyme, we will use all for IMS systems.

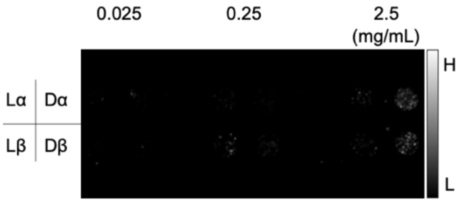

Fig. 2. The MS imaging of peptide that including *m/z* 1311.70 1312.05.

REFERENCES:

[1] N. Fujii *et al.,* Biochim. Biophys. Acta, **1860** (2016) 183-191.
[2] J. McMahon *et al.,* J. Am. Soc. Mass. Spectrrom., **11** (1995) 1047-1058.

CO6-25

Molecular dynamics analysis of oxidative folding enzyme ER-60 with solution scattering measurement

A. Okuda, M. Shimizu, K. Morishima, R. Inoue, R. Urade and M. Sugiyama

Institute for Integrated Radiation and Nuclear Science, Kyoto University

INTRODUCTION: ER-60 is a multi-domain oxidative protein folding enzyme with the domain order **a**-**b**-**b**-**b'**-**a'**. The **a** and **a'** domains contain catalytically active cysteine pairs. During oxidative protein folding, ER-60 is thought to adopt specific domain conformations essential for its function. It is also hypothesized that its overall structure dynamically fluctuates in response to the redox state of the active cysteine pairs in solution [1]. Neutron scattering is a valuable technique for investigating such structural dynamics in solutions. It exploits the large difference in neutron scattering length between hydrogen and deuterium, making it particularly useful for studying multi-domain proteins like ER-60. In a 100% deuterated solvent, 75% deuterated proteins become scatteringly invisible, allowing selective observation of hydrogenated domains in multi-domain proteins. Applying this method to multi-domain proteins, the domain of the hydrogenated domains could be selectively observed. To elucidate the structure–function relationships of ER-60, we aim to analyze individual domain structures using inverse contrast-matching small-angle neutron scattering (iCM-SANS) [2]. For this purpose, segmentally deuterated ER-60 proteins were prepared by connecting individual domains using the ligation enzyme OaAEP [3].

EXPERIMENTS: The 75% deuterated (d) and hydrogenated (h) domains were expressed in E. coli cultured in M9 medium containing 75% deuterium and LB medium without deuterium, respectively [4]. The purified domains were mixed in buffer containing 200 mM Tris-HCl (pH 7.4) / 150 mM NaCl. Then, 0.2 μM of the ligation enzyme OaAEP was added to the mixture, and the protein ligation reaction was performed at 20°C for 64 hours. The results of ligation reactions were confirmed by SDS-PAGE. SAXS measurements were performed at 25 °C with 4 hours of exposure- time using a NANOPIX (Rigaku, Tokyo, Japan). The sample-to-detector distance was set to 1330 mm and 300 mm. The q range was from 0.01 to 0.80 $Å^{-1}$.

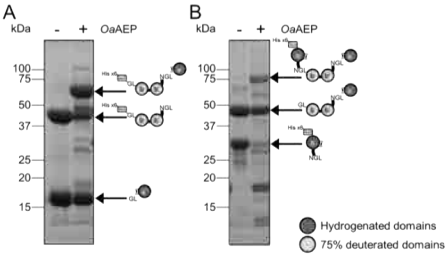

Fig. 1. The ligation products from (A) (*h*)**a'** and (*d*)**bb'** domains and (B) (*h*)**a** and (*d*)**bb'**-(*h*)**a'** domains of ER-60 by *Oa*AEP.

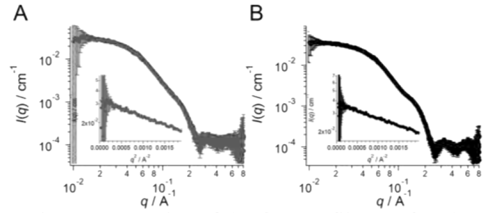

Fig. 2. The SAXS profiles of (A) (*h*)**a**-(*d*)**bb'**-(*h*)**a'** and (B)WT ER-60. the radius of gyration (R_g) of these are 32.8 ± 0.4 Å and 32.0 ± 0.2 Å, respectively. Inset panels are guinier plots of them.

RESULTS: The progress of the first-step ligation reaction, (d)**bb'** and (h) **a'**, and the second-step liga-tion reaction , (h)**a** and (d)**bb'**-(h)**a'**, were observed, indicating that ER-60 with hydrogenated **a** and **a'** domains and deuterated **bb'** domains was pre-pared (Fig. 1). In the SAXS profiles of (h)**a**-(d)**bb'**-(h)**a'** and WT ER-60 showed no significant differences between each other (Fig. 2). Currently, we are proceeding with SANS experiments and analysis of these samples.

REFERENCES:

[1] A. Okuda *et al.,* Sci Rep., **11** (2021) 5655.
[2] M. Sugiyama *et al.,* J. Appl. Cryst, **47** (2014) 430-435.
[3] A. Okuda *et al.,* Angew Chem Int Ed Engl., **62** (2023) e202214412.
[4] A. Okuda *et al.,* Biophys Physicobiol., **18** (2021) 16-27.

CO6-26

^{10}B-enriched nitroimidazole derivative as a functional drug for hypoxia-targeting boron-neutron capture therapy

K. Tanabe,[1] T. Nishihara,[1] T. Ozasa[1] and M. Suzuki[2]

[1]Department of Chemistry and Biological Science, College of Science and Engineering, Aoyama Gakuin University
[2]Institute for Integrated Radiation and Nuclear Science, Kyoto University

INTRODUCTION: Boron neutron capture therapy (BNCT) is a well-known radiation therapy based on the nuclear reaction between boron 10 (^{10}B) atoms and thermal neutrons. BNCT is an ideal cancer treatment, however, this therapy relies on finding boron-containing drugs that are selectively taken up by cancer cells. In particular, applications of therapeutic BNCT for hypoxic cells are slow and therefore, their use is an urgent issue. These research contexts prompted us to prepare a novel drug that could be used to treat hypoxic cells and tumor hypoxia by BNCT. We attempted to modify ^{10}B-enriched p-boronophenylalanine (BPA), a BNCT agent in practical use, for treatment of hypoxic cells. We designed a BPA with nitroimidazole unit (BPA-NI) as hypoxia-targeting BNCT agent (BPA-NI, Fig 1), since nitroimidazoles (NIs) are known as an exogeneous marker for hypoxia because of its characteristic reactions in hypoxic cells. Herein, we characterized the selective accumulation of BPA-NI into hypoxic cells and its cytotoxic effect upon thermal neutron irradiation.[1]

****

EXPERIMENTS: The BPA-NI (0 or 250 μM) was administered to the SAS cells and then the cells were incubated for 3 h. After incubation and wash, the cells were irradiated (neutron, 1 MW) for 45 min at KUR. After incubation, WST 8 was added to the cells, and the cell viability assay was performed using Microplate Reader.

****

RESULTS: We selected SAS cells for the target, because of their versatility for BNCT study, and initially, we checked the intracellular accumulation of BPA-NI. It was well-documented that azomethine H formed chelate complexes with boric acid to exhibit an absorption around 400 nm. Using these characteristic absorption of azomethine H and boron compounds, we attempted to compare the amount of BPA-NI in hypoxic or aerobic cells by the measurement of absorption spectra. After incubation of hypoxic or aerobic cells with BPA-NI, cell lysates were harvested. Then, we added azomethine H to the lysate to measure the absorption spectra. We found that absorption at 420 nm from hypoxic cells was stronger than that from aerobic cells, indicating that BPA-NI selectively accumulated in hypoxic cells. We also measured ICP MS and estimated the amount of ^{10}B element in hypoxic cells to be 78 ng per 10^6 cells. Next, we evaluated the cytotoxic effect of BPA-NI upon thermal neutron irradiation. The cells were incubated with BPA-NI (250 μM) for 3 h under hypoxic or aerobic conditions and then, the cells were subjected to irradiation. We found that the cytotoxic activity of BPA-NI against aerobic SAS cells is negligible, while BPA-NI incubated with hypoxic cells showed higher cytotoxic effect than that with aerobic cells. We also confirmed that the nitroimidazole derivative without BPA unit (A-NI) did not show any cytotoxicity. These results strongly indicate that BPA-NI accumulated in hypoxic cells to show selective cytotoxicity.

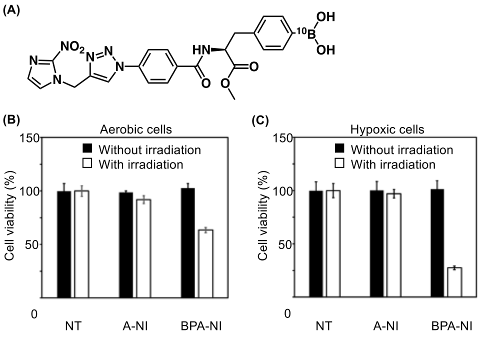

Fig. 1. (A) Chemical structure of BPA-NI. ((B) Cytotoxicity of A-NI and BPA-NI against SAS cells upon thermal neutron irradiation under aerobic (B) or hypoxic conditions (C).

REFERENCES:

[1] K. Tanabe *et al.,* Results Chem., 2025, in press.

CO6-27

Evaluating the Efficacy of Boron Neutron Capture Therapy in Treating Metastatic Central Nerveous System Tumors

Y. Fujikawa, S. Kawabata, H. Yamada, F. Takagi, K. Eza, H. Kashiwagi, T. Takata[1], H. Tanaka[1], M. Suzuki[1], N. Hu[2], S-I. Miyatake[2], T. Takami, and M. Wanibuchi

Department of Neurosurgery, Osaka Medical and Pharmaceutical University
[1] Institute for Integrated Radiation and Nuclear Science, Kyoto University
[2] Kansai BNCT Medical Center, Osaka Medical and Pharmaceutical University

INTRODUCTION: With the remarkable progress in cancer treatment in recent years, the life expectancy of patients with cancer has been extended. On the other hand, the risk of developing metastases including spine or central nervous system are increasing. Moreover, the future challenge will be to extend the prognosis and improve the quality of life of patients with metastases [1]. If it could be shown that boron neutron capture therapy (BNCT), which can selectively destroy cancer cells, is effective, it will be a promising novel treatment option and could also contribute to expanding the application of BNCT. Our laboratory has been conducting research on BNCT mainly for malignant brain tumors such as glioblastoma [2,3]. In this study, we aimed to evaluate the efficacy of BNCT for metastatic cancer rat models.

****

EXPERIMENTS: Rat metastatic brain and spine tumor models were created using 13762 MAT B III rat mammary cancer cells. A solitary metastatic brain tumor model was created to be implanted this tumor cell line into the right brain of the rat through the infusion pump. In addition, a multiple metastatic brain tumor model was created to be injected this cell line into the right internal carotid artery of the rat. Finally, metastatic spine tumor model was created by transplanting subcutaneous tumor mass into the vertebral body of the rat. The rat metastatic tumor models were randomly assigned into three groups: a control group receiving no treatment (untreated), a group subjected to neutron irradiation alone (neutron only), and a BNCT group (The BNCT group received an intravenous injection of BPA at a dose of 250mg/kg, followed by neutron irradiation 2.5 h later). In terms of spine metastasis, Overall survival and any adverse events were assessed post-irradiation.

****

RESULTS: BNCT significantly prolonged overall survival in both solitary and multiple brain metastatic tumor rats. In spine metastasis, BNCT group did not have the superior survival compared to the other groups. However, BNCT group with light hindlimb paresis or no paresis (Basso-Beattie-Bresnahan score more than 16) had significant survival prolongation compared to the other groups.

****

CONCLUSIONS: Our data suggests that BNCT is an effective treatment modality for metastatic central nervous system tumors. Further research is warranted to strengthen the evidence supporting the potential benefits of BNCT for these cancers and to facilitate its translation into clinical practice.

****

REFERENCES:

[1] Y. Fujikawa *et al.,* Cancer Sci., **115** (2024) 2774-2785.
[2] K. Tsujino *et al.,* Neurooncol Adv., **22** (2024) vdae062.
[3] Y. Fujikawa *et al.,* Biology (Basel)., **15** (2023) 1240.

R6122

CO6-28

Investigation of the Biological Impact of Ultra-High Dose Rate Radiation on Normal and Neoplastic Tissues

Tsubasa Watanabe[1], Genki Edward Sato[1], Takushi Takata[2], Yoshinori Sakurai[2], Minoru Suzuki[1], Takashi Mizowaki[3], Hiroki Tanaka[2]

Institute for Integrated Radiation and Nuclear Science, Kyoto University
[1]Particle Radiation Oncology Research Center, Particle Radiation Oncology
[2]Particle Radiation Oncology Research Center, Particle Radiation Medical Physics
[3]Kyoto Univeristy, Department of Radiation Oncology and Image-Applied Therapy

INTRODUCTION: Recent studies suggest that ultra-high dose rate irradiation (≥40 Gy/sec), which is over 1,000 times faster than conventional radiotherapy (≈0.03 Gy/sec), may reduce side effects while maintaining comparable anti-tumor efficacy [1]. If ultra-high dose rates indeed suppress side effects without compromising anti-tumor effects, conventional radiotherapy (e.g., X-rays, γ-rays, protons) may transition to this approach. Specifically, this year we investigated the functional (rather than quantitative) effects of irradiation on immune cells. Additionally, this project seeks to identify optimal radiotherapy approaches from a tumor immunology perspective. Prior to this year, we analyzed how irradiation affects lymphocyte survival rates and immune function.

****

EXPERIMENTS: We aim to clarify the effects of high-dose rate irradiation—which exhibits distinct biological responses compared to conventional X-ray irradiation—on lymphocytes. First, we established in vivo/in vitro irradiation systems for high-dose-rate exposure using electron beams. Next, we administered high-dose-rate irradiation to the head and neck regions of C3H and C57/BL6 mice, confirming that dermatitis in the high-dose-rate group was reduced compared to the conventional dose-rate group, consistent with published reports. Furthermore, lymphocytes isolated from the spleens of C3H mice were irradiated with 0, 2, 4, and 10 Gy using both conventional and high-dose-rate methods. Based on literature indicating the critical role of oxygen concentration in high-dose rate effects, irradiations were conducted under in vitro conditions with varying oxygen levels. Subsequently, using 5% oxygen conditions (validated for high-dose rate effects in mouse skin), additional irradiations of 0, 4, and 10 Gy were performed under both 1% and 5% oxygen conditions.

****

RESULTS: High-dose-rate irradiation to the head and neck regions of C3H and C57/BL6 mice confirmed that dermatitis was reduced in the high-dose-rate group compared to the conventional dose-rate group, consistent with prior reports. Under 0.1% oxygen conditions, no difference in lymphocyte survival rates was observed between high-dose-rate and X-ray irradiation, and no high-dose rate effect was detected at this oxygen level. Using 5% oxygen conditions (previously validated for high-dose rate effects in mouse skin), 0, 4, and 10 Gy irradiations were repeated under both 1% and 5% oxygen levels. However, under all conditions, no irradiation method-dependent differences in lymphocyte survival rates were observed, and in vitro experiments showed no high-dose rate effect regardless of oxygen concentration.

****

REFERENCES:

[1] JD Wilson *et al.*, Front Oncol., (2020) (doi)10.3389/fonc.2019.01563.

CO6-29

Interaction between fibrinogen and amyloid β 1-42 monitired by analytical ultracentrifugation (AUC

Naoki Yamamoto, Ken Morishima[1], Rintaro Inoue[1], Masaaki Sugiyama[1]

Division of Biophysics, Physiology, School of Medicine, Jichi Medical University
[1]Institute for Integrated Radiation and Nuclear Science, Kyoto University

INTRODUCTION: Fibrinogen is a plasma protein functioning for blood clotting. It has been known that the protein possesses chaperone-like function as it inhibits amyloid fibril formation of several proteins [1-3]. We have recently found that the protein also inhibits amyloid fibril formation of amyloid β 1-42 (Aβ42) which is considered to be a cause of Alzheimer's disease [4]. To understand molecular mechanisms of the inhibition, we evaluated the interaction between fibrinogen and Aβ using AUC.

EXPERIMENTS: Aβ42 at 20 μM was incubated with fibrinogen at 37 °C for 1 hour, followed by AUC experiments using a ProteomeLab XL-I analytical-ultracentrifuge (Beckman Coulter, Germany) with an aluminum cell with a volume of 400 μl (optical path: 12 mm). Bovine and human fibrinogen (bFg and hFg, respectively), which are homologous to each other, were used to investi-gate the effect of the difference in the amino acid sequences.

RESULTS: Figure 1 shows the AUC profiles of Aβ42 in the presence of bFg (A) or hFg (B), respectively. Aβ42 retains two peaks at 0.99 S and 4.53 S, corresponding to the monomer and oligomer, respectively. In the presence of bFg of 3 μM, both peaks disappeared, indicating that bFg interacts with these components. When the concentration was 0.3 μM, the peak of the oligomer was still absent, indicating that bFg interacts with the oligomer more strongly than the monomer. In the presence of hFg of 3 μM, the oligomer peak only disappeared, indicating that hFg only interacts with the oligomer at the concentration. These results represent that bFg possesses higher capabilities for the interaction with Aβ42. This might be due to the difference in their amino acid sequences since bFg and hFg possess similar three dimensional structures.

REFERENCES:

[1] Tang *et al.*, Biochem. Biophys. Res. Commun., **378** (2009) 662-667.
[2] Swasthi *et al.,* Biochemistry. **57(44)** (2018) 6270-6273.
[3] N. Yamamoto *et al.,* J. Phys. Chem. B, **126(51)** (2022) 10797-10812.
[4] Manuscript submitted

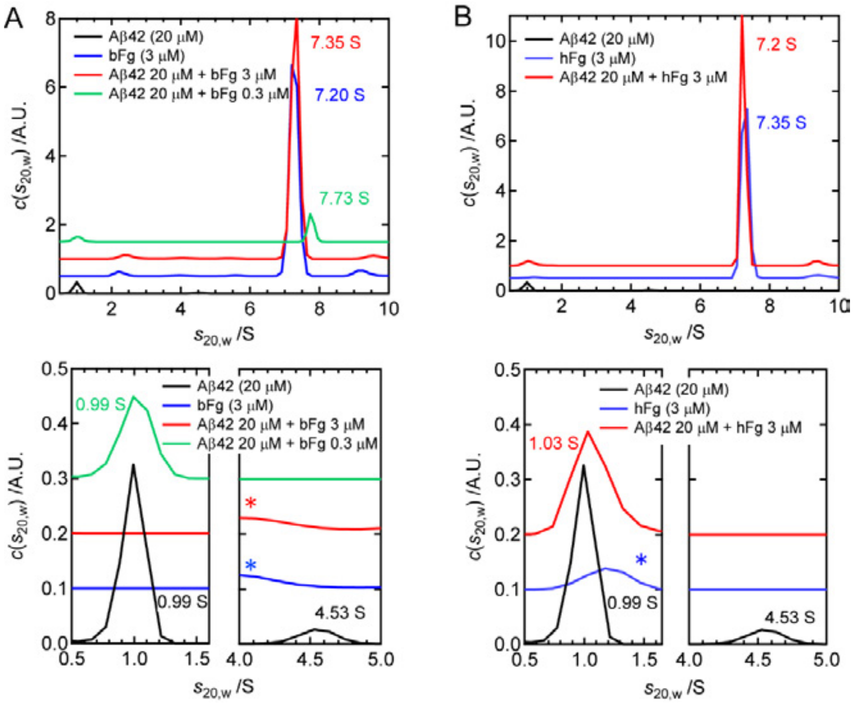

Fig. 1. AUC profiles of Aβ in the presence of bFg (A) or hFg (B), respectively. The top panels show total profiles and the bottom panels are magnified views of the low-S regions corresponding to Aβ42 monomer and oligomer, respectively.

R6154

CO6-30

Radiolabeling of composite natural material chicken eggshell membrane via neutron irradiation 6Li(n,α) 3H reaction

M. Shimizu[1], E. Ohto-Fujita[1], N. Nogawa[2], H. Yoshinaga[3], K. Takamiya[3], A. Enomoto[4], K. Tanoi[5], T. Yamashita[6], Y. Asano[7], Y. Hasebe[8], and Y. Atomi[1]

[1]*Teikyo University, Advanced Comprehensive Research Organization, Division of Open Innovation*
[2]*Isotope Science Center, The University of Tokyo*
[3]*Institute for Integrated Radiation and Nuclear Science, Kyoto University*
[4]*Isotope Facility, Graduate School of Medicine, The University of Tokyo*
[5]*Isotope Facility for Agricultural Education and Research. Graduate school of Agricultual and Life Sciences, University of Tokyo.*
[6]*Department of dermatology, Graduate School of Medicine, The University of Tokyo*
[7]*Department of Dermatology, Tohoku University Graduate School of Medicine*
[8]*Almado, Inc.*

INTRODUCTION: Chicken eggshell membrane (ESM) has been listed as an excellent wound-healing agent in Chinese pharmacopoeia book entries for 400 years. It is a non-woven fabric composed of more than 400 fibrous protein polymers, cross-linked by lysyl-oxidase [1]. We previously found that hydrolyzed ESM provide young extracellular environment to dermal fibroblast [2] , improved skin elasticity and reduced facial wrinkles as cosmetics [3] and improved skin elasticity, respiratory function, and locomotion in healthy adults taking the supplements [4]. Recently, we also reported the potential of ESM and its key components, lysozyme (LYZ) and ovotransferrin (OT), as a promising preventive approach for pulmonary fibrosis [5]. We applied the tritium labeling of organic compounds via the 6Li(n,α)3H reaction, which has been used for radiolabeling of natural products that are difficult to synthesize and for tissue distribution in individuals, to ESM and conducted pilot experiments to determine whether ingested ESM are indeed digested and absorbed and distributed to various tissues. The labeled eggshell membrane was orally administered to mice and was digested and absorbed. The radioactivity derived from the labeled ESM was detected in blood 2 hours after administration, peaking 6 hours later, and was also detected in almost all tissues [6]. The Kyoto University furnace is beneficial for irradiating protein samples because its low power output does not raise the sample temperature during irradiation.

****

EXPERIMENTS: ESM (nano-sized extra-fine form, Almado Inc.) + Li_2CO_3 (1:1 and 1:2 by weight) and SESM (solubilized ESM form, Almado Inc.) + Li_2CO_3 (1:1 and 1:2 by weight) sealed in quartz glass were irradiated under milder conditions (Pn-2, 1 MW, 70 min). After irradiation, samples were transferred to The University of Tokyo for biochemical, in vitro, and in vivo study.

****

RESULTS: The chemical integrity of the protein after Pn-2 irradiation and the peptide size after digestion and absorption into the serum and mouse tissues will be determined using SDS-PAGE and peptide gel. Using cell line, uptake of labeled protein and secretion of ECM (decorin, type III collagen, MMP2) will determine the biological activity of the irradiated protein sample.

****

REFERENCES:

[1] M. Shimizu *et al.*, The journal of Japan Mibyou Association, **30** (2024) 23-26.
[2] E. Ohto-Fujita *et al.*, Cell Tissue Res., **345** (2011) 177-190.
[3] E. Ohto-Fujita *et al.*, Cell Tissue Res., **376** (2019) 123-135.
[4] E. Ohto-Fujita *et al.*, Journal of Fiber Science and Technology **77** (2021) 258-265 .
115-120.
[5] E. Ohto-Fujita *et al.*, Biochem. Biophys. Rep. 2024, **39** (2024) 101806 .
[6] E. Ohto-Fujita *et al.*, Journal of Fiber Science and Technology, **77** (2021) 182-187.

R6155

CO6-31

Solution structure of VAMP722

K. Kato[1,2,3], M. Yagi-Utsumi[1,2,3], H. Yagi[1,2], K. Morishima[4], R. Inoue[4] and M. Sugiyama[4]
[1]*Graduate School of Pharmaceutical Sciences, Nagoya City University*
[2]*Exploratory Research Center on Life and Living Systems (ExCELLS), National Institutes of Natural Sciences*
[3]*Institute for Molecular Science, National Institutes of Natural Sciences*
[4]*Institute for Integrated Radiation and Nuclear Science, Kyoto University*

INTRODUCTION:

VAMP721 (vesicle-associated membrane protein 721) is a plant-specific R-SNARE protein that plays a crucial role in vesicular trafficking to the plasma membrane, where it mediates membrane fusion events essential for polarized secretion and cell expansion. AlphaFold-based structural modeling predicts that VAMP721 adopts a “closed” conformation, in which its SNARE motif folds back onto the N-terminal longin domain, potentially representing an autoinhibited state. In contrast, docking models of VAMP721 in complex with the clathrin adaptor PICALM suggest an “open” conformation, where the SNARE motif is extended and accessible for interaction, implying a possible mechanism of conformation-dependent regulation of protein–protein interactions.

To investigate the conformational state of VAMP721 in solution, we employed small-angle X-ray scattering (SAXS) and analytical ultracentrifugation (AUC). These complementary biophysical techniques provide insights into the overall shape, oligomeric state, and conformational dynamics of VAMP721 under physiological conditions, enabling us to assess whether it predominantly adopts a closed, open, or intermediate ensemble of conformations in solution.

EXPERIMENTS:

Recombinant VAMP721 was expressed in Escherichia coli and purified using GST affinity chromatography. The protein was dissolved in buffer containing 20 mM Tris-HCl (pH 8.0) and 150 mM NaCl. SAXS measurements were performed at 25 °C using a NANOPIX instrument (Rigaku) installed at KURNS. Scattering data were collected over a q-range of 0.010–0.70 Å^{-1} using two sample-to-detector distances (SDDs) of 1333 mm and 300 mm. To minimize the influence of non-specific aggregation on the SAXS profiles, we applied the AUC-SAXS method, an integrated reduction approach combining analytical ultracentrifugation (AUC) and SAXS. AUC measurements were conducted using a ProteomeLab XL-I (Beckman Coulter) at 60,000 rpm and 25 °C.

RESULTS:

Figure 1B shows the experimental SAXS profile of recombinant VAMP721. The scattering curve was compared with theoretical profiles derived from the AlphaFold-predicted closed model and the open conformation observed in PICALM docking simulations. Fitting analysis indicated that VAMP721 exists as a dynamic equilibrium of conformers in solution, comprising approximately 57% open and 43% closed states. These results suggest that VAMP721 samples both conformations in the absence of binding partners, reflecting conformational flexibility that may underlie its regulatory mechanism in vesicle trafficking.

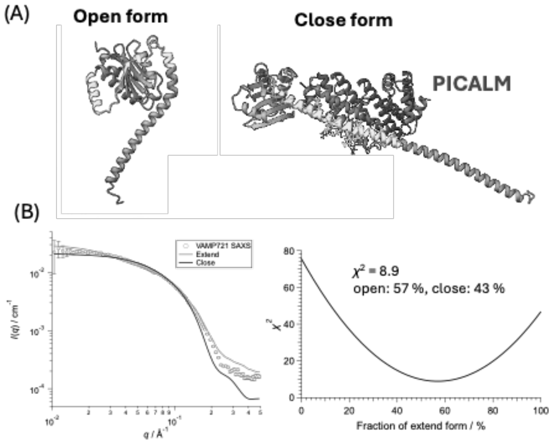

Fig. 1. Solution structure of VAMP721 compared with predicted structural models.
(A) Predicted “closed” and “open” conformation of VAMP721 generated by AlphaFold.
(B) Experimental SAXS profile of recombinant VAMP721 (black dots) compared with theoretical scattering curves calculated from the closed (blue) and open (red) models. The experimental data show better agreement with a possible mixture of conformational states in solution.

CO7-1

Antitumor effect of boron neurton capture therapy in cervical cancer mouse model.

A Toji[1], S Terada[1], S Tsunetoh[1], T Tanaka[1], M Ohmichi[1], J Arima[2], K Taniguchi[2], M Suzuki[3]

[1]*Department of Obstetrics and Gynecology, Osaka Medical and Pharmaceutical University, Takatsuki, Japan*
[2]*Department of general and gastroenterological surgery, Osaka Medical and Pharmaceutical University, Takatsuki, Japan*
[3]*Institute for Integrated Radiation and Nuclear Science, Kyoto University, Asasiro-Nishi, Kumatori-cho, Japan*

INTRODUCTION: In Japan, approximately 10,000 women develop cervical cancer and 2,900 women die from the disease annually. The incidence and mortality rates of cervical cancer in Japan are on the rise.Squamous cell carcinoma (SCC) is the most common histological type at 80%, and adenocarcinoma (Adeno) accounts for about 20%.The main treatment options for cervical cancer are surgery or radiation therapy. However, local and surface lymph nodes recurrence is not uncommon. Thus, new treatment modalities for cervical cancer are needed. In this study, we investigated the efficacy and safety of boron neutron capture therapy (BNCT) for cervical cancer in a mouse model.

EXPERIMENTS: BPA (L-isomer) was supplied by Stella Chemiphar (Osaka, Japan) and converted to fructose complex. 4-6 week-old female nude mice (BALB/c Slc-nu/nu) were purchased from SLC, Japan. Patient-derived xenograft (PDX) was created using cervical cancer tissue (SCC/Adeno). PDX is a procedure in which a patient's tumor tissue is transplanted into immunocompromised mice, and the response to treatment has been reported to be highly consistent with the effect on the patients themselves. [1, 2] Treatment was initiated 4-6 weeks after tumor with matrigel injection into the thighs of mice. Mice were divided into hot control (neutron ir-radiation only) and BNCT (peritoneal BPA followed by neutron irradiation) groups. 2.5 hours before neutron irra-diation, BPA (250 mg/kg) was injected intraperitoneally into mice in the BNCT group. After irradiation, tumor size and mouse weight were measured, and tumor volume was calculated as follows.V=ab2/2

RESULTS: Fig.1 and Fig.2 show that the tumor volume in the hot control and BNCT groups for cervical squamous cell carcinoma and adenocarcinoma PDX model. The tumor was suppressed in the BNCT group than in the hot control group ($P<0.05$). No adverse effects were observed in hot control and BNCT groups after irradiation. The body weight was no remarkable change in the both groups.

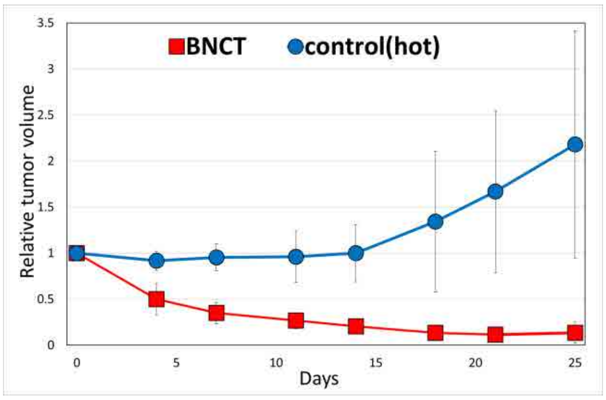

Fig.1 Antitumor effect on subcutaneous PDX (scc) tumor model.
Tumor grows curves in the hot control (irradiation only) and BNCT (irradiation after BPA administration) groups (n=6 in each group).

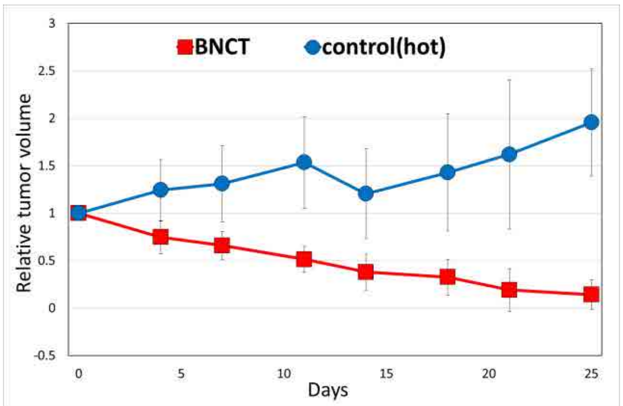

Fig.2 Antitumor effect on subcutaneous PDX (adeno) tumor model.
Tumor grows curves in the hot control (irradiation only) and BNCT (irradiation after BPA administration) groups (n=9 in each group).

REFERENCES:

[1] Shahrokh Abdolahi *et al.*, J. Transl. Med., **20(1)** (2022) 206.
[2] Miyamoto S. *et al.*, Cancers, **14 (12)** (2022) 2969.

CO7-2

The effect of boron neutron capture therapy (BNCT to gastrointestinal stromal tumor cell line GIST-T1

S. Hagihara[1], J. Arima [1], K. Taniguchi[1,2], Y. Inomata[1], A. Miyamoto[1], M. Suzuki[3], and Sang-Woong Lee [1]

Graduate School of Science, Kyoto University
[1]Department of Physics, Niigata University
[2]Accelerator Laboratory, KEK
[3]Faculty of Engineering, Toyama University
[4]Institute for Integrated Radiation and Nuclear Science, Kyoto University

INTRODUCTION: Gastrointestinal stromal tumors (GIST) are the most fre-quent soft-tissue sarcomas substantially arising from the gastrointestinal tract. Surgery is the first choice of treat-ment for primary GISTs. However, local recurrence or metastasis still occurs in 10% to 50% of patients after curative resection. Imatinib mesylate (imatinib) classified in a tyrosine kinase inhibitors is the primary agent of choice used to treat GISTs. On the other hand, drug re-sistance to imatinib poses a major obstacle to treatment efficacy.

In this study, we investigated the effectiveness of
boron neutron capture therapy (BNCT) to GIST-T1 and imatinib-resistant GIST-T1(GIST-T1/IM-R) using the mouse model.

****

EXPERIMENTS: We used Boronophenylalanine (BPA) as a boron compound. In vitro study, Cytotoxicity caused by BNCT with BPA was evaluated by colony forming assay. GIST-T1 and GIST-T1/IM-R cells were incubated with 20 μg B/mL BPA for 2h at 37 ◦C in 5% atmospheric CO2. In vivo study, GIST-T1 cells were concentrated to 2.0×107/100μL in 0.7ml of PBS and 0.3ml of Matrigel and injected into the right leg of each mouse. Animals were divided into three groups; the cold control (no treatment, no neutron irradi-ation), hot control (neutron irradiation only), and BNCT (intraperitoneal BPA administration and neutron irradia-tion) groups.

RESULTS: In vivo study, **Fig.1** showed that tumor volume (mm^3) significantly reduced in the BNCT group compared with that in the cold and hot control groups. In GIST tumors 1h after BNCT, the expression levels of γH2AX significantly increased in the BNCT group. Moreover, in tumor samples collected 72 h after irradiation, the expression levels of cleaved PARP, cleaved caspase-3 and cleaved caspase-8, which are markers of apoptosis, significantly increased in the BNCT group (**Fig.2A, B)** These results indicate that BNCT induces tumor apoptosis through severe DNA damage.

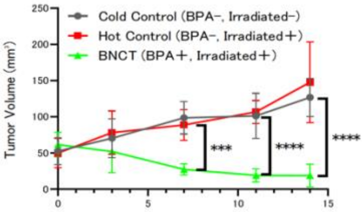

Fig.1 Tumor growth curves of each group after neutron irradiation. (n = 6 for the cold control group; n = 5 for the hot control group; and n = 7 for the BNCT group. Data are presented as the mean ± SD. ***P < 0.001 and ****P < 0.0001).

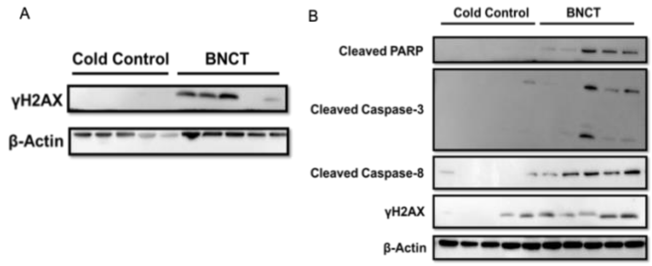

Fig.2 (a) γH2AX protein expression in the cold control (CC) and BNCT groups 1 h after irradiation, as determined by western blotting.(b) Cleaved PARP, Caspase-3, Caspase-8, and γH2AX protein expression levels in the CC and BNCT groups 72 h after irradiation, as determined via western blotting.

****

REFERENCES:

[1] Makiko Sasaki *et al.*, PLOS ONE, April 7, 2021 (doi)10.1371/journal.pone.0249650.

CO7-3

The effect of boron neutron capture therapy (BNCT to liver metastasis of colorectal cancer

Y. Ueda[1], J. Arima [1], K. Taniguchi[1,2], S. Hagihara[1], Y. Inomata[1], N. Kawaguchi [1], M. Suzuki[3], and Sang-Woong Lee [1]

[1] *Department of General and Gastroenterological Surgery, Osaka Medical and Pharmaceutical College, Osaka, Japan*
[2] *Translational Research Program, Osaka Medical and Pharmaceutical College, Osaka, Japan*
[3] *Department of Particle Radiation Oncology, Research Reactor Institute, Kyoto University, Kumatori, Osaka, Japan.*

INTRODUCTION: Management of liver metastases in colorectal cancer is a clinically important issue. However, only 10–15% of patients are eligible for surgery based on the size and number of metastatic lesions. Furthermore, for patients with multifocal, unresectable, or bilateral liver metastases who do not respond to chemotherapy, palliative care is the only option available. In this context, the development and evaluation of new treatment strategies are justified.
In this study, we investigated the effectiveness of boron neutron capture therapy (BNCT) to liver metastasis of colorectal cancer using the mouse model.

EXPERIMENTS: We used Boronophenylalanine (BPA) as a boron compound. Also, we used seven-week-old female BALB/cCrSlc mouse having physiological environment of immunity. Firstly, we established a mouse model of liver metastasis of CRC using DLD-1-Luc cells concentrated to $1.0\times10^6/100\mu L$ in 0.1ml of PBS. The boron concentrations in DLD-1-Luc tumors or surrounding organs at 2h, 4h, 6h after 500mg/kg BPA administration intraperitoneally. (**Figure.1**) According to this result, we considered the effects on the pancreas and decided to inject BPA intraperitoneally at 6h before irradiation. In BNCT study, animals were divided into three groups; the cold control (no treatment, no neutron irradiation), hot control (neutron irradiation only), and BNCT (intraperitoneal BPA administration and neutron irradiation) groups.

Figure.1 Biodistribution

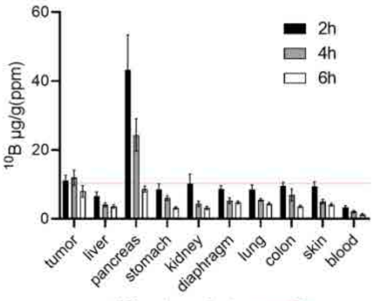

N=7 in each group, Error bar: means ± SE

RESULTS: In the BNCT group, transient weight loss was observed shortly after neutron irradiation, but no significant differences were observed among the groups at the endpoint. (**Figure 2)**
Tumor weight (g) in the BNCT group was significantly reduced compared to the cold control group and showed a decreasing trend compared to the hot control group. Additionally, tumor volume (mm³) in the BNCT group showed a decreasing trend compared to the other two groups, although no significant difference was observed. (**Figure 3)**
No severe adverse effects, including death, were observed in each of the groups.

Figure.2 Body weight

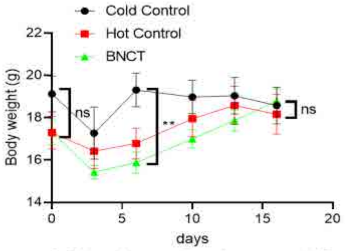

N=8 in each group, Error bar: means ± SE
ns: not significant, **p<0.01

Figure.3 Tumor volume and weight

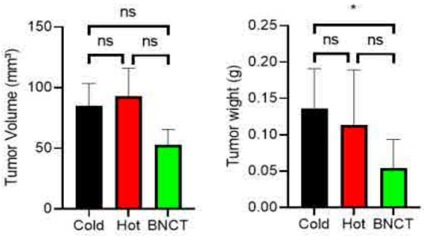

N=8 in each group, Error bar: means ± SE
ns: not significant, *p<0.05

Ongoing study:
Neutron irradiation will be performed 4 hours after BPA administration to investigate the effects on surrounding organs such as the liver and pancreas.
This study will be continued, and the results will be reported in the future.

REFERENCES:

[1] Wittig A. *et al.*, J Cell Mol Med., Aug 13 (2009) (doi)10.1111/j.1582-4934.2009.00856.
[2] Jun Arima *et al.*, Biomed. Pharmacother., 154 (2022) (doi)10.1016j.biopha.2022.113632.

R6003

CO7-4

Development of a Therapeutic Agent for Bone Metastases with Nuclear Imaging and Boron Neutron Capture Therapy

K. Ogawa[1], Y. Akita, K. Tamamura and M. Suzuki[2]

Graduate School of Medical Sciences, Kanazawa University
[1]Institute for Frontier Science Initiative, Kanazawa University
[2]Institute for Integrated Radiation and Nuclear Science, Kyoto University

INTRODUCTION: Boron neutron capture therapy (BNCT) using ^{10}B-labeled agents with companion diagnostics is promising for cancer theranostics. If BNCT and companion positron emission tomography (PET) imaging can be performed with compounds with the same chemical structure, it will be possible to predict the therapeutic and side effects of the compound for BNCT with higher accuracy. Recently, our research group developed a probe, closo-dodecaborate-(Ga-DOTA)-c(RGDfK), containing closo-dodecaborate ($[B_{12}H_{12}]^{2-}$) as a boron cluster, $[^{67/68}Ga]$Ga-DOTA as a stable $^{67/68}$Ga complex for single photon emission computed tomography (SPECT) or PET imaging, and an arginine–glycine–aspartic acid (RGD) peptide targeting $\alpha_v\beta_3$ integrin expressed on the cancer cell membrane [1]. Here, Ga-DOTA-K(ε-closo-dodecaborate)D_{11} (**1**) (Fig. 1), containing closo-dodecaborate ($[B_{12}H_{12}]^{2-}$), $[^{67/68}Ga]$Ga-DOTA, and an aspartic acid peptide as a carrier molecule to bone metastases sites binding to hydroxyapatite [2] was synthesized and evaluated for theranostics of bone metastases. Although we aimed to develop a ^{68}Ga-labeled agent, we used ^{67}Ga ($T_{1/2}$: 3.3 days), which has a long half-life and is easy to handle, and synthesized and evaluated $[^{67}Ga]$**1**.

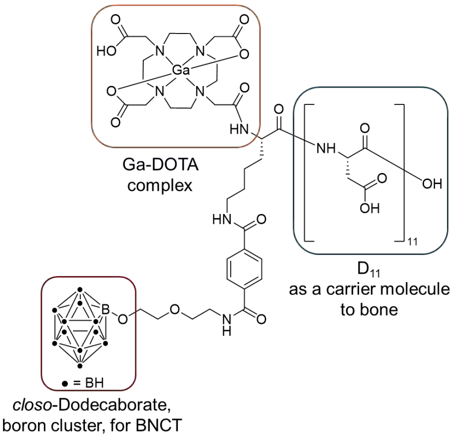

Fig 1. Chemical structure of **1**.

EXPERIMENTS: DOTA-KD_{11} was synthesized by the method of solid-phase peptide synthesis, and the precursor DOTA-K(ε-closo-dodecaborate)D_{11} was synthesized by condensation reaction between DOTA-KD_{11} and N-hydroxysuccinimide ester of closo-dodecaborate-conjugated terephthalic acid. $[^{67}Ga]$**1** was prepared with 91% radiochemical conversion and over 95% radiochemical purity after HPLC purification. Hydroxyapatite (HA) binding assay, biodistribution experiments in normal mice, and SPECT imaging of $[^{67}Ga]$**1** in a normal mouse were performed. In addition, boron accumulation in major organs after injection of DOTA-K(ε-closo-dodecaborate)D_{11} was determined by inductively coupled plasma optical emission spectrometry (ICP-OES).

RESULTS: In the HA binding assay, the binding ratio of $[^{67}Ga]$**1** increased in a HA concentration-dependent manner. In the biodistribution experiments, $[^{67}Ga]$**1** showed high accumulation in bone and low accumulation in non-target tissues except the kidney. SPECT imaging of $[^{67}Ga]$**1** visualized the bone joint. Meanwhile, the boron distribution in normal mice after injection of DOTA-K(ε-closo-dodecaborate)D_{11} determined by ICP-OES analysis was equivalent to that of the distribution of radioactivity after injection of $[^{67}Ga]$**1**.
These results indicate that a combination of PET or SPECT of $[^{67/68}Ga]$**1** and BNCT with **1** could be promising for cancer theranostics.

REFERENCES:

[1] K. Mishiro *et al.,* J. Med. Chem., **65(24)** (2022) 16741-16753.
[2] K. Ogawa *et al.,* PLoS One, **8(12)** (2013) e84335.

CO7-5

Examination of improvement of BNCT treatment efficiency by L-phenylalanine deficiency in mice tumor models

Y. Tamari[1], R. Saba[2], T. Takata[3], M. Suzuki[3], H. Yamazaki[2]

[1]*Department of Medical Information Technology, School of Medical Scinence, Fujita Health University*
[2]*Department of Radiology, Kyoto Prefectural University of Medicine*
[3]*Institute for Integrated Radiation and Nuclear Science, Kyoto University*

INTRODUCTION: L-Boronophenylalanine (L-BPA), a boronated isotope of L-phenylalanine (Phe), is used as a boron drug and is taken up by the tumor through its enhanced metabolism of amino acids. LAT1 is an exchange transporter, releasing one amino acid molecule into the extracel-lular space for the uptake of one amino acid molecule into the cell [1]. However, L-BPA is also taken up by normal cells via LAT2 and other pathways [2], and the improvement of the boron concentra-tion ratio (T/N ratio) between tumor and normal tissues has become an issue. In this study, we at-tempted to improve the therapeutic effect of BNCT by restricting Phe and improving L-BPA up-take.

EXPERIMENTS: 5.0 x 10^5 human tongue carcinoma-derived cell lines SAS were transplanted into the thighs of 6-week-old female nude mice. Two weeks after transplantation, the carcino-ma-bearing mice were fed Phe-free feed, and 500 mg/kg of L-BPA was administered after 24 hours. Carcinoma-bearing mice were fed Phe-free feed for 24 hours, and 2 hours after admin-istration of 500 mg/kg L-BPA, they were neutron irradiated. Neutron-irradiated carcinoma-bearing mice were kept until approximately one month after irradiation, during which time their body weight and tu-mor size were regularly measured.

RESULTS: A mouse tumor model irradiated for 6 minutes at 5 MW in a heavy water facility showed a decrease in tumor size in the neutron-only group compared to the non-irradiated group. Tumor size was further reduced in the BNCT (Phe+) and BNCT (Phe-) groups and was significantly reduced with BNCT (Phe-) compared to BNCT (Phe+). There was no significant decrease in mouse body weight. we plan to investigate the contribution of other amino acid depletion and preload to L-BPA uptake.

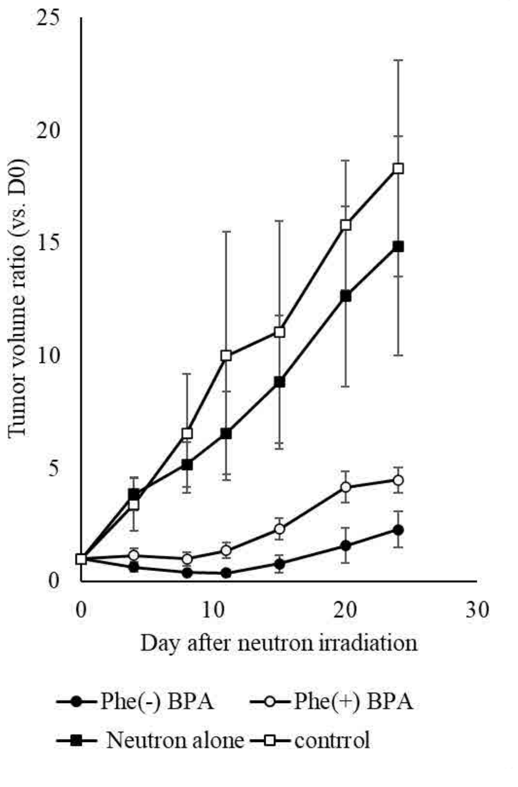

Fig. 1. Change over time in tumor size ratio after Phe-restricted BNCT.

REFERENCES:

[1] A. Wittig *et al.,* Radiat Res., **153** (2000) 173-180.
[2] P. Wongthai *et al.,* Cancer Sci., **106** (2015) 279-286.

CO7-6

Basic research on new BNCT strategies for melanoma

H. Michiue[1], T. Fujimoto[1,2], N. Kanehira[1,2], K. Igawa[1], M. Shirawaka[1] Y. Sakurai[3], N. Kondo[4], T. Takata[3], and M. Suzuki[3]

[1]Neutron Therapy Research Center, Okayama University; 2-5-1, Shikata-cho, Kita-ku, Okayama City, Okayama, Japan.
[2]Department of Gastroenterological Surgery, Okayama University; 2-5-1, Shikata-cho, Kita-ku, Okayama City, Okayama, Japan.

[3]Institute for Integrated Radiation and Nuclear Science, Kyoto University, 2-1010, Asashiro-Nishi, Kumatori-cho, Sennan-gun, Osaka, Japan.

INTRODUCTION: The starting point for melanin synthesis in the body is aromatic amino acids such as phenylalanine and tyrosine, and melanin synthesis is promoted in skin malignancies such as malignant melanoma. Boron-substituted phenylalanine (BPA), which contains boron atoms bound to these amino acids, has been developed as a boron-based drug targeting malignant melanoma. Its efficacy was demonstrated in a 1989 Lancet paper by Mishima et al.: "Treatment of malignant melanoma with single-dose thermal neutron capture therapy: Single-dose thermal neutron capture therapy using 10B compounds targeting malignant melanoma" was published in The Lancet in 1989 by Mishima et al. This clinical study demonstrated the efficacy of BNCT using boron-based drugs characterized by cell-specific uptake and neutron irradiation of tumor tissue.While there have been reports of BNCT for skin malignant tumors such as localized melanoma, we have undertaken a project to evaluate the efficacy of BNCT in combination with immune checkpoint inhibitors to establish its applicability for advanced cancers with lesions outside the irradiation field. This is a challenge to explore new possibilities for BNCT, which has developed as a local therapy.

****

EXPERIMENTS: We purchased the B16-F10 mouse melanoma cell line to create a melanoma model, Mouse anti-PD-1 was intraperitoneally administrated on day 4 or 7 after cell implantation. On the following day, mice were anesthetized, and 500 mg/kg BPA was subcutaneously injected. After 1 h, 5 MW neutron irradiation was performed for 12 min. At day 10 and 13 after implantation, mouse anti-PD1 was intraperitoneally administrated on day 3, 5, 9, and 13. Animal experiments were performed after strict approval by the ethics committees for animal experiments at Okayama University and Kyoto University.

.***

Fig.1

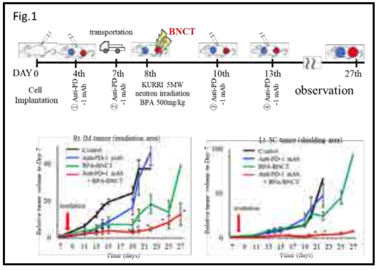

RESULTS: Ex1) We used BPA as an effective boron agent for Pharmacokinetic (PK) evaluation of BPA was performed in a mouse model of advanced-stage melanoma. To establish the model, B16F10 melanoma cells were transplanted intramuscularly in the right thigh and subcutaneously in the left flank. BPA (500 mg/kg) was then administered intraperitoneally or subcutaneously. Subcutaneous administration of BPA resulted in approximately 50 ppm 10B in the right tumor and 12.7 ppm 10B in the left tumor after 1 h. Next, BNCT with immunotherapy (B-NIT) was administered to mice modeling advanced-stage melanoma (Figure 2A). At the neutron-irradiated site, tumor volume ratios on day 22 were 37.6 (control group), 46.4 (anti-PD-1 mAb group), 18.4 (BNCT group), and 3.7 (B-NIT group) (Fig.1). On the other hand, the tumor volume ratio of the shielded remote site was 66.6 (control group), 47.8 (anti-PD-1 mAb group), 24.7 (BNCT group), and 3.9 (B-NIT group), the immune effect was confirmed (Fig.1).

Fig.2

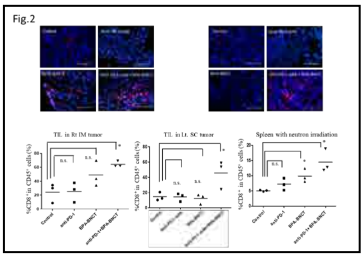

Ex2) In the tumor tissue of the right thigh (irradiation site), a high density of CD8+ T cells was identified in the BNCT and B-NIT on day 22 (Fig.2). Analysis of TILs in the left subcutaneous tumors showed high levels of CD8+ T cells in the B-NIT group compared with other groups (control: 14.4%, anti-PD-1 mAb: 14.1%, BPA-BNCT: 12.1%, B-NIT: 45.6%, Figure 4D). Immunostaining also showed strong intratumor localization of CD8+ cells in the B-NIT (Fig.2).

****

REFERENCES: [1] T. Fujimoto *et al.,* Cancer Sci., **115(10)** (2024) 3231-3247.

CO7-7

Cytosolic Delivery Technology Using Cationic Lipids in BNCT

S. Hirase[1], Y. Araki[1], A. Aoki[1], Y. Hattori[2], M. Kirihata[2], I. Nakase[1]

[1]*Graduate School of Science, Osaka Metropolitan University*
[2]*Research Center for BNCT, Osaka Metropolitan University*

INTRODUCTION: Boron neutron capture therapy (BNCT) is a therapy in which ^{10}B boron is introduced into the target cancer cells, and ^{10}B atoms are transmuted by thermal neutron irradiation, generating α particles and Li recoil nuclei, leading to cell death. BNCT is currently recognized as highly effective in targeting refractory cancers such as brain tumors and head and neck cancer [1]. The ^{10}B compounds such as dodecaborate (BSH) are used in BNCT, however, high concentrations of the boron compounds must be administered continuously to achieve therapeutic effects with current technology (high concentrations of several mM are required in in vitro experiments), and the urgent issue is to improve technology to increase intracellular introduction efficiency and retention rate. In this study, in order to enhance the intracellular delivery of BSH with polyhedral borane anion structure, we evaluate the cellular uptake and BNCT activity using cationic lipids [2] and arginine-rich cell-penetrating peptides (CPPs) [3].

EXPERIMENTS: Lipofectamine LTX as cationic lipid and hexadeca oligoarginine (R16) synthesized by Fmoc-solid phase method were used in the experiments. Fluorescence-labeled BSH (FITC-BSH) was used, and cellular uptake was evaluated by confocal laser microscope and flow cytometer. BNCT activity was examined by irradiating rat C6 glioma cells with thermal neutron beams (Institute for Integrated Radiation and Nuclear Science, Kyoto University) for cancer cell killing activity after internalization of the BSH by the cells.

RESULTS: Mixing FITC-BSH with Lipofectamine LTX markedly increased cellular uptake in C6 glioma cells, and confocal laser microscopy confirmed cytosolic release and nuclear accumulation of the FITC-BSH. In the case of mixing FITC-BSH with R16, the efficacy of cellular uptake was also enhanced, however, only endosomal fluorescent signals were observed in the cells. In the absence of thermal neutron irradiation, no cytotoxicity was observed under each mixing condition. After FITC-BSH was internalized by C6 glioma cells, the cells were irradiated with thermal neutron, and a colony assay was performed. The results showed that a mixture of FITC-BSH and Lipofectamine LTX has superior cancer cell-killing activity. On the other hand, it was also found that when FITC-BSH and R16 were mixed, thermal neutron irradiation induced very low cancer cell-killing activity. The results show that cationic lipids are suitable for intracellular delivery of BSH, and that BSH can be efficiently delivered to the cell nucleus by mixing with lipids, and that its subcellular localization greatly affects the cancer cell-killing activity induced by thermal neutron irradiation [4].

REFERENCES:

[1] Y. Hattori *et al.,* J. Radiat. Res., **64** (2023) 859−869.
[2] S. Futaki, I. Nakase, Acc. Chem. Res., **50** (2017) 2449−2456.
[3] I. Nakase, S. Futaki, Sci. Rep., **5** (2015) 10113.
[4] S. Hirase *et al.,* Biol. Pharm. Bull., **48** (2025) 344−354.

R6017

CO7-8

Neutron irradiation experiments using a novel BPA formulation based on ionic liquids

M. Shirakawa[1], K. Banshoya[2], A. Machida[2], M. Ohnishi[2], T. Takata[3], N. Kondo[3], Y. Sakurai[3], T. Hanafusa[1], K. Igawa[1], H. Michiue[1] and M. Suzuki[3]

[1] *Neutron Therapy Research Center, Okayama University*
[2] *Faculty of Pharmacy and Pharmaceutical Sciences, Fukuyama University*
[3] *Institute for Integrated Radiation and Nuclear Science, Kyoto University*

INTRODUCTION: L-p-boronophenylalanine (BPA) exhibits strong antitumor activity following thermal neutron exposure; however, its limited solubility necessitates high dosing to attain therapeutic outcomes. To address this challenge, our research has focused on the application of ionic liquids (ILs), which we have previously explored and reported [1, 2]. In the present study, we synthesized a novel formulation that has the same or better potential as IL and reported its in vivo antitumor effect after thermal neutron irradiation.

EXPERIMENTS: Three-week-old female BALB/cA mice were obtained from CLEA Japan Inc. (Tokyo, Japan). To establish the tumor model, 2 × 10^6 murine colon carcinoma CT26 cells were subcutaneously inoculated into the right thigh of 4-week-old mice (body weight: 16–20 g), resulting in tumors measuring 6–8 mm in diameter.

Ten days after inoculation, a novel BPA formulation (MS01; 20 µL, equivalent to 14 mg ^{10}B/kg) was administered intravenously prior to neutron irradiation. For comparison, a BPA–sorbitol complex (BPA-Sor) was administered intravenously at a volume of 200 µL. In a separate group, MS01 (200 µL, equivalent to 140 mg ^{10}B/kg) was also administered intravenously.

Two hours after administration, thermal neutron irradiation was performed for 12 minutes at a flux of 5.5–6.1 × 10^9 neutrons/cm^2/s. Tumor growth was monitored until day 26 post-irradiation, and tumor volumes were calculated using a previously described formula [3].

RESULTS: MS01 suppressed tumor growth to a level comparable to that achieved with BPA-Sor, despite being administered in a substantially smaller volume. Furthermore, in the group that received MS01 at the same volume as the BPA-Sor group, a more pronounced antitumor effect was observed, including cases of complete tumor regression.

In addition, no significant adverse effects, such as body weight loss, were observed following the administration of either MS01 or BPA-Sor.

REFERENCES:

[1] M. Shirakawa *et al.,* Patent No. 7525094.
[2] M. Shirakawa *et al.,* Patent No. 7525095.
[3] M. Shirakawa *et. al.,* KURNS PROGRESS REPORT 2021 (2022) 208.

CO7-9

Investigation of boron drug using albumin-binding polymer modified with boron clusters

K. Banshoya[1], A. Machida[1], Y. Kaneo[1], T. Tanaka[1], T. Takata[2], N. Kondo[2], Y. Sakurai[2], M. Suzuki[2], M. Ohnishi[1] and M. Shirakawa[3]

[1] *Faculty of Pharmacy and Pharmaceutical Sciences, Fukuyama University*
[2] *Institute for Integrated Radiation and Nuclear Science, Kyoto University*
[3] *Neutron Therapy Research Center, Okayama University*

INTRODUCTION: Boron neutron capture therapy (BNCT) is theoretically a cell-selective radiotherapy. The anti-tumor effect of BNCT depends on the accumulated concentration of non-radioactive boron isotopes in tumor cells. We developed a new polymerized boron drug, BSH-AB polymer, by combining mercaptoundecahydrododecaborate (BSH) with a serum albumin-binding polymer (AB polymer), which targets malignant tissues via the EPR effect. This study examines the anti-tumor effects of BSH-AB polymers.

EXPERIMENTS: The BSH-AB polymer was synthesized by reacting the thiol group of BSH with the carboxyl group of the AB polymer using a condensation agent. Unreacted BSH was removed by dialysis against distilled water. After dialysis, the BSH-AB polymer was obtained as a powder by lyophilization. To evaluate the antitumor effect, an experiment was conducted using BALB/c mice bearing subcutaneous xenografts of the CT26 mouse colon carcinoma cell line. A dose of 7 mg ^{10}B/kg of BSH-AB polymer was administered via intravenous injection prior to neutron irradiation. Twenty-four hours after injection, thermal neutron irradiation was performed for 12 minutes at a flux of 5.0-5.7 × 10^9 neutrons/cm^2/s. Tumor size was monitored over time following irradiation, and tumor volume was calculated using a previously established formula, continuing until day 24.

RESULTS: As shown in Figure 1, compared to the irradiate-only group, tumor growth tended to be suppressed when thermal neutron irradiation was performed 24 hours after BSH-AB polymer administration. However, this antitumor effect was less pronounced than that observed with the BPA–sorbitol complex administered 2 hours before irradiation. Further research is needed to optimize the timing of thermal neutron irradiation. As shown in Figure 2, no significant side effects (e.g., weight loss) were observed after using BSH-AB polymer, similar to BPA-sorbitol complex.

REFERENCES:

[1] K. Maruyama *et al.,* J. Controlled. Release. **98** (2004) 195-207.

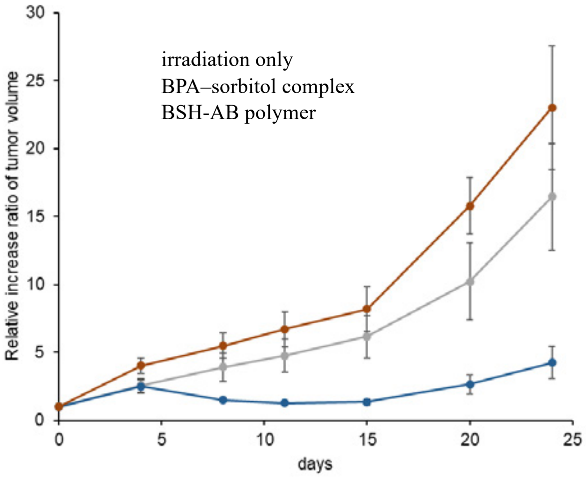

Fig. 1. BNCT effects of BSH-AB polymer.

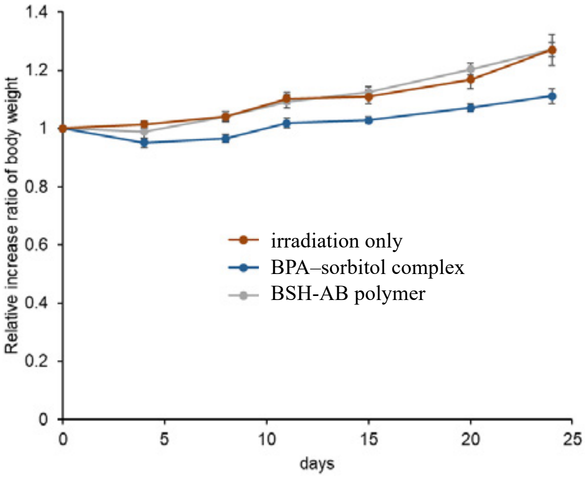

Fig. 2. The ratio of post-BNCT weight changes.

CO7-10

Development of boron rich nanostructure with amphiphilic block polymers as boron agents for BNCT

R. Kawasaki,[1] A. Oshige,[1] K. Yamana,[1] Y. Miura,[1] T. Saito,[1] Y. Sanada,[2] Y. Sakurai,[2] H. Tanaka,[2] M. Suzuki,[2] M. Y. Hattori,[3] M. Kirihata,[3] T. Nishimura,[4] N. Miyamoto,[5] T. Nagasaki,[6] and A. Ikeda[1]

[1]*Applied Chemistry Program, Department of Advanced Science and Engineering, Graduate School of Advanced Science and Engineering, Hiroshima University*

[2]*Institute for Integrated Radiation and Nuclear Science, Kyoto University*

[3]*Research center for BNCT, Osaka Metropolitan University*

[4]*Department of Chemistry and Materials, Faculty of Textile Science, Shinshu University*

[5]*Faculty of Engineering, Aichi Institute of Technology*

[6]*Department of Orthopedic Surgery, Graduate School of Biomedical and Health Sciences, Hiroshima University*

[7]*Department of Applied Chemistry and Bioengineering, Graduate School of Engineering, Osaka Metropolitan University*

INTRODUCTION: Amphiphilic block polymers which possess both hydrophilic and hydrophobic segments in a polymer spontaneously formulate supramolecular nanostructure including polymer micelles and polymer vesicles via self-assembly in aqueous media. These submicron-sized assembly can trap large amounts of pharmaceuticals within their polymer matrixes and their size are advantageous in enhancing deliverability of pharmaceuticals to tumor tissue via EPR effect. In addition, the easiness to fabricate functionality including imaging, targeting, and controlled release properties encouraged to use these nanosystems as drug delivery systems [1]. We designed and synthesized amphiphilic block polymers comprising phenylboronic ester groups as hydrophobic segment and demonstrated the performance of the nanosystem as boron agents for BNCT. Herein, the hydrophobic core or membrane-like structure consisting large amounts of boron atom are advantageous in enhancing the efficiency of boron neutron capture reaction, which can contribute to improve therapeutic efficacy of BNCT.

RESULTS AND DISCUSSION: The amphiphilic polymers comprising phenylboronic ester groups were synthesized by RAFT polymerization using activated polyethylene glycol as a RAFT initiator. To address the effects of polymerization degree of phenylboronic ester group containing monomers to the structure of nanoassembly, we prepared the series of polymers with varying the polymerization degree of the monomers. Both systems formulated nanoassembly with a diameter of 80-150 nm within aqueous media and spherical morphology were found by transmission electron microscopy. To clarify the structure, we measured small angle X-ray scattering for the polymers. Scattering profiles of nanoassembly using polymers with low and high polymerization degree exhibited representative peaks found in polymer vesicles and polymer micelles, respectively.

We next investigated the performance of polymer micelles and polymer vesicles as boron agents for BNCT and L-BPA-sorbitol complex, which is used as clinical drugs, were employed as control. As a result, our polymer systems exhibited higher BNCT activity than L-BPA-sorbitol complex toward SCC VII. For these results, our systems are potentially applicable as boron delivery system for BNCT.

REFERENCES:

[1] W. Y. Fu *et al.,* Biomacromolecules, **25** (2024) 4215-4232.

R6022

CO7-11

Development of a Water-Soluble Small Molecule Boron Carrier Targeting Biotin Receptors for Neutron Capture Therapy

H. Nakamura K. Nishimura[1], S. Tanaka[1], K. Miura, S. Okada, M. Suzuki[2]

Laboratory for Chemistry and Life Science, Institute of Integrated Research, Institute of Science Tokyo
[1] School of Life Science and Technology, Institute of Science Tokyo
[2] Institute for Integrated Radiation and Nuclear Science, Kyoto University

INTRODUCTION: Boron Neutron Capture Therapy (BNCT) has emerged as a promising non-invasive radiotherapeutic modality for the treatment of cancer. 4-Borono-L-phenylalanine (BPA) is known to preferentially accumulate in tumor cells via the L-type amino acid transporter 1 (LAT1). However, the therapeutic efficacy of BPA-based BNCT is limited in tumors with low LAT1 expression, due to its dependency on this transporter. Therefore, the development of novel boron delivery agents, independent of LAT1 expression, is essential for expanding the clinical applicability and efficacy of BNCT. We recently developed a novel boron carrier, pteroyl-closo-dodecaborate-conjugated 4-(p-iodophenyl) butyric acid (PBC-IP) [1]. PBC-IP demonstrated selective uptake by glioma cells at levels 10–20 times higher than those of BPA and exhibited excellent BNCT efficacy in a glioblastoma xenograft mouse model. In this study, we designed a biotinyl-closo-dodecaborate conjugate with an iodophenyl moiety (BBC-IP) [2]. Biotin receptors (BRs) are known to be overexpressed in a variety of cancer cells.

EXPERIMENTS: BBC-IP was designed and synthesized. Tumor-bearing mice (female, 5-6 weeks old) were prepared by injecting subcutaneously (s.c.) a suspension of human head and neck squamous cell carcinoma SAS cells. The tumor-bearing mice were injected i.v. with 200 µL of BBC-IP and BPA in PBS at a 25 mg [^{10}B]/kg dose. At 3 h after injection, the tumors of mice were irradiated with neutrons in the nuclear reactor at a dose range of 3.0–4.2 × 10^{12} neutrons/cm^2. The tumor volume and body weight of the mice were measured after neutron irradiation.

RESULTS: Biodistribution studies revealed that BBC-IP achieved enhanced tumor accumulation (9.7 µg [B]/g, 3 h) in mouse colon tumors, surpassing BPA's accumulation levels (7.2 µg [B]/g, 3 h) at a dose of 15 mg [B]/kg. In contrast, BPA showed significantly higher antitumor efficacy than BBC-IP-HSA (Fig.1A). This observation suggested one possibility that the observed antitumor effects can be attributed to differences in intracellular localization between BBC-IP and BPA. Body weight remained stable across the hot control, BBC-IP, and BPA groups, suggesting minimal systemic toxicity (Fig. 1B).

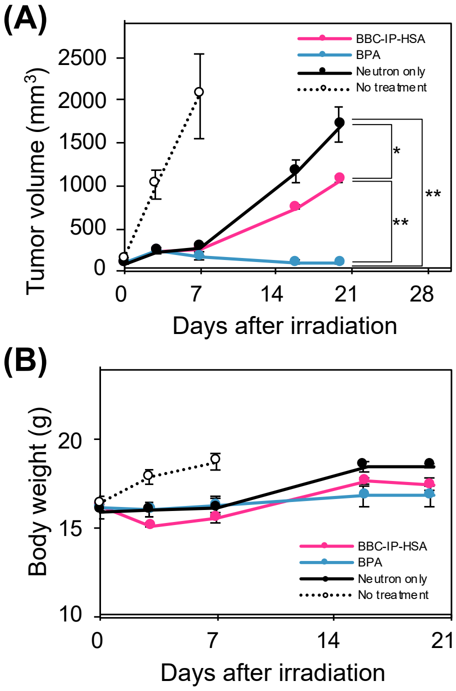

Fig. 1. Anti-tumor effects of BNCT in CT26 tumor-bearing mice. (A) Tumor volume in mice after BNCT with BBC-IP and BPA (25 mg [^{10}B]/kg i.v.). Data are expressed as mean ± SD (n = 4–6). Significance was determined as *$p < 0.05$ and **$p < 0.0001$. (B) Body weight changes of mice after BNCT.

REFERENCES:

[1] K. Nishimura *et al.,* J. Control. Release, **360** (2023) 249–259.

[2] K. Nishimura *et al.,* ACS Omega, **9** (2024) 51631–51640.

CO7-12

BNCT Effect of PBC-IP on Head and Neck Squamous Cell Carcinoma Mouse Model

K. Miura, K. Nishimura[1], M. Suzuki[2], H. Nakamura

Laboratory for Chemistry and Life Science, Institute of Integrated Research, Institute of Science Tokyo
[1]*School of Life Science and Technology, Institute of Science Tokyo*
[2]*Institute for Integrated Radiation and Nuclear Science, Kyoto University*

INTRODUCTION: Boron Neutron Capture Therapy (BNCT) has emerged as a promising non-invasive radiotherapeutic modality for the treatment of cancer. 4-Borono-L-phenylalanine (BPA) is known to preferentially accumulate in tumor cells via the L-type amino acid transporter 1 (LAT1). However, the therapeutic efficacy of BPA-based BNCT is limited in tumors with low LAT1 expression, due to its dependency on this transporter. Therefore, the development of novel boron delivery agents, independent of LAT1 expression, is essential for expanding the clinical applicability and efficacy of BNCT. We recently developed a novel boron carrier, pteroyl-closo-dodecaborate-conjugated 4-(p-iodophenyl) butyric acid (PBC-IP) [1]. PBC-IP demonstrated selective uptake by glioma cells at levels 10–20 times higher than those of BPA and exhibited excellent BNCT efficacy in a glioblastoma xenograft mouse model. Nevertheless, it re-mains to be clarified whether PBC-IP can also be selectively taken up by other cancer cell lines and retain its therapeutic efficacy in BNCT. In this study, we investigated the potential of PBC-IP for the treatment of head and neck cancer, with the aim of expanding its therapeutic applicability. **EXPERIMENTS:** PBC-IP was designed and synthesized according to the previous report [2]. Tumor-bearing mice (female, 5-6 weeks old) were prepared by injecting subcutaneously (s.c.) a suspension of human head and neck squamous cell carcinoma SAS cells. The tumor-bearing mice were injected i.v. with 200 µL of PBC-IP and BPA in PBS at a 25 mg [^{10}B]/kg dose. At 3 h after in-jection, the tumors of mice were irradiated with neutrons in the nuclear reactor at a dose range of 3.0–4.2 × 10^{12} neutrons/cm^2. The tumor volume and body weight of the mice were measured after neutron irradiation.

RESULTS: The therapeutic efficacy of BNCT was evaluated by monitoring tumor volume and body weight following thermal neutron irradiation. Significant tumor suppression was observed in mice treated with either PBC-IP or BPA, whereas rapid tumor progression occurred in both cold and hot control groups. BPA exhibited a more pronounced anti-tumor effect than PBC-IP. Body weight remained stable across the hot control, PBC-IP, and BPA groups, suggesting minimal systemic toxicity [2].

In conclusion, although PBC-IP demonstrates potential as an alternative boron carrier for BNCT, particularly in FR-expressing tumors, BPA remains the preferred agent for BNCT in head and neck cancer due to its higher tumor accumulation and superior therapeutic efficacy.

REFERENCES:

[1] K. Nishimura *et al.,* J. Control. Release, **360** (2023) 249–259.

[2] K. Miura *et al.,* App. Radiat. Isotop., **221** (2025) 111837.

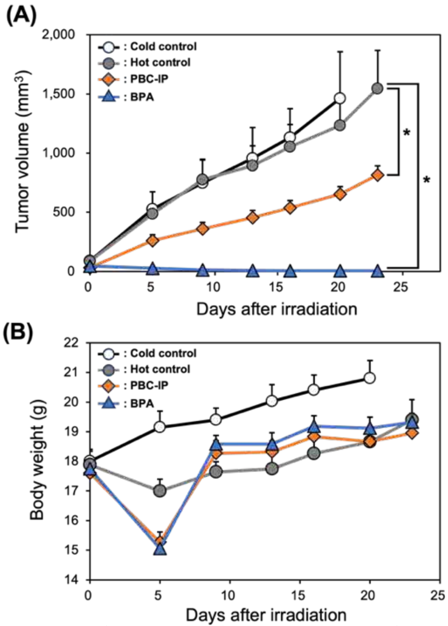

Fig. 1. Anti-tumor effects of BNCT in SAS xenograft model mice. (A) Tumor volume in mice after BNCT with PBC-IP and BPA (25 mg [^{10}B]/kg i.v.). Data are expressed as mean ± SD (n = 4–6). Significance was determined as $*p < 0.05$ using the two-sided Student's t-test. (B) Body weight changes of mice after BNCT.

CO7-13

Construction of novel Boron-containing silica nanoparticles and BNCT experiments

F. Tamanoi[1], K. Matsumoto[1], A. Komatsu[1], Y. Higashi[1] and M. Suzuki[2]

[1]*Institute for Advanced Study, Institute for Integrated Cell-Materials Sciences, Kyoto University*
[2]*Institute for Integrated Radiation and Nuclear Science, Kyoto University*

INTRODUCTION: Two type of boron compounds which are boron phenyl alanine (BPA) and borocaptate (BSH) have been mainly used for BNCT. But, these compounds have problems such as BSH having low uptake into cancer cell and BPA having short retention in tumor. Thus, novel boron compounds which can overcome these problems need to be developed for future BNCT.

We used a new type of mesoporous silica-based nanoparticle (MSN) that is modified with poly-ethylene glycol (PEG) and tetramethylammonium chloride (TMAC) to positively charged on sur-face. This nanoparticle has a large surface area where a large quantity of boron compounds which include BPA or BSH can be loaded. As we previously reported, our silica-based nanoparticle does have the ability to be effectively taken up in cancer cells by endocytosis system. It is also accumu-lated by EPR effect and retained in the tumor after intravenously injected to animal body. In this study, we evaluated the biodistribution of new MSN which has positively charged surface and di-ameter of less than 50 nm.

EXPERIMENTS: We used MSN which was synthesized by sol-gel method using tetraethoxysilane (TEOS) and modified with PEG and TMAC to positively charge on surface. It has the size of less than 50 nm. This MSN was also labeled with Rodamine B dye to trace where it accumulates in mouse body after injection. The MSN was characterized by using TEM, DLS, nitrogen adsorp-tion-desorption analysis and zeta potential. For biodistribution analysis, MSN was intravenously injected to CT26 mouse colon cancer- mouse xenografts at 5 mg/mouse or 2 mg/ mouse, and we dissected tumor and organs which include liver, lung and kidney at 24 hours after injection. Tumor and organs were made into thin sections and the fluorescence of MSN was detected with a confocal microscope.

RESULTS: The analysis showed that the size of MSN was less than 50 nm diameter and had homogenous shapes examined by DLS and TEM microscopy. And then, the surface of MSN was positively charged due to modification with PEG and TMAC. The zeta potential of MSN was 38.29 ±0.77 mV in water. MSN accumulation in the CT26-transplanted mouse was investigated with a confocal microscope after making thin sections. MSN accumulated in the tumor at 24 hours after injection. A maximum level of red fluorescence of MSN was detected in the tumor, whereas it was weakly detected in other organs including liver, kidney and lung.

We are currently attaching boron to MSN. These results suggest that MSN may be an effective boron carrier for BNCT. This MSN may be able to become a new boron reagent for BNCT beyond BPA and BSH if boron compounds are grafted to it.

R6030

CO7-14

Synthesis of PEPT1-targeted boron containing dipeptids for pancreatic cancer therapy

F. Tamanoi[1], K. Matsumoto[1], A. Komatsu[1], Y. Higashi[1] and M. Suzuki[2]

[1]*Institute for Advanced Study, Institute for Integrated Cell-Materials Sciences, Kyoto University*
[2]*Institute for Integrated Radiation and Nuclear Science, Kyoto University*

INTRODUCTION: Peptide transporter 1 (PEPT1) has been noticed because it is expressed on various type of cancer cells. Especially, it has been reported that PEPT1was highly expressed pancreatic cancer PDX model.

We used some of dipeptide which contained ^{10}B that has higher solubility, longer retention ability in the tumor than BPA. These dipeptides are actively taken up into cancer cells by PEPT1 and LAT1 (weakly).

We investigated BNCT efficacy of these ^{10}B-dipeptides or BTS and the vaccine-like effect to distant tumor (uniraddiated tumor) when dipeptides are used.

EXPERIMENTS: We used two types of dipeptides. Dipeptides were intravenously injected to CT26-tansplanted BALB/c mice or FaDu-transplanted nude mice 2 hours before neutron irradiation. Our aim was to investigate whether the BNCT efficacy of dipeptides can be improved compared with BPA by neutron irradiation at KUR. The thermal neutron was irradiated for 6 minnutes at 5MW. After neutron irradiation, tumor volume and body weight measured for 6 weeks after irradiation (up to 42 days after irradiation) to evaluate the BNCT efficacy of dipeptides. For vaccine-like effect evaluation, the CT26-transplanted BALB/C mouse was injected with dipeptides and irradiated with neutron for 6 minutes at 5MW. Two weeks after irradiation, fresh tumor was transplanted on the left leg and was examined the engraftment to evaluate vaccine-like effect induction.

RESULTS:

In previous experiments for tumor accumulation of boron, it has been shown that dipeptides are effective boron carriers. We then investigated BNCT efficacy of these boron compounds. Dipeptides were intravenously injected to CT26-transplanted mice 2 hours before neutron irradiation. These mice were held to 12 mouse holder and placed in front of KUR, and neutron was irradiated. Tumor was almost disappeared on dipeptides-injected mice and tumor regrowth was not observed up to 27 days after BNCT, whereas regrowth was observed on BPA-injected mice. Similar results were observed with FaDu-transplanted nude mice. These results indicate that dipeptides have the potential to strongly cure cancer by BNCT.

We have further carried out vaccine-like effect induction on CT26-transplanted mice which were injected with dipeptides by neutron irradiation. Mice which were transplanted CT26 on right leg was irradiated with neutron, and the tumor was completely eradicated 2 weeks after irradiation. These mice were transplanted CT26 again on left leg for vaccine-like effect observation. As a result, no tumors were observed in the left reg on each mouse, and tumors were completely disappeared from both legs.

We are now preparing the paper to describe these experiments.

In the future, we will investigate the abscopal effect related to BNCT using dipeptides.

R6032

CO7-15

Sensitization of BPA-BNCT by Regulating the Polarity of Tumor-Associated Macrophage Using Shikonin

N. Takabayashi, N. Yasukawa, K. Matsuda, K. Bando, R. Kawasaki[1], N. Kondo[2], Y. Sanada[2], Y. Sakurai[2], M. Suzuki[2]and T. Nagasaki

Graduate School of Engineering, Osaka Metropolitan University
[1] Graduate School of Advanced Science and Engineering, Hiroshima University
[2] Institute for Integrated Radiation and Nuclear Science, Kyoto University

INTRODUCTION: Although boron neutron capture therapy (BNCT) has excellent cancer cell killing ability, in many clinical cases it is ultimately incurable due to recurrence and metastasis. One of the factors for the cancer malignancy is the influence of the cancer microenvironment, represented by tumor-associated macrophages (TAMs). TAMs are broadly divided into M1 and M2 types, with M1 being tumoricidal and M2 being involved in suppressing cancer immunity and cancer cell proliferation and metastasis. In order to enhance the therapeutic effect of BNCT, it is important to control the cancer microenvironment as well as improve boron drugs.[1] It is known that macrophages express dectin-1 as β-1,3-glucan receptor on plasma membrane. In this study, we aim to efficiently and selectively deliver a TAM polarizer to TAM using β-1,3-glucan as a carrier, and evaluate the BNCT sensitization effect by the control of TAM polarity. When M2 macrophage is activated, STAT3, a transcription factor involved in anti-inflammatory responses and cell proliferation, is increased. Shikonin, a naphthoquinone compound produced by plants of the Boraginaceae family, functions as a STAT3 inhibitor and is therefore expected to act as a TAM polarizer.

EXPERIMENTS: To solubilize poorly water-soluble shikonin with β-1,3-glucan, we prepared shikonin/β-1,3-glucan composite nanogels (SKN/GC nanogels) using a dialysis complexation. To examine the inhibitory effect of SKN/GC nanogel on M2 induction in vitro, we used Raw264.7 cells and analyzed the mRNA expression levels of M1 (iNOS) and M2 (Arg-1, CD206) markers in the presence or absence of SKN/GC nanogel upon stimulation with IL-4 and IL-13 by RT-PCR. In vivo, SCC-VII cells (a mouse squamous cell carcinoma cell line) were subcutaneously implanted into C3H mice to prepare tumor-bearing mice. After that, neutron irradiation was performed with BPA-BNCT (250 mg/kg), and SKN/GC nanogel ([SKN] = 100 μM, 200 μl) was administered via the tail vein on the 2nd, 5th, and 7th days after irradiation to evaluate the combined effect. In addition, tumor tissue was excised on the 2nd, 5th, and 14th days. Total RNA was extracted from the excised tumor, and the M1/M2 ratio was analyzed by RT-PCR.

RESULTS: In vitro results showed that the presence of SKN/GC nanogel reduced the expression of M2 markers (Arg-1 and CD206), suppressing M2 progression. In vivo results showed that the combination of BPA-BNCT and SKN/GC nanogel suppressed tumor regrowth from 3 weeks after irradiation. RT-PCR analysis confirmed an increase in M1 markers and suppression of M2 markers from 4 days after neutron irradiation.

These results demonstrated that delivery of shikonin, a STAT3 inhibitor, with a β-1,3-glucan carrier, to dectin-1 cells enhances the anticancer effect of BPA-BNCT by controlling the polarity of TAMs in the cancer microenvironment toward M1-rich conditions.

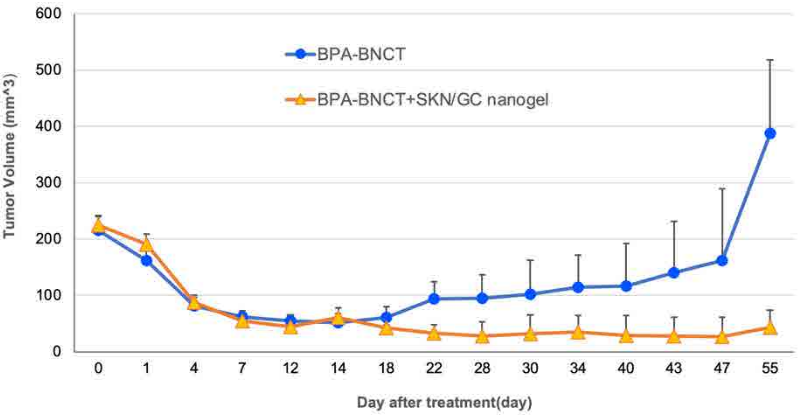

Fig. 1. Tumor suppression effect of BPA-BNCT in the presence or absence of SKN/GC nanogel.

REFERENCES:

[1] N. Yasukawa *et al.*, KURNS Prog. Rep. 2023 (2024) R5151.

CO7-16

Boosting Antitumour Efficacy and Immunity by BNCT with Size-Controlled Nanoparticles

Weian Huang[1], Heon Gyu Kang[1], Xu Han[1], Jie Yu[1], Xiaoxiao Chen[1], Takushi Takata[2], Yoshinori Sakurai[2], Minoru Suzuki[2] & Naoki Komatsu[1*]

[1] Graduate School of Human and Environmental Studies, Kyoto University, Sakyo-ku, Kyoto 606-8501, Japan.

[2]Particle Radiation Oncology Research Center, Institute for Integrated Radiation and Nuclear Science, Kyoto University, 2-1010, Asashiro-nishi, Kumatori-cho, Sennan-gun, Osaka 590-0494, Japan.

Nanoparticles (NPs) hold significant promise in clinical practice especially as drug carriers to cancer. Although various lipid- and protein-based "soft" NPs have been approved in clinical cancer therapies, "hard" inorganic NPs have faced challenges such as low tumour selectivity resulting in poor therapeutic efficacy and potential safety concerns. In BNCT, on the other hand, BPA and BSH have been used clinically, yet they have inherent issues such as low tumour targetability and retentivity. Especially, BPA–BNCT suffers from the long-time infusion of high doses. To overcome these challenges, these boron agents have been conjugated with polymers, encapsulated in micelles or liposomes, and incorporated in inorganic NPs[1],[2], which still required high dosage.

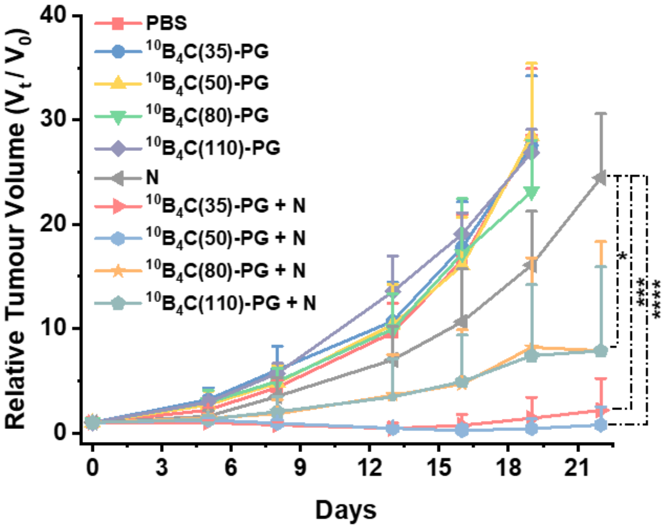

Figure 1. Relative CT26 tumor volume monitored for 22 days at a dosage of 5.1 mg [^{10}B]/kg (mouse) for in vivo BNCT (n = 5), where N indicates neutron irradiation. Statistical analysis of relative tumor volume with one-way ANOVA post Bonferroni test; *$p < 0.05$, **$p < 0.01$, ***$p < 0.001$, ****$p < 0.0001$.

Herein, we firstly establish size-controllable mechanochemical synthesis of $^{10}B_4C$ NPs, which are grafted with poly(glycerol) (PG). Then, the resulting $^{10}B_4C$-PGs are evaluated in their size effect to find that 50 nm core size, or $^{10}B_4C(50)$-PG, shows the higher ^{10}B delivery efficiency than the other sizes; $^{10}B_4C(Y)$-PG (Y = 35, 80 and 110), realizing 88% complete regression (CR) by single bolus intravenous injection at much lower dosage (12 mg / kg (mouse)) than BPA in preclinical studies. Since millions of boron-10 atoms are densely packed in one $^{10}B_4C(50)$-PG particle, its ^{10}B dosage is about five times less than that of BPA. The dosage is further reduced to half by twice neutron irradiation. Besides, antitumour immunity is boosted by $^{10}B_4C(50)$-PG–BNCT to exhibit abscopal ef-fect, in which distant tumours are suppressed or even eradicated.

Overall, $^{10}B_4C(50)$-PG demonstrates great promise as ^{10}B carrier in BNCT for clinical trials.[3]

REFERENCES:

[1] Zhang, Y. *et al.,* Adv. Mater., **35** (2023) e2301479. (doi)10.1002/adma.202301479.

[2] Wang, Y. *et al.,* Small, **18** (2022) e2204044. (doi)10.1002/smll.202204044.

[3] Huang, W. *et al.,* bioRxiv, (2025) 646946. (doi)10.1101/2025.04.02.646946.

CO7-17

Development of boron carriers based on the characteristics of energy metabolism of cancer

R. Yamamoto[1], S. Inoue[1], T. Watanabe[2], Y. Sanada[2], M. Tsuji[1], T. Hirayama[1], and H. Nagasawa[1]

[1] *Laboratory of Medicinal & Pharmaceutical Chemistry, Gifu Pharmaceutical University*
[2] *Institute for Integrated Radiation and Nuclear Science, Kyoto University*

INTRODUCTION: Amino acid transporters such as LAT1 and ASCT2 are highly expressed in cancer cells and promote tumor growth by mediating the uptake of glutamine and essential amino acids. Given their metabolic role, they are being explored as targets for boron delivery in BNCT. We are developing boron cluster–conjugated amino acid analogues that mimic LAT1 substrates to achieve tumor-selective accumulation. Among these, BC2 and BCY2 showed high cellular uptake and greater BNCT efficacy in vitro than the clinical LAT1-targeting agent BPA. However, their limited solubility and physicochemical properties hinder further evaluation in animal models.

In this study, we examined the cellular uptake mechanisms of BC2 and BCY2 using LAT1-deficient cells and a LAT1-specific inhibitor, and additionally initiated an investigation into prodrug strategies to improve their physicochemical properties for in vivo application.

EXPERIMENTS: For boron uptake studies, LAT1-modified SCCVII cells and human glioblastoma T98G cells were treated with boron-containing compounds (BC2, BCY2; 10 µg B/mL) at 37°C for 15 minutes. In LAT1 inhibition studies, T98G cells were pre-incubated with the LAT1-specific inhibitor JPH-203 (10 µM) for 5 minutes before compound treatment. After exposure, cells were washed with cold PBS, lysed in nitric acid, and heated at 75°C for 1 hour to ensure complete dissolution. Boron concentrations in the lysates were then measured by ICP-AES.

As part of our prodrug development efforts, we also synthesized a series of model compounds designed to enable tumor-selective release of the boron carrier via cathepsin B–cleavable linkers. Phenylalanine was used as a model payload, and derivatives with varying linker structures and cleavage sequences were prepared.

RESULTS: As shown in Fig. 1, BC2 uptake was significantly reduced both in LAT1-KO SCCVII cells and in T98G cells treated with JPH-203, whereas BCY2 uptake remained unchanged under either condition. These findings indicate that BC2 is transported in a LAT1-dependent manner, while BCY2 uptake is largely LAT1-independent.

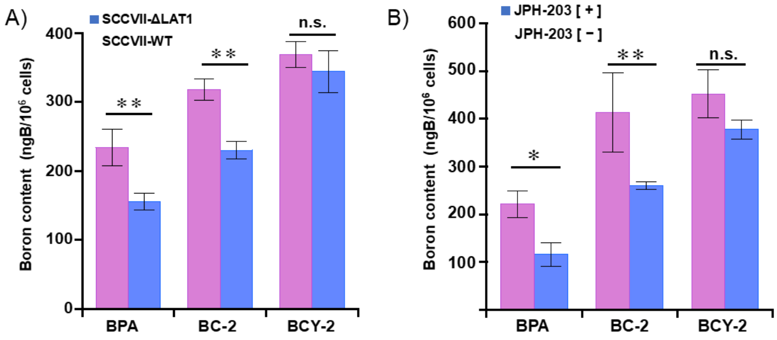

Fig. 1. Effects of boron carriers on cellular boron uptake
A) LAT1-knockout SCCVII cells B) LAT1 inhibition in T98G cells (JPH-203)

As shown in Scheme 1, we successfully synthesized several albumin-binding prodrug derivatives featuring different cathepsin B–responsive linkers. The prodrug function is being assessed using model compounds with phenylalanine as the payload, with the next step being the synthesis of derivatives incorporating BC2 or BCY2.

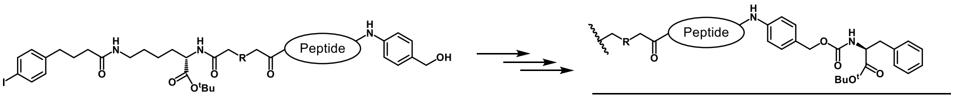

1a, 2a, 2b

S.M.	Peptide	R	result
1a	Val-Cit	C	**1aF, 22% (two steps)**
2a	Val-Cit	C	**2bF, 68% (two steps)**
2b	Phe-Lys	O	**2bF, 9% (two steps)**

Scheme 1. Synthesis of albumin-binding prodrug model compounds with phenylalanine payload

CO7-18

Tumour Growth Suppression by Neutron Capture Therapy using Intratumoral Administration of ^{10}Boro-plex encapsulated Water-in-Oil-in-Water Emulsion

H. Yanagie [1, 2, 3,], M. Yanagawa [4], T. Matsukawa [5], A. Kubota [5], Y. Yanagie [6], M. Suzuki [7], Y. Sakurai[7], T. Takata [7], H. Tanaka [7], M. Nashimoto [3], H. Yamauchi[2, 8], M. Ono [2, 8], T. Sugihara [3], H.Takahashi [1, 2, 9]

[1]Institute of Engineering Innovation, School of Engineering, The University of Tokyo, [2]Cooperative Unit of Medicine & Engineering, The University of Tokyo Hospital, [3]Niigata Univ of Pharmacy & Applied Life Sciences, [4]Joint Faculty of Veterinary Medicine, Kagoshima University, [5]Department of Hygiene, Faculty of Medicine, Juntendo University, [6]Faculty of Medicine, Teikyo University, [7]Kyoto University Institute for Integrated Radiation & Nuclear Science, [8]Department of Cardiac Surgery, The University of Tokyo Hospital, [9]Department of Bioengineering, School of Engineering, The University of Tokyo

INTRODUCTION: We have been continuously developing boron-containing water-in-oil-in-water (WOW) emulsions for application in the multidisciplinary treatment of primary liver cancer using boron neutron capture therapy (BNCT). For effective boron delivery, a two-step targeting process is essential: first targeting involves delivering the drug delivery system (DDS) to the tumor tissue, followed by second targeting, which transports the boron compound into the cancer cells—particularly into the nucleus—via receptors on the cancer cell membrane. Our previously developed boron-containing WOW emulsion has shown the ability to increase boron concen-tration in tumor tissue and achieve tumor shrinkage upon thermal neutron irradiation. However, complete tu-mor eradication has not been achieved, indicating the need for further development of novel boron compounds and DDS strategies. In this study, we report on the basic research conducted prior to hepatic arterial infusion, in which ^{10}Boro-plex was encapsulated in a WOW emulsion, administered intratumorally, and its tumor growth inhibition effect following thermal neutron irradiation was evaluated.

EXPERIMENTS: The internal aqueous phase consisted of the following: 1.2 mL of ^{10}BSH solution (350 mg/mL), 0.12 mL of Lipofectamine 2000, 0.09 mL of sodium hyaluronate (0.25 mL; 10 mg/mL), and 0.09 mL of protamine (0.125 mL; 20 mg/mL). The oil phase consisted of 2 mL of Lipiodol, with surfactants added to each phase. Using our originally developed mixing device, a WOW emulsion was prepared. We prepared mouse colon cancer Colon 26 (5×10^5) model by transplanting to right lower leg. Following the intratumoral injection of 0.2 mL of the emulsion, thermal neutrons at a dose of 3×10^{12} n/cm^2 were irradiated at Institute for Integrated Radiation and Nuclear Science, Kyoto University. Tumor size was measured post-irradiation to evaluate the tumor growth inhibition effect.

RESULTS: Both the WOW emulsion containing ^{10}BSH and that containing the ^{10}Boro-plex complex demonstrated tumor growth inhibition after thermal neutron irradiation compared with non-irradiated group. As the irradiation was performed two hours after intra-tumoral injection in this study, no significant difference in therapeutic effect was observed between the two formulations.

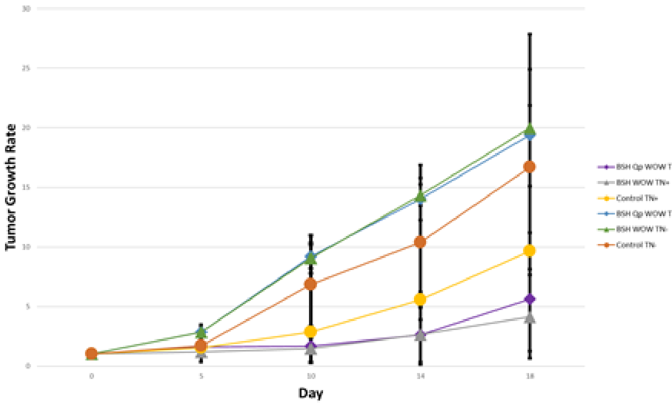

Figure1. Tumor growth suppression in ^{10}BSH Qp-WOW group by NCT was superior compared with non-irradiated group.

REFERENCES:

[1] Yanagie H. *et al.*, Br J Radiol., **90(1074)** (2017) 20170004.

[2] Yanagie H. *et al.*, Appl Radiat Isot., **163** (2020) 109202.

CO7-19

Optimization of polymer-BPA conjugates for non-clinical studies

T. Nomoto, K. Konarita[1,2], D. Tokura[1,2], Shota Tanaka, M. Suzuki[3]

Graduate School of Arts and Sciences, the University of Tokyo
[1]Institute of Integrated Research, Institute of Science Tokyo
[2]School of Life Science and Technology, Institute of Science Tokyo
[3]Institute for Integrated Radiation and Nuclear Science, Kyoto University

INTRODUCTION: 4-Borono-L-phenylalanine (L-BPA), the most potent drug in boron neutron capture therapy (BNCT), selectively accumulates within tumors through the LAT1 transporter [1]. However, L-BPA is sometimes exchanged with extracellular amino acids, such as tyrosine, due to the antiport mechanism of LAT1, resulting in short-term retention in the target tumor and compromising therapeutic efficacy [2]. To address this issue, we discovered that poly(vinyl alcohol) (PVA) can form complexes with L-BPA through boronate esters in aqueous solution. These PVA-L-BPA complexes can then be internalized within tumor cells via LAT1-mediated endocytosis, thereby extending the retention time of BPA [3]. In this study, we prepared PVA formulations with 4-borono-D-phenylalanine (D-BPA) as well as L-BPA and evaluated their BNCT effects.

EXPERIMENTS: PVA formulations with different compositions were administered intravenously to mice bearing subcutaneous CT26 tumors. The tumor was irradiated with epi-/thermal neutrons at 1 MW for 50 minutes using the Kyoto University Research Reactor (KUR) 3 h after injection.

RESULTS: All the PVA formulations demonstrated higher BNCT effects compared to the conventional L-BPA (Fig. 1). Since the PVA formulations exhibited almost complete cure, it was difficult to observe a significant difference in antitumor efficacy between the racemic composition (L:D = 1:1 or 1:2) and L-BPA (L:D = 1:0) in this experimental condition.

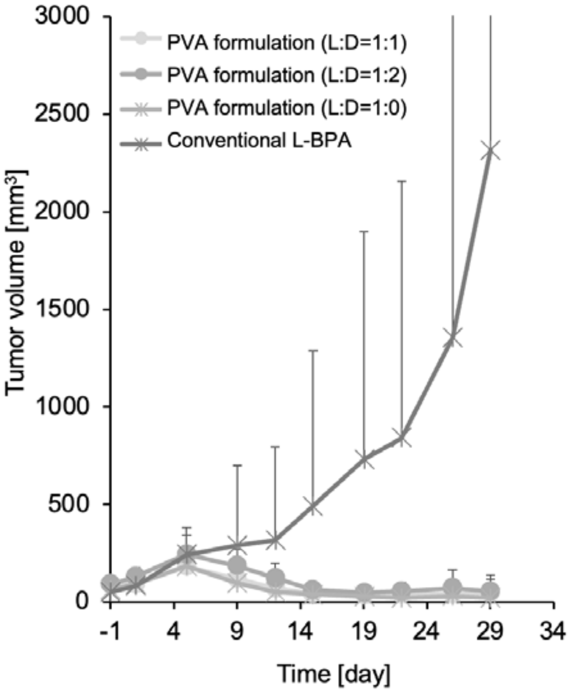

Fig. 1. BNCT effects on subcutaneous CT26 tumors.

REFERENCES:

[1] P. Wongthai *et al.,* Cancer Science, **106** (2015) 279-286.
[2] A. Wittig *et al.,* Radiat. Res., **153** (2000) 173-180.
[3] T. Nomoto *et al.,* Sci. Adv., **6** (2020) eaaz1722.

CO7-20

Development of novel boron delivery systems improving accumulation contrast

T. Nomoto, D. Tokura[1,2], K. Konarita[1,2], Shota Tanaka, M. Suzuki[3]

Graduate School of Arts and Sciences, the University of Tokyo
[1]*Institute of Integrated Research, Institute of Science Tokyo*
[2]*School of Life Science and Technology, Institute of Science Tokyo*
[3]*Institute for Integrated Radiation and Nuclear Science, Kyoto University*

INTRODUCTION: Boron neutron capture therapy (BNCT) is a treatment that uses nuclear reactions between thermal neutrons and boron atoms (^{10}B) to kill cancer cells. In clinical settings, the boron concentration in the tumor must be at least 25 ppm, and the ratio of boron in the tumor to blood (T/B ratio) and the surrounding normal organs (T/N ratio) must be at least 2.5 to achieve an efficient therapeutic effect while minimizing radiation exposure to normal tissue. While many studies have developed drug delivery systems (DDSs) such as polymeric micelles [1] and liposomes [2], these conventional DDSs should exhibit significantly prolonged retention in the bloodstream to enhance the likelihood of leakage from tumor vessels into tumor tissue and subsequent tumor accumulation. Therefore, simply applying conventional DDSs to BNCT does not guarantee a high T/B ratio, and even if high tumor accumulation is achieved, the dose of thermal neutron irradiation is limited and does not lead to improved therapeutic outcomes. In this study, we developed a DDS that can achieve the increased T/B ratio.

EXPERIMENTS: Two types of DDSs were administered to mice bearing subcutaneous CT26 tumors, and thermal neutrons were irradiated to the tumors.

RESULTS: As shown in Fig. 1, the DDS (type II) exhibited antitumor efficacy comparable to conventional L-BPA. The DDS (type II) may be a promising candidate to induce efficient BNCT effects with high T/B and T/N ratios, while advantages from the high ratios needs to be clarified in a future study.

REFERENCES:

[1] H.Cabral *et al.,* Chem. Rev., **118(14)** (2018) 6844-6892.
[2] Theresa M. Allen *et al.,* Advanced Drug Delivery Reviews **65** (2013) 36-48.

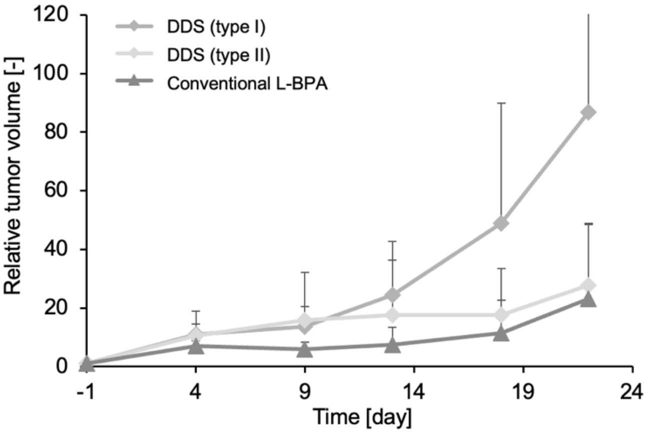

Fig. 1. BNCT effects on subcutaneous CT26 tumors.

CO7-21

Development of Novel Small-molecule Boron Neutron Capture Therapy Drugs Targeting Tumor-specific Enzymatic Activity

S. Kanai[1], J. Tsunetomi[1], M. Suzuki[2], Y. Urano[1,3]

[1] *Graduate School of Pharmaceutical Sciences, The University of Tokyo*
[2] *Institute for Integrated Radiation and Nuclear Science, Kyoto University*
[3] *Graduate School of Medicine, The University of Tokyo*

INTRODUCTION: In boron neutron capture therapy (BNCT), p-boronophenylalanine (BPA), the only approved BNCT agent, is selectively taken up by tumor cells through LAT1, which is a biomarker-transporter over-expressed in tumor cells. However, BPA faces the following challenges: 1) BPA accumulation is insufficient in some types of cancer because of poor LAT1 expression, and 2) BPA gradually leaks out of cells over time. Therefore, the development of new BNCT drugs that target another cancer biomarker and have a mechanism for prolonged intracellular retention is necessary to expand the indications for BNCT and improve therapeutic effect.

In this project, we focused on aminopeptidase activities which were proved to be higher in cancer cells than peripheral normal cells. By last year, we have developed EP-4OCB-FMA, a novel small-molecule carborane-containing drug candidate targeting DPP-4 activity which is known to be upregulated in esophageal cancers in human patients, and conducted BNCT experiments with tumor bearing mice by intratumoral or intravenous injection. This drug is designed to stay inside cells for a long time by generating aza-quinone methide species by being hydrolyzed by DPP-4, which is enough nucleophilic to form a covalent bond with intracellular nucleophiles such as proteins and glutathione. This probe worked well by the intratumoral injection, however, by systemical injection only a small and not enough amount of probe was accumulated in cancer cells, possibly due to the short blood half-life. We also tried to inject higher amount of the probe, however, some side effects were observed due to the toxicity originated from the quinone methide intermediate produced in normal tissues. So this year, we started the development of other probes based on the different molecular mechanisms, Protide-based mechanism [1] and azaquinone methide bearing electron-withdrawing group-based molecular design, which might be safer and show longer blood half-life.

EXPERIMENTS and RESULTS: CB-C2-pSoul-AR was designed and synthesized based on the Protide chemistry to show the reactivity toward carboxypeptidase M (CPM) which is upregulated in some types of cancer cells. By being hydrolyzed by CPM, it yields the carborane derivative bearing phosphate group which show accumulation in cells due to the relatively high hydrophilicity to achieve enough high amount of boron atom. CB-pF-(mCF3)-gGlu was designed based on the azaquinone methide chemistry to have the reactivity toward gamma-glutamyltranspeptidase (GGT) which is known as a good biomarker of breast, oral and hepatic cancers. By the reaction with GGT, it yields azaquinone methide intermediate with electron-withdrawing trifluoromethyl group which shows much lower cytotoxicity than a usual azaquinone methide. After incubating each probe with living target cells, MDCK and MCF-7 for CB-C2-pSoul-AR, A549 and SKOV3 for CB-pF-(mCF3)-gGlu, boron concentration was evaluated. It was found that CB-pF-(mCF3)-gGlu showed enough concentration of boron atoms for BNCT, so we conducted BNCT experiment with this probe, firstly by the intratumoral injection. As a result it was successfully found that tumor growth was suppressed in a drug- and neutron-irradiation-dependent manner. So we now plan to conduct BNCT experiment with intravenous injection next year.

REFERENCES: [1] Y. Kuriki *et al.,* J. Am. Chem. Soc., **146** (2024) 521-531.

CO7-22

Synthesis and evaluation of a novel boron neutron capture therapy agent

H. Kimura[1], M. Suzuki[2]

[1]*Research Center for Experimental Modeling of Human Disease, Kanazawa University*
[2]*Institute for Integrated Radiation and Nuclear Science, Kyoto University*

INTRODUCTION: Neuroendocrine Tumor (NET) is known to be characterized by high expression of somatostatin receptors (SSTRs) on the tumor cell membrane. Somatostatin is a cyclic peptide discovered as a hypothalamic factor that potently inhibits growth hormone secretion from the pituitary gland. There are five subtypes of somatostatin receptors (SSTR1-5), and SSTR2 is highly expressed in NETs. Therefore, somatostatin analogs with high binding to SSTR2 are used for treatment1)-2). Furthermore, Peptide Receptor-mediated Radionuclide Therapy (PRRT), which uses somatostatin analogs as nuclear medicine drugs for NET patients, has recently been implemented in Europe, and LUTATHERA® was approved for manufacturing and marketing in Japan for the first time on June 23, 2021 as a drug for PRRT in Japan. However, there is a need for the development of new therapies with greater therapeutic efficacy. Therefore, in this study, we conducted a basic study on the potential of BNCT for NETs.

EXPERIMENTS: A BSH-labeled SSTR2 agonist-type drug (BSH-TATE) was designed and synthesized. To evaluate the therapeutic effect in BSH-TATE, 400 µg/100 µL of BSH-TATE was administered by tail vein to AR42J cell-bearing mouse models and irradiated with neutron beams 6 hours after administration.

RESULTS: In the saline group, tumor size became too large after 7 days of treatment, and the experiment was terminated due to humane endpoints; in the BSH-TATE group, tumor re-growth was observed after 14 days, but the results suggest that tumor growth can be inhibited (Figure). Multiple neutron irradiation is one possibility to achieve long-term tumor growth inhibition, but since multiple neutron irradiation is not currently allowed in principle in BNCT, we will explore this possibility while evaluating efficacy and safety. The dose administered this time was 400 µg/100 µL, but the dose can be increased with the use of appropriate solubilizing agent, and we consider the dose to be another option to suppress tumor re-growth. In addition, we believe that if the time between administration and neutron irradiation is extended to about 24 hours, the neutron irradiation may be more effective in inhibiting tumor growth because the BSH-TATE is internalized sufficiently.

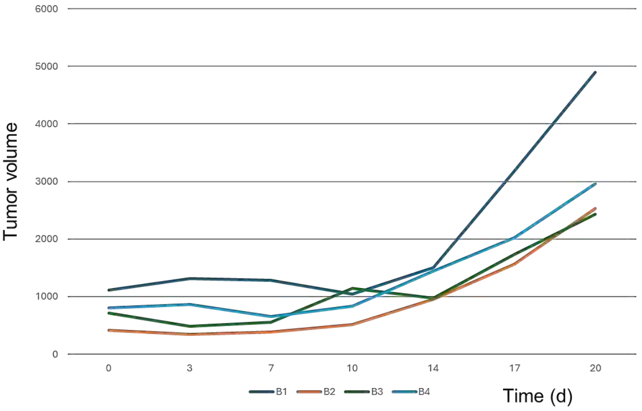

Figure. Tumor Volume Changes after BNCT

REFERENCES:

[1] Ozge Keskin *et al.,* Onco Targets Ther., **6** (2013) 471-483.
[2] Thomas Gunther *et al.,* Phar-macological Reviews, **70** (2018) 763-835.

CO7-23

Measurements of two kinds of thimble-type ionization chambers for an intense epi-thermal neutron beam

T. Matsumoto[1], A. Masuda[1], S. Manabe[1], H. Harano[1], K. Terada[2], H. Tanka[2] and J. Hori[2]

[1]*National Metrology Institute of Japan, National Institute of Advanced Industrial Science and Technology*
[2]*Institute for Integrated Radiation and Nuclear Science, Kyoto University*

INTRODUCTION: The need to ensure traceability to neutron standards at AIST for hospitals performing boron neutron capture therapy (BNCT) has been discussed. For this purpose, we are developing a real-time detector that can measure high-intensity neutrons used in BNCT. It is required that the detector can measure neutrons in appropriate measurement time at standard neutron fields whose fluxes are 4 to 5 orders of magnitude lower than those at BNCT as well.

EXPERIMENTS: Thimble type ionization chambers have been developed as a neutron detector for high intensity neutrons. The ionization chamber is made of aluminum and has a dome shape with a diameter of 13 mm and a length of 15 mm. An aluminum needle-shaped electrode with a diameter of 1 mm is set in the center. We prepared two kinds of chamber. One of chamber was filled with a mixture of ^{3}He gas (0.1 atm) and Kr gas (1.9 atm). Another chamber had 6LiF evaporated on the inner wall and was filled with air as the ionizing gas. Characteristics of the ionization chambers were evaluated using a pulsed white neutron source from an electron linac at the Institute for Integrated Radiation and Nuclear Science of the Kyoto University. The ionization chambers measured neutrons by two-dimensional measurements of neutron time-of-flight and pulse height (PH). In addition, in the current output mode, the measurement was performed by varying the applied voltage for the neutrons in the heavy water facility at the Kyoto University Reactor.

RESULTS: Figure 1 shows a PH spectra obtained from the ionization chambers. Neutron components were clearly observed compared to measurements with a chamber with 3He and Ar gases last year. Figure 2 shows the relations between the applied voltage and output current from the center electrode in the current mode. The applied voltage below 1000 V was the ionization chamber region. In the future, we will evaluate the detection efficiency and stability.

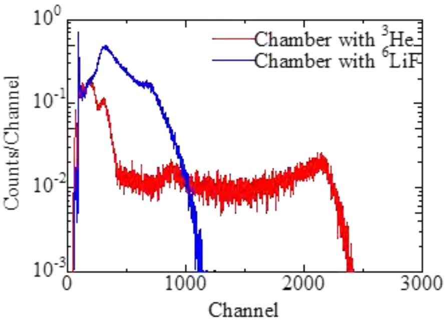

Fig. 1. TOF spectrum for the pulsed neutron source obtained from the electron linac. The thermal bump was clearly observed.

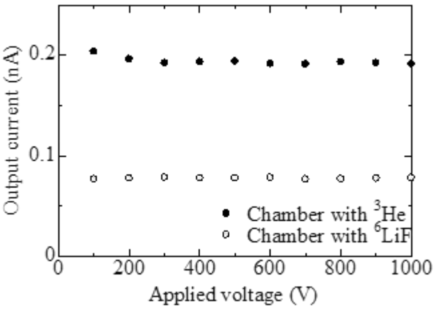

Fig. 2. Relation between applied voltage and output current.

REFERENCES:

[1] K. Kobayashi *et al.,* Annu. Rep. Res. Reactorinst. Kyoto Univ., **22** (1989)142 .

This work was supported by JSPS KAKENHI (21H03755 and 19K12638).

R6077

CO7-24

Development of Nanogels Loaded with Gd(III-Thiacalixarene Complex for Gd-NCT

N. Iki[1], N. Shindo[1], and M. Suzuki[2]

[1]*Graduate School of Environmental Studies, Tohoku University*
[2]*Research Reactor Institute, Kyoto University*

INTRODUCTION: Owing to a large thermal neutron capture cross section, gadolinium attracts growing attention as an alternative to boron in NCT [1]. Because free gadolinium ($[Gd(OH_2)_9]^{3+}$) has toxicity, a safe carrier of Gd to tumor not to release free Gd is required. We found that thiacalix[4]arene-p-tetrasulfonate (TCAS) self-assembled three Gd ions to form a sandwich-type complex, Gd_3TCAS_2 (Fig. 1) [2], the characteristic features of which is high kinetic stability and ^1H relaxation arising from the Gd center [3]. Nano-sized particles are frequently used as a drug carrier toward tumor by enhanced permeability and retention effect. We have so far studied nano-carriers for Gd_3TCAS_2 such as silica nano-particle (NP) [4] and albumin NP (ANP) [5–6] aiming at Gd-NCT. This FY, we introduced a new agent Gd-Nanogel (NG) comprising of Gd_3TCAS_2 and polyethylene imine (PEI) coated with poly(styrene sulfonate) (PSS) and studied the NCT effect.

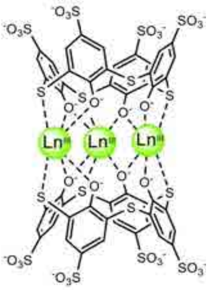

Fig. 1 Ln_3TCAS_2 complex.

EXPERIMENTS: Preparation of NGs. Gd_3TCAS_2-PEI NG [7] was coated with PSS by simply mixing the solutions. Cell experiment. MCF-7 cells were seeded in a 6-well plate at a cell concentration of 1.0 × 10^5 cells/mL and incubated for 24 h. After supernatant was removed, RPMI medium and solution containing Gd agents were added to each well and incubated for 24 hr. The concentration of Gd in the medium to incubate MCF-7 was set to be 12 and 25 μM. After washing with PBS, the cells were detached from the well and transferred to tubes to be irradiated with thermal neutron for 20 min. The cell viability was assessed by the colony assay.

RESULTS: The largest amount of Gd delivered to MCF-7 cells with the Gd_3TCAS_2-PEI-PSS NG was 3.88 ± 1.57 nmol/10^6 cells. The cytotoxicity was not observed up to 100 μM. Cell viability after neutron irradiation suggests that the NCT effect was smaller than that of obtained with Gd_3TCAS_2-PEI NG (Fig. 2), suggesting that the negative charge of Gd_3TCAS_2-PEI-PSS NG led to lower cellular uptake. When incubated with the NG with higher concentration, NCT effect was observed. Studies to increase the cellular uptake by changing the coating materials is now underway.

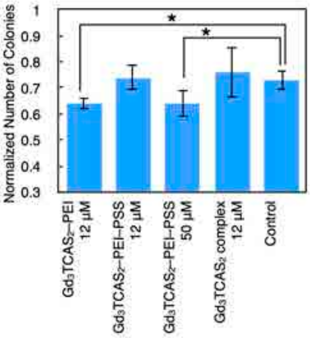

Fig. 2 Cell viability of MCF-7 cells incubated in the presence of Gd agents followed by washing out of free Gd agents and irradiation with thermal neutron. Incubation: 50 μM Gd for 24 h. Neutron fluence: 1.1×10^{12} thermal neutrons cm^{-2}, 1.9×10^{11} epithermal neutrons cm^{-2}.

REFERENCES:

[1] M. Takagaki *et al.,* Future Application of Boron and Gadolinium Neutron Capture Thrapy, in Boron Science, Ed N. S. Hosmane (CRC Press) (2012) 243.
[2] N. Iki *et al.,* Eur. J. Inorg. Chem., **2016** (2016) 5020-5027.
[3] N. Iki *et al.,* Inorg. Chem. **55** (2016) 4000-4005.
[4] T. Yamatoya *et al.,* 31P11-8, p. 105, KURNS Progress Report 2019.
[5] N. Iki *et al.*, R5012, KURNS Progress Report 2024.
[6] N. Iki *et al.,* Colloids Surf. A Physicochem. Eng. Asp., **699** (2024) 134579.
[7] N. Iki *et al.,* The 40th Annual Meeting of the Japan Society of Drug Delivery System, **2024**, Tsukuba.

R6092

CO7-25

Research and Development of New Technology for Boron Neutron Capture Therapy

M. Xu[1], T. Watanabe[4], X. Zhou[1], C. Jin[1], R. Ohgaki[1,2], H. Okanishi[1], H. Tanaka[4], M. Suzuki[4], and Y. Kanai[1,2,3]

[1]*Department of Bio-system Pharmacology, Graduate School of Medicine, The University of Osaka*
[2]*Integrated Frontier Research for Medical Science Division, Institute for Open and Transdisciplinary Research Initiatives (OTRI), , The University of Osaka*
[3]*Premium Research Institute for Human Metaverse Medicine, The University of Osaka*
[4]*Institute for Integrated Radiation and Nuclear Science, Kyoto University*

INTRODUCTION: Boron Neutron Capture Therapy (BNCT) is a cancer treatment modality that involves the selective accumulation of boron-containing compounds within tumor cells, followed by exposure to a neutron beam. Achieving a high intracellular concentration of the boron compound is essential for this nuclear reaction between ^{10}B and thermal neutrons to occur efficiently within cancer cells. Among various boron carriers, L-p-boronophenylalanine (L-BPA) is widely used owing to its preferential uptake by cancer cells through upregulated amino acid transport systems [1]. A major limitation, however, is the swift decline of intracellular L-BPA levels, primarily due to its efflux via specific transporters expressed in cancer cells. This study experimentally verifies a strategy to boost the therapeutic impact of neutron irradiation by inhibiting those transporters mediating L-BPA efflux. Using both in vitro cultured cells and in vivo tumor-bearing mouse models, we assessed whether blocking L-BPA efflux could enhance the effectiveness of BNCT While the studies conducted in FY2022–2023 focused on experimentally validating the underlying concept, in FY2024, we aim to advance toward clinical development by employing the optimized inhibitor's active stereoisomer.

EXPERIMENTS: In the FY2024 study, tumor cells with high expression of transporters responsible for BPA uptake were selected, and the human pancreatic cancer cell lines T3M4 and Suit-2 were used. In the cell-based irradia-tion experiments, T3M4 and Suit-2 cells were first incubated with L-BPA by supplementing it into the culture medium. Following a washing procedure, the cells were further cultured for 60 minutes in the presence or absence of transporter inhibitors that block the efflux of L-BPA. After incubation, cells were collected using Hanks' Balanced Salt Solution (HBSS) and transferred into 1.5 mL microtubes to be used as samples for neutron exposure. As a control, additional samples were prepared by irradiating cells not treated with L-BPA. Cell suspensions were adjusted to appropriate densi-ties post-irradiation and plated onto 10 cm dishes to assess clonogenic survival through colony formation assays.

For the in vivo irradiation studies, tumor models were established by subcutaneous implantation of T3M4 and Suit-2 cell lines into nude mice. L-BPA was administered intravenously via the tail vein at 300 mg/kg. Subsequently, an active stereoisomer of a transporter inhibitor (50 mg/kg), designed to suppress L-BPA efflux, was administered at 1 hour and again at 1.5 hours after L-BPA injection. Control mice received the inhibitor alone, without prior L-BPA administration, before undergoing neutron irradiation. Neutron exposure was performed at a reactor output of 5 MW, with irradiation times set at 30 minutes. Tumor response following neutron treatment was monitored and compared between the inhibitor-treated groups with or without prior L-BPA loading to evaluate therapeutic efficacy.

RESULTS: In the cell-based irradiation studies, T3M4 and Suit-2 cells were exposed to L-BPA and washed. The cells were then divided into three groups. Group 1 was incubated for 60 minutes in RPMI 1640 medium supplemented with an inhibitor targeting the transporter responsible for L-BPA efflux. Group 2 was incubated under identical conditions but without the inhibitor. Group 3 served as a control and consisted of cells not exposed to L-BPA. All groups were then subjected to neutron irradiation. Post-irradiation, colony formation assays were performed under low-density conditions to evaluate cell viability. Results showed no notable difference in survival between Group 2 and Group 3 (non-BNCT), implying that L-BPA was rapidly expelled from the cells and had diminished to subtherapeutic levels within 60 minutes. In contrast, Group 1 exhibited a significantly reduced survival rate compared to Group 2, confirming that inhibition of the efflux transporter enhanced the therapeutic efficacy of BNCT.

For the in vivo studies, T3M4 cells were subcutaneously implanted in the hind limbs of mice to establish tumor-bearing models. Following intravenous L-BPA administration, the mice were allocated into three groups. Group 1 received additional injections of a transporter inhibitor at 1 and 1.5 hours post-L-BPA administration. Group 2 received no inhibitor following L-BPA injection. Group 3 received saline instead of L-BPA, followed by inhibitor injections at the same time points as Group 1. All mice underwent neutron irradiation 2.5 hours after the initial L-BPA or saline administration. Tumor volumes were measured for 18 days post-irradiation. Group 1 displayed a notable reduction in tumor size relative to Group 2, indicating that transporter inhibition substantially improved BNCT efficacy. This supports the effectiveness of the proposed strategy to enhance the therapeutic impact of L–BPA–based BNCT.

REFERENCES: [1] P. Wongthai *et al.,* Cancer Sci., **106** (2015) 279-286.

R6094

CO7-26

Mechanism of Glioma Resistance After BNCT via Small Extracellular Vesicles

Natsuko Kondo[1], Tadatoshi Kinouchi[2], Manabu Natsumeda[3], Eishu Hirata[4], Yoshinori Sakurai[1], and Minoru Suzuki[1]

Graduate School of Science, Kyoto University
[1] Particle Radiation Oncology Research Center, and [2]Division of Radiation Biochemistry, Institute for Integrated Radiation and Nuclear Science, Kyoto University
[3]Department of Neurosurgery, Brain Research Institute, Niigata University,
[4] Division of Tumor Cell Biology and Bioimaging, Cancer Research Institute of Kanazawa University

INTRODUCTION: Boron Neutron Capture Therapy (BNCT) have been applied to recurrent malignant glioma and even after standard therapy (surgery, chemo-radiation therapy) because of the selective damage to the tumor. Especially, glioblastoma (GBM) is the most miserable cancer, whose patient survival is 14.6 months and remarkably resistant to chemo-radiation and immuno-therapy. With BNCT, we achieved better local control and survival benefit in malignant glioma using thermal neutrons produced by the reactor in Kyoto University. However, the recurrence locally or distantly is inevitable after BNCT. And distant recurrences, named cerebrospinal fluid (CSF) space dissemination, more frequently occur after BNCT compared with the cases after standard radiation-chemotherapy. Reasons for recurrence after BNCT have not been fully elucidated. Small extracellular vesicles (sEVs) are small membrane vesicles with sizes ranging from 50 to 150 nm. They serve as functional mediators and promote intercellular communication during physiological and pathological processes. including migration, treatment resistance, and metastasis in cancer. miRNAs are encapsulated in lipid membranes such as extracellular vesicles in blood and body fluids, exist stably, are taken up by the cells they reach, and act negatively on target genes, performing post-translational modification. We investigated miRNAs in sEVs secreted from glioblastoma cells after BNCT using microarray.

EXPERIMENTS:
BPA Treatment and Neutron irradiation
Glioblastoma U87 MG cells were treated with 25 ppm of BPA in the culture media for 2 hours and irradiated with thermal neutrons in plastic tubes for 70 min.
sEVs collection
After irradiation, they were plated into dishes and cultured for 3 days in the 5 % CO2 incubator. Then, sEVs released into the medium were collected by column chromatography.
Measurement of size and concentration of the sEVs
The size distribution profile and concentrations of the sEVs were analyzed with 6. Tunable resistive pulse sensing (TRPS).
Total RNA extraction from sEVs and miRNA microarray analysis
Total RNA was extracted from the sEVs using Toray's 3D-Gene RNA extraction reagent (Toray Industries, Inc., Tokyo, Japan). Comprehensive miRNA expression analysis was performed using a 3D-Gene miRNA Labeling kit and 3D-Gene Human miRNA Oligo Chip Ver. 22 (Toray Industries, Inc.), according to the manufacturer's protocol to detect 2,565 human miRNA sequences.

RESULTS: We detected an increase in 21 individual miRNAs (ratio>2) and a decrease in 2 individual miRNAs (ratio<0.5) in BNCT cells compared to non-irradiated cells. Also, more than 20 miRNAs that associate with poor prognostic markers in glioma were produced or increased after BNCT.

CO7-27

Characterization of Solar Cell-Based Radiation Detectors for BNCT Applications

Y. Okuno, H. Tanaka[1], Y. Sakurai[1], N. Matsubayashi[1]
RAP, RIKEN
[1]Institute for Integrated Radiation and Nuclear Science, Kyoto University

INTRODUCTION: This study focuses on the development of solar cell-based radiation detectors for applications in Boron Neutron Capture Therapy (BNCT), with particular emphasis on the use of hybrid organic–inorganic perovskite (HOIP) solar cells. These devices are investigated for their potential to detect neutrons through the measurement of radiation-induced currents. HOIP solar cells offer unique advantages, including high carrier mobility, strong absorption coefficients, and tunable electronic properties, which make them promising candidates for neutron detection under high-radiation environments. The research aims to characterize the neutron response of these detectors, evaluate their sensitivity and stability, and explore the integration of neutron converter layers such as Boron-10 to enhance their performance. This work contributes to the advancement of compact, low-cost, and real-time radiation monitoring systems for next-generation radiotherapeutic applications.

****

EXPERIMENTS: A neutron detection device was fabricated by coating a 30 μm-thick layer of boron nitride (BN) powder onto a hybrid organic–inorganic perovskite solar cell with the same structural configuration as previously reported in Ref. [1]. Neutron irradiation experiments were conducted using the heavy water neutron beamline of the Kyoto University Research Reactor (KUR). The detector was positioned immediately downstream of the neutron beam extraction port. To measure the radiation-induced current during neutron exposure, the device was connected to a source measure unit (SMU; B2912A, Keysight) located outside the irradiation room via a 10 m-long BNC cable. The measurement was performed under zero applied bias (0 V), with a sampling time of 1 second per data point.

****

RESULTS: Irradiation was performed under conditions equivalent to those used in BNCT treatment. A neutron-induced current of 8.5×10^{-9} A/cm² was measured, which is approximately three orders of magnitude higher than the offset current. This confirms a clear response to neutron flux. During one hour of continuous irradiation, no significant degradation in the current was observed, indicating good stability of the device under neutron exposure. Sharp changes in the output signal were detected during the measurement. These fluctuations coincided with the movement of the reactor control rods, as confirmed by operational records. This correlation demonstrates that the device is capable of detecting neutron flux variations with high temporal resolution. These results show that the device can accurately measure neutron flux under BNCT-equivalent conditions and is suitable for high-precision neutron dosimetry.

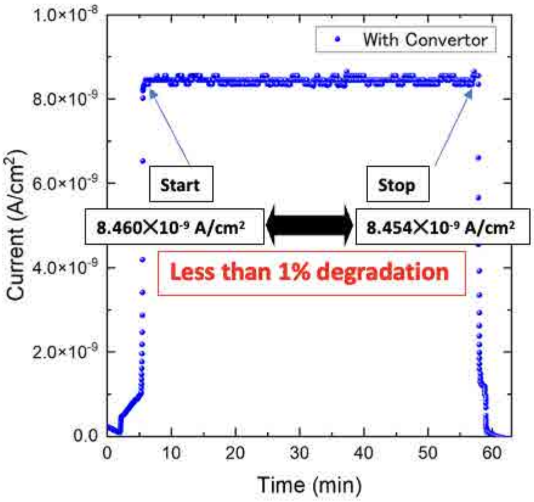

Fig.1. Neutron-induced current characteristics of perovskite solar cells during irradiation

****

REFERENCES:

[1] Y. Okuno *et al.*, ACS Appl. Electron. Mater., **4**, (2022) 3411.

CO7-28

Establishment of innovative BNCT treatment method for intractable bladder cancer

P. Huang[1], K. Igawa[1], Y. Sakurai[2], H. Michiue[1] and M. Suzuki[2]

[1]*Neutron Therapy Research Center, Okayama University*
[2]*Particle Radiation Oncology Research Center, Institute for Integrated Radiation and Nuclear Science, Kyoto University*

INTRODUCTION: Bladder cancer treatment remains a challenge to every urologist. The current first-line treatment for non-muscle invasive bladder cancer is transurethral resection of bladder tumors followed by intravesical Mycobacterium Bovis Bacillus Calmette-Guérin (BCG) immunotherapy. In case of BCG failure, radical cystectomy is the standard of care in high - risk patients. However, many of them are unfit or they refuse to undergo such an intervention; therefore, other treatment options are required. The usefulness of BNCT to urothelial cancer remains unknown. Here we aimed to investigate whether BNCT suppresses in a previously established mouse model of orthotropic bladder cancer.

****

EXPERIMENTS: We constructed BCG-resistant bladder cancer cell lines T24/BCG. In vitro, we investigated the uptake of Boron in various bladder cancer cell lines and normal cell lines through Inductively coupled plasma (ICP). Furthermore, luciferase-expressing T24/BCG cells were implanted in the bladder of nu/nu mice, Neutron irradiation experiments on mouse models of orthotropic bladder cancer.

****

RESULTS: The uptake of boron by various cells is different, but all of them can be effectively taken up and expressed for BNCT treatment. As shown in Fig.1 In Vivo, through intravesical administration of small doses, decreased tumor weight, compared with intravenous systemic administration, intravesical administration has basically no effect on other tissues, organs, liver function, and renal function* *(Data No Shown)*

****

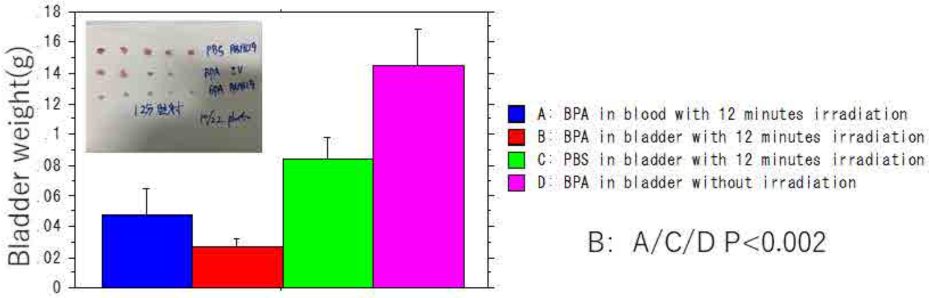

Fig.1 The bladder weight assay of 14 days after Neutron irradiation.

Neutron irradiation for 12 minutes after Boron added for 1 hour

REFERENCES:

[1] T. Fujimoto *et al.,* Biomaterials., **309** (2024)

[2] T. Fujimto *et al.,* Cancer Sci., **115**(2024)

[3] R. Kayama *et al.,* Sci Rep., **14** (2024)

CO7-29

Evaluation of a novel cyclodextrin-based polyrotaxane boron compound for BNCT

Y. Matsumoto[1,2], Y. Sugawara[2], M. Suzuki[3], H. Takeuchi[2], A. Nakaie[2], H. Arase[4], H. Ishiki[4], T. Taharabaru[4], R. Onodera[4], H. Motoyama[4], H. Sakurai[1,2] and T Higashi[4]

[1]*Institute of Medicine, University of Tsukuba*
[2]*Proton Medical Research Center, University of Tsukuba Hospital*
[3]*Institute for Integrated Radiation and Nuclear Science , Kyoto University*
[4]*Graduate School of Pharmaceutical Sciences, Kumamoto University*

INTRODUCTION: Boron neutron capture therapy (BNCT) is an emerging cancer treatment that utilizes the nuclear reaction between boron-10 and thermal neutrons to selectively destroy tumor cells while minimizing damage to the surrounding normal tissue. The effectiveness of BNCT de-pends heavily on the selective delivery and retention of boron compounds within the tumor micro-environment. Among the clinically used boron agents, boronophenylalanine (BPA) is known for its tumor selectivity but has limitations owing to its rapid efflux from tumor cells, necessitating high dosing. In this study, we developed a novel supramolecular boron compound, FPBA-PRX, which is composed of a cyclodextrin-based polyrotaxane (PRX) modified with 4-fluorophenylboronic acid (FPBA). FPBA selectively binds to sialic acid residues that are overexpressed on the surfaces of many tumor cells. Importantly, the FPBA moieties on the PRX backbone are mobile, allowing more efficient and multivalent interactions with tumor cell membranes. We hypothesized that this design would improve tumor-specific accumulation and intracellular uptake of boron compounds, thereby enhancing the therapeutic efficacy of BNCT.

EXPERIMENTS: FPBA-PRX was synthesized via a multi-step process involving α-cyclodextrin, PEG-based axial chains, and FPBA as the boron-containing ligand. A comparison compound, FPBA-CEL (FPBA-modified cellulose), was also synthesized with a similar boron content but without the mobility provided by the polyrotaxane structure. We characterized the physicochemical properties (particle size and ζ-potential) and sialic acid-binding affinity using alizarin red S displacement assays. Cellular uptake was evaluated using TRITC-labeled compounds and analyzed by flow cytometry and confocal microscopy in HeLa and Colon-26 cancer cell lines. For in vivo experiments, Colon-26 tumor-bearing BALB/c mice were intravenously or subcutaneously administered FPBA-PRX or FPBA-CEL. Boron accumulation in tumors and blood was measured using ICP-AES. BNCT efficacy was assessed following thermal neutron irradiation using the Kyoto University Research Reactor, and tumor growth was monitored for several weeks post-treatment.

RESULTS: FPBA-PRX exhibited favorable physicochemical properties, including a particle size of approximately 15 nm and a neutral surface charge, making it suitable for passive tumor targeting via the enhanced permeability and retention (EPR) effect. This compound exhibited strong sialic acid-binding ability and significantly higher cellular uptake in tumor cells than FPBA-CEL or un-modified PRX, attributable to the mobility of the FPBA ligands on the PRX framework. In vivo studies demonstrated superior tumor accumulation of FPBA-PRX compared with that of FPBA-CEL. Importantly, when administered before neutron irradiation, FPBA-PRX resulted in greater boron accumulation in tumors than BPA and significantly inhibited tumor growth compared to BPA. No adverse effects on body weight or blood biochemistry were observed, indicating the safety of this compound. These findings support the use of FPBA-PRX as a promising candidate for tumor-targeted boron delivery in BNCT.

REFERENCES:

[1] Wang J. *et al.,* Sci. Adv., **5** (2019) eaaw4357.
[2] Obayashi S. *et al.,* Oral Oncol., **40** (2004) 474-482.

R6111

CO7-30

Attempts to sensitize tumor cells by exploiting the tumor microenvironment

Y. Sanada, T. Takata, Y. Sakurai, H. Tanaka and T. Watanabe

Institute for Integrated Radiation and Nuclear Science, Kyoto University

INTRODUCTION: Boron neutron capture therapy (BNCT) is a radiotherapy that kills tumor cells via the 10B(n, α)7Li reaction [1]. As reported previously, these high-LET particles produce highly complex DNA damages[2], which can activate cytosolic DNA-mediated signaling pathways, such as interferon response. Since tumor tissues contain various types of cells, it is necessary to take advantages of reporter genes to detect tumor cells-specific signaling. In the present study, we established a targeting vector containing two reporter genes that allows us to monitor expression of Ifnb and ActB genes.

EXPERIMENTS: Targeting vector #1 was generated as described in Fig 1. The targeting vector contained mouse Ifnb promoter, EGFP, mouse Actb promoter, mOrange2 and a neo-resistance marker. SCC VII cells were transfected with targeting vector #1 and CRISPR/Cas9 expression vector, the G418-resistant cell clone was obtained (SCC VII-pIfnb-EGFP/pActb-mOr2 cells).

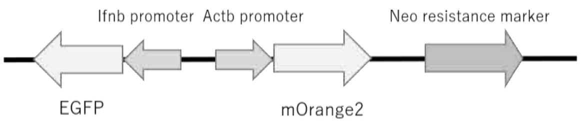

Fig. 1. Targeting vector #1 used for the establishment of SCC VII-pIfnb-EGFP/pActb-mOr2 cells.

RESULTS: Transcriptional induction of Ifnb gene was examined using HT-DNA as a positive control (Fig 2). The upregulation of Ifnb mRNA levels was observed 6 hours after transfection of HT-DNA. There was no increase in Ifnb mRNA level 3 or 24 hours after transfection. Next, we tested if two transgenes are functional. Similar to Ifnb, the reporter EGFP mRNA level was increased 6 hours after transfection of HT-DNA, while the other reporter mOrange2 level was not greatly increased. In this study, we used ActB as an internal control, but also found that HT-DNA transfection possibly influenced ActB mRNA levels. Therefore, mRNA expression level analysis should be performed using multiple internal controls.

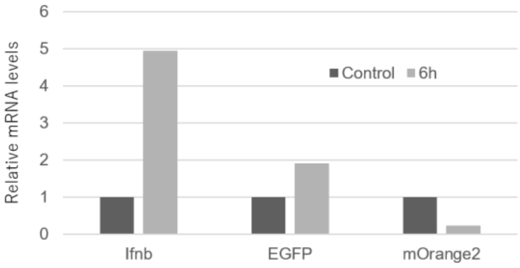

Fig. 2. Relative mRNA levels of Ifnb, and two transfenes EGFP and mOrange2 after HT-DNA transfection. The values are normalized to the mRNA level of Actb at each time point.

REFERENCES:

[1] S. Masunaga *et al.,* Int. J. Rad. Biol., **92** (2016) 187-194.
[2] Y. Sanada *et al.,* Int. J. Rad. Biol., **97** (2021) 1441-1449.

CO7-31

Tumor responses after BNCT at early stages

Y. Tong[1, 2], Gao Zhongming[1], B. Saraswat[1], M. Ishiai[2,3], Y. Sanada[4], Y. Sasaki[1,5], T. Nozaki[1,5], and M. Masutani[1,2,3]

[1] *Dept. of Molecular and Genomic Biomedicine, Center for Bioinformatics and Molecular Medicine, Nagasaki University Graduate School of Biomedical Sciences*
[2] *Central Radioisotope Division, National Cancer Center Research Institute*
[3] *Division of Boron Neutron Capture Therapy, EPOC, National Cancer Center*
[4] *Institute for Integrated Radiation and Nuclear Science, Kyoto University*
[5] *Dept. Pharmacology, Osaka Dental Univ.*

INTRODUCTION: Boron neutron capture therapy (BNCT) is a molecular-targeted cancer therapy that employs high-energy alpha particles and lithium nuclei generated by nuclear reactions and ^{10}B carrier drug that could be preferentially incorporated into cancer cells. We reported the role of HMGB1 and the early effect on proteome after BNCT [1-2]. To optimize the effectiveness of BNCT and to find biomarkers for treatment, we analyzed the response of cancer cells to BNCT further.

EXPERIMENTS: Neutron irradiation experiments at the KUR reactor were carried out at a constant power level of 1 MW in all cases as described [1]. The total physical dose was calculated using the flux-to-dose conversion factor [1]. The relevant data is presented in Tables 1-3.

The cancer cells including human squamous cell line SAS, HSC3 and malignant melanoma A375 cells were incubated with ^{10}B-boronophenylalanine fructose complex (BPA) (Catchem) for 2.0 hrs in suspension. The cell survival was analyzed by colony formation assay and culture supernatants were harvested at 6 and 24 hrs for RNA and protein isolation and molecular analysis.

Mouse melanoma cell lines B16F10 and the variant were grafted to the hind legs and were locally irradiated for 60 min using ^{6}LiF containing shield for thermal neutron. Mice were injected with BPA at 500 mg/kg bodyweight approximately 30 min before irradiation. Mice were euthanized on day 7-14 after irradiation, and blood, tumors, and other organs were analyzed.

RESULTS: The measurement of thermal neutron fluence and doses for cells (Table 1) and mice (Tables 2 & 3 and Fig. 1) were indicated. Modulation of the expression level of SNHG12 caused changes in the early responses of cancer cells to BNCT. The cellular responses of mice to BNCT are being analyzed.

Table 1. Irradiated doses of cells on Dec. 4, 2024 (Rail, irradiation room).

Irradiation time[min]	Position	fluence [/cm2]		[Gy]					
		Thermal neutron [/cm2]	Epi-thermal neutron	Thermal neutron [Gy]	Epi-thermal neutron [Gy]	Fast neutron [Gy]	Gamma-ray [Gy]	Physical Dose [Gy]	B-10** (1ppm)
10	Center	1.2E+12	2.1E+11	1.5E-01	1.7E-02	1.1E-01	1.2E-01	4.0E-01	8.6E-02
60	Center	6.8E+12	1.2E+12	9.1E-01	9.7E-02	6.7E-01	1.1E+00	2.8E+00	5.1E-01
2	Center	2.3E+11	4.1E+10	3.1E-02	3.3E-03	2.3E-02	2.2E-02	7.9E-02	1.7E-02
4	Center	3.8E+11	6.8E+10	5.1E-02	5.4E-03	3.8E-02	2.3E-02	1.2E-01	2.8E-02
6	Center	6.8E+11	1.2E+11	9.0E-02	9.6E-03	6.7E-02	3.8E-02	2.0E-01	5.0E-02
8	Center	8.8E+11	1.6E+11	1.2E-01	1.2E-02	8.7E-02	8.5E-02	3.0E-01	6.5E-02

Table 2. Irradiated doses for local irradiation of mice on Dec.10, 2024 (Cart, irradiation room).

Irradiation time [min]	Position	Fuence [/cm2]		[Gy]					
		Thermal neutron [/cm2]	Epi-thermal neutron	Thermal neutron [Gy]	Epi-thermal neutron [Gy]	Fast neutron [Gy]	Gamma-ray [Gy]	Physical Dose [Gy]	B-10** (1ppm)
60	Center	3.5E+12	6.2E+11	4.6E-01	4.9E-02	3.4E-01	2.3E-01	1.1E+00	2.6E-01
60	Center	3.9E+12	7.0E+11	5.2E-01	5.6E-02	3.9E-01	2.5E-01	1.2E+00	2.9E-01

Table 3. Irradiated doses for local irradiation of mice on February 5, 2025 (Cart, irradiation room). Positions A-C were indicated in Fig. 1.

Irradiation time[min]	Position	Fluence [/cm2]		[Gy]					
		Thermal neutron [/cm2]	Epi-thermal neutron	Thermal neutron [Gy]	Epi-thermal neutron [Gy]	Fast neutron [Gy]	Gamma-ray [Gy]	Physical Dose [Gy]	B-10** (1ppm)
60	Center	3.8E+12	6.8E+11	5.1E-01	5.4E-02	3.8E-01	2.5E-01	1.2E+00	2.8E-01
60	Center	3.9E+12	6.9E+11	5.2E-01	5.5E-02	3.8E-01	2.3E-01	1.2E+00	2.9E-01
	Position A	3.8E+12	6.7E+11	5.0E-01	5.3E-02	3.7E-01	2.3E-01	1.2E+00	2.8E-01
	Position B	3.8E+12	6.7E+11	5.0E-01	5.3E-02	3.7E-01	2.3E-01	1.2E+00	2.8E-01
	Position C	3.8E+12	6.8E+11	5.1E-01	5.4E-02	3.8E-01	2.3E-01	1.2E+00	2.8E-01

Fig. 1. Positions A-C for February 5, 2024. (Cart, irradiation room)

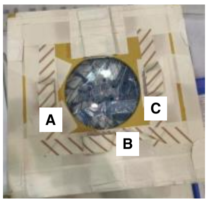

REFERENCES:

[1] Imamichi S. *et al.,* Biology, **11** (2022) 420.
[2] Perico D., *et al.,* Cells, **12(12)** (2023) 1562.
[3] Tong Y. *et al.,* J Oncology., **4(2)** (2024) 1163.
[4] Imamichi S. *et al.,* Appl Radiat Isot., **218** (2025)111648.

R6119

CO7-32

BNCT with a novel boron drug, BBCIP, for a rat brain tumor model

K. Eza, S. Kawabata, Y. Fujikawa ,H. Kashiwagi, H. Tanaka[1], M. Suzuki[1], S-I. Miyatake[2], K.nishimura[3],H.nakamura[3] and M. Wanibuchi

Department of Neurosurgery, Osaka Medical and Pharmaceutical University
[1]Institute for Integrated Radiation and Nuclear Science, Kyoto University
[2]Kansai BNCT Medical Center, Osaka Medical and Pharmaceutical University
[3]School of Life Science and Technology, Tokyo Institute of Technology

INTRODUCTION:

Malignant gliomas diffusely invade normal brain parenchyma, leaving residual tumor cells even after surgical resection. Combination therapy with radiation chemotherapy is the standard of care, however, despite this approach, gliomas remain highly aggressive and and prone to recurrence, leading poor prognosis. Boron neutron capture therapy (BNCT) is a form of particle therapy that selectively destroys tumor cells by incorporating boron compounds and irradiating neutrons.

BNCT is being researched and developed as a treatment for malignant gliomas because of its strong anti-tumor effect at the cellular level, but it has not yet been approved by insurance for malignant brain tumors. The company aims to expand the indication of malignant brain tumors with BNCT using a novel boron-based drug.

****

EXPERIMENTS:

In this study, we used a novel boron compound called BBCIP, designed to target the biotin receptor, specifically the Sodium-dependent Multivitamin Transporter (SMVT). BBCIP is a low-molecular-weight boron carrier that incorporates biotin as a ligand for the biotin receptor, along with an albumin ligand and a boron source. In vivo biodistribution study using a rat brain tumor model, we confirmed sufficient boron accumulation in the tumor when BBCIP was administered via convection-enhanced delivery (CED) [1], a method our group has previously reported. Furthermore, neutron irradiation was performed on the rat brain tumor model after CED administration of this compound. The rat tumor models were randomly as

signed into five groups: a control group receiving no treatment (untreated), a group subjected to neutron irradiation alone (neutron only), a BPA-BNCT group (The BNCT group received an intravenous injection of BPA at a dose of 250mg/kg, followed by neutron irradiation 2.5 h later),a CED BBCIP-BNCT group(The BNCT group received a 200 µL solution of BBC-IP was directly injected into the interstitial space of the brain over 24 h under continuous low positive pressure, followed by neutron irradiation 3h later),and a combination BNCT(BPA and CED BBCIP group) In overall survival and any adverse events were assessed post-irradiation.

****

RESULTS:

CED BBCIP BNCT significantly prolonged overall survival in brain tumor rats. However, the effect was insufficient compared to BPA-BNCT. Conbination BNCT showed prolonged survival, but no significant difference compared to BPA-BNCT.

****

REFERENCES:

[1] K. Tsujino *et al.,* Neurooncol Adv., **22** (2024) vdae062.

CO7-33

Pathological Assessment of Boron Neutron Capture Therapy with CED-Based Delivery of FRα-Targeting PBC-IP in Non-Tumor-Bearing Rats

K. Tsujino[1], K. Nishimura[2], K. Eza[1,] Y. Fujikawa[1], H. Kashiwagi[1], H. Tanaka[3], M. Suzuki[3], S-I. Miyatake[4], M. Wanibuchi[1], H.Nakamura[2] and S. Kawabata[1]

[1]*Department of Neurosurgery, Osaka Medical and Pharmaceutical University*
[2]*School of Life Science and Technology, Institute of Science Tokyo*
[3]*Institute for Integrated Radiation and Nuclear Science, Kyoto University*
[4]*Kansai BNCT Medical Center, Osaka Medical and Pharmaceutical University*

INTRODUCTION

Malignant gliomas diffusely infiltrate brain tissue, making complete resection difficult and leading to recurrence despite standard treatments. We evaluated the safety of boron neutron capture therapy (BNCT) using PBC-IP [1], a boron compound targeting folate receptor alpha (FRα), which is highly expressed in gliomas [2]. PBC-IP was delivered via convection-enhanced delivery (CED), enabling direct distribution into the brain. While its therapeutic potential in tumor models has been reported [3], safety under neutron irradiation in normal brain tissue remains unclear. We therefore assessed pathological effects of CED-administered PBC-IP with BNCT in healthy rats.

EXPERIMENTS

PBC-IP at concentrations of 500 or 1500 μg B/mL (200 μL total volume) was administered into the brain of normal Fischer rats via CED at a rate of 8 μL/h. Neutron irradiation was conducted at 1 and 3 hours after the end of administration to examine the effects at different time points post-delivery. Animals were sacrificed at 2 and 4 weeks after irradiation for pathological examination of the brain and other major organs.

RESULTS

Histopathological evaluation revealed no evident abnormalities in brain tissue or peripheral organs attributable to neutron irradiation in either dose group. These findings suggest that BNCT using PBC-IP administered via CED can be safely performed without inducing discernible tissue damage in non-tumor-bearing models.

DISCUSSION

The safety of boron delivery is crucial for BNCT's clinical use. Our results show that intracerebral PBC-IP via CED causes no significant pathological changes, supporting its tolerability. The lack of damage in brain and peripheral organs suggests a favorable safety profile for future use in tumor-bearing models and clinical studies.

FRα is a promising target due to its high glioma-specific expression and minimal presence in normal tissue. CED effectively bypasses the blood–brain barrier, and the 1–3 hour window for irradiation allows practical flexibility. Further studies should quantify boron distribution at the cellular level and assess long-term safety, including neurobehavioral outcomes. These findings support the development of safer, more targeted BNCT in neuro-oncology.

****

REFERENCES:

[1] Kanemitsu, T. *et al.*, Radiat. Environ. Biophys., **58** (2019) 59–67.
[2] Nishimura, K. *et al.*, J. Control. Release., **360** (2023) 24.
[3] K. Tsujino *et al.,* Neurooncol Adv., **22** (2024) vdae062.

R6124

CO7-34

Exploring Boron Neutron Capture Therapy for Chordoma: Experimental Study

Y. Fujikawa, S. Kawabata, H. Yamada, K. Eza, T. Takata[1], H. Tanaka[1], M. Suzuki[1], N. Hu[2], S-I. Miyatake[2], T. Takami, and M. Wanibuchi

Department of Neurosurgery, Osaka Medical and Pharmaceutical University
[1]Institute for Integrated Radiation and Nuclear Science, Kyoto University
[2]Kansai BNCT Medical Center, Osaka Medical and Pharmaceutical University

INTRODUCTION: Chordomas are rare bone tumors characterized by local invasiveness, high recurrence rates, and relative radioresistance. While treatment modalities such as proton and carbon ion irradiation have been developed in recent years, definitive evidence supporting their clinical efficacy remains limited [1]. This study aimed to evaluate the potential effectiveness of boron neutron capture therapy (BNCT) as a treatment for chordoma through experimental investigations.

****

EXPERIMENTS: ***In vitro:*** U-CH1 and JHC7 human chordoma cell lines were employed in this study. Neutron irradiation was then applied to these two cell lines, BNCT with BPA (10 μg Boron/mL for a 24h exposure before irradiation) (BNCT group), and neutron irradiation without BPA (hot control group), for 0-, 10-, 20- and 30-min (1MW). Assessment of the cell-killing effect was carried out using a colony forming assay. ***In vivo:*** Subcutaneous U-CH1-bearing mice were intravenously administered BPA. After 1 and 3 h, the mice were sacrificed, and the boron concentrations in both the tumor and each organ were measured using Inductively Coupled Plasma Atomic Emission Spectroscopy. The tumor-bearing mice were randomly assigned into four groups: a control group receiving no treatment (untreated; n = 4), a group that was administered BPA intravenously (BPA iv; n = 4), a group subjected to neutron irradiation alone (neutron only; n = 4), and a BNCT group (n = 4). The BNCT group received an intravenous injection of BPA, followed by neutron irradiation (5MW, 15min) 2h later. Relative tumor volume ratios were assessed post-irradiation for 3 months. More detailed information related these methodologies can be obtained by our previous study [2].

****

RESULTS: In the in vitro study, neutron irradiation revealed that the BNCT group demonstrated a more pronounced cell-killing effect than the hot control group in both cell lines. In the in vivo biodistribution of boron, the tumor accumulation was 5.1 μg B/g with a tumor-to-blood ratio (T/Bl) of 1.04 at 1h and 3.6 μg B/g with a tumor-to-blood ratio (T/Bl) of 1.77 at 3h, respectively. Neutron irradiation, especially with i.v. BPA (BNCT), significantly suppressed the tumor growth compared to the untreated or BPA iv group.

****

CONCLUSION: Despite relatively lower boron uptake compared to other malignant tumors, these findings suggest that BNCT could be an effective therapeutic option for chordoma.

****

REFERENCES:

[1] A. Iannalfi *et al.,* Neuro Oncol., **29** (2020) 1348-1358.
[2] Y. Fujikawa *et al.,* Cancer Sci., **115** (2024) 2774-2785.

R6125

CO7-35

Deviation of Important Elements for Activation in Three Types of Ordinary Concrete for Radiation Shielding

K. Kimura, T. Takata[1], Y. Sakurai[1], H. Tanaka[1] and K. Takamiya[1]

Fujita Corporation
[1] Institute for Integrated Radiation and Nuclear Science, Kyoto University

INTRODUCTION: In several years, we performed neutron activation analyses (NAA) to more than several hundreds of samples for radiation shield concrete and raw materials by KUR facilities, including a few types of ordinary concrete and several types of low-activation concrete. Concrete is widely used as radiation shield in nuclear reactors and accelerator facilities because of its flexibility, sufficient supply and low cost. Once these facilities start operating, however, the shielding concrete becomes radioactive by nuclear reaction with neutrons generated. Therefore, it is very important to know their activation property. To estimate the level of activation, we have performed NAA on more than several hundred concrete samples using KUR facilities [1]. In this report, we describe the deviation of important rare elements in eight types of concrete manufactured by different plants.

METHODS: Three types of ordinary concrete by three different JIS (JIS A 5308) qualified concrete plants (Toei, Yoko, and Line, referring plant name, respectively) were prepared and irradiated in KUR, focusing to estimate Eu, Co and Cs (detail procedure was described in the last reports [1]). Eight kinds of concrete are symbolized by type of plant and type of cement in figures (First character indicate name of plant, such as “Toe” meaning Toei concrete, “Yok” meaning Yoko concrete, and “Line” meaning Line concrete. Second character indicate kind of cement, such as “Ord” as Ordinary Portland cement, “Med” as Moderate heat cement, and “Low” as Low heat cement).

RESULTS: Figures show the distribution of deviation for the contents of Eu, Co, and Cs as ratio for the average value, respectively. The ratios of Eu and Co, describing in left figure, are existing in limited ranges within ±10% for Eu and within ±20% for Co, while the ratio of Cs widely disperse up to ± 80%. Considering that past measurements of Cs content have shown large uncertainty, these results indicate that the deviation of Eu and Co is enough small in the concrete with JIS qualified manufacturer plants, under the proper measurement procedure of NAA

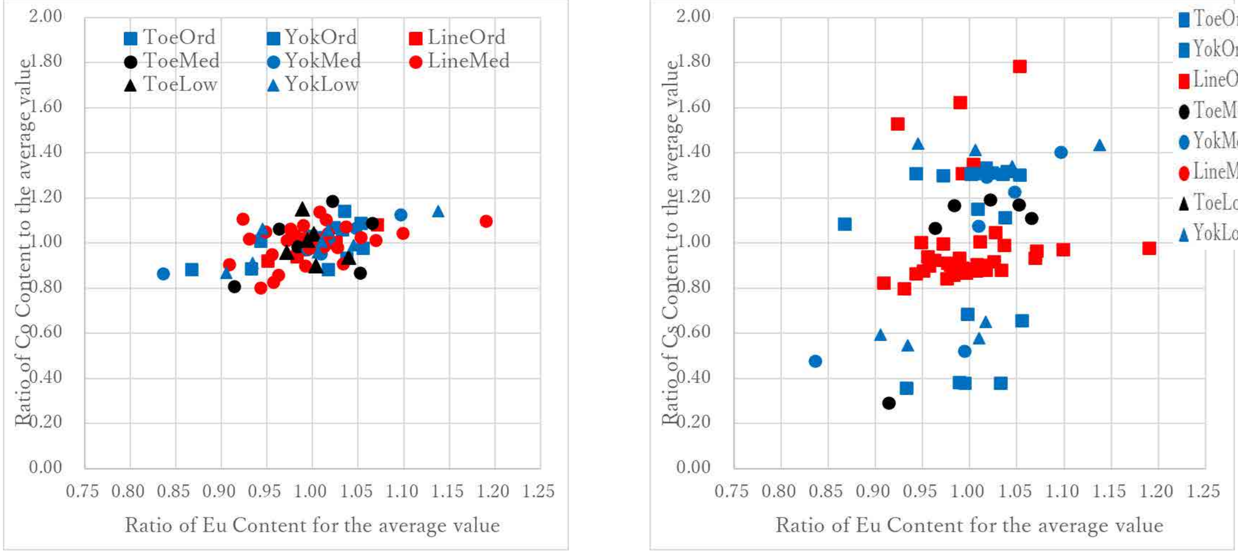

Fig. 1 Ratio of Eu between Co content (Left) and Eu between Cs content (Right) to the average value in several types of ordinary concrete.

REFERENCES:

[1] K. Kimura *et al.,* KURNS Progress Report 2018–2023.

CO7-36

Detection of *p*-Borono-L-phenylalanine (BPA Absorbed in Rice Seeds Using a Boron Neutron Capture Reaction.

T. Kinouchi

Institute for Integrated Radiation and Nuclear Science, Kyoto University

INTRODUCTION: To cope with the decline in paddy rice yields due to global warming, efforts are underway to develop new rice varieties that are resistant to high-temperature injury. However, the frequency of beneficial rice varieties resulting from crossbreeding is relatively low, highlighting the need for breeding methods that can artificially and efficiently produce new varieties. Recently, the application of genome editing technology in breeding has gained attention. Although this method can accurately target specific genes and introduce mutations, it cannot create new varieties that exceed expectations, leading to a reevaluation of methods that induce random mutations on a genome-wide scale. Conversely, the conventional radiation breeding method, which employs gamma rays or fast neutrons, can damage biopolymers and intracellular organelles beyond DNA due to their high energy. This significantly affects the survival rate and physiological functions of rice seeds and their embryonic tissues, thus reducing efficiency. We have developed a novel breeding method to introduce mutations into the rice genome using the Boron Neutron Capture (BNC) reaction, a technique also utilized in cancer therapy. The BNC reaction aims to minimize damage by irradiating rice with low-energy epithermal neutrons, thus efficiently producing new rice varieties. Consequently, we have decided to investigate whether BPA, a neutron-sensitizing reagent, is absorbed by actual rice seeds.

EXPERIMENTS: Materials> Rice seeds (Oryza sativa L. cv. Hinohikari) were kindly gifted from Dr. Segami, Research Institute of Environment, Agriculture and Fisheries, Osaka Prefecture. Boron-10 (^{10}B)-containing neutron-sensitizing reagent, BPA (p-borono-L-phenylalanine) was kindly gifted from Dr. Hattori, Research Center for BNCT, Osaka Metropolitan University.
In situ visualization of BPA in rice seeds> Rice seeds were immersed in BPA solution. (100 ppm) for 24 hrs. Slices (10-μm thickness) of the seeds were mounted onto a solid-state nuclear tracking detector, CR-39 (20 mm×30 mm), and irradiated with epithermal neutrons for 20 min by applying them to the pneumatic tube in the graphite thermal column (Tc-Pn) of Kyoto University Research Reactor (KUR). The irradiated CR-39 plate was etched in 6 M NaOH solution for 60 min at 70°C, and the resulting etch-pits were observed under an optical microscope.

RESULTS: Both Fig. 1(A) and 1(B) show close-up images of cross-sections prepared from the same rice seed, which was immersed in BPA solution (100 ppm). Fig. 1(A) is a bright-field image. Fig. 1(B) is an α-tracking autoradiograph generated by the BNC reaction and reveals the distribution of BPA in the cross-section. The areas enclosed by the circle indicate the embryo. Many etch-pits derived from BPA were imaged throughout the section as small black spots. It was observed that BPA accumulated in the embryo compared to the area not circled (endosperm).

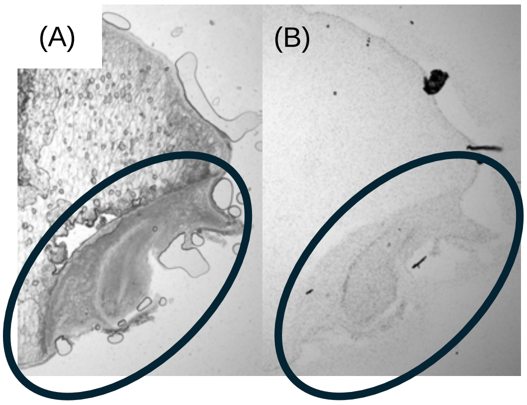

Fig. 1. Detection of BPA absorbed into the rice seed.

CO7-37

Investigation of Potential Adverse Effects of Boron Neutron Capture Therapy on Host Immunity

Tsubasa Watanabe[1], Takushi Takata[2], Yoshinori Sakurai[2], Hiroki Tanaka[2], Minoru Suzuki[1]

Institute for Integrated Radiation and Nuclear Science, Kyoto University
[1]Particle Radiation Oncology Research Center, Particle Radiation Oncology
[2]Particle Radiation Oncology Research Center, Particle Radiation Medical Physics

INTRODUCTION: Boron Neutron Capture Therapy (BNCT) is a form of radiation therapy for cancer that utilizes neutron capture reactions, wherein boron-10 atoms capture thermal neutrons, subsequently undergoing nuclear fission to produce alpha particles and lithium nuclei [1]. Recent studies have revealed that X-ray irradiation does not suppress anti-tumor immune function but rather activates it. To investigate whether BNCT similarly enhances anti-tumor immunity, we have explored the relationship between BNCT and tumor immunomodulation. The purpose of this study is twofold: (1) to determine whether BNCT induces host immune-activating effects, and (2) to evaluate the composition of infiltrating immune cells within tumors post-BNCT, thereby assessing potential adverse impacts on tumor immunity.

****

EXPERIMENTS: Tumor cells were subcutaneously implanted into the hind limbs of C3H/He mice. At 12 days post-implantation, radiation treatment was administered. The control group received X-ray irradiation (20 Gy), while the BNCT group was injected subcutaneously with 500 mg/kg boronophenylalanine (BPA). One hour post-BPA administration, neutron irradiation was delivered to the tumor site using a 5 MW reactor for 12 minutes. Tumor dimensions (height, width, and length) were serially measured under isoflurane anesthesia using digital calipers.

At 72 hours post-irradiation, tumor tissues were excised from three experimental cohorts: untreated controls, X-ray-treated, and BNCT-treated groups. Single-cell suspensions were prepared using the BD Tumor Dissociation Kit (BD Biosciences, #130-096-730) per manufacturer protocol. Cells were stained with fluorochrome-conjugated antibodies against CD45 (leukocyte common antigen), CD3 (T-cells), CD4 (helper T-cells), CD8 (cytotoxic T-cells), Foxp3, CD25, and CD11b (myeloid cells). Flow cytometric analysis (Cytek) quantified immune cell infiltration ratios, with data processed using SpectroFlo software.

****

RESULTS: Initial post-BNCT analysis revealed a transient 32% reduction in anti-tumor immune cell populations compared to untreated controls. However, these populations exhibited time-dependent recovery, reaching baseline levels by Day 21 post-treatment. Tumor volume reduction was significantly greater in BNCT-treated mice versus X-ray cohorts, with no correlation observed between tumor size regression and immune cell depletion. Notably, both BNCT and X-ray groups showed increased proportions of immunosuppressive cells: Inter-group comparison revealed no significant differences in immunosuppressive cell expansion between BNCT and X-ray modalities.

****

REFERENCES:

[1] Rolf F. Barth *et al.*, Cancer Communications (2024) (doi)10.1002/cac2.12581.

CO7-38

Investigation of Potential Adverse Effects of Boron Neutron Capture Therapy on Host Immunity

Tsubasa Watanabe[1], Takafumi Shiagehira[1], Takushi Takata[2], Yoshinori Sakurai[2], Hiroki Tanaka[2], Minoru Suzuki[1]

Institute for Integrated Radiation and Nuclear Science, Kyoto University
[1]Particle Radiation Oncology Research Center, Particle Radiation Oncology
[2]Particle Radiation Oncology Research Center, Particle Radiation Medical Physics

INTRODUCTION: Boron Neutron Capture Therapy (BNCT) is a targeted radiotherapy that utilizes the nuclear capture reaction of thermal neutrons by boron-10, producing high-linear energy transfer (LET) alpha particles and lithium-7 nuclei. The primary boron delivery agent, boronophenylalanine (BPA), is an amino acid analog transported into cells via L-type amino acid transporters LAT1 and LAT2. While cancer cells exhibit elevated LAT1 expression due to metabolic reprogramming, normal tissues also express LAT2, enabling BPA uptake in healthy cells. This unintended accumulation contributes to adverse effects post-BNCT, despite the therapy's theoretical tumor specificity. This study hypothesizes that selective inhibition of LAT1 (tumor-predominant) and LAT2 (normal tissue-expressed) could improve the tumor-to-normal tissue boron concentration ratio. By pre-administering transporter-specific inhibitors prior to BPA infusion, we aim to suppress normal tissue boron uptake while preserving tumor targeting, thereby enhancing BNCT’s therapeutic index.

****

EXPERIMENTS: Tumor Model and Irradiation Protocol: Subcutaneous tumors were established in mice using non-genetically modified cancer cells. At a tumor volume of 150–200 mm, BPA (500 mg/kg) was intravenously administered. Neutron irradiation was performed using a heavy water-based facility, with comparative X-ray cohorts receiving equivalent physical doses (20 Gy). Mice were sacrificed at 7, 14, and 21 days post-irradiation for histopathological analysis of tumor and normal tissues (tongue, liver, skin). Pharmacokinetic Modulation: To assess BPA biodistribution modulation, anticholinergic (atropine, 2 mg/kg) or cholinergic (pilocarpine, 5 mg/kg) agents were administered intraperitoneally 30 minutes prior to BPA. Tissues were digested in a 3:1 mixture of perchloric acid and hydrogen peroxide, followed by boron quantification via inductively coupled plasma atomic emission spectroscopy (ICP-AES). Abdominal Irradiation Study: A separate cohort of tumor-free mice received abdominal X-ray or BNCT irradiation to evaluate gastrointestinal and hepatic toxicity, with organ-specific boron concentrations measured as above.

****

RESULTS: Biodistribution Analysis: Pre-administration of anticholinergic or cholinergic agents failed to alter boron concentrations in normal tissues. No significant differences in tumor boron retention were observed between groups, indicating the tested agents did not modulate LAT1/LAT2-mediated transport under these conditions. Abdominal Toxicity: BNCT induced severe duodenal edema, leading to the irradiated mice death vs. X-ray, correlating with elevated boron levels in intestinal mucosa (14.2 ± 2.3 ppm). Hepatic boron accumulation remained low, consistent with low CBE and minimal hepatotoxicity compared to the CBE of the mucosa.

****

REFERENCES:

[1] Rolf F. Barth*et al.* , Cancer Communications (2024) (doi)10.1002/cac2.12581.

CO7-39

Combining GdNCT and anti-PD-1 immunotherapy to boost abscopal effect

Li Zhao[1], Weian Huang[2], Minoru Suzuki[3] and Naoki Komatsu[2]

[1] *School for Radiological and Interdisciplinary Sciences (RAD-X) and Collaborative Innovation Center of Radiation Medicine of Jiangsu Higher Education Institutions, Soochow University, China*

[2] *Graduate School of Human and Environmental Studies, Kyoto University, Japan* [3] *Institute for Integrated Radiation and Nuclear Science, Kyoto University, Japan*

INTRODUCTION: Gadolinium neutron capture therapy (GdNCT) is a promising binary radiotherapy for cancer treatment, leveraging the nuclear reaction between thermal neutrons and ^{157}Gd, which exhibits an exceptionally high neutron capture cross-section of 254,000 barns. This reaction generates high-LET Auger electrons and low-LET γ-photons, both of which contribute to targeted cancer cell destruction.[1]

The abscopal effect—a phenomenon in which non-irradiated tumors regress alongside directly irradiated lesions following radiotherapy—has shown significant potential in enhancing systemic antitumor efficacy. With the widespread clinical adoption of PD-1/PD-L1 immune checkpoint inhibitors, cancer therapy has entered the era of immunotherapy. Notably, the combination of radiotherapy and immunotherapy has been demonstrated to amplify the antitumor effects of radiation.[2]

Recently, our group has developed poly(glycerol) functionalized Gd nanoparticle (GdNP-PG) that can mediate effective GdNCT of cancer upon intravenous administration. The therapeutic outcomes were further improved when combined with anti-PD-1 immunotherapy.

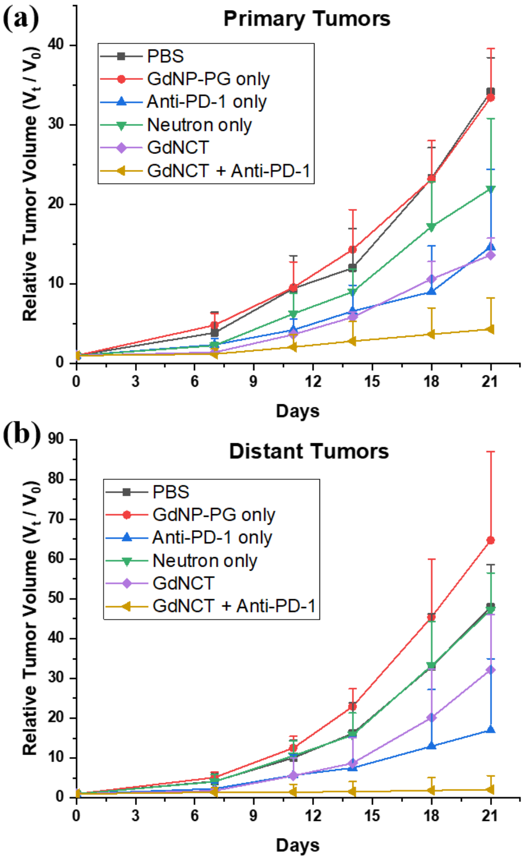

Figure 1. Tumor growth curves of (a) primary tumors inoculated on the right legs; (b) distant tumors inoculated on the right backs. (n = 3)

EXPRIMENTS and RESULTS: In this study, we investigated the abscopal effect induced by the combination of GdNCT and anti-PD-1 therapy in a dual-tumor mouse model (CT26 colon carcinoma). Each mouse bears two tumors: a primary tumor (inoculated on the right leg and subjected to irradiation) and a distant tumor (on the right back but left untreated). For the GdNCT + anti-PD-1 group, mice received thermal neutron irradiation 24 h after GdNP-PG injection, followed by intraperitoneal anti-PD-1 administration on days 1, 5, 8, and 11. As illustrated in Figure 1, the combined treatment significantly suppressed growth in both primary and distant tumors compared to control groups. Remarkably, two-thirds of distant tumors were completely eradicated, demonstrating a pronounced abscopal effect. Further studies are underway to elucidate the underlying mechanisms, including potential modulation of the tumor immune microenvironment.

Reference:

[1] Y-H. Lai *et al.,* Nat. Commun., **14(1)** (2023) 285.
[2] D. Duan *et al.,* CCS Chemistry, **5** (2023) 2589–2602.

CO7-40

Investigation of nano-boron drugs for BNCT

ZhiCheng Zhang[1,2], Qi Dai [1,2], Yaxin Qin [2], Yufan Yang [2], Xiaoyan Sun [2], Qiyao Yang[1], Lihong Liu[1], Minoru Suzuki [3], Min Han[2], Qichun Wei[1]

[1] *Department of Radiation Oncology, Key Laboratory of Cancer Prevention and Intervention, The Second Affiliated Hospital, College of Medicine, Zhejiang University*

[2] *College of Pharmaceutical Sciences, Zhejiang University*

[3] *Division of Particle Radiation Oncology, Particle Radiation Oncology Research Center, Institute for Integrated Radiation and Nuclear Science, Kyoto University*

INTRODUCTION: Boron neutron capture therapy (BNCT) has shown significant efficacy for malignant glioma. However, the boron neutron capturing agent currently used, p-boronophenylalanine (BPA), suffers from poor water-solubility, short tumor retention time, and an inability to monitor real-time boron distribution and concentration within the body. Meanwhile, we constructed nanodrugs including boron agents which were combined with liposome. The therapeutic effect of these nano-drugs after neutron irradiation was evaluated in this experiment.

EXPERIMENTS: The glioma cell line U87MG was seeded onto a 6-well plate, and after 24 hours of incubation, PBS, boronophenylalanine (BPA)-fructose, and two nano-drugs (ANG and Lipo), were added, respectively. After 4 hours of further incubation, the supernatant was discarded, and the cells were collected and counted using trypsin digestion. The cells were then transferred to four 2 mL centrifuge tubes (each tube containing 2×10^4 cells). Each set of four tubes were subjected to neutron irradiation for 0, 15, 30, and 45 minutes, respectively. Following BNCT, cells from each tube were then seeded onto a 6-well plate (1,500 cells/well), with three replicates for each cell sample. After 14 days of further culture, the cells were fixed with 70% ethanol and then stained with crystal violet solution, allowing for the calculation of cell colony formation number.

RESULTS: According to the colony formation results (Figure 1), it can be seen that two nano-drugs (ANG and Lipo) can effectively kill tumor cells at the cellular level, and the effect is slightly stronger than BPA-fructose. Further investigation of the two nano-drugs is warranted. We plan to conduct an in-vivo assay using cancer-baring mice.

Fig.1 Results of colony formation assay

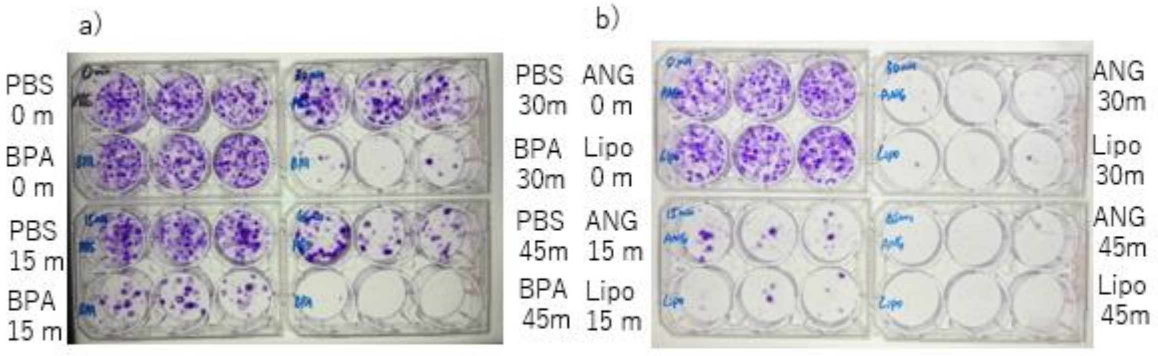

a): Colonies following PBS and BPA exposure (4h) and thermal neutron irradiation (0, 15, 30, and 45 mi).

b): Colonies following two nano-drugs (ANG and Lipo) exposure (4h) and thermal neutron irradiation (0, 15, 30, and 45 mi).

CO7-41

Analysis of the Structural Change of Boron Compounds after Boron Neutron Capture Reaction

H. Ueda, M. Suzuki, Y. Sakurai, T. Takata

Institute for Integrated Radiation and Nuclear Science, Kyoto University

INTRODUCTION:

Boron neutron capture therapy (BNCT) is one of the unique radiotherapies based on the combination of boron compounds and epi-/thermal neutron irradiation. In this treatment, high linear energy transfer (LET) particles, alpha (^{4}He) and lithium (^{7}Li) nucleus, are generated from boron-10 (^{10}B) atom due to the nuclear reaction between ^{10}B atom and neutrons. In 2020, L-4-boronophenylalanine (BPA) is approved as a BNCT agent for the treatment of recurrent head and neck cancer in Japan [1]. Although BPA has been used in BNCT research for decades, the effect of boron neutron capture reaction on the molecular structure of boron compounds is unclear. In this work, we attempted the investigation of structural change of boron-containing molecules after epi-/thermal neutron irradiation.

EXPERIMENTS and RESULTS

The aqueous solution of boron compound was prepared using ^{10}B-enriched BPA purchased from InterPharma (Prague, Czech Republic). The boron concentration was measured by Prompt Gamma-ray Analysis (PGA) and/or Inductively Coupled Plasma Atomic Emission Spectrometry (ICP-AES) using the same standard solutions (1, 2, 5, 10, 20, 50 ppm ^{10}B). Boron solution was poured into Teflon tubes and irradiated with epi-/thermal neutrons using the Heavy Water Neutron Irradiation Facility of the Kyoto University Research Reactor (KUR) operated at 1 MW and/or 5 MW for several times. The activation rate of the samples was evaluated by gamma-ray measurement. The structural change of BPA was analyzed by electrospray ionization mass spectrometry (ESI-MS) after derivatization of the analytes. As a result, tyrosine was observed in the solution of BPA, possibly due to oxidative degradation by hydrogen peroxide which produced by gamma ray irradiation in neutron-mixed beam.

****

REFERENCES:

[1] M. Suzuki, Int. J. Clin. Oncol., **155** (2021) 182-187.
[2] D.D. Pierro *et al.*, Anal. Biochem. **284** (2000) 301-306.
[3] S. Caquani *et al.*, Int. J. Radiat. Oncol. Bioll. Phys. **72** (2008) 562-567.
[4] L. Dick *et al.*, J. Pharm. Biomed. Anal. **56** (2011) 633-636.
[5] G. Halbert *et al.*, Eur. J. Pharm. **48** (2013) 735-739.

R6156

CO7-42

Evaluation of a Retinoid X Receptor-Binding BSH Derivative for Inhibition of Cell Proliferation Under Neutron Irradiation

Atsushi Mashimo[1], Ryuya Otani[2], Natsuko Kondo[3], Yoshinori Sakurai[3], Hiroki Kakuta[1]

[1]*Division of Pharmaceutical Sciences, Okayama University Graduate School of Medicine, Dentistry and Pharmaceutical Sciences.*

[2]*Okayama University, School of Pharmaceutical Sciences.*
[3]*Institute for Integrated Radiation and Nuclear Science, Kyoto University.*

INTRODUCTION: The only ^{10}B boron drug approved for BNCT is borofaran, which is licensed in Japan. To maximize the likelihood of collisions between ^{10}B and thermal neutron beams within cancer cells, borofaran must be administered continuously during neutron irradiation in large doses, such as 500 mg/kg of body weight. Consequently, lower dosages of boron delivery agents are necessary. A recent report indicates that, the dosage of boron medications can be significantly reduced by delivering boron agents directly into the nucleus.[1] Therefore, we focused on boron compounds that bind to nuclear receptors. Although boron compounds targeting nuclear receptors have been reported, there is currently no information regarding the use of these compounds in neutron irradiation. Having previously developed ligands that bind to the retinoid X receptor (RXR), one of the nuclear receptors, we investigated compounds containing ^{10}B that also bind to RXRs. We created CBTF-BSH (**1**) that exhibits RXR-binding characteristics by substituting the fluorescent BODIPY moiety of CBTF-BODIPY (**2**) [2] to BSH, a water soluble boron cluster. The exposure at 100 μM to the human breast cancer cell line MCF-7 gave 1 fmol/cell. In this study, we performed colony formation assay for cells treated with **2**.

****

EXPERIMENTS: Compound **1** was synthesized by authors. The MCF-7 cell line was obtained from RIKEN BioResource. MCF-7 cell were treated with **1** at 100 μM for 24 hours. Subsequently, the cells were collected after washing with PBS and treating with trypsin-EDTA. All resultant cells were then centrifuged in a 15 mL centrifuge tube, the supernatant was aspirated off, and 2 mL of media was added to count the number of cells. After preparing cell suspensions at 5 × 10^4 cells/mL and the suspension was transferred to one milliliter of them into 1.5 mL Eppendorf tubes, and the samples were exposed to a thermal neutron fluence of 1.0 × 10^{12} cm^{-2} (1 MW, 10 min). Following this, the cells were seeded at a density of 5 × 10^3 cells/well in 12-well plates and cultivated for 7 days at 37°C with 5% CO_2. After removing the medium, the cells were fixed in 80% EtOH, stained with crystal violet, washed with Milli-Q water, and the number of colonies was counted. The stained colony area was calculated using the "ImageJ-plugin Colony Area" software [3] and normalized by comparing it with the results of non-irradiated and unexposed cell samples.

****

RESULTS: The combination of **1** and neutron irradiation significantly decreased cell proliferative activity, while exposure to **1** alone had a minimal effect on cell proliferation (Figure 1). These results suggest that boron compounds that bind to nuclear receptors are effective as boron delivery carriers for BNCT and indicate that **1** may be utilized as an intracellular ^{10}B carrier.

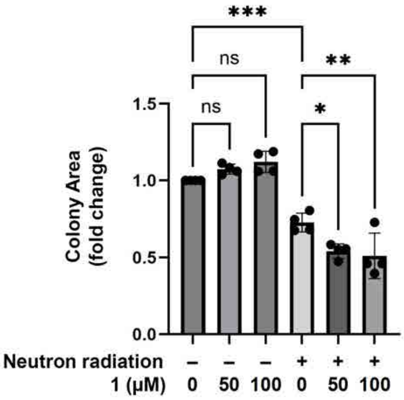

Figure 1. Comparison of the cell proliferative activity of MCF-7 cells following exposure to **1** and neutron irradiation.

****

REFERENCES: [1] *Adv Theory Simul.* **2023**, *6*, 2300163., [2] *ACS Med. Chem. Lett.* **2021** *12*, 1024–9., [3] *PLoS One.* **2014,** *19*, e92444.

CO7-43

Investigation of Boron Neutron Capture Reaction by Iodine-containing BSH Derivatives

Atsushi Mashimo[1], Rui Nozaki[2], Mayuri Inoue[3], Natsuko Kondo[4], Yoshinori Sakurai[4], Hiroki Kakuta[1]

[1]Division of Pharmaceutical Sciences, Okayama University Graduate School of Medicine, Dentistry and Pharmaceutical Sciences.

[2]Okayama University, School of Pharmaceutical Sciences.

[3]Division of Natural Science, Okayama University, Graduate School of Environmental, Life, Natural Science and Technology.

[4]Institute for Integrated Radiation and Nuclear Science, Kyoto University.

INTRODUCTION: Since BNCT relies on the interaction of ^{10}B with neutrons, the concentration of ^{10}B in tumor tissue is critical for the treatment's effectiveness. There are currently no boron agents available that can accurately quantify boron levels in cancerous tissue. We aimed to develop a BNCT drug capable of identifying boron concentrations in malignant tissues. We focused on iodine contrast agents used in X-ray computed tomography because they can noninvasively detect iodine concentrations and are administered in similar large doses to BNCT agents. To test this hypothesis, we designed and synthesized **1**. Additionally, we conducted experiments to evaluate the effects of combining it with the existing drug **A**, which enhances intracellular delivery capacity.

****

EXPERIMENTS: Compound **1** was synthesized by our group. Following 2-hour chemical exposure, cells were harvested by washing with PBS and treated with trypsin-EDTA. All cells were then lysed using RIPA buffer, and the ^{10}B concentration in the resulting samples was measured by ICP-MS. In 6 well plates, cells were cultivated on CR-39 pieces (2 cm square) in the medium and then exposed to a medium containing test compound. Following a wash with PBS, the CR-39 pieces were irradiated. After neutron irradiation, the CR-39 pieces were treated with alkali, and photographed using an optical microscope, and processed.[1][2] Image J was used to analyze the photographs. Colony assays were performed as described in R6163, with samples irradiated. In this study, samples was irradiated with a thermal neutron fluence of 1.1×10^{12} cm^{-2} (1 MW, 10 min).

****

RESULTS: An intracellular boron concentration in MCF7 cells, following a 2-hour exposure to 500 μM of **1** alone or in combination with drug **A**—which enhances the intracellular delivery of BSH —resulted in approximately 3.6-fold and 6-fold higher levels than BSH, respectively (Figure 1A, left four columns). This preference was further supported by the results obtained from CR-39. Additionally, under the combined conditions with drug **A**, **1** (250 μM) yielded similar intracellular boron levels as BSH at half its concentration (500 μM). The effects of compound exposure and neutron irradiation on cell proliferative activity were assessed using a colony formation assay, which demonstrated that the combination of **1** and neutron irradiation significantly reduced cell proliferative activity (Figure 1B). Furthermore, the cell proliferative activity of **1** was decreased in a concentration-dependent manner when combined with drug **A**.

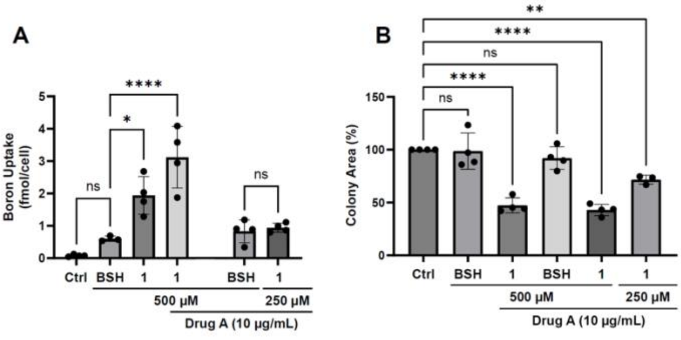

Figure 1. 1 and drug A exposure experiments with MCF7 cells. (A) Intracellular boron concentration. (B) Comparison of cell proliferation ability following neutron

****

REFERENCES: [1] J. Control Release, **330** (2021) 788-796.
[2] Radiat. Res., **191** (2019) 460-465.

CO7-44

Safety of Boronated matrix metalloproteinase ligand 1 *in vivo*

Natsuko Kondo[1], Jonathon Kane[2], Masao Takagaki[3], Yoshinori Sakurai[1] and Daniel P. Becker[2]

[1] *Particle Radiation Oncology Research Center, Institute for Integrated Radiation and Nuclear Science, Kyoto University (KURNS)*

[2] *Department of Chemistry and Biochemistry, Loyola University Chicago*

[3] *Research Center for Nuclear Physics, Osaka University*

INTRODUCTION: BNCT has shown great promise in clinical trials for treatment of glioblas-toma multiforme, malignant gliomas, melanoma, as well as head and neck cancers. Currently, there are only two clinically investigated BNCT drugs, L-boronophenylalanine (L-BPA) and sodium borocaptate (BSH), which are neither tumor-specific, nor do they accumulate in high concentrations within the tumor cells. The effectiveness of BNCT therapy is governed by the selectivity of the drug and the specific accumulation of ^{10}B atoms on tumor cells**.** We indicated the efficacy of new boro-nated matrix metalloproteinase (MMP) ligands for BNCT in vitro [1]. In this study, we proceeded the MMP ligand 1 (B1) to in vivo study, and investigated safety dose.

EXPERIMENTS:

Cells:

We used mouse glioma GL261 cells. They were cultured in DMEM medium with 10% heat-inactivated fetal bovine serum in 5 % CO_2 incubator.

Tests for safety dose of B1:

We dissolved the B1 in DMSO at the dose of 0.886mg/ml (2.5 mmol/L). We mixed this B1 solution with beta cyclodextrin (10mmol/L) and water at the ratio of 1:1:0.5. We evaluated the mixed solu-tion at the dose of 400 and 800 µl (n=3, each). The mice weighted 20g/body.

Mouse orthotopic glioma model:

We used C57BL/6 mice. The GL261 cells were inoculated into the right brain of mice. In brief, 2 x 10^5 GL 261 cells were injected in the location of 2mm right from the bregma, and 3mm depth from the surface of the brain using Hamilton syringe. We created non-irradiated and BNCT groups (n=6 in each group).

BNCT treatment:

Three weeks later, we administrated B1 intraperitoneally and one hour later, irradiated thermal neu-tron to the mouse brains using the heavy water neutron irradiation facility in KUR. After irradiation, the survival time was observed.

RESULTS:

Safety dose of B1 solution: The mice which were administered the 800 µl B1 solution lied down at prone position soon after administration, and they recovered next day. The mice which were administered the 400 µl B1 solution behaved normally after administration. We set the safety dose for the B1 solution at 400 µl/20g body weight. With this safety dose, we treated BNCT to the mouse ortho-topic glioma model and under observation.

REFERENCES:

[1] Flieger S. *et al.,* Carborane-Containing Hydroxamate MMP Ligands for the Treatment of Tumors Using Boron Neutron Capture Therapy (BNCT): Efficacy without Tumor Cell Entry, Int J Mol Sci.,**24(8)**(2023) 6973.

R6165

CO7-45

Investigation of cellular senescence by BNCT

M. Suzuki[1], M. Sakamoto[2]

[1]*Institute for Integrated Radiation and Nuclear Science, Kyoto University*
[2]*Graduate School of Biostudies, Kyoto University*

INTRODUCTION:

Boron neutrons capture therapy (BNCT) is expected to be a novel type of cancer radiotherapy. The mechanism of BNCT is based on the generation of α-particles and lithium nucleus by the nuclear fission reaction between thermal neutron and boron-10 atom. When the thermal neutron is absorbed into the boron-10 atom, the complex is split into helium and lithium nucleus. The two heavy particles have the ability to break double-strand DNA and induce apoptosis of cancer cells [1].

Cell senescence is known to be another cellular physiological status induced by various cytotoxic treatments. Cell senescence is cell growth-inhibited status caused by cell cycle stopping. Radiotherapy has been reported to induce cell senescence in tumor cells. However, the relationship between BNCT and cell senescence has not been reported. The aim of this study is to make it clear that the induction of cell senescence by BNCT and its mechanism.

EXPERIMENTS:

B16F10 cells were incubated in 10cm dishes with 70% confluence and exposed by boronophenylalanine (BPA) 24 hours before thermal neutron irradiation. Before the thermal neutron irradiation, Cells were washed with phosphate-buffered saline (PBS) and collected within the tube after trypsinization, and then, a cell number in each tube was adjusted to 10^6/mL. The suspensions of B16F10 cells were irradiated with thermal neutron beam for 0, 10, 20, 30 min at 1MW power at the Heavy Water Neutron Irradiation Facility (HWNIF). The cells after neutron irradiation were dispersed into 6well plates and incubated 37 °C for 8 days. SA β Gal assay and colony formation assay were carried out to examine whether BNCT induced the cell senescence in the irradiated cells [2]. Next, whole proteins in B16F10 cell were collected at 6, 12, 24 hours after neutron irradiation to examine an expression level of the cell senescence-related proteins such as p21, phosphorylated p21, p53, phosphorylated p53, p38, and phosphorylated p38 by western blotting [3].

RESULTS:

We have performed SAβ Gal assay, Western blotting, colony formation assays to evaluate whether BNCT induced cellular senescence in the irradiated cells. The analysis is currently on going.

REFERENCE:

[1] Locher, G. L., Biological effects and therapeutic possibilities of neutrons, American Journal of Roentgenology and Radium Therapy, **36** (1936)1-13.

[2] Dimri GP, Lee X, Basile G, *et al.,* A biomarker that identifies senescent human cells in culture and in aging skin in vivo., Proc. Natl. Acad. Sci. U S A., **92(20)** (1995) 9363-9367. (doi)10.1073/pnas.92.20.9363.

[3] Sun X, Shi B, Zheng H, *et al.,* Senescence-associated secretory factors induced by cisplatin in mela-noma cells promote non-senescent melanoma cell growth through activation of the ERK1/2-RSK1 pathway, Cell Death Dis., **9(3)** (2018) 260. (doi)10.1038/s41419-018-0303-9.

R6167

CO7-46

Clarification of the normal cell fractionation as a trigger for radiation-induced liver injury

M.Suzuki[1] , T. Shigehira[2]

[1] *Institute for Integrated Radiation and Nuclear Science, Kyoto University*
[2] *Graduate School of Science, Kyoto University*

INTRODUCTION: Even though radiation-induced liver injury is one of the fatal adverse events in radiation therapy, normal cell fractionation, which causes radiation-induced liver injury, is still not clear. By delivering the boron atoms in a particular normal cell fraction and irradiating them with thermal neutrons, it is possible to destroy the targeted normal cell fractions, specifically. The key in this study is the device recognizing a particular normal cell fraction. We used a linker (Linker X) which recognized non parenchymal liver cells and a boron-nanoparticles as a carrier of LinkerX in this study.

EXPERIMENTS: We applied the boron-nanoparticles conjugated with LinkerX and boronophenylalanine (BPA) to Balb/c mice intravenously. The mice were sacrificed 3 hours later, and the livers were resected from the mice. The resected liver was processed to the thin sections (10 μm) and put on CR-39 (solid state nuclear track detector) and irradiated with thermal neutron beam (5MW power) at the Heavy Water Neutron Irradiation Facility (HWNIF). Then, the spatial distribution of boron atoms was analyzed using autoradiography technique described in our previous study [1].

RESULTS: The distributions of the boron-nanoparticles conjugated with LinkerX and boronophenylalanine (BPA) were successfully depicted as dots which were observed with an optical microscope. In the case of the boron-nanoparticles conjugated with LinkerX, the dots seem distributed linearly along the side of hepatocytes, which indicate that the boron-nanoparticles conjugated with LinkerX distributed in non-parenchymal cells. On the other hand, in the case of BPA, the dots distributed homogeneously in the liver.

REFERENCE:

[1] Takeno S, Tanaka H, Watanabe T, Mizowaki T, Suzuki M., Quantitative autoradiography in boron neutron capture therapy considering the particle ranges in the samples., Phys. Medica, **82** (2021) 306–20.

R6168

CO8-1

Detection experiment for nuclear materials positioned away from center

M. Komeda[1], K. Tanabe[2], Y. Toh[1], Y. Kitamura[3], Y. Takahashi[3] and T. Misawa[3]

[1]*Nuclear Science and Engineering Center, Japan Atomic Energy Agency*
[2]*National Research Institute of Police Science*
[3]*Institute for Integrated Radiation and Nuclear Science, Kyoto University*

INTRODUCTION: We have developed a new nuclear material detection method, called the active rotation method, using a neutron rotation machine that rotates a neutron source (Californium-252) at a speed of thousands of rpm. In addition to the rotation machine, we have developed a water Cherenkov neutron detector (WCND) as a low-cost neutron detector. The system for detecting nuclear materials is composed of the neutron rotation machine and WCND, leading to a compact and low-cost. In previous studies, we accomplished to detect lead-shielded high enriched uranium (HEU) using the system [1]. However, in the experiments, the nuclear material was placed at the center of the measurement object. In actual nuclear material detection, nuclear material does not always exist at the center position, for example, nuclear material in a container. Therefore, in this experiment, we worked on the detection of nuclear material placed off-center.

****

EXPERIMENTS: The rotation machine can rotate the disk (32 cm in diameter), where a neutron source is installed at its outer periphery, at a rotation speed between 0 and 4000 rpm. A neutron source of Californium-252 whose reactivity was 1.3 MBq was set in the disk. The size of the WCND is 30x25x30 cm, with four 2 inch PMTs mounted on the ceiling. Polyethylene blocks were placed between the rotating irradiation device and the WCND, and a 20x20x20 cm space was provided inside the polyethylene blocks for measurement sample placement (Figure 1). To investigate the effect of placing the nuclear material away from the central position, the nuclear material was placed at the edge within the measurement space.

****

RESULTS: An example of the measurement results is shown in Figure 2. The measurement time was 10 minutes. By analyzing the spectrum, it was possible to determine the presence of nuclear materials placed at an edge within the measurement space. As a next step for our study, we are going to work on detection nuclear materials in various positions of the measurement space, and development of a more effective data processing method.

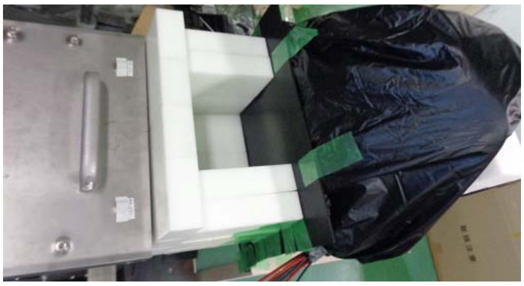

Fig. 1 The rotation machine (left), WCND (right), and sample placement area (middle). The lid is attached during measurement.

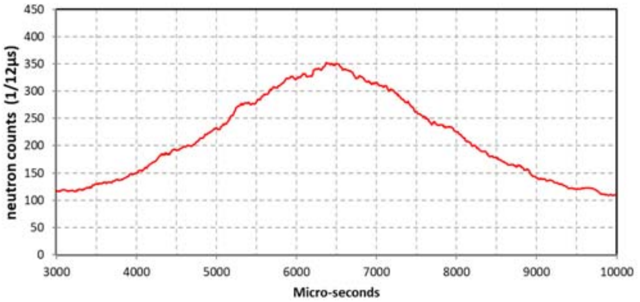

Fig. 2 A sample of the neutron count distribution at a rotation speed of 4000 rpm, in the presence of nuclear materials.

REFERENCES:

[1] K. Tanabe *et al.*, Scientific reports, **14** (2024) 18828.

R6CA01

CO8-2

New boron drug development research targeting pancreatic cancer

H. Michiue[1], T. Fujimoto[1,2], N. Kanehira[1,2], K. Igawa[1], Y. Sakurai[3], N. Kondo[3], T. Takata[3], and M. Suzuki[3]

[1]*Neutron Therapy Research Center, Okayama University; 2-5-1, Shikata-cho, Kita-ku, Okayama City, Okayama, Japan.*

[2]*Department of Gastroenterological Surgery, Okayama University; 2-5-1, Shikata-cho, Kita-ku, Okayama City, Okaya-ma, Japan.*

[3]*Institute for Integrated Radiation and Nuclear Science, Kyoto University, 2-1010, Asashiro-Nishi, Kumatori-cho, Sen-nan-gun, Osaka, Japan.*

INTRODUCTION: Pancreatic cancer refers to malignant tumors that originate in the pancreas, but it gener-ally refers to ductal cancer. Ductal cancer arises from the pancreatic duct epithelium and accounts for 80–90% of ma-lignant tumors in the pancreas. According to national statistics, it is the fifth leading cause of death, following lung cancer, stomach cancer, colorectal cancer, and liver cancer. In recent years, the number of pancreatic cancer patients in Japan has been increasing, with over 30,000 deaths annually.

Despite being a malignant tumor, pancreatic cancer has relatively fewer tumor vessels compared to normal tissue and exhibits interstitial hyperplasia between tumor cells, making it difficult for drugs to reach the tumor.

In the development of drugs for pancreatic cancer, the use of polymer-based DDS formulations with EPR effects (Enhanced Permeability and Retention effect) is considered challenging for future clinical applications. Therefore, we have decided to develop boron-based drugs targeting glucose transporters highly expressed in pancreatic cancer, using glucose as the basis.

****

EXPERIMENTS: In this study, we planned to develop boron-containing drugs targeting pancreatic cancer. Three cell lines were used: PANC0403 and BxPC3, which express high levels of CA19-9, and PANC-1, which express-es low levels of CA19-9. The drugs used were three types of boron-containing agents: glucose-bound BSH, BPA, and BSH. After evaluating the cellular uptake of the drugs, neutron irradiation was performed using a reactor neutron source.

****

RESULTS:

Ex1) The three boron drugs used in this study were Glucose-BSH (G-BSH), BSH, and BPA, with molecular weights of 372.43, 213.88, and 208.21, respectively, and intramolecular boron contents of 0.322, 0.561, and 0.048 ngB, respectively (Fig.1). We treated three pancreatic cell lines, panc0403 and BxPC3 CA19-9-producing cells and PANC-1 CA19-9-non-producing cells with the boron drugs and examined intracellular boron concentrations (Fig. 2). All three cell lines, both CA19-9-producing and CA19-9-non-producing cells, showed low intracellular boron concentrations after treatment with BSH and BPA. In contrast, very high intracellular boron concentrations in the G-BSH group were observed in the panc0403 and BxPC3 CA19-9-producing cells, while low concentrations were observed in the PANC-1 CA19-9-non-producing cells (Fig. 2).

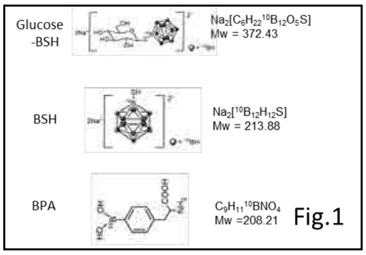

Fig.1

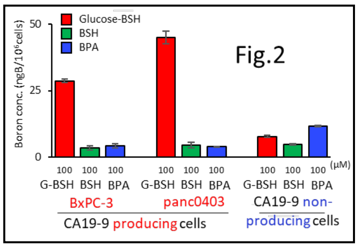

Ex2) We next performed colony formation assays in CA19-9-producing PC cells panc0403 and non-CA19-9-producing PANC-1 cells treated with boron agents and irradiated with neutrons. In panc0403 cells, Glucose-BSH showed superior inhibition of cell proliferation compared with the Control, BPA, and BSH treatments starting from 30 min of irradiation and 45 min (P>0.001). In contrast, none of the boron agents showed significant cell-killing effects in CA19-9-non-producing PANC-1 cells (BPA: P>0.4, BSH: P>0.6) (Fig. 3). Treatment doses were as high as 19.1, 34.9, and 53.2 Gy-Eq each in the Glucose-BSH group of panc0403 cells for 15, 30, and 45 min of irradiation, respectively; the Glucose-BSH group showed 5-fold higher neutron doses than the BPA and BSH groups. These results indicate that Glucose-BSH showed strong cytotoxic activity against CA19-9-producing pancreatic cancer cells upon neutron irradiation.

Fig.3

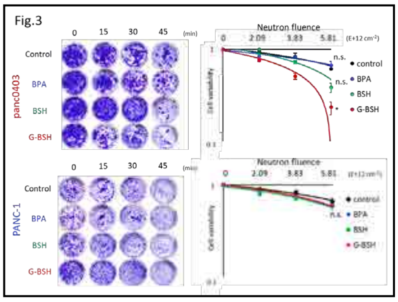

****

REFERENCE: [1] T. Fujimoto *et al.,* Biomaterials, **309** (2024) 122605.

CO8-3

Porocity Distribution Evaluation of Additively Manufactured Workpiece Using Neutron Phase Imaging

Y. Kanbe, Y. Terakawa[1], Y. Seki[1], D. Kono, M. Hino[2]

Graduate School of Engineering, Department of Microengineering, Kyoto University
[1]Institute of Multidisciplinary Research for Advanced Materials, Tohoku University
[2]Institute for Integrated Radiation and Nuclear Science, Kyoto University

INTRODUCTION: Since the porosity distribution in additively manufactured workpiece is highly variable, it is necessary to inspect the porosity distribution to assure the quality of the workpiece. In this study, we investigated the potential of neutron phase imaging as a non-destructive inspection method for porosity distribution. The porosity of samples were measured by the neutron phase imaging and the conventional microscope observation for comparison.

EXPERIMENTS: Samples were prepared by changing fabrication parameters that are laser power, scanning speed, and rotation angle of scanning specifically. The porosity of samples was measured by the neutron phase imaging based on the rigid sphere model proposed by Strobl et al.. The porosity was also measured from the cross sectional image of samples taken by a digital microscope. Samples were cut, embedded into plastic pellets, and polished for observation. The cross sectional image was binarized to extract the pore area. Then, the area ratio of pores relative to the matrix was calculated as porosity.

RESULTS: Figure 1 shows the obtained visibility image of samples. The variation of the porosity depending on the fabrication conditions can be observed from the visibility image. Some samples such as sample 4, 7, 16, and 17 have laminar structured image that indicates the corresponding periodic porosity variation. The porosity measured by the neutron phase imaging had a positive correlation with porosity measured by the microscope. However, the difference of the absolute porosity was up to 20 % and not negligible. The reason for this discrepancy may be the influence of pores with the size larger than the auto correlation length in the neutron phase imaging.

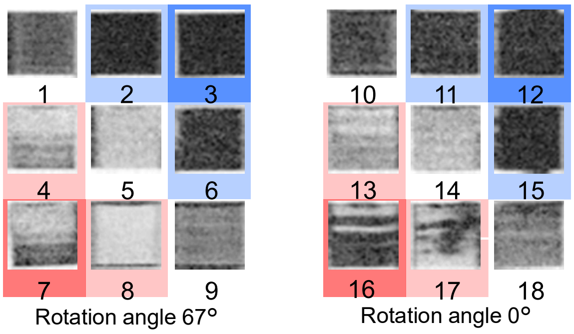

Fig. 1. Visibility image of samples fabricated by different conditions. Black and white colors represent higher and lower porosities, respectively.

REFERENCES:

[1] M. Strobl, Scientific Reports, **4** (2014) 7243.

CO9-1

Preparation method of NaCl–UCl_3 salt

T. Murakami, Y. Sakamura and K. Takamiya[1]

Central Research Institute of Electric Power Industry
[1]Institute for Integrated Radiation and Nuclear Science, Kyoto University

INTRODUCTION: NaCl(66 mol%)–UCl_3(34 mol%) salt (m.p. 796 K) is a promising candidate for a fuel salt of molten chloride salt fast reactor [1]. Reprocessing of the used fuel salt is crucial for effective utilization of nuclear resources. A reasonable reprocessing process for the used fuel salt is expected to be developed by applying pyrochemical technologies which have been established for recycling the used metallic fuel [2–3]. In this study, a chlorination of U metal by $CdCl_2$ in NaCl was studied to prepare NaCl–UCl_3 salt which will be used to obtain the basic properties for developing the pyrochemical reprocessing process of the used fuel salt.

EXPERIMENTS: The preparation of NaCl–UCl_3 salt was performed in a glove box filled with purified Ar gas. A mixture of NaCl(1.515 g)–$CdCl_2$(3.655 g) salt was loaded in Ta crucible (13 mm inner diameter, 35 mm height). Then, the mixture was melted at 823 K together with U metal rod (φ6 mm, 34.426 g) for overnight to convert NaCl–$CdCl_2$ melt to NaCl–UCl_3 melt by proceeding the following chemical reaction.

$$2U + 3CdCl_2 \rightarrow 2UCl_3 + 3Cd \qquad (1)$$

A largely negative value of Gibbs energy of reaction (1) (ΔG = –577 kJ at 823 K) indicates that $CdCl_2$ initially added would be consumed to form UCl_3 and Cd when excess amount of U metal is supplied. Thus, in the present experimental condition, it was expected to form NaCl(1.515 g, 66.1 mol%)–UCl_3(4.588 g, 33.9 mol%) salt and Cd metal (2.238 g) with almost no remaining $CdCl_2$.

RESULTS: After the experiment, the resulting salt, the Cd metal formed, and the U metal rod were recovered (Fig. 1). The weight loss of the U metal rod was 3.218 g which was close to the amount of U metal (3.170 g) to consume all $CdCl_2$ according to reaction (1). The weight of recovered salt was 6.109 g, which agreed well with the expected value (6.103 g = 1.515 g + 4.588 g). The amount of recovered Cd metal (1.505 g) was smaller than the calculated value (2.238 g), which might be explained by that a part of the formed Cd metal would evaporate during the experiment due to its relatively low boiling point (1040 K). These results indicated the feasibility of the method to prepare NaCl–UCl_3 salt with the expected composition using chlorination of U metal by $CdCl_2$ in NaCl. The detailed composition of the obtained NaCl–UCl_3 salt will be quantitatively analyzed in near future.

(a) Formed Cd metal

(b) Recovered salt

Fig. 1. Pictures of (a) formed Cd metal and (b) recovered salt after the experiment.

REFERENCES:

[1] Y. Peng *et al.*, Ann. Nucl. Energy, **214** (2025) 111225.
[2] T. Murakami *et al.*, Proceedings of GLOBAL2024, 7-10 Oct. 2024, Tokyo, Japan, 2B3-04-01.
[3] M. Yamawaki *et al.*, J. Atom. Energ. Soc. JPN (ATOMOΣ), **63** (2021) 791 (in Japanese).

CO9-2

Characterization of tetravalent actinide hydroxide coprecipitated solid phase

T. Kobayashi, Y. Yoshikawa, T. Sasaki, K. Takamiya[1]

Graduate School of Engineering, Kyoto University
[1] Institute for Integrated Radiation and Nuclear Science, Kyoto University

INTRODUCTION: Safety assessment of geological disposal requires a reliable prediction of radionuclide migration behavior under repository conditions. Tetravalent actinides such as Th(IV), U(IV), and Pu(IV) easily precipitate to form amorphous hydroxide ($M(OH)_4$(am)) and play a role in controlling their solubility in groundwater. Under considerable time span during the safety assessment, $M(OH)_4$(am) is expected to transform into more thermodynamically stable crystalline oxide: MO_2(cr) [1]. Although previous studies have investigated to reveal the state of $M(OH)_4$(am) and the process of their transformation to MO_2(cr) for each actinide [2,3], multiple nuclides would coprecipitate under actual disposal conditions. In the case of the coprecipitated solid phase consisting of multiple nuclides with different stabilities, the solubility-limiting solid phase and its transformation process may be different from those consisting of a single nuclide. In this study, coprecipitated solid phases of Th(IV) and Zr(IV) amorphous hydroxide were prepared and aged under elevated temperature conditions. The solid-phase state was investigated using powder X-ray diffraction (PXRD) to interpret the solubility.

EXPERIMENTS: In the experiment, amorphous hydroxide coprecipitates of Th(IV) and Zr(IV) ((Th,Zr)$(OH)_4$(am)) were prepared by an oversaturation method. Mother solutions of Th hydrochloric acid ([Th] = 0.1 M) and Zr hydrochloric acid ([Zr] = 0.1 M) were mixed in a given molar ratio, and the pH was adjusted to 8 or 12 with NaOH. The sample solutions containing the coprecipitated solid phase were settled at 25 or 70 °C for one month. The supernatant of each sample solution was then ultrafiltered (10 kDa membrane), and the metal ion (Th, Zr) concentrations in the filtrate were quantified by ICP-MS. In addition, a portion of the coprecipitated solid phase was dried in a glove box, and the diffraction pattern was measured by a powder X-ray diffractometer (PXRD).

RESULTS: In the PXRD pattern, diffraction peaks corresponding to ZrO_2 (monoclinic) were observed in the case of the sample prepared from only Zr mother solution, and diffraction peaks corresponding to ThO_2 (cubic) were observed when prepared from only Th mother solution. On the other hand, in the samples co-precipitated from a Th and Zr mixed solution, the peaks tended to become broader as the [Th]/[Zr] ratio approached 5/5. This suggests that the coprecipitated solid phase would be more stable as amorphous, consisting of small particles. The solubilities of Th and Zr in the coprecipitated solid phase were found to decrease with decreasing [Th]/[Zr] at the same pH. It is known that when the size of the solid phase particles is sufficiently small, the solubility increases inversely proportional to the particle size due to the particle size effect [3]. Therefore, the solubility of coprecipitated (Th,Zr)$(OH)_4$(am) was interpreted, taking into account the particle size effect on solubility based on the results of PXRD.

REFERENCES:

[1] T. Kobayashi *et al.,* Radiochim. Acta, **101** (2013) 645-651.
[2] D. Rai *et al.,* Radiochim. Acta, **88** (2000) 297-306.
[3] I. Grenthe *et al.,* Chemical Thermodynamics Vol. 14, OECD-NEA (2020).

R6046

CO9-3

Neutron Irradiation of Zn-Coated Stainless Steel Foil

T. Fujii[1], S. Akamatsu[1], A. Uehara[2], S. Fukutani[3],

[1]*Graduate School of Engineering, Osaka University*
[2]*National Institutes for Quantum Science and Technology*
[3]*Institute for Integrated Radiation and Nuclear Science, Kyoto University*

INTRODUCTION: One of the methods to control the accumulation of ^{58}Co and ^{60}Co, which are generated in the nuclear reactors, is to inject Zn into the cooling water. The Zn injection increases ^{65}Zn concentration via the neutron capture of a stable isotope ^{64}Zn. Hence, preparing ^{64}Zn depleted materials is required. In our previous study[1,2], the isotope separation of Zn has been tested by employing solvent extraction and liquid chromatography with a macrocyclic polyether, 1-aza-15-crown-5-ether. Possible magnitudes of isotope fractionation have been found. In the present study, electroplating of Zn onto a stainless steel (SUS304H) foil as a mechanism of depressing ^{58}Co and ^{60}Co was performed. Fragments of the Zn-coated foil were irradiated by neutrons at KUR, and ^{65}Zn generation has been confirmed.

EXPERIMENTS: All chemicals used were analytical grade. A sample solution of 0.1 mol dm^{-3} (M) Zn(NO$_3$)$_2$ was prepared. A stainless steel foil was immersed in the solution and electroplating of Zn onto the foil was performed. As a working electrode, a SUS304H foil of 0.02 mm in thick(5mm in width x 40 mm in length) was used. A reference electrode of Ag/AgCl and a counter electrode of Pt wire were used. The electroplating was run at -1.4 V for 10 to 100 min. After the electroplating, the foil was rinsed by water and dried at room temperature. The dried foil was then cut into pieces of 10mg each. One of the pieces was irradiated in a pneumatic irradiation system of the Kyoto University Research Reactor, where the thermal neutron flux is 2.3 x 10^{13} n/cm^2/sec. After the irradiation, gamma spectrometry was performed.

RESULTS: As shown in Fig. 1, clear gamma spectrum was obtained for the Zn-coated foil. A characteristic gamma-ray of 1115.5 keV emitted from ^{65}Zn was found. This indicates that, even by using ^{64}Zn depleted materials, the Zn coating onto the stainless steels may be possible.

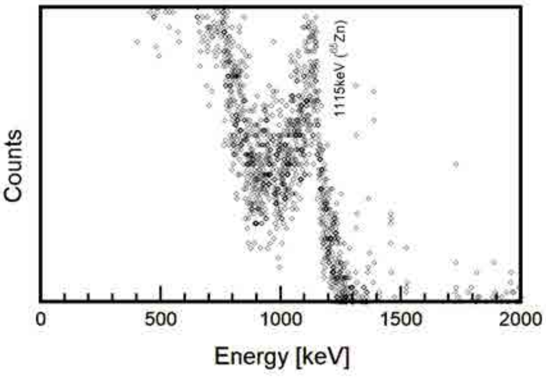

F ig. 1. Gamma spectrum of a Zn-coated stainless steel foil irradiated at KUR

REFERENCES:

[1] S. Akamatsu *et al.*, Proc. 58th KURNS Sci. Mtg., 31(2024).
[2] S. Akamatsu *et al.*, Proc. 58th KURNS Sci. Mtg., 17(2025).

CO9-4

Development of a barium malonate coprecipitation method for the chmiecal study of element 102, nobelium

M. Konno,[1, 3] Y. Kasamatsu,[1, 3] M. Kaneko,[1] H. Kazama,[1] R. Wang,[1, 3] Y. Itakura,[1, 3] E. Khult,[1, 3] K. Shibamoto,[1, 3] R. Kikuchi,[1] K. Takamiya,[2] M. Inagaki,[2] H. Haba,[3] A. Nambu[3]

[1] *Graduate School of Science, Osaka University*
[2] *Institute for Integrated Radiation and Nuclear Science, Kyoto University*
[3] *Nishina Center for Accelerator-Based Science, RIKEN*

INTRODUCTION: Nobelium (No, Z = 102) is an actinide element and has distinctive properties among f-block elements in that it is stable as a divalent cation in aqueous solutions [1]. Previous studies compared the behavior of No with that of transition metals and group 2 elements and concluded that No behaves like group 2 elements as a hard acid. However, due to low production rates and short half-lives of No nuclides, chemical researches on No are very limited. In our group, extraction and coprecipitation methods for heavy elements [2] have been developed and applied to No. As a result, we found that No exhibits soft acid behavior. For further chemical study of No, we plan to investigate the complexation of No^{2+} with oxalic and malonic acids, which are expected to form covalent bonding involving its d- and f-orbitals. These dicarboxylic acids function as chelating ligands, forming stable precipitates with numerous metal ions including group 2 elements. The objective of this study is to investigate the chemical properties of No by comparing chemical bonding properties and ligand size effect on malonate complexation for No and group 2 elements. This paper presents the (co-)precipitation experiments of group 2 elements in malonic acid.

EXPERIMENTS: A) Malonic acid precipitation experiment with macro amounts of group 2 elements. Malonic acid buffer solution at pH = 7 was prepared by dissolving malonic acid (1.370 g) and disodium malonate (3.973 g) in distilled water (200 mL). 10 μL each of ^{47}Ca, ^{85}Sr, or ^{133}Ba were added to the metal (Ca, Sr, or Ba) chloride solution at room temperature and stirred for 5 min to form precipitate. After suction filtration, radioactivity of ^{47}Ca, ^{85}Sr, or ^{133}Ba in the filtrate and collected precipitate were determined by gamma-ray measurement with a Ge detector to evaluate the precipitation yield. B) Coprecipitation experiment of ^{47}Ca and ^{85}Sr with barium malonate. Coprecipitation experiments of ^{47}Ca and ^{85}Sr with Ba selected as the carrier element were performed and the behavior was compared with the precipitation behavior. The ^{47}Ca used in the experiments was produced by thermal neutron irradiation of a ^{nat}CaO target at 5 MW for 1 h at KURNS.

RESULTS: In the precipitation experiments, Ca and Sr were unreactive with malonate ions, while Ba formed crystalline precipitates and chemical reactions reached to equilibrium state within 1 min. From chemical simulation based on the malonate complexes formation constants and dissociation constants of malonic acid, the equilibrium concentration products for Ca and Ba malonate at pH 3 and Sr malonate at pH 4 exceeded their solubility products, suggesting thermodynamically favorable precipitation. The low yields of Ca and Sr are due to their slow reaction kinetics. In the coprecipitation experiments, Ba was selected as the carrier element under malonic acid conditions of pH 7. The co-precipitation yields of Sr were higher than those of Ca with largely different ionic radius from that of Ba. Reaction kinetics of Ca and Sr were fast in the presence of carrier element Ba (faster kinetics). Neutral metal complex concentrations at equilibrium are estimated from chemical simulations, and their proportion reflects coprecipitation efficiency qualitatively. These findings suggest that complex stability in solution influences coprecipitation behavior, and the stability of the No–malonate complex can be examined using the barium malonate coprecipitation method.

REFERENCES:

[1] A. Toyoshima *et al.,* J. Am. Chem. Soc., **131** (2009) 9180-9181.
[2] R. J. Silva *et al.,* Inorg. Chem., **13** (1974) 2233-2237.

R6108

CO10-1

Application of KURAMA-II to Radiation Monitoring of Cement Solidification Facility in Fukushima Prefecture

A. Maekawa, K. Hashimoto and M. Tanigaki[1]

Fukushima Prefectural Centre for Environmental Creation
[1]Institute for Integrated Radiation and Nuclear Science, Kyoto University

INTRODUCTION: KURAMA (Kyoto University Radiation Mapping system)-II is a radiation measurement system characterized by its compactness, autonomous operation, and acquisition of pulse-height spectrum data (Fig. 1) [1]. KURAMA-II measures ambient dose equivalent rate (hereafter referred to as air dose rate) and GPS position and automatically transmits them to a dedicated cloud server. In this study, we used a backpack-style KURAMA-II (Fig. 2) for the cement solidification facility (handling incinerator ash contaminated with radioactive cesium derived from the Fukushima Daiichi NPP accident) to assess whether the radioactive cesium was scattered under demolition.

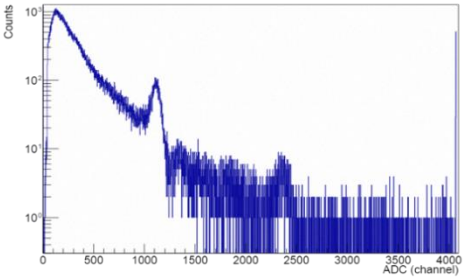

Fig. 1. A typical example of the pulse-height spectrum obtained by KURAMA-II measurement.

Fig. 2. KURAMA-II in a backpack.

EXPERIMENTS: The air dose rates of the cement solidification facility were measured on foot with a KURAMA-II in a backpack. The measurement dates were 20 June 2024 (first), 23 Jul. 2024 (second), and 23 Jan. 2025 (third). The second measurement was carried out during demolition.
A CsI (Tl) scintillation detector (C12137-4034, Hamamatsu Photonics) was used for measurement. The air dose rate and GPS position were measured every second. For the first and second measurements, the air dose rate was measured by walking along the facility's boundary, while the third measurement was carried out in the whole area of the facility. The measurement data were averaged in a 15-meter mesh and visualized to the colored air dose rate maps using GIS software (QGIS 3.28.6).

RESULTS: The air dose rate maps are shown in Fig.3. No apparent differences were found among the three measurements around the facility. As shown in Fig.3(c), no apparent contamination was found in the study area. In conclusion, no clear effect of the demolition of the cement solidification facility on the air dose rate was found in the present study.

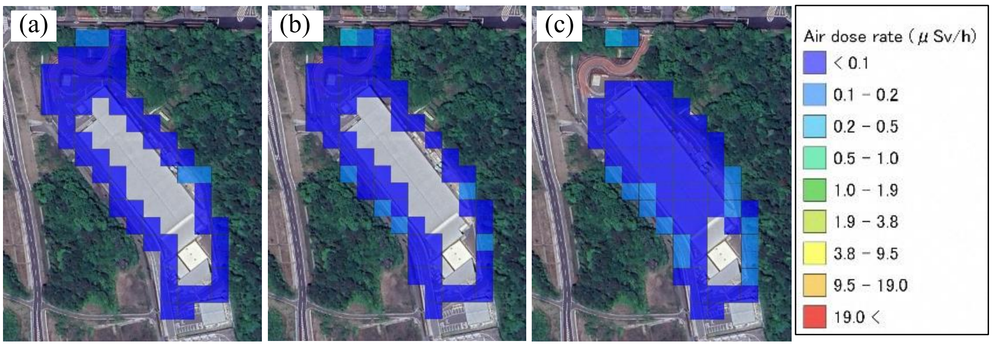

Fig. 3. The air dose rate maps obtained by (a)first, (b)second, and (c)third measurements.

REFERENCES:
[1] M. Tanigaki *et al.,* Nucl. Instrum. Meth. Phys. Res., **781** (2015) 57–64.

R6028

CO10-2

Determination of Chlorine and Bromine Concentration in Plastics in Construction Waste by Neutron Activation Analysis

Y. Yamashita[1], R. Homma[1], S. Fukutani[2], K. Oshita[1], and M. Takaoka[1]

[1]*Department of Environmental Engineering, Graduate School of Engineering, Kyoto University*
[2]*Institute for Integrated Radiation and Nuclear Science, Kyoto University*

INTRODUCTION: In the recycling of waste plastic contained in construction waste (construction waste plastic), there are restrictions on chlorine concentration. However, the elemental composition varies from item to item, and this needs to be clarified. In this study, neutron activation analysis (NAA) was performed on 36 new plastics that can be generated at construction sites to analyze chlorine and bromine concentrations.

EXPERIMENTS: NAA was performed four times for each sample. Samples were irradiated for 3 min with a thermal neutron flux of 2.0-2.4×10^{13} cm^{-2}・sec^{-1} at KURRI. ^{38}Cl ($t^{1/2}$ = 37.18 min, E_γ = 1642, 2168 keV) and ^{80}Br ($t^{1/2}$ = 17.68 min, E_γ = 616, 666 keV) were measured by using a Ge semiconductor detector for 300 sec.

RESULTS: Figure 1 shows a histogram of chlorine concentrations. Chlorine is shown separately on the low and high concentration side because the concentration differs greatly between PVC and non-PVC products. Thirteen samples were below 200 ppm, which is the standard for oil conversion in chemical recycling (the value obtained from interviews with plant manufacturers). The samples exceeding 20% were flooring materials, window frames, and corrugated sheets, which can be assumed to be PVC. These results suggest that chemical recycling with chlorine concentration restrictions should start with packaging and curing, which are non-chlorinated items.

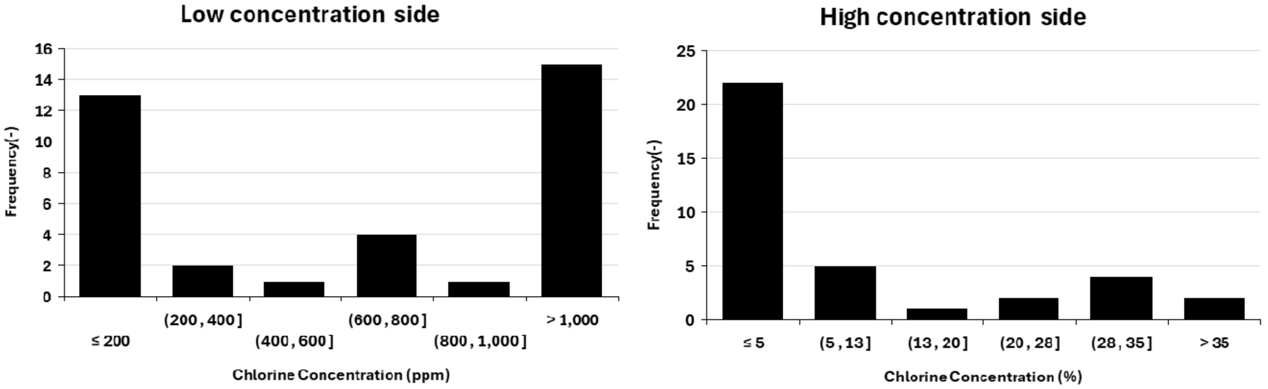

Fig.1. Histograms of chlorine concentrations

Figure 2 shows a histogram of bromine concentration. Most of the 28 samples did not contain bromine, with 28 samples containing less than 200 ppm, and if they did contain bromine, it was in trace amounts. This bromine is considered to be derived from additives.

This experiment made it possible to accurately detect chlorine concentrations on the low side, which is important in plastic recycling, and to classify items that are unsuitable for recycling.

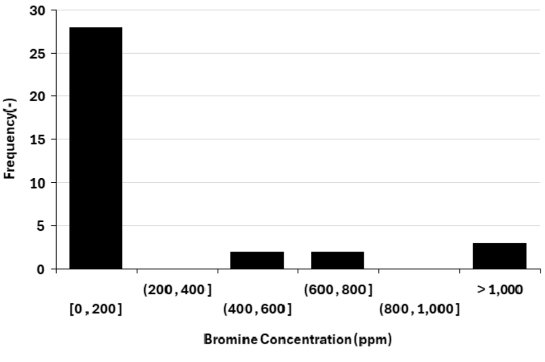

Fig.2. Histograms of bromine concentraitions

CO10-3

Prompt γ-ray Analysis for Chlorine Content in Power Cable Sheath used in a large-scale accelerator facility

G. Yoshida, T. Kimura[1], E. Lee, K. Tsugane, S. Kurita[2], M. Nakada[2], R. Shiobara[3], K. Oishi[3] and H. Yashima[4]

Radiation Science Center, KEK
[1] School of Science and Engineering, University of Tsukuba
[2] Department of Engineering and Technical Service, NIFS
[3] Japan Environment Research Co., Ltd.
[4] Institute for Integrated Radiation and Nuclear Science, Kyoto University

INTRODUCTION: In the previous year, neutron activation analysis (NAA) was conducted to determine chlorine content in power cable jackets used in the KEK 12 GeV proton synchrotron facility. Accurate quantification is essential for evaluating long-lived nuclide production, such as ^{36}Cl, which poses environmental concerns. However, the actual chlorine content in cable materials is often unknown. This year, prompt γ-ray analysis (PGA) was applied to quantify chlorine in the same samples. PGA allows real-time measurement during neutron irradiation and enables rapid assessment. This study compares PGA with NAA in determining chlorine content and assesses its utility for waste characterization.

EXPERIMENTS: The power cable jacket of the septum magnet of KEK-PS was collected, cut into 1-5 mm pieces, washed with water and ethanol, and weighed 100 mg to prepare irradiation samples. The chlorine-containing plastic standards (JSM_P713-1 series) distributed by the JFE Techno-Research Co. were employed as references and prepared in the same way. Samples were irradiated at the horizontal beam port E-3 at a thermal power of 1 MW. The average flux was on the order of 10^4 n/cm^2/s. Prompt γ-rays emitted during irradiation were measured in real-time using a Ge detector (ORTEC) for 5 to 10 minutes.

RESULTS: The γ-ray spectra of the representative sample and standard are shown in Fig. 1. The γ-ray spectra revealed distinguishable peaks at 786 keV and 788 keV for chlorine. A calibration curve based on plastic standards and NaCl showed excellent linearity. Estimated Cl contents in cable insulation were 2–4% higher than those by NAA. Interference by aluminum (e.g., alumina additives) or cobalt may have influenced results. The small sample mass (<0.1 g) relative to the ~1 cm beam diameter may also contribute to uncertainty.

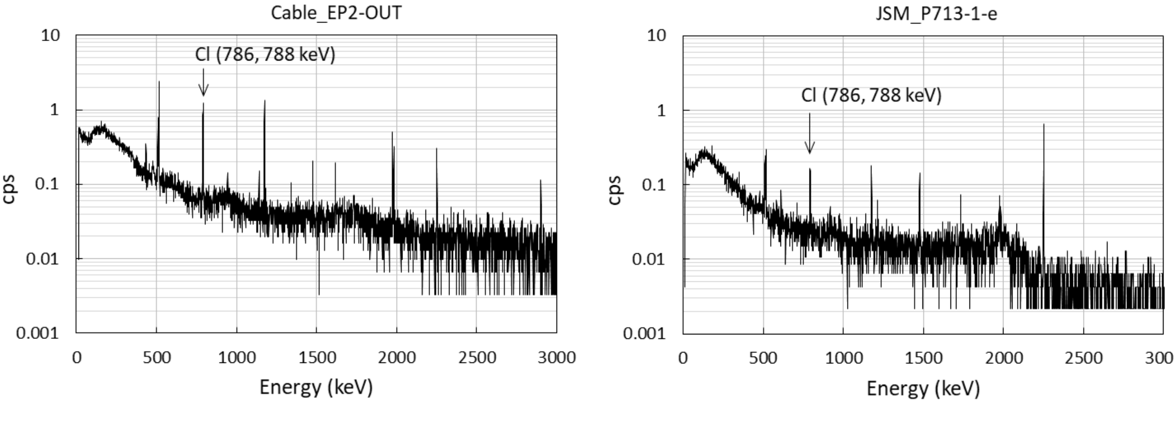

Fig. 1. Prompt γ-ray spectra of representative cable sheath sample (right) and standard (left)

CO10-4

Measurement of Number-Based and Radioactivity-Based Size Distributions of Aerosol Particles Generated in the Accelerator Room of an Electron LINAC Facility Using Screen-Type Diffusion Battery (II)

Y. Oki

Institute for Integrated Radiation and Nuclear Science, Kyoto University

INTRODUCTION: Accelerator safety has become increasingly important in recent years with the advanced use of high-energy and high-intensity accelerators. During accelerator operation, the accelerator room is filled with radioactive gas and radioactive aerosols. Particle size information of the aerosol particles is essential for estimating internal doses and designing exhaust systems in accelerator facilities. This report describes the measurement of the aerosol particle size using a diffusion battery at the electron linac facility, which has been performed for the past several years.

EXPERIMENTS: When fine aerosol particles of about 100 nm or less pass through a stack of wire screens, some of the particles are deposited on the wire surface of the screen by diffusion, depending on the particle size. The percentage of particles that can pass through the screen (penetration ratio) is expressed as a function of particle size, roughness and number of screens, and particle flow rate. By measuring the penetration ratio by varying the number of screens or flow rate, the particle size can be calculated from the theoretical equation.

Radioactive aerosol particles were produced by air irradiation using an irradiation chamber at the electron linac of our institute. The irradiated air containing the aerosol was introduced to a screen-type diffusion battery (SDB) consisting of stacked multiple wire screens and a backup PTFE filter. Simultaneously with the aerosol measurements, the radioactivity of the radioactive gas in the chamber was also measured using an ionization chamber. The SDB measurements were made both by changing the flow rate (Method 1) and the number of screens (Method 2). In Method 1, during irradiated air sampling, the air velocity in the irradiation chamber was always corrected to be constant, as described in the previous report [1]. In Method 2, a method of calculating the penetration ratios by measuring the radioactivity of multiple screens and the backup filter simultaneously using a large format IP was employed [2], instead of the conventional method of repeating the measurement by changing the number of screens,

RESULTS: Since a stable lognormal-type particle size distribution was observed in the SMPS (scanning mobility particle sizer) measurement performed during irradiation, the geometric mean and geometric standard deviation of the particle diameter were calculated, assuming a lognormal particle size distribution, by fitting the penetration ratios obtained by each of the two methods to the theoretical equation [1]. Number-based particle diameter tended to increase with increasing beam current (20-100 μA) in the SDB measurements, ranging from 20 to 60 nm. The size distributions obtained with Methods 1 and 2 were in good agreement, and the results were also in very good agreement with the SMPS measurements. In the radioactivity-based size measurement for ^{13}N-bearing aerosol particles, even a small percentage of radioactive gas deposited on the SDB screen or backup filter would be expected to cause errors in the particle size because the results of the radioactive gas measurements showed that a high percentage of ^{13}N formed in the chamber was present in gaseous form.

REFERENCES:

[1] Y. Oki *et al.,* KURNS Progress Report 2023, CO10-6, 254.
[2] Y. Oki *et al.,* J. Radiat. Prot. Res., **41** (2016) 216-221.

R6135

CO12-1

Effective Measures on Safety, Security, Hygiene and Disaster Prevention in Laboratories

T. Iimoto[1], Y. Cai[1], Q. Jin[1], C. Guh[1], X. Wang[1], T. Kose[1], Y. Taniguchi[1], K. Takamiya[2]

[1]*The University of Tokyo*
[2]*Integrated Radiation and Nuclear Science, Kyoto University*

INTRODUCTION: Important aspects of the study can be found in the following keywords, such as safety, security, hygiene and disaster prevention. Nuclear research reactors are one of the representative facilities together with these keywords under their operation. It is effective to investigate the latest status on practical measures on these keywords in various facilities including nuclear research reactors, to compare each other among facilities, and to discuss more optimized ones for our positive safety management. Through this process, it is also essential to investigate the latest international and/or national regulations and the movement of revision of them. In addition, the development of human resources and public literacy on nuclear science and technology is also within the scope of the research. The total discussion contents and their fruits are directly useful for all relating laboratories.

RESEARCH APPROACH: General research approach is as follows.
- Measures of safety management during operation or standstill status of the real facilities would be investigated. This information would be used for our research discussion on positive and more optimized safety management. - It would not be a single year research, but maybe two to three years of research for one theme. - Information source of facilities would not be only KUR, KUCA or the other facilities in Kyoto University, but also the Kindai university research nuclear reactor or the facility of National Institute of Fusion Science, etc. This research is active joint-research with these related facilities and positive researchers on safety management. - One of the distinctive features of this research is to involve office staff as cooperators as well as re-searchers and technical staff. In The University of Tokyo, most of the members in Division for Environment, Health and Safety are office staff who know the real situation of safety management in laboratories very well.

Concrete discussion targets in FY of 2024 were determined as (1) ‘developing a set of educational videos for radiation protection in English for International Nuclear Science and Technology Academy (INSTA)’ and (2) ‘Investigation of the latest trends in Japan and overseas regarding the optimized management of X-rays’. These were the representative hottest topics in the field of radiation protection and safety.

RESULTS: <CONCEPT AND CONTENTS OF RP-EDU-VIDEO> To support the INSTA activity, the research team developed three English videos entitled as ‘General Risk Management’, ‘Medical Risk Management’, and ‘Chemical Risk Management’, which were planned to be applied in INSTA Phase-1 education. The length of each video was around 30- 45 min. <OPTIMIZED X-RAY MANAGEMENT> The latest activity and movement of Japan Health Physic Society “X-ray Exposure Accident Study WG” and Ministry of Health, Labor and Welfare ”Study Group on Measures to Prevent Radiation Damage from X-ray Equipment” were surveyed and discussed among the research team members.

REFERENCES:
[1] https://www.jstage.jst.go.jp/article/jhps/58/3/58_141/_article/-char/ja
[2] https://www.mhlw.go.jp/stf/newpage_37794.html

R6009

CO12-2

Development of Compensation Method for Faster Measurement with Vanadium Emitter SPND

M. Sasano, R. Tanaka[1], T. Azuma, M. Hayashi, Y. Yoshino[2] and C. H. Pyeon[2]

Advanced technology R&D center, Mitsubishi Electric corporation
[1] Energy systems center, Mitsubishi Electric corporation
[2] Institute for Integrated Radiation and Nuclear Science, Kyoto University

INTRODUCTION: For safety monitoring and control of nuclear reactors, in conventional pressurized water reactors, reactor signals are mainly measured from outside the reactor. For safer reactor control, constant monitoring inside the reactor is required in the future, and measurement inside the reactor is important for more safety opera-tion. For this purpose, the self-powered neutron detector (SPND) is one of the most suitable detectors. SPND is the detector that can obtain the signal from beta-decay associated with activation as a current, and output a current ~10 nA at 10^{12} 1/cm^2/s. SPND is suitable for measurement in high-intensity neutron environment; however, the delay in detector response due to the half-life of beta-decay is of interest in the technical issue. Previously, we examined with the rhodium (Rh) emitter SPND and succeed to compensate the time delay. In this study, we eval-uated techniques to compensate for the larger delay with the vanadium (V) emitter SPDN detector response. **EXPERIMENTS:** Measurement was conducted on 2024/10/31. We started evaluation during the 1 MW power operation. The reactor power changed from 1 MW to 5 MW during the measurement. For the measurement, we obtained current output of the V emitter SPND with an originally developed measurement unit. The period of measurement is 1 second and enough faster than the time of the reactor power increase. From these obtained data, we evaluated the compensated detector response. **RESULTS:** The results of plotting the V emitter SPND output, when the reactor was ramped up to 5 MW from 1 MW, showed that the detector output is raised with a delay of 3.74 min half-life of ^{51}V, which is the time response of the SPND (Fig. 1). The raw output current rose five time as high as that in 1 MW. From ramp up start to maxi-mum reactor power of 5 MW, it took about 20 min (5 half-life). To correct for this time response, we made the attempt to time profile deconvolution with the physical decay model. The computation of deconvolution was based on the following ^{52}V beta-decay, and the correction can be made by deriving f in Eq. (1):

$$\frac{dN}{dt} = -\lambda N + \sigma N^0 f \qquad (1)$$

,

where N and N^0 represent the numbers of ^{52}V and ^{51}V, respectively, σ the neutron capture cross-section of ^{51}V, and f the neutron flux from the reactor. Figure 2 shows the time variation of the raw detector output, the compensated one, and reactor power output. The increase rate in reactor power is 0.015 MW/s. The raw SPND output delayed from the increase. On the other hand, the compensated SPND output completely followed the reactor output. After reaching 5 MW, measurement result was consistent with the small deviation of the reactor power. In the previous study of the Rh emitter SPND, the compensated output slightly delayed from the increase of the reactor power. However, the compensated output completely followed the reactor output in V emitter SPND. This is because that the beta-decay scheme of V is simpler than that of Rh. For simple beta-decay scheme, the uncertainty of the time profile deconvolution is small and correctly calculated.

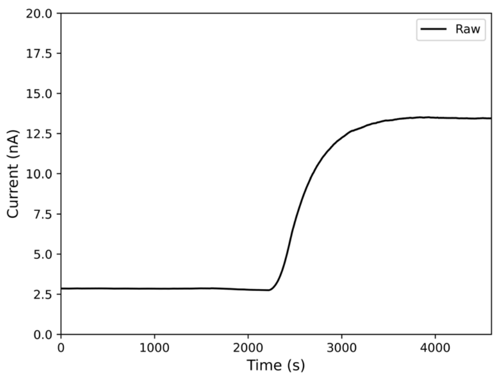

Fig. 1 The plot of normalized V emitter SPND measured current via time.

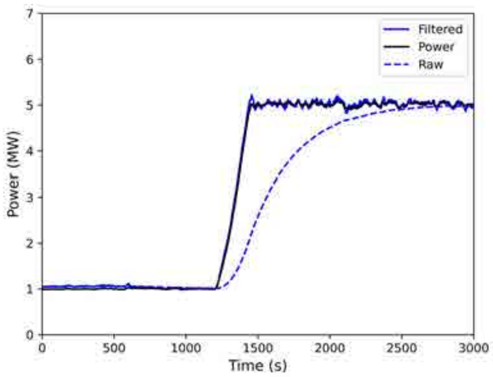

Fig. 2 The plot of V emitter SPND output and reactor power via time.

CO12-3

Measurement of U in commercially available standard solution by EDTA titration method

T. Miura[1], K. Takamiya[2], S. Fukutani[2], H. Yoshinaga[2] and Y. Iinuma[2]

[1]*National Metrology Institute of Japan, Advanced Industrial Science and Technology*
[2]*Institute for Integrated Radiation and Nuclear Science, Kyoto University*

INTRODUCTION: National Metrology Institute of Japan (NMIJ) is responsible for the development of certified reference materials and the establishment of traceability of SI (The International System of Units) to chemical metrology in Japan. To establish SI traceability, the primary method of measurements should be used to characterize the certified reference material1). Uranyl ion is difficult to titrate with EDTA (ethylenediamine-N, N, N', N'-tetraacetic acid) due to its small complexation constant with EDTA. On the other hand, the logarithm of the stability constant between U(IV) and EDTA (Log $K_{U(IV)Y}$) is about 25, which allows titration at low pH (pH 1 to 3) where there is little interference from co-existing metal ions. Approximately 2 mg of U was accurately determined by EDTA titration method with repeatability of less than 0.2 % in the previous study at KURNS3). In this study, the EDTA chelatometric titration method was used to measure U in a commercially available multi-element standard solution.

REAGENT and INSTRUMENTS: Dojindo Laboratories EDTA and Xylenol orange (XO) were purchased from FUJIFILM Wako pure chemicals Corporation. NMIJ CRM Bi standard solution was used for back titration. Other chemical reagents (nitric acid, acetic acid, ammonium acetate, ascorbic acid, etc.,) were analytical grade or JIS special grade. AT-510 automatic titrator (Kyoto Electronics Manufacturing Co. Ltd) was used for titration of U. HORIBA LAQUA F-72 pH meter was used for pH measurement. SPEX XSTC-4507-100 (Lot. No. 7-159-EL) muti-elemental standard solution (Ba, Be, Ca, Cs, K, U, Mg, Na, Rb, Sr, and U; 10 µg/mL) was used for sample solution.

TITRATION METOD: 50 g of sample solution in 50 mL beaker was evaporated to dryness using hot plate. After cooling, the residue was dissolved by 5 mL of 1 % HNO_3. The pH of sample solution adjusted from 3 to 4 by ammonia acetate solution. Excess amounts of 0.002 mol/kg EDTA solution and 100 mg of ascorbic acid were added to the sample solution. The sample solution was then heated and boiled on a hot plate for approximately 10 minutes to form the U(IV)-EDTA complex. After the sample solution was cooled to room temperature, acetic acid was added to the sample solution to adjust the pH from 2 to 3. Finally, 0.005 % XO solution was added to the sample solution and back titrated with 0.002 mol/kg Bi standard solution

RESULTS: U in the SPEX XSTC-457-100 was measured by EDTA titration method. The relative standard deviation of analytical results of U showed sufficient repeatability (0.63 % at sample number of 8). However, a positive bias of about 30 µg was observed in the measured values of U in each sample solution. The cause of this positive bias requires to be elucidated before applying the method to real sample.

REFERENCES:

[1] J. Vogl *et al.,* Metrologia, **55** (2018)211-221.
[2] T. Miura and A. Wada, Front. Chem., **10** (2022) 88863.
[3] T. Miura and K. Takamiya, KURNS progress report 2020 (2021) CO12-4.

R6045

CO12-4

A New Technique of the Micro bunch Interval Measurement in an Electron Linear Accelerator (II

T. Takahashi

Institute for Integrated Radiation and Nuclear Science, Kyoto University

INTRODUCTION: The coherent radiation from short bunches of electrons in an accelerator is useful of analysis of the specification of bunches. For example, it has been used in the high-resolution diagnosis of electron distribution in a bunch [1]. There are two kinds of detector in the millimeter wave region. One is a diode detector with narrow band and high-speed response. The other is a liquid-helium cooled bolometer with wide band and slow response. A bolometer is usually used with a spectrometer, for example a monochromator or an interferometer. In the experiment of FY2024 the frequency-domain measurement with a liquid-helium cooled silicon bolometer was used for the analysis of the micro bunch interval.

EXPERIMENTS: The experiment was performed with KURNS-LINAC. The energy of the electron beam was 39 MeV and the peak beam current measured by CT was 1.9 A. The repetition rate of the macro pulse was 60 pulses/s. Coherent transition radiation (CTR) from a titanium window was guided to the Fourier transform interferometer in the experimental room through the coherent radiation beam line [2]. This interferometer has maximum optical path difference (OPD) of 480 mm. The CTR was detected by the silicon bolometer.

RESULTS: The observed autocorrelation interferogram of CTR emitted from a micro bunch is shown in Fig. 1. The OPD where the intensity is minimum is 0 mm. The observed cross-correlation interferogram of CTR emitted from bunches next to each other is shown in Fig. 2. The OPD where the intensity is minimum is 230.48 mm. The theoretical interval between bunches is 230.47mm because the frequency of microwave of this linac is 1300.79 MHz. Therefore, using this method, measurements of the interval can be taken with an accuracy of 10 microns.

REFERENCES:

[1] Y. Shibata *et al.,* Phys. Rev. E, **50** (1994) 1479-1484.
[2] T. Takahashi *et al.,* Rev. Sci. Instrum., **69** (1998) 3770.

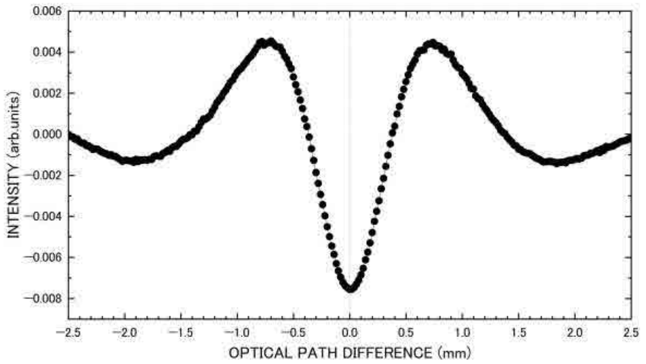

Fig. 1. observed autocorrelation interferogram of CTR emitted from a micro bunch.

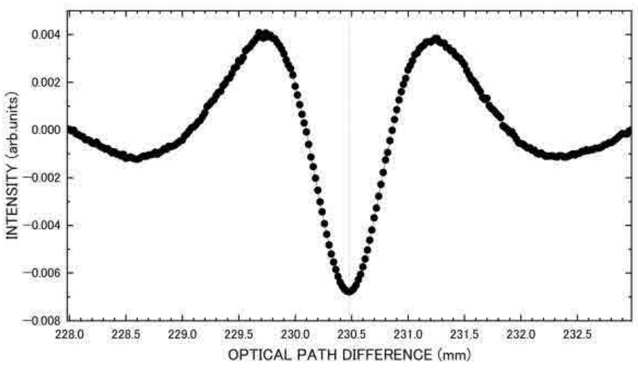

Fig. 2. The observed cross-correlation interferogram of CTR emitted from bunches next to each other.

CO12-5

A texture analysis of the excavated *Haji*-ware of different colour by INAA

M. Tomii, K. Takamiya[1], M. Inagaki[1], Y. Chiba[2], A. Ito[2], M. Kidachi[3], and H. Yoshii[2]

Faculty of Literature, Taisho University
[1] *Institute for Integrated Radiation and Nuclear Science, Kyoto University*
[2] *Graduate School of Letters, Kyoto University*
[3] *College of Letters, Ritsumeikan University*

INTRODUCTION: To investigate the reason for the difference of the medieval low-temperature-fired pottery (Haji-ware) in colour –white/red–, a collection of Haji-ware of 14th century archaeo-logically excavated in the campus of Kyoto University [1] is analysed. The two major types, white larger bowl and reddish medium-sized plate, are done from the single deposition unit. As for the colour difference, some scholars assume that white ones resulted from the water-sieving of clay to decrease iron oxide while others point out that they could result from the reducing condition of firing. Last year, we analysed the different collection of the Haji-ware of the same age and suggested that the colour difference might be due to the difference in clay texture in the light of Na/La concentrations combination, but we did not check the ratio of long-lived nuclides including Fe. This year we there-fore try to check both short-lived and long-lived ones in detail.

EXPERIMENTS: Conventional INAA was applied to determine the elemental composition of samples of the Haji-ware, each of whose main body had been drilled, or scraped, by the alumina drill into fine powder as a sample after removing off the very surface and then had been enclosed in a polyethylene bag [2]. Every of above-mentioned two types of the Haji-ware has seven samples re-spectively from different pieces. Each of the fourteen samples was neutron-irradiated at Pn-3 (1 MW for 90 seconds) for short-lived nuclides, and at Pn-2 (5 MW for 1 hour) for long-lived ones. The gamma-ray spectrometry of the irradiated samples was performed after the irradiation, and the k0-standardization method for determination of concentration of elements was performed. For the k0 method, three standard elements, Au, Lu and Zr, were prepared as a comparator.

RESULTS: Concentrations of twenty elements in almost every fourteen sample were determined with irradiation by Pn-3 and Pn-2: Co, Cr, Cs, Eu, Fe, Ga, Hf, K, La, Mg, Mn, Na, Rb, Sc, Sm, Ta, Tb, Th, Ti, and V. While Na/La concen-trations combination does not necessarily coincide with the colour difference, Fe shows the marked difference along with the colour difference (Figs.1 and 2). These results indicate that the La-rich clay group might usually undergo the process of decreasing Fe_2O_3 to produce white-coloured ware while a little portion in the group occasionally escape the process such as KC11-1199, 1227, and 1228, leading to the reddish ware.

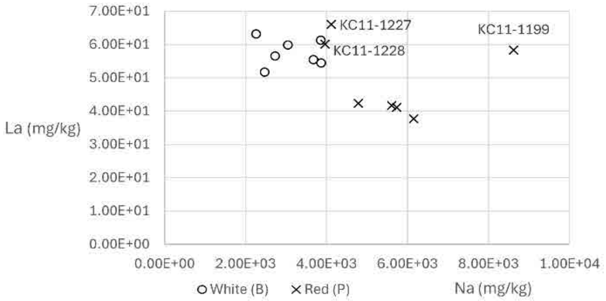

Fig. 1 Distribution of fourteen samples on the concentrations combination of Na with La.

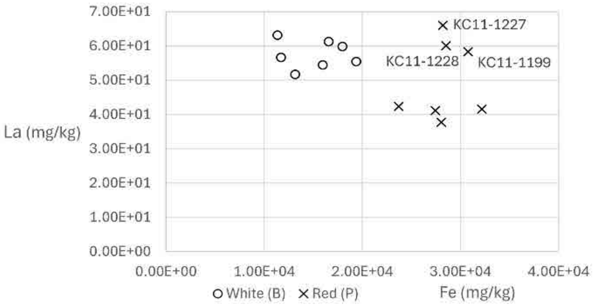

Fig. 2 Distribution of fourteen samples on the concentrations combination of Na with Fe.

REFERENCES:

[1] M. Tomii *et al., Annu. Rept. of Archaeological Researches in KU sites for 2013*. (2015) 5-122.
[2] J. Sterba, *J. Radio. Nucl. Chem.,* **316** (2018) 753-759.

CO12-6

Elucidation of the structural dynamics of E6AP ubiquitin ligase

H. Konno[1], M. Shimizu[2], K. Morishima[2], R. Inoue[2], M. Sugiyama[2]

Graduate School of Science, Kyoto University
[1]Nano Life Science institute, Kanazawa University
[2]Institute for Integrated Radiation and Nuclear Science, Kyoto University

INTRODUCTION: It is known that E6AP (E6-associated protein), a kind of ubiquitin ligase, interacts with E6 protein derived from oncogenic human papilloma virus (HPV 16/18) and the enzyme complex induces ubiquitination of p53 resulting p53 degradation by ubiquitin-proteasome system. To understand the mechanism of p53 ubiquitination by E6AP and E6, we use HS-AFM to observe the structural dynamics of the E6AP/E6 complex. In addition to HS-AFM observation, we analyze the structural dynamics of the E6AP/E6/p53 complex using small-angle X-ray scattering (SAXS) methods.

****

EXPERIMENTS : HS-AFM observation of E6AP, E6AP/E6 and E6AP/E6/p53. HS-AFM imaging of the full-length E6AP, E6AP/E6 complex and E6AP/E6/p53 complex in solution were performed using a laboratory-built HS-AFM setup [1, 2]. SAXS and ultracentrifugation analysis of E6AP. The SAXS was performed using NANOPIX (Rigaku). Changing sample solution, the scattering profiles were measured four times with sample-detector distance of 1330 mm, and data from the first 15 minutes of each measurement were used for analysis. Similarly, the scattering profiles were also measured five times with sample-detector distance of 300 mm, and data from the first 60 minutes of each measurement were used for analysis.

****

RESULTS :HS-AFM observation of E6AP, E6AP/E6 and E6AP/E6/p53. By using of HS-AFM, We found that the importance of the N-terminal region with respect to the p53 binding to E6AP/E6. SAXS and ultracentrifugation analysis of E6AP. The scattering intensity appears to be concentrated in the larger scattering vector (Q) region (Fig. 1). This is due to the effect of aggregation of the HECT domain due to multimerization, and we found that the results may be slightly different from the original structural information. We also performed analytical ultracentrifugation (Fig. 2), and the sample contained not only E6AP alone, but also a degradation product from the protein purification process and a multimerized protein.

****

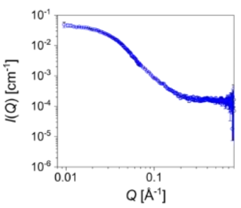

Fig. 1. X-ray scattering profile of full length E6AP.

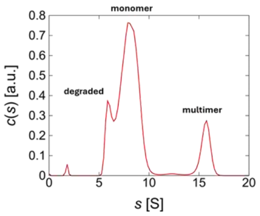

Fig. 2. Analytical ultracentrifugation of full length E6AP

REFERENCES:

[1] T. Uchihashi *et al.,* Nat. Protoc., **7** (2012) 1193-1206.
[2] T. Ando *et al.,* Chem. Rev., **114** (2014) 3120-3188.

CO12-7

Development of an Analog Encoder Module

H. Ohshita[1], H. Endo[1], T. Seya[1], S. Matoba[1] and M. Hino[2]

[1]*Institute of Materials Structure Science, KEK*
[2]*Institute for Integrated Radiation and Nuclear Science, Kyoto University*

INTRODUCTION: The analog encoder (AE) was developed as a readout module for use in pulsed neutron experiments. The AE can measure the TOF and pulse height of the input analog signal. The pulse height can be used to derive the detection position in addition to conducting nγ discrimination. Figure 1 shows the AE, which has four analog inputs and a T0 input for resetting the TOF. The dynamic range of the analog input is 0 to -2 V, and the T0 input is designed for transistor-transistor logic (TTL)- or Nuclear Instrumentation Module (NIM)-level inputs. The signal level of the T0 input can be changed by the internal jumper switch. Both analog and T0 inputs are terminated at 50 Ω. In addition, there are four digital inputs (switchable between TTL and NIM levels). The AE operates at an internal clock speed of 200 MHz, giving it a time accuracy of 5 ns. The data encoded in the AE are transferred to a computer over a 1-Gbps network. Transmission Control Protocol (TCP) communication is used for data transfer between the AE and a computer, whereas User Datagram Protocol (UDP) communication is used for control, such as parameter setting. The analog and digital inputs implemented in the AE operate independently. Therefore, it is necessary to cluster multiple channels in an offline analysis to derive the detection position. When the detection position is derived based on the ratio of the pulse height values of the analog signals output from the four corners of the readout board, the shapes of these signals should be similar, and the data generated by the AE contain parameters for finding such signals. Data encoded from the analog inputs include information on the TOF, maximum pulse height, pulse width, and rise time. Data encoded from digital inputs provide information on TOF and pulse width. Clustering between different channels is performed by setting a time window in offline analysis and collecting events with similar TOFs.

EXPERIMENTS: A neutron irradiation test using a prototype AE was conducted in February 2025 at the KUR CN-3. A scintillation detector was installed downstream of the CN-3 disk chopper. The detector consisted of 0.8-mm-thick enriched lithium glass (Scintacor Ltd., GS-20) and a multi-anode photomultiplier tube (HAMAMATSU PHOTONICS K. K., H12700A-03). The active area of the scintillation detector was 48.5×48.5 mm, and analog signals were output from the four corners of the readout board (HAMAMATSU PHOTONICS K. K., E14340) using a resistance chain. A collimator made of boron carbide was installed in front of the scintillation detector. The aperture of the collimator was 1×1 cm. In the neutron irradiation test, the flight time was measured according to the timing of the disk chopper opening. Figure 2 shows the TOF distribution and two-dimensional hit map obtained from the test. The peak of the TOF distribution corresponds to thermal neutrons of 2 Å. In addition, the two-dimensional hit map represents the beam profile blocked by the collimator. The detection positions were calculated in offline analysis. Future plans include evaluating the validity of the measurement data and improving the AE.

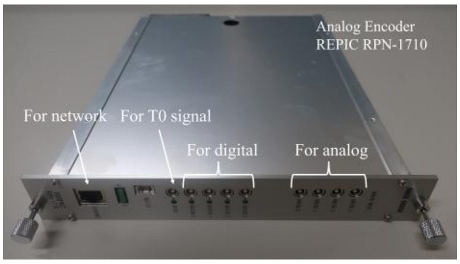

Fig. 1. Picture of the AE.

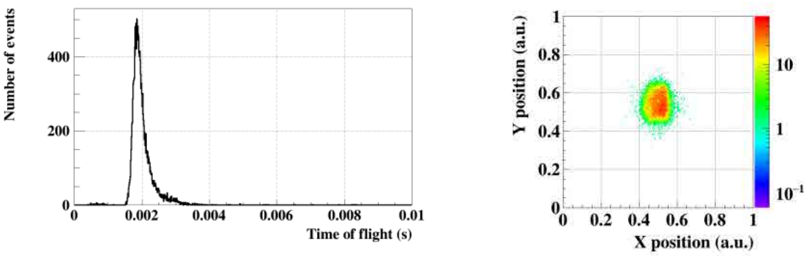

Fig. 2. Test results: TOF distribution (left) and 2D-hit map (right).

CO12-8

Application of KURAMA-II to the analysis of air dose rate distribution around monitoring posts

M. Hosoda[1], M Watanabe[1], H Tanaka[1], M. Tanigaki[2]

[1]*Japan Chemical Analysis Center*
[2]*Institute for Integrated Radiation and Nuclear Science, Kyoto University*

INTRODUCTION: In the nationwide survey of environmental radioactivity levels commissioned by the Nuclear Regulation Authority, air dose rates are measured using portable monitoring posts at about 80 locations in Fukushima Prefecture. Air dose rates obtained by monitoring posts are representative values for each location, and we do not see the detailed distribution of the air dose rate due to the uneven distribution of the artificial radionuclides around the monitoring posts.

In this study, we measured air dose rates around the portable monitoring posts located in a difficult-to-return zone in Fukushima Prefecture by a car-borne survey system KURAMA (Kyoto University Radiation MApping system)-Ⅱ as a walking survey. We analyzed the distribution of the air dose rate and the radioactive cesium using radiation mapping methods.

EXPERIMENTS: We walked with KURAMA-II around the monitoring post at the Kumamachi Elementary School in Okuma Town, Fukushima Prefecture. The data were grouped by a 1 m mesh centered on the monitoring post, and an areal evaluation was performed by displaying the data on a map. From the measured air dose rate data and the pulse-height spectrum data of each mesh, the air dose rate from the natural radioisotopes and that given by the artificial radioisotopes, i.e., Cs-134 and Cs-137, were evaluated respectively using Equation (1) defined in ref. [1],

$$\begin{cases}\dot{D}_n = 0.062x \\ D_a = \dot{D}_t - \dot{D}_n\end{cases} \quad (1)$$

where - $\dot{D}_t$ is the measured air dose rate (μSv/h), x is the counting rates from 1400 to 2000 keV obtained by spectrum data, $\dot{D}_n$ is the air dose rate given by natural radioisotopes, and D_a is that given by the artificial radioisotopes.

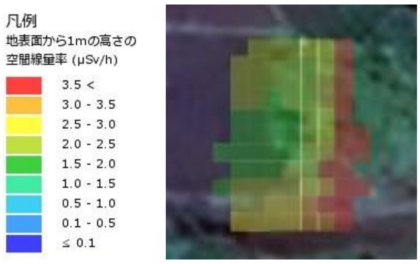

Figure 1. the 1 m × 1 m mesh map of the air dose rate(μSv/h) obtained by the present walking survey.

RESULTS: Figure 1 shows the 1 m × 1 m mesh map of the air dose rate obtained by the present walking survey. The average air dose rate measured by the monitoring post was 2.09 μGy/h, whereas the average air dose rates per 1 m × 1 m mesh obtained by the walking survey ranged from 1.32 to 4.11 μGy/h. The overall average value for all meshes was 2.10 μGy/h, which was similar to the average value from the monitoring posts. Figure 2 shows the map display of the air dose rate given by natural radioisotopes for each mesh calculated by Equation (1). From Figure 1 and 2, the differences in the air dose rates are not due to the uneven distribution of natural radioisotopes but the artificial radioisotopes.

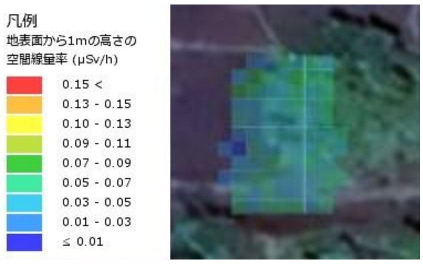

Figure 2. The map display of the air dose rate (μSv/h) given by natural radioisotopes for each mesh calculated by Equation (1).

REFERENCES:

[1] M Ando, N Matsuda and K Saito, "Determination of Parameters for an Equation to Obtain Natural Background Radiation Using KURAMA-II Loaded with C12137-01 CsI(Tl) Detector," *T. J. At. Energy Soc. Jpn.*, **20**[1], 34-39 (2021)

CO12-9

Relationship between Friction Reduction Effect and Solubility in Base Oil of Organic Friction Modifiers

T. Hirayama, H. Gu, N. Yamashita[1] and M. Hino[2]

Department of Mechanical Engineering and Science, Graduate School of Engineering, Kyoto University
[1]Department of Mechanical and System Engineering, Kyoto Institute of Technology
[2]Institute for Integrated Radiation and Nuclear Science, Kyoto University

INTRODUCTION: Lubricants are essential in minimizing frictional forces and reducing surface wear in industrial machinery. This study explored the relationship between the solubility of additives in base oils and their friction-reduction efficacy using cetyl alcohol as a model additive. Atomic force microscope (AFM) friction tests demonstrated that the friction reduction effect of cetyl alcohol varied significantly across the base oils. The solvation free energy was computed using molecular dynamics (MD) simulation to evaluate the solubility of cetyl alcohol in various base oils. A direct proportional relationship between friction reduction and solvation free energy was observed, indicating that additives with lower solubility have better friction-reduction performance. Neutron reflectometry experiments and further MD simulations revealed that lower solubility correlates with stronger adsorption of additives on the substrate. This study quantitatively clarified the relationship between solubility, adsorption, and friction reduction, providing insights into optimizing lubricant formulations for enhanced performance and contributing to a deeper understanding of the mechanisms behind boundary lubrication.

EXPERIMENTS: Cetyl alcohol (>98%, Sigma) was used as a model additive due to its friction-reduction and anti-wear effects in base oils. Seven common organic solvents were used as base oils: dodecane (C12), tetradecane (C14), hexadecane (C16), isocetane (IC), squalane (Sq), dodecylbenzene (DB) and dodecyl acetate (DA). Deuterated cetyl alcohol (CDN Isotopes Inc.) was used to achieve a good contrast of the scattering length density (SLD) with base oils for the NR measurements. Its concentration was set to 0.5 mass% to achieve a more pronounced contrast.

RESULTS: The adsorption behavior of cetyl alcohol molecules on Fe surfaces in various base oils was analyzed using NR. The reflectivity profiles in the left show the experimental data as triangles and the results fitted using GenX 3 software as solid black lines. For Sq, IC, and C16, a leftward shift in the reflectivity profiles was observed upon the introduction of cetyl alcohol, compared with the profiles of the base oil alone.Correlating with the friction experiments, these three solvents exhibited the greatest friction reduction upon the addition of cetyl alcohol. In contrast, for DB and DA, no appreciable shift in the reflectivity profiles was detected, suggesting the absence of an adsorption layer. The pattern of adsorption layer density values is consistent with that of friction reduction: higher adsorption layer densities correlate with more effective friction reduction. We attribute this to the relatively weak adsorption characteristics of alcohols and the challenge of detecting adsorption films at lower concentrations. These results indicate that the lower the solubility of the additive molecules in the base oil, the larger the friction reduction. As confirmed by the NR measurements, the lower the solubility, the denser the additive adsorption film formed, which leads to a reduction in the COF.

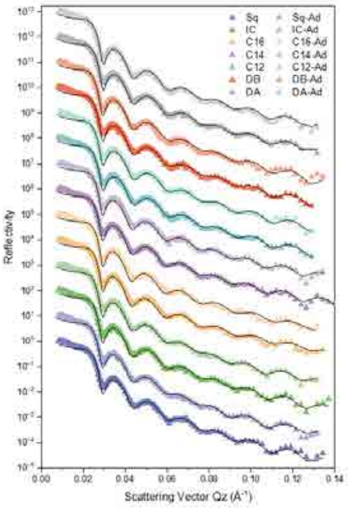

Fig. 1. Reflectivity profiles for all sets of lubricants.

CO12-10

Directional Evaluation of Internal Pores in Additively Manufactured Metal Using Neutron Phase Imaging

Y. Seki, Y. Terakawa[1]. M. Hino[2]

Institute of Multidisciplinary Research for Advanced Materials, Tohoku University
[1]*Graduate School of Engineering, Tohoku University*
[2]*Institute for Integrated Radiation and Nuclear Science, Kyoto University*

INTRODUCTION: Neutron scattering (dark-field) imaging [1, 2] using a Talbot-Lau interferometer can detect small-angle scattering intensity caused by microscopic structures within a sample. When employing an interferometer composed of one-dimensional gratings, the method is sensitive to scattering perpendicular to the grating lines. By rotating the sample with respect to the grating orientation, scattering in different directions can be observed, allowing for the assessment of anisotropy in the microstructure. In this study, we applied this method to an additively manufactured metal sample and investigated the characteristics of internal pores.

EXPERIMENTS: The sample was a 1 cc stainless steel cube fabricated using the laser powder bed fusion method, with laser power and scan speed intentionally set lower than standard process parameters. The sample was first imaged with its stacking direction (z-direction) aligned parallel to the grating lines of the interferometer, as shown in Fig. 1(a) and (b). In this configuration, scattering in the y-direction was detected. The sample was then rotated 90 degrees around the beam axis, and an additional image was acquired to observe scattering in the z-direction, as shown in Fig. 1(c).

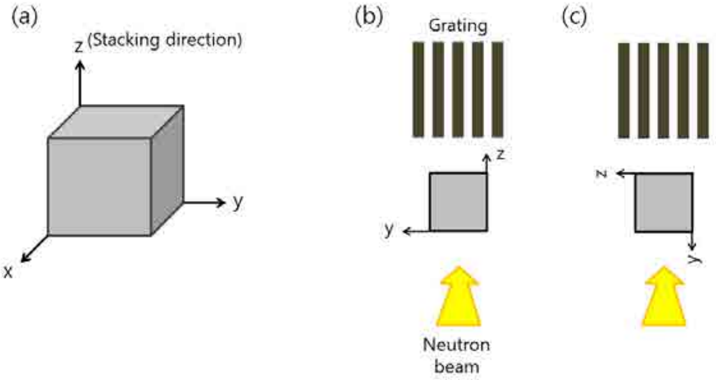

Fig. 1. (a) Coordinate system of the sample. (b) Measurement configuration for scattering in the y-direction. (c) Measurement configuration for scattering in the z-direction.

RESULTS: Figure 2(a) and (b) show the scattering images obtained in the configurations illustrated in Fig. 1(b) and 1(c), respectively. In these scattering images, darker regions correspond to stronger scattering. In Fig. 2(a) and Fig. 2(b), the average visibility reduction within the sample region was 0.40 and 0.30, respectively. These results suggest that the size of pores in the sample tend to be longer in the y-direction and shorter in the z-direction.

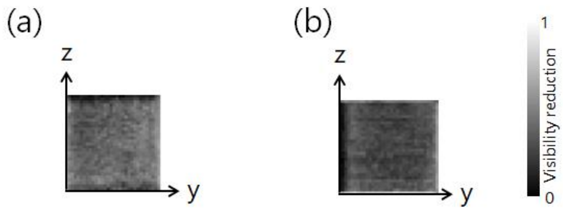

Fig. 2. Scattering images from (a) y-directional and (b) z-directional configurations.

REFERENCES:

[1] W. Yashiro *et al.*, Opt. Exp 18, 16890 (2010). [2] M.Strobl *et al.*, Sci. Rep. 4, 7243 (2014).

CO12-11

Evaluation of the Autocorrelation Length in Neutron Scattering Imaging at the CN-3 Port

Y. Seki, Y. Terakawa[1], T. Higuchi[2], M. Li[2], M. Hino[2]

Institute of Multidisciplinary Research for Advanced Materials, Tohoku University
[1]Graduate School of Engineering, Tohoku University
[2]Institute for Integrated Radiation and Nuclear Science, Kyoto University

INTRODUCTION: In neutron phase imaging using a grating interferometer, scattering imaging (dark-field imaging) [1, 2] can visualize the small-angle scattering intensity caused by microstructures in the sample as a reduction in the visibility of the interference pattern. This reduction is related to the autocorrelation function $\Phi(x)\Phi(x + \Delta x)$ of the phase shift of neutron waves generated in the sample. The parameter representing the spatial shift Δx in the autocorrelation function is called the autocorrelation length, which can be varied by changing the sample position within the interferometer. By performing measurements at various autocorrelation lengths, the characteristics of the microstructures can be quantitatively evaluated. In the current setup of our Talbot-Lau interferometer [3] at the CN-3 port of KUR, the sample is usually placed between the middle phase grating (G1) and the most downstream analyzer grating (G2), which are spaced 140 mm apart. However, depending on the sample size, it is more convenient to place the sample upstream of G1. Therefore, we conducted evaluations of the autocorrelation length with the sample positioned upstream of G1, using a reference sample whose reduction rate as a function of autocorrelation length has been well characterized between G1 and G2.

EXPERIMENTS: The reference sample was a 1 cc cube of aluminum alloy (Al–10%Si–0.4%Mg), additively manufactured using the laser powder bed fusion method with standard process parameters. Micropores with diameters on the order of micrometers induced small-angle neutron scattering. Measurements were performed at six positions located 10 mm, 110 mm, 210 mm, 505 mm, 605 mm, and 705 mm upstream from G1. The exposure time at each position was 640 s, with the reactor thermal power of 5 MW.

RESULTS: Figure 1 shows a plot of the observed visibility reduction rate, averaged over the sample region. The autocorrelation lengths corresponding to each sample position were calculated based on Ref. [2]. The solid line in the figure represents a model curve derived from the reduction rate measured between G1 and G2. Although the maximum autocorrelation length in the G1–G2 configuration is currently 3.4 μm, the curve is extrapolated beyond this range. The model curve and the measured values show good agreement. Furthermore, an autocorrelation length of approximately 4.0 μm was achievable just upstream of G1.

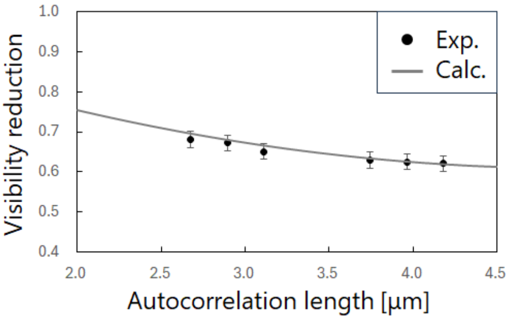

Fig. 1. Comparison of visibility reduction measured upstream of G1 and between G1 and G2.

REFERENCES:

[1] W. Yashiro *et al.*, Opt. Exp 18, 16890 (2010).
[2] M.Strobl *et al.*, Sci. Rep. 4, 7243 (2014).
[3] Y. Seki *et al.*, Rev. Sci. Instrum., 94, 103701 (2023).

CO12-12

Observation of Internal Pore Distribution in Additively Manufactured Metal

Y. Seki, Y. Terakawa[1]. T. Higuchi[2], M. Li[2], M. Hino[2]

Institute of Multidisciplinary Research for Advanced Materials, Tohoku University
[1]Graduate School of Engineering, Tohoku University
[2]Institute for Integrated Radiation and Nuclear Science, Kyoto University

INTRODUCTION: Metal additive manufacturing is a highly promising technique owing to its ability to produce complex geometries with reduced weight and advanced functionality. However, due to the layer-by-layer melting and solidification process, it tends to generate microscopic pores within the material during the fabrication. The porosity of the fabricated material is typically inves-tigated through destructive testing, such as cross-sectional observation using optical microscopy. Currently, it is difficult to non-destructively assess the porosity distribution throughout the overall structure. We are developing a non-destructive technique using neutron phase imaging [1] at the CN-3 port of KUR to visualize the porosity distribution inside additively manufactured metal structures. By observing the small-angle neutron scattering effects caused by micropores using a grating interferometer, we can gain insights into the interior of relatively thick structures. This ap-proach also allows us to observe a wide area over several tens of square centimeters. In this study, we attempted to estimate the distribution of internal pores using a simple method based on imaging from three different directions.

EXPERIMENTS: The observed sample was a 1 cc stainless steel cube fabricated using the laser powder bed fusion method. Since it was produced with a laser power intentionally set above standard process parameters, numerous micropores were expected to be formed within the structure. As shown in Fig. 1(a), the sample was irradiated with neutron beams along the x-, y-, and z-axes, and scattering images were obtained for each direction.

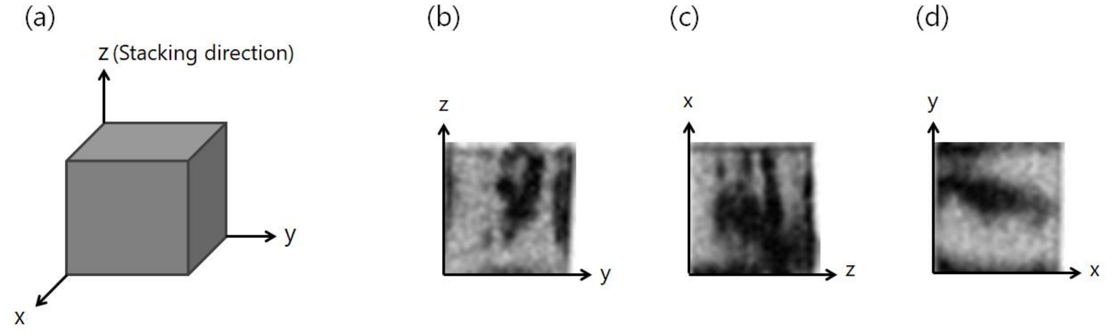

Fig. 1. (a) Coordinate system of the sample. (b) Scattering image observed from x-direction. (c) From y-direction. (d) From z-direction.

RESULTS: Figure 1(b), (c), and (d) shows resultant images observed from three directions. The darker regions in the images correspond to areas with a higher concentration of pores. A simple back-projection of these three images was used to estimate the internal pore distribution, as shown in Figure 2. The figure illustrates an example of the pore distribution on an oblique cross-sectional plane.

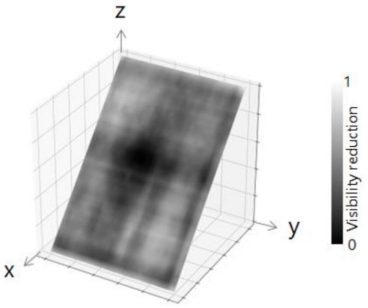

Fig. 2. Estimated internal pore distribution based on three scattering images.

REFERENCES:
[1] Y. Seki *et al*., Rev. Sci. Instrum., 94, 103701 (2023).

CO12-13

Study of Isotope Separation via Chemical Exchange Reaction

R. Hazama, P. Kumsut, T. Yoshimoto, A. Rittirong[1], C. Pitakchaianan, K. Kosinarkaranun, Y. Sakuma[2], T. Fujii[3], T. Fukutani[4], Y. Shibahara[4], and T. Kishimoto[1]

Graduate School of Human Environment, Osaka Sangyo University
[1]Research Center for Nuclear Physics, Osaka University
[2]Laboratory for Zero-Carbon Energy, Institute of Science Tokyo
[3]Graduate School of Engineering, Osaka University
[4]Institute for Integrated Radiation and Nuclear Science, Kyoto University

INTRODUCTION: Chemical isotope separation for calcium and lithium has been studied by liquid-liquid extraction (LLE) with DC18C6 crown-ether [1]. This report describes LLE with 5ml of 30%(w/w) LiCl and 100ml of 0.07M B15C5 dissolved in chloroform.

EXPERIMENTS: Chemical Isotopic exchange occurs according to the following chemical exchange reaction: $^{6}Li^{+}_{(aq)} + ^{7}LiL^{+}_{(org)} \rightarrow ^{6}Li^{+}_{(aq)} + ^{7}LiL^{+}_{(org)}$ (1)
, where L represents macrocyclic polyether (B15-crown-5). Lithium chloride solution (30% LiCl (aq) was mixed in an Erlenmeyer flask with 0.07M B15C5 dissolved in chloroform by the volume ratio of 1/20 (aqueous/organic) by a magnetic stirrer, The extraction time was kept consistent at 1 min and the phase separation time in the separation funnel was 10 min. To retrieve the lithium in the organic phase, 10 ml pure water was mixed with the extraction time and phase separation time of 10 min.

RESULTS: As shown in Fig. 1, the separation factor (α) was obtained by multi-stage LLE (eight iteration) with and without 12 M hydrochloric acid (HCl) at room temperature (22±0.5°C). It is noted that our recent progress in the measurement of isotope ratio for calcium and lithium was carried out by utilizing the cool plasma technique and the result obtained by TIMS was generally consistent [4].

Ref.	Chemical species	Distribution Coefficient (D)	Single stage separation factor	Temperature (°C)	Initial concentration of B15C5
[2]	LiCl	6.0×10^{-2}	1.002±0.002	22±0.5	0.07 M
[3]	LiCl	1.62×10^{-5}	1.002±0.002	25	0.186 M
[3]	LiI	1.58×10^{-3}	1.026±0.002	25	0.186 M
[3]	LiSCN	5.40×10^{-3}	1.032±0.002	25	0.186 M

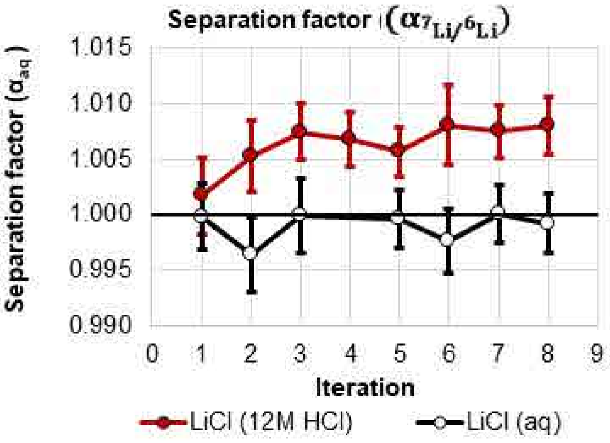

Fig. 1. Separation factor (α) of litium isotope in the aqueous phase with (filled) and without 12M HCl (open). [2].

REFERENCES:

[1] A. Rittirong, Doctor Thesis, OSU (2022).
[2] P. Kumsut, to be published in J. Phys:Conf Series (SPLG2023).
[3] K. Nishizawa *et al.,* J. Nucl. Sci. Tec., **21** (1984) 694: K. Nishizawa *et al.,* J. Nucl. Sci. Tec., **21** (1984) 133.
[4] A. Ishikawa and M.Nomura, in private communication.

CO12-14

Developing a new method for determining ionization chamber response ratio between air and P-10 gas for ^{41}Ar calibration applications

R. Furukawa[1], H. Yashima[2], Y. Soeta[3], R. Ichikawa[3], S. Otsuka[3], H. Murata[3], R. Nagata[4]
and T. Yamada[3,5]

[1]*National Metrology Institute of Japan, Advanced Industrial Science and Technology*
[2]*Institute for Integrated Radiation and Nuclear Science, Kyoto University*
[3]*Graduate School of Science and Engineering Research, Kindai University*
[4]*Fuculty of Science and Engineering, Kindai University*
[5]*Atomic Energy Research Institute, Kindai University*

INTRODUCTION: In order to calibrate gas monitors used in nuclear facilities for measuring radioactive noble gases, use of activity reference measurement standard gases with known activity are essential. Among these gases ^{41}Ar is a representative nuclide released from nuclear reactors. While a primary activity standard for ^{41}Ar is currently under development at the National Metrology Institute of Japan (NMIJ) [1], activity standard for ^{85}Kr have already been established based on measurement using a set of proportional counters of different length [2]. Commercially available gas monitors are typically designed to measure radioactive gas concentration in air, not in P-10 counting gas. Therefore, calibration should ideally be performed using air as the detection medium. However, proportional counters generally do not work well when air is used as the counting gas. In response to this limitation, we designed a calibration system using an inner-through type ionization chamber capable of operating both P-10 gas and air. This system serves as a transfer standard for calibrating gas monitors. To determine ^{41}Ar concentration using the ionization chamber, it is necessary to evaluate in advance its response, specifically, the conversion factor from ionization current into to ^{41}Ar activity concentration. Although preliminary studies have assessed the chamber's response to ^{41}Ar in P-10 gas [1], the response ratio between air and P-10 gas has not yet been established. This study proposes a method to derive that response ratio using a gas substitution and extrapolation technique.

****

EXPERIMENTS: Two 3 ml acrylic containers were filled with pure argon gas. ^{41}Ar gas was produced via ^{40}Ar(n, γ)^{41}Ar reaction by irradiating the gas samples for 60 s at the at the bottom of KUR-SLY reactor operating at 1 MW thermal output. The production of ^{41}Ar was confirmed gamma-ray spectroscopy using a HPGe detector. In the proposed “extrapolation method”, a mixture of ^{41}Ar and P-10 was initially prepared. Half of gases was then evacuated and replaced with dry air. This step was repeated twice, resulting in gas mixtures with P-10 to air ratios of 100 : 0, 50 : 50, and 25 : 75. The ionization current was measured at each stage. To account for dilution effect, measured currents were corrected based on the proportion of P-10 in the mixture and normalized to the current measured at 100% P-10. Assuming the ^{41}Ar activity remained constant throughout, a regression line was fitted to the normalized data using the least-squares method. The intercept of this regression line represents the ionization current corresponding to 100 % air, relative to that for 100 % P-10, thereby yielding the response ratio.

****

RESULTS: The response ratio of the ionization chamber when filled with air compared to P-10 gas was determined to be 0.680. In future work, the reliability of this extrapolation method will be assessed by conducting uncertainty evaluation and comparing it with alternative measurement approaches.

****

REFERENCES:

[1] A. Yunoki *et al.*, KURNS Progress Report 2019, (2020) CO12-5, 275.
[2] A. Yunoki *et al.,* Appl Radiat Isot., **68(7-8)** (2010) 1340-1343.

R6157

CO12-15

Effect of the Charging State of a Lithium-Ion Battery on the Positron Annihilation Characteristics in Graphite Anode

A. Yabuuchi, N. Oshima[1], T. Fujiwara[1], K. Michishio[1], and M. Hino

Institute for Integrated Radiation and Nuclear Science, Kyoto University
[1]National Institute of Advanced Industrial Science and Technology

INTRODUCTION: Positron annihilation spectroscopy typically requires positrons to be injected from the sample surface, limiting its ability to probe the interior of thick samples. In this study, a lithium-ion battery (LIB) was irradiated with thermal neutrons to produce the positron-emitting nuclide ^{64}Cu in the copper foil anode current collector, enabling the investigation of positron annihilation characteristics in the graphite anode. We previously observed changes in positron annihilation characteristics during Li-ion deintercalation (i.e., discharge). To determine whether the observed changes were significant, we evaluated the temporal stability of the *S* parameter under no-charge/discharge conditions in this fiscal year.

EXPERIMENTS: The LIB sample was irradiated with thermal neutrons at the KUR CN-3 port for 24 h at 1 MW and 6 h at 5 MW. Following irradiation, and in accordance with previous experimental protocols, the sample was left for about 24 h before measuring the annihilation gamma-rays emitted from positrons injected into the graphite anode using a high-purity Ge detector. The temporal changes in the Doppler broadening of the annihilation radiation spectrum were characterized using the *S* parameter [1]. A series of measurements was conducted under two conditions: the same LIB sample in a discharged state and a half-charged state.

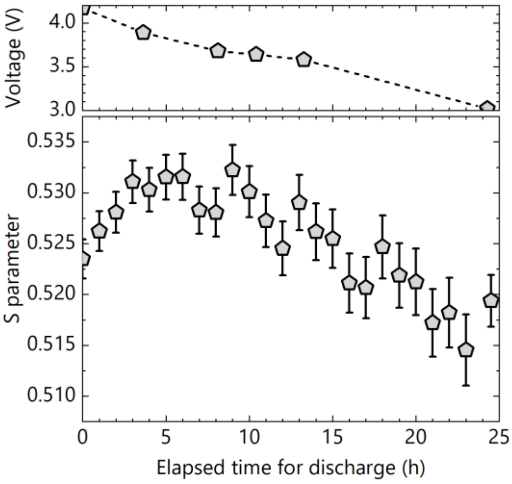

Fig. 1. *S* parameter changes while discharging. The upper panel shows the closed-circuit voltage.

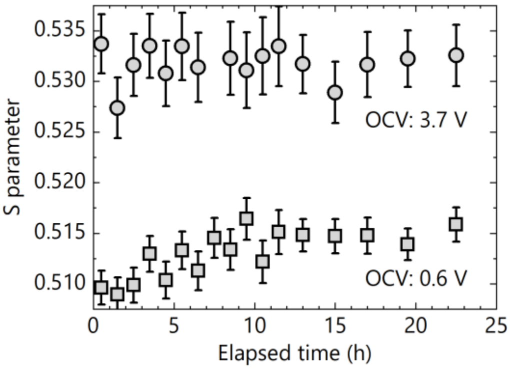

Fig. 2. Time variation of the *S* parameters in different charge states. The open-circuit voltage (OCV) of 0.6 V and 3.7 V correspond to the discharged and half-charged states, respectively.

RESULTS: Figure 1 shows the changes in the *S* parameter during the discharging of a graphite anode from a fully charged state. During discharge, the *S* parameter initially increases and then decreases, consistent with our first-principles calculations. Figure 2 shows the temporal evolution of the *S* parameter measured at open-circuit voltages (OCVs) of 0.6 V (fully discharged state) or 3.7 V (half-charged state), under conditions without charging/discharging during measurements. (Note that an OCV of 0.6 V corresponds to an over-discharged state.) These results indicate that the *S* parameter strongly depends on the LIB's charge state. However, at an OCV of 0.6 V, a gradual increase in the *S* parameter is observed during the first 10 hours, possibly influenced by the 847 keV gamma-ray peak of ^{56}Mn, which has a higher energy than the 511 keV annihilation photopeak. (Mn is present in the cathode material.) Since the half-life of ^{56}Mn (2.6 h) is shorter than that of ^{64}Cu (12.7 h), its influence diminishes over time.

REFERENCES: [1] F. A. Selim, Mater. Charact. **174** (2021) 110952.

R6169

II. PUBLICATION LIST
(APRIL 2024 – MARCH 2025)

1. Slow Neutron Physics and Neutron Scattering

Papers

Development of non-destructive isotope measurement of the natural galena (PbS) using negative muon beams
Terada K., Ninomiya K., Sato A., Tomono D., Kawashima Y., Inagaki M., Nambu A., Kudo T., Osawa T., Kubo M. K.
Journal of Analytical Science and Technology 15(1) (2024) 28 (doi)10.1186/s40543-024-00440-6

Polarized Cold-neutron Reflectometry at JRR-3/MINE2 for the Development of Ultracold-neutron Spin Analyzers for a Neutron EDM Experiment at TRIUMF
Higuchi Takashi, Akatsuka Hiroaki, Brossard Alexis, Fujimoto Derek, Giampa Pietro, Hansen-Romu Sean, Hatanaka Kichiji, Hino Masahiro, Ichikawa Go, Imajo Sohei, Jamieson Blair, Kawasaki Shinsuke, Kitaguchi Masaaki, Mammei Russell, Matsumiya Ryohei, Mishima Kenji, Picker Rüdiger, Schreyer Wolfgang, Shimizu Hirohiko M., Sidhu Steve, Vanbergen Sean
Journal of the Physical Society of Japan, 93(9) (2024) 091009 (doi)10.7566/JPSJ.93.091009

Demonstration with very-cold neutrons of developments in Fourier time-of-flight
Neulinger Thomas, Bernert Karina, Fierlinger Peter, Filter Hanno, Hino Masahiro, Jenke Tobias, Lapeyre Franck, Zimmer Oliver
Nuclear Instruments and Methods in Physics Research Section A: Accelerators, Spectrometers, Detectors and Associated Equipment, 1066 (2024) 169570 (doi)10.1016/j.nima.2024.169570

Study of the boundary friction of high-strength steel during the cold rolling
Shimura Masahiro, Yamashita Naoki, Hino Masahiro, Otsuka Takayuki, Hirayama Tomoko
Tribology - Materials, Surfaces & Interfaces 34 (2025) 912-913 (doi)10.1177/17515831231216387

Proceedings

Development of neutron focusing mirrors and the application for neutron beam optics in the new research reactor at "Monju" site
Masahiro Hino, Takuya Hosobata, Masahiro Takeda, Yutaka Yamagata, Takashi Higuchi, Ryuto Fujitani, Hitoshi Endo
Proceedings of the 59th KURNS Scientific Meeting, Kumatori, Japan/Online (Jan. 30-31, 2025) 57 (in Japanese)

The measurement of a traversal time by neutron spin interferometry
Ryuto Fujitani, Masahiro Hino, Takashi Higuchi
Proceedings of the 59th KURNS Scientific Meeting, Kumatori, Japan/Online (Jan. 30-31, 2025) 42 (in Japanese)

Towards the design of cold neutron source for new research reactor to be constructed on the “Monju” site
Yudai Takita, Mizuki Iriyama, Seiji Tasaki, Yutaka Abe, Masahiro Hino, Masasi Arai
Proceedings of the 59th KURNS Scientific Meeting, Kumatori, Japan/Online (Jan. 30-31, 2025) 39 (in Japanese)

高速度中性子 CT の実用性に関する検討
Naoya Odaira, Daisuke Ito, Yasushi Saito
Proceedings of the 59th KURNS Scientific Meeting, Kumatori, Japan/Online (Jan. 30-31, 2025) 43 (in Japanese)

2. Nuclear Physics and Nuclear Data

Papers

Microscopic Observation of the Anisotropy of the Johari–Goldstein-β Process in Cross-Linked Polybutadiene on Stretching by Time-Domain Interferometry
Mashita Ryo, Saito Makina, Yoda Yoshitaka, Nagasawa Nobumoto, Bito Yasumasa, Kikuchi Tatsuya, Kishimoto Hiroyuki, Seto Makoto, Kanaya Toshiji
ACS Macro Letters 13(7) (2024) 847-852 (doi)10.1021/acsmacrolett.4c00274

Cd-content and temperature dependences of hyperfine fields in $Cd_xFe_{3-x}O_4$
Sato W., Fujii M., Konaka M., Ito T., Hirahara H., Komatsuda S., Taniguchi A., Ohkubo Y.
Applied Radiation and Isotopes 209 (2024) 111320 (doi)10.1016/j.apradiso.2024.111320

An introduction to Spent Nuclear Fuel decay heat for Light Water Reactors: a review from the NEA WPNCS
Rochman Dimitri, Algora Alejandro, Àlvarez-Velarde Francisco, Bardelay Aurélie, Bremnes Øystein, Cabellos Oscar, Cano-Ott Daniel, Capponi Luigi, Carmouze Coralie, Caruso Stefano, Cummings Andrew, Dagan Ron, Fallot Muriel, Fiorito Luca, Giot Lydie, Govers Kevin, Häkkinen Silja, Hannstein Volker, Hoefer Axel, Huynh Tan Dat, Ichou Raphaëlle, Ilas Germina, Juutilainen Pauli, Koszuk Lukasz, Kromar Marjan, Lahaye Sébastien,

Lam James, Laugier Frédéric, Launay Agnés, Léger Vincent, Lecarpentier David, Leppanen Jaakko, Malouch Fadhel, Martin Julie-Fiona, McGinnes David, Mills Robert William, Minato Futoshi, Nauchi Yasushi, Ortego Pedro, Petkov Plamen, Romojaro Pablo, Sato Shunsuke, Seidl Marcus, Shama Ahmed, Simeonov Teodosi, Sjöland Anders, Solans Virginie, Sommer Fabian, Tittelbach Sven, Tsilanizara Aimé, Vlassopoulos Efstathios, Vallet Vanessa, Vasiliev Alexander, Watanabe Tomoaki, Žerovnik Gašper
EPJ Nuclear Sciences & Technologies 10 (2025) 9 (doi)10.1051/epjn/2024010

Spectroscopy of neutron-rich nuclei produced by multinucleon transfer reactions at KISS
Watanabe Yutaka, Hirayama Yoshikazu, Mukai Momo, Niwase Toshitaka, Schury Peter, Rosenbusch Marco, Ishiyama Hironobu, Jeong Sun-Chan, Miyatake Hiroari, Wada Michiharu, Kimura Sota, Iimura Shun, Moon Jun Young, Hashimoto Takashi, Taniguchi Akihiro
EPJ Web of Conferences 306 (2024) 01016 (doi)10.1051/epjconf/202430601016

Quasi-elastic γ-ray scattering study of α process under stretching in crosslinked rubber filled with silica via Mössbauer time-domain interferometry
Mashita Ryo, Yoda Yoshitaka, Bito Yasumasa, Kishimoto Hiroyuki, Seto Makoto, Kanaya Toshiji, Saito Makina
Interactions 245 (2024) 314 (doi)10.1007/s10751-024-02171-x

Synchrotron based conversion electron Mössbauer spectroscopy
Mitsui Takaya, Fujiwara Kosuke, Sakai Seiji, Li Songtian, Okabayashi Jun, Kobayashi Yasuhiro, Seto Makoto
Interactions 245 (2024) 347 (doi)10.1007/s10751-024-02195-3

Thermal Stability of Retained Austenite with Heterogeneous Composition and Size in Austempered Fe-2Mn-1.5Si-0.4C Alloy
Watanabe Miku, Miyamoto Goro, Zhang Yongjie, Morooka Satoshi, Harjo Stefanus, Kobayashi Yasuhiro, Furuhara Tadashi
ISIJ International 64(9) (2025) 1464-1476 (doi)10.2355/isijinternational.ISIJINT-2024-044

Thermal behavior of open-volume defects and absorbed hydrogen atoms in palladium
Sato W., Furumoto M., Shimizu H., Ohkubo Y.
Journal of Applied Physics 135(24) (2024) 245103 (doi)10.1063/5.0207064

Neural network potential for molecular dynamics calculation of UO_2
Konashi Kenji, Kato Nobuhiko, Mori Kazuki, Kurosaki Ken
Journal of Nuclear Materials 607 (2025) 155660 (doi)10.1016/j.jnucmat.2025.155660

Development of a non-destructive carbon quantification method in iron by negative muon lifetime measurement
Ninomiya Kazuhiko, Kubo Michael Kenya, Inagaki Makoto, Yoshida Go, Takeshita Soshi, Tampo Motonobu, Shimomura Koichiro, Kawamura Naritoshi, Strasser Patrick, Miyake Yasuhiro, Ito Takashi U., Higemoto Wataru, Saito Tsutomu
Journal of Radioanalytical and Nuclear Chemistry 333 (2024) 3445-3450 (doi)10.1007/s10967-023-09289-2

Controlling ^{229}Th isomeric state population in a VUV transparent crystal
Hiraki Takahiro, Okai Koichi, Bartokos Michael, Beeks Kjeld, Fujimoto Hiroyuki, Fukunaga Yuta, Haba Hiromitsu, Kasamatsu Yoshitaka, Kitao Shinji, Leitner Adrian, Masuda Takahiko, Guan Ming, agasawa Nobumoto, Ogake Ryoichiro, Pimon Martin, ressler Martin, Sasao Noboru, Schaden Fabian, Schumm Thorsten, Seto Makoto, Shigekawa Yudai, Shimizu Kotaro, Sikorsky Tomas, Tamasaku Kenji, Takatori Sayuri, Watanabe Tsukasa, Yamaguchi Atsushi, Yoda Yoshitaka, Yoshimi Akihiro, Yoshimura Koji
Nature Communications 15(1) (2024) 5536 (doi)10.1038/s41467-024-49631-0

Development of a phoswich imaging detector to simultaneously acquire neutron and gamma photon images
Yamamoto Seiichi, Yoshino Masao, Nakanishi Kohei, Kamada Kei, Yoshikawa Akira, Tanaka Hiroki, Kataoka Jun
Nuclear Instruments and Methods in Physics Research Section A: Accelerators, Spectrometers, Detectors and Associated Equipment 1065 (2024) 169484 (doi)10.1016/j.nima.2024.169484

Giant dipole resonance photofission and photoneutron reactions in U238 and Th232
Filipescu D., Gheorghe I., Goriely S., Tudora A., Nishio K., Ohtsuki T., Wang H., Fan G., Stopani K., Suzaki F., Hirose K., Inagaki M., Lui Y.-W., Ari-izumi T., Miyamoto S., Otsuka T., Utsunomiya H.
Physical Review C 109(4) (2024) 044602 (doi)10.1103/PhysRevC.109.044602

Measurement system requirements for photofission signal detection with coincidence neutron counting method
K. W. Chin, H. Sagara, J. Hori, Y. Takahashi
Progress in Nuclear Science and Technology 7 (2025) 91-96 (doi)10.15669/pnst.7.91

Proceedings

Current Status of Neutron In-beam Mössbauer spectroscopy
M. Yoshida, Y. Kobayashi, M. K. Kubo, S. Kimoto, W. Sato, M. Mihara, J. Miyazaki, T. Nagatomo, Y. Watanabe, I. Chui, and T. Osawa
Proceedings of the Specialists' Meeting on "Nuclear Spectroscopy and Condensed Matter Physics Using Short-Lived Nuclei X", Online (Feb. 7, 2024) 41-46 (in Japanese)

Development of a combined neutron resonance analysis technique as a nondestructive assay for fissile material quantification
F. Rossi, J. Lee, Y. Kodama, K. Hironaka, M. Koizumi, J. Hori, K. Terada, and T. Sano
65th Annual Meeting of the Institute of Nuclear Materials Management, Portland, U.S.A. (Jul. 21-25, 2024)

Identification of β-delayed γ-rays of a short-lived fission product ^{157}Nd using an Isotope
S. Sakakibara, T. Kuga, M. Shibata and A. Taniguchi
Proceedings of the Specialists' Meeting on "Nuclear Spectroscopy and Condensed Matter Physics Using Short-Lived Nuclei X", Online (Feb. 7, 2024) 38-42 (in Japanese)

Laser spectroscopy at KISS
Y. Hirayama, M. Mukai, Y.X. Watanabe, P. Schury, H. Choi, J.Y. Moon, T. Hashimoto, S. Iimura, M. Oyaizu, S.C. Jeong, T. Niwase, M. Tajima, A. Taniguchi, M. Wada, and H. Miyatake
Proceedings of the Specialists' Meeting on "Nuclear Spectroscopy and Condensed Matter Physics Using Short-Lived Nuclei X", Online (Feb. 7, 2024) 32-37 (in Japanese)

Local states of oxide ions in yttria stabilized zirconia (YSZ)
M. Mihara, Y. Otani, M. Ogura, K. Matsuta, M. Fukuda, M. Fukutome, Y. Kimura, G. Takayama, T. Sugisaki, R. Taguchi, T. Izumikawa, N. Noguchi, T. Ohtsubo, D. Nishimura, H. Takahashi, A. Kitagawa, S. Sato, S. Momota
Proceedings of the Specialists' Meeting on "Nuclear Spectroscopy and Condensed Matter Physics Using Short-Lived Nuclei X", Online (Feb. 7, 2024) 8-11(in Japanese)

Mixed-Valence State of Binuclear Ferrocene Derivatives
S. Nakashima
Proceedings of the Specialists' Meeting on "Nuclear Spectroscopy and Condensed Matter Physics Using Short-Lived Nuclei X", Online (Feb. 7, 2024) 12-17 (in Japanese)

Recoilless Fraction on ^{197}Au Mössbauer Spectroscopy
Y. Kobayashi, H. Ohashi and M. Seto
Proceedings of the Specialists' Meeting on "Nuclear Spectroscopy and Condensed Matter Physics Using Short-Lived Nuclei X", Online (Feb. 7, 2024) 1-4 (in Japanese)

Others

Gamma ray spectroscopy for event out of phase of pulsed neutron source for short lived fission products
Y. Nauchi, J. Hori, K. Terada, T. Sano
Symposium on Nuclear Data 2024 (2024)

Development of a High-Voltage Output DAC System for Fast Ion-Shuttling
T. Oshio, R. Nishimoto, T. Higuchi, K. Hayasaka, K. Koike, S. Morisaka, T. Miyoshi, R. Ohira, U. Tanaka
arXiv (2025) (doi)10.48550/arXiv.2412.07363

Precision Spectroscopy of Antiprotonic Atoms for Investigation of Low-energy Antinucleon-nucleus Interactions
Takashi Higuchi, Hiroyuki Fujioka
arXiv (2025) (doi)10.48550/arXiv.2501.08759

Towards Precision Spectroscopy of Antiprotonic Atoms for Probing Strong-field QED
Gonçalo Baptista, Shikha Rathi, Michael Roosa, Quentin Senetaire, Jonas Sommerfeldt, Toshiyuki Azuma, Daniel Becker, Francois Butin, Ofir Eizenberg, Joseph Fowler, Hiroyuki Fujioka, Davide Gamba, Nabil Garroum, Mauro Guerra, Tadashi Hashimoto, Takashi Higuchi, Paul Indelicato, Jorge Machado, Kelsey Morgan, Francois Nez, Jason Nobles, Ben Ohayon, Shinji Okada, Daniel Schmidt, Daniel Swetz, Joel Ullom, Pauline Yzombard, Marco Zito, Nancy Paul
arXiv (2025) (doi)10.48550/arXiv.2501.08893

Novel concept for low-energy antineutron production and its application for antineutron scattering experiments
Alessandra Filippi, Hiroyuki Fujioka, Takashi Higuchi, Luca Venturelli
arxiv (2025) (doi)10.48550/arXiv.2503.06972

3. Reactor Physics and Reactor Engineering

Papers

Evaluation of existing correlations and development of a new correlation for single-phase friction factor in rod bundle assembly
Chalgeri Vikrant Siddharudh, Shen Xiuzhong, Yamamoto Toshihiro
Annals of Nuclear Energy 201 (2024) 110456-110456 (doi)10.1016/j.anucene.2024.110456

Neutron transmission measurements for silica glass at the KURNS-LINAC
Lee Jaehong, Rossi Fabiana, Kodama Yu, Hironaka Kota, Koizumi Mitsuo, Sano Tadafumi, Matsuo Yasunori, Hori Jun-ichi
Annals of Nuclear Energy 211 (2025) 111017 (doi)10.1016/j.anucene.2024.111017

Nuclear education programs with reactor laboratory experiments at zero-powered research reactor facilities in Japan
Pyeon Cheol Ho, Endo Tomohiro, Chiba Go, Watanabe Kenichi, Wakabayashi Genichiro
Annals of Nuclear Energy 204 (2024) 110531 (doi)10.1016/j.anucene.2024.110531

Sensitivity and perturbation analysis of alpha-eigenvalue with time-dependent Monte Carlo perturbation techniques
Yamamoto Toshihiro, Sakamoto Hiroki
Annals of Nuclear Energy 208 (2024) 110756 (doi)10.1016/j.anucene.2024.110756

Extraction method for superimposed coherent transition radiation using Fresnel reflection in a ring-type resonator
Sei Norihiro, Takahashi Toshiharu
Applied Optics 63(18) (2024) 5000 - 5005 (doi)10.1364/AO.525707

Long-Term Estimation of Depositions on Heating Surface During Boiling of Long-Life Coolant
Shinozaki M., Ito D., Odaira N., Ito K., Saito Y. ASME
Journal of Heat and Mass Transfer 146(11) (2024) 111602 (doi)10.1115/1.4065844

Experimental investigation on local flow structures of upward cap-bubbly flows in a vertical large-size square channel
Sun Haomin, Kunugi Tomoaki Yokomine Takehiko, Shen Xiuzhong, Hibiki Takashi
Experimental Thermal and Fluid Science 154 (2024) 111171 (doi)10.1016/j.expthermflusci.2024.111171

Experimental investigation of tritium release behavior from neutron irradiated $LiAlO_2$ with Zr for tritium production in a high-temperature gas-cooled reactor
Isogawa Hiroki, Katayama Kazunari, Kobayashi Seiyo, Matsuura Hideaki, Iinuma Yuto
Fusion Engineering and Design 208 (2024) 114657 (doi)10.1016/j.fusengdes.2024.114657

A full-flow-range drift-flux model for adiabatic and boiling two-phase flows in vertical narrow rectangular flow channels
Shen Xiuzhong, Yamamoto Toshihiro, Nakajima Ken, Hibiki Takashi
International Journal of Thermal Sciences 202 (2024) 109086 (doi)10.1016/j.ijthermalsci.2024.109086

Development of Capacitance Void Fraction Sensor Using X-ray Transmission Imaging
ITO Daisuke, ADACHI Takuya, ODAIRA Naoya, ITO Kei, SAITO Yasushi
JAPANESE JOURNAL OF MULTIPHASE FLOW 39(1) (2025) 47-52 (in Japanese) (doi)10.3811/jjmf.2025.002

Fusion neutron source and array of particle detectors for nondestructive interrogation of special nuclear materials
Masuda Kai, Takahashi Yoshiyuki, Misawa Tsuyoshi, Yamakawa Norio, Scott Thomas B., Bakr Mahmoud
Journal of Applied Physics 136(11) (2024) 114503 (doi)10.1063/5.0225179

Measurements of neutron capture cross-section for nuclides of interest in decommissioning (II):^{58}Fe(n,γ)^{59}Fe
Nakamura Shoji, Shibahara Yuji, Endo Shunsuke, Rovira Gerard, Kimura Atsushi
Journal of Nuclear Science and Technology 62(3) (2025) 300-307 (doi)10.1080/00223131.2024.2427244

Uncertainty quantification of criticality in light-water-moderated and graphite-reflected core with highly enriched uranium fuel at university teaching and research reactor
Shiga Hiroshi, Watanabe Kenichi, Takeda Satoshi, Wakabayashi Genichiro, Yamanishi Hirokuni, Pyeon Cheol Ho
Journal of Nuclear Science and Technology 62(2) (2025) 224-232 (doi)10.1080/00223131.2024.2402363

A Study of Oscillating Magnetic Fields with Neutron Spin Interferometry
Suzuki Takaya, Fujitani Ryuto, Tasaki Seiji, Hino Masahiro, Kitaguchi Masaaki, Oda Tatsuro, Nakamura Riichiro
Journal of the Physical Society of Japan 93(9) (2024) 091008 (doi)10.7566/JPSJ.93.091008

Uncertainty Quantification of ^{237}Np, ^{241}Am, and ^{243}Am Reaction Rates in Highly Enriched Uranium Fuel Cores at Kyoto University Critical Assembly
Pyeon Cheol Ho, Oizumi Akito, Katano Ryota, Fukushima Masahiro
Nuclear Science and Engineering 199(3) (2025) 429-444 (doi)10.1080/00295639.2024.2380624

Nondestructive and active interrogation system for special nuclear material: proof of principle and initial results
Bakr Mahmoud, Masuda Kai, Takahashi Yoshiyuki, Misawa Tsuyoshi, Yamakawa Norio, Scott Tomas
Nuclear Science and Techniques 35(5) (2024) 87 (doi)10.1007/s41365-024-01458-6

Perovskite Nanocrystal-Coated Inorganic Scintillator-Based Fiber-Optic Gamma-ray Sensor with Higher Light Yields
Jegal Seokhyeon, Song Siwon, Park Jae Hyung, Kim Jinhong, Kim Seunghyeon, Lee Sangjun, Pyeon Cheol Ho, Kim Sin, Lee Bongsoo
Photonics 11(10) (2024) 936 (doi)10.3390/photonics11100936

Vortex-induced vibration of double cylinders under different tandem spacing
Guangyun Min
Physics of Fluids 37(2) (2025) 025172 (doi)10.1063/5.0253155

Monte Carlo iterative k-source method for fixed-source calculations in nearly critical subcritical systems
Yamamoto Toshihiro, Sakamoto Hiroki
Progress in Nuclear Energy 173 (2024) 105264 (doi)10.1016/j.pnucene.2024.105264

Performance of the Fully Equipped Spin Flip Chopper for the Neutron Lifetime Experiment at J-PARC
Mishima K, Ichikawa G, Fuwa Y, Hasegawa T, Hino M, Hosokawa R, Ino T, Iwashita Y, Kitaguchi M, Matsuzaki S, Mogi T, Okabe H, Oku T, Okudaira T, Seki Y, Shimizu H E, Shimizu H M, Takahashi S, Tanida M, Yamashita S, Yokohashi M, Yoshioka T
Progress of Theoretical and Experimental Physics 2024(9) (2024) 093G01 (doi)10.1093/ptep/ptae123

Compact and transportable system for detecting lead-shielded highly enriched uranium using ^{252}Cf rotation method with a water Cherenkov neutron detector
Tanabe Kosuke, Komeda Masao, Toh Yosuke, Kitamura Yasunori, Misawa Tsuyoshi, Tsuchiya Ken'ichi, Sagara Hiroshi
Scientific Reports 14(1) (2024) 18828 (doi)10.1038/s41598-024-69526-w

Application of interface-tracking method into condensation simulation
ITO Kei, ODAIRA Naoya, ITO Daisuke, SAITO Yasushi
JAPANESE JOURNAL OF MULTIPHASE FLOW 39(1) (2025) 41-46 (in Japanese) (doi)10.3811/jjmf.2025.001

Effect of fin arrangement on pressure drop characteristics of two-phase flow in a finned rectangular channel.
OKUNAKA Shori, SHINOZAKI Masaru, ODAIRA Naoya, ITO Daisuke, ITO Kei, SAITO Yasushi
JAPANESE JOURNAL OF MULTIPHASE FLOW 38(3) (2024) 289-298 (in Japanese) (doi)10.3811/jjmf.2024.013

Proceedings

Active Shield for Environmental Magnetic Fields
K. Matsuta, Y. Masuda, M. Mihara
Proceedings of the Specialists' Meeting on "Nuclear Spectroscopy and Condensed Matter Physics Using Short-Lived Nuclei X", Online (Feb. 7, 2024) 22-25 (in Japanese)

Development of Muon Spin Imaging Spectroscopy
T. Sugisaki, K. M. Kojima, M. Mihara, Y. Kimura, Y. Mizoi, G. Takayama, D. Nishimura, M. Tanaka, S. Ishitani, G. Morris, D. Arseneau, R. Abasalti, D. Vyas, M. Fukuda, W. Sato, R. Yasuda, R. Taguchi
Proceedings of the Specialists' Meeting on "Nuclear Spectroscopy and Condensed Matter Physics Using Short-Lived Nuclei X", Online (Feb. 7, 2024) 26-31 (in Japanese)

Reduced enrichment project for KUCA fuel and future plan
Tsuyoshi Misawa, Hironobu Unesaki, Yasunori Kitamura and Yoshiyuki Takahashi
Proceedings of the 59th KURNS Scientific Meeting, Kumatori, Japan/Online (Jan. 30-31, 2025) 67-69 (in Japanese)

Reevaluation of Neutron Energy Spectrum in Heavy-Water Neutron Irradiation Facility Using Multifoil Activation Method
Jakkrit Prateepkaew, and Yoshinori Sakurai
Proceedings of the 59th KURNS Scientific Meeting, Kumatori, Japan/Online (Jan. 30-31, 2025) 33 (in Japanese)

Books

Reactor Laboratory Experiments at Kyoto University Critical Assembly
Pyeon Cheol Ho, Chiba Go, Endo Tomohiro, Watanabe Kenichi
Springer Nature Singapore (2024) (ISBN)9789819780693 (doi)10.1007/978-981-97-8070-9

4. Material Science and Radiation Effects

Papers

Discovery of collective nonjumping motions leading to Johari–Goldstein process of stress relaxation in model ionic glass
Saito Makina, Araki Takeaki, Onodera Yohei, Ohara Koji, Seto Makoto, Yoda Yoshitaka, Wakabayashi Yusuke
Acta Materialia 284 (2025) 120536 (doi)10.1016/j.actamat.2024.120536

Three-dimensional surface analysis of iron-based materials using synchrotron Mössbauer source
Fujiwara Kosuke, Mitsui Takaya, Hasegawa Noboru, Nishikino Masaharu, Kobayashi Yasuhiro, Mibu Ko, Shinoda Keiji, Masuda Ryo, Seto Makoto
Applied Physics Express 17(8) (2024) 082002 (doi)10.35848/1882-0786/ad67a8

Extraordinary ^{99}Mo adsorption: utilizing spray-dried mesoporous alumina for clinical-grade generator development
Alowasheeir Azhar, Eguchi Miharu, Fujita Yoshitaka, Tsuchiya Kunihiko, Wakabayashi Ryutaro, Kimura Tatsuo, Ariga Katsuhiko, Hatano Kentaro, Fukumitsu Nobuyoshi, Yamauchi Yusuke
Bulletin of the Chemical Society of Japan 97(10) (2024) uoae099 (doi)10.1093/bulcsj/uoae099

Charge-entropy-stabilized selenide $Ag_xSn_{1-x}Se$
Oudah Mohamed, Takegami Daisuke, Kitao Shinji, Lado Jose L., Meléndez-Sans Anna, Christovam Denise S., Yoshimura Masato, Tsuei Ku-Ding, McNally Graham, Isobe Masahiko, Küster Kathrin, Seto M., Keimer Bernhard, Bonn D. A., Tjeng Liu Hao, Sawatzky George, Takagi Hidenori
Communications Materials 6(1) (2025) 58 (doi)10.1038/s43246-025-00778-3

Achieving effective bonding between W-75Cu composite and CuCrZr alloy via spark plasma sintering
Sang Changcheng, Xu Dang, Fu Kaichao, Chen Ruizhi, Chen Pengqi, Lu Yingwei, Xia Yonghong, Xu Qiu, Cheng Jigui
Fusion Engineering and Design 211 (2025) 114791 (doi)10.1016/j.fusengdes.2024.114791

The correlation of the gamma ray waveform with the vibration phase of the resonant absorber
Yamashita Hiroyuki, Kitao Shinji, Kobayashi Yasuhiro, Seto Makoto
Interactions 245 (2024) 366 (doi)10.1007/s10751-024-02214-3

Investigation of vacancy-type defects in diamond-like carbon films using slow positron beam
Kanda Kazuhiro, Mishima Tomohiro, Akasaka Hiroki, Hori Fuminobu, Yabuuchi Atsushi, Kinomura Atsushi
Japanese Journal of Applied Physics 63(4) (2024) 045503 (doi)10.35848/1347-4065/ad327f

Direct measurement of lattice behavior during femtosecond laser-driven shock front formation in copper
Egashira Naoya, Matsuda Tomoki, Okuchi Takuo, Seto Yusuke, Ito Yusuke, Shobu Takahisa, Nakanii Nobuhiko, Inubushi Yuichi, Togashi Tadashi, Miyanishi Kohei, Mashimo Tsutomu, Sano Tomokazu
Journal of Applied Physics 137 (2025) 105903 (doi)10.1063/5.0253150

Effects of Gamma-ray and neutron irradiation on infrared optical properties of ZnSe and ZnS for ITER divertor thermography
Ushiki Tomohiko, Imazawa Ryota, Kitazawa Sin-Ichi, Ishikawa Masao, Murakami Hidetoshi, Shimizu Kosuke, Sugie Tatsuo, Okazaki Hiroyuki, Seki Masaya, Buenavidez Butch, Kasano Naoto, Katayanagi Yuzi, Nunoya Yoshihiko
Journal of Nuclear Materials 595 (2024) 155047 (doi)10.1016/j.jnucmat.2024.155047

Formulation of high-temperature strength equation of 9Cr-ODS tempered martensitic steels using the Larson–Miller parameter and life-fraction rule for rupture life assessment in steady-state, transient, and accident conditions of fast reactor fuel
Miyazawa Takeshi, Tanno Takashi, Imagawa Yuya, Hashidate Ryuta, Yano Yasuhide, Kaito Takeji, Ohtsuka Satoshi, Mitsuhara Masatoshi, Toyama Takeshi, Ohnuma Masato, Nakashima Hideharu

Journal of Nuclear Materials 593 (2024) 155008 (doi)10.1016/j.jnucmat.2024.155008

He irradiation resistance performance in CrNiCo, CrFeNiCo, and CrFeMnNiCo multi-principal element alloys
Xu Q., Guan H.Q., Huang S.S., Zhong Z.H., Miyamoto M., Yasunaga K., Yabuuch A.
Journal of Nuclear Materials 603 (2025) 155432 (doi)10.1016/j.jnucmat.2024.155432

Improving interfacial microstructure and mechanical properties of ODS-W/Cu joints via anodization treatment and spark plasma sintering
Xu Dang, Fu Kaichao, Sang Changcheng, Chen Ruizhi, Chen Pengqi, Lu Yingwei, Zhu Dahuan, Xu Qiu, Cheng Jigui
Journal of Nuclear Materials 601 (2024) 155351 (doi)10.1016/j.jnucmat.2024.155351

Thermophysical characterization of UFe_3B_2 and USiNi: An experimental study
Sun Yifan, Miyawaki Yuji, Kumagai Masaya, Fujieda Shun, Muta Hiroaki, Kurosaki Ken, Ohishi Yuji
Journal of Nuclear Materials 595 (2024) 155048 (doi)10.1016/j.jnucmat.2024.155048

Creep deformation and rupture behavior of 9Cr-ODS steel cladding tube at high temperatures from 700°C to 1000°C
Imagawa Yuya, Hashidate Ryuta, Miyazawa Takeshi, Onizawa Takashi, Ohtsuka Satoshi, Yano Yasuhide, Tanno Takashi, Kaito Takeji, Ohnuma Masato, Mitsuhara Masatoshi, Toyama Takeshi
Journal of Nuclear Science and Technology 61(6) (2024) 762-777 (doi)10.1080/00223131.2023.2269178

Water extraction of technetium-99m from neutron irradiated porous molybdenum dioxide pellet
Hu Xiangrong, Fujita Yoshitaka, Tsuchiya Kunihiko, Fukutani Satoshi, Hori Jun-ichi, Suzuki Tatsuya
Journal of Radioanalytical and Nuclear Chemistry 333(11) (2024) 6057-6063 (doi)10.1007/s10967-024-09529-z

Diffractometer for element-specific analysis on local structures using a combination of X-ray fluorescence holography and anomalous X-ray scattering
Tajiri Hiroo, Kohara Shinji, Kimura Koji, Halubai Sekhar, Morimoto Haruto, Happo Naohisa, Stellhorn Jens R., Onodera Yohei, Qiao Xvsheng, Urushihara Daisuke, Hu Peidong, Wakihara Toru, Kinoshita Toyohiko, Hayashi Koichi
Journal of Synchrotron Radiation 32(1) (2025) 125-132 (doi)10.1107/S1600577524011366

Evaluation of the effect of composition and firing temperature on pore size distribution of ceramics by SANS measurement
Sugita Tsuyoshi, Yoshida Hirokazu, Kodama Hiroto, Ishigaki Toru, Oba Yojiro
Journal of the Ceramic Society of Japan 132(9) (2024) 548-554 (doi)10.2109/jcersj2.24064

Enhancing Mechanical and Thermal Shock Resistance Properties of W/W-10Cu Joints through a Novel Pre-oxidation Treatment and Infiltration Method
Xu Dang, Zhou Rui, Fu Kaichao, Chen Pengqi, Xu Qiu, Cheng Jigui
Journal of the Japan Society of Powder and Powder Metallurgy 72(Supplement) (2025) S1487-S1493 (doi)10.2497/jjspm.16P-T10-01

Thermoelectric materials for space explorations
Palaporn Dulyawich, Tanusilp Sora-at, Sun Yifan, Pinitsoontorn Supree, Kurosaki Ken
Materials Advances 5(13) (2024) 5351-5364 (doi)10.1039/D4MA00309H

Characterization of δNi_2Si Precipitates in Cu-Ni-Si Alloy by Small-Angle X-ray Scattering, Small-Angle Neutron Scattering, and Atom Probe Tomography
Sasaki Hirokazu, Akiya Syunta, Mihara Kuniteru, Oba Yojiro, Onuma Masato, Uzuhashi Jun, Ohkubo Tadakatsu
MATERIALS TRANSACTIONS 66(1) (2025) 44-49 (doi)10.2320/matertrans.MT-D2024005

Direct observation of the atomic density fluctuation originating from the first sharp diffraction peak in SiO_2 glass
Hirata Akihiko, Sato Shuya, Shiga Motoki, Onodera Yohei, Kimoto Koji, Kohara Shinji
NPG Asia Materials 16(1) (2024) 25 (doi)10.1038/s41427-024-00544-w

Formation of a zirconium oxide crystal nucleus in the initial nucleation stage in aluminosilicate glass investigated by X-ray multiscale analysis
Onodera Yohei, Takimoto Yasuyuki, Hijiya Hiroyuki, Li Qing, Tajiri Hiroo, Ina Toshiaki, Kohara Shinji
NPG Asia Materials 16(1) (2024) 22 (doi)10.1038/s41427-024-00542-y

High-energy extension of the gamma-ray band observable with an electron-tracking Compton camera
Oka Tomohiko, Ogio Shingo, Abe Mitsuru, Hamaguchi Kenji, Ikeda Tomonori, Kubo Hidetoshi, Kurosawa Shunsuke, Miuchi Kentaro, Mizumura Yoshitaka, Nakamura Yuta, Sawano Tatsuya, Takada Atsushi, Takemura Taito, Tanimori Toru, Yoshikawa Kei

Nuclear Instruments and Methods in Physics Research Section A: Accelerators, Spectrometers, Detectors and Associated Equipment 1063 (2024) 169242 (doi)10.1016/j.nima.2024.169242

Effects of precipitates on defect formation and irradiation resistance in CoCrFeNi alloy
Yabuuchi A., Zhong Z.H., Yasunaga K., Watanabe H., Tokitani M., Xu Q.
Nuclear Instruments and Methods in Physics Research Section B: Beam Interactions with Materials and Atoms 555 (2024) 165481 (doi)10.1016/j.nimb.2024.165481

Measurements of displacement cross sections of metals for 120-GeV proton beam irradiation
Iwamoto Yosuke, Matsuda Hiroki, Meigo Shin-ichiro, Yonehara Katsuya, Pellemoine Frederique, Liu Zunping, Lynch Kevin, Yoshida Makoto, Yabuuchi Atsushi, Yoshiie Toshimasa, Hashimoto Shintaro
Nuclear Instruments and Methods in Physics Research Section B: Beam Interactions with Materials and Atoms 557 (2024) 165543 (doi)10.1016/j.nimb.2024.165543

Mechanical Properties and Hydrogen Embrittlement Resistance of the High‐Entropy Alloy CrFeMnNiCo and Its Subsystems
Xu Qiu, Guan Huaqing, Huang Shaosong, Zhong Zhihong, Yabuuchi Atsushi, Sato Koichi
physica status solidi (b) 2024 (2024) 2400162 (doi)10.1002/pssb.202400162

Experimental electronic structures of the Fe^{IV}=O bond in S=1 heme vs. nonheme sites: Effect of the porphyrin ligand
Braun Augustin, Gee Leland B., Waters Max D. J., Jose Anex, Baker Michael L., Mara Michael W., Babicz Jeffrey T., Ehudin Melanie A., Quist David A., Zhou Ang, Kroll Thomas, Titus Charles J., Lee Sang-Jun, Nordlund Dennis, Sokaras Dimosthenis, Yoda Yoshitaka, Kobayashi Yasuhiro, Tamasaku Kenji, Hedman Britt, Hodgson Keith O., Karlin Kenneth D., Que Lawrence, Solomon Edward I.
Proceedings of the National Academy of Sciences 122(8) (2025) e2420205122 (doi)10.1073/pnas.2420205122

Damage caused by He and D plasma exposure in Mo/Zr-added W-Y_2O_3 composites
Ren X.L., Yao G., Luo L.M., Xu Y., Yabuuchi A., Xu Q.
Radiation Effects and Defects in Solids 179(9-10) (2024) 1233-1249 (doi)10.1080/10420150.2024.2332216

Advancing neutron imaging techniques to highest resolution with fluorescent nuclear track detectors
Muneem Abdul, Yoshida Junya, Saito Takehiko R., Ekawa Hiroyuki, Hino Masahiro, Hirota Katsuya, Ichikawa Go, Kasagi Ayumi, Kitaguchi Masaaki, Mishima Kenji, Nabi Jameel-Un, Nakagawa Manami
Scientific Reports 15(1) (2025) 2103 (doi)10.1038/s41598-024-84591-x

Gamma-ray induced luminescence from diamonds
Nakamura Toshihiro, Nishimura Tomoaki, Kuriyama Kazuo, Nakamura Tohru, Kinomura Atsushi
Solid State Communications 396 (2025) 115770 (doi)10.1016/j.ssc.2024.115770

Proceedings

Desorption-induced changes in vacancy-type defects in highly hydrogenated DLC films
Kazuhiro Kanda, Daisuke Niwa, Tomohiro Mishima, Koji Nakanishi, Naoki Fukumuro, Fuminobu Hori, Atsushi Yabuuchi, and Atsushi Kinomura
Proceedings of the 59th KURNS Scientific Meeting, Kumatori, Japan/Online (Jan. 30-31, 2025) 23 (in Japanese)

Development of gas-flow humidity sample environment for neutron scattering experiments
Hiroshi Arima
Proceedings of the 59th KURNS Scientific Meeting, Kumatori, Japan/Online (Jan. 30-31, 2025) 8-9 (in Japanese)

Development of Thin-film Targets for Precision X-ray Spectroscopy of Antiprotonic Calcium Atoms
Takashi Higuchi, Masahiro Hino, Hiroyuki Fujioka
Proceedings of the 59th KURNS Scientific Meeting, Kumatori, Japan/Online (Jan. 30-31, 2025) 25 (in Japanese)

Dynamics of Hydrogen Atoms and Open-volume Defects in Palladium
W. Sato, M. Furumoto, H. Shimizu, and Y. Ohkubo
Proceedings of the Specialists' Meeting on "Nuclear Spectroscopy and Condensed Matter Physics Using Short-Lived Nuclei X", Online (Feb. 7, 2024) 5-7 (in Japanese)

Effect of Pulse Irradiation by Charged Particles on Damage Structures in Metals (2)
T. Yoshiie, A. Kinomura, F. Hori, T. Nishimura

Proceedings of the 43rd Symposium on Materials Science and Engineering Research Center of Ion Beam Technology, Hosei University, Koganei, Tokyo (Dec. 12, 2024) 42-45

Fundamental Resratch on Decommissioning of Reactor Facility
Jun-ichi Hori, Tadafumi Sano, Koichi Takamiya, Satoshi Fukutani, Shoji Nakamura, Yasushi Nauchi, Hiroshi Yashima, Yoshiyuki Takahashi, Kazushi Terada, Jian Zhang, Yasuyuki Fujihara, Ryo Okumura, Hisao Yoshinaga, Yuto Iinuma, Yuji Shibahara, Shunsuke Endo, Rovira Gerard, Atsushi Kimura, Shunsuke Sato
Proceedings of the 59th KURNS Scientific Meeting, Kumatori, Japan/Online (Jan. 30-31, 2025) 10-14 (in Japanese)

High-pressure synthesis of hydrous SiO_2 glass and structural analysis at multiple scales
Shuto Takahashi, Yohei Onodera, Tetsu Kogiso, Rintaro Inoue, Masaaki Sugiyama, Kenji Shimizu, Takayuki Ushikubo, Naotaka Tomioka, Takuo Okuchi
Proceedings of the 59th KURNS Scientific Meeting, Kumatori, Japan/Online (Jan. 30-31, 2025) 48 (in Japanese)

Interaction between hydrogen and defects introduced by H^+ irradiation in B2 type Fe-Al alloy
J. TIAN, S. Miyazumi, Q. Xu, K. Ohsawa, K. Yasunaga, Y. Saito, F. Hori
The 33rd Annual Meeting of MRS-J, Yokohama, Japan (Nov. 14-16, 2024) E3-O17-008

Multiple hydrogen trapping in vacancies introduced by electron irradiation in FeAl alloys
Fuminobu Hori, Shouta Hirayama, Tian Jiaxin, Qiu Xu, Atsushi Yabuuchi, Atsushi Kinomura, Kazuhito Ohsawa, Kazufumi Yasunaga, Sakurai, Minoru Suzuki
Proceedings of the 59th KURNS Scientific Meeting, Kumatori, Japan/Online (Jan. 30-31, 2025) 28 (in Japanese)

合成高分子の分子状態オペランド計測と新機能創生
Hidehito Nakamura, Maiko Ikegami, Takumi Kubota, Yoshiyuki Shirakawa, Hisashi Kitamura
Proceedings of the 59th KURNS Scientific Meeting, Kumatori, Japan/Online (Jan. 30-31, 2025) 20 (in Japanese)

Reviews

ダイヤモンドライクカーボン膜の国際標準規格制定と低速陽電子線を用いた新しい構造解析
神田 一浩
陽電子科学 24 (2025) 9-18 (in Japanese)

5. Geochemistry and Environmental Science

Papers

Atomistic Mechanism of Al Substitution Effects on the Ferroelastic Post-stishovite Transition by High-Pressure Single-Crystal X-Ray Diffraction
Zhang Yanyao, Chariton Stella, Prakapenka Vitali B., Okuchi Takuo, Lin Jung-Fu
American Mineralogist 110 (2025) (doi)10.2138/am-2023-9257

Hydrogen incorporation mechanism in the lower-mantle bridgmanite
Purevjav Narangoo, Tomioka Naotaka, Yamashita Shigeru, Shinoda Keiji, Kobayashi Sachio, Shimizu Kenji, Ito Motoo, Fu Suyu, Gu Jesse, Hoffmann Christina, Lin Jung-Fu, Okuchi Takuo
American Mineralogist 109(6) (2024) 1036-1044 (doi)10.2138/am-2022-8680

Single-crystal X-ray diffraction on the structure of (Al, Fe)-bearing bridgmanite in the lower mantle
Fu Suyu, Chariton Stella, Zhang Yanyao, Okuchi Takuo, Prakapenka Vitali B., Lin Jung-Fu
American Mineralogist 109(5) (2024) 872 - 881 (doi)10.2138/am-2023-8969

Tritium concentration in the modern commercial D_2O reagents
Ohta Tomoko, Fukutani Satoshi, Kubota Takumi, Mahara Yasunori
Analytical Sciences 40(10) (2024) 1927 - 1930 (doi)10.1007/s44211-024-00615-6

Positive correlations between ^{137}Cs and fungal tracers in Fukushima aerosols: Implication for enhanced nighttime fungal spore emission with radioactivity from forest soil to the atmosphere
Kawamura Kimitaka, Kunwar Bhagawati, Kita Kazuyuki, Hayashi Naho, Igarashi Yasuhito
Atmospheric Pollution Research 16(3) (2025) 102407 (doi)10.1016/j.apr.2025.102407

Microtremor Full-Wavefield Modeling of Effective Phase Velocity and Horizontal-to-Vertical Spectral Ratio at Kyoto Reference Borehole Site: Comparison with Surface-Wavefield Modeling Based on a Velocity Structure with a Cap Layer

Uebayashi Hirotoshi, Arai Hiroshi, Cho Ikuo, Yoshida Kunikazu, Ohori Michihiro, Yamada Koji
Bulletin of the Seismological Society of America 114(4) (2024) 2099-2117 (doi)10.1785/0120230067

Origin of Philippine Sea Basins During Subduction Initiation in the Western Pacific
Ishizuka, O., Tani, K., Taylor, R. N., Umino, S., Sakamoto, I., Yokoyama, Y., Ogitsu, I., Shimoda, G., Harigane, Y., Sato, T., Ohara, Y., Conway, C.E., Perez, A., Fujii, M., Kusano, Y., Yagi, M., Sekimoto S.
Geochemistry, Geophysics, Geosystems 25(5) (2024) e2023GC011291 (doi)10.1029/2023GC011291

In-situ gamma-ray measurement to estimate depth distribution of ^{137}Cs in farmland in Fukushima Prefecture
Momota Sadao, Okuda Yoshihiro, Tanigaki Minoru, Ohkubo Yoshitaka, Saito Takashi
Journal of Environmental Radioactivity 282 (2025) 107610 (doi)10.1016/j.jenvrad.2024.107610

Hydrogen Dissolution Mechanisms in Bridgmanite by First‐Principles Calculations and Infrared Spectroscopy
Zhang Yanyao, Tsuchiya Jun, Li ChingChien, Ye Zefang, Yan Wei, Okuchi Takuo, Karato Shun-ichiro, Kung Jennifer, Lin Jung-Fu
Journal of Geophysical Research: Solid Earth 130(1) (2025) e2024JB030403 (doi)10.1029/2024JB030403

Artificial formation of alpha recoil tracks using an americium source
Nakashima Taiki, Hasebe Noriko, Yokoyama Akihiko, Yamada Norihiro, Takamiya Koichi, Iinuma Yuto
Radiation Measurements 173 (2024) 107087 (doi)10.1016/j.radmeas.2024.107087

Proceedings

Aerosols in radiation facilities
Yuichi Oki
Proceedings of the 59th KURNS Scientific Meeting, Kumatori, Japan/Online (Jan. 30-31, 2025) 70-71 (in Japanese)

Concentration distribution on the particle size for Al, Ca in the Kosa particle
Norio Ito, Hisao Yoshinaga
Proceedings of the 59th KURNS Scientific Meeting, Kumatori, Japan/Online (Jan. 30-31, 2025) 22 (in Japanese)

Current Status of Radiation Monitoring Based on KURAMA-II
Minoru Tanigaki
Proceedings of the 59th KURNS Scientific Meeting, Kumatori, Japan/Online (Jan. 30-31, 2025) 19 (in Japanese)

Detailed provenancial studies of excavated low-fired ceramics by INAA
Makoto Tomii, Koichi Takamiya, Makoto Inagaki, Atsushi Ito, Masaaki Kidachi, Yutaka Chiba, and Hideo Yoshii
Proceedings of the 59th KURNS Scientific Meeting, Kumatori, Japan/Online (Jan. 30-31, 2025) 34 (in Japanese)

Search for uranium-containing particles originated from the Hiroshima Atomic Bomb
Koichi Takamiya, Naoki Toe, Makoto Inagaki, Yuichi Oki, Satoshi Fukutani, Hiroshi Yashima, Yuji Shibahara, Tomohiro Adachi, Yasuhito Igarashi
Proceedings of the 59th KURNS Scientific Meeting, Kumatori, Japan/Online (Jan. 30-31, 2025) 18 (in Japanese)

6. Life Science and Medical Science

Papers

Physical Isolation of Single Protein Molecules within Well‐Defined Coordination Cages to Enhance Their Stability
Ebihara Risa, Nakama Takahiro, Morishima Ken, Yagi‐Utsumi Maho, Sugiyama Masaaki, Fujita Daishi, Sato Sota, Fujita Makoto
Angewandte Chemie International Edition 64(7) (2025) e202419476 (doi)10.1002/anie.202419476

Induction of Paraptotic Cell Death in Cancer Cells by Triptycene–Peptide Hybrids and the Revised Mechanism of Paraptosis II
Nii Mayuka, Yamaguchi Kohei, Tojo Toshifumi, Narushima Nozomi, Aoki Shin
Biochemistry 63(17) (2024) 2111-2130 (doi)10.1021/acs.biochem.4c00085

Changing the gravity vector direction by inverted culture enhances radiation-induced cell damage
Mizoguchi Yuma, Kamimura Masao, Kitabatake Kazuki, Uchiumi Fumiaki, Aoki Shin, Tsukimoto Mitsutoshi
Biochemistry and Biophysics Reports 39 (2024) 101792 (doi)10.1016/j.bbrep.2024.101792

Charge manipulation of the human insulin B chain C-terminal to shed light on the complex mechanism of insulin fibrillation
Shahsavani Mohammad Bagher, Hoshino Masaru, Kumar Ashutosh, Yousefi Reza
Biochimica et Biophysica Acta (BBA) - General Subjects 1868(4) (2024) 130578 (doi)10.1016/j.bbagen.2024.130578

Amodiaquine Analogs Are Potent Inhibitors of Interleukin-6 Production Induced by Activation of Toll-Like Receptors Recognizing Pathogen Nucleic Acids
Takenaka Yohei, Tanaka Tomohiro, Otaki Shotaro, Kanbe Azusa, Morita Tomoe, Yokoi Kenta, Sekiguchi Saki, Nakamura Koki, Satoh Hidetoshi, Tojo Toshifumi, Uchiumi Fumiaki, Kitabatake Kazuki, Aoki Shin, Tsukimoto Mitsutoshi
Biological and Pharmaceutical Bulletin 47(12) (2024) 2101 - 2118 (doi)10.1248/bpb.b24-00639

Structure–Activity Relationship Analysis of Fluoxetine for Suppression of Inflammatory Cytokine Production
Takenaka Yohei, Tanaka Ryu, Kitabatake Kazuki, Uchiumi Fumiaki, Aoki Shin, Kuramochi Kouji, Tsukimoto Mitsutoshi
Biological and Pharmaceutical Bulletin 47(5) (2024) 946-954 (doi)10.1248/bpb.b24-00083

Synthesis of new functionalized bioactive S-substituted indolyl-triazoles as cytotoxic and apoptotic agents through multi-targeted kinase inhibition
Boraei Ahmed T.A., Nafie Mohamed S., Barakat Assem, Tanaka Tomohiro, Kawano Koshu, Tojo Toshifumi, Aoki Shin, Sarhan Ahmed A.M.
Bioorganic Chemistry 156 (2025) 108154 (doi)10.1016/j.bioorg.2025.108154

Revealing an origin of temperature-dependent structural change in intrinsically disordered proteins
Inoue Rintaro, Oda Takashi, Nakagawa Hiroshi, Tominaga Taiki, Ikegami Takahisa, Konuma Tsuyoshi, Iwase Hiroki, Kawakita Yukinobu, Sato Mamoru, Sugiyama Masaaki
Biophysical Journal 124(3) (2025) 540-548 (doi)10.1016/j.bpj.2024.12.022

Deciphering the sub-Golgi localization of glycosyltransferases via 3D super-resolution imaging
Yagi Hirokazu, Tateo Seigo, Saito Taiki, Ohta Yusaku, Nishi Emiko, Obitsu Saemi, Suzuki Tatsuya, Seetaha Supaphorn, Hellec Charles, Nakano Akihiko, Tojima Takuro, Kato Koichi
Cell Structure and Function 49(2) (2024) 47-55 (doi)10.1247/csf.24008

Comprehensive Search for Genes Involved in Thalidomide Teratogenicity Using Early Differentiation Models of Human Induced Pluripotent Stem Cells: Potential Applications in Reproductive and Developmental Toxicity Testing
Kato Yu, Inaba Takeshi, Shinke Koudai, Hiramatsu Noriko, Horie Tetsuhiro, Sakamoto Takuya, Hata Yuko, Sugihara Eiji, Takimoto Tetsuya, Nagai Noriaki, Ishigaki Yasuhito, Kojima Hajime, Nagano Osamu, Yamamoto Naoki, Saya Hideyuki
Cells 14(3) (2025) 215 (doi)10.3390/cells14030215

NDT‐C11 as a Viable Novel Detergent for Single Particle Cryo‐EM
Jiko Chimari, Li Jiannan, Moon Youngsun, Tanaka Yoshito, Gopalasingam Chai C., Shigematsu Hideki, Chae Pil Seok, Kurisu Genji, Gerle Christoph
ChemPlusChem 89(10) (2024) e202400242 (doi)10.1002/cplu.202400242

Structural basis of sugar recognition by SCF^{FBS2} ubiquitin ligase involved in NGLY1 deficiency
Satoh Tadashi, Yagi‐Utsumi Maho, Ishii Nozomi, Mizushima Tsunehiro, Yagi Hirokazu, Kato Ryuichi, Tachida Yuriko, Tateno Hiroaki, Matsuo Ichiro, Kato Koichi, Suzuki Tadashi, Yoshida Yukiko
FEBS Letters 598(18) (2024) 2259-2268 (doi)10.1002/1873-3468.15003

Identification of potential C1-binding sites in the immunoglobulin CL domains
Yanaka Saeko, Kodama Atsuji, Nishiguchi Shigetaka, Fujita Rina, Shen Jiana, Boonsri Pornthip, Sung Duckyong, Isono Yukiko, Yagi Hirokazu, Miyanoiri Yohei, Uchihashi Takayuki, Kato Koichi
International Immunology 36(8) (2024) 405-412 (doi)10.1093/intimm/dxae017

Molecular Characterization of the MoxR AAA+ ATPase of Synechococcus sp. Strain NKBG15041c
Mano Kota, Noi Kentaro, Oe Kumiko, Mochizuki Takahiro, Morishima Ken, Inoue Rintaro, Sugiyama Masaaki, Noguchi Keiichi, Shinohara Kyosuke, Yohda Masafumi, Yamada Akiyo
International Journal of Molecular Sciences 25(18) (2024) 9955 (doi)10.3390/ijms25189955

Molecular tag for promoting N-glycan maturation in the cargo receptor-mediated secretion pathway
Yagi Hirokazu, Yamada Rino, Saito Taiki, Honda Rena, Nakano Rio, Inutsuka Kengo, Tateo Seigo, Kusano Hideo, Nishimura Kumiko, Yanaka Saeko, Tojima Takuro, Nakano Akihiko, Furukawa Jun-ichi, Yagi-Utsumi Maho, Adachi Shungo, Kato Koichi
iScience 27(12) (2024) 111457 (doi)10.1016/j.isci.2024.111457

Profile of miRNAs in small extracellular vesicles released from glioblastoma cells treated by boron neutron capture therapy
Kondo Natsuko, Kinouchi Tadatoshi, Natsumeda Manabu, Matsuzaki Juntaro, Hirata Eishu, Sakurai Yoshinori, Okada Masayasu, Suzuki Minoru
Journal of Neuro-Oncology 168(1) (2024) 91-97 (doi)10.1007/s11060-024-04649-8

Single-Molecule Kinetic Observation of Antibody Interactions with Growing Amyloid β Fibrils
Yagi-Utsumi Maho, Kanaoka Yui, Miyajima Shogo, Itoh Satoru G., Yanagisawa Katsuhiko, Okumura Hisashi, Uchihashi Takayuki, Kato Koichi
Journal of the American Chemical Society 146(46) (2024) 31518 (doi)10.1021/jacs.4c08841

Human F-ATP synthase as a drug target
Gerle Christoph, Jiko Chimari, Nakano Atsuki, Yokoyama Ken, Gopalasingam Chai C., Shigematsu Hideki, Abe Kazuhiro
Pharmacological Research 209 (2024) 107423 (doi)10.1016/j.phrs.2024.107423

Characterization of different-sized human αA-crystallin homomers and implications to Asp151 isomerization
Sun Jiayue, Matsubara Toshiya, Koide Tamaki, Lampi Kirsten J., David Larry L., Takata Takumi
PLOS ONE 33(7) (2024) e0306856 (doi)10.1371/journal.pone.0306856

Asymmetric fluctuation of overlapping dinucleosome studied by cryoelectron microscopy and small-angle X-ray scattering
Shimizu Masahiro, Tanaka Hiroki, Nishimura Masahiro, Sato Nobuhiro, Nozawa Kayo, Ehara Haruhiko, Sekine Shun-ichi, Morishima Ken, Inoue Rintaro, Takizawa Yoshimasa, Kurumizaka Hitoshi, Sugiyama Masaaki
PNAS Nexus 3(11) (2024) 484 (doi)10.1093/pnasnexus/pgae484

Characterization of βB2-crystallin tryptophan mutants reveals two different folding states in solution
Sun Jiayue, Morishima Ken, Inoue Rintaro, Sugiyama Masaaki, Takata Takumi
Protein Science 33(7) (2024) e5092 (doi)10.1002/pro.5092

Crystal structure of GTP-dependent dephospho-coenzyme A kinase from the hyperthermophilic archaeon, Thermococcus kodakarensis
Akiko Kita, Yuna Ishida, Takahiro Shimosaka, Yuta Michimori, Kira Makarova, Eugene Koonin, Haruyuki Atomi, and Kunio Miki
Proteins: Structure, Function, and Bioinformatics 92(6) (2024) 768-775 (doi)10.1002/prot.26666

Dynamics of side chains in poly(quinoxaline-2,3-diyl)s studied via quasielastic neutron scattering
Inoue R., Nagata Y., Tominaga T., Sato S., Kawakita Y., Yamawaki T., Morishima K., Suginome M., Sugiyama M.
The Journal of Chemical Physics 161(5) (2024) 054905 (doi)10.1063/5.0215603

Proceedings

Analysis of minerals in the gum which consumed by small primates.
Hiroo Imai, Arisa Ishimura, Takashi Hayakawa, Leonardo Melo, Valdir Luna, Maria Adélia, Michiko Fukushima
Proceedings of the 59th KURNS Scientific Meeting, Kumatori, Japan/Online (Jan. 30-31, 2025) 40 (in Japanese)

Competitive complex formation of cyanobacterial circadian clock proteins
Ken Morishima, Ritsuki Sakamoto, Masaaki Sugiyama
Proceedings of the 59th KURNS Scientific Meeting, Kumatori, Japan/Online (Jan. 30-31, 2025) 31 (in Japanese)

Crystal structure of the complex between extradiol dioxygenase and its inhibitor
Akiko Kita, Tetsuo Ishida, Hiroyuki Tanaka, Kihachiro Horiike, and Kunio Miki
Proceedings of the 59th KURNS Scientific Meeting, Kumatori, Japan/Online (Jan. 30-31, 2025) 29 (in Japanese)

Development of a Nanogel-Based Neutron Capture Therapy Agent Utilizing a Gadolinium-Thiacalixarene Complex as a Physical Crosslinker
Nanaho Shindo, Ryota Sawamura, Ryunosuke Karashimada, Minoru Suzuki, Nobuhiko Iki
Proceedings of the 59th KURNS Scientific Meeting, Kumatori, Japan/Online (Jan. 30-31, 2025) 35 (in Japanese)

Development of new rice variety using boron neutron capture reaction (tentative name: RONOHIKARI)
Tadatoshi Kinouchi, Yoshihide Hattori, Shuhei Segami, Yuki Oba, Hiroshi Yashima, Yasuhito Igarashi, Yoko Fujikawa, Mitsunori Kirihata
Proceedings of the 59th KURNS Scientific Meeting, Kumatori, Japan/Online (Jan. 30-31, 2025) 47 (in Japanese)

Improvement of Mo-SAXS
Yojiro Oba, Rintaro Inoue, Ken Morishima, Masaaki Sugiyama
Proceedings of the 59th KURNS Scientific Meeting Kumatori, Japan/Online (Jan. 30-31, 2025) 32 (in Japanese)

Mechanism of amyloid fibril formation by serum amyloid protein A
Masaru Hoshino, Taishi Okunish, Ken Morishima, Rintaro Inoue, Masaaki Sugiyama
Proceedings of the 59th KURNS Scientific Meeting Kumatori, Japan/Online (Jan. 30-31, 2025) 30 (in Japanese)

Practical Application Strategy for Protein Ligation with Enzyme
Aya Okuda, Masahiro Shimizu, Rintaro Inoue, Reiko Urade, and Masaaki Sugiyama
Proceedings of the 59th KURNS Scientific Meeting Kumatori, Japan/Online (Jan. 30-31, 2025) 55 (in Japanese)

Response of cyanobacterial circadian rhythm to external environments and the origin of its robustness.
Ritsuki Sakamoto, Ken Morishima, Masahiro Shimizu, Rintaro Inoue, Masaaki Sugiyama
Proceedings of the 59th KURNS Scientific Meeting Kumatori, Japan/Online (Jan. 30-31, 2025) 38 (in Japanese)

SAXS for the nucleosomes containing histones of malaria parasite
Shoko Sato, Mariko Dacher, Ken Morishima, Rintaro Inoue, Kankichi Murayama, Mistuo Ogasawara, Naoki Horikoshi, Yoshimasa Takizawa, Masaaki Sugiyama, Hitoshi Kurumizaka
Proceedings of the 59th KURNS Scientific Meeting Kumatori, Japan/Online (Jan. 30-31, 2025) 56 (in Japanese)

Structural analysis of a multidomain protein from hyperthermophilic archaea at physiological temperature
Takashi Oda, Rintaro Inoue, Ken Morishima, Naoki Aizawa, Aya Okuda, Takayuki Oku, Mamoru Sato, Masaaki Sugiyama
Proceedings of the 59th KURNS Scientific Meeting Kumatori, Japan/Online (Jan. 30-31, 2025) 44 (in Japanese)

Study on the temperature dependent oligomer dissociation of sHsps from methanogens
Masafumi Yohda, Nina Kurokawa, Mima Ogawa, Wakaba Naka, Ken Morishima, Rintaro Inoue, Masaaki Sugiyama
Proceedings of the 59th KURNS Scientific Meeting Kumatori, Japan/Online (Jan. 30-31, 2025) 21 (in Japanese)

Reviews

Beyond “Switch ON”
Ken MORISHIMA
POLYMERS 73(1) (2024) 27 (doi)10.1295/kobunshi.73.1_27 (in Japanese)

Ensemble Modeling of Biomolecules by Small-angle X-ray Scattering and Coarse-grained Molecular Dynamics Simulation
Masahiro SHIMIZU, Masaaki SUGIYAMA
Seibutsu Butsuri 64(4) (2024) 209 - 213 (doi)10.2142/biophys.64.209 (in Japanese)

Investigation of Crystallin Folding Pathway Using Spontaneous Fluorescence
Takumi Takata
The Journal of The Japanese Society for Cataract Research 36(1) (2024) 74-81 (doi)10.14938/cataract.36-022 (in Japanese)

Others

Conserved loop of a phase modifier endows protein condensates with fluidity
Honoka Kawamukai, Motonori Matsusaki, Takanari Tanimoto, Mai Watabe, Ken Morishima, Shunsuke Tomita, Yoichi Shinkai, Tatsuya Niwa, Taro Mannen, Hiroyuki Kumeta, Hitoki Nanaura, Kotona Kato, Takuya Mabuchi, Yuichiro Aiba, Takeru Uehara, Noriyoshi Isozumi, Yoshika Hara, Shingo Kanemura, Hiroyoshi Matsumura, Kazuma Sugie, Koichiro Ishimori, Takahiro Muraoka, Masaaki Sugiyama, Masaki Okumura, Eiichiro Mori, Takuya Yoshizawa, Tomohide Saio
bioRxiv (2024) (doi)10.1101/2024.07.03.601791

7. Neutron Capture Therapy

Papers

Extracellular Vesicles Comprising Carborane Prepared by a Host Exchanging Reaction as a Boron Carrier for Boron Neutron Capture Therapy
Kawasaki Riku, Oshige Ayano, Kono Nanami, Yamana Keita, Hirano Hidetoshi, Miura Yamato, Yorioka Ryuji, Bando Kaori, Tabata Anri, Yasukawa Naoki, Sadakane Masahiro, Sanada Yu, Suzuki Minoru, Takata Takushi, Sakurai Yoshinori, Tanaka Hiroki, Yimiti Dilimulati, Miyaki Shigeru, Adachi Nobuo, Mizuta Ryosuke, Sasaki Yoshihiro, Akiyoshi Kazunari, Hattori Yoshihide, Kirihata Mitsunori, Nagasaki Takeshi, Ikeda Atsushi
ACS Applied Materials & Interfaces 16(36) (2024) 47137-47149 (doi)10.1021/acsami.4c07650

A Water-Soluble Small Molecule Boron Carrier Targeting Biotin Receptors for Neutron Capture Therapy
Nishimura Kai, Tanaka Shota, Miura Kazuki, Okada Satoshi, Suzuki Minoru, Nakamura Hiroyuki
ACS Omega 9(52) (2024) 51631-51640 (doi)10.1021/acsomega.4c09388

4H-SiC 64 pixels CMOS image sensors with 3T/4T-APS arrays
Meguro Tatsuya, Tsutsumi Masayuki, Takeyama Akinori, Ohshima Takeshi, Tanaka Yasunori, Kuroki Shin-Ichiro **Applied Physics Express 17(8) (2024) 081005 (doi)10.35848/1882-0786/ad665f**

Accelerator neutron sources for BNCT: Current status and some pointers for future development
Green Stuart, Phoenix Ben, Nakamura Satoshi, Liu Yuan Hao, Shu Diyun, Hu Naonori, Suzuki Shunsuke, Koivunoro Hanna, Kumada Hiroaki, Tanaka Hiroki
Applied Radiation and Isotopes 217 (2025) 111656 (doi)10.1016/j.apradiso.2025.111656

Potential of boron neutron capture therapy (BNCT) for myxofibrosarcoma
Fujimoto Takuya, Andoh Tooru, Sudo Tamotsu, Fujita Ikuo, Sakurai Yoshinori, Takata Takushi, Tanaka Hiroki, Kawamoto Teruya, Yahiro Shunsuke, Nakamura Shotaro, Hara Hitomi, Fukase Naomasa, Akisue Toshihiro, Ichikawa Hideki, Kuroda Ryosuke, Suzuki Minoru
Applied Radiation and Isotopes 217 (2025) 111603 (doi)10.1016/j.apradiso.2024.111603

BNCT pancreatic cancer treatment strategy with glucose-conjugated boron drug
Fujimoto Takuya, Teraishi Fuminori, Kanehira Noriyuki, Tajima Tomoyuki, Sakurai Yoshinori, Kondo Natsuko, Yamagami Masahiro, Kuwada Atsushi, Morihara Akira, Kitamatsu Mizuki, Fujimura Atsushi, Suzuki Minoru, Takaguchi Yutaka, Shigeyasu Kunitoshi, Fujiwara Toshiyoshi, Michiue Hiroyuki
Biomaterials 309 (2024) 122605 (doi)10.1016/j.biomaterials.2024.122605

Evaluating optimal quality assurance and quality control conditions of activation measurements at the accelerator-based boron neutron capture therapy system employing a lithium target
Suzuki Shunsuke, Yagihashi Takayuki, Nitta Kazunori, Yamanaka Masashi, Sato Naoki, Gotoh Shinichi, Sugimoto Satoru, Shiba Shintaro, Nagata Hironori, Tanaka Hiroki
Biomedical Physics & Engineering Express 10(4) (2024) 045028 (doi)10.1088/2057-1976/ad4b1e

Evaluation of dose calculation method with a combination of Monte Carlo method and removal-diffusion equation in heterogeneous geometry for boron neutron capture therapy
Nojiri Mai, Takata Takushi, Sasaki Akinori, Tamari Yuki, Matsubayashi Nishiki, Hu Naonori, Sakurai Yoshinori, Suzuki Minoru, Tanaka Hiroki
Biomedical Physics & Engineering Express 11(2) (2025) 025045 (doi)10.1088/2057-1976/ada7fe

Preliminary outcomes of boron neutron capture therapy for head and neck cancers as a treatment covered by public health insurance system in Japan: Real‑world experiences over a 2‑year period
Takeno Satoshi, Yoshino Yuki, Aihara Teruhito, Higashino Masaaki, Kanai Yasukazu, Hu Naonori, Kakino Ryo, Kawata Ryo, Nihei Keiji, Ono Koji
Cancer Medicine 13(11) (2024) e7250 (doi)10.1002/cam4.7250

Boron neutron capture therapy delays the decline in neurological function in a mouse model of metastatic spinal tumors Fujikawa Yoshiki, Kawabata Shinji, Tsujino Kohei, Yamada Hironori, Kashiwagi Hideki, Yagi Ryokichi, Hiramatsu Ryo, Nonoguchi Naosuke, Takami Toshihiro, Sasaki Akinori, Hu Naonori, Takata Takushi, Tanaka Hiroki, Suzuki Minoru, Wanibuchi Masahiko
Cancer Science 115(8) (2024) 2774 - 2785 (doi)10.1111/cas.16245

Overcoming immunotherapy resistance and inducing abscopal effects with boron neutron immunotherapy (B‑NIT)
Fujimoto Takuya, Yamasaki Osamu, Kanehira Noriyuki, Matsushita Hirokazu, Sakurai Yoshinori, Kenmotsu Naoya, Mizuta Ryo, Kondo Natsuko, Takata Takushi, Kitamatsu Mizuki, Igawa Kazuyo, Fujimura Atsushi, Otani

Yoshihiro, Shirakawa Makoto, Shigeyasu Kunitoshi, Teraishi Fuminori, Togashi Yosuke, Suzuki Minoru, Fujiwara Toshiyoshi, Michiue Hiroyuki
Cancer Science 115(10) (2024) 3231-3247 (doi)10.1111/cas.16298

Novel Drug Delivery Particles Can Provide Dual Effects on Cancer "Theranostics" in Boron Neutron Capture Therapy
Fithroni Abdul Basith, Inoue Haruki, Zhou Shengli, Hakim Taufik Fatwa Nur, Tada Takashi, Suzuki Minoru, Sakurai Yoshinori, Ishimoto Manabu, Yamada Naoyuki, Sauriasari Rani, Sauerwein Wolfgang A. G., Watanabe Kazunori, Ohtsuki Takashi, Matsuura Eiji
Cells 14(1) (2025) 60 (doi)10.3390/cells14010060

Therapeutic Effect of Boron Neutron Capture Therapy on Boronophenylalanine Administration via Cerebrospinal Fluid Circulation in Glioma Rat Models
Kusaka Sachie, Voulgaris Nikolaos, Onishi Kazuki, Ueda Junpei, Saito Shigeyoshi, Tamaki Shingo, Murata Isao, Takata Takushi, Suzuki Minoru
Cells 13(19) (2024) 1610 (doi)10.3390/cells13191610

Boron Agent Delivery Platforms Based on Natural Products for Boron Neutron Capture Therapy
Kawasaki Riku, Miura Yamato, Kono Nanami, Fujita Seiya, Yamana Keita, Ikeda Atsushi
ChemMedChem 19(21) (2024) e202400571 (doi)10.1002/cmdc.202400323

Comparison of lifetime attributable risk of post-irradiation secondary cancer of boron neutron capture therapy, proton beam therapy, and X-ray therapy for pediatric and adolescent and young adult patients
Suzuki Shunsuke, Shiba Shintaro, Tanaka Hiroki, Yamanaka Masashi, Matsumoto Kazuki, Tokuuye Koichi, Omura Motoko
Clinical and Translational Radiation Oncology 51 (2025) 100921 (doi)10.1016/j.ctro.2025.100921

Albumin nanoparticle electrostatically loaded with highly anionic Gd-thiacalixarene complex for MRI-guided neutron capture therapy
Ohama Kohei, Komiya Miku, Yamatoya Takumi, Sawamura Ryota, Karashimada Ryunosuke, Gao Shan, Ozawa Yoshikazu, Osada Kensuke, Aoki Ichio, Nagasaki Takeshi, Suzuki Minoru, Iki Nobuhiko
Colloids and Surfaces A: Physicochemical and Engineering Aspects 699 (2024) 134579 (doi)10.1016/j.colsurfa.2024.134579

Experimental designs for radiobiological characterization of an accelerator-based BNCT system in preclinical studies
Masutani Mitsuko, Imamichi Shoji, Nakamura Satoshi, Shimada Kenji, Itami Jun, Okamoto Hiroyuki, Ishiai Masamichi, Suzuki Minoru, Igaki Hiroshi
Health and Technology 14(5) (2024) 1023-1028 (doi)10.1007/s12553-024-00866-3

Two Years of Clinical Experience with Accelerator-Based Boron Neutron Capture Therapy for Head and Neck Cancer Takeno S., Yoshino Y., Aihara T., Higashino M., Kanai Y., Hu N., Kakino R., Kawata R., Nihei K., Ono K. **International Journal of Radiation Oncology*Biology*Physics 120 (2, Supplement) (2024) e794 (doi)10.1016/j.ijrobp.2024.07.1744**

The Early Response After Radiation Therapy on Three-Dimensional Oral Cancer Model Using Patient-Derived Cancer-Associated Fibroblasts
Yamamoto I, Igawa K, Kondo N, Sakurai Y, Fujimura A, Takabatake K, Huang P, Michiue H, Ibaragi S, Izumi K.
International Journal of Translational Medicine 5(1) (2025) 12 (doi)10.3390/ijtm5010012

Implementation of optically simulated luminescent dosimeter for quality control of gamma ray dose of an accelerator-based neutron source
Hu Naonori, Nakamura Taiki, Kataura Ryusuke, Suga Keita, Mukawa Tetsuya, Akita Kazuhiko, Sasaki Akinori, Nojiri Mai, Matsubayashi Nishiki, Takata Takushi, Tanaka Hiroki, Nihei Keiji, Ono Koji
Journal of Applied Clinical Medical Physics 25(11) (2024) e14493 (doi)10.1002/acm2.14493

Potential for boron neutron capture therapy (BNCT) with ASCT2-targeted boron agents.
Eza Kenichiro, Tsujino Kohei, Kawabata Shinji, Fujikawa Yoshiki, Kashiwagi Hideki, Hutamura Gen, Hiramastu Ryo, Miyatake Sinichi, Tanaka Hiroki, Suzuki Minoru, Wanibuchi Masahiko, Nakamura Hiroyuki, Araki Tomoyuki, Morita Taiki
Journal of Clinical Oncology 42(23_suppl) (2024) 233 (doi)10.1200/JCO.2024.42.23

Active control of pharmacokinetics using light-responsive polymer-drug conjugates for boron neutron capture therapy Tokura Daiki, Konarita Kakeru, Suzuki Minoru, Ogata Keisuke, Honda Yuto, Miura Yutaka, Nishiyama Nobuhiro, Nomoto Takahiro
Journal of Controlled Release 371 (2024) 445-454 (doi)10.1016/j.jconrel.2024.06.006

Poly(vinyl alcohol) potentiating an inert d-amino acid-based drug for boron neutron capture therapy
Konarita Kakeru, Kanamori Kaito, Suzuki Minoru, Tokura Daiki, Tanaka Shota, Honda Yuto, Nishiyama Nobuhiro, Nomoto Takahiro
Journal of Controlled Release 377 (2025) 385-396 (doi)10.1016/j.jconrel.2024.11.017

A national survey of medical staffs' required capability and workload for accelerator-based boron neutron capture therapy
Nakamura Satoshi, Tanaka Hiroki, Kato Takahiro, Akita Kazuhiko, Takemori Mihiro, Kasai Yusaku, Kashihara Tairo, Takai Yoshihiro, Nihei Keiji, Onishi Hiroshi, Igaki Hiroshi
Journal of Radiation Research 65(5) (2024) 712-724 (doi)10.1093/jrr/rrae058

Characterization of acrylic phantom for use in quality assurance of BNCT beam output procedure
Matsubayashi Nishiki, Hu Naonori, Takata Takushi, Sasaki Akinori, Kumada Hiroaki, Nakamura Satoshi, Masuda Akihiko, Tanaka Hiroki
Journal of Radiation Research 66(1) (2025) 10-15 (doi)10.1093/jrr/rrae089

Effect of neutron beam properties on dose distributions in a water phantom for boron neutron capture therapy
Ishikawa Akihisa, Tanaka Hiroki, Nakamura Satoshi, Kumada Hiroaki, Sakurai Yoshinori, Watanabe Kenichi, Yoshihashi Sachiko, Tanagami Yuki, Uritani Akira, Kiyanagi Yoshiaki
Journal of Radiation Research 65(6) (2024) 765-775 (doi)10.1093/jrr/rrae076

Dynamic Expression Profiles of HMGB1 after BNCT and γ-Irradiation in Cancer Cells.
Ying Tong, Shoji Imamichi, Lichao Chen, Satoshi Nakamura, Akira Sato, Yu Sanada, Hiroshi Igaki, Minoru Suzuki, Jun Itami, Masamichi Ishiai, Shinichiro Masunaga, Mitsuko Masutani
Journal on Oncology 4(2) (2024) 1163 (doi)10.52768/2692-563X/1163

Application of stoichiometric CT number calibration method for dose calculation of tissue heterogeneous volumes in boron neutron capture therapy
Hu Naonori, Nakao Minoru, Ozawa Shuichi, Takata Takushi, Tanaka Hiroki, Nihei Keiji, Ono Koji, Suzuki Minoru
Medical Physics 51(6) (2024) 4413 - 4422 (doi)10.1002/mp.17093

Neutron flux evaluation algorithm with a combination of Monte Carlo and removal‐diffusion calculation methods for boron neutron capture therapy
Nojiri Mai, Takata Takushi, Hu Naonori, Sakurai Yoshinori, Suzuki Minoru, Tanaka Hiroki
Medical Physics 51(5) (2024) 3711-3724 (doi)10.1002/mp.16931

TMET-13. SPATIAL METABOLOMIC CHANGES OF NUCLEOTIDE IN THE BRAINS OF ORTHOTOPIC MOUSE GLIOMA MODEL AFTER BORON NEUTRON CAPTURE THERAPY (BNCT)
Kondo Natsuko, Kobayashi Nao, Sakurai Yoshinori, Suzuki MInoru, Yamaguchi Shinichi, Ikegawa Masaya
Neuro-Oncology 26(Supplement_8) (2024) viii290 (doi)10.1093/neuonc/noae165.1151

Nonclinical pharmacodynamics of boron neutron capture therapy using direct intratumoral administration of a folate receptor targeting novel boron carrier
Tsujino Kohei, Kashiwagi Hideki, Nishimura Kai, Fujikawa Yoshiki, Kayama Ryo, Fukuo Yusuke, Hiramatsu Ryo, Nonoguchi Naosuke, Takata Takushi, Tanaka Hiroki, Suzuki Minoru, Hu Naonori, Ono Koji, Wanibuchi Masahiko, Nakai Kei, Nakamura Hiroyuki, Kawabata Shinji
Neuro-Oncology Advances 6(1) (2024) vdae062 (doi)10.1093/noajnl/vdae062

Clinical evaluation of performance, stability, and longevity of an accelerator system designed for boron neutron capture therapy utilising a beryllium target
Hu Naonori, Kakino Ryo, Sasaki Akinori, Yoshikawa Syuushi, Akita Kazuhiko, Takeno Satoshi, Yoshino Yuki, Aihara Teruhito, Nihei Keiji, Nojiri Mai, Matsubayashi Nishiki, Takata Takushi, Tanaka Hiroki, Suzuki Minoru, Ono Koji
Nuclear Instruments and Methods in Physics Research Section A: Accelerators, Spectrometers, Detectors and Associated Equipment 1072 (2025) 170126 (doi)10.1016/j.nima.2024.170126

Developing and validating measurement methods combining ^{6}LiF sintered capsule and Mg_2SiO_4: Tb (TLD-MSO-S) for γ-ray dose evaluation at accelerator-based BNCT system
Suzuki Shunsuke, Yagihashi Takayuki, Nitta Kazunori, Yamanaka Masashi, Shimo Takahiro, Sato Naoki, Matsubayashi Nishiki, Takata Takushi, Sugimoto Satoru, Hashimoto Harumitsu, Shiba Shintaro, Gotoh Shinichi, Nagata Hironori, Tanaka Hiroki
Nuclear Instruments and Methods in Physics Research Section A: Accelerators, Spectrometers, Detectors and Associated Equipment 1064 (2024) 169443 (doi)10.1016/j.nima.2024.169443

Experimental verification of liquid multilayer spectrometer in neutron irradiation field for boron neutron capture therapy
Prateepkaew Jakkrit, Takata Takushi, Tanaka Hiroki, Sakurai Yoshinori
Nuclear Instruments and Methods in Physics Research Section A: Accelerators, Spectrometers, Detectors and Associated Equipment 1065 (2024) 169534 (doi)10.1016/j.nima.2024.169534

Thickness-dependent neutron detection efficiency of LiF-Si-based active neutron detector for boron neutron capture therapy
Takada Masashi, Endo Satoru, Kajimoto Tsuyoshi, Horiguchi Tetsuo, Yamanishi Hirokuni, Yagi Natsumi, Masuda Akihiko, Matsumoto Tetsuro, Tanaka Hiroki, Nunomiya Tomoya, Aoyama Kei, Narita Masataka, Nakamura Takashi
Nuclear Instruments and Methods in Physics Research Section A: Accelerators, Spectrometers, Detectors and Associated Equipment 1064 (2024) 169352 (doi)10.1016/j.nima.2024.169352

Reevaluation of neutron energy spectrum in Heavy-Water neutron irradiation facility of Kyoto University research Reactor using multifoil activation method
Prateepkaew Jakkrit, Sakurai Yoshinori
Nuclear Instruments and Methods in Physics Research Section B: Beam Interactions with Materials and Atoms 557 (2024) 165555 (doi)10.1016/j.nimb.2024.165555

Peptide-functionalized gold nanoparticles for boron neutron capture therapy with the potential to use in Glioblastoma treatment
Zhang Zhicheng, Wang Xin, Dai Qi, Qin Yaxin, Sun Xiaoyan, Suzuki Minoru, Ying Xiaoying, Han Min, Wei Qichun
Pharmaceutical Development and Technology 29(8) (2024) 862-873 (doi)10.1080/10837450.2024.2406044

New technologies for beam spectrometry, quality assurance, real-time monitoring and microdosimetry in BNCT
Kumada Hiroaki, Masuda Akihiko, Tanaka Hiroki, Takada Masashi, Hu Naonori
Radiation Measurements 177 (2024) 107276 (doi)10.1016/j.radmeas.2024.107276

Preliminary study of a compact epithermal neutron absolute flux intensity measurement system for real-time in-vivo dose monitoring in boron neutron capture therapy
Qiu Jiye, Hatano Daisuke, Ge Yulin, Voulgaris Nikolaos, Sagara Kohei, Qiao Zhaopeng, Tamaki Shingo, Kusaka Sachie, Takata Takushi, Murata Isao
Radiation Measurements 178 (2024) 107308 (doi)10.1016/j.radmeas.2024.107308

Translational research of boron neutron capture therapy for spinal cord gliomas using rat model
Kayama Ryo, Tsujino Kohei, Kawabata Shinji, Fujikawa Yoshiki, Kashiwagi Hideki, Fukuo Yusuke, Hiramatsu Ryo, Takata Takashi, Tanaka Hiroki, Suzuki Minoru, Hu Naonori, Miyatake Shin-Ichi, Takami Toshihiro, Wanibuchi Masahiko
Scientific Reports 14(1) (2024) 8265 (doi)10.1038/s41598-024-58728-x

Investigation of converter for assuring beam component fluence by imaging plate in boron neutron capture therapy ‐ Combination with gamma-ray shield to detect fast neutrons
K. Tanaka, T. Kajimoto, Y. Sakurai, T. Takata, H. Tanaka, G. Bengua, S. Endo,
Bulletin of Kyoto Pharmaceutical University 5(1) (2024) 100 -109

Proceedings

A characterization of LCV micelle gel dosimeters for boron neutron capture therapy
Narita Ryosuke, Hayashi Shin-ichiro, Sakurai Yoshinori
13th International Conference on 3D Dosimetry (IC3DDose 2024), Aarhus, Denmark (Jun.17-19, 2024) 012009 (doi)10.1088/1742-6596/2799/1/012009

Assessment of the effects of activation by BNCT on the treatment of companion animals
Yuya Ishikawa, Sachiko Yoshihashi, Atsushi Yamazaki, Akira Uritani, Ryota Iwasaki
Proceedings of the 59th KURNS Scientific Meeting Kumatori, Japan/Online (Jan. 30-31, 2025) 24 (in Japanese)

Basic research to expand BNCT indications for companion animals Minoru Suzuki, Yusuke Wada, Masashi Yanagawa, Riku Kawasaki, Hiroe Kusaka, Sachiko YoshihashiRyota Iwasaki, Ken Nagasaki,
Proceedings of the 59th KURNS Scientific Meeting Kumatori, Japan/Online (Jan. 30-31, 2025) 59-61 (in Japanese)

Basic research to expand BNCT indications for companion animals
Minoru Suzuki, Natsuko Kondo, Ryota Iwasaki, Jun Arima
Proceedings of the 59th KURNS Scientific Meeting Kumatori, Japan/Online (Jan. 30-31, 2025) 62-63 (in Japanese)

Boiling two-phase flow dynamics measurement using neutron imaging
Daisuke Ito
Proceedings of the 59th KURNS Scientific Meeting Kumatori, Japan/Online (Jan. 30-31, 2025) 64-66 (in Japanese)

Development of real-time thermal neutron detector for progress of BNCT
Nishiki Matsubayashi, Hiroki Tanaka, Shunsuke Kurosawa, Akihiro Yamaji, Yoshinori Sakurai, Takushi Takata.
Proceedings of the 59th KURNS Scientific Meeting Kumatori, Japan/Online (Jan. 30-31, 2025) 45 (in Japanese)

Fundamental Study for Dosimetry of BNCT Field Using PVA-GTA-I Gel Dosimeter Ousuke Suzuki, Sachiko Yoshihashi, Atsushi Yamazaki, Akira Uritani, Shin-ichiro Hayashi, Yoshinori Sakurai
Proceedings of the 59th KURNS Scientific Meeting Kumatori, Japan/Online (Jan. 30-31, 2025) 26 (in Japanese)

Fundamental study of BNCT to the field of veterinary medicine
Sachiko Yoshihashi, Akira Niimi, Kazuki Tsuchimoto, Noritaka Kawai, Ryota Iwasaki, Atsushi Yamazaki, Akira Uritani, Yoshinori Sakurai, Minoru Suzuki
Proceedings of the 59th KURNS Scientific Meeting Kumatori, Japan/Online (Jan. 30-31, 2025) 27 (in Japanese)

Measurement of fast neutron flux intensity in Heavy-water neutron irradiation facility of Kyoto University research Reactor
Kohei Sagara, Haruka Asano, Isao Murata, Takushi Takata
Proceedings of the 59th KURNS Scientific Meeting Kumatori, Japan/Online (Jan. 30-31, 2025) 52 (in Japanese)

Others

2方向の中性子照射と患者体位変換で実現した高悪性度髄膜腫へのホウ素中性子捕捉療法
柏木 秀基、川端 信司、辻野 晃平、竹内 孝治、平松 亮、野々口 直助、古瀬 元雅、呼 尚徳、櫻井 良憲、田中 浩基、近藤 夏子、鈴木 実、小野 公二、宮武 伸一、鰐渕 昌彦
日本癌治療学会学術集会抄録集 62 (2024) O87～3 (in Japanese)

ASCT2標的とした BNCTにおける悪性神経膠腫の治療
江座 健一郎、辻野 晃平、川端 信司、藤川 喜貴、柏木 秀基、二村 元、平松 亮、田中 浩基、鈴木 実、宮武 伸一、荒木 倫之、盛田 大輝、中村 浩之、鰐渕 昌彦
日本癌治療学会学術集会抄録集 62 (2024) O87～1 (in Japanese)

ホウ素中性子捕捉療法の進歩と将来展望 転移性脊椎腫瘍に対する新規治療選択肢としてのホウ素中性子捕捉療法の橋渡し研究
藤川 喜貴、川端 信司、辻野 晃平、山田 浩徳、柏木 秀基、二村 元、平松 亮、高田 卓志、鈴木 実、呼 尚徳、宮武 伸一、高見 俊宏、鰐渕 昌彦
日本癌治療学会学術集会抄録集 62 (2024) CCWS5～5 (in Japanese)

脊髄神経膠腫に対するホウ素中性子捕捉療法の適応拡大に向けての橋渡し研究
辻野 晃平、香山 諒、川端 信司、藤川 喜貴、柏木 秀基、福尾 祐介、平松 亮、高田 卓志、田中 浩基、鈴木 実、呼 尚徳、宮武 伸一、高見 俊宏、鰐渕 昌彦
日本癌治療学会学術集会抄録集 62 (2024) O87～2 (in Japanese)

8. Neutron Radiography and Radiation Application

Papers

Impact of high-energy electron beam irradiation on piezoelectric properties of lead zirconate titanate
Takechi Seiji, Maeda Shoki, Tominaga Shuhei, Naruse Ryusei, Takahashi Ayano, Katayama Shinya, Miyachi Takashi, Kobayashi Masanori, Okudaira Osamu, Okada Nagaya, Takahashi Toshiharu, Abe Naoya
Japanese Journal of Applied Physics 63(7) (2024) 078002 (doi)10.35848/1347-4065/ad5e28

Measurement of the response of a ^{6}Li-glass detector to gamma rays by a coincidence method
Ito Fumiaki, Lee Jaehong, Hironaka Kota, Takahashi Tone, Suzuki Satoshi, Mochimaru Takanori, Hori Jun-ichi, Terada Kazushi, Koizumi Mitsuo
Nuclear Instruments and Methods in Physics Research Section A: Accelerators, Spectrometers, Detectors and Associated Equipment 1064 (2024) 169465 (doi)10.1016/j.nima.2024.169465

Development of a method for distinguishing alpha particles from other types of radiation using a high-resolution alpha imager
Morishita Yuki, Sagawa Naoki, Fujisawa Makoto, Kurosawa Shunsuke, Sasano Makoto, Hayashi Masateru, Tanaka Hiroki
Radiation Measurements 181 (2025) 107371 (doi)10.1016/j.radmeas.2024.107371

コンクリートの水分状態が爆裂現象に与える影響
堀合航太、西尾悠平、金準鎬、兼松学
日本建築学会大会学術講演梗概集・建築デザイン発表梗概集 2024 (2024) 69-70 (in Japanese)

Proceedings

Evaluation and development of novel neutron scintillators in KUR
Shunsuke Kurosawa, Hiroki Tanaka, Takushi Takata, Nishiki Matsubayashi, Yusuke Urano, Chihaya Fujiwara, Akihiro Yamaji
Proceedings of the 59th KURNS Scientific Meeting Kumatori, Japan/Online (Jan. 30-31, 2025) 58 (in Japanese)

Measurement of two-phase flow in a finned rectangular channel by X-ray imaging.
Syuto Kondo, Naoya Odaira, Daisuke Ito, Kei Ito, Yasushi Saito
Proceedings of the 59th KURNS Scientific Meeting Kumatori, Japan/Online (Jan. 30-31, 2025) 50 (in Japanese)

9. TRU and Nuclear Chemistry

Papers

Activation imaging of gold nanoparticles for versatile drug visualization: An in vivo demonstration
Koshikawa N., Kikuchi Y., Tanaka K. S., Tokoi K., Mitsukai A., Aoto H., Kadonaga Y., Toyoshima A., Kato H., Ooe K., Takamiya K., Kataoka
Applied Physics Letters 126(10) (2025) 103702 (doi)10.1063/5.0251048

Impact of MA Temporary Storage Process on the Reduction of Final Disposal Burden in the Advanced Nuclear Fuel Cycle
Tomohiro Okamura, Masahiko Nasase, Kenji Takeshita, Takashi Shimada, Yuki Konishi, Keisuke Nishimura, Hitomi Ishida, Tomoo Yamamura
EPJ Web of Conferences 317 (2025) 01009 (doi)10.1051/epjconf/202531701009

Relativistic CASPT2/RASPT2 Program along with DIRAC Software
Masuda Yasuto, Noda Kohei, Iwamuro Sumika, Hada Masahiko, Nakatani Naoki, Abe Minori
Journal of Chemical Theory and Computation 21(3) (2025) 1249-1258 (doi)10.1021/acs.jctc.4c01589

Measurements of neutron capture cross-sections for nuclides of interest in decommissioning: ^{45}Sc, ^{63}Cu, ^{64}Zn, ^{109}Ag, and ^{113}In
Nakamura Shoji, Shibahara Yuji, Endo Shunsuke, Rovira Gerard, Kimura Atsushi
Journal of Nuclear Science and Technology 61(11) (2024) 1415-1430 (doi)10.1080/00223131.2024.2346347

Radium separation from thorium and manufacturing of targets by precipitation method
Yin Feng, Fukutani Satoshi, Toyama Mari, Yamamura Tomoo, Suzuki Tatsuya
Journal of Radioanalytical and Nuclear Chemistry 333(11) (2024) 6039-6046 (doi)10.1007/s10967-024-09496-5

Solvent extraction of selenium in nitric acid: evaluation of multiple extractants and proposal of a novel separation process
Ito K. T. M., Kawakami T., Kato C., Fukutani S., Matsumura T., Fujii T.
Journal of Radioanalytical and Nuclear Chemistry 333(10) (2024) 5183-5189 (doi)10.1007/s10967-024-09681-6

Solvent extraction of tin in nitric acids: evaluation of multiple extractants
Ito K. T. M., Takahashi S., Kato C., Fukutani S., Matsumura T., Fujii T.
Journal of Radioanalytical and Nuclear Chemistry 334(3) (2025) 2467-2475 (doi)10.1007/s10967-025-10003-7

Electron correlation effects on uranium isotope fractionation in U(vi)–U(vi) and U(iv)–U(vi) equilibrium isotopic exchange systems
Sato Ataru, Hada Masahiko, Abe Minori
Physical Chemistry Chemical Physics 26(21) (2024) 15301-15315 (doi)10.1039/D4CP01149J

Solvent Extraction Behaviors of Rhodium and Palladium in Nitric Acid Solutions Using Amide Extractants
ITO Kengo T. M., MORITA Misaki, ARAKI Yuta, KATO Chizu, FUKUTANI Satoshi, MATSUMURA Tatsuro, FUJII Toshiyuki
Solvent Extraction Research and Development, Japan 32(1) (2025) 53-62 (doi)10.15261/serdj.32.53

Proceedings

Chemical and electronic properties of Actinide compounds and their applications
Tomoo Yamamura, Yuji Shibahara, Satoshi Fukutani, Minori Abe, Masahiko Nakase, Kenji Shirasaki, Naoto Ishikawa, Ta-tsuya Suzuki, Masanobu Nogami, Takumi Kubota, Yoshinori Haga, Chihiro Tabata, Tsuyoshi Yaita, Shinsaku Kambe, Toru Kobayashi
Proceedings of the 59th KURNS Scientific Meeting Kumatori, Japan/Online (Jan. 30-31, 2025) 1 - 4 (in Japanese)

Isotope fractionation of zinc using a chemical exchange method with Aza-Crown Ether
Seiya Akamatsu, Kousuke Otsu, Takuma Mototani, Keisuke Nakata, Kazuki Okada, Yuya Nihei, Koutarou Kakutani, Kouki Tamai, Satoshi Fukutani, Ryoichi Nakada, Kazuya Nagaishi, Shigeyuki Wakaki, Akihiro Uehara, Chizu Kato, Toshiyuki Fujii
Proceedings of the 59th KURNS Scientific Meeting Kumatori, Japan/Online (Jan. 30-31, 2025) 17 (in Japanese)

Leaching of europium from calcined cements
Yuya Nihei, Kousuke Otsu, Seiya Akamatsu, Takuma Mototani, Keisuke Nakata, Kazuki Okada, Riku Yanobe, Hiroki Goto, Tatsuro Matsumura, Satoshi Fukutani, Kengo Ito, Chizu Kato, Toshiyuki Fujii
Proceedings of the 59th KURNS Scientific Meeting Kumatori, Japan/Online (Jan. 30-31, 2025) 37 (in Japanese)

Malonate Precipitation and Coprecipitation of Group 2 Elements for Coprecipitation Experiments of Nobelium
Miyu Konno, Masashi Kaneko, Hiroyuki Kazama, Kojiro Nagata, Ryohei Nakanishi, Ruilin Wang, Yudai Itakura, Enni Khult, Kyosuke Shibamoto, Ryotaro Masuda, Koichi Takamiya, Makoto Inagaki, Hiromitsu Haba, Akihiro Nambu, Yoshitaka Kasamatsu
Proceedings of the 59th KURNS Scientific Meeting Kumatori, Japan/Online (Jan. 30-31, 2025) 41 (in Japanese)

Production of medical RI by reactor irradiation
Tomoo Yamamura, Ryo Okumura, Yuji Nakamoto, Yoichi Shimizu, Hiroyuki Kimura, Kazuma Ogawa, Kenji Shirasaki, Koshin Washiyama, Chihiro Tabata
Proceedings of the 59th KURNS Scientific Meeting Kumatori, Japan/Online (Jan. 30-31, 2025) 5-7 (in Japanese)

Solid-liquid extraction experiments of group 2 elements using dithiophosphoric acid with Sr resin system toward the chemical study on element 102, nobelium.
Ruilin Wang, Eisuke Watanabe, Miyu Konno, Yudai Itakura, Enni Khult, Kyosuke Shibamoto, Koichi Takamiya, Hiromitsu Haba, Yudai Shigekawa, Akihiro Nambu, Yousuke Kanayama, Masashi Kaneko, Hiroyuki Kazama, Kojiro Nagata, Yoshitaka Kasamatsu
Proceedings of the 59th KURNS Scientific Meeting Kumatori, Japan/Online (Jan. 30-31, 2025) 51 (in Japanese)

Solubility and solid phase analysis of coprecipitated M(IV) amorphous hydroxides
Taishi Kobayashi, Yuki Yoshikawa, Daiju Matsumura, Atsushi Ikeda-Ohno, Takayuki Sasaki
Proceedings of the 59th KURNS Scientific Meeting Kumatori, Japan/Online (Jan. 30-31, 2025) 36 (in Japanese)

Study of dynamic isotope effects in molybdenum Kazuki Okada, Ryoichi Nakada, Kazuya Nagaishi, Satoshi Fukutani, Akihiro Uehara, Chizu Kato, Toshiyuki Fujii
Proceedings of the 59th KURNS Scientific Meeting Kumatori, Japan/Online (Jan. 30-31, 2025) 46 (in Japanese)

Study of Isotope Separation via Chemical Exchange Reaction
Ryuta Hazama, Takaaki Yoshimoto, Kumsut Pantiwa, Anawat Rittirong, Yoichi Sakuma, Toshiyuki Fujii, Satoshi Fukutani, Yuji Shibahara
Proceedings of the 59th KURNS Scientific Meeting Kumatori, Japan/Online (Jan. 30-31, 2025) 49 (in Japanese)

10. Health Physics and Waste Management

Papers

Improved data analysis techniques for calculating more accurate radon and thoron exhalation rates from building interior solid walls
Sakoda Akihiro, Ishimori Yuu, Jin Qianhao, Iimoto Takeshi
Applied Radiation and Isotopes 207 (2024) 111180 (doi)10.1016/j.apradiso.2024.111180

Seasonal Variations in Radon and Thoron Exhalation Rates from Solid Concrete Interior Walls Observed Using In Situ Measurements
Sakoda Akihiro, Ishimori Yuu, Hasan Md. Mahamudul, Jin Qianhao, Iimoto Takeshi
Atmosphere 15(6) (2024) 701 (doi)10.3390/atmos15060701

Advancing Sustainable Development Goals through Enhanced Literacy in Nuclear Science and Technology: Emphasizing Hands-On Experiences
Saengkaew Phannee, Chanyotha Supitcha, Pengvanich Phongphaeth, Srijaroen Benjawan, Phruksarojanakun Phiphat, Cherdchu Chainarong, Takaki Rieko, Iimoto Takeshi
Perspectives on Global Development and Technology 23(1-2) (2024) 32-44 (doi)10.1163/15691497-12341672

Practical cut-off value for radon concentration in indoor air using an activated-charcoal radon collector
Yasuoka Yumi, Takemoto June, Omori Yasutaka, Kawamoto Nanaho, Goda Nao, Nagahama Hiroyuki, Muto Jun, Tokonami Shinji, Hosoda Masahiro, Iimoto Takeshi, Mukai Takahiro
Radiation Protection Dosimetry 200(16-18) (2024) 1701-1705 (doi)10.1093/rpd/ncae108

Consideration of Reasonable Protection for Naturally Occurring Radioactive Materials Based on an Actual Case Study
Hiromi Koike, Takeshi Iimoto
RADIOISOTOPES 74(1) (2025) 55-62 (in Japanese) (doi)10.3769/radioisotopes.740101

Reviews

Review of Articles Related to the Accident of TEPCO’s Fukushima Daiichi Nuclear Power Station Published in the Japanese Journal of Health Physics: Overview (Secondary Publication)
Yokoyama Sumi, Nabatame Kuniaki, Suzuki Akira, Iimoto Takeshi
Journal of Radiation Protection and Research 49(4) (2024) 151-155 (doi)10.14407/jrpr.2024.00038

The complexities in interpreting Argon isotopes Assis
Fernandes Vera, Burgess Ray, Sumino Hirochika
Methods and Applications of Geochronology (2024) 297-343 (doi)10.1016/B978-0-443-18803-9.00006-7

第1回国際原子力科学オリンピック（INSO）開催！ 背景、目的、成果と所感
Yuichi TSUNOYAMA, Yu IGARASHI, Takeshi IIMOTO
FBNews 577 (2025) 13 - 17 (in Japanese)

11. Accelerator Physics

Papers

Development of a strip-shaped X-ray mapping system for 9-cell superconducting cavities
Kuriyama Y., Iwashita Y., Fuwa Y., Tongu H., Hayano H., Geng R.L.
Journal of Instrumentation 19(9) (2024) P09037 (doi)10.1088/1748-0221/19/09/P09037

Negative muon beam generation with muon catalyzed fusion
Mori Yoshiharu, Uesugi Tomonori, Ishi Yoshihiro
Journal of Instrumentation 19(5) (2024) P05001 (doi)10.1088/1748-0221/19/05/P05001

Accuracy verification of protoacoustic measurements in a heterogeneous phantom by an optical hydrophone
Chen Ye, Kasamatsu Koki, Kuriyama Yasutoshi, Uesugi Tomonori, Ishi Yoshihiro, Murakami Taichi, Hidani Sena, Caulfield Michael, Unlu Mehmet Burcin, Rohringer Wolfgang, Matsuura Taeko
Medical Physics 52(3) (2025) 1893-1902 (doi)10.1002/mp.17575

Beam stacking experiment at a fixed field alternating gradient accelerator
Uesugi T., Ishi Y., Kuriyama Y., Mori Y., Jolly C., Kelliher D. J., Lagrange J.-B., Letchford A. P., Machida S., de Boer D. W. Posthuma, Rogers C. T., Yamakawa E., Topp-Mugglestone M.
Physical Review Accelerators and Beams 28(1) (2025) 012803 (doi)10.1103/PhysRevAccelBeams.28.012803

Muonic x-ray measurement for the nuclear charge distribution: The case of stable palladium isotopes
Saito T. Y., Niikura M., Matsuzaki T., Sakurai H., Igashira M., Imao H., Ishida K., Katabuchi T., Kawashima Y., Kubo M. K., Miyake Y., Mori Y., Ninomiya K., Sato A., Shimomura K., Strasser P., Taniguchi A., Tomono D., Watanabe Y.
Physical Review C 111(3) (2025) 034313 (doi)10.1103/PhysRevC.111.034313

Proceedings

Development of UHDR irradiation field in KURNS-LINAC
Nishiki Matsubayashi, Hiroki Tanaka, Toshiharu Takahashi, Naoya Abe, Tsubasa Watanabe
Proceedings of the 59th KURNS Scientific Meeting Kumatori, Japan/Online (Jan. 30-31, 2025) 15-16 (in Japanese)

Evaluation of the fast neutron intensity from the target using the time-of-flight method with He-3 detector at KUANS.
Mizuki Iriyama, Seiji Tasaki
Proceedings of the 59th KURNS Scientific Meeting Kumatori, Japan/Online (Jan. 30-31, 2025) 53 (in Japanese)

Improving Beam Commissioning by Fast Computation of Magnetic Field of Accelerator Magnets Considering Magnetic Hysteresis
Onchi Yoshitake, Sugahara Kengo, Ahagon Akira, Ishi Yoshihiro, Hane Yoshiki
2024 IEEE 21st Biennial Conference on Electromagnetic Field Computation (CEFC) Jeju, Korea (Jun. 2-5, 2024) 01-02 (doi)10.1109/CEFC61729.2024.10586120

Plan for equipment related to neutron activation analysis and radioisotope production in the new research reactor at Monju site
Makoto Inagaki, Koichi Takamiya, Tsutomu Miura, Kohshin Washiyama, Kazuhiko Akiyama, Takahito Osawa, Yoshitaka Kasamatsu, Naoki Shirai, Kunihiko Tsuchiya, Go Yoshida, Nobuhiro Sato
Proceedings of the 59th KURNS Scientific Meeting Kumatori, Japan/Online (Jan. 30-31, 2025) 54 (in Japanese)

Plan for terahertz-wave source of superimposed coherent transition radiation using ring-type resonator at LEBRA
N. Sei, H. Ogawa, K. Hayakawa, T. Sakai, T. Tanaka, Y. Hayakawa, Y. Takahashi, T. Takahashi
Proceedings of the 32nd Linear Accelerator Conference Chicago (Aug. 25-30, 2024) 709-712.

12. Other

Papers

Quantitative Analysis of Total Fluorine in ABS Resin (for Perfluoroalkyl Substance Analysis: NMIJ CRM 8155-a)
Nobuyasu HANARI, Eriko YAMAZAKI, Keisuke NAKAMURA, Ayaka WADA, Tsutomu MIURA
BUNSEKI KAGAKU 74(1-2) (2025) 7-11 (in Japanese) (doi)10.2116/bunsekikagaku.74.7

Nuclear power, resilience, and energy security under a vulnerability-based approach
Shoki Kosai and Hironobu Unesaki
Cleaner Energy Systems 7 (2024) 100107 (doi)10.1016/j.cles.2024.100107

Thermally Stable Heteroleptic Trans-Bis(Chelate) Ruthenium(II) Complex Bearing 2,2'-Bipyridine and Acetylacetonato: Synthesis, Isomerization, and Crystal Structure
Toyama Mari, Fujimoto Daichi, Kawakami Yusuke, Tanaka Shiho
European Journal of Inorganic Chemistry 27(32) (2024) e202400243 (doi)10.1002/ejic.202400243

Bayesian Flow Network Framework for Chemistry Tasks
Tao Nianze, Abe Minori
Journal of Chemical Information and Modeling 65(3) (2025) 1178-1187 (doi)10.1021/acs.jcim.4c01792

Development and characterization of magnetic-based biodegradable periodic mesoporous organosilica nanoparticles for enhanced biomedical applications
Ta Hanh Kieu Thi, Mai Ngoc Xuan Dat, Nguyen Hanh-Vy Tran, Matsumoto Kotaro, Phan Thang Bach, Tamanoi Fuyuhiko, Doan Tan Le Hoang
Journal of Industrial and Engineering Chemistry 142 (2025) 563-569 (doi)10.1016/j.jiec.2024.07.061

Complexes exhibiting trans (Cl)-$RuCl_2(dmso\text{-}S)_2$ geometry with methyl-picolinate-type neutral N,O-ligands: Synthesis, structural characterization, and chemical behavior analysis in aqueous solutions
Toyama Mari, Onishi Yuto, Tanaka Nobuyoshi, Nagao Noriharu
Journal of Molecular Structure 1321(Part 2) (2025) 139964 (doi)10.1016/j.molstruc.2024.139964

Towards an Integrated Verification Scheme for the FM(C)T
Hirokazu Kumekawa, Hironobu Unesaki
Journal of Nuclear Material Management 51(3) (2024) 4-19

Quantification of bulk elemental composition for C-type asteroid Ryugu samples with nondestructive elemental analysis using muon beam
Ninomiya Kazuhiko, Osawa Takahito, Terada Kentaro, Wada Taiga, Nagasawa Shunsaku, Chiu I-Haun, Nakamura Tomoki, Takahashi Tadayuki, Miyake Yasuhiro, Kubo M. Kenya, Takeshita Soshi, Taniguchi Akihiro, Umegaki Izumi, Watanabe Shin, Azuma Toshiyuki, Katsuragawa Miho, Minami Takahiro, Mizumoto Kazumi, Shimomura Koichiro, Takeda Shin'ichiro, Morita Tomoyo, Kikuiri Mizuha, Amano Kana, Kagawa Eiichi, Furukawa Yoshihiro, Yurimoto Hisayoshi, Noguchi Takaaki, Okazaki Ryuji, Yabuta Hikaru, Naraoka Hiroshi, Sakamoto Kanako, Tachibana Shogo, Yada Toru, Nishimura Masahiro, Nakato Aiko, Miyazaki Akiko, Yogata Kasumi, Abe Masanao, Okada Tatsuaki, Usui Tomohiro, Yoshikawa Makoto, Saiki Takanao, Tanaka Satoshi, Terui Fuyuto, Nakazawa Satoru, Watanabe Sei-ichiro, Tsuda Yuichi
Meteoritics & Planetary Science 59(8) (2024) 2044-2057 (doi)10.1111/maps.14135

Purity Determination of High-Purity BeO using Gravimetric Analysis with Stepwise Conversions of Weighing Form of Be
Tsutomu Miura
Talanta Open 11 (2024) 100307 (doi)10.1016/j.talo.2024.100307

A Systematic Consolidation of Talking Points for Negotiation toward the Realization of FMCT
Hirokazu KUMEKAWA, Hironobu UNESAKI
Transactions of the Atomic Energy Society of Japan 23(4) (2024) 130-148 (in Japanese) (doi)10.3327/taesj.J24.001

Relationship between friction reduction effect and solubility in base oil of organic friction modifiers
Gu Haiyang, Hirayama Tomoko, Yamashita Naoki, Xu Jimin, Yamada Masako
Tribology International 22 (2025) 110304 (doi)10.1016/j.triboint.2024.110304

森林土壌における水溶態安定セシウムの鉛直分布について
寺島龍平、池上麻衣子、福谷哲
環境衛生工学研究 38 (2024) 144-146 (in Japanese)

森林土壌における Cs-137 の鉛直分布について
寺島龍平、池上麻衣子、福谷哲
Symposium on Soil and Groundwater Contamination and Radiation 29 (2024) 320-325 (in Japanese)

Proceedings

Towards Lamb shift spectroscopy of antihydrogen atoms at the GBAR $\bar{\mathrm{H}}$ beam line
Tanaka T. A., Blumer Philipp Peter, Janka Gianluca, Ohayon Ben, Regenfus Christian, Crivelli Paolo, Kuroda Naofumi, Tsukida Rin, Higuchi Takashi, Tanaka Kazuo S.
International Conference on Exotic Atoms and Related Topics and Conference on Low Energy Antiprotons (EXA/LEAP 2024) Vienna (Aug 26-30, 2024) 044 (doi) 10.1063/5.0251048

Reviews

From the Discovery of Radiation and Radioactivity to the Beginning of World War II—Surveying Original Papers—
Tetsuji Imanaka
RADIOISOTOPES 74(1) (2024) 39-54 (in Japanese)

原子力の未来に向けて、原子の灯ふたたび
Ken Kurosaki
Journal of the Atomic Energy Society of Japan 66(5) (2024) 228-229 (doi)10.3327/jaesjb.66.5_228 (in Japanese)

中性子放射化分析法
三浦勉
Bunseki 9 (2024) 329-330 (in Japanese)

Others

Provenancial study by neutron activation analysis on the roof-tiles with stamp impression excavated from the garrison of the Tosa domain in Kyoto
冨井眞、高宮幸一、伊藤淳史、木立雅朗、千葉豊、吉井秀夫

Annual Meeting of the Japan Society for Scientific Studies on Cultural Property Abstracts (2024) 178-179 (in Japanese)

機器中性子放射化分析による幕末京都の 土佐藩白川邸から出土した刻印瓦の胎土分析
冨井眞、高宮幸一、稲垣誠、伊藤淳史、木立雅朗、千葉豊、吉井秀夫
京都大学構内遺跡調査研究年報 2024 (2025) (in Japanese)

［空虚］の中のメモリー 浪江、大熊、双葉ー福島第一原発事故
高垣雅緒、香川則子
PASKEN JOURNAL 33 (2024) 23-33 (in Japanese)

KURNS Progress Report 2024

Issued in June 2025

Issued by the Institute for Integrated Radiation and Nuclear Science,
Kyoto University
Kumatori-cho, Sennan-gun, Osaka 590-0494 Japan

Tel. +81-72-451-2300
Fax. +81-72-451-2600

In case that corrections are made, overwrite the modified version
in the following webpage:
https://www.rri.kyoto-u.ac.jp/PUB/report/PR/ProgRep2024/ProgRep2024.html

---